Scuola Normale Superiore

Classe di Scienze

Corso di Perfezionamento in
Matematica per le Tecnologie Industriali e la Finanza

Anno Accademico 2015

Ph.D. Thesis

Modeling dispersed gas–particle turbulence in volcanic ash plumes

Candidate

Dr. Matteo Cerminara

Advisors

Prof. Luigi Carlo Berselli
Università di Pisa

Dr. Tomaso Esposti Ongaro
Istituto Nazionale di Geofisica e
Vulcanologia, Sezione di Pisa

Pisa, Italy – 2016

... to ***Fiamma****,*

who patiently supported and sustained me.
With Love.

Abstract

This PhD thesis focuses on numerical and analytical methods for simulating the dynamics of volcanic ash plumes.

The study starts from the fundamental balance laws for a multiphase gas–particle mixture, reviewing the existing models and developing a new set of Partial Differential Equations (PDEs), well suited for modeling multiphase dispersed turbulence. In particular, a new model generalizing the equilibrium–Eulerian model to two-way coupled compressible flows is developed.

The PDEs associated to the four-way Eulerian-Eulerian model is studied, investigating the existence of weak solutions fulfilling the energy inequalities of the PDEs. In particular, the convergence of sequences of smooth solutions to such a set of weak solutions is showed.

Having explored the well-posedness of multiphase systems, the three-dimensional compressible equilibrium–Eulerian model is discretized and numerically solved by using the OpenFOAM® numerical infrastructure. The new solver is called `ASHEE`, and it is verified and validated against a number of well understood benchmarks and experiments. It demonstrates to be capable to capture the key phenomena involved in the dynamics of volcanic ash plumes. Those are: turbulence, mixing, heat transfer, compressibility, preferential concentration of particles, plume entrainment.

The numerical solver is tested by taking advantage of the newest High Performance Computing infrastructure currently available.

Thus, `ASHEE` is used to simulate two volcanic plumes in realistic volcanological conditions. The influence of model configuration on the numerical solution is analyzed. In particular, a parametric analysis is performed, based on: 1) the kinematic decoupling model; 2) the subgrid scale model for turbulence; 3) the discretization resolution.

In a one-dimensional and steady-state approximation, the multiphase flow model is used to derive a model for volcanic plumes in a calm, stratified atmosphere. The corresponding Ordinary Differential Equations (ODEs) are written in a compact, dimensionless formulation. The six non-dimensional parameters characterizing a multiphase plume are then written. The ODEs is studied both numerically and analytically. Different regimes are analyzed, extracting the first integral of motion and asymptotic solutions. An asymptotic analytical solution approximating the model in the general regime is derived and compared with numerical results. Such a solution is coupled with an electromagnetic model providing the infrared intensity emitted by a volcanic ash plume. Key vent parameters are then retrieved by means of inversion techniques applied to infrared images measured during a real volcanic eruption.

Contents

List of Figures

List of Tables

Notation

a	non-dimensional atmospheric density profile
$\boldsymbol{a}$	acceleration
a_{p}	plume–jet regime control parameter
a_q	jet–plume regime control parameter
A	specific absorption coefficient
A_φ	forcing amplitude of the jet inlet
b	plume radius
$\mathbb{B}$	subgrid-scale Reynolds stress tensor
B_λ	Planck's function
c	speed of sound
c_ℓ	speed of light
C	specific heat
C_{p}	specific heat at constant pressure
C_{v}	specific heat at constant volume
$\mathcal{C}$	compressibility of the velocity field: $\langle\lvert\nabla\cdot\boldsymbol{u}\rvert^2\rangle_\Omega/\langle\lvert\nabla\boldsymbol{u}\rvert^2\rangle_\Omega$
$\mathcal{C}_j$	normalized jth ash class concentration
d	particle diameter
d_{S}	mean Sauter diameter
d	spatial dimension
D	vent diameter; power-law distribution coefficient
$\mathcal{D}$	strain rate tensor
e	internal energy per unity of mass
E	total energy per unity of mass
$\mathcal{E}$	kinetic energy per unity of mass spectrum
f	non-dimensional enthalpy flux; frequency
f	generic field
f_φ	forcing frequency of the jet inlet
$\boldsymbol{f}_j$	drag force per unity of volume acting on the jth particle class
F	enthalpy flux over π
${}_2F_1$, $\mathfrak{F}$	Gauss hypergeometric functions
g	gravitational acceleration norm
g'	reduced gravity
$\boldsymbol{g}$	gravitational acceleration vector
$\hat{\boldsymbol{g}}$	gravitational acceleration versor
$\mathfrak{G}$	Gauss hypergeometric function
$\mathcal{H}$	enstrophy per unity of mass; Heaviside step function

h	enthalpy per unity of mass
H	total enthalpy per unity of mass
$H_{\max}$	volcanic plume maximum height
H_{nbl}	volcanic plume neutral buoyancy level
i	index running over all the chemical components in the fluid phase
I	number of chemical components in the fluid phase; electromagnetic radiation intensity
I_0	background atmospheric radiation
I_L	intensity incident on the detector
$\mathcal{I}$	set of all the indexes i
$\mathbb{I}$	identity tensor
j	index running over all the particle classes
J	number of particle classes
$\mathcal{J}$	set of all the indexes j
k	wavenumber; generic phase index
k_{g}	thermal conductivity
K	kinetic energy per unity of mass; absorption coefficient
K_{t}	subgrid-scale kinetic energy per unity of mass
l_{c}	function for the first integral of motion of `ASHOD`
ℓ_g	stratification length scale
L	length scale; position of the detector along the optical path
L_{M}	Morton length scale
m	mass; non-dimensional momentum flux
M	momentum flux over pi
N	number of grid cells
N_φ	number of modes of the jet inlet forcing
p	pressure of the fluid phase
$\boldsymbol{p}$	inversion parameter vector
$\boldsymbol{q}$	heat flux
q	non-dimensional mass flux
q_ψ	non-dimensional mass flux of the mixture constant anomaly
q_χ	non-dimensional mass flux of the mixture heat capacity anomaly
$\tilde{q}_0$	plume height control parameter
r	radial coordinate
$\hat{r}$	radial unity vector
R	gas constant
Q	mass flux over π
Q_j	heat per unity of volume exchanged from the fluid phase to the jth particle class
$\mathcal{Q}$	subgrid-scale diffusivity vector for the temperature
s	optical path coordinate
S	source term

$\mathbb{S}$	rate-of-shear tensor
$\mathcal{S}$	vorticity tensor
t	time
t_α	non-dimensional temperature profile of the atmosphere
T	temperature
$\mathbb{T}$	stress tensor
$\mathcal{T}$	temporal domain
$\boldsymbol{u}$	velocity vector
U	velocity scale; mean plume axial velocity
U_i	maximum velocity of the jet inlet
U_ϵ	entrainment velocity
$\mathcal{U}$	first integral of motion
v_f	coefficient for the velocity of variation of the enthalpy flux
$v_{f,0}$	non-dimensional square of the Brunt-Väisällä frequency
v_m	coefficient for the velocity of variation of the momentum flux
v_q	coefficient for the velocity of variation of the mass flux
V	volume
$\boldsymbol{w}$	particle settling terminal velocity
$\mathcal{W}$	WALE subgrid model operator
$\boldsymbol{x}$	position vector
x_0	plume height control parameter
y	mass fraction
Y	mean plume mass fraction
$\mathcal{Y}$	subgrid-scale diffusivity vector for the mass fraction
z	axial coordinate
$\hat{z}$	axial unity vector

α	density of the atmosphere
β	gas–particle mixture density for the integral plume model
β_ρ	density ratio parameter
γ	adiabatic index of the gas mixture
γ_c	stability of the plume column
Γ	Gamma function
Γ_1	maximum plume height zeroth-order number: 2.572
Γ_2	maximum plume height first-order number: 0.3802
Γ_nbl	neutral buoyancy level number: 0.7596
δ	grid scale
δ_j	jet regime limit parameter
δ_p	plume regime limit parameter
Δx	smallest space scale of the dynamical problem
ϵ	volumetric concentration
ϵ_t	subgrid-scale energy dissipation
ζ	non-dimensional axial coordinate

η	Kolmogorov length scale
$\eta_\varkappa$	entrainment function
θ	non-dimensional atmospheric thermal gradient
θ_α	atmospheric thermal gradient
θ_f	buoyancy modified thermal gradient
θ_i	boundary layer thickness of the jet inlet
ϑ	azimuth angle
κ	dispersed on carrier mass ratio
$\varkappa$	entrainment coefficient
λ	wavelength
λ_T	Taylor microscale
ν	fluid kinematic viscosity
ξ	smallest resolved LES length scale
μ	fluid dynamic viscosity; total erupted mass
μ_b	fluid bulk viscosity
μ_t	subgrid-scale eddy viscosity
ρ	bulk density
$\hat{\rho}$	density
ϱ	density scale
σ	standard deviation
τ	typical time scale; optical depth
τ_e	eddy turnover time
τ_η	Kolmogorov time scale
υ	molar fraction
ϕ	Boussinesq-likeness parameter
ϕ_c	drag correction function
φ_i	forcing function of the jet inlet
χ	ratio between specific heats
ψ	ratio between the gas constants
ω	Brunt-Väisällä frequency
Ω	spatial domain

Co	Courant number
Ec	Eckert number
Eu	Euler number
Fr	Froude number
Ma	Mach number
Nu	Nusselt number
Pr	Prandtl number
$\mathrm{Pr_t}$	subgrid-scale turbulent Prandtl number
Ra	Rayleigh number
Re	Reynolds number
Ri	Richardson number

St	Stokes number
Str	Strouhal number

$\langle\cdot\rangle$	weighted average
$\langle\cdot\rangle_\Omega$	space domain averaging
$\langle\cdot\rangle_\mathcal{T}$	temporal domain averaging
$\langle\cdot\rangle_j$	jth mass fraction weight average over the domain
$\underline{(\cdot)}$	filtered quantity
$\widetilde{(\cdot)}$	Favre-filtered quantity
$(\cdot)_0$	initial; evaluated at $z = 0$
$(\cdot)_{\mathrm{dg}}$	dusty gas
$(\cdot)_{\mathrm{e}}$	ejected gas phase
$(\cdot)_{\mathrm{f}}$	fluid phase
$(\cdot)_{\mathrm{g}}$	gas phase
$(\cdot)_i$	ith chemical component of the fluid mixture
$(\cdot)_j$	jth particle class
$(\cdot)_{\mathrm{m}}$	gas–particle mixture
$(\cdot)_{\mathrm{r}}$	*two-way* correction due to particle decoupling
$(\cdot)_{\mathrm{rms}}$	root mean square
$(\cdot)_{\mathrm{s}}$	solid phase
$(\cdot)_{\mathrm{Sth}}$	Sutherland law
$(\cdot)_{\mathrm{w}}$	water vapor
$(\cdot)_\alpha$	atmospheric
$(\cdot)_\beta$	gas - particle mixture (integral model)
$(\cdot)_\lambda$	at wavelength λ

Acronyms

APE	Available Potential Energy
ASHEE	Ash Equilibrium–Eulerian
BD	Bresch & Desjardins
CFD	Computational Fluid Dynamics
CFL	Courant–Friedrichs–Lewy condition
DHIT	Decaying Homogeneous and Isotropic Turbulence
DNS	Direct Numerical Simulation
ESF	European Science Foundation
FV	Finite Volume
HPC	High Performance Computing
IAVCEI	International Association of Volcanology and Geochemistry of the Earth Interior
INGV	Istituto Nazionale di Geofisica e Vulcanologia
IR	InfraRed
LES	Large Eddy Simulation
LMV	Laboratoire Magmas et Volcans
MMF	Mixed Mass Fraction
MTT	Morton, Taylor & Turner
MV	Mellet & Vasseur
NBL	Neutral Buoyancy Level
ODE	Ordinary Differential Equation
OGS	Istituto Nazionale di Oceanografia e Geofisica Sperimentale
PDE	Partial Differential Equation
PE	Potential Energy
PIMPLE	mixed PISO–SIMPLE algorithm
PISO	Pressure Implicit with Splitting of Operators
RPE	Reference Potential Energy
RS	Ricou & Spalding
SGS	Subgrid-Scale
SNS	Scuola Normale Superiore
TIR	Thermal InfraRed
TVD	Total Variation Diminishing
UniPi	Università di Pisa
VEI	Volcanic Explosivity Index
1D	One Dimensional
3D	Three Dimensional

Introduction

This thesis concerns the application of mathematical physics to problems arising in the study of volcanic explosive eruptions, and particularly to volcanic ash plumes.

There are two particular mathematical approaches that can be used to describe such phenomena: these are the integral model approach, or equivalently the one-dimensional (1D) approach; and the three-dimensional (3D) Large Eddy Simulation (LES) approach.

Integral models use the self-similarity hypothesis to reduce to one the dimensions of the dynamics: only the main direction of the evolution is modeled, by describing empirically three-dimensional phenomena like turbulence. These kind of models are based on Ordinary Differential Equations (ODEs).

Three-dimensional LES models are based on the discretization of Partial Differential Equations (PDEs), both in space and time. This approach uses the Kolmogorov theory of turbulence, which assumes that turbulence has a universal spectral behavior at the smallest scales.

Each approach has strengths and weaknesses, but their cooperation and comparison with observables allows to improve the understanding of both the physical phenomena and the models themselves.

In this thesis, firstly a mathematical model based on clear physical assumptions is written, in order to make it applicable to the natural phenomenon under analysis. Secondly, it is filtered to separate the large and small scales of turbulence, and a numerical method suitable to resolving the associated three-dimensional discrete problem is developed. The accuracy of the numerical solution is tested against a variety of well known benchmarks. Thirdly, the full tree-dimensional model is approximated by a simpler one-dimensional plume model, in order to find analytical solutions useful to deeply understand the plume phenomenology. Finally, the 1D and 3D model results are compared each others and with the phenomenology of real volcanic eruptions.

In the following section, a qualitative description of the phenomenon under study is presented.

Volcanological phenomenon.

Explosive volcanic eruptions are characterized by the injection from a vent into the atmosphere of a mixture of gases, liquid droplets and solid particles, at high velocity and temperature. In typical magmatic eruptions, solid particles constitute more than 95% of the erupted mass, thus the erupted mixture is much denser than air when it exits the crater. Solid particles are mostly produced

Figure 0.0.1: Strombolian eruption at Stromboli Volcano, June 2006, `www.photovolcanica.com`.

by the brittle fragmentation of a highly viscous magma during its rapid ascent in a narrow conduit [217, 183], with particle sizes and densities spanning over a wide range, depending on the overall character and intensity of the eruption [110, 113]. Magma fragmentation can be either magmatic o phreatomagmatic: the former fragmentation style is due to pressure variation inside the volcano conduit, where dissolved gases and high magma viscosity make the ascending mixture break down fragmenting and creating volcanic ash and pumice [89]. The latter is due to interaction between hot magma and cold water. Walker [213] [among others, see 77] studied the grain-size characteristics of fragmented material produced by a variety of volcanic eruptions. These are polycomponent materials, composed by crystals, pumice or lithic components. Their grain-size extends from tens of centimeters to microns, with most of the mass typically distributed in the *ash* part (i.e. below one millimeter). The grain-size distribution mostly depends on the fragmentation efficiency. Indeed, stronger eruptions are usually richer in fine particles [179]. After fragmentation, the mixture is ejected through the volcanic vent (Fig. 0.0.1).

The fragmented mixture is initially subjected to an expansion in which the pressure equilibrates with the atmospheric pressure [228]. From laboratory experiments, this is expected to occur within less than 20 conduit diameters above the ground [232], i.e. approximatively at the crater exit [228].

After being injected in the atmosphere, the solid part of the volcanic mixture is transported from the vent to different ground positions. The particular path followed by each individual pyroclast depends both on its physical properties (e.g. grain-size) and on the dynamics of the flow. The coarsest particles have a greater fall velocity and rapidly decouple from the mean flow, being deposited closer to

Figure 0.0.2: Subplinian eruption, Calbuco Volcano (Chile), April 22, 2015. Carlos F. Gutierrez/AP.

the vent; the finest components are tightly coupled with the gas phase, and they can be transported much farther by winds (see Fig. 0.0.2). Strongest eruptions can even lead to global-scale ash dispersion.

In explosive eruptions, four main flow regimes can be distinguished:

1. *Volcanic fountains and ballistics*: the coarsest and denser part of the erupted mixture, where turbulence is absent (the flow follows the Bernoulli approximation) and the particles follow a ballistic trajectory.

2. *Volcanic plume*: the part of the erupted mixture that behaves as a turbulent multiphase fluid. It is initially transported upwards because of its momentum. When the inertia is exhausted, volcanic plumes are transported by their buoyancy. Indeed, high mixture temperature and turbulent entrainment of atmospheric air reverse buoyancy signature and make part of the mixture less dense than the surrounding atmosphere. Solid particles are lost by a volcanic plume through gravitational fallout.

3. If mixture temperature is not high enough, if the particle size is too large, or if turbulent entrainment is not efficient enough, the volcanic column will collapse – partially or completely – giving rise to a *pyroclastic density current*, which can flow down the slopes of the volcanic edifice with temperatures up to 1000 °C and velocities up to tens of m/s (Figs. 0.0.3 and 0.0.4).

Volcanic plumes are the focus of the present study. They are qualitatively sketched in Fig. 0.0.5 and photographed in Figs. 0.0.1, 0.0.2, 0.0.4 and 0.0.6.

Figure 0.0.3: Pyroclastic density current generated by the June 1991 Mount Pinatubo Plinian eruption (Philippines). Albert Garcia.

Figure 0.0.4: A relatively small volcanic ash plume and pyroclastic density current generated by early stages of the June 1991 Mount Pinatubo Plinian eruption (Philippines), `volquake.weebly.com/mt-pinatubo-1991.html`.

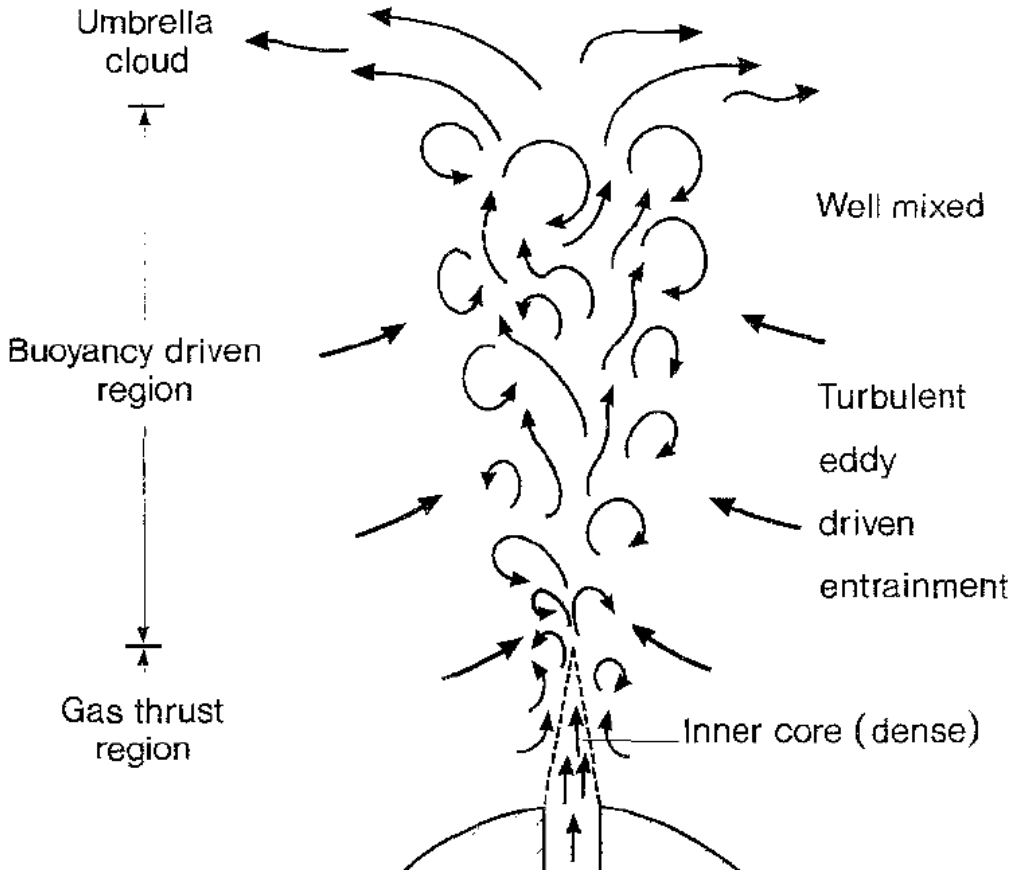

Figure 0.0.5: Volcanic ash plume phenomenology, [225]. The three regions of a volcanic plume development are sketched: jet (or gas thrust region), plume (or buoyancy driven region) and umbrella cloud. The turbulent entrainment erodes the dense inner core and mixes the plume mixture with the atmosphere.

Figure 0.0.6: Subplinian eruption at Mount Etna (Italy), December 5, 2015. Fernando Famiani.

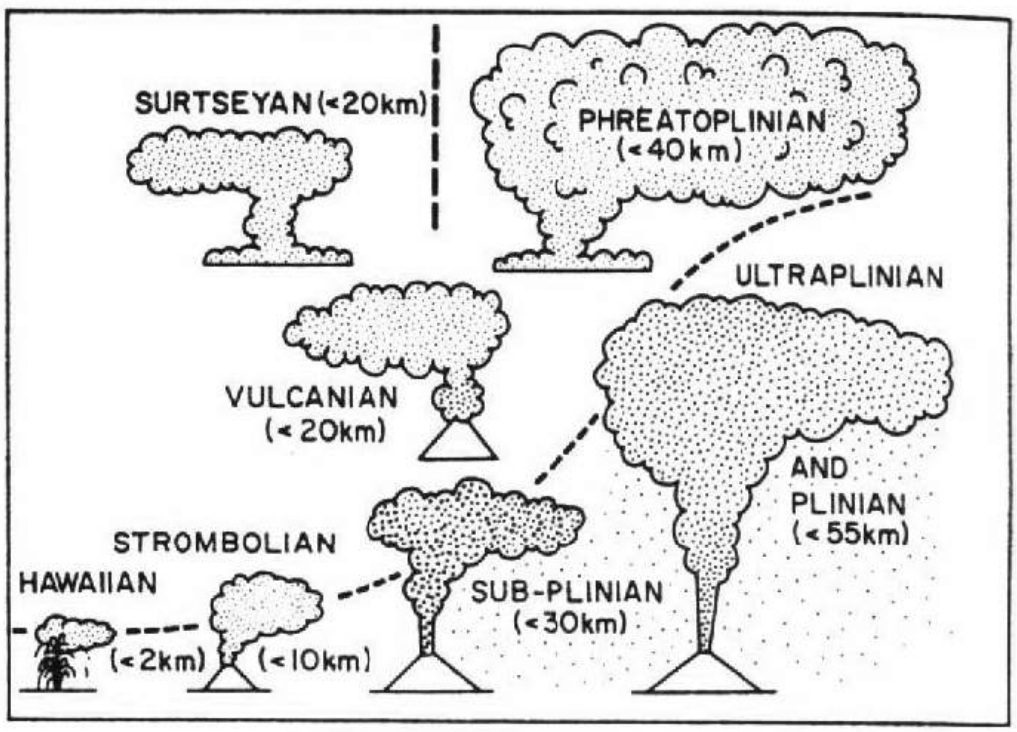

Figure 0.0.7: Classification of eruption styles, and intensity. In bracket is reported the typical maximum plume height for each eruption style, `http://www.vialattea.net/esperti/php/risposta.php?num=7055`.

In order to classify the size and strength of a volcanic eruption, a relative measure of the volume of products has been devised. It is called *Volcanic Explosivity Index*, it is defined:

$$\mathrm{VEI} = \left[\log_{10}\left(\frac{V_{\mathrm{erupted}}}{V_0}\right)\right] \tag{0.0.1}$$

where $V_0 = 10^{-4}\,\mathrm{km}^3$ is a reference volume and V_{erupted} is the volume of eruption products. Alongside this quantity, another indication of the size of a volcanic eruption is given by the plume height (see Fig. 0.0.7). Following Sigurdsson et al. [179], *Hawaiian and Strombolian* eruptions are the least violent (VEI < 2). They are characterized by low magma viscosity (typically basalt or basaltic andesite), which allows the essolved gas to escape from the magma with relative ease. *Vulcanian* eruptions eject material to heights smaller than 20 km and last on the order of seconds to minutes (VEI $\simeq 3$). They are characterized by discrete, violent explosions, with both ballistics and ash particles. They can create shock waves in the atmosphere. *Plinian and Subplinian* eruptions are characterized by the formation of high eruption plumes resulting in atmospheric ash and particle injection and dispersal by winds over huge areas (VEI > 4). They can also create shock waves, pyroclastic density currents and thick fall-out deposit. In this thesis, I present three examples of volcanic plumes extending from vulcanian to plinian.

After having said something about the size of volcanic eruptions, I want to spend a few words about the frequency of these natural phenomena on earth. As reported in Fig. 0.0.8, many volcanic eruptions occur worldwide during a solar year, less frequently as VEI increases. For example, 65 eruptions with VEI ≥ 4 have been reported in the 20th century, of which only 12 with VEI ≥ 5 and 3 with VEI $= 6$, [SIV, WK1]. Both the temporal and spatial distribution of volcanic eruptions is heterogeneous on earth (Fig. 0.0.9).

Finally, volcanic eruptions are dangerous. Historically, there have been many explosive eruptions that have had a big impact. There are mainly four sources of hazard from volcanic eruptions:

- Ballistic pyroclasts and rocks ejected during a explosive eruptions can constitute a serious risk in the vicinity of the crater.
- Pyroclastic density currents can be generated by plume collapses. They are extremely dangerous because they are very hot, mobile and fast. Recalling an historical example, they have been cause of the deaths at Pompei and Ercolano at the foot of the Vesuvio volcano in Italy in 79 a.D.
- Ash fallout from volcanic plumes can endanger the solidity of the roofs of houses and also the health of people and animals who are forced to live for long periods with ash filling the air and covering all surfaces.
- The ash dispersed from a volcanic plume can reach the stratosphere and be dispersed for thousands of kilometers by the wind, endangering the functioning and security of air transport in the affected areas. A recent example of such a hazard is the eruption of the Eyjafjallajökull volcano in Iceland, which led to air travel disruption in northwest Europe for six days from 15 April to 21 April 2010 and also in May 2010, including the closure of airspace over many parts of Europe.

Observing volcanic eruptions.

In order to characterize and understand volcanic eruptions, a number of observables have been used, starting from direct observation and qualitative description of the phenomenon and its consequences, to more quantitative techniques using complex instruments capable to measure a variety of physical and chemical properties. However, an accurate method of measure does not exist yet and easy to measure observables are preferred in this field of study, even if the error associated with these measurements is typically large ($> 10\,\%$).

An example of such an observable is the *plume height*. Even if it is influenced by many different parameters tied both to eruptive and meteorological conditions, typically with a large temporal variability, it has been found that the plume maximum height $H_{\max}$ depends on the steady rate of release of thermal energy in watt at the crater $\dot{Q}_{\mathrm{W}}$, [219]. In particular, the following empirical formula has been broadly used in volcanology:

$$H_{\max} \propto \dot{Q}_{\mathrm{W}}^{1/4}\,, \tag{0.0.2}$$

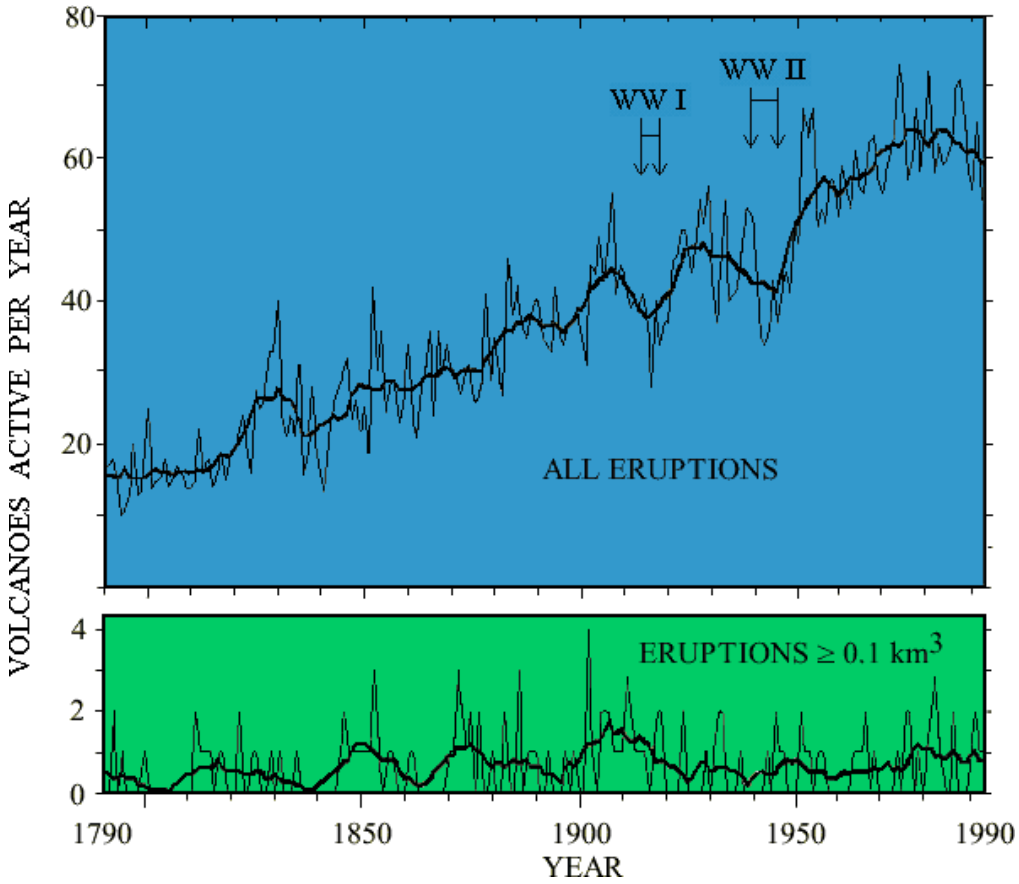

Figure 0.0.8: Number of eruptions in the last two centuries. In the upper panel are reported all the registered eruptions, evidencing the first and second world word periods. The lower panel reports only the eruptions with VEI ≥ 3. The bold line is a windowed time-average.

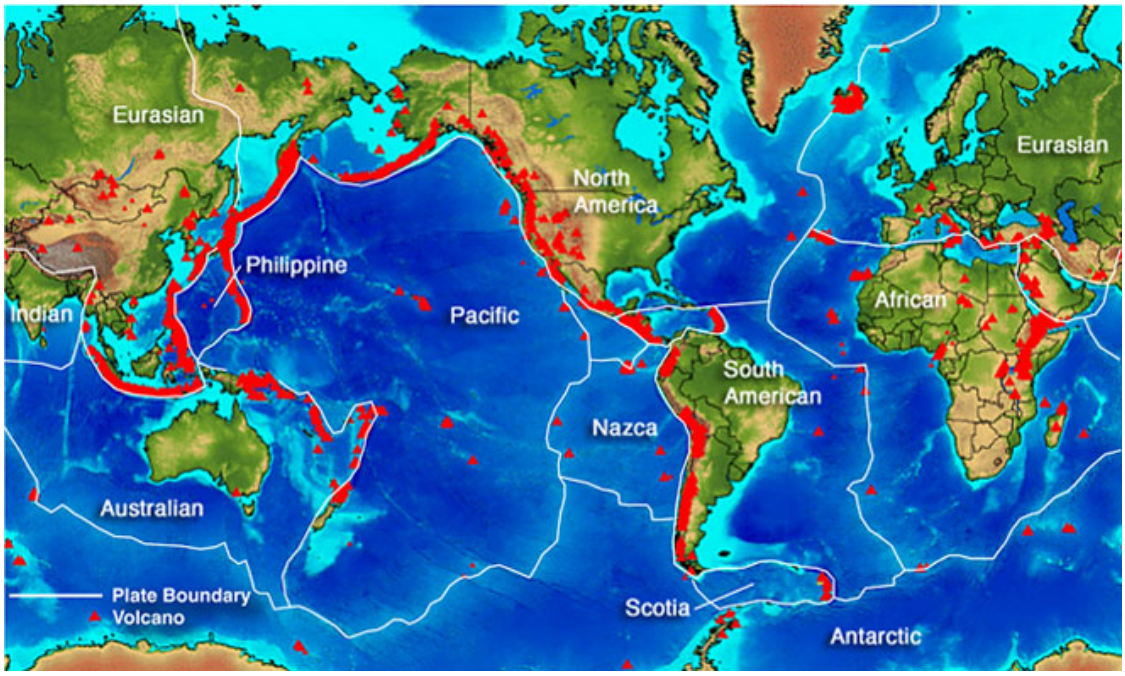

Figure 0.0.9: Global distribution of volcanoes, `http://www.gso.uri.edu/lava/Volcanism/volcanism.html`.

because of its simplicity and the possibility to give an immediate estimation of the plume strength. For this reason, when writing a model for volcanological applications it is very important to retain the model as simple as possible. This is possible by identifying the key phenomena driving the dynamics of the system under study, thus by adopting *ad hoc* assumptions, to be kept in mind when the model is applied to the real phenomenon.

Some of the methodologies used today for observing and studying volcanic eruptions are cited here:

- plume height (cf. Chap. 3 and 6)
- plume shape
- plume and pyroclastic flow deposits, [156, 24, 16]
- remote sensing
  - thermal infrared and visible electromagnetic emission (cf. Chap. 4)
  - radar, sonar and lidar measurements [159, 56]
  - infrasonic acoustic signal (cf. Sec. 5.5 and Chap. 6).

Some of them were introduced decades ago, others are much more recent. In particular, direct measurements have recently become more diffuse.

In this thesis, I compare model results with the following observables: plume height, plume shape, thermal infrared bright emission and infrasonic acoustic signal.

From laboratory to numerical experiments

When possible, comparison with laboratory experiments is useful to get more insight into volcanic plumes. Unfortunately, it is not always possible to scale real geophysical phenomena down to small laboratory experiments. For this reason, numerical models become very important in this field of study. Anyway, they still have a great need of laboratory experiments (see Chap. 5). Indeed, in order to trust the predictions of a numerical model, it must be compared with experiments. When the accuracy of the simulated results reach a satisfactory threshold, a scaling process can be applied to the numerical domain and physical parameters, to mimic as faithful as possible the geophysical natural phenomenon. At this point, comparison of the results of numerical simulations with field observation are desirable.

The numerical simulation post-processing has to be prepared in order to reproduce not only important thermo-fluid dynamics parameters like temperature, density and velocity but also observables quantity. For volcanic plumes, I worked mainly on thermal infrared emission, infrasonic acoustic signal and tephra deposit.

One example of the latter methodology applied to volcanic eruption is the following: turbulence is a key phenomenon in volcanic eruptions because it drives mixing, motion and diffusion of the ash particles inside the erupted mixture. It is indeed ubiquitous in volcanic plumes and pyroclastic density currents. Adversely, turbulence is a very complex behavior of fluids, that even today is not completely understood, especially if the fluid is moving in a complicated geometry or domain.

Additional complications come from the presence of particles dispersed in the carrier fluid [4]. However, computational fluid dynamics has made great progresses in the last decades, furnishing well understood and tested *benchmarks*. These numerical experiments can be used to test the accuracy of numerical solvers in capturing the turbulent dynamics in a specific spatial domain.

The accuracy of the numerical solver developed in this thesis is tested in Chap. 5, where it is stressed against a number of computational fluid dynamics benchmarks. Then, the computational domain is scaled to real volcanological dimensions, for simulating a multiphase fluid dynamics transformation as similar as possible to two real volcanic eruptions.

Volcanic plume modeling.

In a volcanic plume, after the initial decompression, the order of magnitude of particle volumetric concentration very rarely exceed $\epsilon_s \sim 10^{-2}$. Thus, the bulk density of the ejected mixture is less then $\rho_m \lesssim 10\,\mathrm{kg/m^3}$, because the order of magnitude of the ejected fragments density is $\hat{\rho}_s = \rho_m/\epsilon_s \sim 10^3\ \mathrm{kg/m^3}$. Thus, the gas–particle mixture in a volcanic plume con be considered mainly as a dilute suspension in the sense of Elghobashi [59, 60]. This threshold for ϵ_s is overcome in the dense layer forming in pyroclastic density currents [see e.g. 144], and in the plume mixture just outside the conduit, before its decompression [27, 28]. Collisions between ash particles can be disregarded when looking at the dynamics of volcanic ash plume, because of the dilute character of the plume mixture [cf. 138, 227].

The term *volcanic column* will be adopted in this thesis to generically indicate the turbulent eruptive cloud ejected from the vent (e.g. convective/collapsing column). However, I also follow the fluid-dynamic nomenclature, thus *jet* characterizes the inertial regime of the volcanic column and *plume* the buoyancy-driven regime. A *forced plume* is characterized by an initial momentum-driven jet stage, transitioning into a plume. The most important physical phenomena characterizing a volcanic plume are the following:

- *Buoyancy reversal*: The ejected mixture of volcanic ash and gases is denser than the surrounding atmosphere just above the vent, but becomes progressively less dense because of *air entrainment* and heating due to *high plume temperature*.

- *Momentum at the vent*: the high ejection velocity allows eruptive material to reach heights up to some km even if its buoyancy is negative.

- *Atmospheric stratification*: volcanic ash plumes can reach heights up to 50 km, thus their dynamics is strongly influenced by atmospheric stratification. An evidence of this is the *umbrella* forming at the top of ash plumes, above their neutral buoyancy level.

- *Grain size distribution*: grain size distribution of volcanic ash is a key property in the dynamics of volcanic ash plumes. Indeed, it is needed to quantify kinematic and thermal decoupling between particles and the surrounding

fluid, causing *particle settling* and *preferential concentration*. It can change along the volcanic column because of *aggregation* and *sorting*.

- *Meteorological conditions* such as *wind* and *humidity* could influence strongly the plume dynamics.

- *Compressible effects* are important if the mixture is over-pressured at the vent, shock waves are sometimes created and peculiar effects are observed during volcanic eruptions. Moreover, compressibility generates sonic and infrasonic signals that can be used as an observation tool.

The following approaches have been used in the literature for modeling volcanic ash plumes:

1. three-dimensional transient numerical simulations [e.g. 64, 192, 190, 203]: where the fluid dynamics equations are resolved in the three spatial dimensions plus time, to take into account the mean evolution and fluctuations in the system. In geophysical application, it is typically unfeasible to solve all the relevant scales of turbulence, thus a subgrid model have to be used to take into account of the phenomena occurring at scales smaller than the smallest resolved scale (see Sect. 1.4).

2. two-dimensional transient numerical simulations [e.g. 202, 100, 54, 141, 45]: in order to simplify the complexity of the mathematical problem to be solved, average along one spatial dimension is performed. It can be done in cylindrical coordinates, averaging along the angular coordinate, or in a Cartesian system averaging along one horizontal direction.

3. one-dimensional integral models [e.g. 219, 225, 23, 111, 222]: where all the turbulent fluctuations are filtered out and a self-similar profile is assumed at each position along the plume axis. In this way it remains to solve the fluid dynamic equations just along the axial direction. This kind of model are usually stationary because a time average is needed to filter out turbulent fluctuations. Sometimes, the slow evolution with respect to the turbulent one can be modeled in order to capture the plume vertical evolution [170, 224].

Moreover, the multiphase character of the gas–particle mixture can be treated with two different approaches:

- *Eulerian*: each solid phase is considered as a fluid interpenetrating in the carrier gaseous phase, characterized in all points of the domain by its own density, velocity and temperature fields.

- *Lagrangian*: each particle in the domain is modeled individually. It can be considered either like a point (with empirical relationships for the drag force with the carrier fluid) or, in the fully resolved approach, as a body with finite dimensions.

In this thesis, I will always use the Eulerian approach, because the focus is on volcanic ash, thus a large number of relatively small particles. I will use both 3D and 1D models, comparing their results.

Dusty gas modeling of volcanic plumes

Starting from the assumption that the large-scale behavior of volcanic columns is controlled by the *bulk* properties of the eruptive mixture, most of the models for volcanic plumes have considered the eruptive mixture as a *dusty gas* (i.e., they assume that particles are perfectly coupled to the gas phase). This approach is also named *pseudo-gas*. Under such a hypothesis, the multiphase transport equations can be largely simplified and reduce to a set of mass, momentum and energy balance equations for a single fluid having average thermo-fluid dynamic properties (mixture density, velocity and temperature) and equations of state accounting for the incompressibility of the particulate phase and gas covolume [127].

By adopting the dusty gas approximation, volcanic plumes have been studied in the framework of the one-dimensional jet [61] and plume theory [138, 137]. Such models of volcanic plumes have had a formidable role in volcanology to identify the main processes controlling their dynamics and scaling properties [217, 225, 184].

Accordingly, volcanic plume dynamics are schematically subdivided into three main stages (see Fig. 0.0.5):

- The lower, jet phase is driven by the initial flow momentum. When buoyancy reversal does not occur, partial or total collapse of the jet from its maximum thrust height (where the jet has lost all its initial momentum) and generation of pyroclastic density currents are expected.

- Above the jet thrust region, the volcanic plume rise is driven by buoyancy and it is controlled by turbulent mixing until, in the stratified atmosphere, a level of neutral buoyancy is reached.

- Above that height, the plume starts to spread out achieving its maximum height and forming an umbrella ash cloud dispersing in the atmosphere and slowly falling-out.

In one-dimensional, time-averaged models, entrainment of atmospheric air is described by one empirical coefficient (the entrainment coefficient) relating the influx of atmospheric air to the local, vertical plume velocity. The entrainment coefficient also determines the plume shape [104] and can be empirically determined by means of direct field observations or ad-hoc laboratory and numerical measurements. In laboratory and numerical experiments, the ratio between the influx and the vertical plume velocity varies between $0.05 \div 0.1$ in jets and between $0.07 \div 0.15$ in plumes.

Recent studies [189, 188, 63, 33] showed that the entrainment coefficient of volcanic plumes can differ significantly from that found in laboratory experiments.

Further development of volcanic plume models have included the influence of atmospheric stratification and humidity [226, 88], the effect of cross wind [23], loss and reentrainment of solid particles from plume margins [229, 208] and transient effects [170, 224]. However, one-dimensional models strongly rely on the self-similarity hypothesis, whose validity cannot be experimentally ascertained for volcanic eruptions.

To overcome the limitations of one-dimensional models, three-dimensional dusty gas models have been developed to simulate volcanic plumes. Suzuki et al. [192] have developed a three-dimensional dusty gas model (`SK-3D`) able to accurately

resolve the relevant turbulent scales of a volcanic plumes, allowing a first, theoretical determination of the entrainment coefficient [189], without the need of an empirical calibration. The dusty gas approximation is partly relaxed in the `ATHAM` model [143, 90, 203], which is able to simulate particle settling and the microphysics of water in volcanic plumes. `ATHAM` describes the dynamics of gas–particle mixtures by assuming that particles are in kinetic equilibrium with the gas phase only in the horizontal component, whereas along the vertical direction they are allowed to have a differential velocity. Thermal equilibrium is assumed.

In this thesis, I present a method to derive an effective entrainment coefficient from 3D numerical models (Sect. 3.11 and Chap. 6).

Multiphase flow models of volcanic plumes

Notwithstanding all the above advantages, dusty gas models are still limited by the equilibrium assumption, which can be questionable at least for the coarsest part of the granulometric spectrum in a plume. Turbulence is indeed a non-linear multiscale process and the time and space scales of gas–particle interaction may be comparable with some relevant turbulent scales, thus influencing the large-scale behavior of volcanic plumes.

To model non-equilibrium processes, Eulerian multiphase flow models have been developed, which solve the full set of mass, momentum and energy transport equations for a mixture of gas and dispersed particles, treated as interpenetrating fluids, both in subsonic and supersonic regime.

Valentine and Wohletz [202] and Dobran et al. [54], Neri and Dobran [140] have first analyzed the influence of non-equilibrium processes and erupting parameters on the column behavior to identify, by means of two-dimensional numerical simulations, a threshold from collapsing and convective columns. Lately, two-dimensional [52, 45] and three-dimensional numerical simulations [64] has contributed to modify the view of a sharp transition between convecting and collapsing columns in favor of that of a transitional regime, characterized by a progressively increasing fraction of mass collapsing. More recently, the multiphase decompression of a volcanic plume ejected from a conduit has been numerically faced with `PDAC`, studying the influence of particle decoupling on the decompression dynamics, [27, 28]. However, previous works could not investigate in detail the non-equilibrium effects in volcanic plumes, mainly because of their averaged description of turbulence: a detailed resolution of the relevant turbulent scales in three dimensions would indeed be computationally prohibitive for N-phase systems.

The main objective of the present work is therefore to develop a new physical model and a fast three-dimensional numerical code able to resolve the spatial and temporal scales of the interaction between gas and particle in turbulent regime and to describe the kinetic non-equilibrium dynamics and their influence on the *observable* features of volcanic plumes. To this aim, a development of the so-called *equilibrium–Eulerian* approach [71, 4] has been adopted. I generalized it to the compressible, two-way coupling regime, by writing a new set of partial differential equations (cf. Sec. 1.3), suitable for multiphase turbulence in subsonic, transonic and supersonic regimes. It is a generalization of the dusty gas model retaining the kinematic non-equilibrium as a first order correction, with respect to the Stokes

number of the solid particles in the mixture. In this way, it is possible to capture efficiently not only particle settling but also particle preferential concentration, i.e. the non-equilibrium process induced by turbulence.

I refer to this 3D model with the name `ASHEE`: *Ash Equilibrium–Eulerian Model*.

Dispersed multiphase turbulence

In this section the main challenges of the numerical modeling of dispersed multiphase turbulence [see 4, for a review] in volcanic plumes are presented. `ASHEE` is written for flows in such a dynamical regime.

Turbulence is a multiscale physical phenomenon involving many different scales, from the integral scale of the flow to the scale of the smallest eddy of the turbulent field. To overcome observational and laboratory difficulties in understanding this phenomenon, computational fluid dynamics bypasses the shortcomings of analytical methods and integral numerical models by offering Direct Numerical Simulations (DNS), i.e., the simulation of the whole range of spatial and temporal scales in the turbulent flow. With respect to other investigation methods, DNS is more akin to an experiment, and no less valuable for the immense quantity of data it produces, especially at high spatial resolution. Unfortunately, as demonstrated in next sections, the DNS of volcanic plumes is presently computationally unaffordable, because it would require an extremely fine numerical grid. The main idea behind the Large Eddy Simulation (LES) approach adopted in this work is to reduce this computational cost by reducing the range of time- and length-scales that are being solved for via a low-pass filtering of the equations. Such a low-pass filtering effectively removes small-scale information from the numerical solution. However, nonlinearity causes the coupling between the large and the small scales, introducing subgrid-scale (SGS) terms that cannot in general be disregarded [see 211]. To mimic the SGS effect on the large scales, reproducing correctly the resolved turbulent spectrum, SGS models take advantage of the universal character of turbulence at the smallest scales.

The turbulent entrainment process at the interface between two regions at different turbulent intensity (such as the boundary between the plume and the atmosphere) is carried out through two different mechanisms: large-scale eddies are responsible of the engulfment of parcels of air [197], whereas small-scale turbulence controls the so-called nibbling process [129, 10]. Although experimental studies [216] suggest that the nibbling process controls the development of the turbulent/non-turbulent interface, it is still believed that the global rate of entrainment is imposed by the large-scale engulfment [e.g., 194, 43]. Indeed, in turbulent plumes experimental and numerical studies [see e.g., 43, for a review] support the idea that the *rate* of air entrainment is controlled by the dynamics of the large eddies, at the so-called Taylor microscale (see the discussion below). It is therefore necessary to understand to what extent LES is suited to describe turbulent plumes and how important the unresolved (subgrid-scale, SGS) part of the turbulent spectrum (which must be modeled) can be in practical cases of volcanological interest.

In Chap. 5 and 6, I measure the capability and robustness of `ASHEE` in simulating plume turbulent entrainment.

In multiphase turbulence, the broad range of scales of the turbulence interpenetrate the scales of solid particles (described by their grain-size distribution). Balachandar and Eaton [4] showed that in dispersed multiphase turbulence (turbulence in diluted suspensions, $\epsilon_s \lesssim 10^{-3}$), the equilibrium–Eulerian model performances are enhanced in the LES framework. Thus in `ASHEE`, I decide to use the combination of LES and the equilibrium–Eulerian models for simulating volcanic ash plumes.

In the last chapter of this thesis, I quantify the sensitivity to grid resolution of three-dimensional (3D) LES of a volcanic plume, providing an empirical quantitative estimate of the minimum grid size required to minimize the effect of the modeled subgrid turbulence. In the next section, I briefly quantify the range of spatial and temporal scales involved in the dynamics of a volcanic ash plume.

Micro and macro scales of turbulence in volcanic plumes

The smallest scale of turbulent fluctuations in a volcanic plume is given by the Kolmogorov scale [152]

$$\eta = A_\eta D \mathrm{Re}^{-\frac{3}{4}} . \tag{0.0.3}$$

Here, D is the crater diameter, A_η is a constant depending on the geometry of the problem and $\mathrm{Re} = DU/\nu$ is the Reynolds number based on the flow properties at the vent (U is the vent velocity and ν is the kinematic viscosity). Plourde et al. [151] estimated $A_\eta \simeq 5.6$ for a pure plume. The Kolmogorov characteristic time scale of the smallest eddies is $\tau_\eta = \eta^2/\nu$.

The order of magnitude of the integral scale for the plume development is the plume height. This can be estimated as a function of the steady release of thermal energy at the crater $\dot{Q}_\mathrm{W} = \rho_\mathrm{m} U \pi (D/2)^2 C_\beta (T_\beta - T_\alpha)$, by means of the following formula:

$$H_\mathrm{top} = A_\mathrm{W} \dot{Q}_\mathrm{W}^{\frac{1}{4}} . \tag{0.0.4}$$

Wilson et al. [219] estimated $A_\mathrm{W} \simeq 8.2\,(\mathrm{m}^2\,\mathrm{s}^3\,\mathrm{kg}^{-1})^{\frac{1}{4}}$ for volcanic plumes.

When Re is high (in volcanic plumes it typically ranges in $10^6 \div 10^{10}$) the integral and the Kolmogorov scales are separated by many order of magnitude (cf. Eq. (0.0.3)). Between these two scales there exists the so called inertial sub-range, where the turbulent properties of the flow are universal and do not depend on the integral scale configuration. This sub-range is characterized by the Taylor microscale λ_T. Because λ_T depends on the flow configuration, it is difficult to estimate it a-priori.

In Sects. 6.3 and 6.4, I compute this length scale a-posteriori from the results of three-dimensional simulations.

The temporal integral scale t_top can be evaluated thanks to Morton et al. [138], where it depends only on atmospheric parameters:

$$t_\mathrm{top} \simeq \sqrt{\frac{T_1}{g\Gamma(1+n)}} . \tag{0.0.5}$$

Here Γ is the atmospheric adiabatic lapse rate, T_1 is the atmospheric temperature at the vent level and n is the ratio of the vertical temperature gradient to the

lapse rate Γ. In standard atmospheric conditions ($\Gamma = 9.8\,\mathrm{K/km}$ and $n = -0.66$), I obtain $t_{\mathrm{top}} \simeq 100\,\mathrm{s}$.

Degrees of freedom of volcanic plumes

In this section, using scaling arguments, I demonstrate that, although DNS is still not affordable, LES provides a viable approach for modeling volcanic plumes.

On the basis of the scaling analysis above, I am able to estimate the number of degrees of freedom to be resolved to fully simulate a turbulent volcanic plume in a DNS. The number of spatial and temporal degrees of freedom can be given by

$$N_{\mathrm{spatial}} \approx \left(\frac{H_{\mathrm{top}}}{\eta}\right)^3 \tag{0.0.6}$$

$$N_{\mathrm{temporal}} = \frac{t_{\mathrm{top}}}{\tau_\eta}\,. \tag{0.0.7}$$

Thus, the number of degrees of freedom to be resolved in a volcanic simulation is:

$$N_{\mathrm{d.o.f.}} = N_{\mathrm{spatial}} N_{\mathrm{temporal}} = \frac{t_{\mathrm{top}} H_{\mathrm{top}}^3 U}{A_{\mathrm{K}}^5 D^4}\mathrm{Re}^{\frac{11}{4}} = \\ = \frac{t_{\mathrm{top}} A_{\mathrm{W}}^3 (\rho_{\mathrm{m}} C_\beta (T_\beta - T_\alpha))^{\frac{3}{4}}}{A_\eta^5}\frac{U^{\frac{9}{2}} D^{\frac{1}{4}}}{\nu^{\frac{11}{4}}}\,. \tag{0.0.8}$$

Setting the typical values for a volcanic eruption [cf. 219] to $(T - T_\alpha) = 1000\,\mathrm{K}$, $\rho_{\mathrm{m}} = 5\,\mathrm{kg/m^3}$, $C_\beta = 1100\,\mathrm{J/(K\,kg)}$ and $\nu \simeq 2 * 10^{-5}\,\mathrm{m^2/s}$, I obtain (in SI unit):

$$N_{\mathrm{d.o.f.}} = 9.5 * 10^{19} * U^{\frac{9}{2}} D^{\frac{1}{4}}\,, \tag{0.0.9}$$

which is huge, even for "small" volcanic eruptions. The LES approach has been developed to mitigate this unaffordable computational effort. That approach takes advantage of the fact that in a fully turbulent flow the vast majority of modes is below the Taylor microscale [152]. In the LES approach these small scales (far from the integral scales) are modeled by assuming that the spectrum has an universal shape. This approach has been demonstrated to be accurate if the resolved scales ξ are in the inertial range.

For a volcanic plume, it has been numerically observed that the grid resolution at the vent must be at least $\xi \simeq D/10$ [cf. i.e., 233, 192] to approach the inertial sub-range. Therefore, I can recount the number of degrees of freedom for a volcanic LES by using $D/10$ as smallest spatial scale and $D/(10U)$ as smallest temporal scale (instead of the Kolmogorov scales). I obtain:

$$N_{\mathrm{d.o.f.}} = 10^4\,\frac{t_{\mathrm{top}} H_{\mathrm{top}}^3 U}{D^4} = 10^4\,\frac{t_{\mathrm{top}} A_{\mathrm{W}}^3 (\rho_{\mathrm{m}} C_\beta (T_\beta - T_\alpha))^{\frac{3}{4}} U^{\frac{7}{4}}}{D^{\frac{5}{2}}}\,, \tag{0.0.10}$$

or, using the typical values for a volcanic eruption (in SI unit):

$$N_{\mathrm{d.o.f.}} = 6.3 * 10^{14} * U^{\frac{7}{4}} D^{-\frac{5}{2}}\,. \tag{0.0.11}$$

It is worth noting here that, contrary to intuition, larger plumes are less expensive to model than small ones. For example, a Plinian eruption can have (after its initial decompression) $D \simeq 1000\,\mathrm{m}$ and $U \simeq 300\,\mathrm{m/s}$, bringing to $N_{\mathrm{d.o.f.}} \simeq 4.3 * 10^{11}$ while a Strombolian with $D \simeq 10\,\mathrm{m}$ and $U \simeq 10\,\mathrm{m/s}$ brings to $N_{\mathrm{d.o.f.}} = 1.1 * 10^{14}$. Even if these numbers are still very large, they could be mitigated by using non-homogeneous grid geometries, because Re is not homogeneous in the domain.

In Sects. 6.3 and 6.4, I use the `ASHEE` model for the LES of two volcanic plumes.

Mathematical tools

The mathematical pillars supporting this thesis are differential equations, both ordinary and partial [139]. The first issue arising in differential equation is whether they are well posed, i.e. if they satisfy the following properties:

- Existence: a solution exists
- Uniqueness: the solution is unique
- Continuous dependence: the solution's behavior changes continuously with the initial conditions.

While the well-posedness of ordinary differential equations is usually not a big issue, that of partial differential equations related with fluid mechanics is one of the most difficult problems of mathematical analysis. The general problem is still open, making the Navier-Stokes existence and smoothness one of the *Millennium Prize Problems* [51].

In Chap. 2, I explore the stability and existence of weak solutions of certain partial differential equations arising from the physics of multiphase compressible mixtures (see Chap. 1 for the description of such systems).

In the previous section I showed that the degrees of freedom of a volcanic plume are too many to be resolved completely (DNS). Thus, approximations are needed. In this thesis, I follow two approaches:

- In Chap. 3, I show that integral plume models are a particular solution of the full three dimensional problem. In particular, they are a solution of the time-averaged stationary isentropic model, where the horizontal profiles of all the variables are assumed to be *self-similar* [cf., 225, 111]. The resulting mathematical model is an initial value problem described by a system of ODEs, where the only independent variable is the position along the plume axis.
- In Sect. 1.4, I filter the PDEs of the compressible equilibrium–Eulerian model in order to separate large and small scales of turbulence. All the non-linear terms, keeping the interaction between different scales, are modeled by using state-of-the-art SGS models (both static and dynamic) [116, 80]. In Chap. 6 I analyze the influence of different SGS models on the dynamics of a volcanic ash plume.

Once the well posedness of the problem under analysis is established (or hypothesized), *numerical discretization* is needed to solve practically the system.

In Chap. 3, the ODEs of integral plume models are solved using standard commercial codes, in particular the code Maple `http://www.maplesoft.com/products/Maple/`. The numerical method used is a Runge-Kutta Fehlberg method that produces a fifth order accurate solution [176].

Moving to the 3D problem, in Sect. 5.1, I describe the discretization strategy adopted in this thesis for the PDEs of the `ASHEE` model. The software infrastructure I decide to use is OpenFOAM® , an open source finite volume code for computational fluid dynamics, based on `C++`. In this way, the continuous problem is associated to a discrete one: a system of non-linear coupled equations, of size equal to the number of cells in the domain. To solve the latter, the system is firstly linearized, then it is solved by using *linear algebra*. Non-linear terms are thus treated *iteratively*.

High Performance Computing tools

Solving turbulence is computationally very expensive. This is because it is a multiscale phenomenon that in a volcanic eruption has the largest scale of hundreds of meters while the smallest is of the order of $1\,\mu$m. As I showed above, the LES of a volcanic plume has a number of degrees of freedom of the order of $N_{\text{d.o.f}} \simeq 10^{12}$. `ASHEE` is able to solve approximatively $10^4\, N_{\text{d.o.f.}}/\text{s}$ on a today's single core CPU (this is the order of magnitude of the performances of standard finite-volume solvers). Thus, the LES I am considering here would take something like 10 y to be solved. This makes such a simulation unfeasible on a single core. Today it is possible to speed up numerical simulations by using parallel supercomputers (High Performance Computing, HPC), that allow users to use tens of thousands processors contemporary. HPC are needed to perform LESs of volcanic plumes at decent resolution.

`ASHEE` parallel performances are satisfactorily up to one thousand of processors. The most resolved LESs of the two volcanic plumes presented in Chap. 6 have respectively $5.2{*}10^{12}$ ([weakPlume]) and $8.8{*}10^{11}$ ([strongPlume]) degrees of freedom, needing respectively about 25 and 5 days to be solved on 1024 processors.

In Sect. 5.1, I discuss the parallel performances of the `ASHEE` code, showing that presently it scales up to 1024 processors. Increasing the number of processors used, the main bottleneck on parallel performances is the communications between different processors. In `ASHEE`, the most of the communication is requested by the linear algebra algorithm needed to construct and invert the matrices of the discretized system [42, 44].

The present HPC challenge in the scientific community is to identify these bottlenecks and speed up computation flops towards the exascale [209, 55]. Nowadays, special attention is given by the HPC community to linear algebra problems related to partial differential equations.

The research presented in this thesis sets within the context of this challenge.

Thesis résumé

I briefly describe the contents of each chapter to help the reader to focus on its interests.

The derivation of the fluid dynamic model describing the non-equilibrium gas–particle mixture is described in detail in Chap. 1. The PDEs of models used in dispersed multiphase turbulence are described in this chapter, together with the boundary conditions used throughout this thesis. Moreover, in this chapter I discuss the subgrid scale models used for the LESs of chapters 5, 6.

In Chap. 2 the barotropic Eulerian-Eulerian model in a four-way formulation is studied from the point of view of the existence of weak solutions fulfilling the energy inequality associated to the PDE problem.

Chap. 3 focuses on mean integral models for volcanic plumes in a calm stratified atmosphere. Starting from the PDEs of the dusty gas model, the integral model ODEs are written and studied in its dimensionless formulation.

Chap. 4 uses such integral models to retrieve vent key parameters inverting the information provided by infrared images of a real volcanic eruption.

The discretization procedure, the algorithm and the numerical code development are reported in Chap. 5. Moreover, this chapter focuses on verification and validation issues in the context of applications of the `ASHEE` numerical model to turbulent volcanic plumes.

Finally, Chap. 6 presents numerical simulations of volcanic plumes and discusses some aspects related to numerical grid resolution, subgrid LES models and kinematic decoupling in realistic volcanological conditions.

Related scientific documentation

Publications

Some of the physical modeling issues discussed in Chap. 1, the coupled integral-infrared electromagnetic model (Chap. 3 and 4), some of the numerical simulations and the numerical algorithm presented in Chap. 5 and 6 have been documented through the international publications:

- [8]: Berselli, L. C., Cerminara, M., and Iliescu, T. (2015). Disperse Two-Phase Flows, with Applications to Geophysical Problems. *Pure Appl. Geophys.*, **172**(1):181–196.

- [30]: Cerminara, M., Berselli, L. C., Esposti Ongaro, T., and Salvetti, M. V. (2015a). Direct numerical simulation of a compressible multiphase flow

through the fast Eulerian approach. In Fröhlich, J., Kuerten, H., Geurts, B. J., and Armenio, V., editors, *Direct Large-Eddy Simul. IX*, volume **XX** of ERCOFTAC Series, page 700. Springer.

- [34]: Cerminara, M., Esposti Ongaro, T., Valade, S., and Harris, A. J. (2015b). Volcanic plume vent conditions retrieved from infrared images: A forward and inverse modeling approach. *J. Volcanol. Geotherm. Res.*, **300**:129–147.

- [201]: Valade, S., Harris, A. J., and Cerminara, M. (2014). Plume Ascent Tracker: Interactive Matlab software for analysis of ascending plumes in image data. *Comput. Geosci.*, **66**:132–144.

- [31]: Cerminara, M., Esposti Ongaro, T., and Berselli, L. C. (2016a). ASHEE-1.0: a compressible, equilibrium–Eulerian model for volcanic ash plumes. *Geosci. Model Dev.*, **9**(2):697–730.

- [39]: Costa, A., Suzuki, Y. J., Cerminara, M., Devenish, B. J., Esposti Ongaro, T., Herzog, M., Van Eaton, A. R., Denby, L., Bursik, M. I., de' Michieli Vitturi, M., Engwell, S., Neri, A., Barsotti, S., Folch, A., Macedonio, G., Girault, F., Carazzo, G., Tait, S., Kaminski, É., Mastin, L. G., Woodhouse, M. J., Phillips, J. C., Hogg, A. J., Degruyter, W., and Bonadonna, C. (2016). Results of the eruptive column model inter-comparison study. *J. Volcanol. Geotherm. Res.*, **In press**.

- [188]: Suzuki, Y. J., Costa, A., Cerminara, M., Esposti Ongaro, T., Herzog, M., Van Eaton, A. R., and Denby, L. (2016). Inter-comparison of three-dimensional models of volcanic plumes. *J. Volcanol. Geotherm. Res.*, **Accepted**.

- [63]: Esposti Ongaro, T. and Cerminara, M. (2015). Non-equilibrium processes in ash-laden volcanic plumes: new insights from 3D multiphase flow simulations. *J. Volcanol. Geotherm. Res.*, **In press**.

- [33]: Cerminara, M., Esposti Ongaro, T., and Neri, A. (2016b). Large eddy simulation of gas–particle kinematic decoupling and turbulent entrainment in volcanic plumes. *J. Volcanol. Geotherm. Res.*, **Accepted**.

The results discussed in this thesis have been presented in a number of national and international conferences, schools and workshops. The author refer to its website [MCW] for a complete list and abstracts of these presentations.

Issues presented in Chap. 2, 3 and part of Chap. 1, 5, and 6 originally appear in the present document.

Projects

The author of the thesis has been involved in the following projects:

- Research grant (OGS): "Impatto ambientale di eruzioni vulcaniche esplosive e rischio vulcanico". *Mar. 2016–Today.*

- Research fellowship (Università di Pisa): "Soluzioni numeriche per le equazioni di evoluzione di flussi multifase". *Dec. 2015–Feb. 2016.*
- Research grant (INGV), DPC-V1 and FP7 Supersites MED-SUV projects: "Multiphase modeling and 2D/3D numerical simulations of the non-equilibrium dynamics in gas particles flows for the study of turbulent plumes and pyroclastic density currents". *Oct. 2014–Nov. 2015.*
- Research grant (SNS): "Modellistica di Flussi Turbolenti multifase in regime comprimibile con applicazioni allo studio dei plumes vulcanici". *Dec. 2013–May 2014.*
- Collaborator in the DPC–V1 project (INGV): "Valutazione della pericolosità vulcanica in termini probabilistici". *May–June 2014.*
- Principal Investigator (CINECA): ISCRA C project "VolcAshW": 1.0 Mh of computational time. *Oct. 2015–July 2016.*
- Principal Investigator (CINECA): ISCRA C project "VolcAshP": 2.2 Mh of computational time. *Jan.-Oct. 2015.*
- Principal Investigator (CINECA): ISCRA B project "VolcFoam": 5 Mh of computational time. *Mar. 2013–Mar. 2014.*
- Collaborator (CINECA): ISCRA C project "GeoFoam": 1 Mh of computational time. *Dec. 2011–Feb. 2013.*
- Collaboratore (INGV–LMV): "Sakurajima Volcano Field Campaign". Experiment executed with high resolution and thermal cameras, infrasonic sensors and meteorological stations. *July–Aug. 2013.*
- Short visit grant in the project MeMoVolc (ESF), INGV, Sezione di Pisa – Université Blaise Pascal, Laboratoire Magmas et Volcans, Clermont-Ferrand, France: Project MoDaPlumes: "Model and Data interaction for volcanic Plumes". *Dec. 2012–Mar. 2013.*
- The models presented in this thesis have been used to participate actively to the research community working on volcanic ash plume modeling. I participate to an international study aimed at inter-comparing many of the models for volcanic plumes used today [39, 188, 33, 63]. *Apr. 2014–Apr. 2016.*

Chapter 1

Multiphase gas–particle flows

In this chapter the models used in this study are written, listing and justifying the various assumptions needed. The reference review paper is Balachandar and Eaton [4], where the research on dispersed multiphase turbulence of last years is well described, and model pros and cons are listed. In Cerminara et al. [31], I discuss the application of the theory of dispersed multiphase turbulence applied to volcanic eruptions.

In order to classify multiphase flows, the first step is to define the way the various phase interact with each others [cf. 8]. Assuming a carrier fluid transporting a particulate phase of particles, I have the following classification:

- *Four-way coupling:* All the possible interactions are important, namely: collisions between particles, effects of particles inertia and energy on the fluid, and effects of the fluid on the particles.
- *Two-way coupling:* Collisions between particles can be disregarded and only interaction between particle and the fluid and vice versa are taken into account.
- *One-way coupling:* The effect of particles on the fluid can be neglected: only the fluid acts on the particles. Particles can be considered as tracers.

Role of particle-particle collisions: Volumetric fraction

The first important physical parameter characterizing the regime is the total volumetric concentration of the particulate phase. Let $i \in \mathcal{I} \equiv \{1, 2 \ldots, I\}$ be the index running over all the gas chemical components and $j \in \mathcal{J} \equiv \{I+1, \ldots, I+J\}$ the index running over all the particle phases. Defining $\epsilon_j = V_j/V$ the volumetric concentration of the jth phase, the particulate phase can be considered dilute if $\epsilon_s \equiv \sum_{\mathcal{J}} \epsilon_j \lesssim O(10^{-3})$. In the dilute regime, the interaction between particles can be neglected. On the other hand, if $O(10^{-2}) < \epsilon_s < 1$, than I have a dense suspension of particles and the four-way coupling has to be taken into account. In dispersed multiphase turbulence the dispersed phase is always assumed to have concentration smaller than or of the order of 10^{-3}, precisely for neglecting particle-particle collisions.

Dispersed regime is dominant in volcanic plumes and in the dilute part of turbulent pyroclastic density currents [see what follows and 31]. In this thesis, I

thus treat just the *dispersed multiphase turbulence regime*, disregarding the four-way coupling and particle-particle interaction.

Role of gas–particle interaction: Stokes number

Another important parameter is the Stokes time. It is the particle relaxation time, measuring the typical time a particle needs to reach kinematic equilibrium with the carrier phase. It is defined, for the jth phase:

$$\tau_j = \frac{d_j^2}{12\beta_\rho \nu\, \phi_{\mathrm{c}}(\mathrm{Re}_j)} \tag{1.0.1}$$

where $\beta_\rho = 3/(2\hat{\rho}_j/\hat{\rho}_{\mathrm{f}} + 1)$ is a function of the particle to fluid density ratio $(\hat{\rho}_j/\hat{\rho}_{\mathrm{f}})$, $\hat{\rho}_j$ is the material density of the phase j, d_j is its diameter, ν is the carrier phase kinematic viscosity, $\mathrm{Re}_j = d_j|\boldsymbol{u}_{\mathrm{f}} - \boldsymbol{u}_j|/\nu$ is the relative particle-fluid Reynolds number and $\phi_{\mathrm{c}}(\mathrm{Re}_j) = 1 + 0.15\mathrm{Re}_j^{0.687}$ is a correction for finite Reynolds number ($\mathrm{Re}_j < 10^3$) [4, 3, 37]. In the case of heavy particles ($\hat{\rho}_j/\hat{\rho}_{\mathrm{f}} \gg 1$) the expression (1.0.1) for the Stokes time reduces to:

$$\tau_j = \frac{\hat{\rho}_j\, d_j^2}{18\mu\, \phi_{\mathrm{c}}(\mathrm{Re}_j)} \tag{1.0.2}$$

where here μ is the carrier fluid dynamic viscosity.

In order to infer about the kinematic equilibrium between particles and fluid, the Stokes time has to be compared with the fastest time scale of the carrier flow dynamics, namely τ_{f}. The Stokes number is defined as the ratio between these two time scales: $\mathrm{St}_j \equiv \tau_j/\tau_{\mathrm{f}}$.

This non-dimensional group is the parameter characterizing the capability of the particulate phase to follow the dynamic of the carrier fluid. It also suggests the more suitable approach to be used for that particular class of particles. As reported in Balachandar and Eaton [4], the different approaches can be classified as follows:

- $\mathrm{St}_j < 10^{-3}$ *dusty gas*
- $10^{-3} < \mathrm{St}_j < 0.2$ *equilibrium–Eulerian*
- $\mathrm{St}_j > 0.2$ *Eulerian*
- $\mathrm{St}_j > 1$ *Lagrangian*

Moreover, if the size of the particles is larger than the size of the smallest spatial scale of the dynamical problem Δx, than the shape of the particles has to be taken into account and the so called *fully resolved* approach has to be used. Detailed investigation of the different approaches performances can be found for example in Elghobashi [59, 60], Ferry and Balachandar [71, 72], Ferry et al. [74], Rani and Balachandar [158], Shotorban and Balachandar [177], Cencini et al. [29], Boffetta et al. [13] .

Even if, in principle, the Eulerian approach does not have a limitation on the Stokes number, Lagrangian approach is more suitable if $\mathrm{St}_j > 1$, because uniqueness

of particle velocity field cannot be guaranteed in the Eulerian one [see Sect. 1.6.3 and 3].

In this thesis, I will always assume that the particle size is smaller than Δx so that the *point-like assumption* for particles can be used. Moreover, I will not use the Lagrangian approach but only *Eulerian*-like ones (Eulerian, equilibrium–Eulerian or dusty gas models). I opted for this choice because the number of particles involved in a volcanic eruption is huge and the Stokes number for ash particles ($d_j < 1$ mm) is usually smaller than 0.2 [cf. Chap. 6 and 31]. The Lagrangian approach could be added on the Eulerian model in future work for taking into consideration particles with larger diameter.

1.1 Eulerian multiphase flow model - [eulerian]

In the Eulerian approach the carrier and dispersed phases are considered as interpenetrating fluid media. Their properties are calculated defining the state of each phases in field representation [cf. e.g. 41, 57, 76, 141]. Thus, each field $\mathfrak{f}$ is function of position and time, namely $\mathfrak{f} = \mathfrak{f}(\boldsymbol{x}, t)$.

1.1.1 Conservation equations

I assume the mixture is composed by a carrier fluid composed by I chemical components and J classes of solid particles, being the dispersed phases. Consequently, the equations of conservation of mass, momentum and energy for such a mixture can be written [cf. 68, 127, 141, 86, 80, 8, 64]:

$$\partial_t(\rho_i) + \nabla \cdot (\rho_i \, \boldsymbol{u}_\mathrm{f}) = 0 \,, \quad i \in \mathcal{I} \tag{1.1.1a}$$

$$\partial_t(\rho_j) + \nabla \cdot (\rho_j \, \boldsymbol{u}_j) = S_j \,, \quad j \in \mathcal{J} \tag{1.1.1b}$$

$$\partial_t(\rho_\mathrm{f} \, \boldsymbol{u}_\mathrm{f}) + \nabla \cdot (\rho_\mathrm{f} \, \boldsymbol{u}_\mathrm{f} \otimes \boldsymbol{u}_\mathrm{f}) + \nabla p = \nabla \cdot \mathbb{T} + \rho_\mathrm{f} \, \boldsymbol{g} - \sum_{j \in \mathcal{J}} \boldsymbol{f}_j \tag{1.1.1c}$$

$$\partial_t(\rho_j \, \boldsymbol{u}_j) + \nabla \cdot (\rho_j \, \boldsymbol{u}_j \otimes \boldsymbol{u}_j) = \rho_j \, \boldsymbol{g} + \boldsymbol{f}_j + S_j \, \boldsymbol{u}_j \,, \quad j \in \mathcal{J} \tag{1.1.1d}$$

$$\begin{aligned} &\partial_t(\rho_\mathrm{f} e_\mathrm{f}) + \nabla \cdot (\rho_\mathrm{f} \boldsymbol{u}_\mathrm{f} e_\mathrm{f}) + p \, \nabla \cdot \boldsymbol{u}_\mathrm{f} = \\ &\qquad = \mathbb{T} : \nabla \boldsymbol{u}_\mathrm{f} - \nabla \cdot \boldsymbol{q} + \sum_{j \in \mathcal{J}} [(\boldsymbol{u}_\mathrm{f} - \boldsymbol{u}_j) \cdot \boldsymbol{f}_j - \mathrm{Q}_j] \end{aligned} \tag{1.1.1e}$$

$$\partial_t(\rho_j \, e_j) + \nabla \cdot (\rho_j \, \boldsymbol{u}_j e_j) = \mathrm{Q}_j + S_j \, e_j \,, \quad j \in \mathcal{J} \tag{1.1.1f}$$

where $\rho_\cdot = \rho_\cdot(\boldsymbol{x}, t)$ is the bulk density field (which can also be seen as the volumetric fraction times the material density: $\rho_\cdot = \epsilon_\cdot \hat{\rho}_\cdot$), $\boldsymbol{u}_\cdot = \boldsymbol{u}_\cdot(\boldsymbol{x}, t)$ the velocity vector field, $p = p(\boldsymbol{x}, t)$ is the fluid pressure field, $\mathbb{T} = \mathbb{T}(\boldsymbol{x}, t)$ is the stress tensor field (the stress terms are neglected in the solid phase in the approximation of dilute regime), $\boldsymbol{g}$ is the gravitational acceleration, $\boldsymbol{f}_j = \boldsymbol{f}_j(\boldsymbol{x}, t)$ is the drag force per unity of volume acting on the jth particle class, e is the internal energy per unity of mass, $\boldsymbol{q} = \boldsymbol{q}(\boldsymbol{x}, t)$ is the fluid heat flux, $\mathrm{Q}_j = \mathrm{Q}_j(\boldsymbol{x}, t)$ is the heat per unity of volume exchanged between the fluid phase and the jth particle class, $(\boldsymbol{u}_\mathrm{f} - \boldsymbol{u}_j) \cdot \boldsymbol{f}_j$ is the

dissipation due to the decoupling and drag of the jth particle phase on the carrier phase, and S_j is the source (or sink) term for the jth class particle. Subscript $(\cdot)_j$ stands for the jth particle class phase, $(\cdot)_\mathrm{f}$ is the fluid phase, while $(\cdot)_i$ is the ith chemical component of the fluid phase, so that $\rho_\mathrm{f} = \sum_\mathcal{J} \rho_i$ and[1] $e_\mathrm{f} = \sum_\mathcal{J} \rho_i\, e_i/\rho_\mathrm{f}$. In Eq. (1.1.1c) and Eqs. (1.1.1d), the term containing $\boldsymbol{f}_j$ is respectively the reaction and the action of the fluid on the particles, while in Eq. (1.1.1e) $\boldsymbol{f}_j$ is in the term accounting for the drag dissipation. The term Q_j in Eq. (1.1.1e) and Eqs. (1.1.1f) is respectively the heat transmitted from the jth solid phase to the fluid and vice versa. Here the symbol $\mathbb{A} : \mathbb{B}$ stands for the scalar product between two tensors:

$$\mathbb{A} : \mathbb{B} = \sum_{i,j=1}^{\mathsf{d}} \mathbb{A}_{i,j}\mathbb{B}_{i,j}\,.$$

in d spatial dimensions.

Lagrangian derivatives

In order to make calculations with these equations it is useful to remember that if a bulk density ρ is fulfilling the continuity equation through a velocity $\boldsymbol{u}$, then I can easily switch from the Eulerian to the Lagrangian representation of the convective term of a field $\mathfrak{f}(\boldsymbol{x}, t)$:

$$\partial_t \rho + \nabla \cdot (\rho \boldsymbol{u}) = 0 \quad \Rightarrow \tag{1.1.2}$$

$$\partial_t(\rho\,\mathfrak{f}) + \nabla \cdot (\rho \boldsymbol{u}\,\mathfrak{f}) = \rho\, \mathrm{d}_{\boldsymbol{u}}\mathfrak{f}\,, \quad \text{where} \quad \mathrm{d}_{\boldsymbol{u}}(\cdot) \equiv \partial_t(\cdot) + \boldsymbol{u} \cdot \nabla(\cdot)\,. \tag{1.1.3}$$

It is useful to recall here the definition of a streamline of $\boldsymbol{u}$ starting at $\boldsymbol{x}_0$, as the trajectory $\boldsymbol{X}(\boldsymbol{x}_0, t)$ fulfilling:

$$\mathrm{d}_t \boldsymbol{X}(\boldsymbol{x}_0, t) = \boldsymbol{u}(\boldsymbol{X}(\boldsymbol{x}_0, t), t) \tag{1.1.4}$$

$$\boldsymbol{X}(\boldsymbol{x}_0, 0) = \boldsymbol{x}_0\,. \tag{1.1.5}$$

The total derivative of a field $\mathfrak{f}(\boldsymbol{x}, t)$ in a point $\boldsymbol{x} = \boldsymbol{X}(\boldsymbol{x}_0, t)$ is in this way equivalent to the Lagrangian derivative:

$$\mathrm{d}_t \mathfrak{f}(\boldsymbol{X}(\boldsymbol{x}_0, t), t) = \partial_t \mathfrak{f} + \nabla \mathfrak{f} \cdot \mathrm{d}_t \boldsymbol{X}(\boldsymbol{x}_0, t) = \mathrm{d}_{\boldsymbol{u}}\mathfrak{f}\,. \tag{1.1.6}$$

Thus, if a field $\mathfrak{f}$ has Lagrangian derivative equal to zero, it is constant along streamlines:

$$\mathrm{d}_{\boldsymbol{u}}\mathfrak{f} = 0 \quad \Leftrightarrow \quad \mathfrak{f}(\boldsymbol{X}(\boldsymbol{x}_0, t), t) = \mathfrak{f}(\boldsymbol{x}_0, 0)\,. \tag{1.1.7}$$

Total energy and enthalpy

By using these relationships, it is useful to rewrite the energy balance equations in a different form. Defining the total energy of the fluid $E_\mathrm{f} = e_\mathrm{f} + \frac{1}{2}|\boldsymbol{u}_\mathrm{f}|^2$ and of the

[1] Notice that by summing up all Eqs. (1.1.1a) I get back the continuity equation for ρ_f.

jth particle class $E_j = e_j + \frac{1}{2}|\boldsymbol{u}_j|^2$, and using the momentum balance equations, they become:

$$\partial_t(\rho_\mathrm{f} E_\mathrm{f}) + \nabla\cdot(\rho_\mathrm{f}\boldsymbol{u}_\mathrm{f}\, E_\mathrm{f} + p\boldsymbol{u}_\mathrm{f} - \mathbb{T}\cdot\boldsymbol{u}_\mathrm{f} + \boldsymbol{q}) = \rho_\mathrm{f}\boldsymbol{u}_\mathrm{f}\cdot\boldsymbol{g} - \sum_{j=1}^{J}[\boldsymbol{u}_j\cdot\boldsymbol{f}_j + \mathrm{Q}_j] \tag{1.1.8}$$

$$\partial_t(\rho_j E_j) + \nabla\cdot(\rho_j\boldsymbol{u}_j\, E_j) = \rho_j\boldsymbol{u}_j\cdot\boldsymbol{g} + \boldsymbol{u}_j\cdot\boldsymbol{f}_j + \mathrm{Q}_j + S_j E_j\,, \tag{1.1.9}$$

while balance for the kinetic energies $K_\mathrm{f} = \frac{1}{2}|\boldsymbol{u}_\mathrm{f}|^2$ and $K_j = \frac{1}{2}|\boldsymbol{u}_j|^2$ reads:

$$\rho_\mathrm{f}\,\mathrm{d}_{\boldsymbol{u}_\mathrm{f}} K_\mathrm{f} + \boldsymbol{u}_\mathrm{f}\cdot\nabla p = \boldsymbol{u}_\mathrm{f}\cdot(\nabla\cdot\mathbb{T}) + \rho_\mathrm{f}\boldsymbol{u}_\mathrm{f}\cdot\boldsymbol{g} - \sum_{j=1}^{J}\boldsymbol{u}_\mathrm{f}\cdot\boldsymbol{f}_j \tag{1.1.10}$$

$$\rho_j\,\mathrm{d}_{\boldsymbol{u}_j} K_j = \rho_j\boldsymbol{u}_j\cdot\boldsymbol{g} + \boldsymbol{u}_j\cdot\boldsymbol{f}_j\,. \tag{1.1.11}$$

By comparing Eqs. (1.1.1f), (1.1.9) and (1.1.11), it is worth noting that the work resulting from the fluid drag on the particles affects only the particle kinetic energy while it is not influencing its internal energy [cf. 127]. In order to write the balance equation of the total energy of the mixture, I sum up the total energy of all the the phases, obtaining:

$$\begin{aligned}\partial_t\left(\rho_\mathrm{f}E_\mathrm{f} + \sum_{\mathcal{J}}\rho_j E_j\right) + \nabla\cdot\left(\rho_\mathrm{f}\boldsymbol{u}_\mathrm{f}E_\mathrm{f} + \sum_{\mathcal{J}}\rho_j\boldsymbol{u}_j E_j\right) = \\ = \nabla\cdot(-p\boldsymbol{u}_\mathrm{f} + \mathbb{T}\cdot\boldsymbol{u}_\mathrm{f} - \boldsymbol{q}) + \left(\rho_\mathrm{f}\boldsymbol{u}_\mathrm{f} + \sum_{\mathcal{J}}\rho_j\boldsymbol{u}_j\right)\cdot\boldsymbol{g} + \sum_{\mathcal{J}} S_j E_j\,.\end{aligned} \tag{1.1.12}$$

Another form to write the energy balance equations is the enthalpy formulation. By defining $H_\mathrm{f} = h_\mathrm{f} + K_\mathrm{f} = e_\mathrm{f} + p/\rho_\mathrm{f} + K_\mathrm{f}$ and $H_j = h_j + K_j = e_j + K_j$, I obtain:

$$\begin{aligned}\partial_t(\rho_\mathrm{f}H_\mathrm{f}) + \nabla\cdot(\rho_\mathrm{f}\boldsymbol{u}_\mathrm{f}H_\mathrm{f}) = \\ = \partial_t p + \nabla\cdot(\mathbb{T}\cdot\boldsymbol{u}_\mathrm{f} - \boldsymbol{q}) + \rho_\mathrm{f}(\boldsymbol{g}\cdot\boldsymbol{u}_\mathrm{f}) - \sum_{j\in\mathcal{J}}[\boldsymbol{u}_j\cdot\boldsymbol{f}_j + \mathrm{Q}_j]\end{aligned} \tag{1.1.13}$$

$$\partial_t(\rho_j\, H_j) + \nabla\cdot(\rho_j\,\boldsymbol{u}_j H_j) = \rho_j\boldsymbol{u}_j\cdot\boldsymbol{g} + \boldsymbol{u}_j\cdot\boldsymbol{f}_j + \mathrm{Q}_j + S_j\, H_j\,, \quad j\in\mathcal{J}\,. \tag{1.1.14}$$

Summing up all these equations, I obtain a variant of the total energy Eq. (1.1.12):

$$\begin{aligned}\partial_t\left(\rho_\mathrm{f}H_\mathrm{f} + \sum_{j}\rho_j H_j\right) + \nabla\cdot\left(\rho_\mathrm{f}\boldsymbol{u}_\mathrm{f}H_\mathrm{f} + \sum_{j}\rho_j\boldsymbol{u}_j H_j\right) = \\ = \partial_t p + \nabla\cdot(\mathbb{T}\cdot\boldsymbol{u}_\mathrm{f} - \boldsymbol{q}) + \left(\rho_\mathrm{f}\boldsymbol{u}_\mathrm{f} + \sum_{j}\rho_j\boldsymbol{u}_j\right)\cdot\boldsymbol{g} + \sum_{\mathcal{J}} S_j H_j\,.\end{aligned} \tag{1.1.15}$$

Hypothesis, pros and cons

Summarizing, the *physical hypothesis* behind the Eulerian model presented in Eqs. (1.1.1) are the following:

- the particulate phase is dilute, i.e. $\epsilon_\mathrm{s} \lesssim 10^{-3}$. This means that particle–particle interactions are disregarded (two-way coupling).

- particle are assumed point-like: particle diameter has to be much smaller than the smallest resolved scale: $d_\mathrm{s}/\Delta x < 1$. The influence if particle shape is not modeled directly, but empirical relationships can be inserted in constitutive relationships.

- the carrier and the dispersed phases are considered as interpenetrating fluid media, described in field representation.

The *main advantages* of the Eulerian approach, in comparison with other methods, are:

- An increase in the number of particles does not add complexity to the problem, in opposition to the Lagrangian approach, where each particle is modeled separately.

- In principle, there is no restriction in the decoupling strength (namely, the Stokes number) that can be modeled with this methodology [86, 141], even if a Lagrangian approach is more suitable if $\mathrm{St} > 1$ [cf. 4].

- Since there are no limitations in St, shock–particle interaction can be captured by these equations [see e.g. 168, 27, 28].

On the other hand, the Eulerian approach has the following *disadvantages*:

- Drag force is a function of the relative velocity between the particle and the fluid velocity fields: $\boldsymbol{f}_j = \boldsymbol{f}_j(\boldsymbol{u}_\mathrm{f} - \boldsymbol{u}_j)$ and it can be very important with respect to other terms in Eqs. (1.1.1c), (1.1.1d) in the two-way regime.
  For this reason, special care must be taken in solving numerically the gas–particle kinematic coupling. It is very important to take into account the contribution of the drag terms into the momentum equations in an accurate way, to avoid problems for the numerical solution. This difficulty is not present in models such as the dusty gas or the equilibrium–Eulerian ones, where the drag term is absorbed into a formulation that is more similar to the standard Navier-Stokes equations (for a more detailed description cf. Secs. 1.3 and 1.2).

- In the case of polydispersed mixtures the number of equations to be solved and the complexity of the resulting system grows dramatically: defining with d the spatial dimension of the problem, the number of equations to be solved is indeed $I + (2 + \mathsf{d})J + \mathsf{d} + 1$, so that, for each new particle class, $(2 + \mathsf{d})$ new equations need to be solved. On the other hand, as discussed in Secs. 1.3 and 1.2, the equilibrium–Eulerian and the dusty gas approaches need just $I + J + \mathsf{d} + 1$ equations, making much lighter adding particle classes (for each new particle class just 1 equation more is needed, i.e. $(1 + \mathsf{d})J$ equations less).

1.1.2 Constitutive equations

Since I am interested in atmospheric applications, in this thesis I assume that the carrier fluid is a mixture of ideal gases. For this reason, in what follows, I substitute the subscript $(\cdot)_{\mathrm{f}}$ with $(\cdot)_{\mathrm{g}}$.

Equations of state

Using the equation of state for gases, I can put in relation ρ_{g}, ρ_i, p, e_{g}, e_i and the gas temperature T_{g}:

$$p = \sum_{i\in\mathcal{I}} \hat{\rho}_i R_i T_{\mathrm{g}} = \frac{\rho_{\mathrm{g}}}{1-\epsilon_{\mathrm{s}}} R\, T_{\mathrm{g}} \qquad R = \sum_{i\in\mathcal{I}} \frac{\rho_i}{\rho_{\mathrm{g}}} R_i \qquad \rho_{\mathrm{g}} = \sum_{i\in\mathcal{I}} \rho_i \tag{1.1.16}$$

$$e_i = C_{\mathrm{v},i}\, T_{\mathrm{g}} \qquad e_{\mathrm{g}} = \sum_{i\in\mathcal{I}} \frac{\rho_i}{\rho_{\mathrm{g}}} e_i = C_{\mathrm{v}}\, T_{\mathrm{g}} \tag{1.1.17}$$

$$C_{\mathrm{v}} = \sum_{i\in\mathcal{I}} \frac{\rho_i}{\rho_{\mathrm{g}}} C_{\mathrm{v},i} \qquad C_{\mathrm{p}} = C_{\mathrm{v}} + R \qquad \gamma = \frac{C_{\mathrm{p}}}{C_{\mathrm{v}}} \tag{1.1.18}$$

where R_i is the gas constant of the ith chemical component of the gas, R is the gas constant of the gas mixture, $C_{\mathrm{v},i}$ is the specific heat at constant volume of the ith chemical component, C_{v} and C_{p} are the specific heats of the gas phase at constant volume and pressure respectively, and γ is the adiabatic index of the gas mixture. I also assume that the fluid is composed by perfect gases, so the specific heats of each chemical component are constants.
In this thesis I will use two versions of the former ideal gas formulation:

- The dilute approximation $\epsilon_{\mathrm{s}} \lesssim 10^{-3}$ would allow the approximation:

  $$p = \rho_{\mathrm{g}} R T_{\mathrm{g}}\,, \tag{1.1.19}$$

  which has been utilized in volcanology by Suzuki et al. [192].

- the complete version of the ideal gas of a mixture of gases and solid particles with density ρ_{m} can be rearranged by using the mass fractions y_i and y_j:

  $$\frac{1}{\rho_{\mathrm{m}}} = \sum_{j\in\mathcal{J}} \frac{y_j}{\hat{\rho}_j} + \sum_{i\in\mathcal{I}} \frac{y_i R_i T_{\mathrm{g}}}{p}\,. \tag{1.1.20}$$

  In particular, I will use this version of the ideal gas in the equilibrium–Eulerian model discussed in Sect. 1.3.

I now move to the diffusion terms $\nabla\cdot\mathbb{T}$ and $\nabla\cdot\boldsymbol{q}$.

Stress tensors

The term $\nabla\cdot\mathbb{T}$ can be written using the compressible expression for the stress tensor of each chemical component of the gas mixture. Defining υ_i the molar

fraction of the ith gas component, I have [cf. 91, 141, 80, 68]

$$\mathbb{T} = \sum_{i\in\mathcal{I}} \upsilon_i \mathbb{T}_i = 2\mu\mathbb{S} \qquad \mu \equiv \sum_{i\in\mathcal{I}} \upsilon_i \mu_i \tag{1.1.21}$$

$$\mathbb{T}_i = 2\mu_i\mathbb{S} = 2\mu_i \left(\mathcal{D} - \frac{1}{\mathsf{d}}\,\mathrm{Tr}(\mathcal{D})\,\mathbb{I}\right) \tag{1.1.22}$$

where $\mathbb{S}$ is the rate-of-shear tensor (namely the deviatoric part of the strain rate tensor), $\mathcal{D} = \mathrm{Sym}(\nabla \boldsymbol{u}_\mathrm{f})$ is the strain rate tensor[2] (namely the symmetric part of the velocity gradient), and $\mathbb{I}$ is the identity tensor. Here I do not take into account (as usually done) the volume viscosity μ_b that is adding to the stress tensor a contribution proportional to the rate-of-expansion [115, 68][3]

$$\mathbb{T}_\mathrm{volume} = \mu_\mathrm{b}\,\mathrm{Tr}(\mathcal{D})\,\mathbb{I}\,. \tag{1.1.23}$$

This term can be important for specific compressible fluid in presence of shock waves or sound propagation. In order to compare the notation used here with others [cf. 70], in the special case where the dynamic and volume viscosity are constant, the divergence of the stress tensor can be written:

$$\nabla\cdot\mathbb{T} = \mu\,\Delta\,\boldsymbol{u} + \left(\frac{\mathsf{d}-2}{\mathsf{d}}\mu + \mu_\mathrm{b}\right)\nabla(\nabla\cdot\boldsymbol{u})\,. \tag{1.1.24}$$

In the applications faced in the present work, I will always consider the volume viscosity negligible and the dynamic viscosity of the gaseous component will be considered constant or depending on the temperature by the Sutherland law:

$$\mu_i = \mu_i(T) = \frac{\mu_\mathrm{Sth}\,T^{\frac{3}{2}}}{T + T_\mathrm{Sth}}\,, \tag{1.1.25}$$

where μ_Sth and T_Sth are two constants depending on the fluid. Using data from [NIS], I obtain results presented in Tab. 1.1.1.

fluid	temperature interval	μ_Sth	T_Sth
air	$100 \div 1500\,\mathrm{K}$	$(1.5697 \pm 0.0009) * 10^{-6}\,\mathrm{Pa\ s}$	$(144 \pm 1)\,\mathrm{K}$
steam	$375 \div 1275\,\mathrm{K}$	$(2.528 \pm 0.003) * 10^{-6}\,\mathrm{Pa\ s}$	$(1130 \pm 2)\,\mathrm{K}$

Table 1.1.1: Sutherland law constants obtained by fitting data from [NIS].

Heat flux

As usually done, the heat flux $\boldsymbol{q}$ is defined through the Fourier law

$$\boldsymbol{q} = -k_\mathrm{g}\,\nabla T_\mathrm{g}\,, \tag{1.1.26}$$

[2]Notice that the trace of the strain rate tensor is the divergence of the velocity field: $\mathrm{Tr}\,\mathcal{D} = \nabla\cdot\boldsymbol{u}_\mathrm{f}$.

[3]Imposing the second principle of thermodynamics it has to hold $\mu > 0$, $\mu_\mathrm{b} \geq 0$.

while the particle-particle heat flux has been disregarded because negligible in dispersed multiphase turbulence ($\epsilon_j \lesssim 10^{-3}$). The gas phase Prandtl number is defined:

$$\mathrm{Pr_g} = \frac{\mu\, C_\mathrm{p}}{k_\mathrm{g}}\,. \tag{1.1.27}$$

Throughout all this work, I will use for atmospheric air the assumption $\mathrm{Pr_g} = 0.71$, as a good approximation of the temperature dependence of the thermal conductivity on temperature [80].

Gas–particle drag

As reported in Clift et al. [37], Magnaudet and Eames [126], Ferry and Balachandar [71], Bagchi and Balachandar [1], Balachandar and Eaton [4] the following semi-empirical relation expresses the drag force $\boldsymbol{f}_j$ acting on the jth particle class:

$$\boldsymbol{f}_j = \frac{6\epsilon_j(3-\beta_\rho)\mu}{d_j^2}(\boldsymbol{u}_\mathrm{g}-\boldsymbol{u}_j)\phi_\mathrm{c}(\mathrm{Re}_j)+\beta_\rho\rho_j \mathrm{d}_{\boldsymbol{u}_\mathrm{g}}\boldsymbol{u}_\mathrm{g}-\rho_j\beta_\rho\boldsymbol{g}+\frac{\beta_\rho\rho_j}{d_j}\sqrt{12\nu\phi_\mathrm{c}(\mathrm{Re}_j)}\,\mathcal{L}(\boldsymbol{u}_\mathrm{g}-\boldsymbol{u}_j) \tag{1.1.28}$$

where $\mathcal{L}$ is a linear operator taking into account the Basset history and the Saffman lift terms and $\beta_\rho = 3/(2\hat{\rho}_j/\hat{\rho}_f + 1)$ [37]. Since I am interested in the heavy particles limit ($\beta_\rho \to 0$), the pressure gradient, the added mass, the Basset history and the Saffman terms can be disregarded [71, 2]. In this regime, the above relation rewrites (here I used the Stokes time defined in Eq. (1.0.2)):

$$\boldsymbol{f}_j = \frac{18\epsilon_j\mu}{d_j^2}(\boldsymbol{u}_\mathrm{g}-\boldsymbol{u}_j)\phi_\mathrm{c}(\mathrm{Re}_j) = \frac{\rho_j}{\tau_j}(\boldsymbol{u}_\mathrm{g}-\boldsymbol{u}_j) \tag{1.1.29}$$

$$\tau_j = \frac{\hat{\rho}_j\, d_j^2}{18\mu\,\phi_\mathrm{c}}. \tag{1.1.30}$$

This relationship has a linear dependency on the fluid-particle relative velocity only if $\mathrm{Re}_j \ll 1$, so that $\phi_\mathrm{c} \simeq 1$ and the classic Stokes drag expression is recovered. On the other hand, if the relative Reynolds number Re_j grows, non-linear effects become much more important. In this case, I am using the empirical Schiller-Naumann relationship [cf. 41]:

$$\phi_\mathrm{c}(\mathrm{Re}_j) = 1 + 0.15\,\mathrm{Re}_j^{0.687} \tag{1.1.31}$$

which has been used and tested in a number of papers [see e.g. 4, 214, 16]. In particular, Wang and Maxey [214] shows nonlinear effects due to correction (1.1.31) on the dynamics of point-like particles falling out in an homogeneous and isotropic turbulent surrounding. This is equivalent to defining the following drag coefficient for an individual particle:

$$C_\mathrm{D}(\mathrm{Re}_j) = \frac{24}{\mathrm{Re}_j}(1 + 0.15\,\mathrm{Re}_j^{0.687})\,. \tag{1.1.32}$$

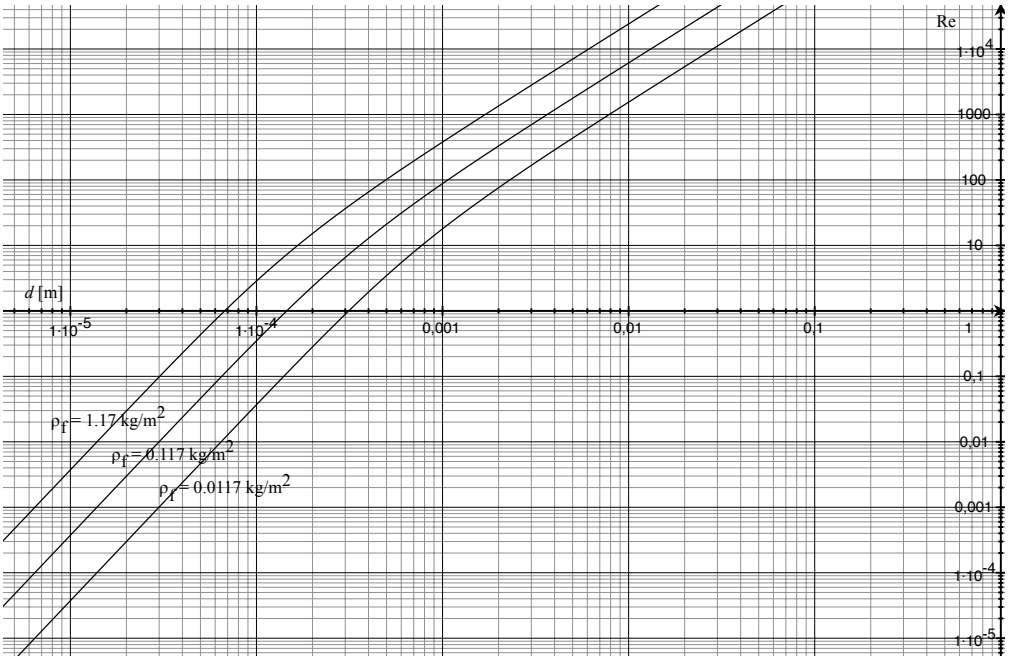

Figure 1.1.1: Function $\mathrm{Re}_j(d_j)$ for a falling particle with: $\hat{\rho}_j = 2000\,\mathrm{kg/m^3}$ in an ambient fluid with $\mu = 1.846 * 10^{-5}$ Pa s and $\rho_\mathrm{g} = 1.17$, 0.117, or 0.0117 $\mathrm{kg/m^3}$.

I recall here the terminal velocity that can be found by setting $\boldsymbol{u}_\mathrm{g} = 0$ in Eq. (1.1.1d) and (1.1.29) [cf. 37]:

$$\boldsymbol{w}_j = \sqrt{\frac{4 d_j \hat{\rho}_j}{3 C_\mathrm{D} \rho_\mathrm{g} g}}\, \boldsymbol{g} = \tau_j\, \boldsymbol{g}\,. \tag{1.1.33}$$

Correction used in Eq. (1.1.32) is valid if $\mathrm{Re}_j < 10^3$, that is the threshold I am using in this work. However, this bound is well observed for volcanic ash particles: In figure 1.1.1, it is worth noting that, for particles smaller than 1 mm, Re_j remains always smaller than 10^3. If regimes with a bigger decoupling need to be explored, different empirical corrections have to be used for ϕ_c [cf. 141, 22]. As discussed in Chap. 6, maximum values of Re_j are reached during particle settling and fallout.

Using formula (1.1.32) and (1.1.33), it is possible to estimate Re_j of a falling particle with diameter d_j. In Cerminara et al. [31] an approximated inverse expression for the needed equation in Re_j is founded:

$$\mathrm{Re}_j = \frac{\hat{\rho}_\mathrm{g} d_j |\boldsymbol{w}_j|}{\mu} = \frac{\hat{\rho}_\mathrm{g} d_j \tau_j |\boldsymbol{g}|}{\mu} = \frac{\hat{\rho}_\mathrm{g} \hat{\rho}_j d_j^3 |\boldsymbol{g}|}{18\mu^2\, \phi_\mathrm{c}(\mathrm{Re}_j)} = \frac{\mathrm{Re}_j^*}{\phi_\mathrm{c}(\mathrm{Re}_j)}\,, \tag{1.1.34}$$

where

$$\mathrm{Re}_j^* \equiv \frac{\hat{\rho}_\mathrm{g} \hat{\rho}_j d_j^3 |\boldsymbol{g}|}{18\mu^2}\,, \tag{1.1.35}$$

is the uncorrected Reynolds number. The resulting expression is:

$$\mathrm{Re}_j = \frac{\mathrm{Re}_j^*}{1 + 0.315\,(\mathrm{Re}_j^*)^{0.4072}}\,, \tag{1.1.36}$$

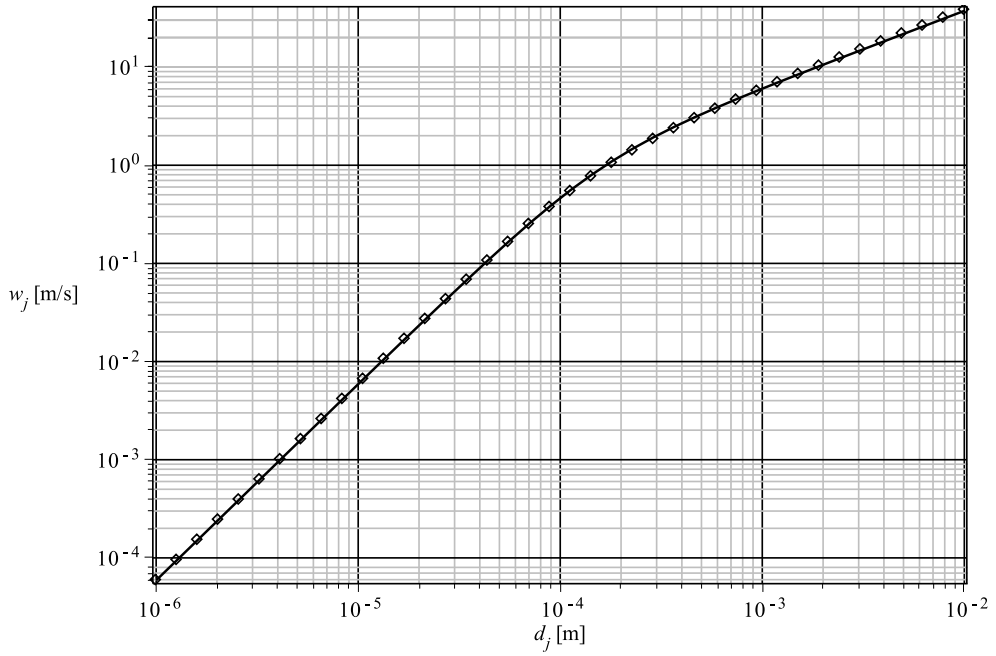

Figure 1.1.2: Selling velocity $\boldsymbol{w}(d_j)$ of a falling particle with diameter d_j. Properties are: $\hat{\rho}_j = 2000\,\mathrm{kg/m^3}$ in an ambient fluid with $\mu = 1.846 * 10^{-5}\,\mathrm{Pa\,s}$ and $\rho_\mathrm{g} = 1.17\,\mathrm{kg/m^3}$. Exact solution of Eq. (1.1.34) (points) and approximation based on Eq. (1.1.36) (solid line).

which, substituted in τ_j, allows a straightforward calculation of $\boldsymbol{w}_j$. In Fig. 1.1.2 the settling velocity is shown, as resulting from Eq. (1.1.34) and (1.1.36) respectively. Approximation (1.1.36) works very well for ash particles.

Gas–particle heat transfer

Finally, the heat transfer per unit of volume from the jth particle class to the fluid has to be defined. As reported in Neri et al. [141], it depends on the mixture properties by:

$$\mathrm{Q}_j = \frac{\rho_j\, C_j}{\tau_{T,j}}(T_\mathrm{g} - T_j) \tag{1.1.37}$$

$$\tau_{T,j} \equiv \frac{2}{\mathrm{Nu}_j}\frac{\hat{\rho}_j\, C_j}{k_\mathrm{g}}\frac{d_j^2}{12}\,, \tag{1.1.38}$$

where T_j and C_j are respectively the temperature and the specific heat of the jth solid phase (so that $e_j = C_j T_j$); $\tau_{T,j}$ is its thermal equilibrium time, and Nu_j is its Nusselt number. In general terms, it depends on Re_j and Pr_g [cf. 141], while if Re_j is small enough, $\mathrm{Nu}_j = 2$ and $\tau_{T,j} = \hat{\rho}_j\, C_j\, d_j^2/(12\, k_\mathrm{g})$. In the dispersed hypothesis the empirical relationship used by Neri et al. [141] reduces to:

$$\mathrm{Nu}_j(\mathrm{Re},\mathrm{Pr}) = 2\left(1 + 0.7\,\mathrm{Re}^{0.2}\mathrm{Pr}^{1/3}\right) + 0.13\,\mathrm{Re}^{0.7}\mathrm{Pr}^{1/3}\,. \tag{1.1.39}$$

It is interesting to compare thermal and kinematic equilibrium times in order to have an indication on the disequilibrium nature of the jth phase. Defining

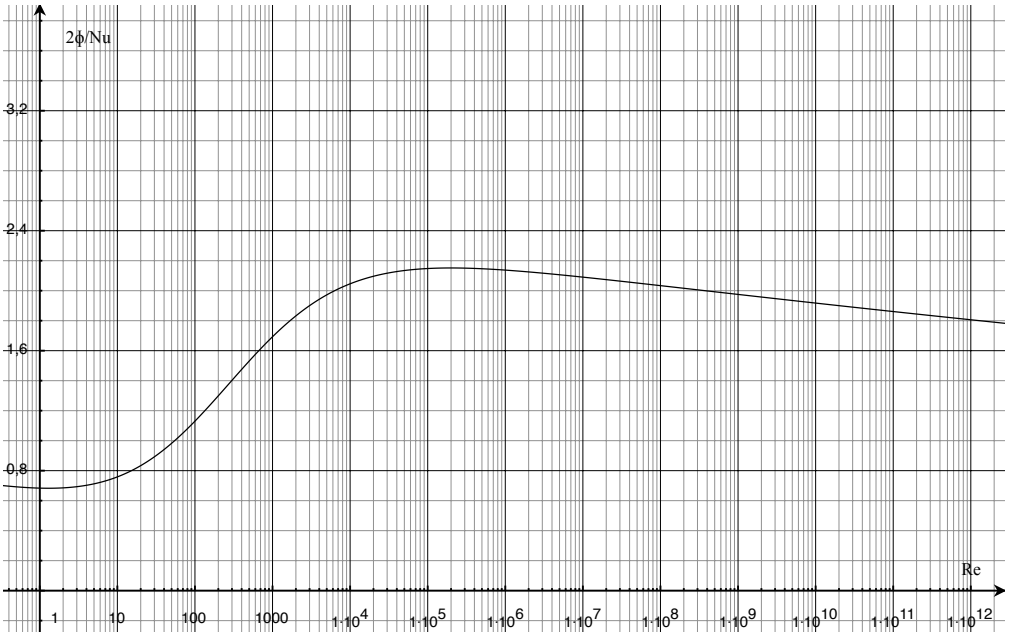

Figure 1.1.3: The correction factor $2\phi_c/\mathrm{Nu}_j$ as a function of Re_j, fixing the Prandtl number of atmospheric air to $\mathrm{Pr}_g = 0.71$.

$\mathrm{Pr}_j = \mu\, C_j/k_g$, I have

$$\frac{\tau_{T,j}}{\tau_j} = \frac{3}{2}\frac{\mu\, C_j}{k_g}\frac{2\,\phi_c(\mathrm{Re}_j)}{\mathrm{Nu}_j(\mathrm{Re}_j,\mathrm{Pr}_g)} = \frac{3}{2}\frac{2\phi_c}{\mathrm{Nu}_j}\,\mathrm{Pr}_j\,. \tag{1.1.40}$$

In order to estimate this correction, firstly notice that factor $2\phi_c/\mathrm{Nu}_j$ tends to 1 if $\mathrm{Re}_j \to 0$ and, as shown in figure 1.1.3, it remains smaller than $\simeq 2$. Successively, the particle jth class Prandtl number Pr_j is order 1 for typical volcanic applications. Indeed, $\mu \simeq 10^{-5}$, $C_j \simeq 10^3$ and $k_g \simeq 10^{-2}$, so that $\mathrm{Pr}_j \simeq 1$. This means that *the thermal equilibrium time is typically of the same order of the kinematic one*. This bound will be very useful writing the equilibrium–Eulerian and the dusty gas models, because it ensures that the thermal Stokes number is always of the same order of the kinematic one, at least for volcanic ash finer than 1 mm.

Hypothesis

Summarizing, additional *physical hypothesis* used for constitutive relationships presented in this section are:

- carrier fluid is an ideal gas composed by perfect gases;
- the stress tensor is described by Eqs. (1.1.21), (1.1.22), and the gas components are Newtonian fluids with dynamical viscosity either constant or described by the Sutherland law reported in Eq. (1.1.25);
- carrier gas Prandtl number is assumed constant;
- particles are much more heavier than the carrier fluid: $\hat{\rho}_s/\hat{\rho}_f \gg 1$, and the particle relative Reynolds number is smaller than 10^3. In this way it is

justified using momentum and temperature exchange corrections reported in Eqs. (1.1.31) and (1.1.39).

I will refer to the model described in the last two sections as [eulerian].

1.1.3 Non-dimensionalization and scaling

In order to put Eqs. (1.1.1) in dimensionless form, the following characteristic scales of the system are defined: L the length scale, U the velocity, L/U the temporal scale, ϱ_g the reference gas density, ϱ_j the jth dispersed phase reference density, P the reference pressure, T_0 the reference temperature, C_0 the reference specific heat, μ_0 the reference viscosity and k_0 the reference conductivity. By using this numbers, the following dimensional transformations are defined:

$$
\begin{aligned}
&\rho_i \to \varrho_\mathrm{g}\,\rho_i && \rho_j \to \varrho_j\,\rho_j && p \to P\,p \\
&\boldsymbol{u}_\mathrm{g} \to U\,\boldsymbol{u}_\mathrm{g} && \boldsymbol{u}_j \to U\,\boldsymbol{u}_j && e_\mathrm{g} \to C_0 T_0\,e_\mathrm{g} \\
&e_j \to C_0 T_0\,e_j && \nabla \to 1/L\,\nabla && \partial_t \to U/L\,\partial_t \\
&\mathbb{T} \to \mu_0 U/L\,\mathbb{T} && k_\mathrm{g} \to k_0\,k_\mathrm{g} && C_j \to C_0\,C_j\,,
\end{aligned}
$$

gravitational acceleration $\boldsymbol{g} = g\,\hat{\boldsymbol{g}}$ and the following dimensionless groups:

$$
\begin{aligned}
&\text{Reynolds} && \mathrm{Re} = \frac{\varrho_\mathrm{g}\rho_\mathrm{g} U L}{\mu_0} && \text{inertial on viscous forces} \\
&\text{Euler} && \mathrm{Eu} = \frac{P}{\varrho_\mathrm{g}\rho_\mathrm{g} U^2} && \text{pressure on inertial forces} \\
&\text{Froude} && \mathrm{Fr} = \frac{U^2}{Lg} && \text{inertial on gravitational forces} \\
& && \kappa_j = \frac{\varrho_j \rho_j}{\varrho_\mathrm{g}\rho_\mathrm{g}} && j\text{th phase relative mass} \\
&\text{Eckert} && \mathrm{Ec} = \frac{U^2}{C_0 T_0} && \text{kinetic energy on enthalpy} \\
&\text{Prandtl} && \mathrm{Pr} = \frac{\mu_0 C_0}{k_0} && \text{viscous on thermal diffusion rate} \\
&\text{Stokes} && \mathrm{St}_j = \frac{\tau_j U}{L} && j\text{th phase kinematic decoupling} \\
& && \mathrm{St}_{T,j} = \frac{\tau_{T,j} U}{L} = \frac{3\phi_\mathrm{c}}{\mathrm{Nu}_j}\mathrm{Pr}_j\mathrm{St}_j && j\text{th phase thermal decoupling}
\end{aligned}
$$

where in the last relation, formula (1.1.40) is used. Some of these dimensionless groups contain the non-dimensionalized bulk densities ρ_g and ρ_j. Even if they have been made dimensionless, notice that their value can change significantly in the domain. By using these definitions, Eqs. (1.1.1) can be written in dimensionless

Lagrangian form:

$$\partial_t(\rho_i) + \nabla \cdot (\rho_i \, \boldsymbol{u}_\mathrm{g}) = 0 \,, \quad i \in \mathcal{I} \tag{1.1.41a}$$

$$\partial_t(\rho_j) + \nabla \cdot (\rho_j \, \boldsymbol{u}_j) = 0 \,, \quad j \in \mathcal{J} \tag{1.1.41b}$$

$$\mathrm{d}_{\boldsymbol{u}_\mathrm{g}} \boldsymbol{u}_\mathrm{g} = -\mathrm{Eu}\, \nabla p + \frac{1}{\mathrm{Re}} \nabla \cdot \mathbb{T} + \frac{1}{\mathrm{Fr}} \hat{\boldsymbol{g}} - \sum_{j \in \mathcal{J}} \frac{\kappa_j}{\mathrm{St}_j} (\boldsymbol{u}_\mathrm{g} - \boldsymbol{u}_j) \tag{1.1.41c}$$

$$\mathrm{d}_{\boldsymbol{u}_j} \boldsymbol{u}_j = \frac{1}{\mathrm{Fr}} \hat{\boldsymbol{g}} + \frac{\kappa_j}{\mathrm{St}_j} (\boldsymbol{u}_\mathrm{g} - \boldsymbol{u}_j) \,, \quad j \in \mathcal{J} \tag{1.1.41d}$$

$$\begin{aligned} \mathrm{d}_{\boldsymbol{u}_\mathrm{g}} e_\mathrm{g} = -\mathrm{Eu}\, \mathrm{Ec}\, p \, \nabla \cdot \boldsymbol{u}_\mathrm{g} + \frac{\mathrm{Ec}}{\mathrm{Re}} \, \mathbb{T} : \nabla \boldsymbol{u}_\mathrm{g} + \frac{1}{\mathrm{RePr}} \, \nabla \cdot (k_\mathrm{g} \nabla T_\mathrm{g}) + \\ + \sum_{j \in \mathcal{J}} \left[\frac{\kappa_j}{\mathrm{St}_j} \, \mathrm{Ec} \, |\boldsymbol{u}_\mathrm{f} - \boldsymbol{u}_j|^2 - \frac{\kappa_j}{\mathrm{St}_{T,j}} (T_\mathrm{g} - T_j) \right] \end{aligned} \tag{1.1.41e}$$

$$\mathrm{d}_{\boldsymbol{u}_j} e_j = \frac{\kappa_j}{\mathrm{St}_{T,j}} (T_\mathrm{g} - T_j) \,, \quad j \in \mathcal{J} \,. \tag{1.1.41f}$$

Here, formula (1.1.3) is used for the convective terms.

In volcanic plumes, the typical scales defined above can vary significantly. Variability orders of magnitude are the following:

$$\begin{aligned} U &= 1 \div 300 \,\mathrm{m/s} & L &= 1 \div 1000 \,\mathrm{m} \\ \varrho_\mathrm{g} &= 0.1 \div 1 \,\mathrm{kg/m^3} & \varrho_j &= 1 \div 10 \,\mathrm{kg/m^3} \\ P &= 10^4 \div 10^7 \,\mathrm{Pa} & C_0 &= 10^3 \,\mathrm{J/kg\ K} \\ \mu_0 &= 10^{-5} \,\mathrm{Pa\ s} & k_0 &= 10^{-2} \,\mathrm{W/m\ K} \\ T_0 &= 100 \div 1000 \,\mathrm{K} & g &= 10 \,\mathrm{m/s^2} \end{aligned}$$

from which, ranging from small to large volcanic ash plume

$$\begin{aligned} \mathrm{Re} &= 10^5 \div 10^{11} & \mathrm{Eu}^{-1} &= 10^{-4} \div 1 \\ \mathrm{Fr} &= 10^{-1} \div 10^2 & \mathrm{Pr} &= 1 \\ \kappa_j &< 10 & \mathrm{Ec} &= 10^{-6} \div 10^{-1} \\ \mathrm{St}_j &= 10^{-6} \div 100 & \mathrm{St}_{T,j} &= 10^{-8} \div 10 \end{aligned}$$

This large variability makes difficult to reproduce the full dynamics of volcanic plumes at the laboratory scale.

1.1.4 The barotropic approximation - [barEulerian]

When conduction of heat, its generation by dissipation of mechanical energy, and heat transfer between the gas and the particles can be disregarded [†], the flow

[†] This regime can be identified through the non-dimensional groups, when:

$$\mathrm{Re} \gg \mathrm{Ec} \qquad \mathrm{Re} \gg \mathrm{Pr}^{-1} \qquad \mathrm{St}_j \gg \kappa_j \, \mathrm{Ec} \qquad \mathrm{St}_{T,j} \gg \kappa_j \,.$$

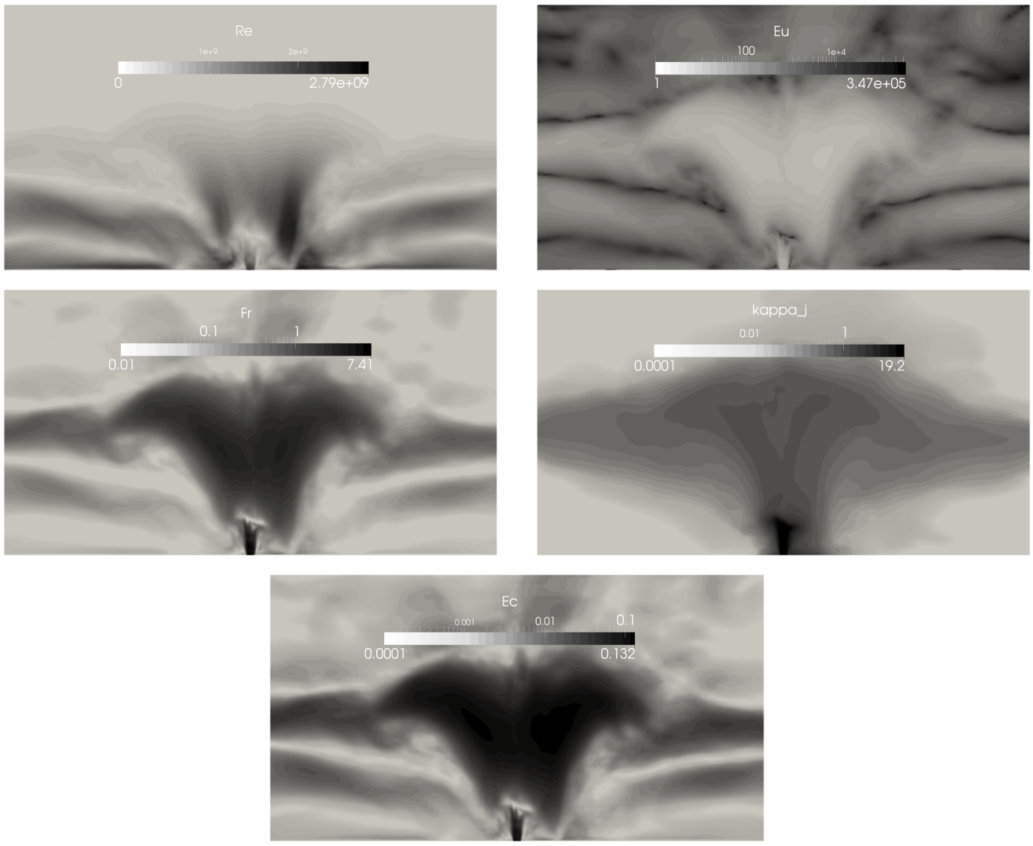

Figure 1.1.4: Dimensionless groups in a slice inside a time-averaged solution of the volcanic plume system. Slices dimensions are around 50x90 km^2.

becomes isentropic and energy equation (1.1.1e) simplifies as follows:

$$\partial_t(\rho_\mathrm{g} C_\mathrm{v} T_\mathrm{g}) + \nabla \cdot (\rho_\mathrm{g} C_\mathrm{v} T_\mathrm{g} \boldsymbol{u}_\mathrm{g}) = -p \nabla \cdot \boldsymbol{u}_\mathrm{g} \,. \tag{1.1.42}$$

Transforming this equation in Lagrangian form (see Eq. (1.1.3)) and using the continuity equation (1.1.1a) $\nabla \cdot \boldsymbol{u}_\mathrm{g} = -\mathrm{d}_{\boldsymbol{u}_\mathrm{g}} \rho_\mathrm{g} / \rho_\mathrm{g}$, I obtain:

$$\rho_\mathrm{g} \, \mathrm{d}_{\boldsymbol{u}_\mathrm{g}} (C_\mathrm{v} T_\mathrm{g}) = -\frac{p}{\rho_\mathrm{g}} \, \mathrm{d}_{\boldsymbol{u}_\mathrm{g}} \rho_\mathrm{g} \tag{1.1.43}$$

It is worth noting that C_v is constant along the gas streamlines. Indeed, using Eq. (1.1.1a) and $\sum_i \rho_i = \rho_\mathrm{g}$, I obtain $\mathrm{d}_{\boldsymbol{u}_\mathrm{g}} \rho_i = -\rho_i \nabla \cdot \boldsymbol{u}_\mathrm{g}$, $\mathrm{d}_{\boldsymbol{u}_\mathrm{g}} \rho_\mathrm{g} = -\rho_\mathrm{g} \nabla \cdot \boldsymbol{u}_\mathrm{g}$ and:

$$\mathrm{d}_{\boldsymbol{u}_\mathrm{g}} C_\mathrm{v} = \sum_{i=1}^{I} C_{\mathrm{v},i} \, \mathrm{d}_{\boldsymbol{u}_\mathrm{g}} \left(\frac{\rho_i}{\rho_\mathrm{g}} \right) = \sum_{i=1}^{I} C_{\mathrm{v},i} \left(\frac{1}{\rho_\mathrm{g}} \mathrm{d}_{\boldsymbol{u}_\mathrm{g}} \rho_i - \frac{\rho_i}{\rho_\mathrm{g}^2} \mathrm{d}_{\boldsymbol{u}_\mathrm{g}} \rho_\mathrm{g} \right) = 0 \,. \tag{1.1.44}$$

Thanks to this result and to the ideal gas law in the dilute approximation (1.1.19), Eq. (1.1.42) reads:

$$\frac{\mathrm{d}_{\boldsymbol{u}_\mathrm{g}} T}{T} = \frac{R}{C_\mathrm{v}} \frac{\mathrm{d}_{\boldsymbol{u}_\mathrm{g}} \rho_\mathrm{g}}{\rho_\mathrm{g}} = (\gamma - 1) \frac{\mathrm{d}_{\boldsymbol{u}_\mathrm{g}} \rho_\mathrm{g}}{\rho_\mathrm{g}} \,, \tag{1.1.45}$$

leading to the classic expressions (recall that both R and C_v are constant along streamlines of $\boldsymbol{u}_\mathrm{g}$):

$$\frac{T}{T_0} = \left(\frac{\rho_\mathrm{g}}{\rho_{\mathrm{g},0}}\right)^{\gamma-1} \tag{1.1.46}$$

$$\frac{p}{p_0} = \left(\frac{\rho_\mathrm{g}}{\rho_{\mathrm{g},0}}\right)^{\gamma}, \tag{1.1.47}$$

where, by defining $\boldsymbol{X}_\mathrm{g}(\boldsymbol{x}_0, t)$ the trajectory starting in $\boldsymbol{x}_0$ and driven by $\boldsymbol{u}_\mathrm{g}$, the adiabatic index of the gas mixture is defined as:

$$\gamma\left(\boldsymbol{X}_g(\boldsymbol{x}_0, t), t\right) = \gamma(\boldsymbol{x}_0, 0) = \frac{R(\boldsymbol{x}_0, 0)}{C_\mathrm{v}(\boldsymbol{x}_0, 0)}\,. \tag{1.1.48}$$

As stated at the beginning of this section, the isentropic (barotropic) assumption is valid when the viscous heat and heat flux are negligible and when the solid phase mass fraction y_s is much smaller than 1 ($\kappa_j \ll 1$, one-way coupling), so that the heat transfer between the particles and the gas can be disregarded. I will refer to the model described in this section as [barEulerian].

In volcanic plumes, the Reynolds number is huge, thus the first assumption on viscous heat and heat flux are typically fulfilled. On the other hand, only when the solid phase mass fraction is much smaller than 1 the heat transfer between the gas and the particles can be disregarded, limiting the applicability of the [barEulerian] only in the region of the domain where the one-way approximation can be considered valid.

1.2 Dusty gas model - [dusty]

As pointed out in Marble [127], Balachandar and Eaton [4] and in the introduction of chapter 1, if $\mathrm{St}_j < 10^{-3}$, then the jth particulate phase can be considered kinematically coupled with the carrier gaseous phase: $\boldsymbol{u}_\mathrm{g} = \boldsymbol{u}_j = \boldsymbol{u}$. Moreover, these two phases can also be considered thermodynamically coupled because $\mathrm{St}_{T,j} \approx \mathrm{St}_j$ (cf. Eq. (1.1.40)). In other words, if the particles are small enough, they can be considered as a unique phase $(\cdot)_\mathrm{s}$ with $\tau_\mathrm{s} \to 0$, $\boldsymbol{u}_\mathrm{s} \to \boldsymbol{u}_\mathrm{g} = \boldsymbol{u}$ and $T_\mathrm{s} \to T_\mathrm{g} = T$. However, it is worth noting that the volumetric particle force $\boldsymbol{f}_\mathrm{s} = \rho_\mathrm{s}(\boldsymbol{u}_\mathrm{f} - \boldsymbol{u}_\mathrm{s})/\tau_\mathrm{s}$ remains finite while $\tau_\mathrm{s} \to 0$. This limit can be performed by reducing the particle radius while the number of particle (n) increases, so that $\rho_\mathrm{s} = n m_\mathrm{s}$ remains constant. As described in Marble [127], this limit is affordable by summing up both the momentum Eqs. (1.1.1d), (1.1.1c) and energy Eqs. (1.1.1f), (1.1.1e). All the terms containing $\boldsymbol{f}_j$ and Q_j cancel . In this way, I get:

$$\partial_t(\rho_\mathrm{m}\boldsymbol{u}) + \nabla\cdot(\rho_\mathrm{m}\boldsymbol{u}\otimes\boldsymbol{u}) + \nabla p = \nabla\cdot\mathbb{T} + \rho_\mathrm{m}\boldsymbol{g} \tag{1.2.1}$$

$$\partial_t\left[(\rho_\mathrm{g}C_\mathrm{v} + \rho_\mathrm{s}C_\mathrm{s})T\right] + \nabla\cdot\left[(\rho_\mathrm{g}C_\mathrm{v} + \rho_\mathrm{s}C_\mathrm{s})T\boldsymbol{u}\right] + p\,\nabla\cdot\boldsymbol{u} = \mathbb{T} : \nabla\boldsymbol{u} - \nabla\cdot\boldsymbol{q} \tag{1.2.2}$$

where here the mixture bulk density is defined as $\rho_\mathrm{m} = \rho_\mathrm{g} + \rho_\mathrm{s} = \sum_i \rho_i + \sum_j \rho_j$. It is also useful to define the mass fractions $y_\mathrm{g} = \rho_\mathrm{g}/\rho_\mathrm{m}$, $y_\mathrm{s} = \rho_\mathrm{s}/\rho_\mathrm{m}$, $y_i = \rho_i/\rho_\mathrm{m}$ and

$y_j = \rho_j/\rho_\mathrm{m}$, so that $y_\mathrm{g} + y_\mathrm{s} = \sum_i y_i + \sum_j y_j = 1$. By using these definitions and Eqs. (1.1.1a), (1.1.1b) the dusty gas model writes:

$$\partial_t \rho_\mathrm{m} + \nabla \cdot (\rho_\mathrm{m} \boldsymbol{u}) = 0 \tag{1.2.3a}$$
$$\partial_t (\rho_\mathrm{m} y_\mathrm{s}) + \nabla \cdot (\rho_\mathrm{m} y_\mathrm{s} \boldsymbol{u}) = 0 \tag{1.2.3b}$$
$$\partial_t (\rho_\mathrm{m} \boldsymbol{u}) + \nabla \cdot (\rho_\mathrm{m} \boldsymbol{u} \otimes \boldsymbol{u}) + \nabla p = \nabla \cdot \mathbb{T} + \rho_\mathrm{m} \boldsymbol{g} \tag{1.2.3c}$$
$$\partial_t (\rho_\mathrm{m} C_\mathrm{m} T) + \nabla \cdot (\rho_\mathrm{m} C_\mathrm{m} T \boldsymbol{u}) + p \nabla \cdot \boldsymbol{u} = \mathbb{T} : \nabla \boldsymbol{u} - \nabla \cdot \boldsymbol{q} \tag{1.2.3d}$$

where $C_\mathrm{m} = (y_\mathrm{g} C_\mathrm{v} + y_\mathrm{s} C_\mathrm{s}) = \sum_\mathcal{I} (y_i C_{\mathrm{v},i}) + \sum_\mathcal{J} (y_j C_j)$ is the mixture specific heat. Moreover, the mixture gas constant can be defined in the same way $R_\mathrm{m} = \sum_\mathcal{I} (y_i R_i) + \sum_\mathcal{J} (y_j R_j)$ so that (cf. Eqs. (1.1.19) and (1.1.20))

$$p = \begin{cases} \rho_\mathrm{m} R_\mathrm{m} T = \rho_\mathrm{g} R T & \text{in the dilute case,} \\ \dfrac{\sum_i \rho_i R_i T}{1 - \sum_j \rho_j / \hat{\rho}_j} & \text{otherwise.} \end{cases} \tag{1.2.4}$$

It is worth noting here that the solid phase is defined as $R_j = 0$, so that $R_\mathrm{m} = y_\mathrm{g} R$ and the former expression for p is equivalent to Eqs. (1.1.19) and (1.1.20). The form of the stress tensor $\mathbb{T}$ and heat flux $\boldsymbol{q}$ remains the same, as specified in Eqs. (1.1.21), (1.1.22), (1.1.25) and (1.1.26). Alternatively, Eq. (1.2.3a) or Eq. (1.2.3b) can be replaced by

$$\partial_t (\rho_\mathrm{m} y_\mathrm{g}) + \nabla \cdot (\rho_\mathrm{m} y_\mathrm{g} \boldsymbol{u}) = 0 \,, \tag{1.2.5}$$

and Eq. (1.2.3d) can be replaced by the balance for the mixture total energy $E_\mathrm{m} = C_\mathrm{m} T + K_m = C_\mathrm{m} + \frac{1}{2}|\boldsymbol{u}|^2$, or the total enthalpy $H_\mathrm{m} = h_\mathrm{m} + K_\mathrm{m} = E_\mathrm{m} + p/\rho_\mathrm{m}$:

$$\partial_t (\rho_\mathrm{m} E_\mathrm{m}) + \nabla \cdot (\rho_\mathrm{m} E_\mathrm{m} \boldsymbol{u}) + \nabla \cdot (p \boldsymbol{u}) = \nabla \cdot (\mathbb{T} \cdot \boldsymbol{u} - \boldsymbol{q}) + \rho_\mathrm{m} \boldsymbol{u} \cdot \boldsymbol{g} \,, \tag{1.2.6}$$
$$\partial_t (\rho_\mathrm{m} H_\mathrm{m}) + \nabla \cdot (\rho_\mathrm{m} H_\mathrm{m} \boldsymbol{u}) - \partial_t p = \nabla \cdot (\mathbb{T} \cdot \boldsymbol{u} - \boldsymbol{q}) + \rho_\mathrm{m} \boldsymbol{u} \cdot \boldsymbol{g} \,. \tag{1.2.7}$$

I will refer to the model described in this section as [dusty].

1.2.1 The barotropic approximation - [barDusty]

If conduction of heat and its generation by dissipation of mechanical energy can be neglected in the [dusty] model, the flow becomes isentropic and the local conservation of energy becomes (see Eq. (1.2.3d)):

$$\partial_t (\rho_\mathrm{m} C_\mathrm{m} T) + \nabla \cdot (\rho_\mathrm{m} C_\mathrm{m} T \boldsymbol{u}) = -p \nabla \cdot \boldsymbol{u} \,. \tag{1.2.8}$$

Using the Lagrangian derivative, Eq. (1.1.3) (ρ_m is fulfilling a continuity equation, Eq. (1.2.3a)), and the expression for $\nabla \cdot \boldsymbol{u}$ obtained from the continuity Eq. (1.2.3a), I obtain

$$\rho_\mathrm{m} \mathrm{d}_{\boldsymbol{u}} (C_\mathrm{m} T) = p \frac{\mathrm{d}_{\boldsymbol{u}} \rho_\mathrm{m}}{\rho_\mathrm{m}} \,. \tag{1.2.9}$$

It is worth noting here that C_m is constant along the streamlines of the vector field $\boldsymbol{u}$. Indeed, using again Eq. (1.1.3) in Eqs. (1.2.3b) and (1.2.5), I obtain

$$\mathrm{d}_{\boldsymbol{u}} y_\mathrm{g} = 0 \tag{1.2.10}$$

$$\mathrm{d}_{\boldsymbol{u}} y_\mathrm{s} = 0\,, \tag{1.2.11}$$

i.e. the mass fractions are constant along streamlines. This fact, together with the ideal gas law (1.2.4) in dilute approximation, allows to write

$$\frac{\mathrm{d}_{\boldsymbol{u}} T}{T} = \frac{R_\mathrm{m}}{C_\mathrm{m}} \frac{\mathrm{d}_{\boldsymbol{u}} \rho_\mathrm{m}}{\rho_\mathrm{m}}\,. \tag{1.2.12}$$

Since y_g and y_s are constants along streamlines, $R_\mathrm{m}/C_\mathrm{m} = \gamma_\mathrm{m} - 1$ is also constant along streamlines:

$$\begin{aligned}\gamma_\mathrm{m}(\boldsymbol{X}(\boldsymbol{x}_0,t),t) = \frac{C_\mathrm{m}+R_\mathrm{m}}{C_\mathrm{m}} = \frac{C_\mathrm{p} y_\mathrm{g}(\boldsymbol{X}(\boldsymbol{x}_0,t),t) + C_\mathrm{s} y_\mathrm{s}(\boldsymbol{X}(\boldsymbol{x}_0,t),t)}{C_\mathrm{v} y_\mathrm{g}(\boldsymbol{X}(\boldsymbol{x}_0,t),t) + C_\mathrm{s} y_\mathrm{s}(\boldsymbol{X}(\boldsymbol{x}_0,t),t)} = \\ = \frac{C_\mathrm{p} y_\mathrm{g}(\boldsymbol{x}_0,0) + C_\mathrm{s} y_\mathrm{s}(\boldsymbol{x}_0,0)}{C_\mathrm{v} y_\mathrm{g}(\boldsymbol{x}_0,0) + C_\mathrm{s} y_\mathrm{s}(\boldsymbol{x}_0,0)} = \gamma_\mathrm{m}(\boldsymbol{x}_0,0)\,.\end{aligned} \tag{1.2.13}$$

By defining $\chi_\mathrm{v,s} = C_\mathrm{s}/C_\mathrm{v}$ and $\kappa(\boldsymbol{x},t) = y_\mathrm{s}(\boldsymbol{x},t)/y_\mathrm{g}(\boldsymbol{x},t) = \rho_\mathrm{s}/\rho_\mathrm{g}$, the previous expression becomes:

$$\gamma_\mathrm{m}(\boldsymbol{X}(\boldsymbol{x}_0,t),t) = \gamma_\mathrm{m}(\boldsymbol{x}_0,0) = \frac{C_\mathrm{m}+R_\mathrm{m}}{C_\mathrm{m}} = \frac{\gamma + \chi_\mathrm{v,s}\kappa(\boldsymbol{x}_0,0)}{1+\chi_\mathrm{v,s}\kappa(\boldsymbol{x}_0,0)}\,. \tag{1.2.14}$$

Using this result in Eq. (1.2.12), and the ideal gas law again, the classic barotropic expression for a perfect gas, modified for the dusty gas model, is found:

$$\frac{T}{T_0} = \left(\frac{\rho_\mathrm{m}}{\rho_{\mathrm{m},0}}\right)^{\gamma_\mathrm{m}-1} \tag{1.2.15}$$

$$\frac{p}{p_0} = \left(\frac{\rho_\mathrm{m}}{\rho_{\mathrm{m},0}}\right)^{\gamma_\mathrm{m}}\,. \tag{1.2.16}$$

I will refer to the model described in this section as [barDusty].

In volcanic eruptions, this model extends the applicability of [barEulerian] to two-way coupled systems (the mass fraction of the solid phase can be comparable to that of the gas phase), where gas–particle disequilibrium can be disregarded ($\mathrm{St_s} < 10^{-3}$).

In App. 1.6.1, the speed of sound of the [dusty] model, in the barotropic approximation, is found:

$$c_\mathrm{dg} = \left(\frac{\partial p}{\partial \rho_\mathrm{m}}\right)^{1/2}_\mathrm{isentropic} = \sqrt{\frac{\gamma_\mathrm{m} p}{\rho_\mathrm{m}}}\,. \tag{1.2.17}$$

There, it is worth noting that the speed of sound of a gas–particle mixture decreases with respect to that of the carrier gas phase because the mixture density ρ_m increases and the specific heat ratio decreases, because of the presence of the solid particles.

1.2.2 Incompressible limit

In the incompressible regime, the dusty gas model Eqs. (1.2.3) is equivalent to the variable-density Navier-Stokes equation [120]:

$$\nabla \cdot \boldsymbol{u} = 0 \tag{1.2.18}$$

$$\mathrm{d}_{\boldsymbol{u}} \rho_{\mathrm{m}} = 0 \tag{1.2.19}$$

$$\rho_{\mathrm{m}} \mathrm{d}_{\boldsymbol{u}} \boldsymbol{u} + \nabla p = \mu \Delta \boldsymbol{u} + \rho_{\mathrm{m}} \boldsymbol{g} \,, \tag{1.2.20}$$

where the incompressible version of the stress tensor Eq. (1.1.24) is used.

This equations set is also equivalent to the Boussinesq approximation of the compressible Navier-Stokes equations, except that there is no diffusion for the density perturbation in Eq. (1.2.19) [i.e. infinite Prandtl number, cf. 8].

1.2.3 Homogeneous case

If the initial condition is homogeneous i.e., if $y_{\mathrm{s}}(\boldsymbol{x}, 0) = y_0$ then the dusty gas model significantly simplifies because the mass fractions y_{g} and y_{s} should remain constant thanks to Eqs. (1.2.10) and (1.2.11). In this case, also C_{m} and R_{m} remain constant in the domain, Eq. (1.2.3b) becomes useless and Eqs. (1.2.3a), (1.2.3c), (1.2.3d) reduce to the compressible Navier-Stokes equation for a perfect gas with gas constant R_{m} and specific heat at constant volume C_{m}.

1.3 Equilibrium–Eulerian model - [eqEu]

This chapter focuses on the model I have written for the volcanological application. It generalizes originally the equilibrium–Eulerian model by Ferry and Balachandar [71] to the compressible two-way coupled regime.

The equilibrium–Eulerian model is an extension of the dusty gas model written to take into account particle kinematic decoupling, retaining the numerical advantages and simplifications of [dusty]. The model is driven by the assumption that the particle velocity field $\boldsymbol{u}_j$ can be seen as equal to the gas velocity plus a decoupling velocity. In this case the [eulerian] model can be rearranged in a convenient form, based on mixture properties, as derived in the next section. The equilibrium–Eulerian model uses asymptotic solutions to find explicitly the decoupling velocity (see Sects. 1.3.2, 1.6.2 and 1.6.3), simplifying significantly the model formulation.

In the following the Eulerian model is written in the more convenient "mixture" formulation, where the focus moves to the mass averaged fields. This formulation has the advantage to be independent from the explicit form of the gas–particle drag terms, keeping their effects just through the decoupling terms.

1.3.1 The Eulerian model in "mixture" formulation

Let the particle velocity field be:

$$\boldsymbol{u}_j = \boldsymbol{u}_{\mathrm{g}} + \boldsymbol{v}_j \,. \tag{1.3.1}$$

Recalling the definition for the mass fraction and the mixture density given above Eq. (1.2.2), the mixture velocity field $\boldsymbol{u}_\mathrm{m}$ is defined through the mass weighted average:

$$\boldsymbol{u}_\mathrm{m} = \boldsymbol{u}_\mathrm{g} - \boldsymbol{u}_\mathrm{r} \tag{1.3.2}$$

$$\boldsymbol{u}_\mathrm{r} = -\sum_{j\in\mathcal{J}} y_j \boldsymbol{v}_j \tag{1.3.3}$$

so that $\boldsymbol{u}_\mathrm{m} = \sum_\mathcal{I} y_i \boldsymbol{u}_\mathrm{g} + \sum_\mathcal{J} y_j \boldsymbol{u}_j$.

Advection with respect the mixture velocity

Let a generic field $\mathfrak{f}$ be associated to the gas phases ($\mathfrak{f}_i$), to the solid phases ($\mathfrak{f}_j$), and to the mixture ($\mathfrak{f}_\mathrm{m} = \sum_\mathcal{I} y_i \mathfrak{f}_i + \sum_\mathcal{J} y_j \mathfrak{f}_j$). The advection terms for $\mathfrak{f}$ can be rewritten by using the following results:

$$\sum_\mathcal{I} \rho_i \mathfrak{f}_i + \sum_\mathcal{J} \rho_j \mathfrak{f}_j = \rho_\mathrm{m} \mathfrak{f}_\mathrm{m} \tag{1.3.4}$$

$$\begin{aligned}\sum_\mathcal{I} \rho_i \mathfrak{f}_i \boldsymbol{u}_\mathrm{g} + \sum_\mathcal{J} \rho_j \mathfrak{f}_j \boldsymbol{u}_j &= \rho_\mathrm{m} \mathfrak{f}_\mathrm{m} \boldsymbol{u}_\mathrm{m} + \rho_\mathrm{m} \sum_\mathcal{J} y_j \boldsymbol{v}_j (\mathfrak{f}_j - \mathfrak{f}_\mathrm{m}) = \\ &= \rho_\mathrm{m} \mathfrak{f}_\mathrm{m} (\boldsymbol{u}_\mathrm{m} + \boldsymbol{v}_\mathfrak{f})\,,\end{aligned} \tag{1.3.5}$$

where

$$\boldsymbol{v}_\mathfrak{f} = \frac{\sum_\mathcal{J} y_j \boldsymbol{v}_j (\mathfrak{f}_j - \mathfrak{f}_\mathrm{m})}{\mathfrak{f}_\mathrm{m}}\,, \tag{1.3.6}$$

can be defined when $\mathfrak{f}_\mathrm{m} \neq 0$. This velocity field takes into account the kinematic decoupling $\boldsymbol{v}_j$, correcting the advection term of $\mathfrak{f}_\mathrm{m}$.

Continuity equations

Summing up over i and j all Eqs. (1.1.1a) and (1.1.1b), the continuity equation for the mixture is:

$$\partial_t \rho_\mathrm{m} + \nabla \cdot (\rho_\mathrm{m} \boldsymbol{u}_\mathrm{m}) = S_\mathrm{m}\,, \tag{1.3.7}$$

where $S_\mathrm{m} = \sum_\mathcal{J} S_j$, while those of the phases are:

$$\partial_t (\rho_\mathrm{m} y_i) + \nabla \cdot (\rho_\mathrm{m} \boldsymbol{u}_\mathrm{g} y_i) = 0\,, \quad i \in \mathcal{I} \tag{1.3.8}$$

$$\partial_t (\rho_\mathrm{m} y_j) + \nabla \cdot [\rho_\mathrm{m} (\boldsymbol{u}_\mathrm{g} + \boldsymbol{v}_j) y_j] = S_j\,, \quad j \in \mathcal{J}\,. \tag{1.3.9}$$

It is worth noting that the mixture density follows the classical continuity equation with velocity field $\boldsymbol{u}_\mathrm{m}$.

Momentum equations

Summing up over i and j the gas and particle momentum Eqs. (1.1.1c) and (1.1.1d), and using Eqs. (1.3.4) and (1.3.5) with $\mathfrak{f} = \boldsymbol{u}$, I obtain

$$\partial_t(\rho_\mathrm{m}\boldsymbol{u}_\mathrm{m}) + \nabla\cdot(\rho_\mathrm{m}\boldsymbol{u}_\mathrm{m}\otimes\boldsymbol{u}_\mathrm{m} + \rho_\mathrm{m}\mathbb{T}_\mathrm{r}) + \nabla p = \nabla\cdot\mathbb{T} + \rho_\mathrm{m}\boldsymbol{g} + \sum_{j\in\mathcal{J}} S_j\,\boldsymbol{u}_j\,, \quad (1.3.10)$$

where

$$\mathbb{T}_\mathrm{r} = \sum_{j\in\mathcal{J}}(y_j\boldsymbol{v}_j\otimes\boldsymbol{v}_j) - \boldsymbol{u}_\mathrm{r}\otimes\boldsymbol{u}_\mathrm{r}\,. \quad (1.3.11)$$

This equation for the momentum balance is the classical compressible Navier-Stokes equation with the substitution $\boldsymbol{u}_\mathrm{g}\to\boldsymbol{u}_\mathrm{m}$ and the addition of the term $\nabla\cdot(\rho_\mathrm{m}\mathbb{T}_\mathrm{r})$ which takes into account the effects of particle decoupling on momentum (two-way coupling).

Enthalpy equations

The same technique I used for the momentum equations can be used for the enthalpy Eq. (1.1.15), by using $\mathfrak{f} = H = h + K$ and defining

$$H_\mathrm{m} = h_\mathrm{m} + K_\mathrm{m} \quad (1.3.12)$$

$$h_\mathrm{m} = \sum_{\mathcal{I}} y_i h_i + \sum_{\mathcal{J}} y_j h_j = \sum_{\mathcal{I}} y_i e_i + \sum_{\mathcal{J}} y_j e_j + \frac{p}{\rho_\mathrm{m}} \quad (1.3.13)$$

$$K_\mathrm{m} = \sum_{\mathcal{I}} y_i K_i + \sum_{\mathcal{J}} y_j K_j = \frac{1}{2}|\boldsymbol{u}_\mathrm{m}|^2 + \frac{1}{2}\sum_{\mathcal{J}} y_j|\boldsymbol{v}_j|^2 - \frac{1}{2}|\boldsymbol{u}_\mathrm{r}|^2\,. \quad (1.3.14)$$

By rewriting the total enthalpy Eq. (1.1.15) with respect the mixture velocity (use Eqs. (1.3.4) and (1.3.5)), I obtain:

$$\begin{aligned}\partial_t(\rho_\mathrm{m}h_\mathrm{m}) + \nabla\cdot[\rho_\mathrm{m}h_\mathrm{m}(\boldsymbol{u}_\mathrm{m}+\boldsymbol{v}_h)] + \partial_t(\rho_\mathrm{m}K_\mathrm{m}) + \nabla\cdot[\rho_\mathrm{m}K_\mathrm{m}(\boldsymbol{u}_\mathrm{m}+\boldsymbol{v}_K)] = \\ = \partial_t p + \nabla\cdot(\mathbb{T}\cdot\boldsymbol{u}_\mathrm{g} - \boldsymbol{q}) + \rho_\mathrm{m}(\boldsymbol{g}\cdot\boldsymbol{u}_\mathrm{m}) + \sum_{j\in\mathcal{J}} S_j(h_j + K_j)\,, \quad (1.3.15)\end{aligned}$$

where

$$\boldsymbol{v}_h = \boldsymbol{u}_\mathrm{r} + \frac{\sum_{\mathcal{J}} y_j h_j \boldsymbol{v}_j}{h_\mathrm{m}} = \frac{\sum_{\mathcal{J}} y_j(h_j - h_\mathrm{m})\boldsymbol{v}_j}{h_\mathrm{m}} \quad (1.3.16a)$$

$$\boldsymbol{v}_K = \boldsymbol{u}_\mathrm{r} + \frac{\sum_{\mathcal{J}} y_j K_j \boldsymbol{v}_j}{K_\mathrm{m}} = \frac{\sum_{\mathcal{J}} y_j(K_j - K_\mathrm{m})\boldsymbol{v}_j}{K_\mathrm{m}}\,, \quad (1.3.16b)$$

taking into account of the combined effect due to kinematic decoupling and difference between the enthalpy ($\boldsymbol{v}_h$) and kinetic energy ($\boldsymbol{v}_K$) of the mixture and of the jth specie.

The Eulerian model in "mixture" formulation

Summarizing, the [eulerian] model can be rearranged by using the mixture mass, velocity and enthalpy definitions:

$$\partial_t \rho_\mathrm{m} + \nabla \cdot (\rho_\mathrm{m} \boldsymbol{u}_\mathrm{m}) = S_\mathrm{m} \tag{1.3.17a}$$

$$\partial_t (\rho_\mathrm{m} y_i) + \nabla \cdot (\rho_\mathrm{m} \boldsymbol{u}_\mathrm{g} y_i) = 0\,, \quad i \in \mathcal{I} \tag{1.3.17b}$$

$$\partial_t (\rho_\mathrm{m} y_j) + \nabla \cdot [\rho_\mathrm{m} (\boldsymbol{u}_\mathrm{g} + \boldsymbol{v}_j) y_j] = S_j\,, \quad j \in \mathcal{J} \tag{1.3.17c}$$

$$\partial_t (\rho_\mathrm{m} \boldsymbol{u}_\mathrm{m}) + \nabla \cdot (\rho_\mathrm{m} \boldsymbol{u}_\mathrm{m} \otimes \boldsymbol{u}_\mathrm{m} + \rho_\mathrm{m} \mathbb{T}_\mathrm{r}) + \nabla p = \\ = \nabla \cdot \mathbb{T} + \rho_\mathrm{m} \boldsymbol{g} + \sum_{j \in \mathcal{J}} S_j \boldsymbol{u}_j \tag{1.3.17d}$$

$$\partial_t (\rho_\mathrm{m} h_\mathrm{m}) + \nabla \cdot [\rho_\mathrm{m} h_\mathrm{m} (\boldsymbol{u}_\mathrm{m} + \boldsymbol{v}_h)] = \\ = \partial_t p - \partial_t (\rho_\mathrm{m} K_\mathrm{m}) - \nabla \cdot [\rho_\mathrm{m} K_\mathrm{m} (\boldsymbol{u}_\mathrm{m} + \boldsymbol{v}_K)] + \\ + \nabla \cdot (\mathbb{T} \cdot \boldsymbol{u}_\mathrm{g} - \boldsymbol{q}) + \rho_\mathrm{m} (\boldsymbol{g} \cdot \boldsymbol{u}_\mathrm{m}) + \sum_{j \in \mathcal{J}} S_j (h_j + K_j) \tag{1.3.17e}$$

with ρ_m, y_i and y_j defined as for Eq. (1.2.2); $\boldsymbol{u}_\mathrm{r}$, $\mathbb{T}_\mathrm{r}$ and $\boldsymbol{v}_h\,, \boldsymbol{v}_K$ are defined in Eqs. (1.3.3), (1.3.11) and (1.3.16) respectively; p is given by the perfect gas law Eq. (1.1.20); $\mathbb{T}$ is defined in Eqs. (1.1.21), (1.1.22) and (1.1.25); C_m and R_m are the mixture specific heat and gas constant, given below Eq. (1.2.3d); and $\boldsymbol{q}$ is defined in Eq. (1.1.26).

Note that the explicit form of $\boldsymbol{v}_j$ has not be used for deriving Eqs. (1.3.17), which can therefore be used for any multiphase flow model with I phases moving with velocity $\boldsymbol{u}_\mathrm{g}$ and temperature T, and J phases each moving with velocity $\boldsymbol{u}_j = \boldsymbol{u}_\mathrm{g} + \boldsymbol{v}_j$ and temperature T_j. With respect to the [eulerian] model written in Eqs. (1.1.1), this formulation is not closed because the closure equations for $\boldsymbol{v}_j$ and T_j are missing. In the [dusty] model, a perfect local coupling between the phases is assumed, so that $\boldsymbol{v}_j = 0$ and $T_j = T_\mathrm{g}$. In this case Eqs. (1.3.17) are equivalent to Eqs. (1.2.3). In the next section and in Apps. 1.6.2 and 1.6.3, I show that it is possible to find an asymptotic approximation – valid for small Stokes number – to the particles momentum equation, giving $\boldsymbol{v}_j$ as a function of the mixture properties.

1.3.2 The equilibrium–Eulerian asymptotic solution for the particle momentum

In this section I review the equilibrium–Eulerian model, as the first-order asymptotic solution of the particles momentum equation valid for small Stokes number.

In order to obtain the dusty gas model, I did a formal limit $\tau_j \to 0$ for each solid phase j, keeping constant its bulk density $\rho_j = n\, m_j$. If the particles radius is allowed to grow, τ_j increases and the particle velocity can no longer be considered to be equal to the fluid velocity: y_j begins to exhibit spatial variations even if initially constant because $\boldsymbol{v}_j \neq 0$. Maxey [131], Ferry and Balachandar [71] developed a first-order approximation of the particles momentum balance equations (1.1.1d)

using the Stokes law (1.1.29) and a perturbative approach. The Lagrangian form of the particle momentum equations with the Stokes law is (use Eq. (1.1.3) in Eq. (1.1.1d)):

$$\partial_t \boldsymbol{u}_j + \boldsymbol{u}_j \cdot \nabla \boldsymbol{u}_j = \frac{1}{\tau_j}(\boldsymbol{u}_\mathrm{g} - \boldsymbol{u}_j) + \boldsymbol{g}\,. \tag{1.3.18}$$

In section 1.6.2, I derive formally $\boldsymbol{u}_j$ as a function of $\boldsymbol{u}_\mathrm{g}$, by using asymptotic expansion techniques. By defining

$$\boldsymbol{a}_\mathrm{g} = \partial_t \boldsymbol{u}_\mathrm{g} + \boldsymbol{u}_\mathrm{g} \cdot \nabla \boldsymbol{u}_\mathrm{g}\,, \tag{1.3.19}$$

and the terminal fallout velocity $\boldsymbol{w}_j = \tau_j \boldsymbol{g}$ (which I consider at the leading order), I obtain a correction to the particle velocity field up to first order in τ_j:

$$\boldsymbol{v}_j = \boldsymbol{u}_j - \boldsymbol{u}_\mathrm{g} = \boldsymbol{w}_j - \tau_j(\boldsymbol{a}_\mathrm{g} + \boldsymbol{v}_j \cdot \nabla \boldsymbol{u}_\mathrm{g}) + O(\tau_j^2)\,. \tag{1.3.20}$$

The explicit first-order expression $\boldsymbol{v}_j(\boldsymbol{u}_\mathrm{g})$ can be found in two ways:

- by substituting the term $\boldsymbol{v}_j \cdot \nabla \boldsymbol{u}_\mathrm{g}$ with $\boldsymbol{w}_j \cdot \nabla \boldsymbol{u}_\mathrm{g} + O(\tau_j)$, as in Ferry and Balachandar [71]:
$$\boldsymbol{v}_j = \boldsymbol{w}_j - \tau_j(\boldsymbol{a}_\mathrm{g} + \boldsymbol{w}_j \cdot \nabla \boldsymbol{u}_\mathrm{g})\,. \tag{1.3.21}$$
- by defining the matrix $\mathbb{G}_j = \mathbb{I} + \tau_j(\nabla \boldsymbol{u}_\mathrm{g})^\mathrm{T}$, as in Ferry et al. [74]:
$$\boldsymbol{v}_j = \mathbb{G}_j^{-1} \cdot (\boldsymbol{w}_j - \tau_j \boldsymbol{a}_\mathrm{g})\,. \tag{1.3.22}$$

This first-order model has been tested in a number of papers. Some of them are cited here: Ferry and Balachandar [71, 72], Ferry et al. [74], Ferry and Balachandar [73], Rani and Balachandar [158], Shotorban and Balachandar [177, 178], Cantero et al. [25], Boffetta et al. [13]. In what follows, I will always use model (1.3.22).

As above, also an explicit first-order expression $\boldsymbol{v}_j(\boldsymbol{u}_\mathrm{m})$ can be found. Indeed, by defining $\boldsymbol{a}_\mathrm{m} = \partial_t \boldsymbol{u}_\mathrm{m} + \boldsymbol{u}_\mathrm{m} \cdot \nabla \boldsymbol{u}_\mathrm{m}$, $\boldsymbol{w}_\mathrm{r} = -\sum_\mathcal{J} y_j \boldsymbol{w}_j$[†], and noting that $\boldsymbol{a}_\mathrm{g} = \boldsymbol{a}_\mathrm{m} + \boldsymbol{w}_\mathrm{r} \cdot \nabla \boldsymbol{u}_\mathrm{m} + O(\tau_j)$, I obtain:

$$\boldsymbol{v}_j = \boldsymbol{w}_j - \tau_j(\boldsymbol{a}_\mathrm{m} + \boldsymbol{w}_\mathrm{r} \cdot \nabla \boldsymbol{u}_\mathrm{m} + \boldsymbol{v}_j \cdot \nabla \boldsymbol{u}_\mathrm{m}) + O(\tau_j^2)\,, \tag{1.3.23}$$

implying the following modification to Eqs. (1.3.21) and (1.3.22), respectively:

$$\boldsymbol{v}_j = \begin{cases} \boldsymbol{w}_j - \tau_j(\boldsymbol{a}_\mathrm{m} + \boldsymbol{w}_\mathrm{r} \cdot \nabla \boldsymbol{u}_\mathrm{m} + \boldsymbol{w}_j \cdot \nabla \boldsymbol{u}_\mathrm{m}) \\ \mathbb{G}_j^{-1} \cdot [\boldsymbol{w}_j - \tau_j(\boldsymbol{a}_\mathrm{m} + \boldsymbol{w}_\mathrm{r} \cdot \nabla \boldsymbol{u}_\mathrm{m})], \quad \text{with} \quad \mathbb{G}_j = \mathbb{I} + \tau_j(\nabla \boldsymbol{u}_\mathrm{m})^\mathrm{T}\,. \end{cases} \tag{1.3.24}$$

Stokes time for particles with generic density

I finally remark that the assumption of heavy particles ($\beta_\rho \to 0$) can be relaxed [as also shown in 71], and the Stokes time becomes:

$$\tau_j \to \tau_j(1 - \beta_\rho) = \frac{(\hat{\rho}_j - \hat{\rho}_\mathrm{g})\, d_j^2}{18\mu\, \phi_\mathrm{c}}\,. \tag{1.3.25}$$

From this expression, it is worth noting that the first-order correction term changes sign moving from heavy particles (e.g. ash in air) to light particles (e.g. bubbles in water): in a turbulent flow, heavy particles tend to escape from eddies while light particles tend to be caught by them (preferential concentration).

[†]recall that $\mathrm{d}_{\boldsymbol{u}_j} y_j = 0$, thus $\mathrm{d}_{\boldsymbol{u}_j} \boldsymbol{w}_\mathrm{r} = 0$ because $\boldsymbol{w}_j$ is considered as a constant at the leading order, see Sect. 1.6.2.

Thermal decoupling

As pointed out in Eq. (1.1.40) and below, in the physical regime selected here, thermal Stokes time is of the same order of magnitude of the kinematic one. However, this regime has been thoroughly analyzed in the incompressible case by Ferry and Balachandar [73], demonstrating that the error made by assuming thermal equilibrium is at least one order of magnitude smaller than that on the momentum equation (at equal Stokes number), thus justifying the limit $T_j \to T_\mathrm{g} = T$ as already done for the dusty gas model.

Under this thermal coupling approximation, the mixture enthalpy defined in Eq. (1.3.13) can be easily written in terms of T:

$$h_\mathrm{m} = \sum_{\mathcal{J}} y_i h_i + \sum_{\mathcal{J}} y_j h_j = C_\mathrm{m} T + \frac{p}{\rho_\mathrm{m}} \tag{1.3.26}$$

$$C_\mathrm{m} = \sum_{\mathcal{J}} y_i C_{\mathrm{v},i} + \sum_{\mathcal{J}} y_j C_j \,. \tag{1.3.27}$$

I will refer to this model as [eqEu]. They are the PDEs implemented in the ASHEE numerical model.

Discussion

I notice that in the Navier-Stokes equations it is critical to accurately take into account the non-linear terms contained by the conservative derivative $\partial_t(\rho\boldsymbol{u}) + \nabla\cdot(\rho\boldsymbol{u}\otimes\boldsymbol{u})$ because they are the origin of the major difficulties in turbulence modeling. A large advantage of the multiphase models written in formulation (1.3.17) is that the drag ($\sum_\mathcal{J} \boldsymbol{f}_j$) and heat exchange ($\sum_\mathcal{J} \mathrm{Q}_j$) terms have been absorbed into the conservative derivatives for the mixture. This fact allows the numerical solver to implicitly and accurately solve the particles contribution on mixture momentum and energy, using the same numerical techniques developed in Computational Fluid Dynamics for the Navier-Stokes equations.

The new kinematic decoupling terms proportional to $\mathbb{T}_\mathrm{r}$, $\boldsymbol{v}_h$ and $\boldsymbol{v}_K$ arising in the momentum and enthalpy Eqs. (1.3.17d) and (1.3.17e) are easier to handle numerically than the drag and heat exchange ones. Indeed, in the small Stokes number (strong coupling) two-way regime, the latter terms are big and important, while the former are small (first-order). More insight about those new terms can be obtained writing them in the forms (cf. Eq. (1.3.5)):

$$\sum_{j\in\mathcal{J}} y_j \boldsymbol{v}_j(\mathfrak{f}_j - \mathfrak{f}_\mathrm{m}) = (1-y_\mathrm{s})\sum_{j\in\mathcal{J}} y_j \boldsymbol{v}_j(\mathfrak{f}_j - \mathfrak{f}_\mathrm{g}) + \sum_{j,k\in\mathcal{J}} y_j y_k \boldsymbol{v}_j(\mathfrak{f}_j - \mathfrak{f}_k)\,, \tag{1.3.28}$$

with $\mathfrak{f} = \boldsymbol{u}, h, K$, respectively. Four observations are noteworthy: 1) they are first-order in y_s (recall that $y_j \le y_\mathrm{s}$); 2) they are first-order in the decoupling velocity $|\boldsymbol{v}_j|$; 3) they are first-order with respect $(1-y_\mathrm{s})$ in the mono-disperse case $J=1$, or when there is $j\in\mathcal{J}$ such that $y_\mathrm{s} - y_j \ll 1$; 4) they are first-order in the difference between the particle and the mixture property $(\mathfrak{f}_j - \mathfrak{f}_\mathrm{m})$. Thus, $\mathbb{T}_\mathrm{r}$ is second-order in the decoupling velocity $|\boldsymbol{v}_j|$, because $|\mathfrak{f}_j - \mathfrak{f}_\mathrm{m}| = |\boldsymbol{u}_j - \boldsymbol{u}_\mathrm{m}| = O(|\boldsymbol{v}_j|)$. For this reason Ferry and Balachandar [71] neglected it. However, I keep this term

because of the presence of the settling velocity $\boldsymbol{w}_j$ in $\boldsymbol{v}_j$, which is at the leading order. For the same reason, I keep the term containing $\boldsymbol{v}_K$. I keep also $\boldsymbol{v}_h$ because $(h_j - h_\mathrm{m})$ can in principle be at the leading order.

The dusty gas and equilibrium–Eulerian models in mixture formulation (1.3.17) are thus best suited for solving multiphase systems in which the particles are strongly coupled with the carrier fluid and the bulk density of the particles is not negligible with respect to that of the fluid.

1.4 LES modeling

Turbulence is a multiscale physical phenomenon involving many different scales from the scale of the flow domain to the scale of the smallest eddy of the turbulent field. In order to model it, numerical simulations are needed, where the continuous space-time domain is mapped into a discrete one with $N_{d.o.f.}$ number of degree of freedom. In this section the PDEs of the `ASHEE` model (1.3.17) are filtered in order to separate the *large scales* from the the *subgrid scales*. While the former degrees of freedom are directly calculated, in LES the latter are modeled. In particular, in this thesis I will use selected subgrid-scale (SGS) models. They are presented in section.

1.4.1 Equations filtering

Let a filtered or large-scale flow quantity be denoted by an overbar (δ is the filter scale):

$$\bar{\mathfrak{f}} = \int_\Omega G(\boldsymbol{x} - \boldsymbol{x}'; \delta)\mathfrak{f}(\boldsymbol{x}')\mathrm{d}\boldsymbol{x}' \,. \tag{1.4.1}$$

Some example of LES filters $G(\boldsymbol{x}; \delta)$ used in compressible turbulence are reviewed in Garnier et al. [80]. Moreover, in compressible turbulence it is defined another filter, called the Favre filter:

$$\tilde{\mathfrak{f}} = \frac{\overline{\rho_\mathrm{m}\mathfrak{f}}}{\bar{\rho}_\mathrm{m}} \,. \tag{1.4.2}$$

Firstly, this filter is applied to the equilibrium–Eulerian model fundamental equation (1.3.20) modified as follows:

$$\boldsymbol{u}_j = \boldsymbol{u}_\mathrm{g} + \boldsymbol{w}_j - \tau_j(\partial_t \boldsymbol{u}_\mathrm{m} + \boldsymbol{u}_\mathrm{m} \cdot \nabla \boldsymbol{u}_\mathrm{m} + (\boldsymbol{w}_\mathrm{r} + \boldsymbol{u}_j - \boldsymbol{u}_\mathrm{g}) \cdot \nabla \boldsymbol{u}_\mathrm{m}) + O(\tau_j^2) \tag{1.4.3}$$

moving the new second order terms into $O(\tau_j^2)$, using $\mathrm{d}_{\boldsymbol{u}_j} y_j = 0$, defining:

$$\boldsymbol{w}_\mathrm{r} = -\sum_j y_j \boldsymbol{w}_j \,, \tag{1.4.4}$$

and recalling that at the leading order $\tilde{\boldsymbol{u}}_\mathrm{m} \simeq \tilde{\boldsymbol{u}}_\mathrm{g} - \tilde{\boldsymbol{w}}_\mathrm{r}$. Multiplying the new expression for $\boldsymbol{u}_j$ by ρ_m and Favre-filtering, at the first order I obtain:

$$\tilde{\boldsymbol{u}}_j = \tilde{\boldsymbol{u}}_\mathrm{g} + \tilde{\mathbb{G}}^{-1} \cdot \left[\boldsymbol{w}_j - \tau_j(\tilde{\boldsymbol{a}}_\mathrm{m} + \tilde{\boldsymbol{w}}_\mathrm{r} \cdot \nabla \tilde{\boldsymbol{u}}_\mathrm{m}) - \frac{\tau_j}{\bar{\rho}_\mathrm{m}} \nabla \cdot \mathbb{B} \right] \,, \tag{1.4.5}$$

where I have used $\tilde{a}_\mathrm{m} = \partial_t \tilde{\boldsymbol{u}}_\mathrm{m} + \tilde{\boldsymbol{u}}_\mathrm{m} \cdot \nabla \tilde{\boldsymbol{u}}_\mathrm{m}$, $\tilde{\tau}_j = \tau_j$ and consequently $\tilde{\boldsymbol{w}}_j = \boldsymbol{w}_j$ because the Stokes time changes only at the large scale and it can be considered constant at the filter scale. Moreover, I have defined the subgrid-scale Reynolds stress tensor:

$$\mathbb{B} = \bar{\rho}_\mathrm{m}(\widetilde{\boldsymbol{u}_\mathrm{m} \otimes \boldsymbol{u}}_\mathrm{m} - \tilde{\boldsymbol{u}}_\mathrm{m} \otimes \tilde{\boldsymbol{u}}_\mathrm{m}) \,. \tag{1.4.6}$$

As discussed and tested in Shotorban and Balachandar [178], the subgrid terms can be considered $O(\tau_j)$ and neglected when it is multiplied by first order terms. I will use this approximation in what follows referring to it as the *Balachandar approximation*.

I recall here the Boussinesq eddy viscosity hypothesis:

$$\mathbb{B} = \frac{2}{\mathsf{d}} \bar{\rho}_\mathrm{m} K_\mathrm{t} \mathbb{I} - 2\mu_\mathrm{t} \tilde{\mathbb{S}}_\mathrm{m} \,, \tag{1.4.7}$$

where the deviatoric part of the subgrid stress tensor can be modelled with an eddy viscosity μ_t times the rate-of-shear tensor $\mathbb{S}_\mathrm{m}$ (cf. Eq. (1.1.22) for its definition with $\boldsymbol{u}_\mathrm{f}$ in place of $\boldsymbol{u}_\mathrm{m}$). The first term on the right hand side of the previous equation is the isotropic part of the subgrid-scale tensor, proportional to the subgrid-scale kinetic energy K_t. While in incompressible turbulence the latter term is absorbed into the pressure, it must be modelled for compressible flows [cf. 136, 230]. Ducros et al. [58] showed another way to treat this term by absorbing it into a new *macropressure* and *macrotemperature* [cf. also 116, 123]. I recall here also the eddy diffusivity viscosity model [cf. also 136]: any scalar $\mathfrak{f}$ transported by $\boldsymbol{u}_\mathrm{m}$ generates a subgrid-scale vector that can be modeled with the large eddy variables. I have:

$$\bar{\rho}_\mathrm{m}(\widetilde{\boldsymbol{u}_\mathrm{m}\mathfrak{f}} - \tilde{\boldsymbol{u}}_\mathrm{m}\tilde{\mathfrak{f}}) = -\frac{\mu_\mathrm{t}}{\mathrm{Pr}_\mathrm{t}} \nabla \tilde{\mathfrak{f}} \,, \tag{1.4.8}$$

where Pr_t is the subgrid-scale turbulent Prandtl number.

The Favre filter defined in Eq. (1.4.2) is applied to Eqs. (1.3.17) [for the application of the Favre filter to the compressible Navier-Stokes equations cf. 62, 136, 80], obtaining:

$$\partial_t \bar{\rho}_\mathrm{m} + \nabla \cdot (\bar{\rho}_\mathrm{m} \tilde{\boldsymbol{u}}_\mathrm{m}) = \tilde{S}_\mathrm{m} \tag{1.4.9a}$$

$$\partial_t (\bar{\rho}_\mathrm{m} \tilde{y}_i) + \nabla \cdot (\bar{\rho}_\mathrm{m} \tilde{\boldsymbol{u}}_\mathrm{g} \tilde{y}_i) = -\nabla \cdot \mathcal{Y}_i \,, \quad i \in \mathcal{I} \tag{1.4.9b}$$

$$\partial_t (\bar{\rho}_\mathrm{m} \tilde{y}_j) + \nabla \cdot [\bar{\rho}_\mathrm{m} (\tilde{\boldsymbol{u}}_\mathrm{g} + \tilde{\boldsymbol{v}}_j) \tilde{y}_j] = \tilde{S}_j - \nabla \cdot \mathcal{Y}_j \,, \quad j \in \mathcal{J} \tag{1.4.9c}$$

$$\begin{aligned} &\partial_t (\bar{\rho}_\mathrm{m} \tilde{\boldsymbol{u}}_\mathrm{m}) + \nabla \cdot (\bar{\rho}_\mathrm{m} \tilde{\boldsymbol{u}}_\mathrm{m} \otimes \tilde{\boldsymbol{u}}_\mathrm{m} + \bar{\rho}_\mathrm{m} \tilde{\mathbb{T}}_\mathrm{r}) + \nabla \bar{p} = \\ &\qquad = \nabla \cdot \tilde{\mathbb{T}} + \bar{\rho}_\mathrm{m} \boldsymbol{g} + \sum_{j \in \mathcal{J}} \tilde{S}_j (\tilde{\boldsymbol{u}}_\mathrm{g} + \tilde{\boldsymbol{v}}_j) - \nabla \cdot \mathbb{B} \end{aligned} \tag{1.4.9d}$$

$$\begin{aligned} &\partial_t (\bar{\rho}_\mathrm{m} \tilde{h}_\mathrm{m}) + \nabla \cdot [\bar{\rho}_\mathrm{m} (\tilde{\boldsymbol{u}}_\mathrm{m} + \tilde{\boldsymbol{v}}_h) \tilde{h}_\mathrm{m}] = \\ &\quad = \partial_t \bar{p} - \partial_t (\bar{\rho}_\mathrm{m} \tilde{K}_\mathrm{m}) - \nabla \cdot [\bar{\rho}_\mathrm{m} (\tilde{\boldsymbol{u}}_\mathrm{m} + \tilde{\boldsymbol{v}}_K) \tilde{K}_\mathrm{m}] + \\ &\qquad + \nabla \cdot (\tilde{\mathbb{T}} \cdot \tilde{\boldsymbol{u}}_\mathrm{g} - \tilde{\boldsymbol{q}}) + \bar{\rho}_\mathrm{m} (\boldsymbol{g} \cdot \tilde{\boldsymbol{u}}_\mathrm{m}) + \sum_{j \in \mathcal{J}} \tilde{S}_j (\tilde{h}_j + \tilde{K}_j) - \nabla \cdot (\mathcal{Q} + \mathcal{Q}_K) \,, \end{aligned} \tag{1.4.9e}$$

where

$$\mathcal{Y}_i = \bar{\rho}_\mathrm{m}(\widetilde{y_i \boldsymbol{u}_\mathrm{g}} - \tilde{y}_i \tilde{\boldsymbol{u}}_\mathrm{g}) = -\frac{\mu_\mathrm{t}}{\mathrm{Pr}_\mathrm{t}} \nabla \tilde{y}_i \tag{1.4.10a}$$

$$\mathcal{Y}_j = \bar{\rho}_\mathrm{m}(\widetilde{y_j \boldsymbol{u}_j} - \tilde{y}_i \tilde{\boldsymbol{u}}_j) = -\frac{\mu_\mathrm{t}}{\mathrm{Pr}_\mathrm{t}} \nabla \tilde{y}_j \tag{1.4.10b}$$

$$\mathbb{B} = \bar{\rho}_\mathrm{m}(\widetilde{\boldsymbol{u}_\mathrm{m} \otimes \boldsymbol{u}_\mathrm{m}} - \tilde{\boldsymbol{u}}_\mathrm{m} \otimes \tilde{\boldsymbol{u}}_\mathrm{m}) = \frac{2}{\mathsf{d}} \bar{\rho}_\mathrm{m} K_\mathrm{t} \mathbb{I} - 2\mu_\mathrm{t} \tilde{\mathbb{S}}_\mathrm{m} \tag{1.4.10c}$$

$$\mathcal{Q} = \bar{\rho}_\mathrm{m}(\widetilde{h_\mathrm{m} \boldsymbol{u}_\mathrm{m}} - \tilde{h}_\mathrm{m} \tilde{\boldsymbol{u}}_\mathrm{m}) = -\frac{\mu_\mathrm{t}}{\mathrm{Pr}_\mathrm{t}} \nabla \tilde{h}_\mathrm{m} \tag{1.4.10d}$$

$$\mathcal{Q}_K = \bar{\rho}_\mathrm{m}(\widetilde{K_\mathrm{m} \boldsymbol{u}_\mathrm{m}} - \tilde{K}_\mathrm{m} \tilde{\boldsymbol{u}}_\mathrm{m}) = -\frac{\mu_\mathrm{t}}{\mathrm{Pr}_\mathrm{t}} \nabla \tilde{K}_\mathrm{m}\,, \tag{1.4.10e}$$

are respectively: the subgrid eddy diffusivity vector of the ith phase; of the jth phase; the subgrid-scale stress tensor; the diffusivity vector of the enthalpy and of the kinetic energy. Other approximations have been used to derive the former LES model: the viscous and source terms in momentum and energy equations, and the pressure-dilatation and conduction terms in the energy equations are all non-linear terms and I here treat them as done by Erlebacher et al. [62], Moin et al. [136]. The subgrid terms corresponding to the former non-linear terms could be neglected so that, for example, $\overline{p \nabla \cdot \boldsymbol{u}_\mathrm{g}} \simeq \bar{p} \nabla \cdot \tilde{\boldsymbol{u}}_\mathrm{g}$. In particular, this term has been neglected also in presence of shocks [82, cf.]. I refer to Vreman [210] for an *a priori* and *a posteriori* analysis of all the neglected terms of the compressible Navier-Stokes equations. Moreover, in the `ASHEE` model the mixture specific heat C_m and the mixture gas constant R_m vary in the domain because y_i and y_j vary. Thus, also the following approximations should be done, coherently with the other approximations used: $\tilde{h}_\mathrm{m} = \widetilde{C_\mathrm{m} T + p/\rho_\mathrm{m}} \simeq \tilde{C}_\mathrm{m} \tilde{T} + \bar{p}/\bar{\rho}_\mathrm{m}$ and $\widetilde{R_\mathrm{m} T} \simeq \tilde{R}_\mathrm{m} \tilde{T}$.

The model written in Eqs. (1.4.9) is actually the one which has been discretized. The discretization strategy can be found in Sect. 5.1.

In the next sections I discuss various subgrid models, both static and dynamic. In what follows, I will use the notation [noM] when no subgrid model is applied (so that $\mu_\mathrm{t} = K_\mathrm{t} = 0$).

1.4.2 Compressible Smagorinsky model – [sma]

As described in Yoshizawa [231], Fureby [79], the compressible Smagorinsky model assumes that the the subgrid viscosity μ_t and energy dissipation ϵ_t, defined as [cf. 152, 80, 36] [4]:

$$K_\mathrm{t} = \frac{1}{2}\left(\widetilde{|\boldsymbol{u}_\mathrm{m}|^2} - |\tilde{\boldsymbol{u}}_\mathrm{m}|^2\right) \tag{1.4.11}$$

$$\epsilon_\mathrm{t} = \frac{2\mu}{\bar{\rho}_\mathrm{m}}\left(\widetilde{\mathbb{S}_\mathrm{m} : \mathcal{D}_\mathrm{m}} - \tilde{\mathbb{S}}_\mathrm{m} : \tilde{\mathcal{D}}_\mathrm{m}\right)\,; \tag{1.4.12}$$

[4] Note that to obtain the balance equation for K_t the average of the scalar product of the velocity and the momentum equations minus the product of this averaged quantities must be done.

can be modelled as follows [cf. 85]:

$$\mu_{\mathrm{t}} = c_k \bar{\rho}_{\mathrm{m}} \delta \sqrt{K_{\mathrm{t}}} \tag{1.4.13}$$

$$\epsilon_{\mathrm{t}} = c_e K_{\mathrm{t}}^{\frac{3}{2}} / \delta \,, \tag{1.4.14}$$

with c_k and c_e two constants to be determined and δ the filter scale. By assuming the local equilibrium

$$\tilde{\mathcal{D}}_{\mathrm{m}} : \mathbb{B} + \bar{\rho}_{\mathrm{m}}\, \epsilon_{\mathrm{t}} = 0 \,, \tag{1.4.15}$$

I obtain an equation in $\sqrt{K_{\mathrm{t}}}$:

$$\frac{c_e}{\delta} K_{\mathrm{t}} + \frac{2}{\mathsf{d}} \nabla \cdot \tilde{\boldsymbol{u}}_{\mathrm{m}} \sqrt{K_{\mathrm{t}}} - 2 c_k \delta\, \tilde{\mathcal{D}}_{\mathrm{m}} : \tilde{\mathbb{S}}_{\mathrm{m}} = 0 \,. \tag{1.4.16}$$

If the flow is incompressible, or if the compressible part of the previous equation (that proportional to $\nabla \cdot \tilde{\boldsymbol{u}}_{\mathrm{m}}$) can be neglected, I recover the classical Yoshizawa and Smagorinsky model [cf. 180, 230]:

$$\bar{\rho}_{\mathrm{m}}\, K_{\mathrm{t}} = \frac{2 c_k \delta^2}{c_e} \bar{\rho}_{\mathrm{m}}\, |\tilde{\mathcal{D}}_{\mathrm{m}}|^2 \tag{1.4.17}$$

$$\mu_{\mathrm{t}} = \sqrt{\frac{2 c_k^3}{c_e}} \bar{\rho}_{\mathrm{m}} \delta^2\, |\tilde{\mathcal{D}}_{\mathrm{m}}| \,, \tag{1.4.18}$$

with the Smagorinsky constant $C_{\mathrm{S}} = \sqrt[4]{c_k^3 / c_e}$. On the other hand, for the compressible version of this model, the second degree Eq. (1.4.16) must be resolved in order to find $\sqrt{K_{\mathrm{t}}}$ and, consequently, μ_{t}. Substituting this result into Eq. (1.4.8) I have a model for all the considered subgrid terms.

Summarizing, this LES model has three constants: c_k, c_e and Pr_{t}. In what follows, when referring to the Smagorinsky model, I will use the following values, respectively: 0.094, 1.048, 1 [cf. 79]. I will refer to this subgrid model as [sma].

1.4.3 Subgrid-scale K-equation model – [oneEqEddy]

Following Yoshizawa [231], Fureby [79], Chai and Mahesh [36] the local equilibrium hypothesis can be released and K_{t} can be found by solving an *a posteriori* balance equation:

$$\partial_t(\bar{\rho}_{\mathrm{m}} K_{\mathrm{t}}) + \nabla \cdot (\bar{\rho}_{\mathrm{m}} \boldsymbol{u}_{\mathrm{m}} K_{\mathrm{t}}) - \nabla \cdot ((\mu + \mu_{\mathrm{t}}) \nabla K_{\mathrm{t}}) = -\tilde{\mathcal{D}}_{\mathrm{m}} : \mathbb{B} - \bar{\rho}_{\mathrm{m}}\, \epsilon_{\mathrm{t}} \,, \tag{1.4.19}$$

where the right hand side is the same of the previous paragraph.

This model is the compressible counterpart of the Turbulent Kinetic Energy (TKE) model [cf. 35]. I will refer to this subgrid model as [oneEqEddy].

1.4.4 WALE model – [wale]

The wall-adapting local eddy-viscosity (WALE) subgrid model, introduced by Nicoud and Ducros [142], accounts for the effects of both the strain and the rotation

rate of the smallest resolved turbulent fluctuations. It shows also a good behavior near the walls, so it is used in the literature for the large eddy simulations of complex geometries [cf. 123]. In this model, the subgrid viscosity is written in the generic form $\mu_\mathrm{t} = \bar{\rho}(c_w\,\delta)^2\mathcal{O}(\boldsymbol{x},t)$ and the operator $\mathcal{O}$ is chosen in order to fulfil the following major properties: it should be invariant for translations and rotations; it should be easily calculated for any domain grid; it should depend on both the strain and rotation rates; it well behaves near the walls, going naturally to zero in the right way. Nicoud and Ducros [142] found that such an operator can be written as follows:

$$\mu_\mathrm{t} = \bar{\rho}_\mathrm{m}(c_w\delta)^2\frac{|\mathcal{V}_\mathrm{m}|^3}{|\tilde{\mathcal{D}}_\mathrm{m}|^5 + |\mathcal{V}_\mathrm{m}|^{\frac{5}{2}}} \equiv \bar{\rho}_\mathrm{m}c_w^2\delta^2\,\tilde{\mathcal{W}}_\mathrm{m}\,, \tag{1.4.20}$$

where $\mathcal{V}_\mathrm{m}$ is the symmetric and deviatoric part of the velocity gradient:

$$\mathcal{V}_\mathrm{m} = \mathrm{dev}\left(\mathrm{Sym}\left(\nabla\tilde{\boldsymbol{u}}_\mathrm{m}\cdot\nabla\tilde{\boldsymbol{u}}_\mathrm{m}\right)\right)\,, \tag{1.4.21}$$

and $\tilde{\mathcal{W}}_\mathrm{m}$ is the WALE model operator (as a function of $\tilde{\boldsymbol{u}}_\mathrm{m}$), which contains both the strain and rotation rate. The Yoshizawa model (Eq. (1.4.13)) and the eddy diffusivity model (Eq. (1.4.8)) close the system. I will refer to this subgrid model as [wale].

1.4.5 Moin dynamical model – [moin]

Moin et al. [136] applied the ideas of Bardina et al. [5] and Germano et al. [84] to the compressible Navier-Stokes equations. The key idea of these models (the dynamics subgrid models) is to use the spectral information contained into the resolved fields to dynamically quantify the constants appearing in the LES model. In order to achieve this objective, a test filter $\hat{(\cdot)}$ of width $\hat{\delta}$ must be defined and a key assumption must be made: the test-filtered subgrid terms can be modelled using the same formal expression used for the Favre-filtered subgrid quantities. In other terms [cf. 36], for any subgrid term of the form $a = \widetilde{\alpha\beta} - \tilde{\alpha}\tilde{\beta}$ I assume that, on the test-filter level, $A = \widehat{\widetilde{\alpha\beta}} - \hat{\tilde{\alpha}}\hat{\tilde{\beta}}$ holds. Germano's identity is $L = A - \hat{a} = \widehat{\tilde{\alpha}\tilde{\beta}} - \hat{\tilde{\alpha}}\hat{\tilde{\beta}}$ depending only on resolved quantity. If the subgrid model can be written $a = c_a m$, than at the test-filter level I have $A = c_a M$, with the same constant and M that takes the same functional form of m but with the test-filtered quantities. Germano's identity become $L = c_a(M - \hat{m})$. Since both the left and right hand side are computable by resolved variables filtering, c_a can be obtained dynamically from the latter equation. In order to avoid computational instabilities, regularization through least square error minimization and volume averaging is needed [cf. 119, and discussion below]. In this thesis I will use an average over the cell faces to compute the filter $\hat{(\cdot)} = \langle\cdot\rangle$, so that $\hat{\delta}/\delta = 2$, the optimal value found by Spyropoulos and Blaisdell [185].

Moin et al. [136] used Eqs. (1.4.17), (1.4.18) and (1.4.8) to model respectively the subgrid kinetic energy, the eddy viscosity and the eddy diffusivity. Applying

the procedure I described above and defining $c_D = \sqrt{2c_k^3/c_e}$, I obtain:

$$\operatorname{dev}(\mathbb{B}) = \operatorname{dev}(\overline{\rho_\mathrm{m}\boldsymbol{u}_\mathrm{m}\otimes\boldsymbol{u}_\mathrm{m}} - \overline{\rho_\mathrm{m}\boldsymbol{u}_\mathrm{m}}\otimes\overline{\rho_\mathrm{m}\boldsymbol{u}_\mathrm{m}}/\bar\rho_\mathrm{m}) = -2c_D\bar\rho_\mathrm{m}\delta^2|\tilde{\mathcal{D}}_\mathrm{m}|\,\tilde{\mathbb{S}}_\mathrm{m} \tag{1.4.22}$$

$$\operatorname{dev}\left(\widehat{\overline{\rho_\mathrm{m}\boldsymbol{u}_\mathrm{m}\otimes\boldsymbol{u}_\mathrm{m}}} - \widehat{\overline{\rho_\mathrm{m}\boldsymbol{u}_\mathrm{m}}}\otimes\widehat{\overline{\rho_\mathrm{m}\boldsymbol{u}_\mathrm{m}}}/\hat{\bar\rho}_\mathrm{m}\right) = -2c_D\hat{\bar\rho}_\mathrm{m}\hat\delta^2|\hat{\tilde{\mathcal{D}}}_\mathrm{m}|\,\hat{\tilde{\mathbb{S}}}_\mathrm{m}\,. \tag{1.4.23}$$

The difference between the latter equation and the average of the former gives rise to the deviatoric part of the Leonard stresses ($\operatorname{dev}(\mathcal{L})$):

$$\operatorname{dev}\left(\bar\rho_\mathrm{m}\widehat{\tilde{\boldsymbol{u}}_\mathrm{m}\otimes\tilde{\boldsymbol{u}}_\mathrm{m}} - \widehat{\bar\rho_\mathrm{m}\tilde{\boldsymbol{u}}_\mathrm{m}}\otimes\widehat{\bar\rho_\mathrm{m}\tilde{\boldsymbol{u}}_\mathrm{m}}/\hat{\bar\rho}_\mathrm{m}\right) = 2c_D\delta^2\left(\bar\rho_\mathrm{m}\widehat{|\tilde{\mathcal{D}}_\mathrm{m}|\,\tilde{\mathbb{S}}_\mathrm{m}} - \frac{\hat\delta^2}{\delta^2}\,\hat{\bar\rho}_\mathrm{m}|\hat{\tilde{\mathcal{D}}}_\mathrm{m}|\,\hat{\tilde{\mathbb{S}}}_\mathrm{m}\right) \equiv 2c_D\mathcal{M}\,. \tag{1.4.24}$$

This tensor equation is overdetermining c_D. Lilly [119] proposed to find c_D in order to minimize the least square error $\Delta_\mathrm{Lilly}(c_D) = |\operatorname{dev}(\mathcal{L}) - 2c_D\mathcal{M}|^2$. By imposing $\Delta'_\mathrm{Lilly} = 0$, I obtain

$$c_D = \frac{1}{2}\frac{\operatorname{dev}(\mathcal{L}) : \mathcal{M}}{\mathcal{M} : \mathcal{M}}\,. \tag{1.4.25}$$

Using the fact that $\mathcal{M}$ is traceless and averaging this result thorough the spatial filter $\langle\cdot\rangle$ [cf. 84, 136], I finally obtain:

$$c_D = \frac{1}{2}\frac{\langle\mathcal{L} : \mathcal{M}\rangle}{\langle\mathcal{M} : \mathcal{M}\rangle}\,. \tag{1.4.26}$$

Moving to the subgrid-scale kinetic energy, I define $c_I = c_k/c_e$ and the test-filter level model for the kinetic energy

$$\hat{\bar\rho}_\mathrm{m}\,\mathcal{K}_\mathrm{t} = \frac{1}{2}\left(\widehat{\overline{\rho_\mathrm{m}|\boldsymbol{u}_\mathrm{m}|^2}} - |\widehat{\bar\rho_\mathrm{m}\tilde{\boldsymbol{u}}_\mathrm{m}}|^2/\hat{\bar\rho}_\mathrm{m}\right) = 2c_I\hat\delta^2\hat{\bar\rho}_\mathrm{m}|\hat{\tilde{\mathcal{D}}}_\mathrm{m}|^2\,, \tag{1.4.27}$$

so that from Eqs. (1.4.11) and (1.4.17), I obtain:

$$\hat{\bar\rho}_\mathrm{m}\mathcal{K}_\mathrm{t} - \widehat{\bar\rho_\mathrm{m}K_\mathrm{t}} = \frac{1}{2}\left(\widehat{\bar\rho_\mathrm{m}|\tilde{\boldsymbol{u}}_\mathrm{m}|^2} - |\widehat{\bar\rho_\mathrm{m}\tilde{\boldsymbol{u}}_\mathrm{m}}|^2/\hat{\bar\rho}_\mathrm{m}\right) = 2c_I\delta^2\left(\frac{\hat\delta^2}{\delta^2}\hat{\bar\rho}_\mathrm{m}|\hat{\tilde{\mathcal{D}}}_\mathrm{m}|^2 - \widehat{\bar\rho_\mathrm{m}|\tilde{\mathcal{D}}_\mathrm{m}|^2}\right) \equiv c_I\,\mathcal{F}\,, \tag{1.4.28}$$

and

$$c_I = \frac{\langle(\hat{\bar\rho}_\mathrm{m}\mathcal{K}_\mathrm{t} - \widehat{\bar\rho_\mathrm{m}K_\mathrm{t}})\,\mathcal{F}\rangle}{\langle\mathcal{F}^2\rangle}\,. \tag{1.4.29}$$

Finally, the eddy diffusivity model Eq. (1.4.8) with Eq. (1.4.18) gives:

$$\overline{\rho_\mathrm{m}\boldsymbol{u}_\mathrm{m}h_\mathrm{m}} - \overline{\rho_\mathrm{m}\boldsymbol{u}_\mathrm{m}}\,\overline{\rho_\mathrm{m}h_\mathrm{m}}/\bar\rho_\mathrm{m} = -c_h\delta^2\bar\rho_\mathrm{m}|\tilde{\mathcal{D}}_\mathrm{m}|\nabla\tilde h_\mathrm{m}\,, \tag{1.4.30}$$

with $c_h = c_I/\mathrm{Pr_t}$, from which:

$$\mathcal{P} \equiv \bar{\rho}_\mathrm{m}\widehat{\tilde{\boldsymbol{u}}_\mathrm{m}\tilde{h}_\mathrm{m}} - \widehat{\bar{\rho}_\mathrm{m}\tilde{\boldsymbol{u}}_\mathrm{m}}\,\widehat{\bar{\rho}_\mathrm{m}\tilde{h}_\mathrm{m}}/\hat{\bar{\rho}}_\mathrm{m} = c_h\delta^2\left(\bar{\rho}_\mathrm{m}|\widehat{\tilde{\mathcal{D}}_\mathrm{m}|\nabla\tilde{h}_\mathrm{m}} - \frac{\hat{\delta}^2}{\delta^2}\hat{\bar{\rho}}_\mathrm{m}\,|\hat{\tilde{\mathcal{D}}}_\mathrm{m}|\nabla\hat{\tilde{h}}_\mathrm{m}\right) \equiv c_h\mathcal{R}\,. \tag{1.4.31}$$

Again, after regularization I obtain:

$$c_h = \frac{\langle\mathcal{P}\,\mathcal{R}\rangle}{\langle\mathcal{R}^2\rangle}\,. \tag{1.4.32}$$

In order to increase stability and to fulfill the entropy second principle of thermodynamics I bound the dynamical coefficients with both an upper and lower limits. In particular, I choose the coefficients $c.$ so that:

$$c. < 100 \tag{1.4.33}$$
$$\mu_\mathrm{t} + \mu \geq 0 \tag{1.4.34}$$
$$K_\mathrm{t} > 0 \tag{1.4.35}$$
$$\frac{\mu_\mathrm{t}\tilde{C}_\mathrm{m}}{\mathrm{Pr_t}} + k_\mathrm{g} \geq 0\,. \tag{1.4.36}$$

In this way, the effect of the back-scatter are taken into account (negative subgrid diffusion) without breaking the second principle of thermodynamics. I will refer to this subgrid model as [moin].

1.4.6 Dynamical Smagorinsky model – [dynSma]

I want here to follow the same approach used by Moin et al. [136] for determining dynamically the constants of the model described in Sec. 1.4.2. As described in the previous section, the first assumption is that the test-filtered subgrid terms can be modeled as the Favre-filtered one. Using this hypothesis for the deviatoric part of the subgrid-stress tensor, I have:

$$\mathrm{dev}\,(\overline{\rho_\mathrm{m}\boldsymbol{u}_\mathrm{m}\otimes\boldsymbol{u}_\mathrm{m}} - \overline{\rho_\mathrm{m}\boldsymbol{u}_\mathrm{m}}\otimes\overline{\rho_\mathrm{m}\boldsymbol{u}_\mathrm{m}}/\bar{\rho}_\mathrm{m}) = -2c_k\bar{\rho}_\mathrm{m}\delta\sqrt{K_\mathrm{t}}\,\tilde{\mathbb{S}}_\mathrm{m} \tag{1.4.37}$$
$$\mathrm{dev}\left(\widehat{\overline{\rho_\mathrm{m}\boldsymbol{u}_\mathrm{m}\otimes\boldsymbol{u}_\mathrm{m}}} - \widehat{\overline{\rho_\mathrm{m}\boldsymbol{u}_\mathrm{m}}}\otimes\widehat{\overline{\rho_\mathrm{m}\boldsymbol{u}_\mathrm{m}}}/\hat{\bar{\rho}}_\mathrm{m}\right) = -2c_k\hat{\bar{\rho}}_\mathrm{m}\hat{\delta}\sqrt{\mathcal{K}_\mathrm{t}}\,\hat{\tilde{\mathbb{S}}}_\mathrm{m}\,, \tag{1.4.38}$$

where

$$\hat{\bar{\rho}}_\mathrm{m}\mathcal{K}_\mathrm{t} = \frac{1}{2}\left(\widehat{\overline{\rho_\mathrm{m}|\boldsymbol{u}_\mathrm{m}|^2}} - \hat{\bar{\rho}}_\mathrm{m}|\hat{\tilde{\boldsymbol{u}}}_\mathrm{m}|^2\right) = \widehat{\bar{\rho}_\mathrm{m}K_\mathrm{t}} + \frac{1}{2}\left(\widehat{\bar{\rho}_\mathrm{m}|\tilde{\boldsymbol{u}}_\mathrm{m}|^2} - |\widehat{\bar{\rho}_\mathrm{m}\tilde{\boldsymbol{u}}_\mathrm{m}}|^2/\hat{\bar{\rho}}_\mathrm{m}\right)\,. \tag{1.4.39}$$

The test-filtered difference between Eq. (1.4.38) and Eq. (1.4.37) gives rise to the deviatoric part of the Leonard stresses ($\mathrm{dev}(\mathcal{L})$):

$$\mathrm{dev}\left(\bar{\rho}_\mathrm{m}\widehat{\tilde{\boldsymbol{u}}_\mathrm{m}\otimes\tilde{\boldsymbol{u}}_\mathrm{m}} - \widehat{\bar{\rho}_\mathrm{m}\tilde{\boldsymbol{u}}_\mathrm{m}}\otimes\widehat{\bar{\rho}_\mathrm{m}\tilde{\boldsymbol{u}}_\mathrm{m}}/\hat{\bar{\rho}}_\mathrm{m}\right) = 2c_k\delta\left(\bar{\rho}_\mathrm{m}\widehat{\sqrt{K_\mathrm{t}}}\,\tilde{\mathbb{S}}_\mathrm{m} - \frac{\hat{\delta}}{\delta}\hat{\bar{\rho}}_\mathrm{m}\sqrt{\mathcal{K}_\mathrm{t}}\,\hat{\tilde{\mathbb{S}}}_\mathrm{m}\right) \equiv 2c_k\mathcal{M}\,, \tag{1.4.40}$$

and, from least square error minimization [cf. 119], c_k is dynamically obtained as a function of the subgrid kinetic energy K_t:

$$c_k = \frac{1}{2}\frac{\langle \mathrm{dev}(\mathcal{L}) : \mathcal{M}\rangle}{\langle \mathcal{M} : \mathcal{M}\rangle}\,. \tag{1.4.41}$$

Moving to c_e, unfortunately it cannot be modeled with the standard dynamical procedure because the turbulent dissipation is a small-scale phenomenon and no dissipation can be seen at the large scale, making the Germano identity useless in this context [cf. 85, 80]. Thus, I will use a constant value for this constant: $c_e = 1.048$.

Similarly to what done in the previous section, the eddy diffusivity model Eq. (1.4.8) with Eq. (1.4.13) gives:

$$\overline{\rho_\mathrm{m}\boldsymbol{u}_\mathrm{m}h_\mathrm{m}} - \overline{\rho_\mathrm{m}\boldsymbol{u}_\mathrm{m}}\,\overline{\rho_\mathrm{m}h_\mathrm{m}}/\bar{\rho}_\mathrm{m} = -c_h\delta\bar{\rho}_\mathrm{m}\sqrt{K_\mathrm{t}}\nabla\tilde{h}_\mathrm{m}\,, \tag{1.4.42}$$

where, this time, $c_T = c_k/\mathrm{Pr}_\mathrm{t}$. Taking the difference between the Favre and test filter level models, I obtain:

$$\mathcal{P} \equiv \widehat{\bar{\rho}_\mathrm{m}\tilde{\boldsymbol{u}}_\mathrm{m}\tilde{h}_\mathrm{m}} - \widehat{\bar{\rho}_\mathrm{m}\tilde{\boldsymbol{u}}_\mathrm{m}}\,\widehat{\bar{\rho}_\mathrm{m}\tilde{h}_\mathrm{m}}/\hat{\bar{\rho}}_\mathrm{m} = c_h\delta\left(\bar{\rho}_\mathrm{m}\widehat{\sqrt{K_\mathrm{t}}}\nabla\tilde{h}_\mathrm{m} - \frac{\hat{\delta}}{\delta}\hat{\bar{\rho}}_\mathrm{m}\sqrt{\mathcal{K}_\mathrm{t}}\nabla\hat{\tilde{h}}_\mathrm{m}\right) \equiv c_h\mathcal{R}\,. \tag{1.4.43}$$

Again, after regularization I obtain:

$$c_h = \frac{\langle \mathcal{P}\,\mathcal{R}\rangle}{\langle \mathcal{R}^2\rangle}\,. \tag{1.4.44}$$

The coefficients of this model were bounded as done in the previous section. I will refer to this subgrid model as [dynSma].

1.4.7 Dynamical K-equation model – [dynOneEqEddy]

The model described in Sec. 1.4.3 can be modified by using the dynamic constants c_k and c_h as described in the previous section. In this way I have a dynamical subgrid model resolving the equation for the subgrid kinetic energy (Eq.(1.4.19)). I will refer to this subgrid model as [dynOneEqEddy].

1.4.8 Dynamical WALE model - [dynWale]

In order to make [wale] dynamical, it is sufficient to follow the same steps of Sec. 1.4.5 making the substitution $|\tilde{\mathcal{D}}_\mathrm{m}| \to \tilde{\mathcal{W}}_\mathrm{m}$ in Eqs. (1.4.24), (1.4.28) and (1.4.31) because the only difference between [wale] and [sma] (Eqs. (1.4.17) and (1.4.18)) is that.

1.5 Boundary conditions

The boundary conditions used throughout this thesis are intended to reproduce: 1) closed walls thermally insulated; 2) closed walls at fixed temperature; 3) closed walls with slip boundary condition for the velocity field; 4) closed walls with particle deposit; 5) atmospheric, reflecting boundary conditions; 6) periodic boundary conditions; 7) jet inlet boundary conditions. In the following I enumerate their description.

In this section, I refer to the boundary of the domain with $\partial\Omega$ and to its outward normal versor with $\boldsymbol{n}$.

1.5.1 Closed wall – [wall]

To simulate a closed wall, the following conditions are requested in $\partial\Omega$:

$$\boldsymbol{u} = \boldsymbol{u}_j = 0 \tag{1.5.1}$$
$$\nabla T \cdot \boldsymbol{n} = 0 \tag{1.5.2}$$
$$\nabla y_i \cdot \boldsymbol{n} = 0 \tag{1.5.3}$$
$$\nabla y_j \cdot \boldsymbol{n} = 0\,, \tag{1.5.4}$$

if the wall is thermally insulated, otherwise, if it is at fixed temperature

$$T = T_{\partial\Omega}\,. \tag{1.5.5}$$

The boundary condition above is a no-slip one. If a slip boundary condition is imposed, the velocity on the boundary would respect:

$$\boldsymbol{u}_\mathrm{g} \cdot \boldsymbol{n} = \boldsymbol{u}_j \cdot \boldsymbol{n} = 0\,. \tag{1.5.6}$$

When the deposited particles needs to be extracted from the domain a source term S_j is implemented in the cell right above the boundary:

$$S_j = \nabla \cdot (\rho_\mathrm{m} y_j \boldsymbol{v}_j)|_{\partial\Omega}\,. \tag{1.5.7}$$

In all the cases above, the boundary condition for ∇p is evaluated on the basis of the boundary condition on the velocity field, cf. Eq. (1.3.17d).

1.5.2 Atmospheric boundary condition – [atmo]

In order to emulate the behavior of an open boundary, the following conditions are used in $\partial\Omega$ (here $\boldsymbol{u}_\mathrm{m} = \boldsymbol{u}$):

$$\text{if } \boldsymbol{u}\cdot\boldsymbol{n} \geq 0 \quad \begin{cases} p = p_{\partial\Omega} \\ \boldsymbol{n}\cdot\nabla\boldsymbol{u} = 0 \\ \boldsymbol{n}\cdot\nabla T = 0 \\ \boldsymbol{n}\cdot\nabla y_i = 0 \\ \boldsymbol{n}\cdot\nabla y_j = 0 \end{cases} \tag{1.5.8}$$

$$\text{if } \boldsymbol{u}\cdot\boldsymbol{n} < 0 \quad \begin{cases} p = p_{\partial\Omega} - \frac{1}{2}\rho_\mathrm{m}|\boldsymbol{u}_\mathrm{m}|^2 \\ \boldsymbol{u}_\parallel = \boldsymbol{u} - \boldsymbol{u}_\perp = \boldsymbol{u} - (\boldsymbol{u}\cdot\boldsymbol{n})\boldsymbol{n} = \boldsymbol{u}_{\parallel,\partial\Omega} \\ \boldsymbol{n}\cdot\nabla\boldsymbol{u}_\perp = 0 \\ T = T_{\partial\Omega} \\ y_i = y_{i,\partial\Omega} \\ y_j = y_{j,\partial\Omega}\,. \end{cases} \tag{1.5.9}$$

Usually, $\boldsymbol{u}_{\parallel,\partial\Omega} = 0$, $y_{\mathrm{air},\partial\Omega} = 1$ and for all the mass fractions different from atmospheric air, $y_{i,\partial\Omega} = y_{j,\partial\Omega} = 0$. The particle velocity $\boldsymbol{u}_j$ is evaluated on the basis of $\boldsymbol{u}$. In presence of waves, this boundary condition is fully reflective.

1.5.3 Forced jet inlet – [jet]

In order to mimic the experimental radial profile of jet inlets measured in experiments, I implemented the following boundary condition, which includes turbulence fluctuations and forcing. The values of the temperature, of all the mass fractions and of the velocity fields are prescribed at the inlet. The boundary condition for ∇p is evaluated on the basis of $\boldsymbol{u}$, as in the closed wall boundary condition, above. The velocity profile at the inlet is $\boldsymbol{u} = \boldsymbol{u}(r,\vartheta,t) = \boldsymbol{u}_0(r,t)\varphi(\vartheta,t)$. In particular, the time average of the vertical inlet velocity profile has the following form [cf. 116, 233]:

$$\langle\boldsymbol{u}_0\rangle_\mathcal{T}(r) = \frac{1}{2}U_\mathrm{i}\hat{z}\left(1 - \tanh\left(\frac{b_0}{4\theta_\mathrm{i}}\left(\frac{r}{b_0} - \frac{b_0}{r}\right)\right)\right), \tag{1.5.10}$$

where b_0 is the inlet radius with boundary layer [cf. 116]

$$\theta_\mathrm{i} = \frac{b_0}{11.2} \quad \left(\Leftrightarrow \frac{b_0}{4\theta_\mathrm{i}} = 2.8\right), \tag{1.5.11}$$

so that its radial average is

$$U_0 = \frac{2}{b_0^2}\int_0^{b_0} r\,\mathrm{d}r\,\langle\boldsymbol{u}_0\rangle_\mathcal{T}(r) \simeq 0.8987440385 * U_\mathrm{i} \simeq 0.90 * U_\mathrm{i}\,. \tag{1.5.12}$$

To introduce inlet turbulent fluctuations, Eq. (1.5.10) is multiplied by a random white noise fluctuation with standard deviation σ_0. Moreover, to excite the inflow

Eq. (1.5.10) is multiplied by a fluctuating axial forcing to the inlet profile as previously done by Menow and Rizk [133], Zhou et al. [233]:

$$\varphi_{\mathrm{i}}(\vartheta,t) = 1 + A_\varphi \sqrt{\frac{2}{N_\varphi}} \sum_{n=1}^{N_\varphi} \sin\left(\frac{2\pi f_\varphi t}{n} + \vartheta\right) \tag{1.5.13}$$

$$f_\varphi = \frac{U_{\mathrm{i}}}{2b_0}\,\mathrm{Str} \tag{1.5.14}$$

$$\langle \varphi_{\mathrm{i}} - 1 \rangle_{\mathcal{T}} = 0 \tag{1.5.15}$$

$$\sqrt{\langle |\varphi_{\mathrm{i}} - 1|^2 \rangle_{\mathcal{T}}} = A_\varphi\,, \tag{1.5.16}$$

in order to fasten plume turbulent development. Here Str is the Strouhal number of the forcing.

Asymmetric forcing

In volcanic simulations, I also used an asymmetric forcing function to emulate the nontrivial behavior of such systems. That function is described below:

$$\varphi(t,\vartheta) = 1 + A_\varphi \sqrt{\frac{2}{2+(N_\varphi-1)^2}} \left[\sin(2\pi f_\varphi t) + \sin(2\pi f_\varphi t + \vartheta) + (N_\varphi - 1)\sin(\vartheta)\right] \tag{1.5.17}$$

$$\langle \varphi - 1 \rangle_{\mathcal{T}} = A_\varphi \sqrt{\frac{2(N_\varphi-1)^2}{2+(N_\varphi-1)^2}}\,\sin\vartheta \tag{1.5.18}$$

$$\langle \varphi - 1 \rangle_{\Omega\times\mathcal{T}} = 0 \tag{1.5.19}$$

$$\sqrt{\langle |\phi - 1|^2 \rangle_{\mathcal{T}}} = A_\varphi \sqrt{\frac{2}{2+(N_\varphi-1)^2}}\,\sqrt{1 + \cos\vartheta + (N_\varphi-1)^2 \sin^2\vartheta} \tag{1.5.20}$$

$$\sqrt{\langle |\phi - 1|^2 \rangle_{\Omega\times\mathcal{T}}} = A_\varphi\,. \tag{1.5.21}$$

1.6 Appendices

1.6.1 Dusty gas model spectrum

In this section, the spectrum of the dusty gas model is found, i.e. the eigenvalues of the hyperbolic problem associated to that model. For notation simplicity, the calculations are performed in one spatial dimension x, defining also $u = \boldsymbol{u}\cdot\boldsymbol{x}$. Neglecting the diffusive and source terms in the model (1.2.3b), (1.2.3c), (1.2.5), (1.2.6), it is possible to find a flow function $F(\Psi)$ and its Jacobian $J_F = F'(\Psi)$ so that the equations can be compactly rewritten:

$$\partial_t \Psi + \partial_x F(\Psi) = 0 \quad \Leftrightarrow \quad \partial_t \Psi + J_F\,\partial_x \Psi = 0 \tag{1.6.1}$$

by defining

$$\Psi = \begin{pmatrix} \rho_{\mathrm{g}} \\ \rho_{\mathrm{s}} \\ \rho_{\mathrm{m}}\,u \\ \rho_{\mathrm{m}}\,E_{\mathrm{m}} \end{pmatrix} \equiv \begin{pmatrix} q_1 \\ q_2 \\ q_3 \\ q_4 \end{pmatrix}, \quad F = u\,\Psi + \begin{pmatrix} 0 \\ 0 \\ p \\ p\,u \end{pmatrix}, \quad J_{F,ij} = \frac{\partial F_i}{\partial \Psi_j} \tag{1.6.2}$$

and $p = p(q_1, q_2, q_3, q_4)$; $u = q_3/(q_1 + q_2)$. In particular, by using the ideal gas law in the dilute approximation, the functional expression of the pressure turns out to be:

$$p = \frac{R\, q_1}{q_1\, C_{\rm v} + q_2 C_{\rm s}} \left(q_4 - \frac{1}{2} \frac{q_3^2}{q_1 + q_2} \right) . \tag{1.6.3}$$

The expression of J_F can be easily calculated, obtaining:

$$J_F = \begin{pmatrix} u - u\, y_{\rm g} & -u\, y_{\rm g} & y_{\rm g} & 0 \\ -u\, y_{\rm s} & u - u\, y_{\rm s} & y_{\rm s} & 0 \\ \partial_1 p - u^2 & \partial_2 p - u^2 & 2u + \partial_3 p & \partial_4 p \\ u\, \partial_1 p - u\, \dfrac{p}{\rho_{\rm m}} - u E_{\rm m} & u\, \partial_2 p - u\, \dfrac{p}{\rho_{\rm m}} - u E_{\rm m} & u\, \partial_3 p + \dfrac{p}{\rho_{\rm m}} - E_{\rm m} & u + u\, \partial_4 p \end{pmatrix} \tag{1.6.4}$$

where, recalling that $\kappa = \rho_{\rm s}/\rho_{\rm g}$ and $\chi_{\rm v,s} = C_{\rm s}/C_{\rm v}$,

$$\begin{aligned} \partial_1 p &= \frac{\kappa \chi_{\rm v,s}}{1 + \kappa \chi_{\rm v,s}} \frac{p}{\rho_{\rm g}} + \frac{\gamma - 1}{1 + \kappa \chi_{\rm v,s}} \left(\frac{1}{2} u^2 \right) \\ \partial_2 p &= \frac{-\chi_{\rm v,s}}{1 + \kappa \chi_{\rm v,s}} \frac{p}{\rho_{\rm g}} + \frac{\gamma - 1}{1 + \kappa \chi_{\rm v,s}} \left(\frac{1}{2} u^2 \right) \\ \partial_3 p &= -\frac{\gamma - 1}{1 + \kappa \chi_{\rm v,s}}\, u \\ \partial_4 p &= \frac{\gamma - 1}{1 + \kappa \chi_{\rm v,s}} . \end{aligned} \tag{1.6.5}$$

The eigenvalues of matrix J_F turn out to be:

$$\sigma(J_F) = \begin{pmatrix} u \\ u \\ u + c_{\rm dg} \\ u - c_{\rm dg} \end{pmatrix} \tag{1.6.6}$$

where (cf. Eqs. (1.2.14) and (1.2.16))

$$c_{\rm dg} = \sqrt{\frac{\gamma + \kappa \chi_{\rm v,s}}{(1 + \kappa)(1 + \kappa \chi_{\rm v,s})} \frac{p}{\rho_{\rm g}}} = \sqrt{\frac{\gamma_{\rm m} p}{\rho_{\rm m}}} = \left(\frac{\partial p}{\partial \rho_{\rm m}} \right)^{1/2}_{\rm isentropic} \tag{1.6.7}$$

is the speed of sound of the dusty gas [cf. 127]). If $\kappa = 0$, the speed of sound of the carrier phase is recovered.

In a volcanic ash plume $\chi_{\rm v,s}$ is of order one while κ can reach values up to order ten. Anyway, a typical value for κ near the vent is order one. In order to give an idea of the variation of the speed of sound due to the presence of ash inside a volcanic plume, $c_{\rm dg}$ is compared with the speed of sound in the gas phase $c_{\rm g} = \sqrt{\gamma\, p/\rho_{\rm g}}$:

$$\frac{c_{\rm dg}}{c_{\rm g}} = \sqrt{\frac{1 + \kappa \chi_{\rm v,s}/\gamma}{(1 + \kappa)(1 + \kappa \chi_{\rm v,s})}} \simeq \sqrt{\frac{1}{2}} \simeq 0.71 . \tag{1.6.8}$$

Thus, the net effect of the presence of ash inside the plume is to decrease the speed of sound of the mixture. Quantitatively, the atmospheric speed of sound (around 340 m/s) decreases to $\simeq 240\,\mathrm{m/s}$ using typical values in standard conditions.

1.6.2 Derivation of the equilibrium–Eulerian model through asymptotic expansion

Equation (1.3.18) is non-linear because of the convective term $\boldsymbol{u}_j \cdot \nabla \boldsymbol{u}_j$ but also because of the correction term $\phi_\mathrm{c}(\mathrm{Re}_j)(\boldsymbol{u}_\mathrm{g} - \boldsymbol{u}_j)$ in the Stokes drag force (cf. Eq. (1.1.29)). As pointed out and analyzed in Wang and Maxey [214], the latter non-linear term can be considered as slowly-variable and treated as a constant in the following analysis.

Here I want to solve Eq. (1.3.18) using an asymptotic expansion technique. Indeed, letting $1/\tau_j \to +\infty$ and considering $t \gg \tau_j$, it is possible to formally solve that equation. In the volcanological applications presented in this thesis, there are some zone in the domain where the gravitational effect (particle fallout) is dominant, thus I must consider the term $\boldsymbol{w}_j = \tau_j \boldsymbol{g}$ at the leading order. In other words, I must consider $\boldsymbol{g} = O(\boldsymbol{u}_\mathrm{g}/\tau_j)$ and rewrite Eq. (1.3.18) in terms of the terminal velocity $\boldsymbol{w}_j = \tau_j \boldsymbol{g}$ already defined in Eq. (1.1.33). Then, multiplying Eq. (1.3.18) by e^{t/τ_j} and calling $\boldsymbol{V} = \boldsymbol{u}_j\, e^{t/\tau_j}$, I get

$$\partial_t \boldsymbol{V} + \boldsymbol{u}_j \cdot \nabla \boldsymbol{V} = \big(\frac{1}{\tau_j}(\boldsymbol{u}_\mathrm{g} + \boldsymbol{w}_j)\big)\, e^{t/\tau_j} \tag{1.6.9}$$

that is a transport equation, with solution

$$\boldsymbol{V}(\boldsymbol{X}(\boldsymbol{x}_0, t), t) = \boldsymbol{V}_0(\boldsymbol{x}_0) + \int_0^t \frac{1}{\tau_j}\big(\boldsymbol{u}_\mathrm{g}(\boldsymbol{X}(\boldsymbol{x}_0, s), s) + \boldsymbol{w}_j\big)\, e^{s/\tau_j} \mathrm{d}s\,, \tag{1.6.10}$$

with $\boldsymbol{X}(\boldsymbol{x}_0, t)$ such that

$$\mathrm{d}_t \boldsymbol{X}(\boldsymbol{x}_0, t) = \boldsymbol{u}_j(\boldsymbol{X}(\boldsymbol{x}_0, t), t) \tag{1.6.11}$$

$$\boldsymbol{X}(\boldsymbol{x}_0, 0) = \boldsymbol{x}_0\,. \tag{1.6.12}$$

Thus, I have formally obtained $\boldsymbol{u}_j$:

$$\boldsymbol{u}_j(\boldsymbol{X}(\boldsymbol{x}_0, t), t) = \boldsymbol{u}_{j,0}(\boldsymbol{x}_0) e^{-t/\tau_j} + (1 - e^{-t/\tau_j})\, \boldsymbol{w}_j + \int_0^t \frac{1}{\tau_j} \boldsymbol{u}_\mathrm{g}(\boldsymbol{X}(\boldsymbol{x}_0, t-s), t-s)\, e^{-\frac{s}{\tau_j}} \mathrm{d}s \tag{1.6.13}$$

where $\boldsymbol{u}_j(\boldsymbol{X}(\boldsymbol{x}_0, t), t)$ is the velocity of the particle "$\boldsymbol{x}_0$" evaluated in its position at time t. In order to carry out the asymptotic expansion, I perform the Taylor expansion of $\boldsymbol{u}_\mathrm{g}$ around $s = 0$:

$$\boldsymbol{u}_\mathrm{g}(\boldsymbol{X}(\boldsymbol{x}_0, t-s), t-s) = \sum_{n=0}^{+\infty} \frac{(-1)^n}{n!} \frac{\mathrm{d}^n \boldsymbol{u}_\mathrm{g}}{\mathrm{d}t^n}(\boldsymbol{X}(\boldsymbol{x}_0, t), t)\, s^n\,. \tag{1.6.14}$$

Using the relation

$$\int \frac{1}{\tau_j} s^n e^{-\frac{s}{\tau_j}} \mathrm{d}s = -e^{-\frac{s}{\tau_j}} \sum_{k=0}^{n} \frac{n!}{k!}\, \tau_j^{n-k} s^k \tag{1.6.15}$$

and assuming that the series converges uniformly, I get

$$\int_0^t \frac{1}{\tau_j}\boldsymbol{u}_{\mathrm{g}}(\boldsymbol{X}(\boldsymbol{x}_0,t-s),t-s)\,e^{-\frac{s}{\tau_j}}\,\mathrm{d}s = \int_0^t \frac{1}{\tau_j}\sum_{n=0}^{+\infty}\frac{(-1)^n}{n!}\frac{\mathrm{d}^n\boldsymbol{u}_{\mathrm{g}}}{\mathrm{d}t^n}(\boldsymbol{X}(\boldsymbol{x}_0,t),t)\,s^n\,e^{-\frac{s}{\tau_j}}\,\mathrm{d}s$$
$$= -\sum_{n=0}^{+\infty}(-1)^n\frac{\mathrm{d}^n\boldsymbol{u}_{\mathrm{g}}}{\mathrm{d}t^n}(\boldsymbol{X}(\boldsymbol{x}_0,t),t)\,e^{-\frac{s}{\tau_j}}\sum_{k=0}^{n}\frac{1}{k!}\,\tau_j^{n-k}s^k\,\Big|_0^t$$
$$= \sum_{n=0}^{+\infty}(-1)^n\,\tau_j^n\,\frac{\mathrm{d}^n\boldsymbol{u}_{\mathrm{g}}}{\mathrm{d}t^n}(\boldsymbol{X}(\boldsymbol{x}_0,t),t)\,\left[1-\sum_{k=0}^{n}\frac{1}{k!}\,\left(\frac{t}{\tau_j}\right)^k e^{-\frac{t}{\tau_j}}\right].$$

Thus

$$\boldsymbol{u}_j(\boldsymbol{X}(\boldsymbol{x}_0,t),t)-\boldsymbol{u}_{\mathrm{g}}(\boldsymbol{X}(\boldsymbol{x}_0,t),t)-\boldsymbol{w}_j = \big(\boldsymbol{u}_{j,0}(\boldsymbol{x}_0)-\boldsymbol{u}_{\mathrm{g}}(\boldsymbol{X}(\boldsymbol{x}_0,t),t)-\boldsymbol{w}_j\big)e^{-t/\tau_j}+$$
$$-\tau_j\frac{\mathrm{d}\boldsymbol{u}_{\mathrm{g}}}{\mathrm{d}t}(\boldsymbol{X}(\boldsymbol{x}_0,t),t)\left(1-e^{-t/\tau_j}-\frac{t}{\tau_j}e^{-t/\tau_j}\right)+$$
$$+\tau_j^2\frac{\mathrm{d}^2\boldsymbol{u}_{\mathrm{g}}}{\mathrm{d}t^2}(\boldsymbol{X}(\boldsymbol{x}_0,t),t)\left(1-e^{-t/\tau_j}-\frac{t}{\tau_j}e^{-t/\tau_j}-\frac{1}{2}\left(\frac{t}{\tau_j}\right)^2 e^{-t/\tau_j}\right)+O(\tau_j^3)\,.$$

If I now consider $t \gg \tau_j$, neglecting the transient phase in which particles reach the equilibrium with the fluid[†], I obtain

$$\boldsymbol{u}_j(\boldsymbol{X}(\boldsymbol{x},t),t) = \boldsymbol{u}_{\mathrm{g}}(\boldsymbol{X}(\boldsymbol{x},t),t)+\boldsymbol{w}_j-\tau_j\frac{\mathrm{d}\boldsymbol{u}_{\mathrm{g}}}{\mathrm{d}t}(\boldsymbol{X}(\boldsymbol{x},t),t)+$$
$$+\tau_j^2\frac{\mathrm{d}^2\boldsymbol{u}_{\mathrm{g}}}{\mathrm{d}t^2}(\boldsymbol{X}(\boldsymbol{x},t),t)+O(\tau_j^3)\,, \quad (1.6.16)$$

which, using Eq. (1.6.11), gives:

$$\boldsymbol{u}_j = \boldsymbol{u}_{\mathrm{g}}+\boldsymbol{w}_j-\tau_j(\partial_t\boldsymbol{u}_{\mathrm{g}}+\boldsymbol{u}_j\cdot\nabla\boldsymbol{u}_{\mathrm{g}})+O(\tau_j^2)\,. \quad (1.6.17)$$

Note that I here obtain the same expansion of Maxey [131] reported and discussed in Ferry and Balachandar [71] and Balachandar and Eaton [4].

1.6.3 Uniqueness of the particle velocity field

Ferry and Balachandar [71] noted that the formal manipulations used to obtain result (1.3.20) are based on the assumption that there is a unique Eulerian field representation of the particle velocity $\boldsymbol{u}_j(\boldsymbol{x},t)$, given a carrier phase velocity field $\boldsymbol{u}_{\mathrm{g}}$. They showed that this is the case if the particles are sufficiently small, where how small the particles needs to be depends on the flow field. It can be expected that for particles with characteristic time τ_j smaller than a certain time-scale of the fluid, any two different initial velocity field $\boldsymbol{v}_1$ and $\boldsymbol{v}_2$ converge exponentially fast to $\boldsymbol{u}_j$. To be more precise, they demonstrated the following theorem:

[†]For this reason the model is known as equilibrium–Eulerian model.

Theorem 1.6.1. *Let $\Omega_1(t)$ be a material volume for the velocity field $\boldsymbol{v}_1(\boldsymbol{x},t)$. Defining*

$$\delta(t) = \sup_{\boldsymbol{x}\in\Omega_1(t)} |\boldsymbol{v}_1(\boldsymbol{x},t) - \boldsymbol{v}_2(\boldsymbol{x},t)|^2 \tag{1.6.18}$$

with $\boldsymbol{v}_1$ and $\boldsymbol{v_2}$ fulfilling Eq. (1.3.18) as $\boldsymbol{u}_j$, then $\delta(t) \leq \delta(0)e^{-2t\left(\frac{1}{\tau_j}+\sigma_2\right)}$, with

$$\sigma_2 = \inf_{\substack{\boldsymbol{x}\in\Omega(0)\\ 0<t'<t}} \sigma_{\min}(\boldsymbol{x},t')\,,$$

and $\sigma_{\min}$ the smallest eigenvalue of the strain rate tensor $\mathcal{D} = \mathrm{Sym}(\nabla\boldsymbol{v}_2)$.

Thus, if $\tau_j\sigma_2 > -1$ a unique particle velocity field $\boldsymbol{u}_j = \boldsymbol{v}_1 = \boldsymbol{v}_2$ can be considered to exist after transients have decayed. Note that σ_2 is the maximal compressional strain of the flow, over the entire domain and time. The velocity field $\boldsymbol{u}_j$ should be though as an *equilibrium* particle velocity field, asymptotically valid after the decay of initial transients.

If the condition $\tau_j\sigma_2$ is violated, then $\boldsymbol{u}_j$ becomes a multi-valued particle velocity field in finite time. To deal with such a condition, a Boltzmann-like approach has to be considered to study the evolution of a particle distribution function in the phase space $(\boldsymbol{x},\boldsymbol{u},t)$.

It is worth noting that this result does not show the uniqueness of a particle velocity. It is well know that in turbulence the particle velocity can easily become chaotic, being very sensitive to initial conditions. Ferry and Balachandar [71] discussed the convergence of the particle velocity field, not of individual particles.

Chapter 2

On weak solutions of the two-phase Eulerian model

This chapter concerns with the most theoretical part of the thesis, regarding results of mathematical analysis of stability and existence of solutions for certain multiphase systems involved in volcanology (Eqs. (2.2.1)). Here I explain how to adapt results know for the single phase equations, in order to give a rigorous foundation of the results for the two- (or even multi-) phase problems I consider for volcanic plumes.

The existence of weak solutions (and the related question of stability of sequences of smooth solutions) represents a very technical problem which was still open when this thesis started to be assembled. In particular, the existence of weak solutions for the compressible barotropic Navier-Stokes is well established since the end of 20th century mainly due to the work of Lions [121] and Feireisl [68] (and coworkers). Even this single-phase system (with positive constant viscosities) requires some very delicate steps as the use of the notion of renormalized solutions and compensated compactness to prove convergence of approximating sequences. In particular, the mathematical tools needed to deal with a variable density and a compressible flow are sensibly more sophisticated than those required to handle weak solutions of the incompressible and homogeneous Navier-Stokes equations.

The mathematical analysis of problems with viscosity depending on the density has been considered first by Vauigant and Kazhikhov [207] and more recently by Bresch and Desjardins [17] and Mellet and Vasseur [132]. For this system (again single-phase) the situation is even more complex, since additional difficulties arise to handle convergence in regions where the density vanishes and more refined estimates are needed.

When this thesis started, only partial results of stability of smooth solutions and of existence on modified systems were known. Consequently the main theoretical part which I decided to address is to prove related results for system with two phases, combining techniques and estimates which were known separately for the two systems. Only very recently (April 2015) the problem has been solved independently by Vasseur and Yu [206, 205] and Li and Xin [117] in two technical reports still waiting for publication in peer reviewed journals. This is why I slightly changed this chapter, in order at least to explain the modifications needed to adapt these new results to the two-phase systems considered in the thesis.

Most of this chapter will be devoted to the description of the mathematics of the problems and to the study of the stability of weak solutions of model (1.1.1) under the barotropic assumption (1.1.47) for two phases: one gas and one particle class (continuum modeling particles as discussed in the previous chapter). In order to take into account the interaction between particles (*four-way coupling*), in this chapter I will consider a modified version of model (1.1.1). In particular, I insert two new terms in the equation for the momentum balance of the solid phase: a barotropic pressure terms and a viscous term. In order to follow the literature with the most theoretical results, the notation of this chapter is independent (slightly different) from that used in the rest of the thesis.

2.1 Mathematical preliminaries

In this section, I recall the mathematical tools I will use to define weak solutions and to prove the theorems of stability and existence. In particular, I will recall the definition of some functional space, and of the fundamental concepts of the theory of distributions and functional analysis.

Since I mainly work in the periodic setting all functions are considered to be 2π-periodic along the coordinate axes. Hence Ω will be either the d-dimensional torus or a smooth bounded open set.

By using a standard notation, I denote by $C^k(\Omega)$ the space of continuous functions together with derivatives up to the order k, while $L^p(\Omega)$ is the space of p-summable Lebesgue functions which are Banach spaces endowed with natural norms. I denote with $\mathcal{D}(\Omega)$ the space of infinitely differentiable functions with compact support and with the following notion of convergence $v_n \to v$ if

$$\begin{aligned}&\text{There exists a compact set } K \subset \Omega \text{ such that}\\ &\text{a) } \operatorname{supp}(v_n) \subset K \quad \forall n \in \mathbb{N}\\ &\text{b) } \max_K |D^\alpha v_n - D^\alpha v| \to 0 \quad \forall \alpha \in \mathbb{R}^{\mathsf{d}}\,,\end{aligned}$$

where $D^\alpha \equiv \frac{\partial^{\alpha_1+\cdots+\alpha_{\mathsf{d}}}}{\partial x_1^{\alpha_1}\ldots\partial x_{\mathsf{d}}^{\alpha_{\mathsf{d}}}}$. By $\mathcal{D}'(\Omega)$ I denote the space of linear continuous functionals on $\mathcal{D}(\Omega)$. The elements of $\mathcal{D}'$ are called generalized functions, or distributions. The symbol $\langle f, v\rangle$ denotes the value of the functional $f \in \mathcal{D}'$ at the point $v \in \mathcal{D}$.

I define the derivative of a distribution f_α as follows:

$$\langle f_\alpha, v\rangle = (-1)^{|\alpha|}\langle f, D^\alpha v\rangle \quad \forall v \in \mathcal{D}(\Omega)\,. \tag{2.1.1}$$

Since for smooth functions distributional derivatives are equal to the classical ones, I use the same symbol D^α to denote the classical and also the distributional derivatives.

By using a standard notation, I will denote by $W^{k,p}(\Omega)$ the Sobolev space of (classes of equivalence of) functions in $L^p(\Omega)$, together with distributional derivatives up to the order $k \in \mathbf{N}$:

$$W^{k,p}(\Omega) = \{u :\, D^\alpha u \in L^p(\Omega) \quad \forall\, \alpha \text{ such that } |\alpha| = 0, \ldots, k\}\,, \tag{2.1.2}$$

with the norms

$$\|u\|_{W^{k,p}} = \left(\sum_{|\alpha|=0}^{k} \|D^\alpha u\|_{L^p}^p \right)^{1/p} , \tag{2.1.3}$$

$$\|u\|_{W^{k,\infty}} = \max_{|\alpha|\leq k} \|D^\alpha u\|_{L^\infty} . \tag{2.1.4}$$

The fundamental properties of the Sobolev spaces are the following:

- $W^{k,p}(\Omega)$ is a Banach space, an Hilbert space in the special case $p = 2$ with inner product

$$(u, v)_{k,\Omega} = \int_\Omega \sum_{|\alpha|=0}^{k} D^\alpha u \, D^\alpha v \mathrm{d}x . \tag{2.1.5}$$

- the space $W^{k,p}$ is separable $\forall p \in [1, \infty)$
- the space $W^{k,p}$ is reflexive $\forall p \in (1, \infty)$
- the space $C^\infty(\overline{\Omega})$ is dense in $W^{k,p}$ $\forall p \in [1, \infty)$

I recall that, if $u \in W^{1,p}$, then

$$u^+ = \begin{cases} u & \text{a.e. in} \quad \{u > 0\} \\ 0 & \text{a.e. in} \quad \{u \leq 0\} \end{cases} \tag{2.1.6}$$

belongs to $W^{1,p} \quad \forall p \in (1, \infty)$ and

$$\partial_j u^+ = \begin{cases} \partial_j u & \text{a.e. in} \quad \{u > 0\} \\ 0 & \text{a.e. in} \quad \{u \leq 0\} . \end{cases} \tag{2.1.7}$$

For Sobolev spaces, trace values of functions are well defined, and $W_0^{1,p}(\Omega)$ is the subspace of functions with vanishing trace. By $W^{-k,p}(\Omega)$ I denote the topological dual space of $W^{k,p}(\Omega)$ (in the non-periodic setting, the dual of the subspace of functions in $W_0^{k,p}(\Omega)$) [see 21].

Moreover, the Green's formula holds true:

$$\int_\Omega u \partial_i v = -\int_\Omega \partial_i u \, v + \int_{\partial\Omega} u \, v \, n_i \quad \forall u \in W^{1,p}, \quad v \in W^{1,p'} , \tag{2.1.8}$$

where $p' = \frac{p}{p-1}$ and n here denotes the normal unit exterior vector at the boundary $\partial\Omega$, which is well defined if the domain Ω is Lipshitz continuous.

Of fundamental importance are the following results.

Theorem 2.1.1 (Sobolev, Kondrashov & Rellich, Imbedding theorems)**.** *a) Let $k \geq 0$ and $1 \leq p \leq \infty$ and Ω be a bounded Lipschitz domain. Then*

$$W^{k,p}(\Omega) \hookrightarrow L^q(\Omega) \quad \text{where} \quad \frac{1}{q} = \frac{1}{p} - \frac{k}{\mathsf{d}}, \quad \text{if} \quad k < \frac{\mathsf{d}}{p},$$
$$W^{k,p}(\Omega) \hookrightarrow L^q(\Omega) \quad \forall q \in [1,\infty), \quad \text{if} \quad k = \frac{\mathsf{d}}{p},$$
$$W^{k,p}(\Omega) \hookrightarrow C^{0,k-\mathsf{d}/p}(\overline{\Omega}), \quad \text{if} \quad \frac{\mathsf{d}}{p} < k < \frac{\mathsf{d}}{p} + 1,$$
$$W^{k,p}(\Omega) \hookrightarrow C^{0,\alpha}(\overline{\Omega}) \quad \forall \alpha \in (0,1), \quad \text{if} \quad k = \frac{\mathsf{d}}{p} + 1,$$
$$W^{k,p}(\Omega) \hookrightarrow C^{0,1}(\overline{\Omega}), \quad \text{if} \quad k > \frac{\mathsf{d}}{p} + 1.$$

b) Let $k > 0$, $1 \leq p \leq \infty$. Then

$$W^{k,p}(\Omega) \hookrightarrow\hookrightarrow L^q(\Omega) \quad \forall q \in [1,p^*) \quad \text{with} \quad \frac{1}{p^*} = \frac{1}{p} - \frac{k}{\mathsf{d}}, \quad \text{if} \quad k < \frac{\mathsf{d}}{p},$$
$$W^{k,p}(\Omega) \hookrightarrow\hookrightarrow L^q(\Omega) \quad \forall q \in [1,\infty), \quad \text{if} \quad k = \frac{\mathsf{d}}{p},$$
$$W^{k,p}(\Omega) \hookrightarrow\hookrightarrow C(\overline{\Omega}), \quad \text{if} \quad k > \frac{\mathsf{d}}{p}.$$

The symbols $\hookrightarrow$ and $\hookrightarrow\hookrightarrow$ denote the continuous and compact imbedding, respectively.

I have the following interpolation inequality:

Theorem 2.1.2 (Interpolation)**.** *Let be given $0 \leq s_j < \infty$, $1 \leq p_j \leq \infty$, $j = 0, 1$, and define s and p as follows: $s = (1-\theta)s_0 + \theta s_1$ and, $\frac{1}{p} = \frac{1-\theta}{p_0} + \frac{\theta}{p_1}$ for $0 \leq \theta \leq 1$. Then there exists $C > 0$ such that*

$$\|f\|_{W^{s,p}} \leq C \, \|f\|^{1-\theta}_{W^{s_0,p_0}} \, \|f\|^{\theta}_{W^{s_1,p_1}}, \quad f \in W^{s_0,p_0} \cap W^{s_1,p_1}, \tag{2.1.9}$$

where $W^{s,p}$ is the fractional Sobolev space, defined as follows: given $s = [s] + \{s\}$, with $[\cdot]$ the floor function, then $W^{s,p}$ is the space of functions $v \in W^{[s],p}$, such that

$$I_\alpha(v) = \int_\Omega \int_\Omega \frac{|D^\alpha v(x) - D^\alpha v(y)|^p}{|x-y|^{\mathsf{d}+p\{s\}}} \mathrm{d}x\mathrm{d}y < \infty, \quad \text{for} \quad |\alpha| = [s]. \tag{2.1.10}$$

The space $W^{s,p}$ is equipped with the norm

$$\|v\|_{W^{s,p}} = \left(\|v\|^p_{W^{[s],p}} + \sum_{|\alpha|=[s]} I_\alpha(v) \right)^{1/p}. \tag{2.1.11}$$

Similar results are also true for the space-periodic Sobolev spaces with minor changes, and I refer to Brezis [21], Temam [196].

Functions with values in Banach spaces

Since I will work with time evolution problems, I need functions depending on time and with values in Banach spaces. If $v(x,t)$ is a function of the space variable $x \in \Omega$ and time $t \in [0,T]$, it is suitable to separate this variables and consider v as a function $v(t) = v(\cdot,t)$ which for each $t \in [0,T]$ attains a value $v(t)$ that is a function of x and belongs to a space of functions depending on x. In other words $v(t)$ represents the mapping

$$x \mapsto [v(t)](x)\,. \tag{2.1.12}$$

Let $(X, \|\cdot\|)$ a Banach space, I say that a function $v : [0,T] \to X$ is continuous at $t_0 \in [0,T]$ if

$$\lim_{t\to t_0} \|v(t) - v(t_0)\| = 0\,. \tag{2.1.13}$$

By $C(0,T;X)$ I denote the space of continuous functions on the interval $[0,T]$ with values in X, and it is a Banach space with the norm

$$\|v\|_{C(0,T;X)} = \max_{t\in[0,T]} \|v(t)\|\,. \tag{2.1.14}$$

I will need to define the integral of a function with values in X (Bochner integral). A mapping $f : [0,T] \to X$ is a simple function if there exists $B_i \subset [0,T]$, measurable and such that $B_i \cap B_j = \emptyset$ and $\cup_1^n B_i = [0,T]$ and $c_i \in X$, such that

$$f(t) = \sum_{i=1}^{n} \chi_{B_i}(t) c_i\,, \tag{2.1.15}$$

where

$$\chi_{B_i}(t) = \begin{cases} 1 & \text{if} \quad t \in B_i \\ 0 & \text{elsewhere.} \end{cases} \tag{2.1.16}$$

The Bochner integral of a simple function f is

$$\int_0^T f(t)\mathrm{d}t = \sum_{i=1}^{n} c_i |B_i|\,. \tag{2.1.17}$$

Definition 2.1.1 (Bochner integral)**.** *I say that $v : [0,T] \to X$ is Bochner integrable if there exists a sequence v_n of simple functions, such that*

$$\lim_{n\to\infty} \|v_n(t) - v(t)\| = 0\,, \quad \textit{a.e. in} \quad t \in [0,T] \quad \textit{(strongly measurable)} \tag{2.1.18}$$

and

$$\lim_{n\to\infty} \int_0^T \|v_n(t) - v(t)\|\mathrm{d}t = 0\,. \tag{2.1.19}$$

The Bochner integral is then defined as follows:

$$\int_0^T v(t)\mathrm{d}t = \lim_{n\to\infty} \int_0^T v_n(t)\mathrm{d}t\,. \tag{2.1.20}$$

A function $v : [0,T] \to X$ is differentiable at t_0 if there exists $w \in X$ such that

$$\lim_{h\to 0} \left\| \frac{v(t_0+h)-v(t_0)}{h} - w \right\| = 0\,, \tag{2.1.21}$$

and $v'(t_0) = w$ is the strong derivative of v at t_0.

Theorem 2.1.3. *a) If u is Bochner integrable in $[0,T]$ and $t_0 \in [0,T]$ and $\xi \in X$, then the function*

$$v(t) = \xi + \int_{t_0}^{t} u(s)\mathrm{d}s \tag{2.1.22}$$

is continuous in $[0,T]$, differentiable a.e. in $t \in (0,T)$ and

$$\frac{\mathrm{d}v}{\mathrm{d}t}(t) = u(t) \quad \textit{for a.e.} \quad t \in [0,T]\,. \tag{2.1.23}$$

b) Let $u, v : [0,T] \to X$ be Bochner integrable. Then Eq. (2.1.22) is equivalent to

$$\int_0^T u(t)\phi(t)\mathrm{d}t = -\int_0^T v(t)\phi'(t)\mathrm{d}t\,, \quad \forall \phi \in C_0^\infty([0,T])\,, \tag{2.1.24}$$

or

$$\frac{\mathrm{d}}{\mathrm{d}t}\langle \eta, v\rangle = \langle \eta, u\rangle\,, \quad \forall \eta \in X^*\,. \tag{2.1.25}$$

In particular, I will use the Bochner integral to deal with Banach spaces $W^{k,p}(0,T;X)$ defined as follows:

$$W^{k,p}(0,T;X) = \{v \in L^p(0,T;X) : \frac{\mathrm{d}^j v}{\mathrm{d}t^j} \in L^p(0,T;X)\,, \quad j = 1,\,\ldots,\,k\}\,, \tag{2.1.26}$$

where $k \in \mathbb{N}$ and $p \in [1,\infty]$. The norm of $v \in W^{k,p}(0,T;X)$ is defined

$$\|v\|_{W^{k,p}(0,T;X)} = \left(\sum_{j=1}^{k} \left\| \frac{\mathrm{d}^j f}{\mathrm{d}t^j} \right\|^p_{L^p(0,T;X)} \right)^{1/p}\,, \tag{2.1.27}$$

where $L^p(0,T;X)$ is the space of strongly measurable functions such that

$$\int_0^T \|v(t)\|^p \mathrm{d}t < \infty\,,$$

with obvious modifications when $p = \infty$. $L^p(0,T;X)$ is a Banach space. If X is reflexive and $p \in (1,\infty)$, then $L^p(0,T;X)$ is reflexive with

$$(L^p(0,T;X))^* = L^{p'}(0,T;X^*)\,.$$

Finally, I define the spaces with weak topologies as follows:

$$C_w(0,T;X) = \{f : [0,T] \to X : \langle f, \xi\rangle \in C(0,T)\,, \quad \forall \xi \in X^*\}\,. \tag{2.1.28}$$

The theory of time evolution partial differential equations requires most often the following Sobolev imbedding of abstract spaces.

Theorem 2.1.4. *Let $v \in L^2(0,T;W_0^{1,2}(\Omega)) \cap W^{1,2}(0,T;(W_0^{1,2}(\Omega))^*)$, then*

$$v \in C(0,T;L^2) \quad \textit{and} \quad \frac{\mathrm{d}}{\mathrm{d}t}\|v(t)\|_{L^2}^2 = 2\langle v'(t), v(t)\rangle\,, \quad \textit{for a.e.} \quad t \in [0,T]\,. \tag{2.1.29}$$

For further detail on Bochner spaces and real Banach-valued functions, see for instance Feireisl and Novotny [69].

In the application of the Faedo-Galerkin method, after having constructed appropriate approximate solutions, the main difficulties are concerned with taking the limits of non-linear quantities involving the approximate solutions. For this reason, one has to show some compactness of the approximating sequence, and one of the most known result is the classical Aubin-Lions lemma, which is a consequence of the Arzelà-Ascoli theorem for equibounded and equicontinuous functions.

Theorem 2.1.5 (Aubin-Lions)**.** *Let X, B and Y Banach spaces, such that*

$$X \hookrightarrow\hookrightarrow B \hookrightarrow Y\,. \tag{2.1.30}$$

Let v_n sequence bounded in $L^q(0,T;B) \cap L^1([0,T];X)$ for some $q \in (1,\infty]$, and such that $\frac{\mathrm{d}v_n}{\mathrm{d}t}$ is bounded in $L^1(0,T;Y)$. Then I can extract a subsequence $v_{n(k)}$ and $v \in L^p(0,T;B)$ for any $p \in [1,q)$, such that

$$\lim_{k\to\infty} \|v_{n(k)} - v\|_{L^p(0,T;B)} = 0\,. \tag{2.1.31}$$

For basic properties of Sobolev spaces and introduction to the theory of weak solutions for parabolic problems see also the very clear introductory presentation in Dautray and Lions [46, 47].

2.2 Definition of the mathematical problem

As first results I prove the stability of solutions of the bi-phase Eulerian equations of a compressible iso-entropic fluid $(\cdot)_\mathrm{f}$ and a dispersed particulate phase $(\cdot)_\mathrm{s}$. In particular the main concern is that of proving certain a priori estimates by assuming that the solution is smooth enough to perform the calculations below. Since I will treat weak solutions, an appropriate standard setting is that of Sobolev spaces.

In the sequel, I will mainly prove the basic energy estimate and also the counterpart of the estimate proved by Mellet and Vasseur [132] for a single fluid, which I will denote by (MV).

The model I consider is the bi-phase and iso-entropic version of Eqs. (1.1.1):

$$\partial_t \rho_\mathrm{f} + \nabla\cdot(\rho_\mathrm{f}\,\boldsymbol{u}_\mathrm{f}) = 0, \tag{2.2.1a}$$

$$\partial_t(\rho_\mathrm{f}\boldsymbol{u}_\mathrm{f}) + \nabla\cdot(\rho_\mathrm{f}\,\boldsymbol{u}_\mathrm{f}\otimes\boldsymbol{u}_\mathrm{f}) + a\nabla\rho_\mathrm{f}^\gamma - \nabla\cdot\mathbb{T}_\mathrm{f} = \frac{\rho_\mathrm{s}}{\tau_\mathrm{s}}(\boldsymbol{u}_\mathrm{s}-\boldsymbol{u}_\mathrm{f}), \tag{2.2.1b}$$

$$\partial_t \rho_\mathrm{s} + \nabla\cdot(\rho_\mathrm{s}\,\boldsymbol{u}_\mathrm{s}) = 0, \tag{2.2.1c}$$

$$\partial_t(\rho_\mathrm{s}\boldsymbol{u}_\mathrm{s}) + \nabla\cdot(\rho_\mathrm{s}\,\boldsymbol{u}_\mathrm{s}\otimes\boldsymbol{u}_\mathrm{s}) + b\nabla\rho_\mathrm{s}^{\gamma_\mathrm{s}} - \nabla\cdot\mathbb{T}_\mathrm{s} = -\frac{\rho_\mathrm{s}}{\tau_\mathrm{s}}(\boldsymbol{u}_\mathrm{s}-\boldsymbol{u}_\mathrm{f})\,, \tag{2.2.1d}$$

where (in this chapter $\lambda \equiv \mu_{\rm b} - \frac{2}{3}\mu$)

$$\mathbb{T}_{\rm f} = 2\mu\,\mathcal{D}_{\rm f} + \lambda(\nabla\cdot\boldsymbol{u}_{\rm f})\,\mathbb{I} = 2\mu\,\mathbb{S}_{\rm f} + \mu_{\rm b}(\nabla\cdot\boldsymbol{u}_{\rm f})\,\mathbb{I}, \tag{2.2.2}$$

$$\mathbb{T}_{\rm s} = 2\nu_{\rm s}\rho_{\rm s}\mathcal{D}_{\rm s} = 2\nu_{\rm s}\rho_{\rm s}\mathbb{S}_{\rm s} + \frac{2}{3}\nu_{\rm s}\rho_{\rm s}(\nabla\cdot\boldsymbol{u}_{\rm s})\,\mathbb{I}\,, \tag{2.2.3}$$

are the stress tensors for the two phases. Moreover, I recall that $\boldsymbol{u}_\cdot(\boldsymbol{x},t)$, $\rho_\cdot(\boldsymbol{x},t)$ are respectively the velocity and bulk density fields, functions of time $t \in (0,T)$ and space $\boldsymbol{x} \in \Omega$. The subscripts $(\cdot)_{\rm f}$ and $(\cdot)_{\rm s}$ denote the fluid and solid phase respectively. Here Ω is either the whole space $\mathbb{R}^3$ or the block $]0,2\pi[^3$ endowed with periodic boundary conditions. These assumptions are needed to freely perform many integration by parts without boundary terms which will be not under control.

I recall that $\mathcal{D}_\cdot = \mathrm{Sym}(\nabla\boldsymbol{u}_\cdot)$ denotes the strain (or deformation) tensor of the vector $\boldsymbol{u}_\cdot$, while $\mathbb{S}_\cdot = \mathrm{dev}(\mathrm{Sym}(\nabla\boldsymbol{u}_\cdot))$ denotes rate-of-shear tensor of the vector field $\boldsymbol{u}_\cdot$, and $\mathbb{I}$ is the identity tensor. I have introduced here a barotropic pressure for both the gaseous phase $a\,\rho_{\rm f}^{\gamma}$ (cf. Eq. (1.1.47)) and the solid phase $b\,\rho_{\rm s}^{\gamma_{\rm s}}$ with two positive constants a and b. The fluid phase pressure is motivated by the barotropic assumptions (cf. Sect. 1.1.4). The fluid dynamic viscosity μ will be considered as a constant in this chapter. Further details on the constitutive laws for the solid phase are given in the next section. The reader interested only in the mathematical aspects can go directly to Sect. 2.3.

2.2.1 Some discussion on the granular stress tensor

The solid phase pressure and viscosity can be physically justified as a small (for $b \simeq 0$) interaction between the solid particles (collisions), which can occur even if in an extremely small manner, due to the assumption of dilute suspension. Indeed, starting from the Boltzmann equations, the Cauchy stress tensor of a granular fluid can be written as

$$\sigma_{\rm s} = (-p_{\rm s} + \mu_{{\rm b},s}\nabla\cdot\boldsymbol{u}_{\rm s})\mathbb{I} + 2\mu_{\rm s}\mathbb{S}_{\rm s}\,. \tag{2.2.4}$$

At the leading order in $\rho_{\rm s}$, defining $\theta_{\rm s}$ the granular temperature I have:

$$p_{\rm s} = \rho_{\rm s}\theta_{\rm s}\,, \quad \text{the analogous of the ideal gas law,} \tag{2.2.5}$$

$$\mu_{\rm s} = c_1\theta_{\rm s}^{\delta_1} + \alpha_1\mu_{\rm b,s}\,, \tag{2.2.6}$$

$$\mu_{\rm b,s} = c_2\rho_{\rm s}^2\theta_{\rm s}^{\delta_2}\,. \tag{2.2.7}$$

For a more detailed review on granular flows, cf. Orsucci [144]. There the values are: $\delta_1 = \delta_2 = \frac{1}{2}$; $\alpha_1 = \frac{3}{5}$; $\gamma_{\rm s} = \frac{5}{3}$. Since in the dilute approximation collisions are rare, dissipation can be disregarded in the granular energy balance, leading to a result similar to that recalled in Sect. 1.1.4:

$$p_{\rm s} \propto \rho_{\rm s}^{\gamma_{\rm s}}\,, \quad \theta_{\rm s} \propto \rho_{\rm s}^{\gamma_{\rm s}-1}\,. \tag{2.2.8}$$

If the particles can be considered spheres, $\gamma_{\rm s} = 5/3$ (as in the monatomic gas case). If the solid particles are not spheres they could have more degrees of freedom, resulting in a different value for $\gamma_{\rm s}$. For the sake of generality, in this chapter the

heat capacity ratio has been left a parameter in the pressure $p_\mathrm{s} \propto \rho_\mathrm{s}^{\gamma_\mathrm{s}}$, and in the granular temperature $\theta_\mathrm{s} \propto \rho_\mathrm{s}^{\gamma_\mathrm{s}-1}$. On the contrary, I choose $\delta_1 = 3/2$ and $\gamma_\mathrm{s} = 5/3$ for the dynamic viscosity, so that (recall $\theta_\mathrm{s} \propto \rho_\mathrm{s}^{\gamma_\mathrm{s}-1}$)

$$\mu_\mathrm{s} \propto (\theta_\mathrm{s})^{\delta_1} \propto (\rho_\mathrm{s})^{\delta_1(\gamma_\mathrm{s}-1)} \propto \rho_\mathrm{s} \quad \Rightarrow \quad \mu_\mathrm{s} = \nu_\mathrm{s}\rho_\mathrm{s}\,. \tag{2.2.9}$$

Moreover, I choose δ_2 such that $\mu_{\mathrm{b,s}} = \frac{2}{3}\mu_\mathrm{s}$ (or $\lambda_{\mathrm{b,s}} = 0$), so that I can use the result of Bresch and Desjardins [19], where a special relationship is needed between the bulk and dynamic viscosity. That relationship, also recalled in Remark 2.3.1 below, requests $\mu_{\mathrm{b},s}(\rho_\mathrm{s}) - \frac{2}{3}\mu_\mathrm{s}(\rho_\mathrm{s}) = 2\rho_\mathrm{s}\mu_\mathrm{s}'(\rho_\mathrm{s}) - 2\mu_\mathrm{s}(\rho_\mathrm{s})$. In the following, I prove that the functional form chosen here for μ_s, $\mu_{\mathrm{b,s}}$ is enough for proving the stability of Eqs. (2.2.1) even if the granular viscosity goes to zero with the granular density.

2.3 On the main stability result

Thanks to the second principle of the thermodynamics, viscosity coefficients should satisfy:

$$\mu > 0\,, \qquad \mu_\mathrm{b} \geq 0\,, \qquad \nu_\mathrm{s} > 0\,;$$

a, b are positive constants and the two adiabatic constants are subject to the following constraints (that I need for proving Theorem 2.3.1):

$$\gamma > \frac{3}{2} \quad \text{and} \quad 1 < \gamma_\mathrm{s} < 3\,. \tag{2.3.1}$$

Coupling between the two phases is described through the Stokes drag force

$$\boldsymbol{f}_d = \frac{\rho_\mathrm{s}}{\tau_\mathrm{s}}(\boldsymbol{u}_\mathrm{s} - \boldsymbol{u}_\mathrm{f}),$$

where τ_s is the Stokes time, as described in Sec. 1.1.2 and defined in Eq. (1.0.2). In this chapter I will consider the case $\mathrm{Re}_\mathrm{s} < 1$ so that, as previously discussed, τ_s can be treated as a positive constant. In order to have a Cauchy problem, I prescribe the following initial conditions:

$$\rho_\cdot(\boldsymbol{x}, 0) = \rho_{\cdot,0}(\boldsymbol{x}) \geq 0, \quad \rho_\cdot \boldsymbol{u}_\cdot(\boldsymbol{x}, 0) = \boldsymbol{m}_{\cdot,0}(\boldsymbol{x}). \tag{2.3.2}$$

I give now the precise notion of weak solution for the system I consider

Definition 2.3.1. *I say that* $(\rho_\mathrm{f}, \boldsymbol{u}_\mathrm{f}, \rho_\mathrm{s}, \boldsymbol{u}_\mathrm{s})$ *is a weak solution to system* (2.2.1) *if*

$$\begin{aligned}
&\rho_\mathrm{f} \geq 0\,,\\
&\rho_\mathrm{f} \in L^\infty(0, T; L^\gamma(\Omega))\,,\\
&\boldsymbol{u}_\mathrm{f} \in L^2(0, T; W_0^{1,2}(\Omega))\,,
\end{aligned}$$

and the equations (2.2.1a)-(2.2.1b) *are satisfied in the sense of distributions. Moreover the equation* (2.2.1a) *is satisfied in the sense of renormalized solutions, that is*

$$b(\rho_\mathrm{f})_t + \nabla\cdot(b(\rho_\mathrm{f})\boldsymbol{u}_\mathrm{f}) + (b'(\rho_\mathrm{f})\rho_\mathrm{f} - b(\rho_\mathrm{f}))\nabla\cdot\boldsymbol{u}_\mathrm{f} = 0, \text{ in the sense of distributions,}$$

(2.3.3)

for all $b \in C^1(\mathbb{R})$ *such that* $b'(z) = 0$ *for all* $z \in \mathbb{R}$ *large enough. Moreover,*

$$\begin{aligned}
&\rho_{\rm s} \geq 0\,,\\
&\rho_{\rm s} \in L^\infty(0,T;L^1(\Omega)\cap L^{\gamma_{\rm s}}(\Omega))\,,\\
&\sqrt{\rho_{\rm s}} \in L^\infty(0,T;W^{1,2}(\Omega))\,,\\
&\sqrt{\rho_{\rm s}}\boldsymbol{u}_{\rm s} \in L^\infty(0,T;L^2(\Omega))\,,\\
&\rho_{\rm s}\mathcal{D}_{\rm s} \in L^2(0,T;W^{-1,1}_{loc}(\Omega))\,,
\end{aligned}$$

the density of particles $\rho_{\rm s}$ *is non-negative and the couple* $(\rho_{\rm s}, \sqrt{\rho_{\rm s}}\boldsymbol{u}_{\rm s})$ *satisfies*

$$\partial_t \rho_{\rm s} + \nabla\cdot(\sqrt{\rho_{\rm s}}\,\sqrt{\rho_{\rm s}}\boldsymbol{u}_{\rm s}) = 0 \qquad \textit{in the sense of distributions}\,;$$

while the momentum of particles $\boldsymbol{m}_{\rm s} \equiv \rho_{\rm s}\boldsymbol{u}_{\rm s}$ *satisfies for all smooth vector valued functions* $\phi_{\rm s}$ *with compact support and such that* $\phi_{\rm s}(T,0) = 0$ *[see 132, Sect. 2]*

$$\begin{aligned}
&\int_\Omega \boldsymbol{m}_{\rm s}\phi_{\rm s}(0){\rm d}x + \int_0^T \sqrt{\rho_{\rm s}}(\sqrt{\rho_{\rm s}}\boldsymbol{u}_{\rm s})\partial_t\phi_{\rm s} + \sqrt{\rho_{\rm s}}\otimes\sqrt{\rho_{\rm s}}\boldsymbol{u}_{\rm s} : \nabla\phi_{\rm s}\,{\rm d}\boldsymbol{x}{\rm d}t\\
&+ b\int_0^T\int_\Omega \rho_{\rm s}^{\gamma_{\rm s}}\nabla\cdot\phi_{\rm s}\,{\rm d}x{\rm d}t - 2\nu_{\rm s}\int_0^T\langle\rho_{\rm s}\mathcal{D}_{\rm s},\nabla\phi_{\rm s}\rangle\,{\rm d}t = \frac{1}{\tau_{\rm s}}\int_0^T\int_\Omega \rho_{\rm s}(\boldsymbol{u}_{\rm s}-\boldsymbol{u}_{\rm f})\phi_{\rm s}\,{\rm d}\boldsymbol{x}{\rm d}t\,.
\end{aligned}$$

Finally, the energy inequality (2.3.10) *holds true.*

The main result of this chapter is the stability of smooth solutions stated in Theorem 2.3.1. More precisely, I show that, given a sequence of smooth solutions which are solutions of Eqs. (2.2.1) then, they converge, up to extraction of subsequences, to a weak solution. This is one of the main results needed to show theorems of existence of weak solutions. A very peculiar problem arises when considering fluids with density dependent viscosity (even not coupled with a standard Newtonian fluid): It is rather technical to show that the sequence of smooth solutions is pre-compact and I will sketch the adaption of the proofs (taken from the cited references) to the present setting in the next theorem. On the other hand this relies heavily on proving some special entropy-type estimates developed first by Bresch et al. [20] and based on "roughly speaking" testing the momentum equation for particles by $2\nabla\log(\rho_{\rm s})$. (In the sequel I will use the now common name of BD – for Bresch and Desjardins – entropy). Then this entropy inequality, which becomes (2.3.13) in the present setting, can be used to produce as in Mellet and Vasseur [132] the logarithmic-bound

$$\rho_{\rm s}\frac{1+|\boldsymbol{u}_{\rm s}|^2}{2}\log(1+|\boldsymbol{u}_{\rm s}|^2) \in L^\infty(0,T;L^1(\Omega))\,,$$

which is crucial to prove the strong convergence of the density. The main difference with the classical compressible Navier-Stokes system is that there is not a satisfactory control on the velocity $\boldsymbol{u}_{\rm s}$ in the set $\{\rho_{\rm s} = 0\}$ (in that region one can properly define only the momentum $\mathbf{m}_{\rm s}$ and the velocity is set $\boldsymbol{u}_{\rm s} = \mathbf{0}$ as in [132, Lemma 4.6], even if this choice is quite arbitrary, as commented therein).

The main difficulty is that of constructing such approximate sequence of solutions. For a while, after appearance of the cited papers (which deal only with the single-phase equations, that for the solid part) it has been argued that the most difficult point has been solved. Then it appeared that the question is very subtle, since it was not clear at all how to construct such approximate solutions. In particular, the technical difficulty is that of constructing smooth approximate solutions satisfying the BD entropy condition. The situation is similar to having a priori estimates, but without having a theorem of existence: It could be that the solutions do not exist at all! Some results concerning existence with a drag-term as in Bresch and Desjardins [18, 19] made the feeling that the problem probably can be solved, or at least can be treated adding the drag term $\rho_{\mathrm{s}}|\boldsymbol{u}_{\mathrm{s}}|\boldsymbol{u}_{\mathrm{s}}$ also to the present set of equations. The solution of this problem, again for the single-phase problem arrived when most part of the thesis has been completed in Vasseur and Yu [206, 205], Li and Xin [117]. Hence, from one side I am safe that my results can be adapted to cover also this case. On the other hand many technical points have to be considered and I have sketched the proof of the same result for the coupled system, but it is too long and technical to be reproduced here. So in the final section of this chapter I will only explain the main ideas and how the system has to be regularized in order to obtain the existence of sequence of weak solutions as those claimed in the statement of the stability theorem. I then prove the following original result

Theorem 2.3.1. *Let Ω as before and let γ and γ_{s} satisfy* (2.3.1)*. Let $\big((\rho_{\mathrm{f}})_n, (\boldsymbol{u}_{\mathrm{f}})_n, (\rho_{\mathrm{s}})_n, (\boldsymbol{u}_{\mathrm{s}})_n\big)_{n\in\mathbb{N}}$ be a sequence of smooth solutions of* (2.2.1) *satisfying the energy inequalities* (2.3.10)*,* (2.3.13) *and* (2.3.25) *with initial data:*

$$(\rho_{\mathrm{f}})_n(\boldsymbol{x},0) = (\rho_{\mathrm{f},0})_n(\boldsymbol{x})\,, \tag{2.3.4a}$$
$$(\rho_{\mathrm{s}})_n(\boldsymbol{x},0) = (\rho_{\mathrm{s},0})_n(\boldsymbol{x})\,, \tag{2.3.4b}$$
$$(\rho_{\mathrm{f}})_n(\boldsymbol{u}_{\mathrm{f}})_n(\boldsymbol{x},0) = (\boldsymbol{m}_{\mathrm{f},0})_n(\boldsymbol{x}) = (\rho_{\mathrm{f},0})_n(\boldsymbol{u}_{\mathrm{f},0})_n(\boldsymbol{x})\,, \tag{2.3.4c}$$
$$(\rho_{\mathrm{s}})_n(\boldsymbol{u}_{\mathrm{s}})_n(\boldsymbol{x},0) = (\boldsymbol{m}_{\mathrm{s},0})_n(\boldsymbol{x}) = (\rho_{\mathrm{s},0})_n(\boldsymbol{u}_{\mathrm{s},0})_n(\boldsymbol{x})\,, \tag{2.3.4d}$$

such that

$$(\rho_{\mathrm{f},0})_n \geq 0\,, \quad (\rho_{\mathrm{f},0})_n \to \rho_{\mathrm{f},0} \text{ in } L^1(\Omega)\,, \quad (\rho_{\mathrm{f},0})_n(\boldsymbol{u}_{\mathrm{f},0})_n \to \rho_{\mathrm{f},0}\boldsymbol{u}_{\mathrm{f},0} \text{ in } L^1(\Omega)\,, \tag{2.3.5}$$

$$(\rho_{\mathrm{s},0})_n \geq 0\,, \quad (\rho_{\mathrm{s},0})_n \to \rho_{\mathrm{s},0} \text{ in } L^1(\Omega)\,, \quad (\rho_{\mathrm{s},0})_n(\boldsymbol{u}_{\mathrm{s},0})_n \to \rho_{\mathrm{s},0}\boldsymbol{u}_{\mathrm{s},0} \text{ in } L^1(\Omega)\,, \tag{2.3.6}$$

and, given C a constant independent from n,

$$\int_\Omega \left[\frac{1}{2}(\rho_{\mathrm{f},0})_n|(\boldsymbol{u}_{\mathrm{f},0})_n|^2 + \frac{1}{2}(\rho_{\mathrm{s},0})_n|(\boldsymbol{u}_{\mathrm{s},0})_n|^2 + \frac{a}{\gamma-1}(\rho_{\mathrm{f},0})_n^{\gamma} + \frac{b}{\gamma_{\mathrm{s}}-1}(\rho_{\mathrm{s},0})_n^{\gamma_{\mathrm{s}}}\right]\mathrm{d}\boldsymbol{x} < C\,, \tag{2.3.7}$$

$$\int_\Omega \frac{1}{(\rho_{\mathrm{s},0})_n}\left|\nabla(\rho_{\mathrm{s},0})_n\right|^2 \mathrm{d}\boldsymbol{x} < C\,, \tag{2.3.8}$$

$$\int_\Omega (\rho_{\mathrm{s},0})_n \frac{1+|(\boldsymbol{u}_{\mathrm{s},0})_n|^2}{2}\ln(1+|(\boldsymbol{u}_{\mathrm{s},0})_n|^2)\mathrm{d}\boldsymbol{x} < C\,. \tag{2.3.9}$$

Then, up to a sub-sequence, $\big((\rho_{\mathrm{f}})_n, \sqrt{(\rho_{\mathrm{f}})_n}(\boldsymbol{u}_{\mathrm{f}})_n, (\rho_{\mathrm{s}})_n, \sqrt{(\rho_{\mathrm{s}})_n}(\boldsymbol{u}_{\mathrm{s}})_n\big)$ converges strongly to a weak solution of (2.2.1) *satisfying the energy inequalities* (2.3.10)*,* (2.3.13)

and (2.3.25). *In particular,* $(\rho_{\rm f})_n$ *converges strongly in* $C_w(0,T;L^\gamma(\Omega))$, $(\boldsymbol{u}_{\rm f})_n$ *converges strongly in* $C_w(0,T;L^{\frac{2\gamma}{\gamma-1}}(\Omega))$, $\sqrt{(\rho_{\rm s})_n}(\boldsymbol{u}_{\rm s})_n$ *converges strongly in* $L^2_{\rm loc}([0,T]\times\Omega)$, $(\rho_{\rm s})_n$ *converges strongly in* $C^0((0,T);L^{3/2}_{\rm loc}(\Omega))$ *and* $(\rho_{\rm s})_n(\boldsymbol{u}_{\rm s})_n$ *converges strongly in* $L^2(0,T;L^1_{\rm loc}(\Omega))$, *for any* $T>0$.

2.3.1 Proof of the main result

In this section I give a summary of the main steps needed to prove Theorem 2.3.1. The very core of the proof, as in most of the results about partial differential equations is that of using energy-type estimates (test the equation by the solution itself or by functions of the solution and integrate by parts), together with compactness results to extract converging sub-sequences. The solution I construct is weak and there are not results of uniqueness (which will require much more regularity of the solution), so different sub-sequences may converge to different solutions.

I start by observing that a first very-basic inequality is obtained by multiplying Eq. (2.2.1b) by $\boldsymbol{u}_{\rm f}$, Eq. (2.2.1d) by $\boldsymbol{u}_{\rm s}$, integrating by parts, adding the results, and using the continuity equation of the fluid and of the particle phase. It follows the energy inequality:

$$\begin{aligned}\frac{d}{dt}\int_\Omega \big[\frac{1}{2}\rho_{\rm f}|\boldsymbol{u}_{\rm f}|^2+\frac{1}{2}\rho_{\rm s}|\boldsymbol{u}_{\rm s}|^2+\frac{a}{\gamma-1}\rho_{\rm f}^\gamma+\frac{b}{\gamma_{\rm s}-1}\rho_{\rm s}^{\gamma_{\rm s}}\big]{\rm d}\boldsymbol{x}\\ +\int_\Omega\big[2\mu|\mathcal{D}_{\rm f}|^2+\lambda(\nabla\cdot\boldsymbol{u}_{\rm f})^2\big]{\rm d}\boldsymbol{x}\\ +\int_\Omega 2\nu_{\rm s}\rho_{\rm s}|\mathcal{D}_{\rm s}|^2{\rm d}\boldsymbol{x}+\int_\Omega\frac{\rho_{\rm s}}{\tau_{\rm s}}|\boldsymbol{u}_{\rm s}-\boldsymbol{u}_{\rm f}|^2{\rm d}\boldsymbol{x}\le 0\,. \quad (2.3.10)\end{aligned}$$

In particular, I am assuming that the solution $(\rho_{\rm f},\boldsymbol{u}_{\rm f},\rho_{\rm s},\boldsymbol{u}_{\rm s})$ exists and is smooth enough to perform the calculations and to give meaning to all integrals appearing in (2.3.10). The same inequality is obviously satisfied also by the sequence of smooth solutions $\big((\rho_{\rm f})_n,(\boldsymbol{u}_{\rm f})_n,(\rho_{\rm s})_n,(\boldsymbol{u}_{\rm s})_n\big)_{n\in\mathbb{N}}$.

The equations for the gas phase

The energy inequality for the fluid part is a consequence of (2.3.10). The stability of the unknowns concerning the fluid part – that is of the sequences $(\rho_{\rm f})n,(\boldsymbol{u}_{\rm f})_n$ – is then a consequence of well-established results as those obtained by Lions [121], Feireisl [67].

By the a priori estimate I obtain that

$$\begin{aligned}&(\rho_{\rm f})_n\to\rho_{\rm f}\quad\text{in } C_w(0,T;L^\gamma(\Omega)),\\ &(\boldsymbol{u}_{\rm f})_n\to\boldsymbol{u}_{\rm f}\quad\text{weakly in } L^2(0,T;W^{1,2}_0(\Omega)),\\ &(\rho_{\rm f})_n(\boldsymbol{u}_{\rm f})_n\to\rho_{\rm f}\boldsymbol{u}_{\rm f}\quad\text{in } C_w(0,T;L^{\frac{2\gamma}{\gamma+1}}(\Omega)),\end{aligned}$$

where $g\in C_w(0,T;X)$ means the space of bounded functions with values in the Banach space X and such that are continuous with respect to the weak topology, that is such that if $t_n\to t$ then

$$<g(t_n),\phi>\to<g(t),\phi>\qquad\forall\,\phi\in X^*.$$

Then, by using a special test function concerned with the inversion of the divergence operator, one can obtain that [see 67, Prop. 3.1]

$$\int_0^T \int_\Omega \rho_{\rm f}^{\gamma+\theta} \,{\rm d}\boldsymbol{x}{\rm d}t \le C \quad \text{for} \quad \theta = \frac{2\gamma}{3} - 1\,. \tag{2.3.11}$$

I recall that "formally" this result is obtained by using as test function $\psi(t)\mathcal{B}[\rho_{\rm f}^\theta]$, for $\psi \in C_0^\infty(0,T)$, $0 \le \psi \le 1$, and $\mathcal{B} = (\mathcal{B}_1, \mathcal{B}_2, \mathcal{B}_3)$ such that $\nabla \cdot \mathcal{B} = \rho_{\rm f}^\theta$. I am writing formally since one has to perform some smoothing and also one could not use directly the function $z \to z^\theta$ but an approximation satisfying growth conditions which allow to use the results about renormalized solutions of the transport equation for the density $\rho_{\rm f}$ as those in DiPerna and Lions [53].

Remark I am writing that the test function is $\psi(t)\mathcal{B}[\rho_{\rm f}^\theta]$, since I am mainly considering the equation for the momentum of the fluid. More precisely one should test both momentum equations by test functions $(\psi(t)\mathcal{B}[\rho_{\rm f}^\theta], 0)$. Since I will handle in different steps the fluid and the particles, I will use often this convention, meaning that I am, whenever possible, separating problems and techniques coming from the two different constitutive equations, which require a slightly different techniques. In particular, for the fluid part the compactness argument is more complex, while for the particles' equation the a priori estimates need more work.

The above estimates can be used to show [by standard compactness results typical of nonlinear partial differential equations, see 21, 65] that

$$\begin{aligned}
&(\rho_{\rm f})_n^\gamma \to p \quad \text{weakly in } L^{\frac{\gamma+\theta}{\gamma}}(\Omega),\\
&(\rho_{\rm f})_n (\boldsymbol{u}_{\rm f})_n \otimes (\boldsymbol{u}_{\rm f})_n \to \rho_{\rm f}\,\boldsymbol{u}_{\rm f} \otimes \boldsymbol{u}_{\rm f} \quad \text{in the sense of distributions.}
\end{aligned}$$

Clearly, the major difficulty is to show that $p = \rho_{\rm f}^\gamma$, or equivalently that $(\rho_{\rm f})_n$ converges strongly, at least in $L^1(\Omega)$, to $\rho_{\rm f}$.

In particular, one of the main steps is that of showing the remarkable property that the *effective flux* $(\rho_{\rm f})_n^\gamma - (\lambda+2\mu)\nabla\cdot(\boldsymbol{u}_{\rm f})_n$ is more regular than its components. In fact I have the following result

$$\begin{aligned}
\lim_{n\to+\infty} \int_0^T \int_\Omega \psi\,\phi\,(a\left((\rho_{\rm f})_n^\gamma - (\lambda+2\mu)\nabla\cdot(\boldsymbol{u}_{\rm f})_n\right) T_k(\rho_{{\rm f}_n})\,{\rm d}\boldsymbol{x}{\rm d}t\\
= \int_0^T \int_\Omega \psi\,\phi\,(a\left(\rho_{\rm f}^\gamma - (\lambda+2\mu)\nabla\cdot\boldsymbol{u}_{\rm f}\right) T_k(\rho_{{\rm f}_n})\,{\rm d}x{\rm d}t,
\end{aligned}$$

for all $\psi \in C_0^\infty(0,T)$ and $\phi \in C_0^\infty(\Omega)$ (or smooth and periodic in the periodic setting). Here T_k is a family of cut-off operators, defined as

$$T_k(z) = k\,T(z/k) \qquad k \in \mathbb{N} \text{ and } z \ge 0,$$

where T is a smooth and concave function such that $T(z) = z$ for $z \le 1$, while $T(z) = 2$ for $z \ge 3$. The introduction of $T_k(z)$ is due to technical reasons, if one could directly use $(\rho_{\rm f})_n$ instead of $T_k((\rho_{\rm f})_n)$ the proof would be shorter.

The discovery of the special properties of the effective flux is due to to many authors in slightly different contexts [see 174, 101, 121]. A simplification and

extension to the technique to the range of all $\gamma > \frac{3}{2}$ can be found for instance in Feireisl et al. [70]. This result is again a consequence of the use of a suitable test function still related with the inversion of the divergence and on the use of the compactness coming from the div-curl lemma. In particular one has to test the momentum equation by $\psi\,\phi_j A[\rho_{\rm f}]$, where A_j is a linear operator which is defined in terms of Fourier variables by the symbol $\mathcal{A}_j(\xi) = \frac{-i\,\xi_j}{|\xi|^2}$, after extending by zero $\rho_{\rm f}$ off the domain. In the space periodic case this is done more simply by Fourier series with $\mathcal{A}_j(k) = \frac{-i\,k_j}{|k|^2}$. The main fact is that on the operator $\mathcal{A}_j(\xi)$ one can use the classical theory of Mikhlin multipliers (to produce suitable L^p estimates). In addition taking the partial derivative $\partial_{x_k} A_j[v] = \mathcal{R}_{kj}[v]$ (for any function v) one gets an operator related with the Riesz transform and a very special commutation/compactness property (coming form the div-curl lemma) can be deduced [see the details in 70, Sec. 3.4]. The only difference is the further integral

$$\frac{1}{\tau_{\rm s}} \int_0^T \int_\Omega \psi\,\phi\,(\rho_{\rm s})_n((\boldsymbol{u}_{\rm s})_n - (\boldsymbol{u}_{\rm f})_n) \cdot A[(\rho_{\rm f})_n]\,{\rm d}\boldsymbol{x}{\rm d}t,$$

in the right hand side of the equivalent of [70, Eq. (3.4)] and which can be easily shown to pass to the limit, by using the further compactness I will prove later on for the particles' quantities. See Sec. 2.3.1.

In addition, a relevant technical step needed to handle oscillations can be borrowed from the results of Jiang and Zhang [107] and in particular exactly the same proof valid for the equations with only the fluid will show that the oscillations of $(\rho_{\rm f})_n$ stay bounded, at least in $L^{\gamma+1}(\Omega)$. This will show that the limit $\rho_{\rm f}$ satisfies the mass conservation equation in the renormalized sense and one can write the equation (2.3.3) with $b = L_k$ for

$$L_k(z) = \begin{cases} z\log(z) & 0 \le z < k \\ z\log(k) + z\displaystyle\int_k^z \frac{T_k(\sigma)}{\sigma^2}\,d\sigma & z \ge k. \end{cases}$$

This can be then used to show that $(\rho_{\rm f})_n \log(\rho_{\rm f})_n$ converges in $C_w(0,T;L^\alpha(\Omega))$ for all $1 \le \alpha < \gamma$. Finally, by passing to the limit as $k \to +\infty$ one obtains that

$$(\rho_{\rm f})_n \log(\rho_{\rm f})_n \to \rho_{\rm f}\log(\rho_{\rm f}) \qquad \forall\, t \in [0,T],$$

which in turns implies the strong convergence in $L^1(\Omega)$ of the sequence $(\rho_{\rm f})_n$.

The equations for the solid phase

When passing to consider the system with density dependent viscosity, one main obstruction to reproduce the proof is that the uniform control on $(\boldsymbol{u}_{\rm s})_n$ in $W^{1,2}(\Omega)$ is not available and only an inequality weighted with $(\rho_{\rm s})_n$ holds true. This is one of the motivations for more precise and sophisticated estimates.

To this end, I consider another a priori estimate, which is obtained by following the result in Mellet and Vasseur [132] and which will be the main tool to study the stability of solutions for what concerns the solid part.

Here and in what follows it holds $|\mathbb{T}|^2 = \sum_{i,j} |\mathbb{T}_{ij}|^2$ and $\mathbb{T} : \mathbb{U} = \sum_{i,j} \mathbb{T}_{i,j}\mathbb{U}_{i,j}$. Moreover, it is possible to show that for smooth solutions

$$\rho_{(\cdot)}(x,0) \geq 0 \quad \Rightarrow \quad \rho_{(\cdot)}(x,t) \geq 0, \quad \forall\, t > 0\,.$$

In order to prove the counterpart of MV estimates, it is useful to define the following quantities, depending only on time (and their counterpart when applied to the approximating sequence)

$$\begin{aligned}
K_{\rm f} &= \int_\Omega \frac{1}{2}\rho_{\rm f}\,|\boldsymbol{u}_{\rm f}|^2\,{\rm d}\boldsymbol{x}, & K_{\rm s} &= \int_\Omega \frac{1}{2}\rho_{\rm s}\,|\boldsymbol{u}_{\rm s}|^2\,{\rm d}\boldsymbol{x},\\
K_\rho &= \int_\Omega \frac{1}{2}\rho_{\rm s}\left|\boldsymbol{u}_{\rm s} + \frac{2}{\rho_{\rm s}}\nabla\rho_{\rm s}\right|^2\,{\rm d}\boldsymbol{x}, & P_{\rm f} &= \int_\Omega \frac{a}{\gamma-1}\rho_{\rm f}^\gamma\,{\rm d}\boldsymbol{x},\\
P_{\rm s} &= \int_\Omega \frac{b}{\gamma_{\rm s}-1}\rho_{\rm s}^{\gamma_{\rm s}}\,{\rm d}\boldsymbol{x}, & P_\rho &= \int_\Omega 2b\gamma_{\rm s}\rho_{\rm s}^{\gamma_{\rm s}-2}|\nabla\rho_{\rm s}|^2\,{\rm d}\boldsymbol{x},\\
F_\mu &= \int_\Omega \left[\mu|\nabla\boldsymbol{u}_{\rm f}|^2 + (\lambda+\mu)(\nabla\cdot\boldsymbol{u}_{\rm f})^2\right]{\rm d}\boldsymbol{x}, & F_{\rm s} &= \int_\Omega 2\rho_{\rm s}|\mathcal{D}_{\rm s}|^2\,{\rm d}\boldsymbol{x},\\
F_\rho &= \int_\Omega \frac{\rho_{\rm s}}{2}|\nabla\boldsymbol{u}_{\rm s} - \nabla\boldsymbol{u}_{\rm s}^t|^2\,{\rm d}\boldsymbol{x}, & F_\tau &= \int_\Omega \frac{\rho_{\rm s}}{\tau_{\rm s}}|\boldsymbol{u}_{\rm s} - \boldsymbol{u}_{\rm f}|^2\,{\rm d}\boldsymbol{x}.
\end{aligned}$$

With the above quantities the energy inequality (2.3.10) can be rewritten as follows:

$$\mathrm{d}_t(K_{\rm f} + K_{\rm s} + P_{\rm f} + P_{\rm s}) + F_\mu + F_{\rm s} + F_\tau \leq 0\,. \tag{2.3.12}$$

The main a priori estimate which allows to handle the solid part is obtained in the following lemma.

Lemma 2.3.2. *The following entropy inequality [which is the analog of the BD from 20] holds for smooth solutions of* (2.2.1)*:*

$$\mathrm{d}_t(K_{\rm f} + K_\rho + P_{\rm f} + P_{\rm s}) + P_\rho + F_\mu + F_\rho + (1-\epsilon)F_\tau \leq \frac{1}{\epsilon\,\tau_{\rm s}}(K_\rho + K_{\rm s})\,. \tag{2.3.13}$$

for all $\epsilon > 0$.

Proof. It is important to observe that the differential inequality (2.3.13) concerns some very special combinations of quantities related with density and velocity of the solid phase. This can be understood as a special kind of entropy inequality, which will give some strong convergence and which will make possible to overcome the problems concerned with the vanishing of $\rho_{\rm s}$. Especially the fact that $\int_\Omega \frac{|\nabla\rho_{\rm s}|^2}{\rho_{\rm s}}\,{\rm d}\boldsymbol{x}$ is bounded will be used in the sequel.

Remark In the original papers Bresch and Desjardins [19] and also in Mellet and Vasseur [132] some slightly more general version of the viscosity is studied and the stress tensor which can be handled is

$$2h(\rho_{\rm s})\mathcal{D}_{\rm s} + g(\rho_{\rm s})\nabla\cdot\boldsymbol{u}_{\rm s}\mathbb{I}, \quad \text{with } g(z) = 2z\,h'(z) - 2h(z),$$

with $h' \geq \nu > 0$, $h(0) \geq 0$, $|g'(z)| \leq \nu^{-1}h'(z)$, $\nu h(z) \leq 2h(z) + 3g(z) \leq \nu^{-1}h(z)$ and, for some small $\epsilon > 0$, $\liminf_{z\to+\infty} h(z)z^{-\gamma_{\rm s}-\epsilon} > 0$.

Following for instance Mellet and Vasseur [132], I want to deal with the time derivative $\mathrm{d}_t K_\rho$ and use the equations to rewrite the inequality in a equivalent way. By using Eq. (2.2.1c) and with several integration by parts I find the following identity

$$\begin{aligned}
\frac{d}{dt}\int_\Omega \frac{2}{\rho_\mathrm{s}}|\nabla\rho_\mathrm{s}|^2\,\mathrm{d}\boldsymbol{x} &= \int -\frac{2}{\rho_\mathrm{s}^2}|\nabla\rho_\mathrm{s}|^2\partial_t\rho_\mathrm{s} + \frac{4}{\rho_\mathrm{s}}\nabla\rho_\mathrm{s}\cdot\nabla(\partial_t\rho_\mathrm{s})\,\mathrm{d}\boldsymbol{x}\\
&= \int_\Omega \frac{2}{\rho_\mathrm{s}^2}|\nabla\rho_\mathrm{s}|^2\nabla\cdot(\rho_\mathrm{s}\boldsymbol{u}_\mathrm{s}) - \frac{4}{\rho_\mathrm{s}}\nabla\rho_\mathrm{s}\cdot\nabla(\nabla\cdot(\rho_\mathrm{s}\boldsymbol{u}_\mathrm{s}))\mathrm{d}\boldsymbol{x}\\
&= \int_\Omega -\frac{2}{\rho_\mathrm{s}^2}|\nabla\rho_\mathrm{s}|^2\nabla\cdot(\rho_\mathrm{s}\boldsymbol{u}_\mathrm{s}) + \frac{4}{\rho_\mathrm{s}}\Delta\rho_\mathrm{s}\nabla\cdot(\rho_\mathrm{s}\boldsymbol{u}_\mathrm{s})\mathrm{d}\boldsymbol{x}\\
&= \int_\Omega -\frac{2}{\rho_\mathrm{s}}|\nabla\rho_\mathrm{s}|^2\nabla\cdot\boldsymbol{u}_\mathrm{s} + \rho_\mathrm{s}\nabla\cdot\Big(\boldsymbol{u}_\mathrm{s}\frac{2}{\rho_\mathrm{s}^2}|\nabla\rho_\mathrm{s}|^2\Big) + \frac{4}{\rho_\mathrm{s}}\Delta\rho_\mathrm{s}\nabla\cdot(\rho_\mathrm{s}\boldsymbol{u}_\mathrm{s})\,\mathrm{d}\boldsymbol{x}\\
&= \int_\Omega -\frac{4}{\rho_\mathrm{s}^2}\boldsymbol{u}_\mathrm{s}\cdot\nabla\rho_\mathrm{s}\,|\nabla\rho_\mathrm{s}|^2 + \frac{4}{\rho_\mathrm{s}}\nabla\rho_\mathrm{s}\otimes\boldsymbol{u}_\mathrm{s} : \nabla(\nabla\rho_\mathrm{s}) + \frac{4}{\rho_\mathrm{s}}\Delta\rho_\mathrm{s}\nabla\cdot(\rho_\mathrm{s}\boldsymbol{u}_\mathrm{s})\,\mathrm{d}\boldsymbol{x}\\
&= \int_\Omega -\frac{4}{\rho_\mathrm{s}}\nabla\rho_\mathrm{s}\otimes\nabla\rho_\mathrm{s} : \nabla\boldsymbol{u}_\mathrm{s} + 4\Delta\rho_\mathrm{s}\nabla\cdot\boldsymbol{u}_\mathrm{s}\mathrm{d}\boldsymbol{x}. \quad (2.3.14)
\end{aligned}$$

Then, by using Eqs. (2.2.1c) and (2.2.1d) I obtain

$$\begin{aligned}
\frac{d}{dt}\int_\Omega 2\boldsymbol{u}_\mathrm{s}\cdot\nabla\rho_\mathrm{s}\,\mathrm{d}\boldsymbol{x} &= \int_\Omega \frac{2}{\rho_\mathrm{s}}\nabla\rho_\mathrm{s}\cdot\partial_t(\rho_\mathrm{s}\boldsymbol{u}_\mathrm{s}) + \frac{2}{\rho_\mathrm{s}}(\nabla\cdot(\rho_\mathrm{s}\boldsymbol{u}_\mathrm{s}))^2\,\mathrm{d}\boldsymbol{x}\\
&= \int_\Omega \frac{2}{\rho_\mathrm{s}}\nabla\rho_\mathrm{s}\cdot\Big(-\nabla\cdot(\rho_\mathrm{s}\boldsymbol{u}_\mathrm{s}\otimes\boldsymbol{u}_\mathrm{s}) - b\nabla\rho_\mathrm{s}^{\gamma_\mathrm{s}} + \nabla\cdot(2\rho_\mathrm{s}\mathcal{D}_\mathrm{s}) - \frac{\rho_\mathrm{s}}{\tau_\mathrm{s}}(\boldsymbol{u}_\mathrm{s}-\boldsymbol{u}_\mathrm{f})\Big)\\
&\quad + \frac{2}{\rho_\mathrm{s}}(\nabla\cdot(\rho_\mathrm{s}\boldsymbol{u}_\mathrm{s}))^2\,\mathrm{d}\boldsymbol{x}\,.
\end{aligned}$$

Now I have $\int_\Omega -\frac{2}{\rho_\mathrm{s}}\nabla\rho_\mathrm{s}\cdot b\nabla\rho_\mathrm{s}^{\gamma_\mathrm{s}}\mathrm{d}\boldsymbol{x} = -P_\rho$, and (I use explicitly coordinates in this calculations, which otherwise could be hard to follow)

$$\begin{aligned}
\int_\Omega \frac{2}{\rho_\mathrm{s}}\nabla\rho_\mathrm{s}\cdot\big(\nabla\cdot(2\rho_\mathrm{s}\mathcal{D}_\mathrm{s})\big)\,\mathrm{d}\boldsymbol{x} &= \int_\Omega \partial_i(2\ln\rho_\mathrm{s})\partial_j(\rho_\mathrm{s}\partial_i u_{p,j}) + \partial_i(2\ln\rho_\mathrm{s})\partial_j(\rho_\mathrm{s}\partial_j u_{p,i})\,\mathrm{d}\boldsymbol{x}\\
&= \int_\Omega \partial_i(2\ln\rho_\mathrm{s})\partial_j(\rho_\mathrm{s}\partial_i u_{p,j}) + \partial_j(2\ln\rho_\mathrm{s})\partial_i(\rho_\mathrm{s}\partial_j u_{p,i})\,\mathrm{d}\boldsymbol{x}\\
&= \int_\Omega \frac{4}{\rho_\mathrm{s}}\nabla\rho_\mathrm{s}\otimes\nabla\rho_\mathrm{s} : \nabla\boldsymbol{u}_\mathrm{s} - 4\Delta\rho_\mathrm{s}\nabla\cdot\boldsymbol{u}_\mathrm{s}\,\mathrm{d}\boldsymbol{x}\,. \quad (2.3.15)
\end{aligned}$$

I note Eq. (2.3.14) and (2.3.15) are one the opposite of the other.

Moreover, I get:

$$\begin{aligned}
&\int_\Omega -\frac{2}{\rho_\mathrm{s}}\nabla\rho_\mathrm{s}\cdot\big(\nabla\cdot(\rho_\mathrm{s}\boldsymbol{u}_\mathrm{s}\otimes\boldsymbol{u}_\mathrm{s})\big) + \frac{2}{\rho_\mathrm{s}}(\nabla\cdot(\rho_\mathrm{s}\boldsymbol{u}_\mathrm{s}))^2\,\mathrm{d}\boldsymbol{x}\\
&\qquad = \int_\Omega 2\nabla\cdot(\rho_\mathrm{s}\boldsymbol{u}_\mathrm{s})\nabla\cdot\boldsymbol{u}_\mathrm{s} - 2\nabla\rho_\mathrm{s}\otimes\boldsymbol{u}_\mathrm{s} : \nabla\boldsymbol{u}_\mathrm{s}\,\mathrm{d}\boldsymbol{x}\\
&\qquad = \int_\Omega 2\rho_\mathrm{s}(\nabla\cdot\boldsymbol{u}_\mathrm{s})^2 - 2\rho_\mathrm{s}\partial_j(u_{\mathrm{s},j}\partial_i u_{\mathrm{s},i}) - 2\nabla\rho_\mathrm{s}\otimes\boldsymbol{u}_\mathrm{s} : \nabla\boldsymbol{u}_\mathrm{s}\,\mathrm{d}\boldsymbol{x}\\
&\qquad = \int_\Omega -2\rho_\mathrm{s}u_{\mathrm{s},j}\partial_i\partial_j u_{\mathrm{s},i} - 2\nabla\rho_\mathrm{s}\otimes\boldsymbol{u}_\mathrm{s} : \nabla\boldsymbol{u}_\mathrm{s}\,\mathrm{d}\boldsymbol{x} = \int 2\rho_\mathrm{s}\partial_i u_{\mathrm{s},j}\partial_j u_{p,i}\,\mathrm{d}\boldsymbol{x}\,.
\end{aligned}$$

Adding the energy equality Eq. (2.3.12) to $\frac{d}{dt}\int_\Omega \left[2\boldsymbol{u}_\mathrm{s}\cdot\nabla\rho_\mathrm{s}+\frac{2}{\rho_\mathrm{s}}|\nabla\rho_\mathrm{s}|^2\right]\mathrm{d}\boldsymbol{x}+P_\rho$ gives:

$$\frac{d}{dt}(K_\mathrm{f}+K_\rho+P_\mathrm{f}+P_\mathrm{s})+P_\rho+F_\mu+F_\tau= \\ =\int_\Omega -2\rho_\mathrm{s}\big(|\mathcal{D}_\mathrm{s}|^2-\partial_i u_{p,j}\partial_j u_{p,i}\big)-\frac{2}{\tau_\mathrm{s}}\nabla\rho_\mathrm{s}\cdot(\boldsymbol{u}_\mathrm{s}-\boldsymbol{u}_\mathrm{f})\,\mathrm{d}\boldsymbol{x},$$

which yields

$$\mathrm{d}_t(K_\mathrm{f}+K_\rho+P_\mathrm{f}+P_\mathrm{s})+P_\rho+F_\mu+F_\tau+F_\rho=\int_\Omega -\frac{2}{\tau_\mathrm{s}}\nabla\rho_\mathrm{s}\cdot(\boldsymbol{u}_\mathrm{s}-\boldsymbol{u}_\mathrm{f})\,\mathrm{d}\boldsymbol{x}\,.$$

Moreover, by using Hölder inequality, I have

$$\begin{aligned}\int_\Omega -2\nabla\rho_\mathrm{s}\cdot(\boldsymbol{u}_\mathrm{s}-\boldsymbol{u}_\mathrm{f})\,\mathrm{d}\boldsymbol{x}&=-\int_\Omega \rho_\mathrm{s}^{\frac{1}{2}}(\frac{2}{\rho_\mathrm{s}}\nabla\rho_\mathrm{s}+\boldsymbol{u}_\mathrm{s})\rho_\mathrm{s}^{\frac{1}{2}}(\boldsymbol{u}_\mathrm{s}-\boldsymbol{u}_\mathrm{f})\,\mathrm{d}\boldsymbol{x}\\&\quad+\int_\Omega \rho_\mathrm{s}^{\frac{1}{2}}\boldsymbol{u}_\mathrm{s}\rho_\mathrm{s}^{\frac{1}{2}}(\boldsymbol{u}_\mathrm{s}-\boldsymbol{u}_\mathrm{f})\,\mathrm{d}\boldsymbol{x}\\&\le\frac{1}{2\epsilon}\int_\Omega \rho_\mathrm{s}\big|\boldsymbol{u}_\mathrm{s}+\frac{2}{\rho_\mathrm{s}}\nabla\rho_\mathrm{s}\big|^2\,\mathrm{d}\boldsymbol{x}+\frac{\epsilon}{2}\int_\Omega\rho_\mathrm{s}|\boldsymbol{u}_\mathrm{s}-\boldsymbol{u}_\mathrm{f}|^2\,\mathrm{d}\boldsymbol{x}\\&\quad+\frac{1}{2\epsilon}\int_\Omega\rho_\mathrm{s}|\boldsymbol{u}_\mathrm{s}|^2\,\mathrm{d}\boldsymbol{x}+\frac{\epsilon}{2}\int_\Omega\rho_\mathrm{s}|\boldsymbol{u}_\mathrm{s}-\boldsymbol{u}_\mathrm{f}|^2\,\mathrm{d}\boldsymbol{x}\,,\end{aligned}$$

which ends the proof of the Lemma. □

By using Lemma 2.3.2 and recalling the energy estimate (2.3.10), I get the following estimates (with all bounds independent of n), which are valid for the approximating sequence

$$\sqrt{\rho_\mathrm{f}}\,\boldsymbol{u}_\mathrm{f}\in L^\infty(0,T;L^2(\Omega))\,, \tag{2.3.16}$$
$$\rho_\mathrm{f}\in L^\infty(0,T;L^1(\Omega)\cap L^\gamma(\Omega))\,, \tag{2.3.17}$$
$$\boldsymbol{u}_\mathrm{f}\in L^2(0,T;W^{1,2}(\Omega))\,, \tag{2.3.18}$$
$$\sqrt{\rho_\mathrm{s}}\,\boldsymbol{u}_\mathrm{s}\in L^\infty(0,T;L^2(\Omega))\,, \tag{2.3.19}$$
$$\sqrt{\rho_\mathrm{s}}\in L^\infty(0,T;W^{1,2}(\Omega))\,, \tag{2.3.20}$$
$$\sqrt{\rho_\mathrm{s}}\,\nabla\boldsymbol{u}_\mathrm{s}\in L^2(0,T;L^2(\Omega))\,, \tag{2.3.21}$$
$$\rho_\mathrm{s}\in L^\infty(0,T;L^1(\Omega)\cap L^{\gamma_\mathrm{s}}(\Omega))\,, \tag{2.3.22}$$
$$\nabla\rho_\mathrm{s}^{\frac{\gamma_\mathrm{s}}{2}}\in L^2(0,T;L^2(\Omega))\,. \tag{2.3.23}$$

Using Sobolev embedding theorem $W^{1,2}(\Omega)\hookrightarrow L^6(\Omega)$ which is valid for three space variables, I have that $\rho_\mathrm{s}^{\gamma_\mathrm{s}}$ is bounded in $L^1(0,T;L^3(\Omega))\cap L^\infty(0,T;L^1(\Omega))$. Thus standard convex interpolation in Lebesgue spaces gives also

$$\rho_\mathrm{s}^{\gamma_\mathrm{s}}\in L^{\frac{5}{3}}(0,T\times\Omega)\,. \tag{2.3.24}$$

I now prove the basic inequality [which is an adaption to the multiphase system of those in 132] that will be used in the compactness argument, since this will give the control of a quantity *logarithmically better* than the momentum $\rho_\mathrm{s}\,\boldsymbol{u}_\mathrm{s}$.

Lemma 2.3.3. *Let $\varphi : \mathbb{R}^+ \to \mathbb{R}$ be a smooth function such that there exists a positive constant λ for which hold $\varphi'(s) \geq \lambda s$ and $\varphi(s) = 0 \Leftrightarrow s = 0$. Than, for all $\epsilon_{1,2} > 0$ and $\delta > 0$, smooth solutions of Eqs. (2.2.1) satisfy the following inequality:*

$$\begin{aligned}
&\mathrm{d}_t \int_\Omega \rho_\mathrm{s}\varphi(|\boldsymbol{u}_\mathrm{s}|)\,\mathrm{d}\boldsymbol{x} + \left(1 - \frac{3\epsilon_1}{2}\right)\int_\Omega 2\rho_\mathrm{s}\frac{\varphi'}{|\boldsymbol{u}_\mathrm{s}|}|\mathcal{D}_\mathrm{s}|^2\,\mathrm{d}\boldsymbol{x} \leq \\
&\leq \int_\Omega 2\Phi\rho_\mathrm{s}|\nabla\boldsymbol{u}_\mathrm{s}|^2\,\mathrm{d}\boldsymbol{x} - \frac{1}{\tau_\mathrm{s}}\int_\Omega \rho_\mathrm{s}|\boldsymbol{u}_\mathrm{s}|\,\varphi'(|\boldsymbol{u}_\mathrm{s}|)\,\mathrm{d}\boldsymbol{x} + \frac{1}{\tau_\mathrm{s}}\int_\Omega \rho_\mathrm{s}\frac{\boldsymbol{u}_\mathrm{f}\cdot\boldsymbol{u}_\mathrm{s}}{|\boldsymbol{u}_\mathrm{s}|}\,\varphi'(|\boldsymbol{u}_\mathrm{s}|)\,\mathrm{d}\boldsymbol{x} \\
&\qquad + \frac{b^2}{2\epsilon_2}\left[\int \rho_\mathrm{s}\left(1 + \frac{\epsilon_2}{\epsilon_1}\frac{\varphi'}{|\boldsymbol{u}_\mathrm{s}|}\right)^{\frac{2}{\delta}}\mathrm{d}x\right]^{\frac{\delta}{2}} * \left[\int_\Omega \left(\rho_\mathrm{s}^{2\gamma_\mathrm{s}-1-\frac{\delta}{2}}\right)^{\frac{2}{2-\delta}}\mathrm{d}x\right]^{\frac{2}{2-\delta}},
\end{aligned}$$

where $\Phi = \left|\varphi'' - \frac{\varphi'}{|\boldsymbol{u}_\mathrm{s}|}\right| + \frac{\epsilon_2}{4}\left(\varphi'' - \frac{\varphi'}{|\boldsymbol{u}_\mathrm{s}|}\right)^2$.

Proof. Let $\varphi(|\boldsymbol{u}_\mathrm{s}|)$ be a smooth function such that $\varphi' \geq 0$ and $\varphi(|\boldsymbol{u}_\mathrm{s}|) = 0 \Leftrightarrow |\boldsymbol{u}_\mathrm{s}| = 0$. I have that $\partial\varphi(|\boldsymbol{u}_\mathrm{s}|) = \varphi'(|\boldsymbol{u}_\mathrm{s}|)\frac{\boldsymbol{u}_\mathrm{s}}{|\boldsymbol{u}_\mathrm{s}|}\cdot\partial\boldsymbol{u}_\mathrm{s}$, so it is convenient to write the dot product of $\varphi'(|\boldsymbol{u}_\mathrm{s}|)\frac{\boldsymbol{u}_\mathrm{s}}{|\boldsymbol{u}_\mathrm{s}|}$ with Eq. (2.2.1d). I analyze the terms in the momentum equation one by one.

The equations of continuity make possible to switch between the Eulerian and the Lagrangian formulation of the inertial term for each phase:

$$\partial_t(\rho\, f) + \nabla\cdot(\rho\,\boldsymbol{u}\, f) = \rho(\partial_t f + \boldsymbol{u}\cdot\nabla f), \quad \forall\,\text{smooth } f(t,\boldsymbol{x})\,.$$

Using this property for every Cartesian component of $\boldsymbol{u}_\mathrm{s}$ and for the scalar $\varphi(|\boldsymbol{u}_\mathrm{s}|)$, the inertial term in Eq. (2.2.1d) becomes:

$$\begin{aligned}
&\rho_\mathrm{s}(\partial_t\boldsymbol{u}_\mathrm{s} + \boldsymbol{u}_\mathrm{s}\cdot\nabla\boldsymbol{u}_\mathrm{s})\cdot\varphi'(|\boldsymbol{u}_\mathrm{s}|)\frac{\boldsymbol{u}_\mathrm{s}}{|\boldsymbol{u}_\mathrm{s}|} \\
&\qquad = \rho_\mathrm{s}(\partial_t\varphi(|\boldsymbol{u}_\mathrm{s}|) + \boldsymbol{u}_\mathrm{s}\cdot\nabla\varphi(|\boldsymbol{u}_\mathrm{s}|)) = \partial_t(\rho_\mathrm{s}\varphi(|\boldsymbol{u}_\mathrm{s}|)) + \nabla\cdot(\rho_\mathrm{s}\boldsymbol{u}_\mathrm{s}\varphi(|\boldsymbol{u}_\mathrm{s}|))\,.
\end{aligned}$$

I then integrate over Ω, producing $\mathrm{d}_t\int_\Omega \rho_\mathrm{s}\,\varphi(|\boldsymbol{u}_\mathrm{s}|)$ and many other terms to be estimated.

Multiplying and integrating the diffusion term, I get

$$\begin{aligned}
&-\int_\Omega \nabla\cdot(2\rho_\mathrm{s}\mathcal{D}_\mathrm{s})\cdot\varphi'(|\boldsymbol{u}_\mathrm{s}|)\frac{\boldsymbol{u}_\mathrm{s}}{|\boldsymbol{u}_\mathrm{s}|}\,\mathrm{d}\boldsymbol{x} = \int_\Omega 2\rho_\mathrm{s}\mathcal{D}_\mathrm{s} : \nabla\left(\varphi'\frac{\boldsymbol{u}_\mathrm{s}}{|\boldsymbol{u}_\mathrm{s}|}\right)\mathrm{d}\boldsymbol{x} \\
&= \int_\Omega 2\rho_\mathrm{s}\mathcal{D}_\mathrm{s} : \left[\varphi'\frac{\nabla\boldsymbol{u}_\mathrm{s}}{|\boldsymbol{u}_\mathrm{s}|} + \left(\varphi'' - \frac{\varphi'}{|\boldsymbol{u}_\mathrm{s}|}\right)\frac{(\nabla\boldsymbol{u}_\mathrm{s}\cdot\boldsymbol{u}_\mathrm{s})\otimes\boldsymbol{u}_\mathrm{s}}{|\boldsymbol{u}_\mathrm{s}|^2}\right]\mathrm{d}\boldsymbol{x} \\
&\qquad = \int_\Omega 2\rho_\mathrm{s}\frac{\varphi'}{|\boldsymbol{u}_\mathrm{s}|}|\mathcal{D}_\mathrm{s}|^2\,\mathrm{d}\boldsymbol{x} + \int_\Omega 2\rho_\mathrm{s}\left(\varphi'' - \frac{\varphi'}{|\boldsymbol{u}_\mathrm{s}|}\right)\frac{(\mathcal{D}_\mathrm{s}\cdot\boldsymbol{u}_\mathrm{s})\cdot(\nabla\boldsymbol{u}_\mathrm{s}\cdot\boldsymbol{u}_\mathrm{s})}{|\boldsymbol{u}_\mathrm{s}|^2}\,\mathrm{d}\boldsymbol{x}\,.
\end{aligned}$$

In particular, thanks to the Cauchy-Schwartz inequality:

$$\left|\int_\Omega 2\rho_\mathrm{s}\left(\varphi'' - \frac{\varphi'}{|\boldsymbol{u}_\mathrm{s}|}\right)\frac{(\mathcal{D}_\mathrm{s}\cdot\boldsymbol{u}_\mathrm{s})\cdot(\nabla\boldsymbol{u}_\mathrm{s}\cdot\boldsymbol{u}_\mathrm{s})}{|\boldsymbol{u}_\mathrm{s}|^2}\right|\mathrm{d}\boldsymbol{x} \leq \int_\Omega 2\rho_\mathrm{s}\left|\varphi'' - \frac{\varphi'}{|\boldsymbol{u}_\mathrm{s}|}\right||\nabla\boldsymbol{u}_\mathrm{s}|^2\,\mathrm{d}\boldsymbol{x}.$$

I now pass to the pressure term. I notice that $|\mathcal{D}|^2 = \sum_i(\partial_i u_i)^2 + \sum_{j>i}\frac{1}{2}[(\partial_i u_j)^2 + (\partial_j u_i)^2]$ from which

$$(\nabla\cdot\boldsymbol{u})^2 \leq \sum_i\sum_j \partial_i u_i\partial_j u_j \leq \sum_i\sum_j \frac{1}{2}[(\partial_i u_i)^2 + (\partial_j u_j)^2] \leq 3|\mathcal{D}|^2\,.$$

Integration by parts gives us that $\forall\, \epsilon_{1,2} > 0$:

$$\begin{aligned}
&\left| \int_\Omega b \nabla \rho_{\mathrm{s}}^{\gamma_{\mathrm{s}}} \cdot \varphi' \frac{\boldsymbol{u}_{\mathrm{s}}}{|\boldsymbol{u}_{\mathrm{s}}|} \,\mathrm{d}\boldsymbol{x} \right| = \left| \int_\Omega b \rho_{\mathrm{s}}^{\gamma_{\mathrm{s}}} \left[\varphi' \frac{\nabla \cdot \boldsymbol{u}_{\mathrm{s}}}{|\boldsymbol{u}_{\mathrm{s}}|} + \left(\varphi'' - \frac{\varphi'}{|\boldsymbol{u}_{\mathrm{s}}|} \right) \frac{\boldsymbol{u}_{\mathrm{s}} \otimes \boldsymbol{u}_{\mathrm{s}} : \nabla \boldsymbol{u}_{\mathrm{s}}}{|\boldsymbol{u}_{\mathrm{s}}|^2} \right] \mathrm{d}\boldsymbol{x} \right| \\
&\leq \left(\int_\Omega \frac{\varphi'}{|\boldsymbol{u}_{\mathrm{s}}|} b^2 \rho_{\mathrm{s}}^{2\gamma_{\mathrm{s}}-1} \,\mathrm{d}\boldsymbol{x} \right)^{\frac{1}{2}} \left(\int_\Omega \frac{\rho_{\mathrm{s}} \varphi'}{|\boldsymbol{u}_{\mathrm{s}}|} (\nabla \cdot \boldsymbol{u}_{\mathrm{s}})^2 \,\mathrm{d}x \right)^{\frac{1}{2}} + \\
&+ \left(\int_\Omega \rho_{\mathrm{s}} \left(\varphi'' - \frac{\varphi'}{|\boldsymbol{u}_{\mathrm{s}}|} \right)^2 |\nabla \boldsymbol{u}_{\mathrm{s}}|^2 \,\mathrm{d}\boldsymbol{x} \right)^{\frac{1}{2}} \left(\int_\Omega b^2 \rho_{\mathrm{s}}^{2\gamma_{\mathrm{s}}-1} \,\mathrm{d}\boldsymbol{x} \right)^{\frac{1}{2}} \\
&\leq \frac{1}{2\epsilon_1} \int_\Omega \frac{\varphi'}{|\boldsymbol{u}_{\mathrm{s}}|} b^2 \rho_{\mathrm{s}}^{2\gamma_{\mathrm{s}}-1} \,\mathrm{d}\boldsymbol{x} + \frac{\epsilon_1}{2} \int_\Omega \rho_{\mathrm{s}} \frac{\varphi'}{|\boldsymbol{u}_{\mathrm{s}}|} (\nabla \cdot \boldsymbol{u}_{\mathrm{s}})^2 \,\mathrm{d}\boldsymbol{x} + \\
&+ \frac{1}{2\epsilon_2} \int_\Omega b^2 \rho_{\mathrm{s}}^{2\gamma_{\mathrm{s}}-1} \,\mathrm{d}x + \frac{\epsilon_2}{2} \int \rho_{\mathrm{s}} \left(\varphi'' - \frac{\varphi'}{|\boldsymbol{u}_{\mathrm{s}}|} \right)^2 |\nabla \boldsymbol{u}_{\mathrm{s}}|^2 \,\mathrm{d}\boldsymbol{x} \\
&\leq \frac{b^2}{2\epsilon_2} \left[\int \rho_{\mathrm{s}} \left(1 + \frac{\epsilon_2}{\epsilon_1} \frac{\varphi'}{|\boldsymbol{u}_{\mathrm{s}}|} \right)^{\frac{2}{\delta}} \mathrm{d}x \right]^{\frac{\delta}{2}} \left[\int_\Omega \left(\rho_{\mathrm{s}}^{2\gamma_{\mathrm{s}}-1-\frac{\delta}{2}} \right)^{\frac{2}{2-\delta}} \mathrm{d}x \right]^{\frac{2-\delta}{2}} \\
&\qquad + \frac{3\epsilon_1}{2} \int_\Omega \rho_{\mathrm{s}} \frac{\varphi'}{|\boldsymbol{u}_{\mathrm{s}}|} |\mathcal{D}_{\mathrm{s}}|^2 \,\mathrm{d}\boldsymbol{x} + \frac{\epsilon_2}{2} \int_\Omega \rho_{\mathrm{s}} \left(\varphi'' - \frac{\varphi'}{|\boldsymbol{u}_{\mathrm{s}}|} \right)^2 |\nabla \boldsymbol{u}_{\mathrm{s}}|^2 \,\mathrm{d}\boldsymbol{x} \,.
\end{aligned}$$

Putting all together, Eq. (2.2.1d) gives the Lemma. □

Now, choosing $\varphi(|\boldsymbol{u}_{\mathrm{s}}|) = \frac{1+|\boldsymbol{u}_{\mathrm{s}}|^2}{2} \ln(1+|\boldsymbol{u}_{\mathrm{s}}|^2)$ and $\epsilon_1 = \epsilon_2 = \epsilon$, I get

$$\begin{aligned}
&\mathrm{d}_t \int_\Omega \rho_{\mathrm{s}} \frac{1+|\boldsymbol{u}_{\mathrm{s}}|^2}{2} \ln(1+|\boldsymbol{u}_{\mathrm{s}}|^2) \,\mathrm{d}\boldsymbol{x} + \left(1 - \frac{3\epsilon}{2} \right) \int_\Omega 2\rho_{\mathrm{s}} (1+\ln(1+|\boldsymbol{u}_{\mathrm{s}}|^2)) |\mathcal{D}_{\mathrm{s}}|^2 \,\mathrm{d}\boldsymbol{x} \\
&\leq \int_\Omega 2(2+\epsilon)\rho_{\mathrm{s}} |\nabla \boldsymbol{u}_{\mathrm{s}}|^2 \,\mathrm{d}\boldsymbol{x} + \frac{b^2}{2\epsilon} \Big[\int_\Omega \rho_{\mathrm{s}} (2+\ln(1+|\boldsymbol{u}_{\mathrm{s}}|^2))^{\frac{2}{\delta}} \,\mathrm{d}\boldsymbol{x} \Big]^{\frac{\delta}{2}} * \Big[\int_\Omega \left(\rho_{\mathrm{s}}^{2\gamma_{\mathrm{s}}-1-\frac{\delta}{2}} \right)^{\frac{2}{2-\delta}} \mathrm{d}\boldsymbol{x} \Big]^{\frac{2-\delta}{2}} \\
&- \frac{1}{\tau_{\mathrm{s}}} \int_\Omega \rho_{\mathrm{s}} |\boldsymbol{u}_{\mathrm{s}}|^2 \left(1 + \ln(1+|\boldsymbol{u}_{\mathrm{s}}|^2) \right) \mathrm{d}\boldsymbol{x} + \frac{1}{\tau_{\mathrm{s}}} \int_\Omega \rho_{\mathrm{s}} \boldsymbol{u}_{\mathrm{f}} \cdot \boldsymbol{u}_{\mathrm{s}} \left(1 + \ln(1+|\boldsymbol{u}_{\mathrm{s}}|^2) \right) \mathrm{d}\boldsymbol{x} \,.
\end{aligned} \tag{2.3.25}$$

The first term on the right hand belongs to $L^1(0,T)$ thanks to (2.3.21), while $\int_\Omega \rho_{\mathrm{s}} (2+\ln(1+|\boldsymbol{u}_{\mathrm{s}}|^2))^{\frac{2}{\delta}} \,\mathrm{d}\boldsymbol{x}$ thanks to (2.3.19) and (2.3.22). Then, since in three dimensions $\rho_{\mathrm{s}}^{\gamma_{\mathrm{s}}}$ is bounded in $L^{5/3}(0, T \times \Omega)$, thus (for small δ) $\int_{[0,T]\times\Omega} \left(\rho_{\mathrm{s}}^{2\gamma_{\mathrm{s}}-1-\frac{\delta}{2}} \right)^{\frac{2}{2-\delta}} \mathrm{d}\boldsymbol{x}\,\mathrm{d}t$ it is bounded, provided that $\gamma_{\mathrm{s}} < 3$.

On the right hand side remains the term $\int_\Omega \rho_{\mathrm{s}} |\boldsymbol{u}_{\mathrm{s}}|^2 (1+\ln(1+|\boldsymbol{u}_{\mathrm{s}}|^2)) \,\mathrm{d}\boldsymbol{x}$ –which is treatable with the Gronwall Lemma– and $\int_\Omega \rho_{\mathrm{s}} \boldsymbol{u}_{\mathrm{s}} \cdot \boldsymbol{u}_{\mathrm{f}} (1+\ln(1+|\boldsymbol{u}_{\mathrm{s}}|^2)) \,\mathrm{d}\boldsymbol{x}$. Making use of (2.3.18), (2.3.19), (2.3.20) and the usual Sobolev embeddings, the integral $\int_\Omega \rho_{\mathrm{s}} \boldsymbol{u}_{\mathrm{s}} \cdot \boldsymbol{u}_{\mathrm{f}} \,\mathrm{d}\boldsymbol{x}$ it is bounded, thus I have to deal only with $\int_\Omega \rho_{\mathrm{s}} \boldsymbol{u}_{\mathrm{s}} \cdot \boldsymbol{u}_{\mathrm{f}} \ln(1+|\boldsymbol{u}_{\mathrm{s}}|^2) \,\mathrm{d}\boldsymbol{x}$.

I have that $\ln(1+|\boldsymbol{u}_{\mathrm{s}}|^2) \,\mathrm{d}\boldsymbol{x}$ is bounded by $|\boldsymbol{u}_{\mathrm{s}}|^\epsilon$ for all $\epsilon > 0$. Using Hölder inequality, I get for all $0 < \epsilon < \frac{2}{3}$

$$\begin{aligned}
\int_\Omega \rho_{\mathrm{s}} \boldsymbol{u}_{\mathrm{s}} \cdot \boldsymbol{u}_{\mathrm{f}} \ln(1+|\boldsymbol{u}_{\mathrm{s}}|^2) \,\mathrm{d}\boldsymbol{x} &\leq \int_\Omega \rho_{\mathrm{s}}^{\frac{1-\epsilon}{2}} |\boldsymbol{u}_{\mathrm{f}}| |\rho_{\mathrm{s}}^{\frac{1}{2}} \boldsymbol{u}_{\mathrm{s}}|^{1+\epsilon} \,\mathrm{d}\boldsymbol{x} \\
&\leq \|\rho_{\mathrm{s}}\|^{\frac{1-\epsilon}{2}}_{L^{\frac{3(1-\epsilon)}{2-3\epsilon}}(\Omega)} \|\boldsymbol{u}_{\mathrm{f}}\|_{L^6(\Omega)} \|\rho_{\mathrm{s}}^{\frac{1}{2}} \boldsymbol{u}_{\mathrm{s}}\|^{1+\epsilon}_{L^2(\Omega)} \,,
\end{aligned}$$

that is optimal for $\epsilon \to 0$, thus here I need $\rho_{\rm s} \in L^\infty(0,T;L^q(\Omega))$, for $q > \frac{3}{2}$ that it is given by (2.3.20). Finally, I just proved the following Lemma:

Lemma 2.3.4. *If $\gamma_{\rm s} < 3$ holds, then*

$$\rho_{\rm s}|\boldsymbol{u}_{\rm s}|^2 \ln(1+|\boldsymbol{u}_{\rm s}|^2) \quad \textit{is bounded in } L^\infty(0,T;L^1(\Omega))\,. \tag{2.3.26}$$

Convergence of particles' density.

The estimates proved in the previous lemmas can be used now to get the requested compactness. The first and basic results concerns the square root of the particles' density $\rho_{\rm s}$ (I have seen that this quantity represents, in the formulation I consider an unknown by itself).

Lemma 2.3.5. *Let $(\rho_{\rm s})_n$ be a sequence of solutions, then*

$$\partial_t\sqrt{(\rho_{\rm s})_n} \in L^2(0,T;H^{-1}(\Omega))\,,$$

uniformly with respect to n. This implies that

$$\sqrt{(\rho_{\rm s})_n} \to \sqrt{\rho_{\rm s}} \quad \textit{a.e. and} \quad L^2(0,T;L^2_{\rm loc}(\Omega)) \textit{ strong,} \tag{2.3.27}$$
$$(\rho_{\rm s})_n^{\gamma_{\rm s}} \to \rho_{\rm s}^{\gamma_{\rm s}} \quad L^1_{\rm loc}(0,T\times\Omega) \textit{ strong}\,. \tag{2.3.28}$$

Moreover $(\rho_{\rm s})_n$ converges to $\rho_{\rm s}$ in $C(0,T;L^{3/2}_{\rm loc}(\Omega))$.

Proof. Using Eq. (2.2.1c) and writing derivatives in an explicit way, I get

$$\partial_t\sqrt{(\rho_{\rm s})_n} = \frac{1}{2\sqrt{(\rho_{\rm s})_n}}\partial_t(\rho_{\rm s})_n = -\frac{1}{2}\sqrt{(\rho_{\rm s})_n}\nabla\cdot\boldsymbol{u}_{\rm s} - \boldsymbol{u}_{\rm s}\cdot\nabla\sqrt{(\rho_{\rm s})_n} =$$
$$= -\nabla\cdot(\frac{1}{2}\sqrt{(\rho_{\rm s})_n}\boldsymbol{u}_{\rm s}) + \frac{1}{2}\sqrt{(\rho_{\rm s})_n}\nabla\cdot\boldsymbol{u}_{\rm s}\,.$$

Now, by using the previous estimates (especially (2.3.19) and (2.3.21)) I find that $\partial_t\sqrt{(\rho_{\rm s})_n}$ is bounded in $L^2(0,T;H^{-1}(\Omega))$ which, thanks to Aubin-Lions Lemma [cf. 47], gives the strong convergence in $L^2_{\rm loc}(0,T\times\Omega)$.

Next, the Sobolev embedding $W^{1,2}(\Omega)\hookrightarrow L^6(\Omega)$ and (2.3.22) imply that $(\rho_{\rm s})_n$ is bounded in $L^\infty(0,T;L^6(\Omega))$. Thus, with (2.3.19), I get

$$(\rho_{\rm s})_n(\boldsymbol{u}_{\rm s})_n = \sqrt{(\rho_{\rm s})_n}\,\sqrt{(\rho_{\rm s})_n}(\boldsymbol{u}_{\rm s})_n \in L^\infty(0,T;L^{3/2}(\Omega))\,.$$

The continuity equation for particles gives the boundedness of $\partial_t(\rho_{\rm s})_n$ in $L^\infty(0,T;W^{-1,3/2}(\Omega))$. Moreover, since $\nabla(\rho_{\rm s})_n = 2\sqrt{(\rho_{\rm s})_n}\nabla\sqrt{(\rho_{\rm s})_n}$, I have $(\rho_{\rm s})_n$ bounded in $L^\infty(0,T;W^{1,3/2}(\Omega))$, hence I get also the compactness of $(\rho_{\rm s})_n$ in $C^0(0,T;L^{3/2}_{\rm loc}(\Omega))$. At this level the strong convergence of the density $\rho_{\rm s}$ is easier than that for $\rho_{\rm f}$, but difficulties will arise for the velocity $\boldsymbol{u}_{\rm s}$, especially for its proper definition.

I finally observe that, the bounds coming from by (2.3.24) and $(\rho_{\rm s})_n^{\gamma_{\rm s}} \to \rho_{\rm s}^{\gamma_{\rm s}}$ a.e., yield the strong convergence of particles pressure $\rho_{\rm s}^{\gamma_{\rm s}}$ in $L^1_{\rm loc}([0,T]\times\Omega)$. □

Convergence of particles' momentum.

I now explain the compactness argument which allows to control the momentum $\boldsymbol{m}_{\mathrm{s}} = \rho_{\mathrm{s}}\boldsymbol{u}_{\mathrm{s}}$

Lemma 2.3.6. *Up to a sub-sequence, the momentum $(\boldsymbol{m}_{\mathrm{s}})_n = (\rho_{\mathrm{s}})_n(\boldsymbol{u}_{\mathrm{s}})_n$ converges strongly in $L^2(0,T;L^q_{\mathrm{loc}}(\Omega))$ to some $\boldsymbol{m}_{\mathrm{s}}(\boldsymbol{x},t)$, for all $q \in [1,\frac{3}{2})$. In particular,*

$$(\boldsymbol{m}_{\mathrm{s}})_n \to \boldsymbol{m}_{\mathrm{s}} \quad a.e \quad (\boldsymbol{x},t) \in \Omega \times [0,T]\,.$$

Proof. I have:

$$\nabla\left((\rho_{\mathrm{s}})_n(\boldsymbol{u}_{\mathrm{s}})_n\right) = (\rho_{\mathrm{s}})_n\nabla(\boldsymbol{u}_{\mathrm{s}})_n + (\boldsymbol{u}_{\mathrm{s}})_n\nabla(\rho_{\mathrm{s}})_n = \\ = \sqrt{(\rho_{\mathrm{s}})_n}\,\sqrt{(\rho_{\mathrm{s}})_n}\nabla(\boldsymbol{u}_{\mathrm{s}})_n + 2\sqrt{(\rho_{\mathrm{s}})_n}(\boldsymbol{u}_{\mathrm{s}})_n\nabla\sqrt{(\rho_{\mathrm{s}})_n}\,,$$

hence, bounds (2.3.22), (2.3.21), (2.3.19) give

$$(\boldsymbol{m}_{\mathrm{s}})_n \in L^2(0,T;W^{1,1}(\Omega))\,.$$

Now, I want to use Aubin's Lemma in this setting:

$$(\boldsymbol{m}_{\mathrm{s}})_n \in W^{1,1}(\Omega) \subset\subset L^q(\Omega) \hookrightarrow W^{-2,\frac{4}{3}}(\Omega) \ni \partial_t(\boldsymbol{m}_{\mathrm{s}})_n \quad \forall q \in \left[1,\frac{3}{2}\right)\,.$$

The second and third relationship are given by Rellich-Kondrachov Theorem, therefore I need to prove just the latter inclusion.

I use the momentum equation (2.2.1d), first noticing from the bounds (2.3.19) and (2.3.22) that

$$\nabla\cdot\left(\sqrt{(\rho_{\mathrm{s}})_n}(\boldsymbol{u}_{\mathrm{s}})_n \otimes \sqrt{(\rho_{\mathrm{s}})_n}(\boldsymbol{u}_{\mathrm{s}})_n\right) + b\nabla(\rho_{\mathrm{s}})_n^{\gamma_{\mathrm{s}}} \quad \in L^\infty(0,T;W^{-1,1}(\Omega))\,.$$

Then, I deal with the dissipation term. Using the bounds (2.3.22), (2.3.19),

$$(\rho_{\mathrm{s}})_n\nabla(\boldsymbol{u}_{\mathrm{s}})_n = \nabla\left(\sqrt{(\rho_{\mathrm{s}})_n}\sqrt{(\rho_{\mathrm{s}})_n}(\boldsymbol{u}_{\mathrm{s}})_n\right) - 2\sqrt{(\rho_{\mathrm{s}})_n}(\boldsymbol{u}_{\mathrm{s}})_n \otimes \nabla\sqrt{(\rho_{\mathrm{s}})_n}\,,$$

is bounded in $L^\infty(0,T;W^{-1,\frac{3}{2}}(\Omega)+L^1(\Omega)) \subset L^\infty(0,T;W^{-1,\frac{4}{3}}(\Omega))$ thanks to Rellich-Kondrachov theorem [see 21]. As a consequence, since the drag term $(\rho_{\mathrm{s}})_n((\boldsymbol{u}_{\mathrm{s}})_n - \boldsymbol{u}_{\mathrm{f}})$ is bounded in $L^\infty(0,T;L^{3/2}(\Omega))+L^2(0,T;L^{6/5}(\Omega))$ which is included in $L^2(0,T;W^{-1,\frac{4}{3}}(\Omega)$, I found the desired bound on $\partial_t(\boldsymbol{m}_{\mathrm{s}})_n$. This ends the proof of the lemma. □

Remark I observe that at this point the velocity $\boldsymbol{u}_{\mathrm{s}}$ can be defined in the set $\{\rho_{\mathrm{s}} > 0\}$ as $\boldsymbol{u}_{\mathrm{s}} \equiv \frac{\boldsymbol{m}_{\mathrm{s}}}{\rho_{\mathrm{s}}}$, but I need to prove that the momentum vanishes in the region without particles, that is in $\{\rho_{\mathrm{s}} = 0\}$.

The final step concerns the convergence of $\sqrt{\rho_{\mathrm{s}}}\boldsymbol{u}_{\mathrm{s}}$ and I have the following lemma

Lemma 2.3.7. *The quantity $\sqrt{(\rho_{\rm s})_n}(\boldsymbol{u}_{\rm s})_n$ converges strongly in $L^2_{loc}([0,T]\times\Omega)$ to $\frac{\boldsymbol{m}_{\rm s}}{\sqrt{\rho_{\rm s}}}$ and $\boldsymbol{m}_{\rm s}=0$ almost everywhere in $\{\rho_{\rm s}=0\}$ and I can find a function $\boldsymbol{u}_{\rm s}(t,\boldsymbol{x})$ such that $\boldsymbol{m}_{\rm s}=\rho_{\rm s}\boldsymbol{u}_{\rm s}$ and*

$$(\rho_{\rm s})_n(\boldsymbol{u}_{\rm s})_n\to\rho_{\rm s}\boldsymbol{u}_{\rm s}\quad \textit{strongly in } L^2(0,T;L^p(\Omega)),\ \forall\, p\in[1,3/2[\,,$$
$$\sqrt{(\rho_{\rm s})_n}(\boldsymbol{u}_{\rm s})_n\to\sqrt{\rho_{\rm s}}\boldsymbol{u}_{\rm s}\quad \textit{strongly in } L^2_{loc}([0,T]\times\Omega)\,.$$

In particular $\boldsymbol{u}_{\rm s}=\boldsymbol{m}_{\rm s}/\rho_{\rm s}$ where $\rho_{\rm s}>0$, while $\boldsymbol{u}_{\rm s}=\mathbf{0}$ in $\{\rho_{\rm s}=0\}$. This is a somewhat arbitrary way of defining $\boldsymbol{u}_{\rm s}$. Nothing excludes the chance of having other solutions, with non-zero velocity in the region without particles.

Proof. The proof of this result follows very closely that of [132, Lemma 4.6], since it does not use the equations, but just a priori estimates previously established. It is at this step that I need to use the logarithmic improved bound, since the control of $\int_\Omega \rho_{\rm s}|\boldsymbol{u}_{\rm s}|^2\log(1+|\boldsymbol{u}_{\rm s}|^2)\,{\rm d}\boldsymbol{x}$ grows faster than the momentum. This allows to use standard compactness tools as those recalled in Evans [65]. In particular, one has that $(\boldsymbol{m}_{\rm s})_n/\sqrt{(\rho_{\rm s})_n}$ is bounded in $L^\infty(0,T;L^2(\Omega))$ and this can be used to show, after taking weak limit and with Fatou lemma that $\boldsymbol{m}_{\rm s}$ vanishes almost everywhere where $\rho_{\rm s}=0$. Hence, I can define a velocity by dividing the momentum by the density and setting $\boldsymbol{u}_{\rm s}=0$ where this is not possible, i.e., in the regions without particles. Then it is possible to show that for all $M>0$ the sequence $\sqrt{(\rho_{\rm s})_n}(\boldsymbol{u}_{\rm s})_n\,\chi(|(\boldsymbol{u}_{\rm s})_n|\le M)$ converges almost everywhere to $\sqrt{\rho_{\rm s}}\boldsymbol{u}_{\rm s}\,\chi(|\boldsymbol{u}_{\rm s}|\le M)$, where $\chi(A)$ denotes the indicatrix function of the measurable set A. This in turn implies, by using (2.3.26) that, for all $M>0$

$$\limsup_{n\to+\infty}\int_0^T\int_\Omega|\sqrt{(\rho_{\rm s})_n}(\boldsymbol{u}_{\rm s})_n-\sqrt{\rho_{\rm s}}\boldsymbol{u}_{\rm s}|\,{\rm d}\boldsymbol{x}{\rm d}t\le\frac{C}{\log(1+M^2)}.$$

The arbitrary choice of M implies the requested convergence □

The final step concerns the dissipation term. Again by using the equations and following closely the approach from [132, Lemma 4.7] I have the following result, which is needed to show that $(\rho_{\rm s},\boldsymbol{u}_{\rm s})$ satisfy the equation in the weak sense. In particular it is needed to show that it is possible to pass to the limit in the diffusion term.

Lemma 2.3.8. *The following convergence holds true*

$$(\rho_{\rm s})_n(\nabla\boldsymbol{u}_{\rm s})_n\to\rho_{\rm s}\nabla\boldsymbol{u}_{\rm s}\qquad\textit{in the sense of distributions on } (0,T)\times\Omega,$$
$$(\rho_{\rm s})_n(\nabla\boldsymbol{u}_{\rm s}^T)_n\to\rho_{\rm s}\nabla\boldsymbol{u}_{\rm s}^T\qquad\textit{in the sense of distributions on } (0,T)\times\Omega.$$

Proof. The proof follows just taking a smooth space-time test-function ϕ and rewriting the relevant term as follows

$$\int_0^T\int_\Omega(\rho_{\rm s})_n(\boldsymbol{u}_{\rm s})_n\,\phi\,{\rm d}\boldsymbol{x}{\rm d}t$$
$$=-\int_0^T\int_\Omega\frac{(\rho_{\rm s})_n}{\sqrt{(\rho_{\rm s})_n}}\sqrt{(\rho_{\rm s})_n}(\boldsymbol{u}_{\rm s})_n\,\phi\,{\rm d}\boldsymbol{x}{\rm d}t+\int_0^T\int_\Omega\sqrt{(\rho_{\rm s})_n}(\boldsymbol{u}_{\rm s})_n\frac{1}{\sqrt{(\rho_{\rm s})_n}}\,\phi\,{\rm d}\boldsymbol{x}{\rm d}t,$$

and using the convergence results established before. The term with the transposed part of the matrix of derivatives is then treated in the same way and this implies the convergence for the term $(\rho_{\rm s})_n(\mathcal{D}_{\rm s})_n$ in the weak formulation. □

2.4 On the full system

As explained in the introduction, the result sketched is just that of stability of sequences of solutions. Now, I will just write the complete system (at the continuous level, but remind that also a Galerkin approximation is needed as a first step) which can be used to construct the weak solution, by following the approach of Vasseur and Yu [206, 205]. Details are too long to be reported here and out of the primary scopes of the thesis, so they will appear in a forthcoming paper. I am writing in red the terms which can be used in some very recently established way to approximate the system and to produce a priori estimates which respect the BD entropy and the MV approach. The positive approximation parameters are denoted by ϵ, λ, δ, κ.

In particular, one has to smooth both the density equations in a parabolic way, bay adding a diffusion (Laplace) term. This has as a first consequence that, in order to keep the basic energy balance, a quadratic term $\epsilon\nabla\boldsymbol{u}\nabla\rho$ has to the added to both the momentum equations. For technical reasons concerned with certain estimates (especially to work with the smaller exponent γ and to have densities which are square integrable), one has also to add a further barotropic pressure term with a large enough exponent β in both equations. Then a bi-Laplacian is needed by the particles' momentum equation and a regularizing term involving high powers of $\rho_{\rm s}$. The most important one is nevertheless the term $\kappa\rho_{\rm s}\nabla\left(\frac{\Delta\sqrt{\rho_{\rm s}}}{\sqrt{\rho_{\rm s}}}\right)$ which can be considered as a Bohm potential, and which is motivated also by related results for quantum fluids [1]. The full system reads:

$$\partial_t\rho_{\rm f}+\nabla\cdot(\rho_{\rm f}\boldsymbol{u}_{\rm f})=\epsilon\Delta\rho_{\rm f}\,, \tag{2.4.1a}$$

$$\partial_t\rho_{\rm s}+\nabla\cdot(\rho_{\rm s}\boldsymbol{u}_{\rm s})=\epsilon\Delta\rho_{\rm s}\,, \tag{2.4.1b}$$

$$\begin{aligned}&\partial_t(\rho_{\rm f}\boldsymbol{u}_{\rm f})+\nabla\cdot(\rho_{\rm f}\boldsymbol{u}_{\rm f}\otimes\boldsymbol{u}_{\rm f}+b\rho_{\rm f}^{\gamma}\mathbb{I})-\mu\,\nabla\cdot(\mathcal{D}_{\rm f}-\frac{2}{3}\nabla\cdot\boldsymbol{u}_{\rm f}\mathbb{I})\\&\quad+\delta\rho_f^{\beta}+\epsilon\nabla\boldsymbol{u}_{\rm f}\nabla\rho_{\rm f}=\frac{\rho_{\rm s}}{\tau_{\rm s}}(\boldsymbol{u}_{\rm s}-\boldsymbol{u}_{\rm f})+\rho_{\rm f}\boldsymbol{g}\,,\end{aligned} \tag{2.4.1c}$$

$$\begin{aligned}&\partial_t(\rho_{\rm s}\boldsymbol{u}_{\rm s})+\nabla\cdot(\rho_{\rm s}\boldsymbol{u}_{\rm s}\otimes\boldsymbol{u}_{\rm s}+a\rho_{\rm s}^{\gamma_{\rm s}}\mathbb{I})-\nabla\cdot(\mu_{\rm s}\rho_{\rm s}\mathcal{D}_{\rm s})-\lambda\rho_{\rm s}\nabla\Delta^{9}\rho_{\rm s}\\&\quad+\delta\rho_{\rm s}^{\beta}+\epsilon\nabla\boldsymbol{u}_{\rm s}\nabla\rho_{\rm s}+\eta\Delta^{2}\boldsymbol{u}_{\rm s}=-\frac{\rho_{\rm s}}{\tau_{\rm s}}(\boldsymbol{u}_{\rm s}-\boldsymbol{u}_{\rm f})+\rho_{\rm s}\boldsymbol{g}+\kappa\rho_{\rm s}\nabla\left(\frac{\Delta\sqrt{\rho_{\rm s}}}{\sqrt{\rho_{\rm s}}}\right).\end{aligned} \tag{2.4.1d}$$

The novelty in the results which appeared for the moment as a Technical Report (just in the spring of 2015) [206, 205] is that all regularizing parameter can be taken to zero and the limit will give a weak solution of the model (2.2.1). The details, I am still double-checking are very intricate and they are based on a very specific way of taking limits in a determined order. First one has to pass to the limit in the Galerkin approximation (which I skipped in the system, being the most standard step), then one has to take the following limits

i) $\epsilon\to 0^{+}$;

[1] The quantum Navier-Stokes equations may have a lot of applications, in particular, quantum semiconductors, weakly interacting Bose gases, and quantum trajectories of Bohmian mechanics [see also dissipative models in 109].

ii) $\lambda \to 0^+$;

iii) $\delta \to 0^+$;

iv) $\kappa \to 0^+$;

and use the fact that the approximate system satisfies BD entropy, and using also standard compactness arguments as those explained before.

Chapter 3

Integral plume models

Starting from the balance equations of mass, momentum and energy of the [dusty] model, I formulate an integral 1D model for a polydisperse mixture injected in the atmosphere. I write all the equations, either in their most general formulation or in the more simplified, taking particular care in considering all the underlying hypothesis to make clear when it is possible and appropriate to use them. Moreover, I put all the equations in a non-dimensional form, making explicit all the dimensionless parameters that drive the dynamics of these phenomena. In particular, I find six non-dimensional parameters characterizing in a unique way a stationary multiphase plume in a calm, stratified environment. They are: ϕ, a parameter measuring the importance of the density contrast between the ejected plume mixture and the atmosphere; q_χ, q_ψ, two parameters measuring the multiphaseness of the plume; v_q, the entrainment coefficient; v_m, a modified Richardson number; ℓ_g, a parameter comparing the plume radius with the stratification length. Using the first three parameters a non-dimensional quantity γ_c is developed, measuring the stability of the plume column.

Setting to zero some of these parameters, it is possible to recover some of the existing jet and plume models for single-phase flows, writing – originally – their multiphase counterpart. For each plume regime studied, I find an approximated ODE system and its first integral of motion. Moreover, I write a simplified set of equations for which it is possible to find analytical solutions that can be used to describe the dynamics of multiphase plumes and to find their height analytically.

In Sects. 3.1 and 3.2, I show how to recover a multiphase integral model from the three-dimensional balance equations of mass, momentum, and energy. In Sect. 3.3, I close the mathematical problem with the constitutive equations for a gas–particle mixture. In Sect. 3.4, I put in dimensionless form the integral model in its general formulation, individuating the six independent non-dimensional parameters characterizing a multiphase plume in a stratified environment. Then I study the corresponding mathematical problem in a number of different regimes, namely: 1) the monophase limit (Sect. 3.5); 2) the jet limit (Sect. 3.6); 3) the weak stratification limit (Sect. 3.7); 4) the weak stratification limit in Boussinesq approximation (Sect. 3.8). Finally in Sect. 3.9, I find an analytical solution approximating the more general problem introduced in Sect. 3.4. A graphical abstract is given in Fig. 3.0.1, where all the models and approximations treated in this chapter are schematized.

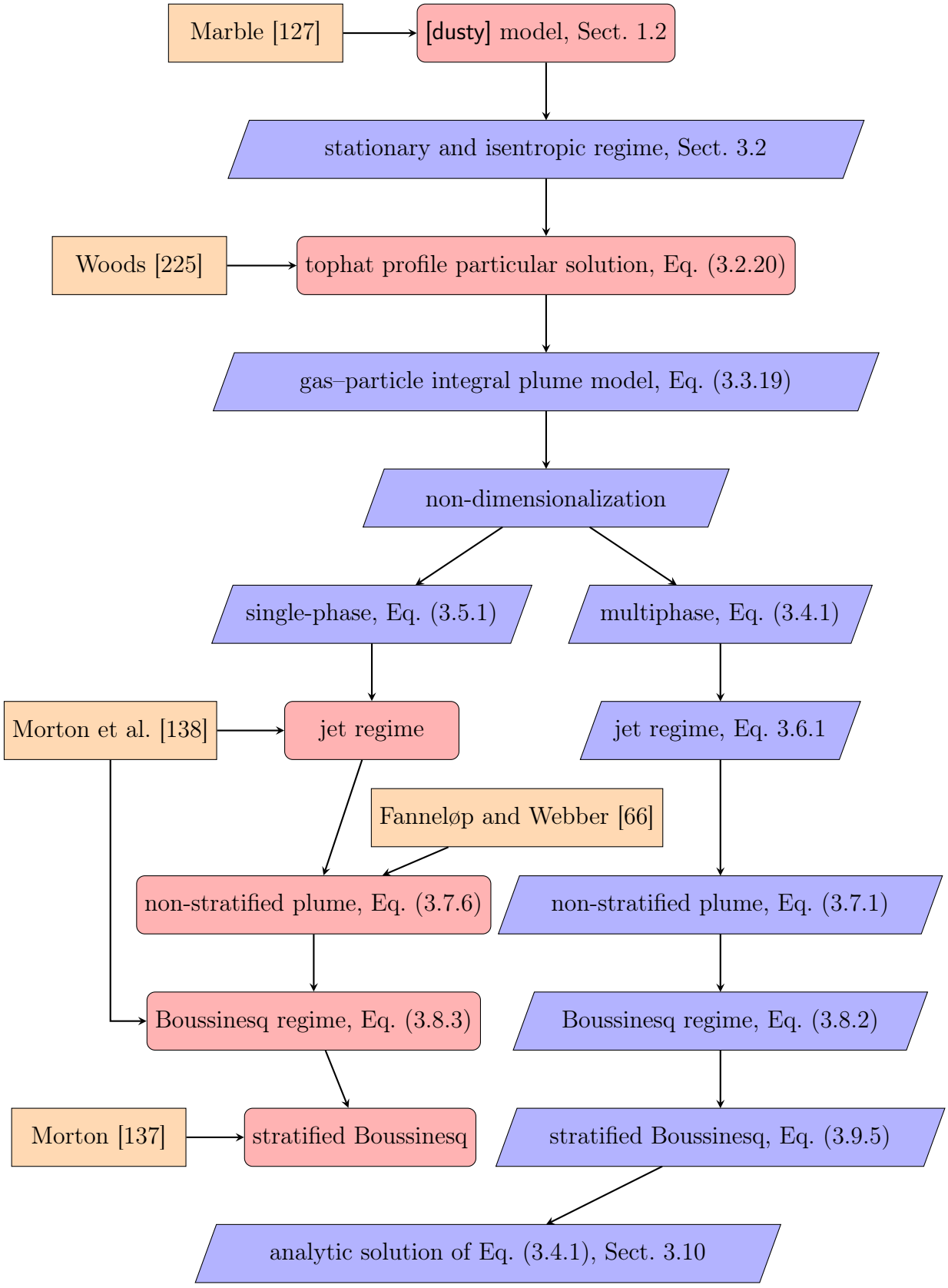

Figure 3.0.1: Flowchart of the present chapter. Red rounded rectangular boxes contain non-original results, which can be found in the literature cited in the orange rectangular boxes. Original results are in the trapezoidal boxes.

3.1 The main assumptions.

To use the [dusty] model (see Sect. 1.2), the following assumptions are necessary:

- Local equilibrium.
- All the phases, either solid or gaseous, move with the same velocity field $\boldsymbol{u}(\boldsymbol{x}, t)$. Marble [127] shows that this assumption is valid if the Stokes time τ_{s} is small compared to the smallest time scale of the evolution problem.
- All the phases, either solid or gaseous, have the same temperature field $T(\boldsymbol{x}, t)$. Marble [127] shows that this assumption is valid if the thermal relaxation time $\tau_{T,\mathrm{s}}$ is small compared to the smallest time scale of the evolution problem.

Here the interest is in the mean behavior of a turbulent buoyant plume. Writing that solution the following assumptions will be used [see 138, 137, 217, 122, 147, 225, 66, 111, 104, 151]:

- The Reynolds number is big enough and turbulence is fully developed, so that it is possible to disregard thermal conduction and shear dissipation.
- Pressure is constant along horizontal sections.
- The profiles of mean vertical velocity and mean density in horizontal sections are of similar form at all heights (self-similar assumption).
- The mean velocity field outside and near the plume is horizontal. An additional assumption on the dependence of the rate of entrainment at the edge of the plume to some characteristic velocity at that height is needed.
- Stationary flow.
- Radial symmetry around the source.

3.2 The multiphase buoyant plume model.

Using the hypothesis given in the previous section, the [dusty] model reviewed in Eqs. (1.2.3) simplifies:

$$\cancel{\partial_t \rho_i} + \nabla \cdot (\rho_i \boldsymbol{u}) = 0\,, \qquad i \in \mathcal{I} \tag{3.2.1a}$$

$$\cancel{\partial_t \rho_j} + \nabla \cdot (\rho_j \boldsymbol{u}) = 0\,, \qquad j \in \mathcal{J} \tag{3.2.1b}$$

$$\cancel{\partial_t \rho_{\mathrm{m}}} + \nabla \cdot (\rho_{\mathrm{m}} \boldsymbol{u}) = 0\,, \tag{3.2.1c}$$

$$\cancel{\partial_t (\rho_{\mathrm{m}} \boldsymbol{u})} + \nabla \cdot \left(\rho_{\mathrm{m}}\, \boldsymbol{u} \otimes \boldsymbol{u} + p \mathbb{I}\right) = \cancel{\nabla \cdot \mathbb{T}} + \rho_{\mathrm{m}}\, \boldsymbol{g}\,, \tag{3.2.1d}$$

$$\cancel{\partial_t (\rho_{\mathrm{m}} E_{\mathrm{m}})} + \nabla \cdot \left[\left(\rho_{\mathrm{m}} E_{\mathrm{m}} + p\right) \boldsymbol{u}\right] = \cancel{\nabla \cdot (u \cdot \mathbb{T}) - \nabla \cdot q} + \rho_{\mathrm{m}}\, \boldsymbol{u} \cdot \boldsymbol{g}\,. \tag{3.2.1e}$$

As suggested in Woods [225], it is convenient to use the specific enthalpy $h_{\mathrm{m}} = e_{\mathrm{m}} + \frac{p}{\rho_{\mathrm{m}}}$ instead of the specific energy e_{m}.

In this way, Eqs. (3.2.1) reduce to:

$$\nabla \cdot (\rho_i \boldsymbol{u}) = 0\,, \qquad i \in \mathcal{I} \tag{3.2.2a}$$

$$\nabla \cdot (\rho_j \boldsymbol{u}) = 0\,, \qquad j \in \mathcal{J} \tag{3.2.2b}$$

$$\nabla \cdot \left(\rho_{\mathrm{m}}\, \boldsymbol{u} \otimes \boldsymbol{u} + p\mathbb{I}\right) = \rho_{\mathrm{m}}\, \boldsymbol{g} \tag{3.2.2c}$$

$$\nabla \cdot \left[\rho_{\mathrm{m}} \left(\frac{|\boldsymbol{u}|^2}{2} + h_{\mathrm{m}}\right) \boldsymbol{u}\right] = \rho_{\mathrm{m}}\, \boldsymbol{u} \cdot \boldsymbol{g}\,. \tag{3.2.2d}$$

3.2.1 The buoyant plume solution.

Coherently with hypothesis of section 3.1, I will look for a solution of Eqs. (3.2.2) in the following form (z is the plume axis coordinate, and $b(z)$ is the plume radius profile):

$$y_k(r,z) = \begin{cases} 1\,, & \text{if } r \geq b(z) \text{ and } k = 1 \\ Y_\alpha(z)\,, & \text{if } r < b(z) \text{ and } k = 1 \\ 0\,, & \text{if } r \geq b(z) \text{ and } k \neq 1 \\ Y_k(z)\,, & \text{if } r < b(z) \text{ and } k \neq 1 \end{cases} \tag{3.2.3a}$$

$$\rho_{\mathrm{m}}(r,z) = \begin{cases} \beta(z)\,, & \text{if } 0 \leq r < b(z) \\ \alpha(z)\,, & \text{if } r \geq b(z) \end{cases} \tag{3.2.3b}$$

$$\boldsymbol{u}(r,z) = \begin{cases} +U(z)\hat{z}\,, & \text{if } 0 \leq r < b(z) \\ -U_\epsilon(z)\hat{r}\,, & \text{if } r = b(z) \\ -u_\epsilon(r,z)\hat{r}\,, & \text{if } r > b(z) \\ u_\epsilon = U_\epsilon & \text{if } r \to b(z) \\ u_\epsilon \to 0 & \text{if } r \gg b(z) \end{cases} \tag{3.2.3c}$$

$$p(r,z) = p(z) \tag{3.2.3d}$$

$$h_{\mathrm{m}}(r,z) = \begin{cases} h_\beta(z)\,, & \text{if } 0 \leq r < b(z) \\ h_\alpha(z)\,, & \text{if } r \geq b(z) \end{cases} \tag{3.2.3e}$$

where $k = i = 1$ is the phase index corresponding to the atmospheric gas, while $k \neq 1$ is the generic index of a phase ejected by the plume vent. Here I am using the so called purely "Top Hat" auto-similar profile. In general – as shown in Morton [137] and discussed after Eqs. (3.2.20) below – it is possible to use other profiles.

Since in the dusty gas model all the phases are completely coupled, in this chapter I will use a simplified notation: I refer to the ejected gas mixture with the subscript $(\cdot)_{\mathrm{e}}$ and to the ejected solid phase with the subscript $(\cdot)_s$. In this way, I define in the plume region $r < b(z)$ the ejected gas and solid particles mass fractions:

$$Y_{\mathrm{e}} = \sum_{i=2}^{I} Y_i \tag{3.2.4}$$

$$Y_{\mathrm{s}} = \sum_{\mathcal{J}} Y_j\,. \tag{3.2.5}$$

I have also defined: the ambient density $\alpha(z)$, the ambient enthalpy $h_\alpha(z)$, the mixture density β, the mixture enthalpy h_β, and the entrainment velocity U_ϵ. For the atmosphere, the profile of pressure $p(z)$, enthalpy $h_\alpha(z)$ and density $\alpha(z)$ must be given. The dependence of U_ϵ on other unknowns (the entrainment model) must be given. Here I express the entrainment velocity U_ϵ as

$$U_\epsilon = \varkappa U \eta_\varkappa (\beta/\alpha) \tag{3.2.6}$$

where $\varkappa$ is the dimensionless entrainment coefficient and $\eta_\varkappa$ is an arbitrary function of the density ratio [see e.g. 66]. When $\eta_\varkappa = 1$ the entrainment model by Morton et al. [138] is used, while if $\eta_\varkappa(x) = \sqrt{x}$ the model is that by Ricou and Spalding [160]. More generally, in the literature there are models where $\eta_\varkappa$ depends on the local Richardson number (see e.g. Carazzo et al. [26]).

3.2.2 The mean conservation equations.

In this section, I substitute the particular solution Eqs. (3.2.3) in the balance Eqs. (3.2.2). In this way, the latter PDE problem moves to an ODE system, where the only independent variable is the height z. The procedure to achieve this result is described in this section.

For each altitude $z \in [0, L]$, a control volume is defined as the cylinder of fixed radius $B > b(z)$ centered above the source $\mathbb{C} = \{(r, z) \in [0, B] \times [z, z + \delta z]\}$ (see Fig. 3.2.1). Using Eqs. (3.2.2a), (3.2.2b), (3.2.3b) and (3.2.3c), and the Gauss theorem, I find:

$$0 = \int_{\mathbb{C}} \left(\sum_{i \in \mathcal{I}} \nabla \cdot (\rho_i \boldsymbol{u}) + \sum_{j \in \mathcal{J}} \nabla \cdot (\rho_j \boldsymbol{u}) \right) = \int_{\mathbb{C}} \nabla \cdot (\rho_{\mathrm{m}} \boldsymbol{u}) = \\ = \beta U \pi b^2|_{z+\delta_z} - \beta U \pi b^2|_z - \alpha u_\epsilon(B, z) 2\pi B \delta z \, .$$

Now, dividing for δz, sending it to 0 and then $B \to b(z)$, the total mass flux conservation is obtained:

$$\mathrm{d}_z(Q) \equiv \mathrm{d}_z(\beta U b^2) = 2\alpha b U_\epsilon \, . \tag{3.2.7}$$

In the general case, the source ejects solid phases that are not in the atmosphere and some gaseous phase that is not included in the ambient composition. Identifying such a phases, respectively, with the index $i \in [2; I]$ and $j \in \mathcal{J} = [I + 1; I + J]$, and using again Eqs. (3.2.2a), (3.2.2b), (3.2.3b) and (3.2.3c), I find that the following mass fluxes are conserved (I am neglecting particle aggregation and fallout):

$$\mathrm{d}_z(Q_i) \equiv \mathrm{d}_z(Y_i \beta U b^2) = 0 \, , \quad \forall i \in [2; I] \, , \tag{3.2.8a}$$
$$\mathrm{d}_z(Q_j) \equiv \mathrm{d}_z(Y_j \beta U b^2) = 0 \, , \quad \forall j \in \mathcal{J} \, , \tag{3.2.8b}$$

while for the atmospheric phase $i = 1 = \alpha$:

$$\mathrm{d}_z(Q_\alpha) \equiv \mathrm{d}_z(Y_\alpha \beta U b^2) = 2\alpha b U_\epsilon \, . \tag{3.2.9}$$

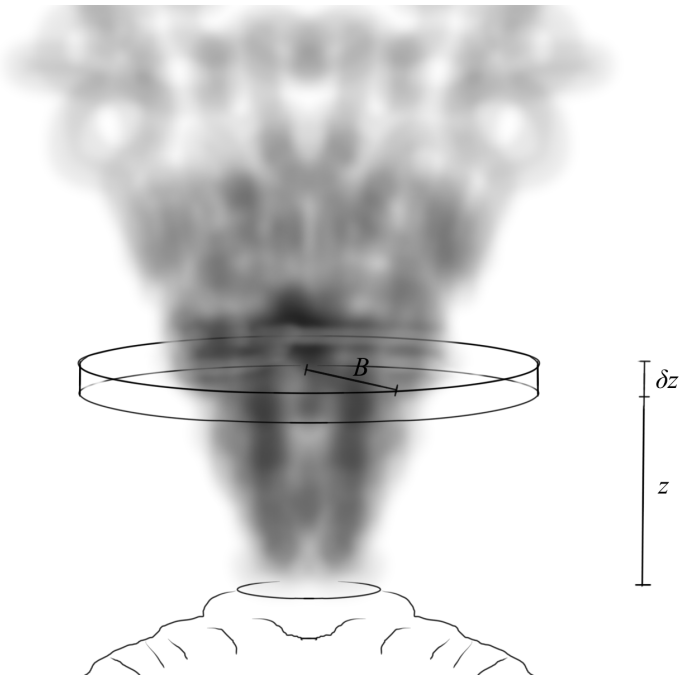

Figure 3.2.1: Sketch of the cylindrical control volume used to find the mean conservation equations. Here B is the cylinder radius, δz its thickness and z its height with respect the vent elevation.

Since the mass flow rate of the erupted gases and particles are conserved, it is useful to define their mass flow rate and mass fraction (respectively $Q_{\mathrm{e,s}}$ and $Y_{\mathrm{e,s}}$):

$$Q_{\mathrm{e}} \equiv \sum_{i=2}^{I} Q_{i,0} = \sum_{i=2}^{I} Q_i = \sum_{i=2}^{I} Y_i \beta U b^2 = Q \sum_{i=2}^{I} Y_i \equiv Q\, Y_{\mathrm{e}}\,, \tag{3.2.10}$$

$$Q_{\mathrm{s}} \equiv \sum_{\jmath} Q_{j,0} = \sum_{\jmath} Q_j = \sum_{\jmath} Y_j \beta U b^2 = Q \sum_{\jmath} Y_j \equiv Q\, Y_{\mathrm{s}}\,. \tag{3.2.11}$$

Putting together Eqs. (3.2.7), (3.2.8), (3.2.9) and

$$Y_\alpha + \sum_{i=2}^{I} Y_i + \sum_{j=I+1}^{I+J} Y_j = Y_\alpha + Y_{\mathrm{e}} + Y_{\mathrm{s}} = 1\,, \tag{3.2.12}$$

I obtain a relationship giving the mass flow rate $Q_\alpha(z)$ as a function of only vent conditions ($Q_{\mathrm{e}}(z) = Q_{\mathrm{e}}(0) \equiv Q_{\mathrm{e}}$, $\quad Q_{\mathrm{s}}(z) = Q_{\mathrm{s}}(0) \equiv Q_{\mathrm{s}}$) and $Q(z)$:

$$Q_\alpha(z) = Q(z) - \left(\sum_{i=2}^{I} Q_i(z) + \sum_{\jmath} Q_j(z) \right) = Q(z) - (Q_{\mathrm{e}} - Q_{\mathrm{s}})\,. \tag{3.2.13}$$

Dividing Eq. (3.2.10), (3.2.11) and (3.2.13) by Q, I obtain a relationship giving all the mass fraction as a function of only vent conditions ($Q_{\mathrm{e,s}}$) and the total mass

flow rate:

$$Y_{\mathrm{e}}(z) = \frac{Q_{\mathrm{e}}}{Q(z)}\,, \tag{3.2.14a}$$

$$Y_{\mathrm{s}}(z) = \frac{Q_{\mathrm{s}}}{Q(z)}\,, \tag{3.2.14b}$$

$$Y_{\alpha}(z) = 1 - \frac{Q_{\mathrm{e}} + Q_{\mathrm{s}}}{Q(z)}\,. \tag{3.2.14c}$$

Dealing with the momentum, the vertical component of Eq. (3.2.2c) and Eqs. (3.2.3b) (3.2.3c) (3.2.3d) yields:

$$\begin{aligned}\frac{1}{\delta z}\int_{\mathbb{C}} -\beta g = -\pi\beta g b^2 - \pi\alpha g(B^2 - b^2) = \frac{1}{\delta z}\int_{\mathbb{C}} \nabla\cdot\left(\beta\, u_z \boldsymbol{u} + p\hat{z}\right) = \\ \frac{\pi}{\delta z}\left[(\beta U^2 b^2 + pB^2)_{z+\delta z} - (\beta U^2 b^2 + pB^2)_z\right] \xrightarrow{\delta z\to 0} \mathrm{d}_z(\pi\beta U^2 b^2) + \pi B^2 \mathrm{d}_z p\,.\end{aligned} \tag{3.2.15}$$

Again, I take the limit $B \to b(z)$, obtaining

$$\mathrm{d}_z(\beta U^2 b^2) = (\alpha - \beta) g b^2. \tag{3.2.16}$$

Here I used $\mathrm{d}_z p = -\alpha g$, stated by Eq. (3.2.2c) together with $p(r,z) = p(z)$ and $u \to 0$ when $r \gg b(z)$.

Turning to the energy balance (3.2.2d) and using the same techniques, I find:

$$\mathrm{d}_z\left[b^2\beta U\left(\frac{U^2}{2} + h_\beta\right)\right] = 2\alpha b U_\epsilon\left(\frac{\cancel{U_\epsilon^2}}{\cancel{2}} + h_\alpha\right) - g\beta U b^2\,. \tag{3.2.17}$$

I neglect the term proportional to U_ϵ^2, to be compared to that proportional to U^2, because the entrainment velocity U_ϵ is typically one order of magnitude smaller than U.

Eq. (3.2.17) could be written in different ways using (3.2.7) and (3.2.16):

$$\mathrm{d}_z\left(\beta U b^2\, h_\beta\right) = h_\alpha\, \mathrm{d}_z(\beta U b^2) + \frac{U^2}{2}\mathrm{d}_z(\beta U b^2) - g\alpha U b^2\,, \tag{3.2.18}$$

that is equivalent to Eq. (8) in Woods [225], or

$$\mathrm{d}_z\left(\beta U b^2\,(h_\beta - h_\alpha)\right) = -\beta U b^2\, \mathrm{d}_z h_\alpha + \frac{U^2}{2}\mathrm{d}_z(\beta U b^2) - g\alpha U b^2\,, \tag{3.2.19}$$

where the dependence on the buoyancy flux and ambient stratification is highlighted.

Finally, I have that Eqs. (3.2.3a)–(3.2.3e) are one mean solution of (3.2.2) if

$$\begin{cases} \mathrm{d}_z(Q_{\mathrm{e}}) = 0\,, \\ \mathrm{d}_z(Q_{\mathrm{s}}) = 0\,, \\ \mathrm{d}_z(\beta U b^2) = 2\alpha b U_\epsilon \\ \mathrm{d}_z(\beta U^2 b^2) = (\alpha - \beta) g b^2 \\ \mathrm{d}_z\left(\beta U b^2\,(h_\beta - h_\alpha)\right) = -\beta U b^2\, \mathrm{d}_z h_\alpha + \frac{U^2}{2}\mathrm{d}_z(\beta U b^2) - g\alpha U b^2\,. \end{cases} \tag{3.2.20}$$

By noting again that Q_e and Q_s are conserved and that Eqs. (3.2.14) hold, here the unknowns are $\beta(z)$, $U(z)$, $b(z)$ and $h_\beta(z)$, provided the knowledge of the ambient density α, the ambient enthalpy h_α and the dependence of U_ϵ on the other unknowns (the entrainment model). I am still lacking one condition. The equation of state of the various phases, together with the full expanded plume hypothesis $p(r, z) = p(z)$, give that last needed condition.

It is important to note that the latter system of equations would not be complicated much by using more complex and realistic self-similar profiles, which just introduce a proportionality factor in the integral equations [e.g. 111, 104]. Indeed, experiments show that the self-similar Gaussian profile best fits the data for a wide range of velocity measurements [147, 111]. In addition, experiments are better reproduced by choosing two different plume radii ($b(z)$ and $\xi_b b(z)$) for the density and the velocity profile (the temperature profile would in this case be determined by the equation of state of the dusty-fluid). However the assumption of a purely top-hat profile is here preferred because it largely simplifies the solution of the electromagnetic model, allowing for an analytical solution when integrating along the optical path (see section 4.4).

Moreover, it is worth noting that solid particles may be lost from the column as a result of kinematic decoupling, thus originating proximal fallout deposits. Typically, this effect has a negligible effect on the column dynamics [e.g. 229, 87, 222, 48, 39]. I neglect it to keep the model as simple as possible, to find an analytical solution, and to develop a more clear reasoning. Integrating this and other phenomena into a more sophisticated model can be achieved by numerical techniques.

Coming back to model (3.2.20), the first equations state that the mass fluxes of volcanic gases and particles must be conserved, so that their value is constant along the plume axis ($\rho_j(z)$ is their bulk density). Acceleration due to gravity is denoted by g. The remaining unknowns are $\beta(z)$, $U(z)$, $b(z)$ and $h_\beta(z)$. The system is closed by opportune equations of state expressing the mixture density as a function of temperature $\beta = \beta(T_\beta)$ (thermal equation of state) and specific heats C_β and C_α (so that $h_\beta = h_\beta(T_\beta)$ caloric equation of state). For a dusty gas, thermodynamic properties are computed locally from the properties of each component of the mixture. Thermodynamic closure equations are reported in the next section.

3.3 The gas–particle thermodynamics.

In order to close the latter system of equations I need constitutive equations. The first I use is the ideal gas law for a gas–particle mixture, Eq. (1.2.4). That law can be used either in its complete form or in its dilute approximation. In the literature, Woods [225] uses the complete form, while Suzuki et al. [192] uses the dilute approximation. I tested both cases using integral models, obtaining very similar results even in the most dense plume studied in this thesis [weakPlume]. Thus, for the sake of simplicity, in what follows I will use the dilute approximation. In this case, the dusty gas constant R_m and specific heat at constant volume C_m

defined in Sec. 1.2 respectively become:

$$R_\beta = Y_\alpha R_\alpha + \sum_{i=2}^{I}(Y_i R_i) = Y_\alpha R_\alpha + Y_\mathrm{e} R_\mathrm{e}\,, \tag{3.3.1}$$

$$C_{\mathrm{v},\beta} = Y_\alpha C_{\mathrm{v},\alpha} + \sum_{i=2}^{I}(Y_i C_i) + \sum_{\mathcal{J}}(Y_j C_j) = Y_\alpha C_{\mathrm{v},\alpha} + Y_\mathrm{e} C_{\mathrm{v,e}} + Y_\mathrm{s} C_\mathrm{s}\,, \tag{3.3.2}$$

where R_α, and $C_{\mathrm{v},\alpha}$, $C_{\mathrm{v,e}}$ and C_s are respectively the gas constant and the specific heat at constant volume for the atmosphere, the ejected gas mixture and the ejected solid phase. I also define the specific heat at constant pressure of the atmosphere, of the ejected gas mixture and of the plume:

$$C_\alpha = C_{\mathrm{v},\alpha} + R_\alpha\,, \tag{3.3.3}$$

$$C_\mathrm{e} = C_{\mathrm{v,e}} + R_\mathrm{e}\,, \tag{3.3.4}$$

$$C_\beta = C_{\mathrm{v},\beta} + R_\beta = Y_\alpha C_\alpha + Y_\mathrm{e} C_\mathrm{e} + Y_\mathrm{s} C_\mathrm{s}\,. \tag{3.3.5}$$

I rewrite the defined thermodynamic properties of the ejected gas and of the particles as follows

$$R_\mathrm{e} = \frac{1}{Y_\mathrm{e}} \sum_{i=2}^{I} Y_i\, R_i\,, \tag{3.3.6}$$

$$C_\mathrm{e} = \frac{1}{Y_\mathrm{e}} \sum_{i=2}^{I} Y_i\, (C_i + R_i)\,, \tag{3.3.7}$$

$$C_\mathrm{s} = \frac{1}{Y_\mathrm{s}} \sum_{\mathcal{J}} Y_j\, C_j\,, \tag{3.3.8}$$

noticing that all these quantities are – coherently – conserved along z[1].

I now use the ideal gas law (1.2.4). Since in Eq. (3.2.3d) $p(r,z) = p(z)$ is assumed, at a given height the pressure inside the plume is the same of that outside the plume:

$$p = \beta R_\beta T_\beta = \alpha R_\alpha T_\alpha\,. \tag{3.3.9}$$

Here the temperatures T_β and T_α are defined by using the definitions for the enthalpy and the specific heats:

$$h_\alpha = C_\alpha T_\alpha \tag{3.3.10}$$

$$h_\beta = (Y_\alpha C_\alpha + Y_\mathrm{e} C_\mathrm{e} + Y_\mathrm{s} C_\mathrm{s})\, T_\beta = C_\beta T_\beta\,. \tag{3.3.11}$$

It is worth noting that the definition $h_\beta = C_{\mathrm{v},\beta} T_\beta + p/\beta$ is also fulfilled.

With these definitions, the plume internal-external enthalpy differential rewrites as follows:

$$\beta(C_\beta T_\beta - C_\alpha T_\alpha) = \alpha C_\alpha T_\alpha \frac{R_\alpha C_\beta}{R_\beta C_\alpha} - \beta C_\alpha T_\alpha\,. \tag{3.3.12}$$

[1]It is sufficient to multiply both numerator and denominator of the right hand sides by Q, and notice that $Y_k Q = Q_k = Q_{k,0}$ (see Sect. 3.2.2 above).

Then, using Eqs. (3.2.12), (3.2.10), (3.2.11) and defining $\chi_\mathrm{s} = \frac{C_\mathrm{s}}{C_\alpha}$, $\chi_\mathrm{e} = \frac{C_\mathrm{e}}{C_\alpha}$, $\psi_\mathrm{e} = \frac{R_\mathrm{e}}{R_\alpha}$, Eq.(3.3.12) can be written in a convenient form:

$$\beta(C_\beta T_\beta - C_\alpha T_\alpha) = C_\alpha T_\alpha \left[(\alpha - \beta) + \alpha \frac{\chi_\mathrm{s} Q_\mathrm{s} + (\chi_\mathrm{e} - \psi_\mathrm{e}) Q_\mathrm{e}}{(Q - Q_\mathrm{s}) + (\psi_\mathrm{e} - 1) Q_\mathrm{e}}\right] . \tag{3.3.13}$$

Now, defining the relative flux of enthalpy

$$F = \left[(\alpha - \beta) + \alpha \frac{\chi_\mathrm{s} Q_\mathrm{s} + (\chi_\mathrm{e} - \psi_\mathrm{e}) Q_\mathrm{e}}{(Q - Q_\mathrm{s}) + (\psi_\mathrm{e} - 1) Q_\mathrm{e}}\right] U b^2 \tag{3.3.14}$$

equation (3.2.19) can be rearranged

$$F' = -(F + Q) \frac{\mathrm{d}_z(C_\alpha T_\alpha)}{C_\alpha T_\alpha} + \frac{U^2 Q'}{2 C_\alpha T_\alpha} - \frac{\alpha g U b^2}{C_\alpha T_\alpha} . \tag{3.3.15}$$

It is useful to define

$$Q_\psi = -Q_\mathrm{s} + (\psi_\mathrm{e} - 1) Q_\mathrm{e} , \tag{3.3.16}$$
$$Q_\chi = (\chi_\mathrm{s} - 1) Q_\mathrm{s} + (\chi_\mathrm{e} - 1) Q_\mathrm{e} , \tag{3.3.17}$$

which are constants along z, so that

$$\boxed{F = \left[(\alpha - \beta) + \alpha \frac{Q_\chi - Q_\psi}{Q + Q_\psi}\right] U b^2 .} \tag{3.3.18}$$

This expression for F – originally found here – represents a modification of the buoyancy flux for a dusty gas plume in the general non-Boussinesq case [cf. 34]. It takes the classic form $(\alpha - \beta) U b^2$ [66, 111] for a single-component gas plume (in such a case $Q_\chi = 0$ and $Q_\psi = 0$). For this reason I will refer to the relative flux of enthalpy F as the *dusty gas buoyancy flux*, a generalization for the multiphase case of the standard buoyancy flux.

This new quantity F, together with the mass flux $Q = \beta U b^2$ and the momentum flux $M = \beta U^2 b^2$ allows to close problem (3.2.20) in its terms:

$$\boxed{\begin{aligned}
Q' &= 2 U_\epsilon(\alpha, Q, M, F) \sqrt{\frac{\alpha Q (F + Q)(Q + Q_\psi)}{M[Q + Q_\chi]}} && \text{(3.3.19a)}\\
M' &= \frac{g F Q}{M} \left[1 - \frac{(F + Q)(Q_\chi - Q_\psi)}{F[Q + Q_\chi]}\right] && \text{(3.3.19b)}\\
F' &= -(F + Q) \frac{(C_\alpha T_\alpha)'}{C_\alpha T_\alpha} + \frac{M^2 Q'}{2 C_\alpha T_\alpha Q^2} - \frac{g(F + Q)(Q + Q_\psi)}{C_\alpha T_\alpha (Q + Q_\chi)} , && \text{(3.3.19c)}
\end{aligned}}$$

where $U = \frac{M}{Q}$, $b = \sqrt{\frac{Q(F+Q)(Q+Q_\psi)}{\alpha M (Q+Q_\chi)}}$ and $\beta = \alpha \frac{Q[Q+Q_\chi]}{(F+Q)(Q+Q_\psi)}$.

3.4 Non-dimensionalization.

It is useful to transform the latter problem in dimensionless form. I choose $Q(z) = Q_0 q(\zeta)$, $M(z) = M_0 m(\zeta)$, $F(z) = F_0 f(\zeta)$ and $z = \ell_0 \zeta$ ($\ell_0 = \frac{Q_0}{\sqrt{\alpha_0 M_0}}$), where $(\cdot)_0$ refers to the vent height. In this way, I have $q(0) = m(0) = f(0) = 1$. It is worth noting that $\zeta = 0$ can correspond to the actual vent elevation as to any height above the vent [cf. 34]. The model in non-dimensional form then is

$$q' = v_q \eta_\varkappa \sqrt{a(\zeta)\, \frac{m(\phi f + q)(q + q_\psi)}{q(q + q_\chi)}} \tag{3.4.1a}$$

$$m' = v_m \frac{q}{m} \left(f - \gamma_c \frac{(\phi f + q)}{(q + q_\chi)} \right) \tag{3.4.1b}$$

$$f' = \frac{v_f}{t_\alpha(\zeta)} \left[(\phi f + q) \left(\theta_f(\zeta) - \frac{q + q_\psi}{q + q_\chi} \right) + \frac{\phi}{2 v_m} \frac{m^2 q'}{q^2} \right], \tag{3.4.1c}$$

where $\eta_\varkappa$ – defined in Eq. (3.2.6) – is the entrainment function, potentially depending on the other variables and parameters; $a(\zeta) \equiv \alpha(\ell_0\zeta)/\alpha_0$, $t_\alpha(\zeta) = T_\alpha(\ell_0\zeta)/T_{\alpha,0}$, $\phi \equiv F_0/Q_0$, $q_\psi \equiv Q_\psi/Q_0$, $q_\chi \equiv Q_\chi/Q_0$, $\gamma_c \equiv \frac{Q_\chi - Q_\psi}{F_0}$, $\theta_f(\zeta) \equiv -\frac{1}{v_f \phi} t'_\alpha(\zeta)$ and

$$v_q = 2\varkappa \tag{3.4.2}$$

$$v_m = \frac{g F_0 Q_0 \ell_0}{M_0^2} = \frac{\phi g \ell_0}{U_0^2} = \mathrm{Ri} \tag{3.4.3}$$

$$v_f = \frac{g Q_0 \ell_0}{F_0\, C_\alpha T_{\alpha,0}} = \frac{g \ell_0}{\phi C_\alpha T_{\alpha,0}} = \frac{g \ell_0}{C_{\beta,0} T_{\beta,0} - C_\alpha T_{\alpha,0}} = \frac{g \ell_0}{\Delta h_0} = \frac{\mathrm{Ec}}{\mathrm{Fr}^2}\,. \tag{3.4.4}$$

I call these last three parameters the rate of variation respectively of q, m, f. In Eq. (3.4.3), I have given a modified definition of the Richardson number $\mathrm{Ri} = \phi g \ell_0 / U_0^2$, because $\phi g = g'$ in the monophase case (g' being the reduced gravity). In Eq. (3.4.4) I used the definition of the Froude number $\mathrm{Fr} = U_0^2/g\ell_0$ and of the Eckert number $U_0^2/\Delta h_0$, where $\Delta h_0 = C_{\beta,0} T_{\beta,0} - C_\alpha T_{\alpha,0}$ is the enthalpy anomaly at the vent. Moreover, I have used Eqs. (3.3.13), (3.3.14) implying $\phi C_\alpha T_{\alpha,0} = C_{\beta,0} T_{\beta,0} - C_\alpha T_{\alpha,0}$. It is also useful to rewrite the physical variables as a function of these new parameters:

$$U = \frac{M_0}{Q_0} \frac{m}{q} \tag{3.4.5a}$$

$$b = \ell_0 \sqrt{\frac{q(\phi f + q)(q + q_\psi)}{a\, m (q + q_\chi)}} \tag{3.4.5b}$$

$$\beta = \alpha\, \frac{q(q + q_\chi)}{(\phi f + q)(q + q_\psi)} \tag{3.4.5c}$$

$$T_\beta = T_\alpha \frac{\phi f + q}{q + q_\chi} \tag{3.4.5d}$$

$$Y_{\mathrm{e\,(s)}} = \frac{Y_{\mathrm{e,0\,(s,0)}}}{q}\,. \tag{3.4.5e}$$

parameter	explicit form	range of variability	description
ϕ	$\dfrac{C_\beta T_{\beta,0} - C_\alpha T_{\alpha,0}}{C_\alpha T_{\alpha,0}}$	$0.3 \div 5$	enthalpy anomaly (Boussinesq hypothesis)
q_ψ	$-Y_{\mathrm{s},0} + (\psi_\mathrm{e} - 1) Y_{\mathrm{e},0}$	$-1 \div 1$	mass flux anomaly due to gas constants
q_χ	$(\chi_\mathrm{s} - 1) Y_{\mathrm{s},0} + (\chi_\mathrm{e} - 1) Y_{\mathrm{e},0}$	$-1 \div 1$	mass flux anomaly due to specific heats
$v_q/2$	$\varkappa$	$0.05 \div 0.3$	entrainment coefficient
v_m	$\dfrac{\phi\, g \ell_0}{U_0^2}$	$10^{-4} \div 10$	modified Richardson number
ℓ_g	$\dfrac{g}{\omega_0^2 \ell_0}$	$10^2 \div 10^5$	stratification length-scale

Table 3.4.1: Independent parameters for a multiphase plume in a stratified atmosphere.

It is worth noting that q_χ, $q_\psi > -1$ because the specific heats and gas constants are positive ($\chi_\cdot$, $\psi_\cdot > 0$) and the sum of the initial mass fraction is smaller than 1 (cf. definition of q_χ, q_ψ in Tab. 3.4.1). Moreover, $\phi > -1$ because $C_{\beta,0} T_{\beta,0} > 0$. Even if these are the general conditions for such parameters, in Tab. 3.4.1 there are summarized the possible ranges for volcanic eruptions.

Moving to the dependent variables, we have that $q'(z) > 0$ as long as the entrainment is positive ($\eta_\varkappa > 0$). Moreover, both q and m are positive defined, otherwise the self-similar solution (3.2.3) is not well-defined ($U < 0$). Coherently, Eq. (3.4.1b) reaches a singularity when $m \to 0^+$. The height at which this situation is reached is defined as the maximum plume height $z = H_\mathrm{max}$.

Model (3.4.1) can be solved numerically. In particular, the numerical method here used is a Runge-Kutta Fehlberg method that produces a fifth order accurate solution [176]. The numerical solution calculated for the 4 plumes of Tab. 3.4.2 is shown in Figs. 3.10.1, 3.10.2, 3.10.3, and 3.10.4. I will refer to this model with the name `ASH1D`.

3.4.1 Atmospheric parameters

Using $\mathrm{d}_z p = -\alpha g$ and the ideal gas law it is possible to obtain the density stratification as a function of the temperature:

$$a(\zeta) = t_\alpha^{-1}(\zeta)\, \exp\left(-\frac{g \ell_0}{R_\alpha T_{\alpha,0}} \int_0^\zeta t_\alpha^{-1}(\zeta')\, \mathrm{d}\zeta' \right) . \tag{3.4.6}$$

For example, if the non-dimensional atmospheric thermal gradient $-t'_\alpha = \theta = \theta_\alpha \ell_0 / T_{\alpha,0}$ is constant, I have $t_\alpha(\zeta) = 1 - \theta\zeta$ and:

$$a(\zeta) = (1 - \theta\zeta)^{\frac{g}{R_\alpha \theta_\alpha} - 1} , \tag{3.4.7}$$

and $\theta_f(\zeta) = \theta_f = \theta / v_f \phi$.

It is also useful to define the Brunt-Väisällä frequency ω. Recalling that the potential temperature is

$$t_{\mathrm{p},\alpha}(\zeta) = t_\alpha(\zeta)\,(a(\zeta)t_\alpha(\zeta))^{-\frac{R_\alpha}{C_\alpha}}\,, \tag{3.4.8}$$

I obtain, in the general case,

$$\omega^2 = \frac{g}{\ell_0}\,\ln(t_{\mathrm{p},\alpha})'(\zeta) = \frac{g^2}{C_\alpha T_{\alpha,0}}\frac{1-\theta_f(\zeta)}{t_\alpha(\zeta)}\,. \tag{3.4.9}$$

This frequency depends on the height z, but it can be approximately be considered as a constant because it varies slowly in our atmosphere: ≈ 10 % of variation in the troposphere. In what follows, I call ω_0 its constant approximation. Using standard average conditions for the troposphere, I find $\omega_0 \simeq 1.13 * 10^{-2}$ Hz. Studying plumes in a stratified atmosphere (cf. Sec. 3.9), it is useful to define

$$v_f\frac{1-\theta_f}{t_\alpha} = \frac{\ell_0\omega^2}{\phi\, g} \simeq \frac{\ell_0\omega_0^2}{\phi\, g} = \frac{1}{\phi\ell_g} \equiv v_{f,0}\,, \tag{3.4.10}$$

showing that the new parameter $v_{f,0}$ can be recovered by knowing the enthalpy anomaly ϕ and the non-dimensional stratification length scale $\ell_g \equiv g/\omega_0^2\ell_0$. In other words, the more $v_{f,0}$ increases the more the vent dimensions corrected with the enthalpy anomaly are comparable with the stratification length scale.

3.4.2 From dimensionless to dimensional parameters

All these non-dimensional parameters characterize the multiphase plume and give the possibility to classify through them all the possible regimes. I summarize in Tab. 3.4.1 six of them, which are *the independent non-dimensional parameters sufficient to characterize a multiphase plume in a calm environment*. In order to fix ideas, I show there the range of variability of those independent parameters for Strombolian to Plinian volcanic eruptions.

Indeed, the knowledge of these parameters and of the thermodynamic properties of the atmosphere allows to retrieve the physical dimensional parameters. I report

here all the inversion relationships needed:

$$\ell_0 = \frac{g}{\omega_0^2 \ell_g} \qquad \text{see footnote}^2 \tag{3.4.11a}$$

$$b_0 = \ell_0 \sqrt{\frac{(1+\phi)(1+q_\psi)}{1+q_\chi}} \tag{3.4.11b}$$

$$\beta_0 = \alpha_0 \frac{1+q_\chi}{(1+\phi)(1+q_\psi)} \tag{3.4.11c}$$

$$U_0 = \sqrt{\frac{g\phi\ell_0}{v_m}} \tag{3.4.11d}$$

$$T_{\beta,0} = T_{\alpha,0} \frac{1+\phi}{1+q_\chi} \tag{3.4.11e}$$

$$Q_0 = \beta_0 U_0 b_0^2 \tag{3.4.11f}$$

$$M_0 = \beta_0 U_0^2 b_0^2 \tag{3.4.11g}$$

$$F_0 = \phi Q_0 \tag{3.4.11h}$$

$$\gamma_c = \frac{q_\chi - q_\psi}{\phi} \tag{3.4.11i}$$

$$v_f = \frac{g\ell_0}{\phi\, C_\alpha T_{\alpha,0}} \tag{3.4.11j}$$

$$v_{f,0} = \frac{1}{\phi \ell_g} \tag{3.4.11k}$$

$$Y_{e,0} = \frac{q_\chi + (\chi_s - 1)q_\psi}{(\chi_e - 1) + (\chi_s - 1)(\psi_e - 1)} \qquad \text{see footnote}^3 \tag{3.4.11l}$$

$$Y_{s,0} = (\psi_e - 1)Y_{e,0} - q_\psi \tag{3.4.11m}$$

$$Y_{\alpha,0} = 1 - Y_{s,0} - Y_{e,0}\,. \tag{3.4.11n}$$

In Cerminara et al. [34] and in Chap. 4, these inversion relationships have been used to obtain the vent condition of a real volcanic eruption occurred at Santiaguito (Santa Maria Volcano, Guatemala).

In this thesis, I will study only two of all the possible entrainment models introduced in the literature:

- Morton et al. [138], where $\eta_\varkappa = 1$
- Ricou and Spalding [160], where $\eta_\varkappa = \eta_\varkappa(\beta/\alpha) = \left(\frac{q(q+q_\chi)}{(q+\phi f)(q+q_\psi)}\right)^{\frac{1}{2}}$

More elaborate models have been studied in volcanology and fluid dynamics. One example can be found in Carazzo et al. [26] where $\eta_\varkappa$ depends on the local Richardson number.

[2] When stratification is disregarded, no reference length scales are present in the non-dimensional system, thus b_0 must be given and ℓ_0 can be recovered from Eq. (3.4.11b).

[3] In order to have the mass fraction of ejected gas and solids, their thermodynamic properties must be known: namely their specific heat and the gas constant of the ejected gas.

It is worth noting that the mass flux $q(\zeta)$ is a strictly increasing function as long as $\eta_{\varkappa}$ is positive, while the sign of $m'(\zeta)$ depends on the buoyancy sign:

$$\text{sign(buoyancy)} = \text{sign}\left(f - \gamma_{\text{c}}\frac{(\phi f + q)}{(q + q_{\chi})}\right), \tag{3.4.12}$$

because v_m, q, m are strictly positive. For an analysis on the plume buoyancy behavior see Sec. 3.7.1. In Sec. 3.9, I study in detail the evolution of the plume variables under the Boussinesq approximation. However, something can be noted even at this point of the analysis by looking at the full system (3.4.1): 1) the mass flow $q(z)$ is a strictly increasing function because the entrainment models used are positive functions; 2) the momentum flux $m(z)$ has derivative equal to zero when the buoyancy becomes zero. It can be due to two causes, buoyancy reversal or neutral buoyancy level. I denote ζ_{nbl} the neutral buoyancy level; 3) when $m(z) = 0$ system (3.4.1) encounters a singularity. In that point the plume reaches its maximum height ζ_{max}; 3) the enthalpy flux is a strictly decreasing function, because usually in applications the term containing $\left(\theta_f(\zeta) - \frac{q+q_{\psi}}{q+q_{\chi}}\right)$ is dominant and negative.

In the next sections, I discuss some of the approximations applicable to problem (3.4.1). In particular, I find that γ_{c} is the parameter related to the column instability – if $\gamma_{\text{c}} > 1$ then the volcanic column will collapse – and that ϕ is the parameter measuring the importance of the density contrast between the mixture and the atmosphere – if $\phi \ll 1$ then the Boussinesq approximation holds. Moreover, q_{ψ} and q_{χ} are the parameters measuring the multiphaseness of the mixture – if $|q_{\psi}| \simeq |q_{\chi}| \ll 1$ the plume can be considered as a single phase one.

In this thesis I will study three different volcanic eruptions and one experimental plume that I denote, from the weaker to the stronger: [forcedPlume], [Santiaguito], [weakPlume], [strongPlume]. I report in Tab. 3.4.2 all the parameters for these volcanic eruptions, respectively: 1) the physical parameters at the vent – radius, density, temperature, velocity and mass fractions; 2) the mass, momentum and enthalpy flows; the non-dimensionalization length scale and the multiphase Morton length scale (see below); 3) the six independent non-dimensional parameters; 4) the non-dimensional dependent parameters; 5) the non-dimensional plume maximum and neutral buoyancy level height, as obtained from system (3.4.1) with Ricou and Spalding [160] entrainment model [4].

[4] While for [forcedPlume], [Santiaguito], [weakPlume] the atmospheric thermal gradient is constant, for [strongPlume] it is a little bit more complex, because the tropopause is included (cf. Chap. 6).

parameter	[forcedPlume]	[Santiaguito]	[weakPlume]	[strongPlume]
b_0 [m]	0.03175	22.9	26.9	703
β_0 [kg/m^3]	0.622	1.05	4.87	3.51
α_0 [kg/m^3]	1.177	0.972	1.100	1.011
$T_{\beta,0}$ [K]	568	375	1273	1053
$T_{\alpha,0}$ [K]	300	288	270.92	294.66
θ_α [K/km]	6.4	4.4	4.607	$\begin{cases} 6.614, & z < 14889.1\,\mathrm{m} \\ -2.2522, & \text{else} \end{cases}$
U_0 [m/s]	0.881	7.29	135	275
R_α [m^2/s^{2}K]	287	287	287	287
C_α [m^2/s^{2}K]	1004.5	998	1004	1004
ψ_e	–	1.61	1.61	1.61
χ_e	–	1.866	1.803	1.803
χ_s	–	1.102	1.096	1.096
$Y_{\mathrm{e},0}$	0	0.196	0.03	0.05
$Y_{\mathrm{s},0}$	0	0.410	0.97	0.95
$Y_{\alpha,0}$	1	0.394	0	0
πQ_0 [kg/s]	$1.74 * 10^{-3}$	$1.26 * 10^{4}$	$1.5 * 10^{6}$	$1.5 * 10^{9}$
πM_0 [kg m/s^2]	$1.53 * 10^{-3}$	$9.19 * 10^{4}$	$2.02 * 10^{8}$	$4.12 * 10^{11}$
πF_0 [kg/s]	$1.55 * 10^{-3}$	$7.28 * 10^{3}$	$6.35 * 10^{6}$	$4.56 * 10^{9}$
ℓ_0 [m]	0.02308	23.8	56.6	1310
L_M [m]	0.0854	18.4	352	4070
ϕ	0.893	0.58	4.25	3.04
q_ψ	0	-0.290	-0.952	-0.920
q_χ	0	0.212	0.117	0.131
v_q	0.28	0.659	0.2	0.2
v_m	0.261	2.54	0.129	0.517
ℓ_g	$3.33 * 10^{6}$	3230	1360	58.6
γ_c	0	0.869	0.252	0.345
v_f	$8.41 * 10^{-7}$	$1.41 * 10^{-3}$	$4.81 * 10^{-4}$	$1.43 * 10^{-2}$
$v_{f,0}$	$3.36 * 10^{-7}$	$5.34 * 10^{-4}$	$1.73 * 10^{-4}$	$5.61 * 10^{-3}$
ζ_max	1621	23.96	160.4	29.87
$\zeta_\mathrm{max}/\zeta_\mathrm{nbl}$	1.318	1.306	1.354	1.574

Table 3.4.2: Relevant parameters of the plumes studied in this thesis. Here I used the standard value $\omega_0 = 1.13 * 10^{-2}$ Hz for non-dimensionalization.

3.5 Monophase plume.

If the thermodynamic properties of the ejected fluid are similar to those of the ambient fluid then $|q_\psi| \simeq |q_\chi| \ll 1$. In this case, model (3.4.1) becomes:

$$q' = v_q \eta_\varkappa \sqrt{a(z)\frac{m(\phi f + q)}{q}} \tag{3.5.1a}$$

$$m' = v_m \frac{qf}{m} \tag{3.5.1b}$$

$$f' = \frac{v_f}{t_\alpha(z)}\left[(\phi f + q)(\theta_f(z) - 1) + \frac{\phi}{2v_m}\frac{m^2 q'}{q^2}\right], \tag{3.5.1c}$$

where

$$\eta_\varkappa = 1 \qquad \text{(Morton et al. [138])}$$

$$\eta_\varkappa = \sqrt{\frac{q}{\phi f + q}} \qquad \text{(Ricou and Spalding [160])}.$$

It is worth noting that in the single phase case $C_\beta = C_\alpha$ and $R_\beta = R_\alpha$. Thus, the initial enthalpy anomaly reduces to the initial thermal anomaly or equivalently to the density anomaly:

$$\phi = \frac{T_{\beta,0} - T_{\alpha,0}}{T_{\alpha,0}} \equiv \frac{\Delta T_0}{T_{\alpha,0}} = \frac{\alpha_0 - \beta_0}{\beta_0}. \tag{3.5.2}$$

Consequently the reduced gravity becomes $g' = \phi g$.

3.6 Jet regime

In the jet regime – defined as the one where $m = f = 1$ – Woods [225] pointed out that the Ricou and Spalding [160] model can be used. In this case, Eqs. (3.4.1) simplify a lot, becoming:

$$q' = v_q \qquad m' = 0 \qquad f' = 0\,, \tag{3.6.1}$$

with the easy solution $q(\zeta) = v_q\,\zeta + 1$.

Substituting this solution in Eqs. (3.4.1) and proceeding with the dimensional analysis, it is possible to find ℓ_M, the dimensionless transition length scale between the jet and the plume regime. It is the length scale for which the momentum variation becomes important. From the momentum equation I find:

$$\frac{1}{\ell_{\rm M}} \simeq v_m(v_q \ell_{\rm M} + 1) \simeq v_m v_q \ell_{\rm M} \quad \Rightarrow \quad \ell_{\rm M} = (v_q v_m)^{-\frac{1}{2}}, \tag{3.6.2}$$

from which, back to dimensional units:

$$\boxed{L_M = \left(\frac{U_0^2 \ell_0}{2\varkappa\phi g}\right)^{\frac{1}{2}} .} \tag{3.6.3}$$

This quantity becomes equivalent to that defined in Morton [137] in the single-phase Boussinesq case: $q_\psi = q_\chi = 0$ and $\beta \simeq \alpha$.

The typical length scale of stratification ℓ_S for a jet can be found by using a similar dimensional analysis for Eq. (3.4.1c)

$$\frac{1}{\ell_\mathrm{S}} = v_{f,0}(\phi + 1 + v_q \ell_\mathrm{S}) \simeq v_{f,0} v_q \ell_\mathrm{S} \quad \Rightarrow \quad \ell_S = (v_q v_{f,0})^{-\frac{1}{2}} , \tag{3.6.4}$$

or

$$\frac{\ell_\mathrm{S}}{\ell_\mathrm{M}} = \left(\frac{v_m}{v_{f,0}}\right)^{\frac{1}{2}} = \frac{\phi g}{U_0 \omega_0} \equiv \delta_\mathrm{j} . \tag{3.6.5}$$

This parameter is comparing the rate of variation of m and f. If $\delta_\mathrm{j} < 1$ than stratification has a role in the jet-like part of the plume, on the contrary, if $\delta_\mathrm{j} > 1$ stratification is important just in the plume-like part of the plume. This length scale will be discussed better in the section below dedicated to the plume height.

Usually in jets, atmospheric stratification is not important because of their limited height ($\delta_\mathrm{j} > 1$). I want to explore now when the kinetic correction term could be important. Contrarily to the last two terms, the second term in square brackets in Eq. (3.4.1c) becomes less important as ζ grows. In particular it decreases with $q'/q^2 \propto \zeta^{-2}$. Defining the typical length scale for this term ℓ_K, I have:

$$\frac{1}{\ell_K} \simeq \frac{\phi v_f v_q}{2 v_m (1 + v_q \ell_K)^2} \quad \Rightarrow \quad \ell_K = \frac{1}{v_q}\left[\left(\frac{\phi v_f}{4 v_m} - 1\right) \pm \sqrt{\left(\frac{\phi v_f}{4 v_m} - 1\right)^2 - 1}\right] , \tag{3.6.6}$$

admitting a positive solution if and only if

$$\frac{\phi v_f}{v_m} = \frac{U_0^2}{\Delta h_0} > 8 \quad \Rightarrow \quad \ell_K \simeq \begin{cases} \dfrac{4 v_m}{v_q \phi v_f} = \dfrac{2\Delta h_0}{\varkappa U_0^2} \lesssim 1 \\ \dfrac{\phi v_f}{2 v_q v_m} = \dfrac{U_0^2}{4\varkappa \Delta h_0} \gg 1 . \end{cases} \tag{3.6.7}$$

Thus, the kinetic correction can be important just near the vent or very far from it and only when $\Delta h_0 \ll U_0^2$ (Ec $\gg 1$). In other words, this correction can be important for "cold and fast" jets and far from the jet central height. Generally, in volcanic plumes the Ec number is small (see Sect. 1.1.3), thus the kinetic correction can be disregarded.

3.7 Non stratified plume regime

If stratification and the last term in square brackets of Eq. (3.4.1c) can be disregarded, $f = 1$ and model (3.4.1) becomes

$$q' = v_q \eta_{\varkappa} \sqrt{\frac{m(\phi+q)(q+q_\psi)}{q(q+q_\chi)}} \tag{3.7.1a}$$

$$m' = v_m \frac{q}{m}\left(1 - \gamma_c \frac{(\phi+q)}{(q+q_\chi)}\right) \tag{3.7.1b}$$

$$f' = 0\,. \tag{3.7.1c}$$

This ordinary differential equation has a first integral of motion[5] $\mathcal{U}$ in both the considered cases for $\eta_{\varkappa}$. I found respectively for the entrainment models of Morton et al. [138] and Ricou and Spalding [160]:

$$\mathcal{U}_{\mathrm{MTT}} = 2\int \left(1 - \gamma_c \frac{(\phi+q)}{(q+q_\chi)}\right) \sqrt{\frac{q(q+q_\chi)}{(\phi+q)(q+q_\psi)}}\,\mathrm{d}q - \frac{4v_q}{5v_m} m^{5/2} \tag{3.7.2a}$$

$$\mathcal{U}_{\mathrm{RS}} = q^2(1-\gamma_c) - 2\gamma_c(\phi - q_\chi)\left[q - q_\chi \ln(|q+q_\chi|)\right] - \frac{4v_q}{5v_m} m^{5/2}\,. \tag{3.7.2b}$$

Using this first integral of motion in Eq. (3.7.1a), it is possible to find an implicit solution for the height of the form $\zeta = \zeta(q)$. For the Ricou entrainment model, defining

$$l(q) = q^2(1-\gamma_c) - 2\gamma_c(\phi - q_\chi)\left[q - q_\chi \ln(|q+q_\chi|)\right]\,, \tag{3.7.3}$$

and substituting the corresponding first integral of motion found in Eq. (3.7.2b)

$$\mathcal{U}_{\mathrm{RS}}(q,m) = l(q) - \frac{4v_q}{5v_m} m^{5/2} = \mathcal{U}_{\mathrm{RS}}(1,1) = l(1) - \frac{4v_q}{5v_m}\,, \tag{3.7.4}$$

into Eq. (3.7.1a), I found the following implicit solution:

$$\zeta = \zeta(q) = \int_1^q \mathrm{d}x\, \frac{1}{v_q}\left[\frac{5v_m}{4v_q}\left(l(x) - \mathcal{U}_{\mathrm{RS}}\right)\right]^{-\frac{1}{5}}\,. \tag{3.7.5}$$

Using this solution it is possible to find the height at which the Boussinesq approximation starts to hold: $\zeta = \zeta_{\mathrm{Bou}}$. I choose the value $q = q_{\mathrm{Bou}} = 10\max(|\phi|, |q_\chi|, |q_\psi|)$. In Tab. 3.7.1 are reported the values obtained for the examples considered in this thesis. By comparing those values with $\zeta_{\max}$ reported in Tab. 3.4.2 it is possible to have an idea of the part of the plume where the Boussinesq regime holds.

[5] A first integral of motion is a quantity remaining constant along the motion described by the differential equation. It is also called *constant of motion*.

Under the same hypothesis of this section, the monophase case (3.5.1) becomes equivalent to the model studied in Fanneløp and Webber [66]:

$$q' = v_q \eta_\varkappa \sqrt{\frac{m(\phi+q)}{q}} \tag{3.7.6a}$$

$$m' = v_m \frac{q}{m} \tag{3.7.6b}$$

$$f' = 0\,. \tag{3.7.6c}$$

For the entrainment models of Morton et al. [138] and Ricou and Spalding [160] the first integral of motion are respectively:

$$\mathcal{U}_{\mathrm{MTT}} = \left(q - \frac{3}{2}\phi\right)\sqrt{q(q+\phi)} + \frac{3}{2}\phi^2 \ln\left(\sqrt{q} + \sqrt{q+\phi}\right) - \frac{4v_q}{5v_m} m^{5/2} \tag{3.7.7}$$

$$\mathcal{U}_{\mathrm{RS}} = q^2 - \frac{4v_q}{5v_m} m^{5/2}\,. \tag{3.7.8}$$

3.7.1 Buoyancy reversal and plume stability

In this section, I consider the plume model behavior near the vent, where it is not possible to use the approximation $q \gg |\phi|$, $|q_\chi|$, $|q_\psi|$ (see next section) but $f \simeq 1$ as done in the previous section. Here I will use the Richou entrainment model, however the present analysis is independent from the entrainment model used since the sign of the buoyancy does not depend on $\eta_\varkappa$. In model (3.7.1), the sign of the buoyancy force is determined by:

$$\mathrm{sign}(\text{buoyancy}) = \mathrm{sign}\left(1 - \gamma_{\mathrm{c}} \frac{(\phi+q)}{(q+q_\chi)}\right) = \mathrm{sign}(l'(q))\,. \tag{3.7.9}$$

Here, $l(q)$ is the first integral function defined in Eq. (3.7.3). When $l'(q) < 0$, the plume is negatively buoyant and m decreases. When the condition $l(q) = \mathcal{U}_{\mathrm{RS}}$ is reached, then $m \to 0$ because the first integral $\mathcal{U}_{\mathrm{RS}}$ must be constant. Thus the plume stops (or collapses) and it is not able to reverse its buoyancy.

The behavior of the non-stratified multiphase plume can be better understood by analyzing all the possible configurations. For this purpose, it is useful to define

$$\gamma^* \equiv \frac{1+q_\chi}{1+\phi} = \frac{T_{0,\alpha}}{T_{0,\beta}}\,, \qquad\qquad q_{\min} = \frac{\gamma_{\mathrm{c}}\phi - q_\chi}{1-\gamma_{\mathrm{c}}}\,, \tag{3.7.10}$$

where $l'(q_{\min}) = 0$. I enumerate the following situations for $q \geq 1$ (recall that $q(\zeta) \geq 1$ because it is a strictly increasing function and q_χ, $\phi > -1$) by denoting "C" the cases when the plume collapses and "B" the cases when the plume can reach and sustain the condition of positive buoyancy:

1B) *positive buoyant.* If $\gamma_{\mathrm{c}} \leq 1 \wedge \gamma_{\mathrm{c}} < \gamma^*$
then $l'(q) > 0 \quad \forall\, q \geq 1$ and the plume rises indefinitely.

2B) *zero, then immediately positive buoyant.* If $\gamma_{\mathrm{c}} = \gamma^* < 1 \quad (\Rightarrow\ \phi > q_\chi)$
then $l'(q) > 0 \quad \forall\, q > 1, \quad l'(q) = 0 \quad \text{if} \quad q = 1$

parameter	[forcedPlume]	[Santiaguito]	[weakPlume]	[strongPlume]
ζ_{Bou}	15.77	7.07	82.2	53.9
γ_{c}	0	0.869	0.252	0.345
γ^*	0.528	0.768	0.213	0.280
q_{min}	–	2.22	1.27	1.40
$l(q_{\mathrm{min}}) - \mathcal{U}_{\mathrm{RS}}$	–	0.0388	1.19	0.214
a_q	0.860	1.59	1.65	0.473

Table 3.7.1: Column stability parameters for the plumes studied in this thesis.

3B) *jet with zero buoyancy.* If $\gamma_{\mathrm{c}} = \gamma^* = 1 \quad (\Rightarrow \phi = q_\chi)$
then $l'(q) = 0$ and the plume behaves as a jet.

4BC) *from negative to positive buoyancy.* If $\gamma^* < \gamma_{\mathrm{c}} < 1 \quad (\Rightarrow \phi > q_\chi)$
then $l'(q) < 0 \quad$ when $\quad q < q_{\mathrm{min}}$, the minimum of $l(q)$ is reached in $q = q_{\mathrm{min}}$ and $l'(q) > 0 \quad$ when $\quad q > q_{\mathrm{min}}$. In this case inversion of the buoyancy sign can be possible if the minimum value of $l(q)$ is above the first integral: $l(q_{\mathrm{min}}) - \mathcal{U}_{\mathrm{RS}} > 0$. In the opposite situation $l(q_{\mathrm{min}}) - \mathcal{U}_{\mathrm{RS}} < 0$ the plume is not able to invert its buoyancy and it collapses when $m = 0$, thus when $l(q) = \mathcal{U}_{\mathrm{RS}}$.

5C) *from positive to negative buoyancy.* If $1 < \gamma_{\mathrm{c}} < \gamma^* \quad (\Rightarrow \phi < q_\chi)$
then $l'(q) > 0 \quad$ when $\quad q < q_{\mathrm{min}}$, the maximum of $l(q)$ is reached in $q = q_{\mathrm{min}}$ and $l'(q) < 0 \quad$ when $\quad q > q_{\mathrm{min}}$. In this case the plume always collapses going from positive to negative buoyancy.

6C) *zero, then immediately negative buoyant.* If $\gamma_{\mathrm{c}} = \gamma^* > 1 \quad (\Rightarrow \phi < q_\chi)$
then $l'(q) < 0 \quad \forall\, q > 1, \quad l'(q) = 0 \quad$ if $\quad q = 1$

7C) *negative buoyant.* If $\gamma_{\mathrm{c}} \geq 1 \wedge \gamma_{\mathrm{c}} > \gamma^*$
then $l'(q) < 0 \quad \forall\, q \geq 1$ and the plume collapses being always negative buoyant.

Thus, I can summarize that: 1) if $\gamma_{\mathrm{c}} > 1$ the plume starts or becomes negative buoyant and collapses; 2) γ^* must be compared with γ_{c} to know the initial buoyancy of the plume: if $\gamma_{\mathrm{c}} < \gamma^* (>)$ then the plume is initially positive (negative) buoyant; 3) if $\gamma_{\mathrm{c}} < 1$ then the plume is or can become positive buoyant, buoyancy reversal occurs if $l(q_{\mathrm{min}}) - \mathcal{U}_{\mathrm{RS}} > 0$. In Tab. 3.7.1, I report all of these parameters for the plumes studied in this thesis. While [forcedPlume] is positive buoyant, the other three plumes are initially negative buoyant. For all of them, buoyancy reversal occurs.

3.8 Non stratified Boussinesq regime

In the Boussinesq limit, it holds: $q \gg |\phi|, |q_\chi|, |q_\psi|$. It is worth noting that under this approximation the reduced gravity g' can be written via ϕ:

$$\phi g \simeq \frac{\alpha_0 - \beta_0}{\alpha_0} g = g' . \tag{3.8.1}$$

Moreover, the two entrainment models here considered become equivalent and Eqs. (3.4.1) reduce to:

$$\boxed{\begin{aligned} q' &= v_q \sqrt{m} && \text{(3.8.2a)} \\ m' &= v_m \left(1 - \gamma_c\right) \frac{q}{m} && \text{(3.8.2b)} \\ f' &= 0 . && \text{(3.8.2c)} \end{aligned}}$$

which is the multiphase version of the celebrated model introduced by Morton et al. [138]:

$$\begin{aligned} q' &= v_q \sqrt{m} && \text{(3.8.3a)} \\ m' &= v_m \frac{q}{m} && \text{(3.8.3b)} \\ f' &= 0 . && \text{(3.8.3c)} \end{aligned}$$

Thus, I have found that the equations for a multiphase plume in a calm environment under the Boussinesq approximation are equivalent to the monophase Morton et al. [138] model with the following modification:

$$v_m \to v_m (1 - \gamma_c) . \tag{3.8.4}$$

3.8.1 Analytic solution

Model (3.8.2) has the following first integral:

$$\mathcal{U}_{\mathrm{MTT}} = \mathcal{U}_{\mathrm{RS}} = \mathcal{U} = q^2 - \frac{4 v_q}{5 v_m (1 - \gamma_c)} m^{5/2} \tag{3.8.5}$$

$$\mathcal{U} = 1 - a_q \tag{3.8.6}$$

$$a_q \equiv \frac{4 v_q}{5 v_m (1 - \gamma_c)} , \tag{3.8.7}$$

The values of a_q for the plume examples studied in this thesis are reported in Tab. 3.7.1. From this expression and Eq.(3.8.2a), I found the implicit solution:

$$\zeta = \zeta(q) = \frac{|a_q|^{\frac{1}{5}}}{v_q} \int_1^q \mathrm{d}x \, \left| x^2 - 1 + a_q \right|^{-\frac{1}{5}} . \tag{3.8.8}$$

This solution has two branches, depending on the sign of $(1 - \gamma_c)$, thus on the sign of a_q. If $a_q < 0$, the column is unstable with implicit solution (cf. App. 3.12 for the

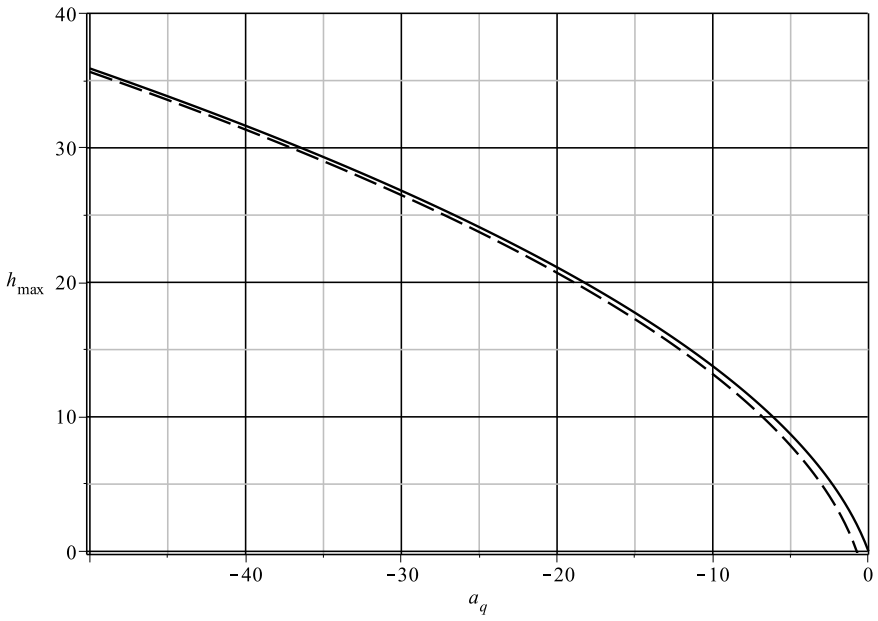

Figure 3.8.1: The height of collapse of a multiphase plume in a non-stratified stable atmosphere as a function of the parameter a_q defined in Eq. (3.8.7). Here, the exact formula Eq. (3.8.10) is compared with its asymptotic expansion Eq. (3.8.11), in the case $v_q = 0.2$.

definition of the Gaussian hypergeometric functions $\mathfrak{F}_b$ and $\mathfrak{G}_b$):

$$\zeta = \frac{(-a_q)^{\frac{1}{5}}}{v_q(1-a_q)^{\frac{1}{5}}}\left[q\,\mathfrak{F}_{-\frac{1}{5}}\left(\frac{q^2}{1-a_q}\right) - \mathfrak{F}_{-\frac{1}{5}}\left(\frac{1}{1-a_q}\right)\right] . \tag{3.8.9}$$

The maximum height is reached when $q_{\max} = \sqrt{1-a_q}$:

$$H_{\max}/\ell_0 = \frac{(-a_q)^{\frac{1}{5}}}{v_q(1-a_q)^{\frac{1}{5}}}\left[\sqrt{1-a_q}\,\mathfrak{F}_{-\frac{1}{5}}(1) - \mathfrak{F}_{-\frac{1}{5}}\left(\frac{1}{1-a_q}\right)\right] . \tag{3.8.10}$$

In Fig. 3.8.1 I show the behavior of $H_{\max}/\ell_0$ for $v_q = 0.2$, comparing it with the following asymptotic expansion ($\mathfrak{F}_{-1/5}(1) \simeq 1.150$):

$$\boxed{H_{\max}/\ell_0 = \frac{1}{v_q}\left(\mathfrak{F}_{-\frac{1}{5}}(1)\,\sqrt{-a_q} - 1\right) + O\left((-a_q)^{-\frac{1}{2}}\right) .} \tag{3.8.11}$$

Thus, the maximum height of a collapsing multiphase plume in Boussinesq regime behaves approximately as $\sqrt{-a_q}$.

On the other hand, if $a_q > 0$, the column is stable, rising indefinitely with this law (see App. 3.12):

$$\zeta = \frac{5}{3v_q}a_q^{\frac{1}{5}}\left[q^{\frac{3}{5}}\mathfrak{G}_{-\frac{1}{5}}\left(\frac{1-a_q}{q^2}\right) - \mathfrak{G}_{-\frac{1}{5}}(1-a_q)\right] . \tag{3.8.12}$$

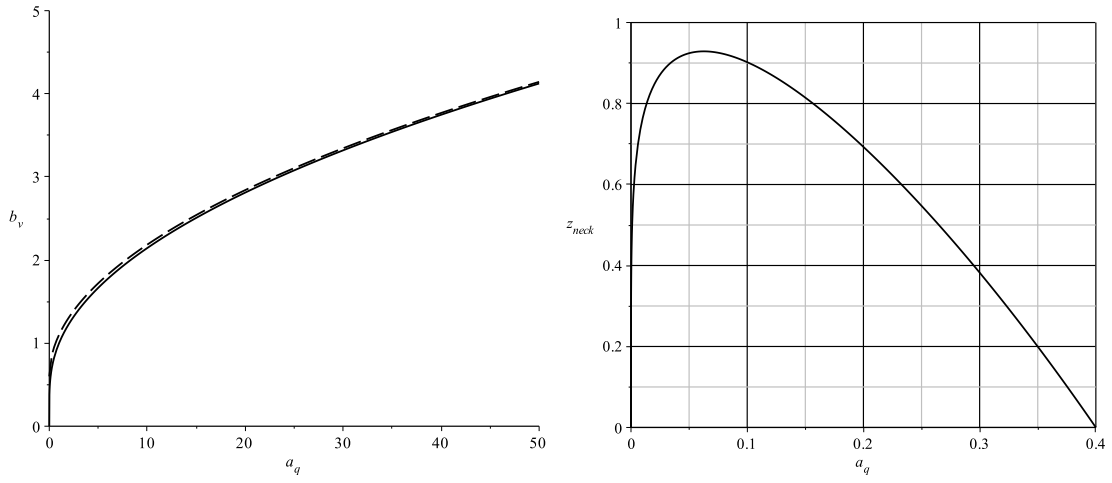

(a) Virtual radius b_v **(b)** Necking height ζ_neck

Figure 3.8.2: a) The virtual radius b_v as a function of a_q. The virtual radius tends to zero when $a_q \to 0$ and increases with a square root law as a_q increases (cf. Eq. (3.8.15)). b) Height of the plume radius necking ζ_neck as predicted by Eq. (3.8.18).

The asymptotic expansion $\mathfrak{G}(x) = 1 + O(x)$ allows to find the self-similar solution:

$$q(\zeta) = \left(\frac{3v_q}{5a_q^{\frac{1}{5}}} \zeta + \mathfrak{G}_{-\frac{1}{5}}(1-a_q) \right)^{\frac{5}{3}} \propto \zeta^{\frac{5}{3}} \tag{3.8.13a}$$

$$m(\zeta) = \left[\frac{1}{a_q} \left(q^2(\zeta) - 1 \right) + 1 \right]^{\frac{2}{5}} \propto \zeta^{\frac{4}{3}} . \tag{3.8.13b}$$

From here it is possible to extract the asymptotic plume radius evolution:

$$b(\zeta) = \frac{q(\zeta)}{\sqrt{m(\zeta)}} = \frac{3}{5} v_q \, \zeta + a_q^{\frac{1}{5}} \, \mathfrak{G}_{-\frac{1}{5}}(1-a_q) . \tag{3.8.14}$$

In this formula, the famous result of Morton et al. [138] can be recognized: the plume spread $b'(\zeta)$ is asymptotically constant and equal to $\frac{3}{5} v_q = \frac{6}{5} \varkappa$. Moreover, I found the initial virtual radius of the asymptotic plume and its asymptotic approximation,

$$b_\mathrm{v} = a_q^{1/5} \, \mathfrak{G}_{-\frac{1}{5}}(1-a_q) \simeq 0.5012 \sqrt{a_q} + 0.6 . \tag{3.8.15}$$

The virtual plume radius is the intercept between $z = 0$ and the radius of the equivalent plume spreading from a point source at $z = z_\mathrm{v} = -\frac{5a_q^{1/5}}{3v_q} \, \mathfrak{G}_{-\frac{1}{5}}(1-a_q)$. In Fig. 3.8.2a, the behavior of $b_\mathrm{v}(a_q)$ and of its asymptotic approximation is shown. Finally, it is worth noting that the derivative of the plume radius has a simple expression thanks to the first integral (3.8.5)

$$b'(\zeta) = v_q \left[\frac{3}{5} - \frac{2(1-a_q)}{5 a_q m^{5/2}} \right] , \tag{3.8.16}$$

from which

$$b'(0) = v_q \left[\frac{3}{5} - \frac{2(1-a_q)}{5 a_q} \right] , \tag{3.8.17}$$

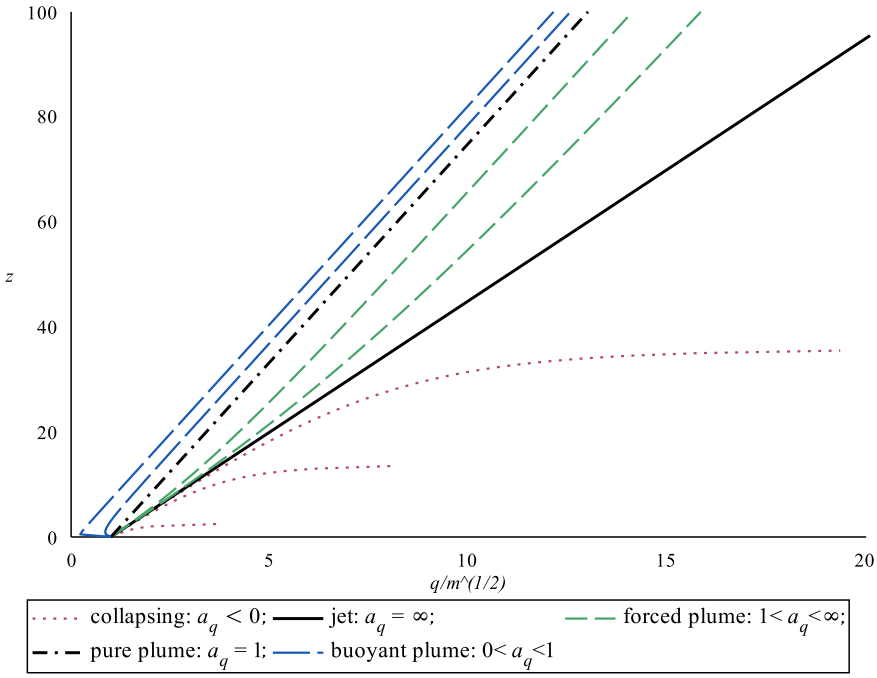

Figure 3.8.3: Evolution of the plume radius $b(z) = q/\sqrt{m}$ in all the admissible regimes of model (3.8.2) with $v_q = 0.2$. Starting from the lower graph, I choose: $a_q = -1, -10, -50, \infty, 50, 10, 1, 0.1, 0.0001$.

is the plume radius slope at $\zeta = 0$. Another important property is the necking height $\zeta = \zeta_{\rm neck}$, where $b'(\zeta_{\rm neck}) = 0$. It exists only when $0 < a_q < 2/5$:

$$\zeta_{\rm neck} = \frac{5}{3v_q} a_q^{\frac{1}{5}} \left[\left(\frac{5}{3}(1-a_q) \right)^{\frac{3}{10}} \mathfrak{G}_{-\frac{1}{5}} \left(\frac{3}{5} \right) - \mathfrak{G}_{-\frac{1}{5}} (1-a_q) \right] . \tag{3.8.18}$$

As shown in Fig. 3.8.2b, the necking height never exceeds $\zeta = 1$.

All the possible regimes of model (3.8.2) are summarized in Fig. 3.8.3. Ranging from $a_q = 0^-$ to $a_q = 0^+$ passing through $a_q = \infty$, I have shown that: 1) (*collapsing regime*) when $a_q < 0$ the plume is collapsing, $b'(0) > v_q$, and its height increases as a_q decreases (cf. Fig. 3.8.1); 2) (*jet regime*) when $a_q \to \infty$ then model Eq. (3.8.2) reduces to the jet model (3.6.1) with $b(z) = v_q z + 1$; 3) (*forced plume regime*) when $a_q > 1$ the initial slope is $\frac{3v_q}{5} < b'(0) < v_q$, and the plume starts behaving as a jet until $z < \ell_{\rm M}$ (cf. (3.6.2) and Morton [137]), then it moves to the plume-like behavior. As shown in Figs. 3.8.3, 3.8.2a, $\ell_{\rm M}$ and $b_{\rm v}$ increase with a_q; 4) (*pure plume regime*) when $a_q = 1$ the solution of model (3.8.2) highly simplifies and asymptotic expansions coincide with the exact solution. In particular, I have $b(z) = \frac{3v_q}{5} z + 1$. There is not a jet-like interval in this regime; 5) (*buoyant plume regime*) when $0 < a_q < 1$ I have $b'(0) < \frac{3v_q}{5}$, and the plume radius reach its asymptotic slope $\frac{3v_q}{5}$ rapidly, after a small necking interval. In particular, if $0 < a_q < 2/5$ there exist $\zeta_{\rm neck} > 0$ where $b'(\zeta_{\rm neck}) = 0$. When $a_q \to 0$ the solution corresponds to the "zero-entrainment" case, in agreement with the non-turbulent Bernoulli approximation.

3.9 Boussinesq plume regime in a stratified environment

The Boussinesq approximation, with atmospheric stratification reduces (3.4.1) to:

$$q' = v_q \sqrt{a(\zeta)\, m} \tag{3.9.1}$$

$$m' = v_m \frac{q}{m}(f - \gamma_c) \tag{3.9.2}$$

$$f' = -v_f \frac{1 - \theta_f(\zeta)}{t_\alpha(\zeta)}\, q\,. \tag{3.9.3}$$

Considering the atmospheric stratification only at the first order, the following approximation can be applied to the latter system (cf. Eqs. (3.4.9) and (3.4.10)):

$$a(\zeta) \simeq 1 \qquad\qquad v_f \frac{1 - \theta_f(\zeta)}{t_\alpha(\zeta)} \simeq v_{f,0}\,, \tag{3.9.4}$$

allowing to write the multiphase plume model in a stratified calm atmosphere:

$$q' = v_q \sqrt{m} \tag{3.9.5a}$$

$$m' = v_m \frac{q}{m}(f - \gamma_c) \tag{3.9.5b}$$

$$f' = -v_{f,0}\, q\,. \tag{3.9.5c}$$

This model reduces to the same model introduced by Morton [137] in the monophase case:

$$q' = v_q \sqrt{m} \tag{3.9.6a}$$

$$m' = v_m \frac{qf}{m} \tag{3.9.6b}$$

$$f' = -v_{f,0}\, q\,, \tag{3.9.6c}$$

where $v_{f,0}$ is proportional to the Brunt-Väisällä frequency ω_0^2 (cf. Woods [227] and Eq (3.4.10)).

3.9.1 Analytic solution

In order to find the first integrals of motion, system (3.9.5) can be written in this form:

$$\frac{\mathrm{d}q}{v_q\sqrt{m}} = \frac{m\,\mathrm{d}m}{v_m q(f - \gamma_c)} = -\frac{\mathrm{d}f}{v_{f,0} q}\,. \tag{3.9.7}$$

By using the last equation multiplied by $q(f - \gamma_c)$, I obtain the first conserved quantity (recall that $f_0 = m_0 = 1$):

$$\mathcal{U}_m = \frac{v_{f,0}}{v_m} m^2 + (f - \gamma_c)^2 = (1 - \gamma_c)^2 + \frac{v_{f,0}}{v_m}\,. \tag{3.9.8}$$

$\mathcal{U}_m$ is a very interesting quantity, because it holds whatever the entrainment model is. Indeed, it is found just by using the conservation of mass and enthalpy in system (3.9.5), which are independent from the entrainment model. Moreover, this conserved quantity tells that m reaches its maximum value

$$m_{\max} = \sqrt{1 + \frac{v_m}{v_{f,0}}(1-\gamma_c)^2}\,, \tag{3.9.9}$$

when $f = \gamma_c$. In other words, the flux of momentum is maximum when the flux of buoyancy $(f - \gamma_c)$ is zero: *neutral buoyancy level*.
Additionally, this first integral of motion gives the value of the enthalpy flux when the plume reaches its maximum height. I define the maximum height of the plume as the point $\zeta = \zeta_{\max}$ where $m = 0$, thus the minimum value of the enthalpy flux should be

$$f(\zeta_{\max}) \equiv f_{\min} = \gamma_c - \sqrt{\mathcal{U}_m}\,, \tag{3.9.10}$$

because f is a strictly decreasing function of ζ (cf. Eq. (3.9.5c)). Thus, increasing the height ζ from 0 to $\zeta_{\max}$ lets f decrease from 1 to $f_{\min}$; while m increases from 1 $(f = 1)$ to $m_{\max}$ $(f = \gamma_c)$, then it decreases to 0 when $f = f_{\min}$. These observations will be very useful in the next sections of this chapter.

Moving back to Eq. (3.9.7), it is easy to show that:

$$q\,\mathrm{d}q = -\frac{v_q}{v_{f,0}}\sqrt{m}\,\mathrm{d}f = -\frac{v_q v_m^{1/4}}{v_{f,0}^{5/4}}\left(\mathcal{U}_m - (f-\gamma_c)^2\right)^{1/4}\,\mathrm{d}f\,, \tag{3.9.11}$$

from which I obtain another first integral of motion:

$$\mathcal{U}_q = q^2 + \frac{2v_q v_m^{1/4}}{v_{f,0}^{5/4}}\mathcal{U}_m^{1/4}(f-\gamma_c)\,\mathfrak{F}_{\frac{1}{4}}\left(\frac{(f-\gamma_c)^2}{\mathcal{U}_m}\right)\,, \tag{3.9.12}$$

where $\mathfrak{F}_{\frac{1}{4}}(x) = {}_2F_1\left(-\frac{1}{4}, \frac{1}{2}; \frac{3}{2}; x\right)$ is the hypergeometric function defined when $x < 1$ in App. 3.12 and $\mathfrak{F}_{\frac{1}{4}}(1) = \pi^{3/2}\sqrt{2}/(6\,\Gamma^2(3/4)) \simeq 0.8740$[6]. Noting that $x\mathfrak{F}_{\frac{1}{4}}(x^2)$ is a strictly increasing function bounded in $[-1, 1]$, I have that, as f decrease from 1 to $\gamma_c - \sqrt{\mathcal{U}_m}$, q must increase from 1 to

$$q_{\max}^2 = 1 + \frac{2v_q v_m^{1/4}}{v_{f,0}^{5/4}}\mathcal{U}_m^{1/4}\left[(1-\gamma_c)\mathfrak{F}_{\frac{1}{4}}\left(\frac{(1-\gamma_c)^2}{\mathcal{U}_m}\right) + \sqrt{\mathcal{U}_m}\,\mathfrak{F}_{\frac{1}{4}}(1)\right]\,. \tag{3.9.13}$$

By using again Eq. (3.9.5c) with (3.9.12), the implicit solution of problem (3.9.5) is found:

$$\boxed{\zeta = \frac{1}{v_{f,0}}\int_f^1 \mathrm{d}f'\left[\mathcal{U}_q - \frac{2v_q v_m^{1/4}}{v_{f,0}^{5/4}}\mathcal{U}_m^{1/4}\,(f'-\gamma_c)\,\mathfrak{F}_{\frac{1}{4}}\left(\frac{(f'-\gamma_c)^2}{\mathcal{U}_m}\right)\right]^{-\frac{1}{2}}\,.} \tag{3.9.14}$$

[6]Here $\Gamma(x)$ is the Gamma function.

parameter	[forcedPlume]	[Santiaguito]	[weakPlume]	[strongPlume]
$1-x_0$	$6.445*10^{-7}$	$5.763*10^{-3}$	$1.198*10^{-3}$	$1.244*10^{-2}$
$\tilde{q}_0$	$2.024*10^{-8}$	$9.810*10^{-4}$	$1.280*10^{-4}$	$8.396*10^{-3}$
δ_p	$1.135*10^{-3}$	0.1078	$4.898*10^{-2}$	0.1592
a_p	0.9321	0.5183	0.4828	1.691
ζ_max	1533	25.98	168.1	32.58
$\zeta^{(1)}_\mathrm{max}$	1531	25.18	165.5	30.79
$\zeta^{(0)}_\mathrm{max}$	1538	28.81	177.8	39.23
$\zeta_\mathrm{max}/\zeta_\mathrm{nbl}$	1.318	1.364	1.341	1.408
$\zeta^{(1)}_\mathrm{max}/\zeta^{(1)}_\mathrm{nbl}$	1.318	1.379	1.348	1.442

Table 3.9.1: Plume parameters useful for estimate the plume height of the four plume examples of this thesis.

In order to better understand the behavior of the solution in different regimes, it is useful to define (see also Eq. (3.6.5)):

$$\delta_\mathrm{p} \equiv \left(\frac{v_{f,0}}{(1-\gamma_\mathrm{c})^2 v_m}\right)^{\frac{1}{2}} = \frac{1}{|1-\gamma_\mathrm{c}|}\frac{U_0\omega_0}{\phi g} \qquad \text{plume limit parameter} \tag{3.9.15}$$

$$\delta_\mathrm{j} \equiv (|1-\gamma_\mathrm{c}|\delta_\mathrm{p})^{-1} = \frac{\phi g}{U_0\omega_0} \qquad \text{jet limit parameter} \tag{3.9.16}$$

which are comparing $U_\phi = U_0/\phi$ with $U_g = g/\omega_0 \simeq 925$ m/s and γ_c with 1. As shown in the next section, when δ_p is small ($U_\phi \ll U_g$ and $\gamma_\mathrm{c} < 1$) the solution has mainly a plume-like behavior, on the contrary, when $\delta_\mathrm{j} \ll 1$, the solution behaves manly as a jet.

In the plume limit regime ($\delta_\mathrm{p} \ll 1$), any power of $\mathcal{U}_m$ can be simplified to (see Eq. (3.9.8)):

$$\mathcal{U}_m^\gamma = |1-\gamma_\mathrm{c}|^{2\gamma}\left(1+\delta_\mathrm{p}^2\right)^\gamma = |1-\gamma_\mathrm{c}|^{2\gamma}\left(1+\gamma\delta_\mathrm{p}^2+O(\delta_\mathrm{p}^4)\right)\,. \tag{3.9.17}$$

This approximation, leads to the limit

$$q_\mathrm{max} \simeq \begin{cases} 2\sqrt{\dfrac{v_q}{v_m(1-\gamma_\mathrm{c})}\mathfrak{F}_{\frac{1}{4}}(1)}\,\delta_\mathrm{p}^{-5/4} & \text{if} \quad \gamma_\mathrm{c} < 1 \\ 1 & \text{if} \quad \gamma_\mathrm{c} > 1 \end{cases} \tag{3.9.18a}$$

$$m_\mathrm{max} \simeq \delta_\mathrm{p}^{-1} \tag{3.9.18b}$$

$$f_\mathrm{min} \simeq \begin{cases} 2\gamma_\mathrm{c}-1 & \text{if} \quad \gamma_\mathrm{c} < 1 \\ 1 & \text{if} \quad \gamma_\mathrm{c} > 1\,. \end{cases} \tag{3.9.18c}$$

Thus, in this regime two distinct behaviors can be recognized: when $\gamma_\mathrm{c} > 1$ the multiphase plume is too heavy and slow to reach its height of positive buoyancy and it collapses. On the contrary, when $\gamma_\mathrm{c} < 1$, the plume is able to reach its buoyancy

reversal height and it can rise into the atmosphere. During its ascent, f varies approximately in $[2\gamma_c - 1, 1]$, while q and m reach a much larger value the more δ_p is small.

On the other hand, in the jet limit regime ($\delta_j \ll 1$):

$$\mathcal{U}_m^\gamma = \left((1-\gamma_c)^2 + \delta_j^{-2}\right)^\gamma \simeq \delta_j^{-2\gamma} \tag{3.9.19a}$$

$$q_{\max} \simeq 1 + \frac{v_q}{v_m}\mathfrak{F}_{\frac{1}{4}}(1)\,\delta_j \tag{3.9.19b}$$

$$m_{\max} \simeq 1 + \frac{1}{2}(1-\gamma_c)^2\delta_j^2 \tag{3.9.19c}$$

$$f_{\min} \simeq -\delta_j^{-1}\,. \tag{3.9.19d}$$

In this case q and m reach maximum values near 1, while f decreases the more the more δ_j is small.

3.9.2 Plume height

Eq. (3.9.14) gives the opportunity to write an analytic expression for the maximum height reached by a plume described by Eqs. (3.9.5). Indeed, the maximum plume height ($m = 0$) is reached when $f = f_{\min}$ (cf. Eq. (3.9.10)). Thus, by substituting $f = f_{\min}$ in the integral lower limit, and performing a change of variable in the integral with $x = (f - \gamma_c)/\sqrt{\mathcal{U}_m}$, I obtain (see definition for $\mathcal{U}_m$ in Eq. (3.9.8)):

$$\zeta_{\max} = \frac{1}{v_q^{\frac{1}{2}}(v_m v_{f,0})^{\frac{1}{4}}}\left(\frac{v_m(1-\gamma_c)^2 + v_{f,0}}{v_{f,0}}\right)^{\frac{1}{8}} \mathfrak{h}(x_0, \tilde{q}_0) \tag{3.9.20a}$$

$$\mathfrak{h}(x_0, \tilde{q}_0) = \frac{1}{\sqrt{2}}\int_{-1}^{x_0} \mathrm{d}x\, \left[\tilde{q}_0 + x_0\,\mathfrak{F}_q(x_0^2) - x\mathfrak{F}_q(x^2)\right]^{-\frac{1}{2}}, \tag{3.9.20b}$$

$$x_0 = (1-\gamma_c)\left(\frac{v_m}{v_m(1-\gamma_c)^2 + v_{f,0}}\right)^{\frac{1}{2}} \tag{3.9.20c}$$

$$\tilde{q}_0 = \frac{(v_m v_{f,0})^{\frac{1}{2}}}{2v_q}\left(\frac{v_{f,0}}{v_m(1-\gamma_c)^2 + v_{f,0}}\right)^{\frac{3}{4}}\,. \tag{3.9.20d}$$

where $\mathfrak{h}(x_0, \tilde{q}_0)$ is a function defined in $[-1, 1] \times [0, \infty)$. It is worth noting that with this substitution the neutral buoyancy level height can be easily obtained by substituting the lower bound of the integral $x = -1$ with $x = 0$ (cf. Eqs. (3.9.9) and (3.9.10)).

In Fig. 3.9.1, I represent the values assumed by $\mathfrak{h}(x_0, \tilde{q}_0)$ in $(x_0, \tilde{q}_0) \in (-1, 1) \times (0, 1)$. It is worth noting that this function has a maximum in $\mathfrak{h}(1, 0) = \Gamma_1 \simeq 2.572$. Approaching this point, the function increases suddenly. This figure must be read keeping in mind four main regimes: 1) $x_0 \to 1^-$ when $\gamma_c < 1$ and $\delta_p \ll 1$. In this case the *plume regime* is reached, near the singular point $(x_0, \tilde{q}_0 = (1, 0)$, thus the column initially has enough momentum to reach its buoyancy reversal height

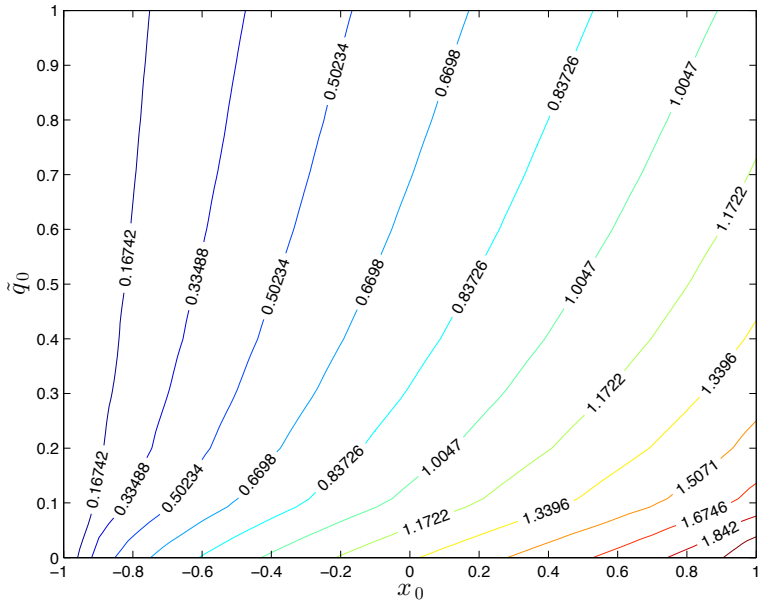

Figure 3.9.1: Contour plot of the plume height function $\mathfrak{h}(x_0, \tilde{q}_0)$ defined in Eq. (3.9.20). This function assumes its maximum in $\mathfrak{h}(1,0) = \Gamma_1 \simeq 2.572$, and it is a strictly decreasing function of $\tilde{q}_0$. When $x_0 \to 1^-$ the *plume regime* is reached.

and enough enthalpy to rise until its maximum; 2) when $\gamma_c > 1$ and $\delta_p \ll 1$, the *collapsing plume regime* is reached, near the point $(x_0, \tilde{q}_0) = (-1, 0)$; 3) when $\delta_j \ll 1$ the *jet regime* is reached, near the line $x_0 = 0$. In general, γ_c is the parameter controlling the column stability: when $\gamma_c < 1$ then $0 < x_0 < 1$, the column is not collapsing and when $x_0 \to 1$ the column behaves as a plume, while $x_0 \to 0^+$, the column behaves as a jet.

The expression found for the plume height is the multiphase version of that found in Morton [137]. The behavior of $\mathfrak{h}$ near $(x_0, \tilde{q}_0) = (1, 0)$ is the more interesting from a volcanological point of view, and it can be studied by using asymptotic expansion techniques for $\delta_p \ll 1$ (plume regime). In this case, Eqs. (3.9.20) can be highly simplified. Indeed by using Eq. (3.9.15), I have:

$$x_0 = \text{sign}(1-\gamma_c)\left(1 - \frac{1}{2}\delta_p^2 + O(\delta_p^4)\right) \simeq 1 - \frac{1}{2}\delta_p^2 \tag{3.9.21}$$

$$\tilde{q}_0 = |1-\gamma_c|\,\frac{v_m}{2v_q}\delta_p^{5/2} + O(\delta_p^{9/2}) \simeq (1-\gamma_c)\,\frac{v_m}{2v_q}\delta_p^{5/2} = \frac{1}{2}a_p\delta_p^{5/2} \tag{3.9.22}$$

$$a_p \equiv (1-\gamma_c)\,\frac{v_m}{v_q}\,, \qquad \text{see footnote}^7 \tag{3.9.23}$$

because $\gamma_c < 1$ near $x_0 = 1$. Moreover, if $x \simeq 1$, the hypergeometric function can be approximated as follows:

$$x\mathfrak{F}(x^2) = \int (1-x^2)^{\frac{1}{4}}\,\mathrm{d}x \simeq 2^{1/4}\int (1-x)^{\frac{1}{4}} = -\frac{2^{9/4}}{5}(1-x)^{\frac{5}{4}} + \mathfrak{F}(1)\,. \tag{3.9.24}$$

[7] Recall that $a_p = \frac{4}{5a_q}$, see Eq. (3.8.7).

With these information and $a_{\rm p}$ small enough, say

$$a_{\rm p} < 2^{3/4} + \frac{4}{5} \simeq 2.5\,, \tag{3.9.25}$$

it is possible to show that:

$$\frac{1}{\sqrt{2}} \int_{-1}^{x_0} \mathrm{d}x \left[\tilde{q}_0 + x_0\, \mathfrak{F}_q(x_0^2) - x \mathfrak{F}_q(x^2)\right]^{-\frac{1}{2}} \simeq \Gamma_1 \left[1 - \Gamma_2 \left(1 + a_{\rm p}^{5/12}\right)\, \delta_{\rm p}^{3/4}\right]\,, \tag{3.9.26}$$

where

$$\Gamma_1 = \frac{1}{\sqrt{2}} \int_{-1}^{1} \mathrm{d}x \left[\mathfrak{F}_q(1) - x \mathfrak{F}_q(x^2)\right]^{-\frac{1}{2}} \simeq 2.572$$
$$\Gamma_2 \simeq 0.3802\,.$$

In this "plume regime", the analytic formulation for the plume height given in (3.9.20) simplifies to the first order approximation:

$$\zeta_{\rm max}^{(1)} = H_{\rm max}^{(1)}/\ell_0 = \frac{\Gamma_1}{v_q\, a_{\rm p}^{\frac{1}{2}}\, \delta_{\rm p}^{\frac{3}{4}}} \left[1 - \Gamma_2 \left(1 + a_{\rm p}^{\frac{5}{12}}\right) \delta_{\rm p}^{\frac{3}{4}}\right]\,, \tag{3.9.27}$$

while the zeroth order approximation is:

$$\zeta_{\rm max}^{(0)} = H_{\rm max}^{(0)}/\ell_0 = \frac{\Gamma_1}{v_q\, a_{\rm p}^{\frac{1}{2}}\, \delta_{\rm p}^{\frac{3}{4}}}\,. \tag{3.9.28}$$

This last approximation holds in the limit $\delta_{\rm p} \to 0$, which is equivalent to the pure plume solution with initial mass and momentum equal to zero and finite initial flux of buoyancy.

In Fig. 3.9.2, I show the good behavior of Eq. (3.9.27) when $\delta_{\rm p} < 0.3$ and $a_{\rm p} < 5$. It is worth noting from Tab. 3.4.2 that this parameter range is the most interesting from the point of view of volcanic plumes. Fig. 3.9.2 compares the first order, the zeroth order and the exact solution (3.9.20). It shows that the first order approximation behaves very well in the selected parameter range. On the other hand, by considering the first order approximation instead of the zeroth order allows to avoid an error up to 100 % when $\delta_{\rm p} \simeq 0.3$ and $a_{\rm p} = 5$ ($H_{\rm max} \simeq H_{\rm max}^{(1)} \simeq 0.5 H_{\rm max}^{(0)}$). I observe also that Fig. 3.9.2 is a zoom on the singularity at the bottom right of Fig. 3.9.1, since $\tilde{q}_0 \propto \delta_{\rm p}^{5/2}$.

In the literature, the problem of obtaining the maximum plume height starting from the monophase ($\gamma_{\rm c} = 0$) formulation of the plume model in a stratified environment, Eq (3.9.6) has been studied in Morton et al. [138]. He found $\zeta_{\rm max,M} \simeq 2.805$ in his non-dimensionalization. The same result can be recovered in the zero order approximation, by noting that the conversion factor from the present non-dimensionalization to that used by Morton et al. [138] is

$$\zeta_{\rm M} = 2^{\frac{1}{8}} v_{f,0}^{\frac{3}{8}} v_q^{\frac{1}{2}} v_m^{\frac{1}{8}}\, \zeta = 2^{\frac{1}{8}} v_q a_{\rm p}^{\frac{1}{2}} \delta_{\rm p}^{\frac{3}{4}}\, \zeta\,, \tag{3.9.29}$$

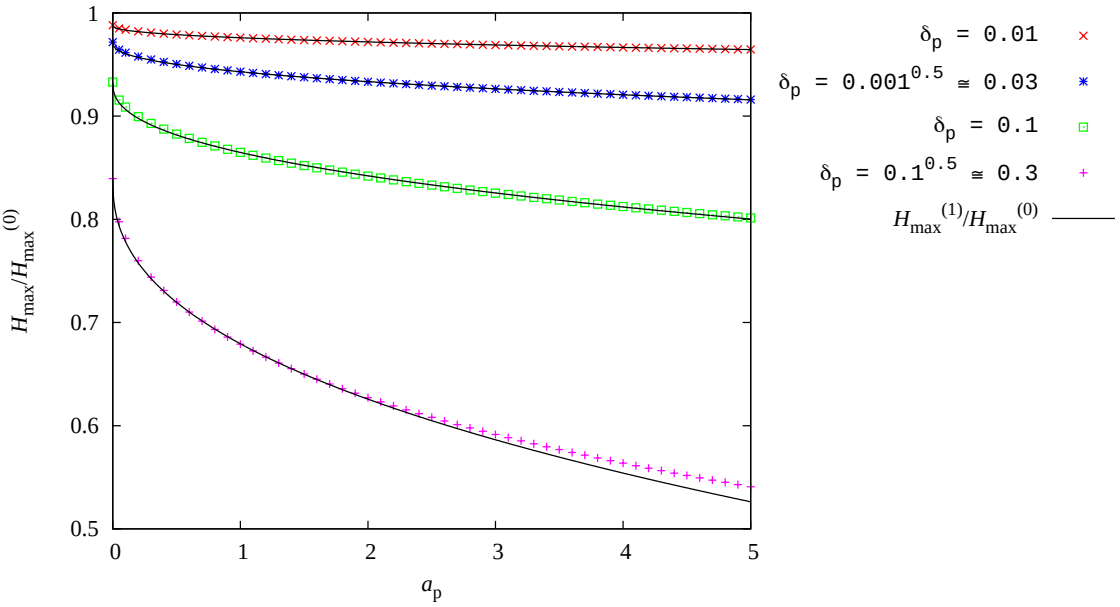

Figure 3.9.2: Comparison of the exact formula Eq. (3.9.20) for the plume height of model (3.9.5) with the first order approximation Eq. (3.9.27) over the zeroth order approximation Eq. (3.9.30).

from which $\zeta_{\max,\mathrm{M}} = 2^{\frac{1}{8}}\,\Gamma_1 \simeq 2.805$. Turning to dimensional variables, at the zeroth order is recovered the famous relationship:

$$H_{\max}^{(0)} = \frac{\Gamma_1}{\sqrt{2\varkappa}}\left(\frac{\phi g U_0 \ell_0^2}{\omega_0^3}\right)^{\frac{1}{4}} = \frac{\Gamma_1}{\sqrt{2\varkappa}}\left(\frac{\phi g Q_0}{\alpha_0\omega_0^3}\right)^{\frac{1}{4}}, \tag{3.9.30}$$

telling that the maximum plume height to the power four is proportional to the mass flow rate times the enthalpy anomaly and inversely proportional to the cube of the Brunt-Väisällä frequency. In the monophase case, when the Ricou and Spalding [160] entrainment model can be considered a good approximation for the dynamics of the first part of the plume, this result is valid even if the Boussinesq approximation is not valid (see Eq. (3.9.1)).

In volcanological applications the zero order formula is widely used. Here, a correction to that formula is written, for the multiphase case in both the zeroth and first order formulation. In dimensional variables, the multiphase first order formulation of the plume height reads:

$$H_{\max} = \frac{\Gamma_1}{\sqrt{2\varkappa}}\left(\frac{\phi^* g Q_0}{\alpha_0\omega_0^3}\right)^{\frac{1}{4}}\left\{1-\Gamma_2\left[1+\left(\frac{\phi^* g \ell_0}{2\varkappa U_0^2}\right)^{\frac{5}{12}}\right]\left(\frac{U_0\omega_0}{\phi^* g}\right)^{\frac{3}{4}}\right\} \tag{3.9.31}$$

$$\phi^* \equiv (1-\gamma_\mathrm{c})\phi = \phi - [\chi_\mathrm{s} Y_{\mathrm{s},0} + (\chi_\mathrm{e} - \psi_\mathrm{e}) Y_{\mathrm{e},0}]\ . \tag{3.9.32}$$

which significantly increases the accuracy of the plume height, keeping a simple analytic formulation (see Tab. 3.9.1). The only difference between the monophase and the multiphase formulation is in the factor $(1-\gamma_\mathrm{c})$, through the substitution $\phi \to \phi^*$.

I remind that this Taylor series approximation holds when $\delta_\mathrm{p} \ll 1$ which is equivalent to $U_0/\phi < g/\omega_0 \simeq 925\,\mathrm{m/s}$. This last condition gives a lower limit for ϕ

and than to the vent temperature:

$$\phi > \frac{U_0\omega_0}{g} \quad \Rightarrow \quad \frac{\Delta T_0}{T_{\alpha,0}} > \frac{U_0\omega_0}{g}\,. \tag{3.9.33}$$

If the vent temperature is much smaller than this lower bound, than the plume behaves more likely to a jet, and integral (3.9.20) must be evaluated without the approximation $\delta_\mathrm{p} \ll 1$.

In the opposite condition $\delta_\mathrm{j} = \delta_\mathrm{p}^{-1} \to 0$ (jet limit), $x_0 \to \delta_\mathrm{j} \ll 1$ holds. In this regime, the function $\mathfrak{h}(x_0, \tilde{q}_0)$ does not have a strong singularity as in the case $x_0 \to 1$ (cf. Fig. 3.9.1) and Eq. (3.9.20) can be safely approximated at the zeroth order as (use the fact that $x\mathfrak{F}(x^2) \simeq x$ in $x \in [-1, 0]$):

$$H_\mathrm{max} \simeq \ell_0 \frac{1}{v_q\left(\sqrt{\tilde{q}_0 + \tilde{q}_0^2} + \tilde{q}_0\right)}\,, \qquad \tilde{q}_0 = \frac{(v_m v_{f,0})^{\frac{1}{2}}}{2v_q} = \frac{\ell_0\omega_0}{4\varkappa U_0}\,. \tag{3.9.34}$$

If also $\tilde{q}_0 \ll 1$ this expression further simplifies giving the following expression for the maximum jet height:

$$H_\mathrm{max} \simeq \left(\frac{U_0\ell_0}{\varkappa\omega_0}\right)^{\frac{1}{2}}\,. \tag{3.9.35}$$

As a first order approximation one can use $\ell_0 \simeq b_0$ and invert this expression to find the inlet velocity from the jet height.

3.9.3 Neutral buoyancy level and plume height inversion

By recalling that the neutral buoyancy level (nbl) is reached when $f = 0$, it is easy to modify Eqs. (3.9.20) and (3.9.27) to find H_nbl:

$$H_\mathrm{nbl}/\ell_0 = \frac{1}{v_q^{\frac{1}{2}}(v_m v_{f,0})^{\frac{1}{4}}}\left(\frac{v_m(1-\gamma_\mathrm{c})^2 + v_{f,0}}{v_{f,0}}\right)^{\frac{1}{8}} \mathfrak{h}_\mathrm{nbl}(x_0, \tilde{q}_0) \tag{3.9.36}$$

$$\mathfrak{h}_\mathrm{nbl}(x_0, \tilde{q}_0) = \frac{1}{\sqrt{2}}\int_0^{x_0} \mathrm{d}x\,\left[\tilde{q}_0 + x_0\,\mathfrak{F}_q(x_0^2) - x\mathfrak{F}_q(x^2)\right]^{-\frac{1}{2}}\,, \tag{3.9.37}$$

$$H^{(1)}_\mathrm{nbl}/\ell_0 = \frac{\Gamma_1}{v_q\, a_\mathrm{p}^{\frac{1}{2}}\,\delta_\mathrm{p}^{\frac{3}{4}}}\left[\Gamma_\mathrm{nbl} - \Gamma_2\left(1 + a_\mathrm{p}^{\frac{5}{12}}\right)\delta_\mathrm{p}^{\frac{3}{4}}\right]\,, \tag{3.9.38}$$

$$\Gamma_\mathrm{nbl} = 1 - \frac{1}{\sqrt{2}\,\Gamma_1}\int_{-1}^{0} \mathrm{d}x\,\left[\mathfrak{F}_q(1) - x\mathfrak{F}_q(x^2)\right]^{-\frac{1}{2}} \simeq 0.7596\,. \tag{3.9.39}$$

Thus a first-order modification of the result of Turner [200] is found:

$$\boxed{\frac{H^{(1)}_\mathrm{max}}{H^{(1)}_\mathrm{nbl}} = \frac{1}{\Gamma_\mathrm{nbl}} + \frac{\Gamma_2(1-\Gamma_\mathrm{nbl})}{\Gamma^2_\mathrm{nbl}}\left(1 + a_\mathrm{p}^{\frac{5}{12}}\right)\delta_\mathrm{p}^{\frac{3}{4}}\,.} \tag{3.9.40}$$

At the zeroth order I find $H^{(0)}_{\rm max}/H^{(0)}_{\rm nbl} = 1/\Gamma_{\rm nbl} \simeq 1.316$ in agreement with $H_{\rm max}/H_{\rm nbl} = 1.3$ obtained by Turner [200].

Thus, the ratio between the maximum plume height and its neutral buoyancy level is a constant $\Gamma^{-1}_{\rm nbl} \simeq 1.3$ when $\delta_{\rm p}$ is small enough, and it grows with $\delta_{\rm p}^{3/4}$.

The neutral buoyancy level of a plume can be observed by measuring the height where the plume umbrella begins to spread up. Here, I want to show that, alongside the mass eruption rate, an additional information on the vent temperature can be retrieved measuring not only the maximum plume height but also the neutral buoyancy level. By knowing $H_{\rm nbl}$, $H_{\rm max}$, $\ell_0 \simeq b_0$ and the entrainment $v_q = 2\varkappa$, it is possible to invert Eqs. (3.9.27) and (3.9.38) in order to find $\delta_{\rm p}$ and $a_{\rm p}$ or equivalently U_0, ϕ and β_0. Defining $h_{\rm nbl} = H_{\rm max}/H_{\rm nbl}$ and $h_{\rm max} = H_{\rm max}/\ell_0$, I find

$$(a_{\rm p})^{-\frac{1}{2}} + (a_{\rm p})^{-\frac{1}{12}} = a_h \tag{3.9.41a}$$

$$a_h = \frac{v_q h_{\rm max}(h_{\rm nbl}\Gamma_{\rm nbl} - 1)}{\Gamma_1\Gamma_2 h_{\rm nbl}(1-\Gamma_{\rm nbl})} \tag{3.9.41b}$$

$$(a_{\rm p})^{-\frac{1}{2}} \simeq \frac{a_h^6}{1 - 0.41a_h^2 + 1.4a_h^3 + 1.39a_h^4 + a_h^5} \tag{3.9.41c}$$

$$\delta_{\rm p}^{\frac{3}{4}} = \frac{\Gamma_1 h_{\rm nbl}(1-\Gamma_{\rm nbl})}{v_q h_{\rm max}(h_{\rm nbl}-1)}\,(a_{\rm p})^{-\frac{1}{2}} \tag{3.9.41d}$$

$$U_0 = \frac{\ell_0\omega_0}{v_q a_{\rm p}\delta_{\rm p}} \tag{3.9.41e}$$

$$\phi^* = (1-\gamma_{\rm c})\phi = \frac{\omega_0^2\ell_0}{v_q g\, a_{\rm p}\delta_{\rm p}^2} \quad \overset{\text{Boussinesq approximation}}{\Rightarrow} \quad \beta_0 \simeq \frac{\alpha_0}{1+\phi^*}\,, \tag{3.9.41f}$$

a well posed problem when $h_{\rm nbl} > \Gamma^{-1}_{\rm nbl} \simeq 1.316$. The first equation can be solved looking for the unique positive root with respect $x = (a_{\rm p})^{-1/2}$ (cf. Fig. 3.9.3). In Eq. (3.9.41c) an approximate analytic solution is given, which has a good behavior both in the asymptotic ($a_h \to 0$ and $a_h \to \infty$) and intermediate regime ($0.5 < a_h < 5$). In conclusion, the first order approximation for the plume height gives an additional information allowing to find both U_0 and ϕ^* in contrast with the zero order approximation which needs an additional hypothesis on ϕ^* to give the mass flux.

In order to fix ideas, an example fulfilling the Boussinesq approximation is given. Suppose to have a plume injected in a stratified atmosphere at standard conditions ($T_{\alpha,0} = 300$ K, $\alpha_0 = 1.177$ kg/m^3), with $\ell_0 = 10$ m, $\phi = 0.3$, $q_\psi = -0.05$, $q_\chi = 0.05$, $v_m = 0.1$. These conditions correspond to: $U_0 \simeq 17.2$ m/s, $T_0 = 371$ K, $\beta_0 \simeq 1$ kg/m^3, $b_0 = 10.8$ m, $Y_{\rm e,0} \simeq 5.23$ wt.% (water) and $Y_{\rm s,0} \simeq 8.19$ wt.% (ash with $C_{\rm s} = 1100$ J/kg K). Solving Eqs. (3.4.1) with the Ricou and Spalding [160] model ($\varkappa = 0.14$), I obtain $H_{\rm max}/\ell_0 \simeq 105.53$ and $h_{\rm nbl} = 1.327$, slightly bigger than $\Gamma^{-1}_{\rm nbl} \simeq 1.316$. Now, in the inverse approach, I assume to know $H_{\rm max}/\ell_0$, $h_{\rm nbl}$, $v_q = 0.28$ and $\ell_0 \simeq b_0 = 10.8$ m. Substituting these values in Eqs. (3.9.41), the problem can be inverted recovering the initial velocity and density. With the first order approximation, I obtain:

$$U_{0,\rm inverted} \simeq 16.1\,{\rm m/s} \tag{3.9.42}$$

$$\beta_{0,\rm inverted} \simeq 0.885\,{\rm kg/m^3}\,, \tag{3.9.43}$$

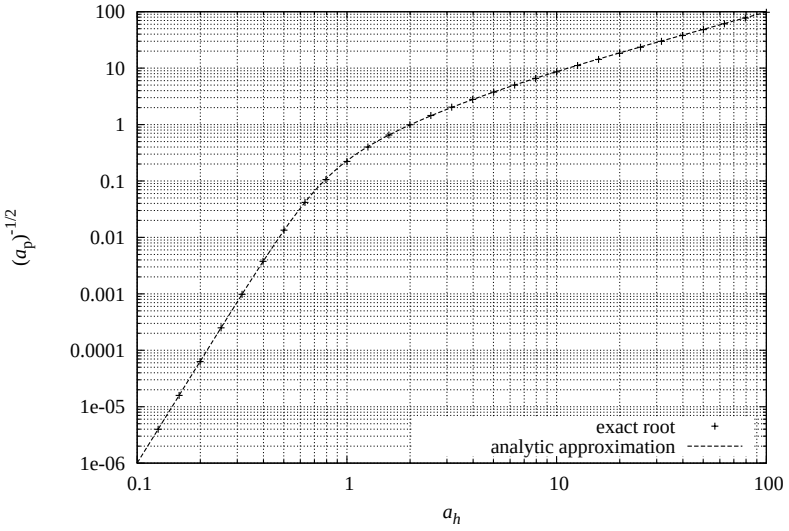

Figure 3.9.3: Root of Eq. (3.9.41a) as a function of a_h and its analytic approximation, Eq. (3.9.41c).

with less than 12 % of error with respect to the "real" values.

3.10 Analytic solution for a non-Boussinesq plume in a stratified environment

In this section I want to find an analytic solution approximating the behavior of the `ASH1D` model (3.4.1) in its complete form. The strategy that I will follow here will bring to an update of the results presented in Cerminara et al. [34]. The resulting analytical model will be called `ASH0D`.

Both Eqs. (3.7.5) and (3.8.8) admit the same asymptotic solution fulfilling the initial condition $q(0) = 1$ [8]:

$$q(\zeta) = \left(\frac{3v_q}{5a_q^{1/5}}\,\zeta + 1 \right)^{\frac{5}{3}}, \qquad \text{where} \quad a_q = \frac{4v_q}{5v_m(1-\gamma_c)}\,. \tag{3.10.1}$$

Thus this solution approximates the plume model (3.4.1) in both the Boussinesq and non-Boussinesq regime. The difference between these two regimes appears in the asymptotic solution when I choose which first integral of motion to use, either

[8] In Eqs. (3.8.13) are the asymptotic solution of system (3.8.2), written in a form such that it is possible to find the virtual radius b_v. However, that solution does not fulfill initial conditions for q and m. To write an asymptotic solution respecting the initial condition it is more convenient to use $q(\zeta)$ in the form given in this section.

$\mathcal{U}$ (Eq. (3.8.5)) or $\mathcal{U}_{\rm RS}$ (Eq. (3.7.4)), thus in the form of m:

$$m(\zeta) = \left[\frac{1}{a_q}\left(q^2(\zeta) - 1\right) + 1\right]^{\frac{2}{5}}, \qquad \text{or} \tag{3.10.2}$$

$$m(\zeta) = \left\{\frac{1}{a_q}\left[(l_{\rm c}(q(\zeta)) - l_{\rm c}(1)\right] + 1\right\}^{\frac{2}{5}}, \qquad \text{with} \tag{3.10.3}$$

$$l_{\rm c}(q) = q^2 - \frac{2\gamma_{\rm c}(\phi - q_\chi)}{1-\gamma_{\rm c}}\left[q - q_\chi \ln(|q + q_\chi|)\right]. \tag{3.10.4}$$

These asymptotic expansions are equivalent to Eqs. (3.8.13), with correct initial conditions $m(0) = 1$ and $q(0) = 1$. In what follows, I will use the latter Eq. (3.10.3) as asymptotic expansion for the momentum flux, because it works better than the former equation in the non-Boussinesq regime. Indeed, even if this solution has been found by applying the approximation $q \gg 1$ to Eqs. (3.4.1), I want to extend its applicability to plumes in non-Boussinesq regime. I will describe a strategy to hold this task, after having introduced atmospheric stratification.

The only difference between Eqs. (3.8.2) – from where I have extracted the latter asymptotic solution – and the Eqs. (3.9.5) – for a stratified atmosphere – is the variability of $f(\zeta)$. In the former system f is considered as constant and equal to 1, while in the latter one it is considered as a function $f = f(\zeta)$. However, in the previous section is shown that $f(z)$ is a slowly varying function, because $v_{f,0}$ is usually very small with respect to the rate of variation of the other equations involved, namely v_q and v_m. Thus, one strategy to look for an analytic solution of the problem in a stratified atmosphere could be to consider the asymptotic solution (3.10.1) valid also for problem (3.9.5), and use it for finding $f(\zeta)$. In particular, substituting $q(\zeta)$ in (3.9.5c), I obtain:

$$f(\zeta) = 1 - \frac{v_{f,0}}{2(1-\gamma_{\rm c})v_m}(m(\zeta)^2 - 1), \tag{3.10.5}$$

with $m(\zeta)$ defined in Eqs. (3.10.2). Now, I recall the first integral of motion found in Eq. (3.9.8)

$$\mathcal{U}_m = (1-\gamma_{\rm c})^2 + \frac{v_{f,0}}{v_m} = (f-\gamma_{\rm c})^2 + \frac{v_{f,0}}{v_m}m^2, \tag{3.10.6}$$

and I try to substitute Eq. (3.10.5) in it. I find:

$$(f-\gamma_{\rm c})^2 = (1-\gamma_{\rm c})^2 + \frac{v_{f,0}}{v_m}(1-m^2) + \frac{v_{f,0^2}}{4(1-\gamma_{\rm c})^2 v_m^2}(1-m^2)^2. \tag{3.10.7}$$

This result differs from Eq. (3.9.8) just because of the term

$$\frac{v_{f,0}^2}{4(1-\gamma_{\rm c})^2 v_m^2}(1-m^2)^2 = \frac{1}{4}(1-\gamma_{\rm c})^2\delta_{\rm p}^2\,(1-m^2)^2, \tag{3.10.8}$$

where I have used the definition of $\delta_{\rm p} = v_{f,0}/(1-\gamma_{\rm c})^2 v_m$. The latter term is $O(\delta_{\rm p}^2)$, thus it can be disregarded in the plume regime ($\delta_{\rm p} \ll 1$) with respect the other two terms in the right-hand-side of Eq. (3.10.7), which are respectively $O(1)$ and $O(\delta_{\rm p})$.

parameter	[forcedPlume]	[Santiaguito]	[weakPlume]	[strongPlume]
$\zeta_{\max}$	1621	23.96	160.4	29.87
$\zeta_{\max}^{(\mathrm{asy})}$	1493	26.20	165.2	33.31
$\Delta\zeta/\zeta$	7.9%	9.3%	3.0%	11.5%
ζ_{nbl}	1230	18.35	118.5	18.98
$\zeta_{\mathrm{nbl}}^{(\mathrm{asy})}$	1150	19.90	125.7	24.87
$\Delta\zeta/\zeta$	6.5%	8.4%	6.1%	31.0%

Table 3.10.1: Comparison between the height of the plume as evaluated from the numerical (`ASH1D`, Eq. (3.4.1)) and analytical (`ASHOD`) one-dimensional plume model.

By noting that $\mathcal{U}_m$ is approximatively conserved by the asymptotic solution found in this section, I have corroborated the fact that this solution is approximating the complete solution in the plume regime.

Having the enthalpy flux evolution $f(\zeta)$, it is possible to calculate the maximum plume height and neutral buoyancy level by using $m_{\max}$ and $f_{\min}$ given respectively in Eqs. (3.9.9) and (3.9.10). In Tab. 3.10.1 I recall the maximum plume height and neutral buoyancy level as obtained from model (3.4.1), comparing it with the asymptotic results $\zeta_{\max}^{(\mathrm{asy})}$, $\zeta_{\mathrm{nbl}}^{(\mathrm{asy})}$.

Now I move to face the non-Boussinesq regime. The strategy proposed in Cerminara et al. [34] is to use the asymptotic solution in the complete inversion formulas for U, b, β, T_β, Y_{e} and Y_{s} reported in Eq. (3.4.5). The behavior of this approximation is showed in Figs. 3.10.1, 3.10.2, 3.10.3, 3.10.4. There I notice that the solution works surprisingly well for all the presented plumes. In particular, the temperature and density profiles are well captured for all the cases. The best behavior is recorded in the non-Boussinesq monophase plume (recall $\phi = 0.893$). The asymptotic solution behaves worse for the plume radius and the plume axial velocity in the upper part, where the stratification play the most important role. Anyway, the plume maximum height is captured with less than 12 % of error for all the plumes. The neutral buoyancy level of the [strongPlume] has a larger error because of the jet-like part, where the enthalpy flux increases. Systematically, the asymptotic mass flux is overestimated with respect model (3.4.1). This error presents with more evidence in [strongPlume], and directly reflects in the underestimation of the mass fractions along the plume axis.

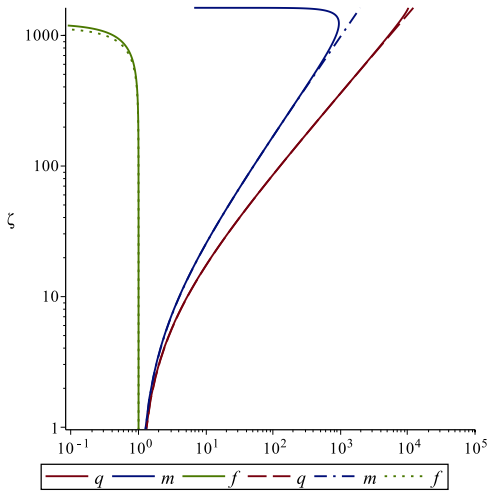

(a) mass, momentum and enthalpy fluxes

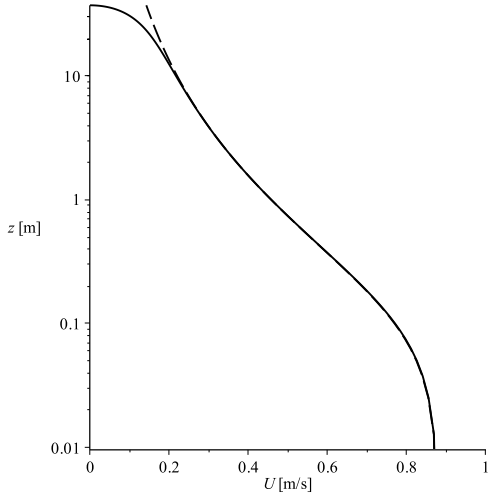

(b) axial velocity

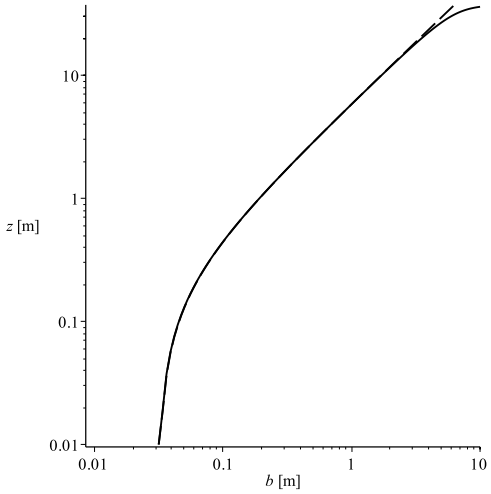

(c) plume radius

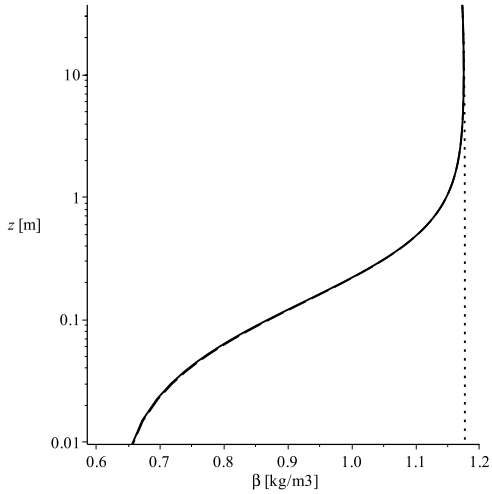

(d) plume density

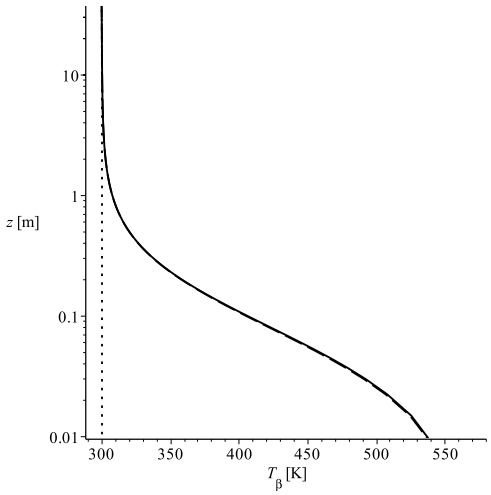

(e) plume temperature

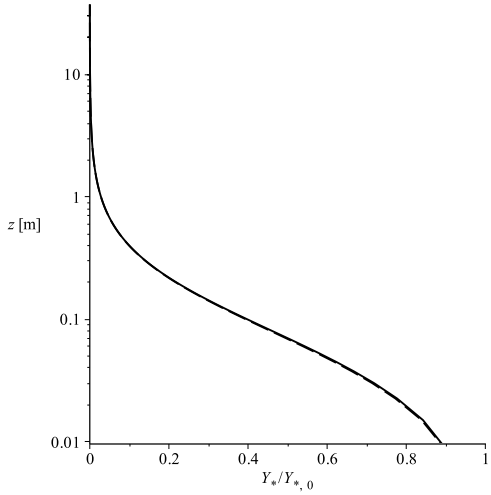

(f) tracer mass fraction

Figure 3.10.1: [forcedPlume]: Vertical evolution of the non-dimensional fluxes q, m, f (log-log scale), of the plume radius b (log-log scale) and of the dimensional physical parameters U, β, T_β, $Y_{e\,(s)}$, in (linear-log) scale. Solid lines correspond to the numerical solution of model (3.4.1), while dashed lines are evaluated by using the analytic asymptotic solution Eqs. (3.10.1), (3.10.3), (3.10.5).

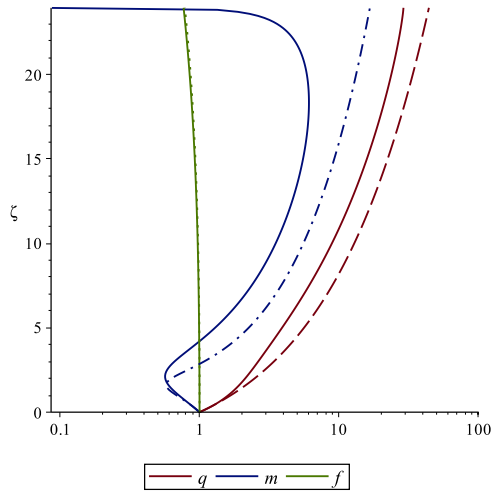

(a) mass, momentum and enthalpy fluxes

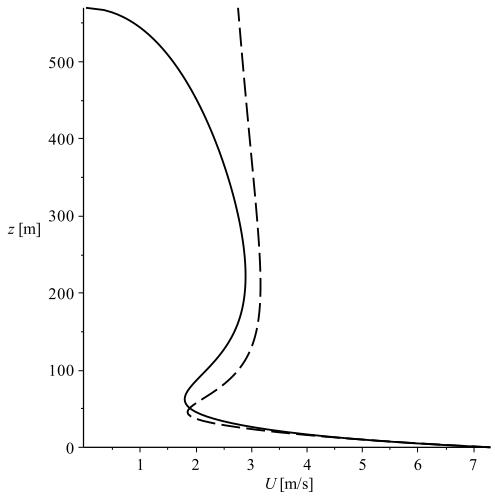

(b) axial velocity

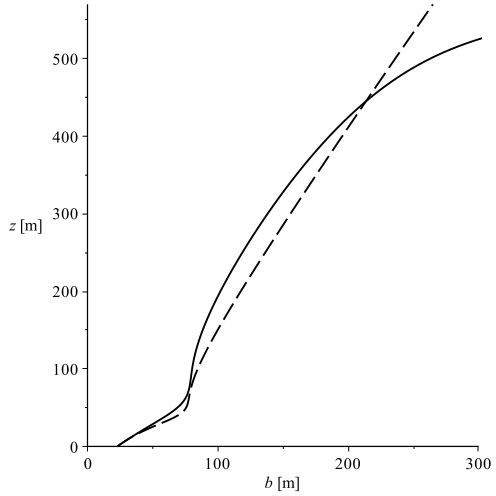

(c) plume radius

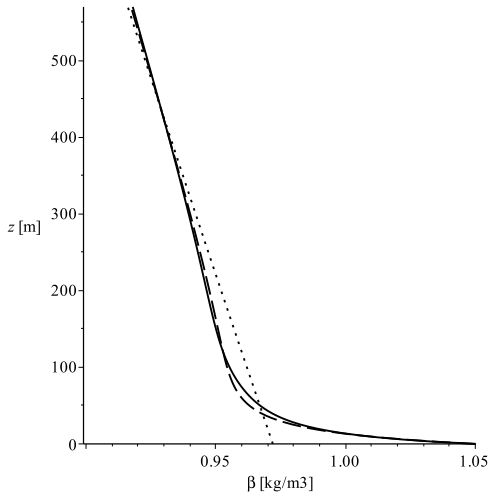

(d) plume density

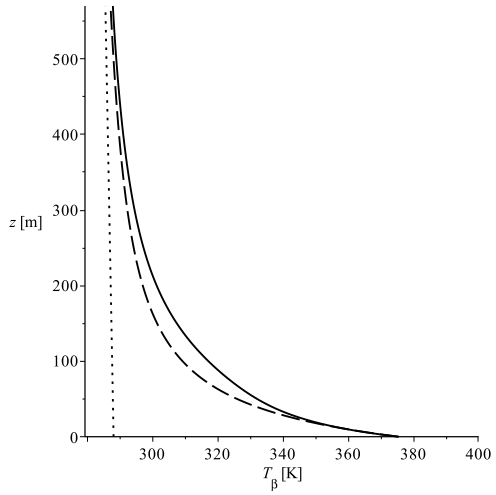

(e) plume temperature

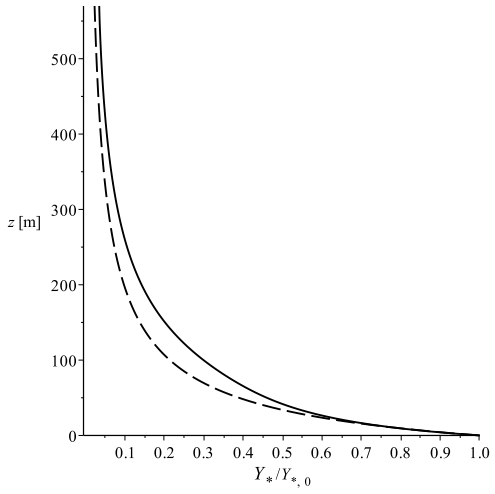

(f) plume mass fractions

Figure 3.10.2: [Santiaguito]: Vertical evolution of the non-dimensional fluxes q, m, f (log-linear scale) and of the dimensional physical parameters U, b, β, T_β, $Y_{e\,(s)}$. Solid lines correspond to the numerical solution of model (3.4.1), while dashed lines are evaluated by using the analytic asymptotic solution Eqs. (3.10.1), (3.10.3), (3.10.5).

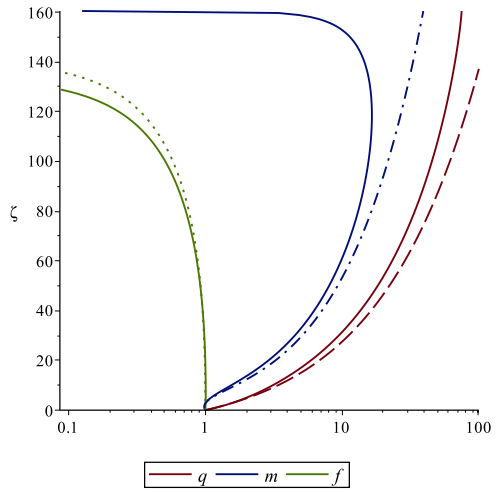

(a) mass, momentum and enthalpy fluxes

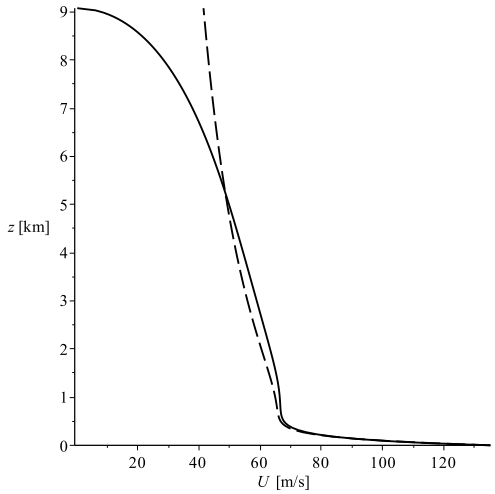

(b) axial velocity

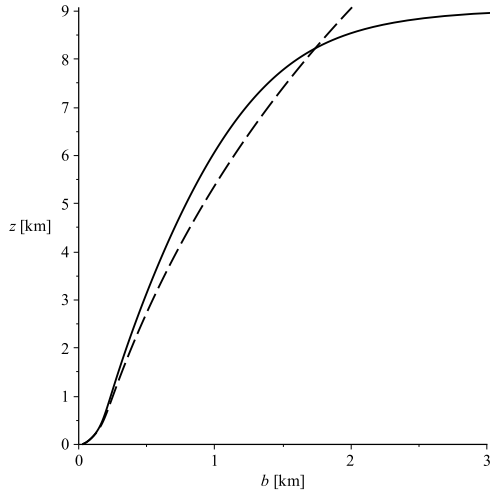

(c) plume radius

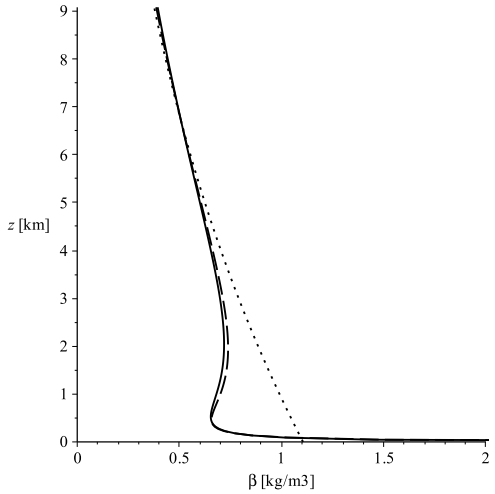

(d) plume density

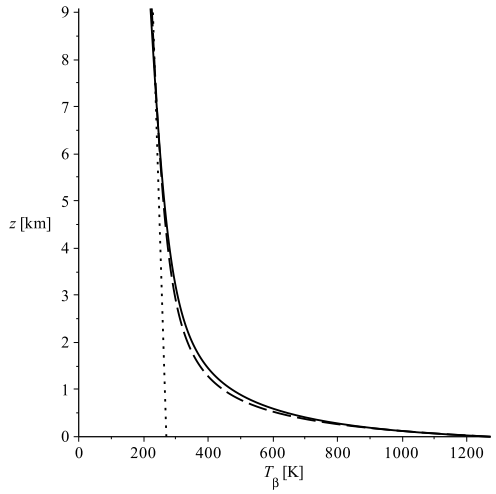

(e) plume temperature

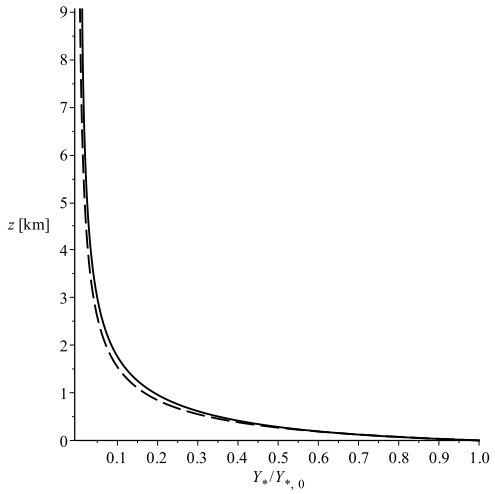

(f) plume mass fractions

Figure 3.10.3: [weakPlume]: Vertical evolution of the non-dimensional fluxes q, m, f (log-linear scale) and of the dimensional physical parameters U, b, β, T_β, $Y_{e\,(s)}$. Solid lines correspond to the numerical solution of model (3.4.1), while dashed lines are evaluated by using the analytic asymptotic solution Eqs. (3.10.1), (3.10.3), (3.10.5).

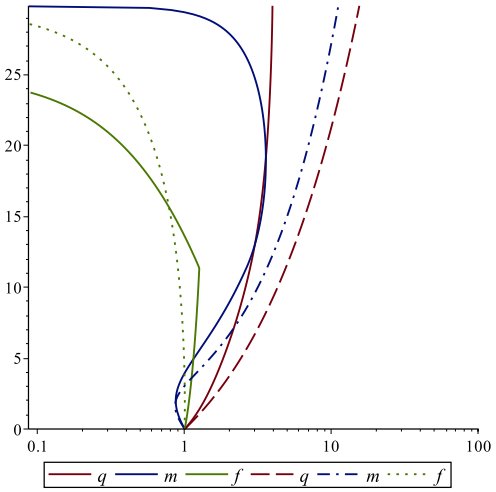

(a) mass, momentum and enthalpy fluxes

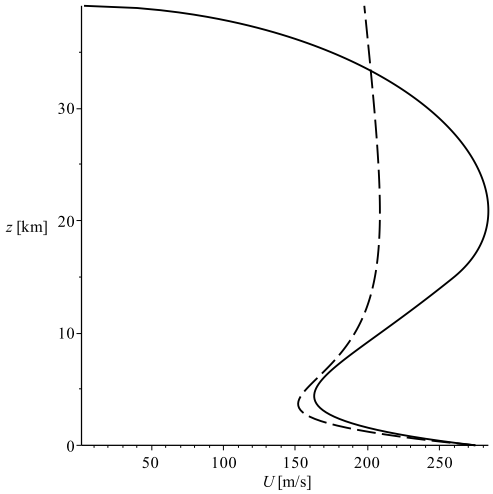

(b) axial velocity

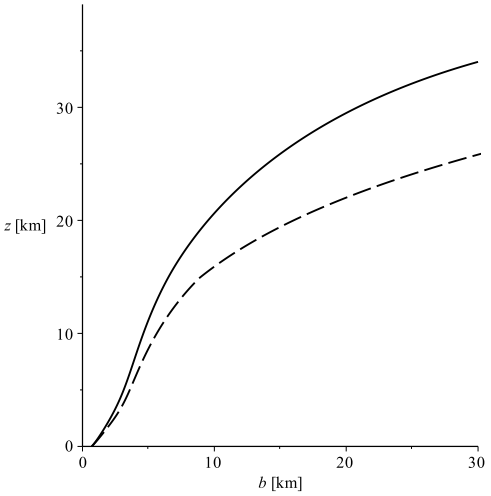

(c) plume radius

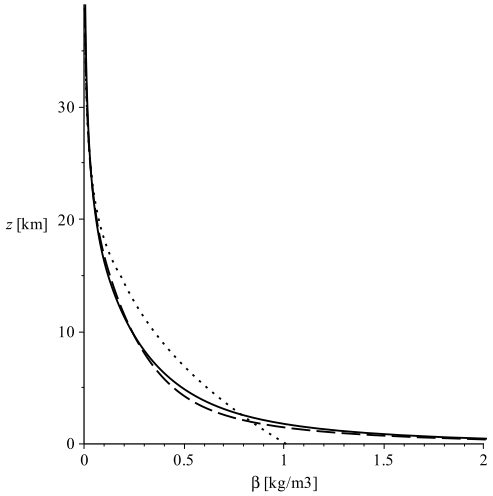

(d) plume density

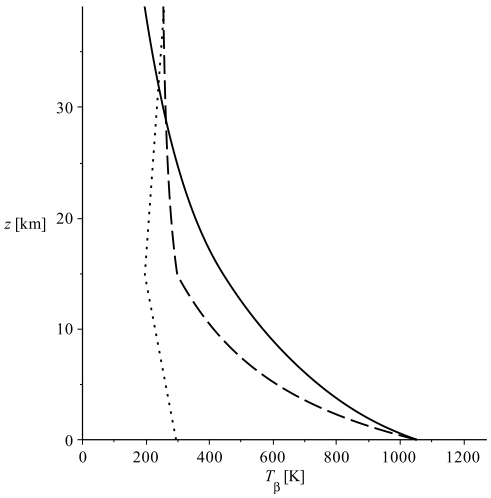

(e) plume temperature

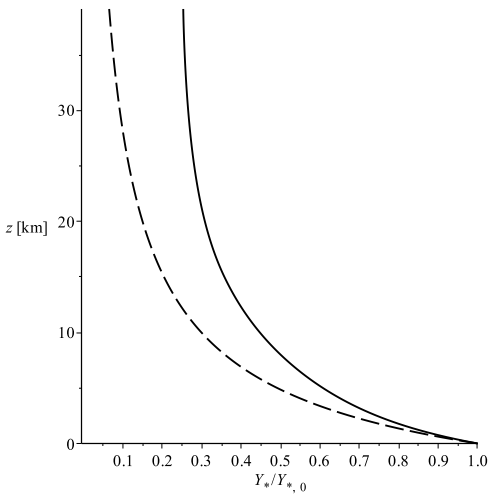

(f) plume mass fractions

Figure 3.10.4: [strongPlume]: Vertical evolution of the non-dimensional fluxes q, m, f (log-linear scale) and of the dimensional physical parameters U, b, β, T_β, $Y_{e\,(s)}$. Solid lines correspond to the numerical solution of model (3.4.1), while dashed lines are evaluated by using the analytic asymptotic solution Eqs. (3.10.1), (3.10.3), (3.10.5).

3.11 Comparison between results of 3D and integral plume models

Integral models for plumes describe the evolution with height (the axial unity vector being $\hat{z}$) of three main variables: the flux of mass, momentum and buoyancy. The purpose of these kind of models is to reproduce – as accurately as possible – the behavior of these three parameters under the hypothesis that the plume is stationary. Moving to the 3D models, they give the plume variables as a function of time and space. In order to compare results, I have first of all to average the 3D result over a time window where the solution can be considered stationary. The second step to do in order to coherently compare the two kind of models is to define the three fluxes also in the 3D case. I choose to define it as described below.

Given $\Omega \times \mathcal{T}$, the space-time domain, a first average over $\mathcal{T}$ of a generic 3D variable $\mathfrak{f}(\boldsymbol{x}, t)$ is performed:

$$\bar{\mathfrak{f}} = \langle \mathfrak{f} \rangle_{\mathcal{T}}(\boldsymbol{x}) = \int_{\mathcal{T}} \mathfrak{f}(\boldsymbol{x}, t)\, \mathrm{d}t\,. \tag{3.11.1}$$

For keeping the notation as simple as possible, in this section I use $\bar{(\cdot)}$ in place of $\langle\cdot\rangle_{\mathcal{T}}$. I define a plume subset $\Omega_{\mathrm{plm}}(z) \subset \Omega_z$, where Ω_z is the plane orthogonal to $\hat{z}$ at height z. Subset Ω_{plm} is identified by two thresholds: the averaged mixture velocity has positive axial component and the mass fraction of a tracer $\bar{y}_{\mathrm{tracer}}$ is larger than a minimum threshold $y_{\min}$:

$$\Omega_{\mathrm{plm}} = \{(x_1, x_2) \in \Omega_z \,|\quad \bar{\boldsymbol{u}}_{\mathrm{m}} \cdot \hat{z} \geq 0 \quad \text{and} \quad \bar{y}_{\mathrm{tracer}} \geq y_{\min}\}\,. \tag{3.11.2}$$

I refer to the integral over this domain as:

$$\mathfrak{f}(z) = \langle \mathfrak{f}(\boldsymbol{x}) \rangle_{\Omega_{\mathrm{plm}}} \equiv \int_{\Omega_{\mathrm{plm}}} \mathrm{d}x_1 \mathrm{d}x_2\, \mathfrak{f}(x_1, x_2, z)\,. \tag{3.11.3}$$

In particular, I define respectively the mass flux, the kth mass fraction, the momentum flux and the buoyancy flux as follows:

$$\pi Q = \langle \bar{\rho}_{\mathrm{m}}\, \bar{\boldsymbol{u}}_{\mathrm{m}} \cdot \hat{z} \rangle_{\Omega_{\mathrm{plm}}} \equiv \pi \beta U b^2 \tag{3.11.4a}$$

$$\pi Q_k = \langle \bar{\rho}_{\mathrm{m}} \bar{y}_k\, \bar{\boldsymbol{u}}_{\mathrm{m}} \cdot \hat{z} \rangle_{\Omega_{\mathrm{plm}}} \equiv \pi \beta Y_k U b^2 \tag{3.11.4b}$$

$$\pi M = \left\langle \bar{\rho}_{\mathrm{m}} (\bar{\boldsymbol{u}}_{\mathrm{m}} \cdot \hat{z})^2 \right\rangle_{\Omega_{\mathrm{plm}}} \equiv \pi \beta U^2 b^2 \tag{3.11.4c}$$

$$\pi F = \left\langle \left(\frac{1 + \sum_k (\chi_k - 1)\bar{y}_k}{1 + \sum_k (\psi_k - 1)\bar{y}_k}\, \rho_\alpha - \bar{\rho}_{\mathrm{m}} \right) (\bar{\boldsymbol{u}}_{\mathrm{m}} \cdot \hat{z}) \right\rangle_{\Omega_{\mathrm{plm}}} \equiv \pi \left(\frac{1 + Y_\chi}{1 + Y_\psi} \alpha - \beta \right) U b^2\,, \tag{3.11.4d}$$

where $Y_\psi = \sum_k (\psi_k - 1) Y_k$, $Y_\chi = \sum_k (\chi_k - 1) Y_k$ and $k \in \mathcal{I} \cup \mathcal{J}$ (with nil gas constant of the solid phase $\psi_j = 0$). Moreover, $\alpha(z) = \langle \rho_\alpha(\boldsymbol{x}, 0) \rangle_{\Omega_{\mathrm{plm}}}$. I choose this method for obtaining the one-dimensional integral fluxes because of two reasons: 1) it is the three-dimensional counterpart of what I have defined in Secs. 3.2.1 and 3.3, thus it holds even in non-Boussinesq regime [9]; 2) it is independent on the shape of the radial profile of the plume.

[9] A similar approach for the Boussinesq regime has been developed in Kaminski et al. [111].

By defining $Q_\psi = Y_\psi Q$ and $Q_\chi = Y_\chi Q$, the plume variables can be recovered by using the same inversion formulas given in 3.4.5. I recall them in their dimensional form:

- plume radius $b(z) = \sqrt{\frac{Q(F+Q)(Q+Q_\psi)}{\alpha M(Q+Q_\chi)}}$
- plume density $\beta(z) = \alpha \frac{Q(Q+Q_\chi)}{(F+Q)(Q+Q_\psi)}$
- kth averaged mass fractions $Y_k(z) = \frac{Q_k}{Q}$
- plume temperature $T(z) = T_\alpha \frac{F+Q}{Q+Q_\chi}$
- plume velocity $U(z) = \frac{M}{Q}$
- entrainment coefficient

$$\varkappa(z) = \frac{Q'}{2\alpha U b}\,, \tag{3.11.5}$$

where $(\cdot)'$ is the derivative along the plume axis and $T_\alpha = p/R_\alpha\alpha$ is the atmospheric temperature profile.

It is worth noting that the methodology described in this section allows plume modelers to coherently compare results obtained from one-dimensional integral models with data obtained from complex three-dimensional simulations. Moreover, the entrainment coefficient $\varkappa$ – the key empirical parameter for one-dimensional models – can be easily obtained for three-dimensional fields. In Chap. 6, I will give some example of the results obtained by using this averaging procedure for the post-processing of three-dimensional plume simulations. The same procedure has been used also for the IAVCEI (International Association of Volcanology and Geochemistry of the Earth Interior) plume model intercomparison initiative [39]. It consisted in performing a set of simulations using a standard set of input parameters so that independent results could be meaningfully compared and evaluated, discussing different approaches, and identifying crucial issues of state of the art of models.

3.12 Appendix

Gauss hypergeometric functions

Gauss hypergeometric functions ${}_2F_1([\cdot,\cdot]\,;[\cdot];x)$ are useful in order to perform integrals of the form:

$$\int (x^c - a)^b \,\mathrm{d}x\,. \tag{3.12.1}$$

${}_2F_1([\cdot,\cdot]\,;[\cdot];x)$ is the hypergeometric function defined when $x \leq 1$ as:

$${}_2F_1([r,s];[t];x) = \sum_{n=0}^{\infty} \frac{(r)_n (s)_n}{(t)_n} \frac{x^n}{n!}\,, \tag{3.12.2}$$

$$(a)_n = \begin{cases} 1 & n = 0 \\ a(a+1)\ldots(a+n+1) & n > 0\,. \end{cases} \tag{3.12.3}$$

In thesis I have to deal with integrals in which $c = 2$, thus I define

$$\mathfrak{F}_b(x) \equiv {}_2F_1\left(\left[-b, \frac{1}{2}\right]; \left[\frac{3}{2}\right]; x\right) \tag{3.12.4}$$

$$\mathfrak{G}_b(x) \equiv {}_2F_1\left(\left[-b, -b-\frac{1}{2}\right]; \left[\frac{1}{2}-b\right]; x\right)\,, \tag{3.12.5}$$

so that

$$\int (a - x^2)^b \mathrm{d}x = a^b x\, \mathfrak{F}_b\left(\frac{x^2}{a}\right) + C \qquad \text{if} \quad x^2 < a \tag{3.12.6}$$

$$\int (x^2 - a)^b \mathrm{d}x = \frac{x^{1+2b}}{1+2b}\, \mathfrak{G}_b\left(\frac{a}{x^2}\right) + C \qquad \text{if} \quad x^2 > a\,. \tag{3.12.7}$$

It is worth noting that $\mathfrak{F}_b(1)$ and $\mathfrak{G}_b(1)$ are finite and their value is tied to the Gamma function $\Gamma(x)$ as:

$$\mathfrak{F}_b(1) = \frac{\sqrt{\pi}\,\Gamma(1-b)}{2\,\Gamma(3/2-b)} \tag{3.12.8}$$

$$\mathfrak{G}_b(1) = \frac{2^{2b}\sqrt{\pi}\,\Gamma(1-2b)}{\Gamma(1/2-2b)}\,. \tag{3.12.9}$$

Chapter 4

Electromagnetic model for ash plumes

In this chapter, I present a coupled fluid-dynamic and electromagnetic model for volcanic ash plumes. The plume fluid-dynamics is based upon the integral plume theory developed in the previous chapter. The aim is: 1) to obtain from the model a new observable (measurable) quantity, namely the plume infrared emission; 2) to invert the model in order to retrieve vent parameters from the measured infrared emission. This chapter is based on Cerminara et al. [34].

In a forward approach, the model is able to simulate the plume dynamics from prescribed input flow conditions and generate the corresponding synthetic thermal infrared (TIR) image, allowing a comparison with field-based observations. An inversion procedure is then developed to retrieve vent conditions from TIR images, and to independently estimate the mass eruption rate. The adopted fluid-dynamic model is based on a one-dimensional, stationary description of a self-similar turbulent plume, for which an asymptotic analytical solution is obtained (cf. Sect. 3.10).

The electromagnetic emission/absorption model is based on the Schwarzschild's equation and on Mie's theory for disperse particles, assuming that particles are coarser than the radiation wavelength (about 10 μm) and that scattering is negligible. In the inversion procedure, the model parameters space is sampled to find the optimal set of input conditions which minimizes the difference between the experimental and the synthetic image.

The inversion procedure is applied to an ash plume at Santiaguito (Santa Maria volcano, Guatemala) allowing to retrieve the plume vent parameters for a real eruption: namely mass flow rate, vent radius, velocity, temperature, gas mass ratio, entrainment coefficient and their related uncertainty. Moreover, it is possible to obtain a reliable estimate of the equivalent Sauter diameter of the particle size distribution (i.e. a measure of the mean particle size).

The presented method is general and, in principle, can be applied to the spatial distribution of particle concentration and temperature obtained by any fluid-dynamic model, either integral or multidimensional, stationary or time-dependent, single or multiphase. The method discussed here is fast and robust, thus indicating potential for applications to real-time estimation of ash mass flux and particle size distribution, which is crucial for model-based forecasts of the volcanic ash dispersal process.

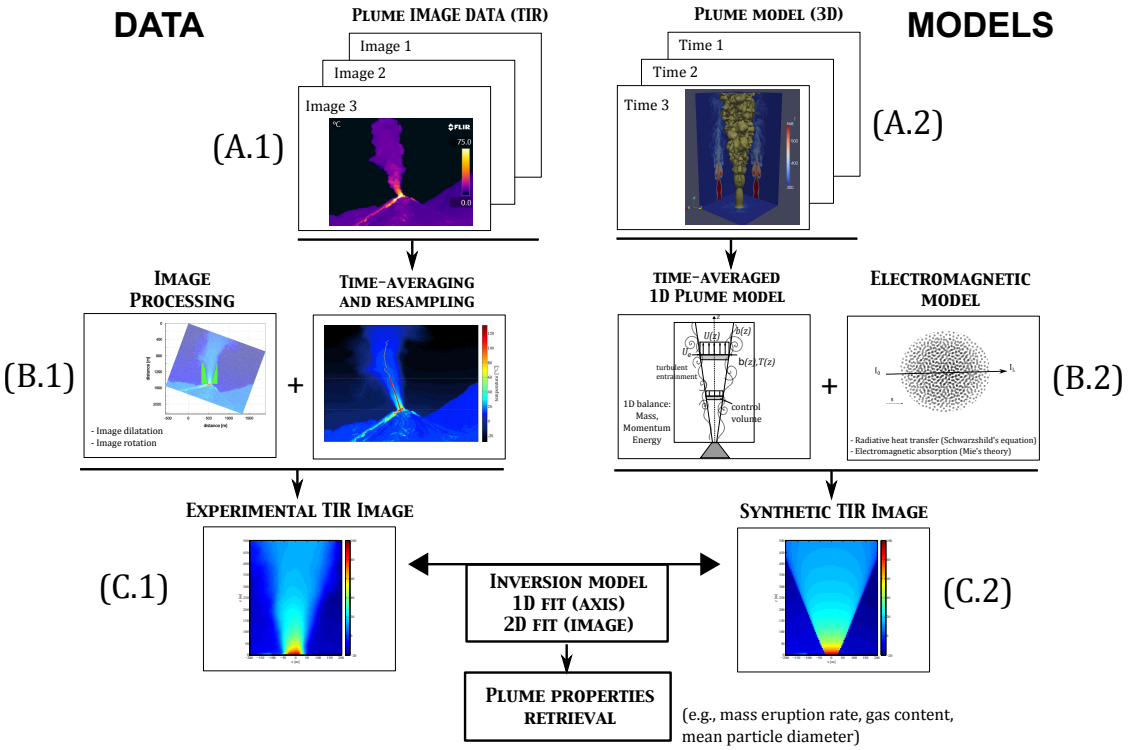

Figure 4.1.1: Schematic overview of the aims and methodology of the work presented in this chapter. (A.1) Volcanic plume emission is recorded using a TIR camera. Modeling of such phenomenon requires 3D numerical models (A.2), able to reproduce the complex fluid-dynamic behavior at various length and time scales. However because such models require high computational power and time, analytical 1D mean plume models (B.2) may be used to predict the mean behavior of volcanic plumes. Such models are time-averaged stationary models, which describe the mean spatial distribution of flow parameters (e.g., particle concentration, temperature, velocity) given a set of input conditions. By coupling an electromagnetic model to the plume model, the TIR emission of the gas–particle mixture is simulated, and a synthetic thermal infrared image (C.2) computed. The mean plume behavior may also be recovered from the recorded image by constructing a "mean image" (B.1), which is a time-averaged image obtained from averaging a sequence of images in a TIR video sequence. In doing this, the time-dependent dynamic fluctuations of the plume are filtered, leaving an image that reflects the mean plume behavior. Image processing is then applied to obtain an image with a vent-centred metric coordinate system, comparable to that created by the forward model. Recursive minimization of the discrepancy between the observed and modelled TIR images is then performed by application of an inversion model (2D when the entire images are compared, or 1D when only the plume central axis is compared), which searches for the best model input-parameters (e.g., ash mass, particle size distribution, etc.) reproducing the observed data.

4.1 Introduction

Despite the advancement of physical models describing eruption conditions and the subsequent atmospheric dispersal of the gas–particle mixture during an explosive eruption, one of the main obstacles to the full understanding of volcanic plume dynamics is the difficulty in obtaining measurements of the ascent dynamics and plume properties, first among them the mass flow rate.

Current understanding of volcanic plume dynamics is largely based on visual observations, field observation (e.g. evolution of the thickness of the deposits around the vent) and on one-dimensional plume models. One of the reasons behind the success of 1D models is also that simple models rely on simple measurements for validation, allowing solution with a limited number of parameters. In the case of integral plume models, one observable is sufficient, namely the plume height. This can be measured using photogrammetry, infrared imaging, satellite remote

sensing, ceilometers, radio and radio-acoustic sounding [e.g., 199]. Under standard eruption conditions (prescribed enthalpy anomaly ϕ), only one adjustable parameter is then needed to fit plume observations, namely a self-similarity coefficient or the entrainment coefficient (cf. Eq. (3.9.30)). This linearly correlates the rate of air entrainment to the average vertical plume velocity [195, 138].

On the contrary, the plume interior is generally invisible to the observer, and there is no way to measure mixture density from simple visual observation. As a result, imaging techniques (here defined as the process by which it is possible to observe the internal part of an object which cannot be seen from the exterior) at different wavelengths are needed to obtain data regarding the plume interior [172].

Thermal infrared cameras have become affordable in the last 15 years and their use in volcanic plume monitoring has become popular [182, 157, 94]. To date they have been used to classify and measure bulk plume properties, such as plume front ascent rates, spreading rates and air entrainment rates for both gas, ash and ballistic rich emissions [97, 149, 165, 215], analysis of particle launch velocities, size distributions and gas densities [98, 49] and particle tracking velocimetry [14]. Recent deployments have involved use of two thermal cameras: one close up to capture the at-vent dynamics as the mixture exits from the conduit and one standing off to obtain full ascent dynamics as the plume ascends to its full extent. Recently, Valade et al. [201] have developed a procedure to extract from TIR images an estimate of the entrainment coefficient and other plume properties including plume bulk density, mass, mass flux and ascent velocity.

However, recovery of the plume ash mass content and grain size distribution in near-real time remains a major challenge. Experiments and modelling by Prata and Bernardo [154, 155] have demonstrated that, under opportune hypotheses (non-opacity of the plume and particle size comparable to the wavelength) thermal cameras can be used for retrieval of ash particle size, mass and optical depth. Such data are crucial for monitoring volcanoes [e.g., 124, 215] and hazard mitigation issues, and especially for the Volcanic Ash Advisory Centers (VAACs) which issue advisories to the aviation community during explosive eruptions. Indeed, VAACs use ash dispersion models (VATD, Volcanic Ash Transport and Dispersion models) to forecast the downstream location, concentration, and fallout of volcanic particles [187]. However, to be accurate, such models require quantification of the plume ash concentration and particle size distribution [128, 15].

In this chapter, I show that recovering this information is possible in a rapid and robust fashion by comparing thermal infrared images that record the emission of a volcanic plume, with synthetic thermal infrared images reconstructed from analytical models. In particular, using fluid dynamical models allows to overcome limitations caused by plume opacity.

The present approach inverts time-averaged thermal image data to reconstruct the temperature, ash concentration, velocity profiles and the grain size distribution within the plume. To do this, I construct a synthetic thermal image of the volcanic plume starting from the spatial distribution of gas and particles obtained from a fluid dynamic model. The method is based on the definition of the infrared (IR) irradiance for the gas-pyroclast mixture. This is derived from the classical theory of radiative heat transfer [135] with the approximation of negligible scattering (Schwarzschild's equation). The model needs to be calibrated to account for the

background atmospheric IR radiation and the material optical properties [94]. The absorption and transmission functions needed to compute the irradiance are derived from Mie's theory [134] and can be related, by means of semi-empirical models, to the local particle concentration, grain size distribution and to the optical thickness of the plume. By applying such an IR emission model to the gas–particle distribution obtained from a fluid dynamic model it is possible to compute a synthetic thermal image as a function of the input conditions. I adopt the one-dimensional, time-averaged plume model described in Sect. 3.10 to simulate the plume profile. The advantage of 1D modelling is that inversion can be performed in a fast and straightforward way by means of minimization of the difference between a synthetic and a measured IR image. However, the method is applicable to any kind of plume model.

In section 4.2, the IR electromagnetic model (equations and approximations) used to produce plume synthetic images is presented. In section 4.3, results obtained in Chap. 3 are applied to the coupled fluid-dynamic-electromagnetic model (forward model) to construct a synthetic thermal image of a volcanic plume. In section 4.4, this model is used to invert experimental TIR data acquired during an explosive event at Santiaguito (Santa Maria volcano, Guatemala) to estimate the flow conditions at the vent. Figure 4.1.1 illustrates the methodology and models developed in the chapter.

4.2 Infrared emission model

Due to the high-temperature of erupted gas and pyroclasts, volcanic plumes emit electromagnetic radiation in the TIR wavelengths (8–14 μm). Every single particle radiates as a function of its temperature (through the Planck's function) and material properties (each material being characterized by its optical properties [153]). On the other hand, part of the emitted radiation is absorbed by neighbouring gas and particles, so that the net transmitted radiation results from the balance between emission and absorption and is a function of the electromagnetic wavelength λ. This balance is expressed by Schwarzschild's equation.

4.2.1 Schwarzschild's equation

Along an optical path, defined by a curvilinear coordinate s (see Fig. 4.2.1), the infinitesimal variation of TIR intensity due to emission at temperature T is proportional to the Planck function

$$B_\lambda(T) = \frac{2h_\mathrm{B}c_\ell^2}{\lambda^5}\frac{1}{e^{\frac{h_\mathrm{B}c_\ell}{\lambda k_\mathrm{B}T}}-1}\,, \tag{4.2.1}$$

multiplied by the infinitesimal length ds: $\mathrm{d}I_\mathrm{emit} = K_\mathrm{emit}B_\lambda \mathrm{d}s$. Here h_B is Planck's constant, c_ℓ is the speed of light and k_B is the Boltzmann constant. On the other hand, the infinitesimal variation due to absorption is proportional to the radiation intensity itself, so that $\mathrm{d}I_\mathrm{abs} = K_\mathrm{abs}I_\mathrm{abs}\mathrm{d}s$. Following Kirchoff's law, the emission and absorption coefficients at a given wavelength λ are equal $K_\mathrm{emit} = K_\mathrm{abs} = K_\lambda$.

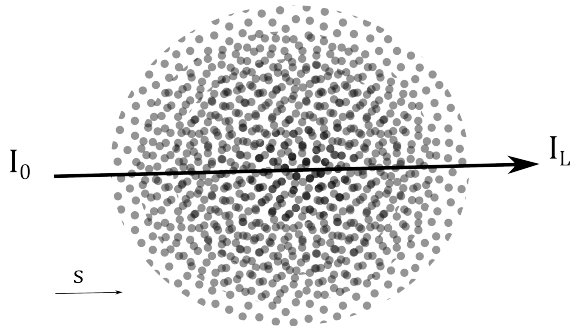

Figure 4.2.1: Schematic configuration of the propagation of a TIR ray inside a heterogeneous medium. The absorption coefficient is proportional to particle concentration. TIR intensity changes along the path due to particle emission/absorption. I indicate with s the curvilinear coordinate along the path, with I_0 being the background intensity and I_L being the measured intensity at distance L from the background position.

Thus, along a ray, this balance is expressed by:

$$\frac{\mathrm{d}I_\lambda}{\mathrm{d}s} = K_\lambda(B_\lambda - I_\lambda)\,. \tag{4.2.2}$$

By solving Eq.(4.2.2) along the optical path (as represented in Figure 4.2.1), for a heterogeneous medium, I find that

$$I_\lambda(L) = I_0 e^{-\tau_L} + \int_0^L K_\lambda(s) B_\lambda(s) e^{-(\tau_L - \tau(s))}\,\mathrm{d}s \tag{4.2.3}$$

where $I_0 = I_\lambda(0)$ is the background atmospheric radiation at the given wavelength and the integral is computed along a straight ray from the source $s = 0$ to $s = L$, this being the detector position. Here τ is the *optical thickness* (or depth), defined as:

$$\tau(s) = \int_0^s K_\lambda(s)\,\mathrm{d}s \tag{4.2.4}$$

and $\tau_L = \tau(L)$. In the next section, I show how $K(s)$ can be derived for a cloud of particles.

Equation (4.2.3) is specific for a given wavelength. However, the measured intensity is the result of integration over the detector spectral response, which is a function $\mathrm{sr}(\lambda) \in [0, 1]$. The spectral response function of the instrument utilized here is represented by the grey-shaded region in Fig. 4.2.2. Therefore, the measured average intensity can be expressed as:

$$I = \langle I_\lambda \rangle \equiv \frac{\int \mathrm{sr}(\lambda) I_\lambda \mathrm{d}\lambda}{\int \mathrm{sr}(\lambda)\,\mathrm{d}\lambda} \tag{4.2.5}$$

where – throughout all this chapter – $\langle\cdot\rangle$ is the operation of averaging over the spectral response. While it is possible to compute numerically this expression for the present model, I adopted a common practice of approximating I as a function of an absorption coefficient weight-averaged over the response function (cf. Fig. 4.2.2 and

Prata and Bernardo [155]) and assuming a slow variation of B_λ over the detector window [see also 94]. In other words, it is possible to simplify the expression of the averaged intensity by substituting in formula (4.2.3) K_λ with $\langle K_\lambda \rangle$, I_0 with $\langle I_0 \rangle$ and B_λ with $\langle B_\lambda \rangle \simeq B_{\hat{\lambda}} \equiv B$, where $\hat{\lambda} = 10\,\mu$m is chosen to best fulfil the latter approximation when T is in the interval $250 \div 400$ K. I also use the function $B(T)$ to convert computed intensity into brightness temperature.

In what follows, when the subscript λ is omitted, I refer to these approximations.

4.2.2 Absorption coefficient of the particulate phase

The absorption coefficient for a cloud of disperse spherical particles can be derived from Mie's theory [134, 93]. Accordingly, the absorption coefficient of N homogeneous spheres with radius r_j in a volume V can be written as:

$$K_\lambda = \frac{1}{V} \sum_{j=1}^{N} \pi r_j^2 \kappa_j(\lambda,\, r_j,\, n_j,\, k_j)\,,$$

where here κ_j is the efficiency factor of absorption and $n_j - ik_j$ is the complex refractive index of the jth sphere.

As shown by Hänel and Dlugi [93], if $r_j > r_{\min} = \dfrac{n_j^2 + 2}{16\pi k_j}\,\lambda$, then κ_j can be approximated to 1. In this regime – the high frequency optical limit – absorption no longer depends on the particle size, material or detection wavelength. It simply corresponds to the total cross section of the dispersed particles:

$$K_\mathrm{s} = \frac{1}{V} \sum_{j=1}^{N} \pi r_j^2\,.$$

For the case of volcanic particles [using the values for pumice reported by 153, (Tab. 1) and $\lambda = 14\,\mu$m], I obtain that this limiting size is around $r_{\min} \simeq 8\,\mu$m. Because in volcanic ash plumes most of the particle mass is usually distributed in ash coarser than this lower limit, throughout this chapter I will consider $\kappa_j = 1$. By using this approximation, the absorption due to particles smaller than $r_{\min}$ is overestimated.

By expressing the volume V in terms of the density and particle concentration ϵ_s, the absorption coefficient can be written in terms of the Sauter diameter d_S of the particle distribution, i.e.

$$K_\mathrm{s} = \frac{3}{4}\epsilon_\mathrm{s}\frac{\sum_j r_j^2}{\sum_j r_j^3} = \frac{3}{2}\frac{\epsilon_\mathrm{s}}{\overline{d^3}/\overline{d^2}} = \frac{3}{2}\frac{\epsilon_\mathrm{s}}{d_\mathrm{S}} \tag{4.2.6}$$

or, in terms of the particle microscopic density $\hat{\rho}_\mathrm{s}$ and the particle bulk density ($\rho_\mathrm{s} = \epsilon_\mathrm{s}\hat{\rho}_\mathrm{s}$)

$$K_\mathrm{s} = \frac{3}{2 d_\mathrm{S} \hat{\rho}_\mathrm{s}}\,\rho_\mathrm{s} = A_\mathrm{s}\rho_\mathrm{s}\,. \tag{4.2.7}$$

Here I have introduced the specific absorption coefficient of the particles A_s which represents the cross section of the particulate phase per unit of mass (having the dimensions of $[m^2/kg]$). Because K_s does not depend on the wavelength, it is worth noting $\langle K_s \rangle = K_s$ and $\langle A_s \rangle = A_s$. The Sauter diameter d_S represents the mean particle diameter that gives the same volume/surface area ratio as the original particle size distribution. In 4.6.1 it is shown how to compute the Sauter diameter for two sample grain size distributions.

4.2.3 Retrieval of grain size distribution from the optical thickness

In the most general case, the absorption coefficient K_s depends on the position s along the optical path through $\rho_s(s)$ (medium heterogeneity) and $A_s(s)$ (non-homogeneity of the grain-size distribution). For volcanic plumes, while the former effect is related to the mixture dilution due to air entrainment and adiabatic expansion, the latter can be ascribed to kinetic decoupling, gravitational settling and particle aggregation [78]. The optical thickness (Eq. 4.2.4) can be very sensitive to the grain size distribution of the particulate cloud, making its reconstruction from τ a potentially ill-posed problem. This fact is particularly critical if one tries to obtain information on the grain size distribution of a heterogeneous mixture by analyzing a single optical path (i.e., one image pixel). This problem has been envisaged by Prata and Bernardo [154, 155] by assuming particle concentration, temperature and specific absorption coefficient as constant along the optical path. This allowed them to retrieve the total particle mass along the integration path. However, in case of an opaque plume or where the image is saturated, only part of the mass can be measured (to have an idea of the opaqueness of the plume analysed in this chapter, cf. Fig. 4.4.7). To overcome this problem, thermofluid dynamic and aggregation models can be used to put further constrains to the spatial distribution of the mixture density, temperature and grain-size distribution, as a function of vent initial conditions. In this chapter I use this strategy to obtain the vent conditions from a plume image, by using the thermofluid dynamic model presented in Sect. 3.10.

When the changes in the grain size distribution can be considered of second-order (see discussion in Sect. 3.2.2), A_s would keep the same value in the whole plume. In such a case, the Sauter diameter does not change in the plume and Eq. (4.2.4) can be rewritten as:

$$\tau(s) = A_s \int_0^s \rho_s(s)\, \mathrm{d}s\,. \tag{4.2.8}$$

By adopting a thermofluid dynamic model to constrain the density distribution along the optical path, it is possible to isolate the dependency of the optical thickness on the grain size distribution. In particular, the optical thickness is inversely proportional to the Sauter diameter of the particle grain size distribution.

4.2.4 Absorption by atmospheric and volcanic gases

Thermal cameras used to monitor volcanic plumes are typically installed at distances of several kilometres from the source. This allows safe measurements, and the full ascent history from vent to point of stagnation to be imaged. Over such distances, the effect of atmospheric absorption will be non-negligible [94]. This effect becomes more important as humidity increases, because water droplets have high absorption properties at TIR wavelengths. Volcanic gases also have a significant effect on absorbing emitted radiation in the TIR [169]. Therefore, to apply Eq.(4.2.3) the absorption coefficients of the atmospheric and volcanic gases need be taken into account.

Absorption by gases can be computed using Eq.(4.2.2), so that the resulting coefficient is the sum of the coefficient of the N_{ph} phases:

$$K_\beta = \sum_i^{N_{\mathrm{ph}}} K_i \,.$$

Analogously to the expression of K_{s} for particles, the absorption coefficient for gases can also be expressed as the product of the specific absorption coefficient A_i (which depends only on gas material properties) multiplied by the gas bulk density $K_i(\boldsymbol{x}) = A_i\,\rho_i(\boldsymbol{x})$.

For example, in volcanic ash plumes one may want to consider the presence of water vapor, carbon dioxide and sulfur dioxide. In such a case, at any point $\boldsymbol{x}$:

$$K_\beta = \sum_k^{N_{\mathrm{ph}}} K_k = \sum_k^{N_{\mathrm{ph}}} A_k\,\rho_k(\boldsymbol{x}); \qquad k = \mathrm{s,\ w,\ CO_2,\ SO_2,\ Air} \tag{4.2.9}$$

In Fig. 4.2.2 I report the spectral behavior of water vapor, carbon dioxide and sulfur dioxide. In this figure I also report their weighted average over the detector spectral response. Throughout this chapter I will use these values for the gas specific absorption coefficients.

It is worth noting that for typical eruptive conditions (involving water vapor as the main volcanic gas), while A_{s} and A_{w} are of the same order of magnitude, $A_{\mathrm{CO_2}}$ and $A_{\mathrm{SO_2}}$ are more than one order of magnitude larger. For this reason, even if the mass fraction of the latter two gases is usually very small (less than 1 %), their optical contribution cannot be neglected. I discuss quantitatively this effect in 4.6.2.

4.2.5 Atmospheric background radiation

The background atmospheric radiation (the first term of Eq. 4.2.3) also contributes to the detected TIR radiance. Whereas the centre of an ash plume is generally opaque to transmission of background thermal radiation (meaning that this term is negligible along an optical path crossing the axis of an ash plume), part of the background atmospheric radiation can be transmitted through a gaseous plume or through the diffuse margins of an ash-laden plume, where particle concentration is much lower. The treatment of background radiation begins with

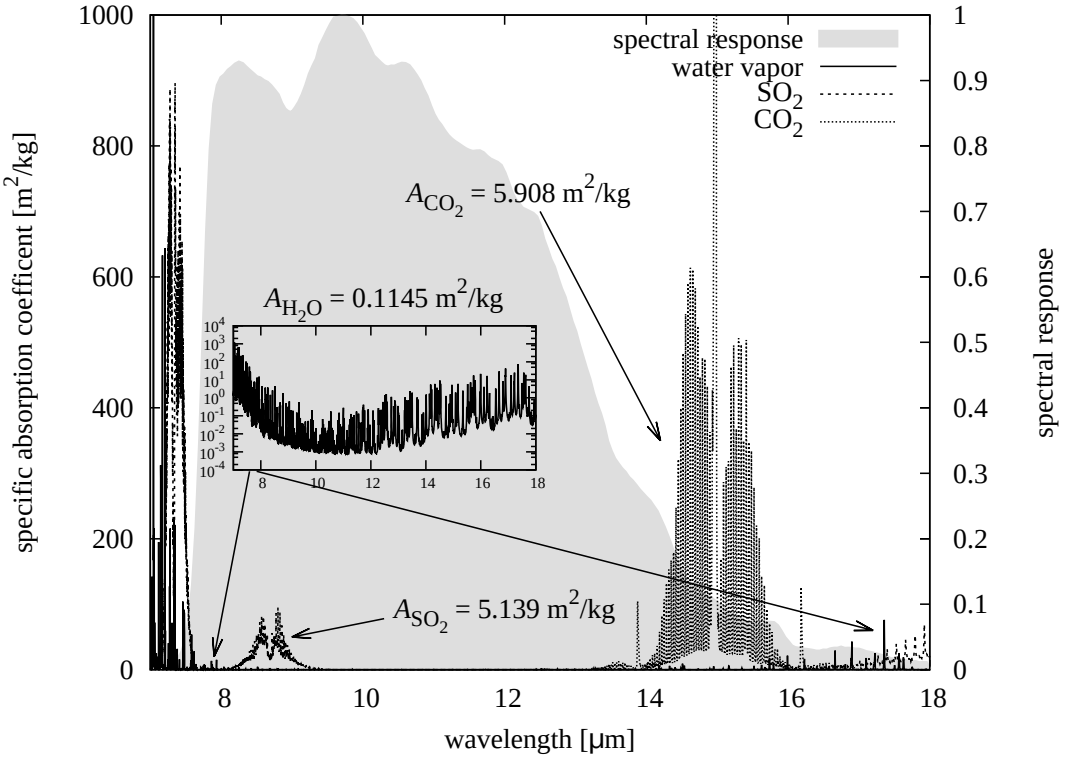

Figure 4.2.2: Typical spectral response of a FLIR camera (grey-shaded line) in the spectral window $7 \div 18\,\mu$m with the specific absorption spectra of water vapor (solid line), SO_2 (dashed line) and CO_2 (dotted line) at standard conditions (296 K, 1 atm). Weighted averages of the absorption coefficients of the three gases over the spectral response A_i are reported in the panel. In the small plot, a logarithmic zoom of the water vapor has been drawn. Data are retrieved from the HITRAN 2012 database [164].

an estimate of the spectral radiance in the absence of the plume at a distance L from the source, L being larger than the distance of the observer from the plume axis (see Fig. 4.3.1). I will show in section 4.4 how this can be done in practical cases.

In summary, the at-detector spectral radiance I associated with the emission/absorption balance from a gas–particle mixture in the atmosphere can be computed using an electromagnetic model by specifying the following variables and parameters along each optical path received by a detector:

- the Sauter diameter d_S of the particle distribution (Eq. 4.2.6);
- the spatial distribution of particle volumetric concentration ϵ_s (Eq. 4.2.6);
- the spatial distribution of temperature T (Eq. 4.2.1);
- the specific absorption coefficients weighted over the detector spectral response A_i for each gas species (Eq. (4.2.9) and Fig. 4.2.2);
- the bulk density distribution ρ_i of each gas species (Eq. 4.2.9).

Whereas the specific absorption coefficient of each material can be obtained from laboratory measurements, the spatial distribution of gas and particles, plus their variation in density and temperature needs to be derived from a fluid-dynamic model that describes the dynamics of the volcanic plume for specific vent conditions. In the following of this chapter I will use the analytical model developed in Sect. 3.10.

4.3 Coupled forward model

Thanks to fluid dynamic models, the bulk density ρ_k of each gaseous and solid component can be considered as given at every point of the domain (Figure 4.3.1). For each component, the specific absorption coefficients A_k are assumed to be known. Now,

1. The absorption coefficient of the mixture K_β can be estimated at any point by using Eq. (4.2.9).

2. Along every ray in Figure 4.3.1 the optical thickness $\tau(s)$ can be calculated (Eq. 4.2.4) by integrating K_β along the ray trajectory (which is assumed to be a straight line).

3. The Planck function of the mixture (Eq. 4.2.1) can be computed at each point of the domain as a function of the local temperature.

4. Finally, the background radiation I_0 is estimated at some point behind the plume (e.g., at $s = 0$ in Fig. 4.3.1), taken as the image horizon.

With these ingredients, the radiation intensity can be computed along a discrete number of rays forming the electromagnetic image of the domain Ω. It is worth noting that, usually, the output image of commercial devices gives the temperature rather than the intensity. To derive the temperature image from the TIR intensity, Planck's function has to be inverted (cf. Sec. 4.2).

Geometric approximations

To simplify the problem, the following geometric approximations are adopted:

- the camera is far enough from the plume so that rays can be considered as parallel;

- rays are assumed to cross the plume axis orthogonally;

- effect of plume bending (due to wind) are corrected by means of image processing techniques.

With these hypotheses, the geometric configuration required to construct the IR image is sketched in Fig. 4.3.1b, where the plume axis is oriented normally to the image plane at $r = 0$. Radius $b(z)$ depends on the height above the vent and the concentration and temperature fields are constant inside the circle and zero outside.

By adopting a top-hat assumption for the plume profile, the radiant intensity can be computed analytically under the further simplification that the emission/absorption of the atmosphere can be neglected. This is reasonable if the distance of the camera from the plume is not too large, indicatively less than about 10 km (based on atmospheric absorption in standard conditions at middle latitudes). In this case, the absorption coefficient is taken equal to zero outside the plume, whereas the value of $K_\beta(z)$ within the plume can be computed starting from the

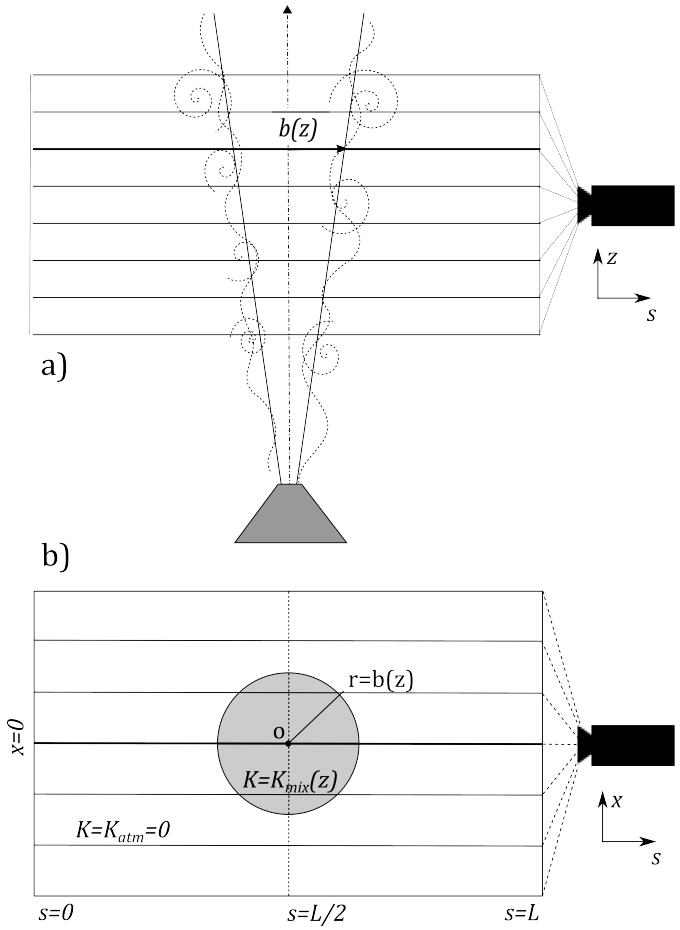

Figure 4.3.1: Geometric configuration adopted for the calculation of the IR intensity. a) Side view. b) Top view of a cutting plane orthogonal to the plume axis (point **o**). The plume radius is represented by the gray-shaded region (top-hat approximation).

analytical solution of the plume model, by expressing the mixture density β in terms of the non-dimensional variable q (Eqs. 3.4.5c and 3.10.1) [1]

$$K_\beta(z) = A_\mathrm{s}\rho_\mathrm{s} + A_\mathrm{e}\rho_\mathrm{e} = (A_\mathrm{s}q_\mathrm{s} + A_\mathrm{e}q_\mathrm{e})\,\frac{\beta}{q} = (A_\mathrm{s}q_\mathrm{s} + A_\mathrm{e}q_\mathrm{e})\,\alpha\frac{(q+q_\chi)}{(\phi+q)(q+q_\psi)} \quad (4.3.1)$$

with $K_\beta(z)$ depending on z only through $q = q(z)$. I also define the specific absorption coefficient of the mixture

$$A_\beta = (A_\mathrm{s}q_\mathrm{s} + A_\mathrm{e}q_\mathrm{e}) \quad (4.3.2)$$

so that $K_\beta = A_\beta\,\beta/q$ and A_β is an initial mixture parameter that does not depend on the position along the plume.

With reference to Fig. 4.3.1b), along each ray I identify the points s_1 and s_2 where the ray crosses the edge of the plume. For $-b < x < b$ their coordinates are $s_1 = L/2 - \sqrt{b^2 - x^2}$ and $s_2 = L/2 + \sqrt{b^2 - x^2}$ and the optical thickness is then

[1] Here I choose $f = 1$ for the sake of simplicity, because it can be considered constant for the [Santiaguto] plume, cf. Fig. 3.10.2 and Cerminara et al. [34].

simply

$$\tau(s,z) = \begin{cases} 0 & 0 < s < s_1 \\ K_\beta(z)\,(s - s_1) & s_1 < s < s_2 \\ K_\beta(z)\,(s_2 - s_1) & s_2 < s < L \end{cases} \tag{4.3.3}$$

Because in this example the optical thickness of the atmosphere is assumed zero, I find that

$$\tau_L(z) = K_\beta(z)\,(s_2 - s_1) = 2K_\beta(z)\sqrt{b^2 - x^2}\,\mathcal{H}(b^2 - x^2)$$

where $\mathcal{H}$ is the Heaviside step function. With these hypotheses, the Planck function depends only on the vertical coordinate z through $T_\beta(z)$ (Eqs. 3.4.5d and 4.2.1). By solving the integral, I obtain:

$$I_L(x,z) = I_0 e^{-\tau_L} + B(z)\left(1 - e^{-\tau_L}\right) \tag{4.3.4}$$

The synthetic TIR image of the plume given in Figure 3.10.2 is shown in Figure 4.4.3c, which will be discussed in the next section (I_0 has been computed by using the measured atmospheric brightness temperature, Fig. 4.4.2a).

4.4 Inverse model and application

The coupled fluid–electromagnetic model described in the previous sections provides a synthetic infrared image of a gas–particle plume, that I have called $I_L(x,z)$. This is a non-linear function of the flow conditions at the vent and of the material properties of volcanic gases and particles and of the atmosphere. More specifically, assuming that the material properties are known and neglecting the emission/absorption contribution of the atmosphere, the synthetic image can be expressed as a function of the plume model boundary values and parameters, and of the specific absorption coefficient of the mixture A_β (given by Eq. 4.3.2):

$$I_L = I_L(v_q, v_m, \ell_0, \phi, q_\chi, q_\psi, A_\beta)\,. \tag{4.4.1}$$

Using the algebraic transformations given in Eqs 3.4.11 and Sect. 4.6.2, I can express I_L as a function of $(b_0, U_0, T_0, Y_\mathrm{w}, Y_\mathrm{s}, \varkappa, d_\mathrm{S})$ where b_0, U_0, T_0, Y_w, Y_s are the plume radius, velocity, temperature, vapor and ash mass fraction at $z = 0$, $\varkappa$ is the air entrainment coefficient and d_S is the equivalent Sauter diameter of the grain size distribution. Note that $z = 0$ may not correspond to the vent emission level but instead to the minimum height of the acquired image.

This synthetic image can now be compared to the actual TIR images captured during the volcanic event. I will demonstrate in this section how it is possible to estimate the parameters in Eq. (4.4.1) by means of inversion procedures. To do this, TIR images must be preliminary processed in order to obtain an average experimental intensity image $I_E(x,z)$ and a background image $I_0(x,z)$. The minimum of the difference $||I_E - I_L|| = f(v_q, v_m, \ell_0, \phi, q_\chi, q_\psi, A_\beta)$ is then sought in the parameter space to find the eruptive conditions which best fit the observation.

4.4.1 Image processing

The TIR video used here provides a sequence of $N+1$ IR images $P_i (i = 0, ..., N)$ of a developing plume, acquired at a fixed time rate. Usually, commercial devices automatically convert the digital intensity image registered by the charge coupled device (CCD) into a 8 or 16 bit temperature image. I will here assume that the first image P_0 represents the time immediately before the eruption and that P_1 is the first image of the erupting plume. Because some time is needed for the plume to develop, I will also assume that the flow can be considered stationary between frames P_m and P_f. Under such assumptions, an average TIR image $P_a = \frac{\sum_{i=m}^{f} P_i}{f-m+1}$ can be computed.

By means of image processing techniques [201] the plume trajectory is extracted from P_a and the region of interest along the axis is selected. If the plume axis is bent (as a result of wind or source anisotropy) the images P_0 and P_a are corrected by means of geometric transformations (rotation and dilatation). This is also used to correct possible image distortions associated to camera orientation.

Finally, Eq. (4.2.1) is applied to thermal images P_a and P_0 to obtain the experimental intensity image $I_E(x, z)$ and the atmospheric background $I_0(x, z)$, where z runs along the axial direction and x along the horizontal direction perpendicular to the camera optical axis.

4.4.2 TIR dataset for an ashy plume at Santiaguito

The 1902 eruption of Santa María volcano (Guatemala) formed a crater on its southeastern flank into which, in June 1922, a new lava dome was emplaced [161]. The new dome complex was named Santiaguito, and comprises four main centers: El Caliente, El Brujo, La Mitad, El Monje [162]. Since 1977, Caliente has been the focus of activity which comprises of emission of silicic lava flows [95, 96] and intermittent low intensity explosions producing ash plumes up to 2 km high at a typical frequency of 1.7 explosions per hour [162, 12, 167]. El Caliente was the initial eruptive center and is believed to be coincident with the approximate location of the main conduit [161, 162]. Using digital video, Bluth and Rose [12] proposed a conduit model involving a dacite plug, with ash emissions being due to shear-induced magma fragmentation at the conduit boundaries. Stick-slip events occur 100 to 600 m below the crater [167]. One eruption model involves ascent of the mixture of gas and ash up the fracture zone around the plug, to result in an emission from vents distributed around the edge of the vent area [12, 166].

Excellent views of the Caliente vent, and plume emission events, can be gained from the SE, S and SW. The thermal camera is deployed on a ridge 4.5 km south of, and 1000 m in elevation below, Caliente vent [165] from where a clear view of the activity is achieved. The thermal camera used was a Forward-Looking Infrared Systems ThermaCam™(Model S40). This thermal video camera operates in the 7–14 μm range (cf. Fig. 4.2.2), producing 320 $\times$ 240 pixel calibrated temperature images.

A set of TIR images of an explosive ash emission that occurred at Santiaguito in 2005 [165] is used. The duration of ash emission is about $\Delta t \simeq 300$ s, and was sampled at 30 Hz.

To analyze the TIR images, a subset of images is extracted from the full TIR dataset [201]. It is chosen in a time window where the plume can be considered as stationary and fully developed. It starts $t_{\text{init}} = 45$ s after the beginning of the eruption and ends at $t_{\text{final}} = 255$ s. The time-averaged image is thus calculated (Fig. 4.4.1a) and the temperature values are sampled along the axis, at the points represented by the red dots in panel a) of Fig. 4.4.1. Finally, a region of about 500 m in height is identified (bounded by the horizontal dashed lines in Fig. 4.4.1a), where the flow is stationary. This fact is supported by Fig. 4.4.1b, where fluctuation relative to the mean image are evaluated pixel by pixel. It is worth noting that fluctuation are smaller than 10 % in the selected area and that the fluctuations are mainly due to turbulence [because they have the typical turbulent shape and are of the order of magnitude found for turbulent fluctuations in plumes, 151]). The averaged image is then rotated in order to have the plume axis along the z direction and dilated to partially correct the error due to the camera inclination. The resulting image $T_E(x_i, z_j)$ is shown in Fig 4.4.2b. Executing the same operation to the image acquired before the eruption, a matrix is obtained within which the brightness temperature can be associated to $I_0(x_i, z_j)$ (Fig 4.4.2a).

4.4.3 Two-dimensional inversion procedure

I here present two possible procedures to best-fit the experimental image $I_E(x, z)$ with the synthetic image $I_L(x, z)$ produced by the coupled fluid-electromagnetic model. The first method is based on the two-dimensional fit to the thermal image of Figure 4.4.2b. Because thermal images are already converted into temperature images, I convert the synthetic intensity image I_L into a thermal image $T_L(x_i, z_j)$ by using Eq. (4.2.1).

Inversion is achieved by seeking the minimum of a cost function which measures the difference between the synthetic and the experimental images. To this end, I have chosen the following residual function:

$$\sigma^2(\boldsymbol{p}) = \frac{1}{N * M - N_p} \sum_{i=1}^{N} \sum_{j=1}^{M} \left(T_E(x_i, z_j) - T_L(x_i, z_j; \boldsymbol{p})\right)^2 \tag{4.4.2}$$

where $\boldsymbol{p} = (v_q, v_m, \ell, \phi, \chi, q_\beta, A_\beta)$ is the N_p-dimensional vector of parameters defining σ^2 (in this case, $N_p = 7$) and $N \times M$ is the size of the image matrix. The function σ^2 must be minimized to obtain the vector of optimal input parameters $\boldsymbol{p} = \boldsymbol{p}^*$ for the plume that best fits the thermal observation. In this application, minimization is performed by deploying a genetic algorithm (implemented in MatLab through the function `ga`), but any minimization procedure can be used. In the present case, minimization have required about 50000 trials which took about 10 s on a laptop. The best fitting plume and the difference (in degrees Celsius) between the synthetic and the observed plume are displayed in panels a) and b) of Fig. 4.4.3. The results of the minimization procedure are also reported in Table 4.4.1, together with the ranges of variability specified in the search procedure.

In Fig. 4.4.4 the projection of $\sigma(\boldsymbol{p}^*)$ along each parameter axis, in the neighbours of the minimum, is shown. In this Figure, the shape of the minimum along all the parameters directions appears to be well constrained. A quantitative analysis of

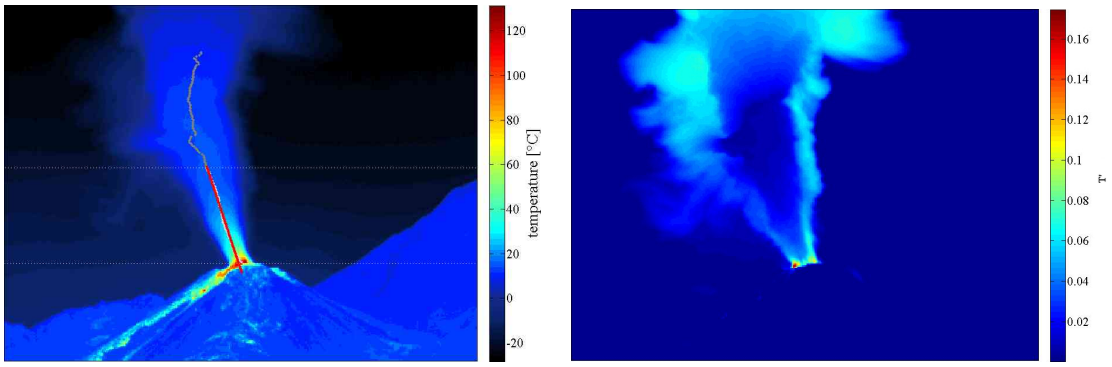

Figure 4.4.1: a) Averaged image computed from a set of thermal infrared images recorded with a FLIR camera, imaging the stationary emission of a sustained volcanic ash plume at Santiaguito. The red dots represent the extracted plume axis [201]. Temperature values along the plume axis are presented in Fig. 4.4.5. b) Relative fluctuation image computed from the same set of images, evidencing turbulence intensity and turbulent entrainment development.

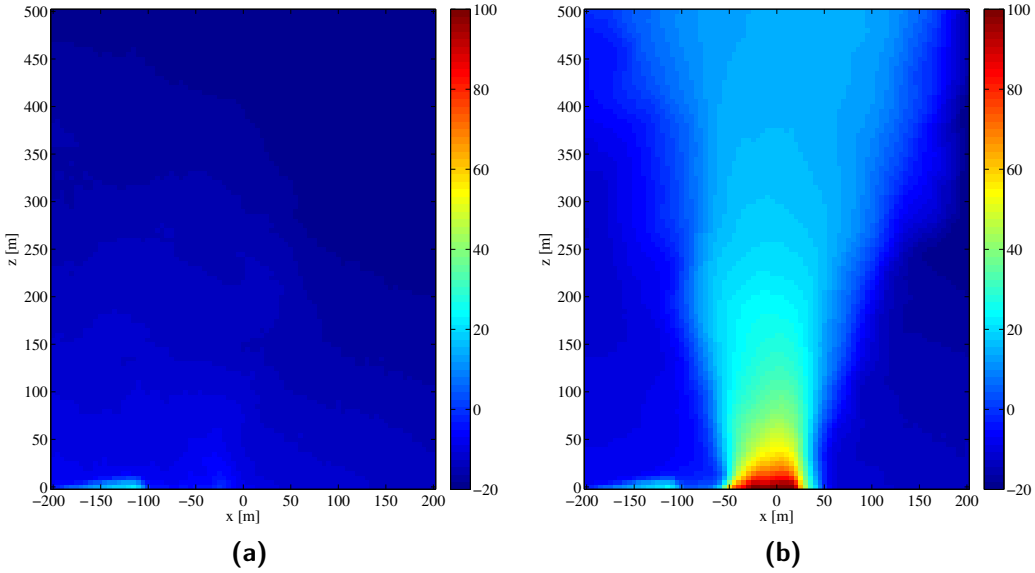

Figure 4.4.2: a) Image of the atmosphere above the volcano before the eruption. b) Averaged image of the volcanic eruption. In both images, horizontal and vertical axes represents the position in meters inside the image, the temperature is represented by the color scale in Celsius degrees.

Parameter	Units	Range	Value
v_q	–	0.5–0.8	0.659 ± 0.004
v_m	–	1.5–3.0	2.17 ± 0.04
ℓ_0	m	25–50	39.8 ± 0.2
ϕ	–	0.1–0.5	0.245 ± 0.002
$\chi \equiv -q_\chi/q_\psi$	–	0.1–1.0	0.55 ± 0.02
$q_\beta \equiv -q_\psi$	–	0.01–0.15	0.086 ± 0.003
A_β	m^2/kg	0.04–0.2	0.0903 ± 0.0007

Table 4.4.1: Result of the two-dimensional minimization procedure. Best fit values of the plume parameters. Here I obtained $\sigma(\boldsymbol{p}^*) = 6.428°$ C.

the correlation matrix is discussed in Sec. 4.4.5. That analysis allows to evaluate the sensitivity of the result on the input parameters and the error associated to the solution. For this test case I obtained $\sigma = 6.428°$ C.

4.4.4 Axial inversion

The second method is based on a one-dimensional fit of the thermal image along the plume axis. The plume axis is defined by a sequence of sampling points in the thermal image (Fig. 4.4.1a). By means of image rotation and dilation, the value of temperature along a selected region of the plume axis can be expressed as a function of the distance from the vent $T_E = T_E(z_j)$ (Fig. 4.4.5) .

Using only the axial points has the advantage that the background intensity is no longer important (because the plume is generally opaque along the axis) and I do not have to deal with problem of the plume edge (see the discussion below). However, the entrainment coefficient cannot be extracted using this procedure, so that I need a complementary analysis to evaluate its value. To do this, a preliminary estimate can be extracted from the 2D images the plume opening angle ($\frac{\mathrm{d}b}{\mathrm{d}z}$), by defining a threshold in the temperature image [201]. In the buoyancy-dominated regime a constant entrainment coefficient can be assumed. This can be correlated with the plume aperture [138, 104] and Eq. (3.8.14) by:

$$k = \frac{5}{6}\frac{\mathrm{d}b}{\mathrm{d}z}\,. \tag{4.4.3}$$

Using this method for this eruption, $k = 0.24$ is obtained. Alternatively, the entrainment coefficient obtained from the two-dimensional fit can be used (Table 4.4.1): $k = v_q/2 \simeq 0.329$.

Subsequently, as for in the two-dimensional case, the synthetic temperature profile $T_L(z)$ is derived from I_λ by means of Eq.(4.2.1). Since κ is independently estimated, the residual function becomes

$$\sigma^2(\boldsymbol{p}) = \frac{\sum_{j=1}^{N}(T_E(z_j) - T_L(z_j;\boldsymbol{p}))^2}{N - N_p} \tag{4.4.4}$$

where now $\boldsymbol{p} = (v_m, \ell, \phi, q_\chi, q_\psi, A_\beta)$, $N_p = 6$ and N is the number sampling points along the plume axis. The result of the minimization of this new cost function is

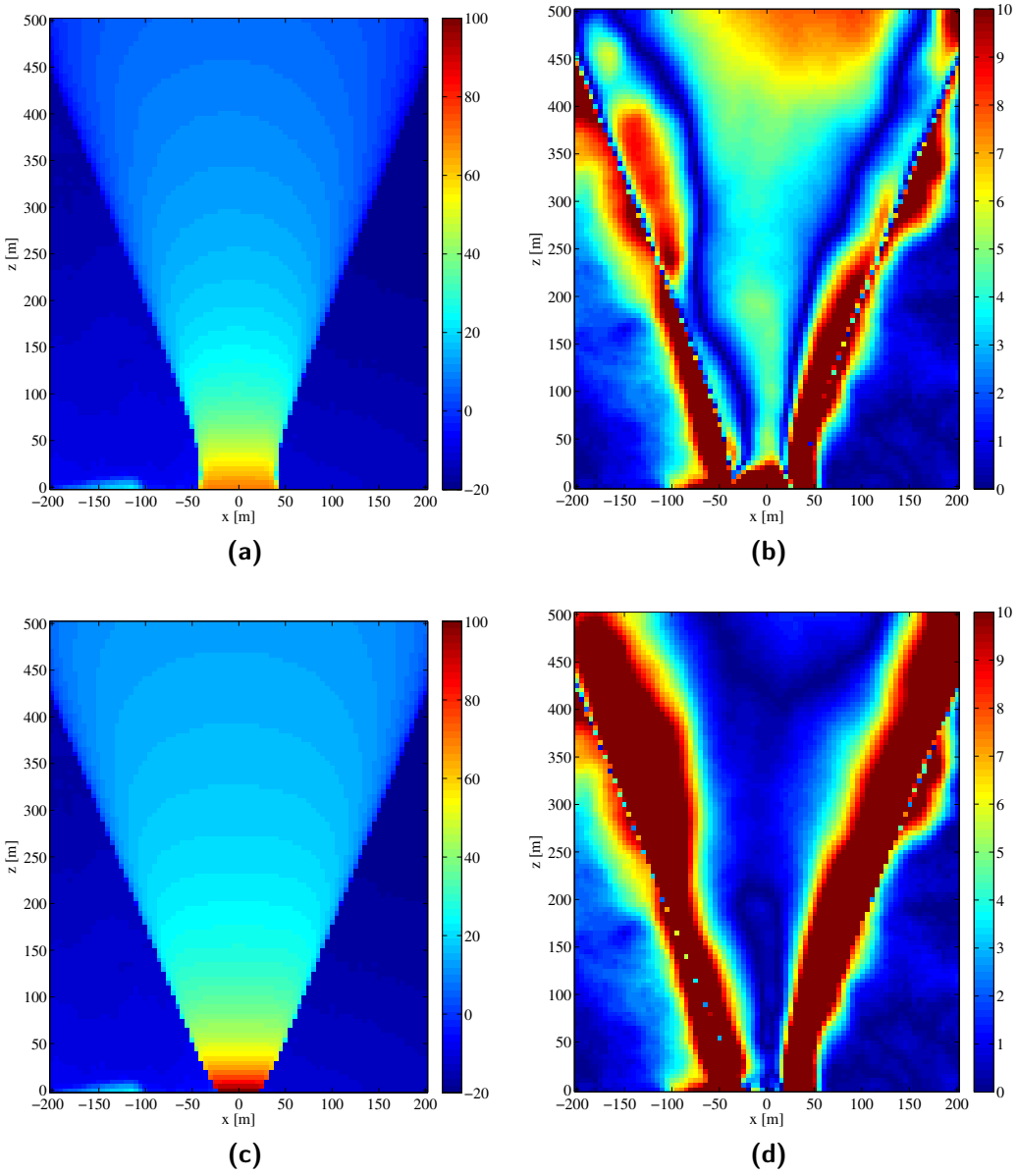

Figure 4.4.3: a,c) Synthetic image of the plume obtained by fitting the experimental data showed in Fig. 4.4.2b (a: two-dimensional fitting, c: axial fitting); b,d) Unsigned difference between the synthetic and the experimental images allowing error quantification and localization (b: two-dimensional fitting, d: axial fitting). In both images, horizontal and vertical axes represents the position (in meters) inside the image. The color scale represents the temperature in degrees Celsius.

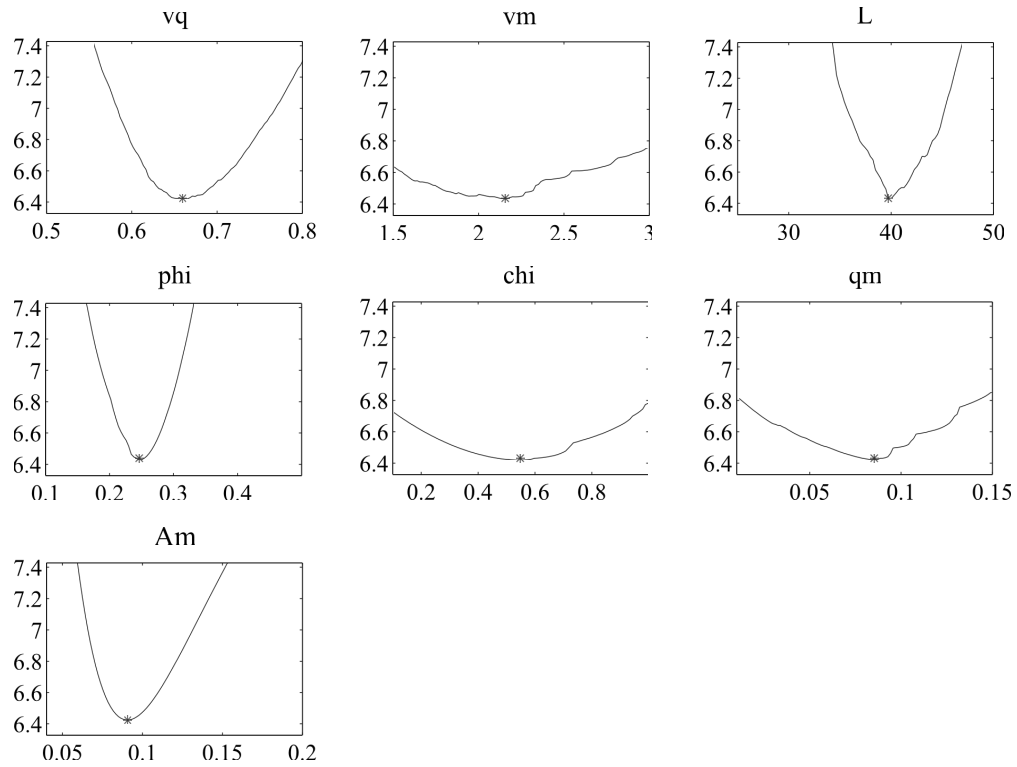

Figure 4.4.4: Two-dimensional inversion procedure. Variation of $\sigma(\boldsymbol{p})$ of Eq. (4.4.2) around p^* as a function of each single parameter, the others being kept fixed ($\boldsymbol{p} = (v_q, v_m, \ell_0, \phi, q_\chi, q_\psi, A_\beta)$). The fit was done using the parameter transformation $\chi \equiv -q_\chi/q_\psi$ and $q_\beta = -q_\psi$. Asterisks mark the value of each component of $\boldsymbol{p}^*$; here I obtained $\sigma(\boldsymbol{p}^*) = 6.428^\circ$ C.

displayed in Fig. 4.4.5 where the fitting function (solid line) is compared with the experimental thermal data (stars). The results of the minimization procedure are also reported in Table 4.4.2, together with the ranges of variability specified in the search procedure.

The corresponding 2D image, constructed by applying the top-hat profile to the one-dimensional plume model, and the difference between the optimal synthetic and the experimental images are displayed in panels c) and d) of Fig. 4.4.3.

In Fig. 4.4.6 I show the projection of $\sigma(\boldsymbol{p}^*)$ along each parameter axis, in the neighbours of the minimum. The error in this case is significantly reduced and all the parameters seem to be better constrained, as also indicated by the much lower value of σ, which, for this test case, is $\sigma = 0.6596^\circ$ C.

Finally, the plume input parameters (as obtained by the transformations (3.4.11) and (4.6.5)) are reported in Table 4.4.3. As a result of the inversion procedure, the eruption mass flow rate (in the stationary regime) can be constrained as $\dot{\mu} = \pi Q = \pi b_0^2 \beta_0 U_0$. To evaluate the total erupted mass μ, some assumption for the non-stationary part of the eruption is needed. For the analyzed eruption, the initial and final part of the emission are much shorter than the stationary one, thus (to the first order) it can be assumed a linear increase of the mass eruption rate between the eruption start and the time $t_{\rm init}$ at which the eruption is stationary. Analogously, a linear decrease of the mass eruption rate is assumed between the time $t_{\rm final}$ and the end of the eruption. Accordingly, $\mu = [\Delta t + (t_{\rm final} - t_{\rm init})] \times \pi Q/2$. In order to evaluate its error, in Table 4.4.3 I used an error on t equal to 10 s.

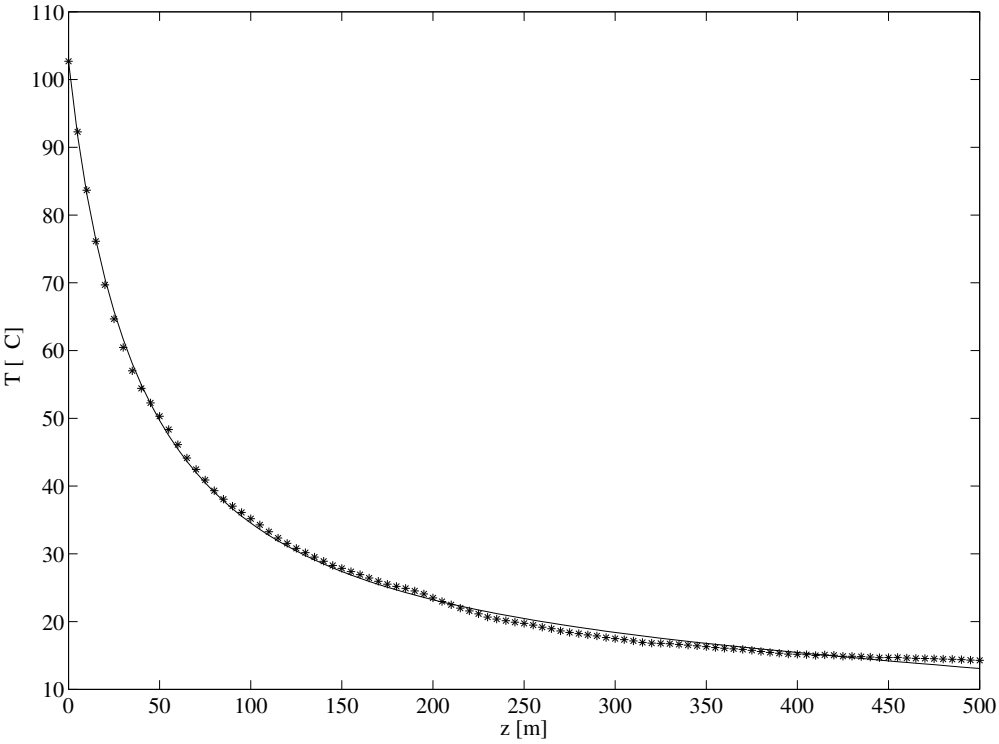

Figure 4.4.5: Result of the one-dimensional fit (solid line) of the experimental thermal image along the axis (stars).

4.4.5 Parameter error estimate

Because the coupled model dependency on input parameters is non-linear, it is difficult, in principle, to ensure that the result of the minimization procedure is unique. This is why the inversion must be done by preliminary constraining the ranges of possible outcomes (third column in tables 4.4.1 and 4.4.2). These can be constrained based on the experience of the operator and on the basis of complementary field observations. In the present application, I have explored also other ranges but only the minima represented in Figures 4.4.6 and 4.4.4 were found. These figures give a view of the multidimensional shape of the minimization function $\sigma(\boldsymbol{p})$, from which the point of minimum is clearly recognizable. The reason for this good behavior of the optimization procedure is that the brightness image is inverted

Parameter	Units	Range	Value
v_q	–	–	0.659 ± 0.004
v_m	–	0.1–0.5	0.34 ± 0.02
ℓ_0	m	10–40	23.8 ± 0.3
ϕ	–	0.1–1.0	0.579 ± 0.003
$\chi \equiv -q_\chi/q_\psi$	–	0.5–1.5	0.73 ± 0.01
$q_\beta \equiv -q_\psi$	–	0.1–0.5	0.29 ± 0.04
A_β	m^2/kg	0.1–1.0	0.215 ± 0.009

Table 4.4.2: Result of the axial minimization procedure. Best fit values of the plume Teen teenparameters. Here I obtained $\sigma(\boldsymbol{p}^*) = 0.6596°$ C.

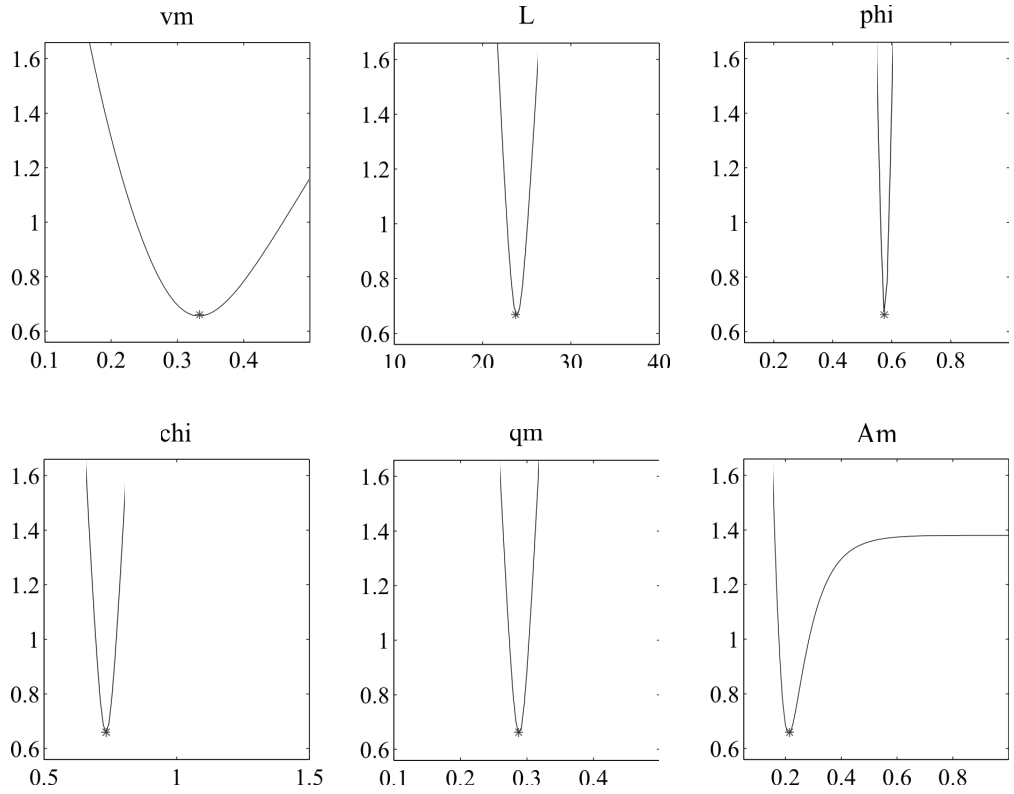

Figure 4.4.6: Axial inversion procedure. Variation of $\sigma(\boldsymbol{p})$ of Eq. (4.4.4) around $\boldsymbol{p}^*$ as a function of each single parameter, the others being kept fixed ($\boldsymbol{p} = (v_q, v_m, \ell_0, \phi, q_\chi, q_\psi, A_\beta)$). The fit was done using the parameter transformation $\chi \equiv -q_\chi/q_\psi$ and $q_\beta = -q_\psi$. Asterisks mark the value of each component of $\boldsymbol{p}^*$; here I obtained $\sigma(\boldsymbol{p}^*) = 0.6596°$ C.

"globally", not pixel by pixel independently. This global inversion procedure uses the constraints coming from the thermofluid dynamic model. To have multiple solutions, two different vent conditions giving the same brightness image must coexist, globally. This is an unlikely condition and here it is shown that – at least for the analyzed plume – this is not the case. Even if part of the plume turns out to be opaque. In Fig. 4.4.7 the contour plot based on the value of the total optical depth τ_L is shown, to give a quantitative measure of the opaqueness of the synthetic plume.

I now analyse the correlation matrix of the minima displayed in Fig. 4.4.4 and 4.4.6. In order to give a quantitative estimation of the standard error of all the parameters, once is found a vector $\boldsymbol{p}^*$ such that $\sigma(\boldsymbol{p}^*)$ is the minimum, I assume that the model can be linearised around that $\boldsymbol{p}^*$. In other words, naming $T_i(\boldsymbol{p})$ the vector of all the measurements, I assume that its derivative does not depend on the parameters: $\partial_{p_k} T_i = Z_{i,k}$. In such a way, as usually done in regression analysis [6], it is possible to formally evaluate all the fit unknowns. In particular, by using Eq. (4.4.2) with $T_L(x_i, y_j) = T_l$ (for $i = 1, \ldots, N$; $j = 1, \ldots, M$; and $l = 1, \ldots, N * M$) I find $(Z^T Z)_{i,j} = (N * M - N_p)\, \sigma(\boldsymbol{p}^*)\, \partial_{i,j}\sigma$ (for $i, j = 1, \ldots, N_p$). It is worth noting that $\partial_{i,j}\sigma$ is calculated by fitting the surface $\sigma = \sigma(\boldsymbol{p})$ with a second order polynomial.

By using the classical formula for the standard error of the parameters, $\mathrm{se}(\boldsymbol{p}_i) = \sigma(\boldsymbol{p}^*) \sqrt{(Z^T Z)^{-1}_{i,i}}$ and by means of error propagation, the confidence inter-

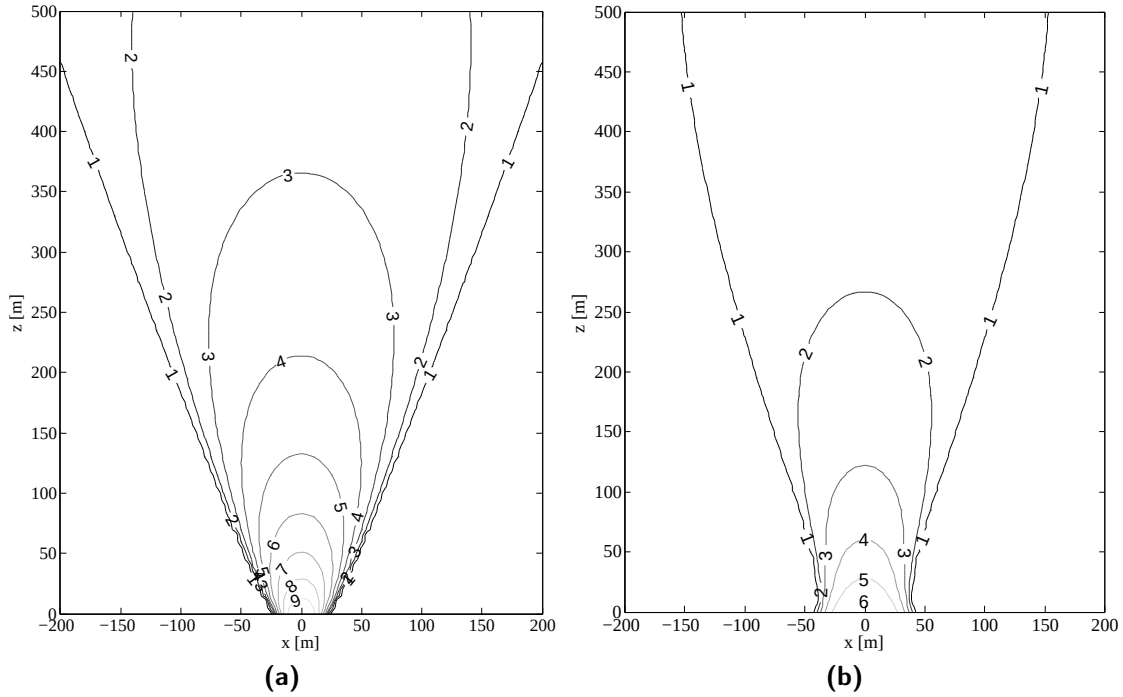

Figure 4.4.7: Contour plot of the optical depth τ_L (see below Eq. (4.2.4)) of the synthetic plume obtained from a) axial fitting; b) two-dimensional fitting. The synthetic plume obtained from axial inversion is more opaque than the plume obtained from two-dimensional inversion.

val of all the parameters involved in both the axial and two-dimensional fit were found (reported in Tables 4.4.1, 4.4.2 and 4.4.3).

4.5 Discussion

Comparison of the synthetic images obtained from two-dimensional (2D) image fitting (panels a) and b) of Fig. 4.4.3) and axial (1D) fitting (panels c) and d) of Fig. 4.4.3) with the experimental averaged image (Fig. 4.4.2b), shows that both inversion procedures have their maximum error along the plume boundaries. This is due to the a-priori assumption of a purely top-hat self-similar profile. This assumption is accurate enough to describe the one-dimensional plume dynamics but is not accurate near the plume margins, where a Gaussian distribution better describes the actual profile. This error is augmented in the coupled model by the fact that 1) the IR absorption depends on the density distribution, so that the top-hat model overestimates the optical thickness near the plume margins and 2) the top-hat model predicts a higher temperature on the plume margins, with respect to the Gaussian distribution. As a consequence, both effects produce a synthetic image displaying higher temperature at the margins. To minimize this error, the 2D inversion procedure (which considers all pixels) underestimates the axial temperature (and the density) to try to balance the overestimates on the margins. In particular, at $z = 0$ the error is larger because of the larger temperature contrast at this location. This argument justifies the lower values of temperature and mass flow rate reported in Table 4.4.3 for the 2D fit with respect to 1D.

Parameter	Units	Axial fit	2D fit
γ	–	0.862 ± 0.1	0.543 ± 0.04
b_0	m	23 ± 1	41.5 ± 0.3
Q_0	10^3 kg/s	4.1 ± 0.5	6.9 ± 0.3
M_0	10^4 kg m/s^2	3.1 ± 0.7	3.1 ± 0.2
U_0	m/s	7.5 ± 0.9	4.5 ± 0.2
T_0	$^\circ$ C	103 ± 3	69.4 ± 0.3
Y_{air}	wt.%	40 ± 6	85 ± 6
Y_{w}	wt.%	20 ± 3	4.2 ± 0.3
Y_{s}	wt.%	41 ± 6	11.1 ± 0.7
d_{S}	mm	2.3 ± 0.8	1.3 ± 0.2
$\dot{\mu}_{\text{w}}$	10^3 kg/s	2.5 ± 0.7	0.9 ± 0.1
$\dot{\mu}_{\text{s}}$	10^3 kg/s	5 ± 1	2.4 ± 0.3
μ_{w}	10^5 kg	6 ± 2	2.3 ± 0.4
μ_{s}	10^5 kg	13 ± 3	6 ± 1

Table 4.4.3: Result of the axial and two-dimensional minimization procedure: physical input parameters for the coupled model. μ_{w} and μ_{s} are the total erupted water vapor and solid masses.

The problem associated with the top-hat assumption is reduced fitting only the axial values, because the integral of the absorption coefficient (i.e. the optical thickness) takes into account the whole density and temperature distribution across the plume. Therefore, the error is significantly lower in a wide region around the axis, whereas larger errors are concentrated near the margins. The better accuracy of the axial fitting procedure is confirmed by the observation that the error σ is comparable to the instrumental accuracy, which is about 0.5° C. In the two-dimensional case, the value of σ corroborates the conclusion that the model is not fully suited to represent the two-dimensional shape of the plume image.

The top-hat assumption is thus more satisfactory when axial inversion is performed; a more accurate description of the plume profile is required to fully invert the two-dimensional image. While assuming a Gaussian profile would be conceptually equivalent to the adopted top-hat hypothesis, the inversion would be computationally more intense, because the coupled model cannot be written analytically. The above observations also allow to assert that the electromagnetic model is accurate enough to represent the IR emission/absorption balance throughout the plume and the error is mainly associated to application of the oversimplified fluid-dynamic model.

Despite these differences, the results of the two procedures are coherent and indicate a mass eruption rate of 7.75×10^3 kg/s in 1D and 3.31×10^3 kg/s in 2D. The observed ash plume has a gas content at $z = 0$ of 59 wt.% in 1D and 89 wt.% in 2D. It is worth recalling here that $z = 0$ does not correspond to the actual vent level but instead to the minimum quota of the analysed thermal image.

At $z = 0$ the amount of entrained air is already significant (40 wt. % in 1D and 85 wt.% in 2D). The high air entrainment recorded here is no doubt a result of emission from a circular vent structure [12, 165]. Both studies record main ash

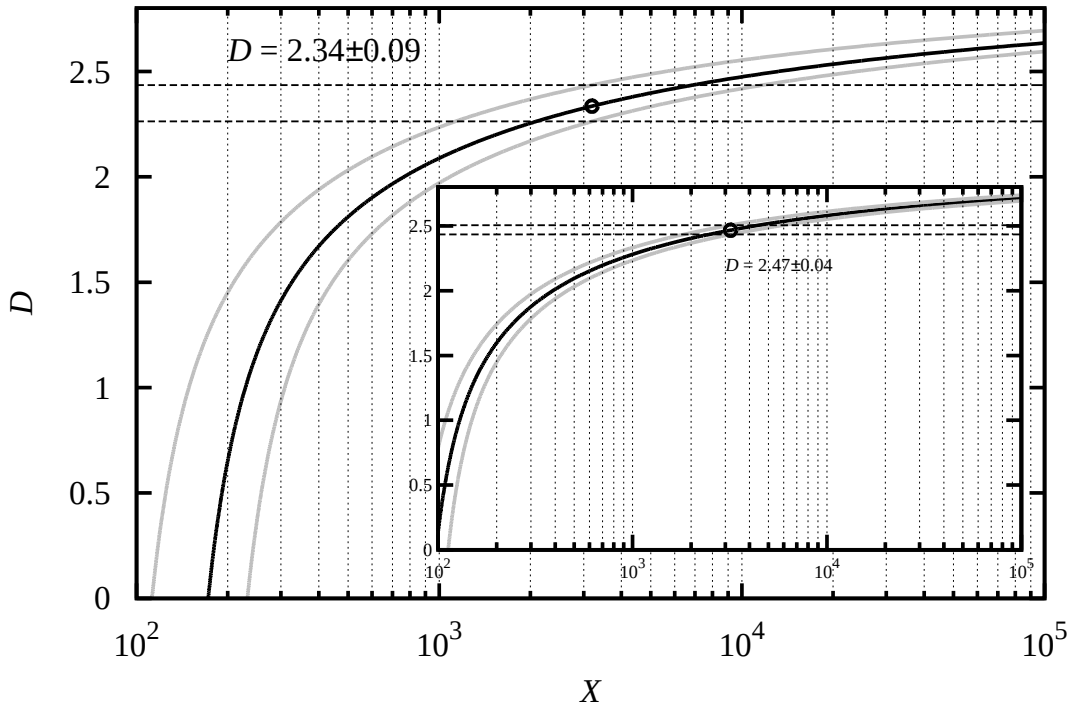

Figure 4.5.1: Function $D(X)$ plotted by fixing d_S/d_{min} in Eq. (4.6.3). The big panel refers to the axial fit Sauter diameter while the small panel has been obtained by using the Sauter diameter from the 2D fit. In each panel, solid black line is associated to the measured Sauter diameter, while solid grey lines corresponds to the error limits. Dashed lines represent the error limits for the selected value of $X = d_{max}/d_{min} = 3.2 * 10^3$.

emission being from sources located around the edge of the roughly circular vent located atop the Caliente dome. This means that the center of the plume at the vent is essentially "hollow", so that air becomes entrapped within the "empty" center of the emission, thereby increasing the amount of air ingestion over cases where enters only across the plume outer surface. This is also responsible for the high entrainment coefficient found ($\varkappa = 0.329$) and for the rapid lowering of the mixture temperature (about 100° C in 1D and 70° C in 2D). The mass fraction of erupted gas, with respect to the total erupted mass, is in any case fairly high (32 wt. % in 1D and 27 wt. % in 2D), so that the plume is dominated by heated air, with a very minor dense ash component, enhancing the buoyancy and explaining why an explosion of such low violence (mean at-vent velocities being just 25 m/s) can ascend to heights of between 2 and 4 km above the vent. I finally notice that the Morton length scale ℓ_M (which characterizes the transition between jet and plume stage) is in this case about 19 m. The transition to buoyancy-dominated plume should be between L_M and $5L_M$, so below about 100 m, which may justify the expression of the entrainment coefficient given in Eq. (4.4.3).

The estimated Sauter diameter is also comparable in the two procedures. To compare the reported values with field observations, I firstly assume a log-normal particle distribution with a 1 standard deviation maximum diameter $\bar{d}+\sigma_d = 950\,\mu$m (based on what was found by Wilson and Self [218] from insitu plume sampling). By using the expression for the mean value $\bar{d}$, the standard deviation σ_d and the mean Sauter diameter (see Sect. 4.6.1 and Eq. (4.6.1)), I find $\bar{d} = 447\,\mu$m, $\sigma_d = 503\,\mu$m (or in phi-units $\mu_{gsd} = 1.754$ and $\sigma_{gsd} = 1.306$) for the axial fit and $\bar{d} = 547\,\mu$m,

$\sigma_d = 403\,\mu$m (or in phi-units $\mu_{\rm gsd} = 1.181$ and $\sigma_{\rm gsd} = 0.949$) for the two-dimensional fit.

Even if the log-normal is the grain size distribution most often assumed in volcanological studies, physical arguments support the hypothesis of power-law distribution for fragmented materials [87]. Assuming a power-law particle distribution (see Sect. 4.6.1) I need to obtain three parameters, namely D, $d_{\rm min}$ and $d_{\rm max}$. At Santiaguito, grain-size distribution is poorly known [171]. $d_{\rm min}$ can be constrained by insitu plume sampling on filters from aircraft [163], where particles smaller than $25\,\mu$m were measured. Setting $d_{\rm min} = 10\,\mu$m in Eq. (4.6.3) I find that resulting D depends weakly on $X = d_{\rm max}/d_{\rm min}$ if X it is large enough (see Fig. 4.5.1). Assuming $d_{\rm max} = 32\,$mm I obtain $D = 2.34 \pm 0.09$ (axial fit) and $D = 2.47 \pm 0.04$ (two-dimensional fit). This low value of D is in accord with the low fragmentation efficiency of the analysed volcanic eruption.

4.5.1 Plume color and visibility

It is worth noting that there are some wavelengths in the visible spectral window ($\lambda < 780\,\mu$m) where the absorption coefficient of atmospheric water vapor at standard density reaches 0.1 m^{-1}, comparable with $A_{\rm w}$ in the IR wavelength window considered in this chapter. Moreover, the specific absorption of the ash particles is also of the same order of magnitude, $A_{\rm s} \simeq 0.1\,{\rm m}^2/{\rm kg}$, because the assumption $d \gg \lambda$ is even more satisfied in the visible waveband. Therefore, it can be roughly said that 1) a high-temperature water-ash plume can be "viewed" by a thermal camera in the 8-14 μm waveband if one can see it with his own eyes 2) a high-temperature water-ash plume that is opaque to the eyes is also opaque to the thermal camera 3) the plume optical thickness will be dominated by the water if $n_{\rm w} \gg Y_{\rm s}$ or by the particles if $Y_{\rm w} \ll Y_{\rm s}$. As suggested by intuition, in the former case one will see a "white" plume, in the latter a "black" plume. Obliviously, in intermediate conditions a lighter or darker gray would be seen. Now, looking at eruptions that occurred at Santiaguito, the plume often appears quite light in tone. This observation supports the argument that the erupted mixture has a high concentration of water.

4.5.2 General applicability of the model

The developed method is general and, in principle, can be applied with any fluid-dynamic model of the plume, either integral or multidimensional, stationary or time-dependent, single or multiphase, potentially including phenomena such as aggregation and particle fallout (discussion in Sect. 3.2.2).

The algorithm could also be easily applied to a more complex geometric configuration [e.g., by introducing an additional entrainment coefficient for a bent plume in a wind field – 223] and atmospheric conditions (e.g., in presence of a significant amount of water vapor), or to more realistic plume models (e.g., assuming a Gaussian plume profile). In such cases, the analytical solution cannot be applied and the coupled model should be solved numerically. It is worth noting that the calibration of the background atmospheric infrared intensity and the information on the atmospheric absorption can be critical in the applications. Thus, experimentalists are

recommended to consider their effects during the acquisition campaigns. Also, the intensity image would be preferable with respect to the temperature image, which is derived from automatic onboard processing by commercial thermal cameras. Furthermore, a narrower waveband is preferable [although the noise-to-signal ratio can be an issue – 154] since the assumption of a weak dependency of the Planck's function on the wavelength (Sect. 4.2) is more justified.

I have not yet tested the method on other explosive events. The discussed test case has been chosen to demonstrate the methodology because it was suited for the image treatment (see below). However, the method is generally applicable to any explosive eruption generating convective plumes (with any proportion of gas and solid) if the following conditions are satisfied: 1) possibility of identifying a temporal windows of stationary regime (fluctuations associated to turbulence, not to variable vent conditions – Fig. 4.4.1b); 2) known atmospheric pressure, temperature, humidity; 3) relatively small distance from the source (< 10 km) and low humidity; 4) knowledge of the spectral response of the camera.

Furthermore, some additional information (if available) can be useful to put further constraints to the choice of the parameter range for the minimization procedure and for obtaining additional parameters (e.g., the parameter characterizing the grain size distribution): 1) maximum plume height; 2) vent radius; 3) exit velocity; 4) proportion of magmatic gas species; 5) maximum (non-ballistic) particle size in the plume.

Despite the non-linearity of the entire system, the minimization procedure appears to be robust (i.e., in the explored parameter range, a unique minimum is found, allowing the quantification of the related errors) and allows the retrieval of the plume vent conditions, namely the vent radius b_0, velocity U_0, temperature T_0, gas mass ratio Y_0, entrainment coefficient $\varkappa$ and the equivalent Sauter diameter d_S of the particle size distribution.

Despite these satisfactory results, it is worth noting that a rigorous validation of the direct model (i.e., the generation of the synthetic image) must still be achieved. Unfortunately, I could not find detailed experimental measurements of the TIR radiation from a turbulent gas–particle plume under controlled injection conditions. This would be extremely useful to calibrate the coupled forward model and to better understand plume visibility issues.

The method developed here to recover ash plume properties is fast and robust. This suggests its potential applications for monitoring other active explosive volcanoes and for real-time estimation of ash mass flux and particle size distribution, which are crucial parameters for model-based projections and simulations. By streaming infrared data to a webtool running, in real-time, the model could provide the input parameters required for ash dispersion models run by VAACs.

4.6 Appendices

4.6.1 Sauter diameter of grain size distributions

I here estimate the mean Sauter diameter in the case of a log-normal and power-low grain size distributions.

It is common in volcanology to assume that the grain size distribution is Gaussian in $\phi_{\rm gsd} = -\log_2(d)$ units, with mean $\mu_{\rm gsd}$ and standard deviation $\sigma_{\rm gsd}$ (i.e., diameters obey a log-normal distribution). In such a case, the normalized particle distribution (in millimetres) can be written:

$$f(x;\mu,\sigma_{\rm gsd}) = \frac{1}{x\ln(2)\sigma_{\rm gsd}\sqrt{2\pi}} e^{-\frac{(\log_2(x)+\mu_{\rm gsd})^2}{2\sigma^2_{\rm gsd}}}$$

and the Sauter mean diameter can be computed analytically as

$$d_{\rm S} = 2^{-\mu_{\rm gsd}+\frac{5}{2}\log(2)\sigma^2_{\rm gsd}}\,. \tag{4.6.1}$$

This means that the mean particle diameter "seen" by the TIR sensor is always larger than the mean diameter $\bar{d} = 2^{-\mu_{\rm gsd}+\frac{1}{2}\log(2)\sigma^2_{\rm gsd}}$. It is useful to recall that the standard deviation for the particle diameter log-normally distributed is $\sigma_d = \bar{d}\sqrt{2^{\log(2)\sigma^2_{\rm gsd}}-1}$.

On the other hand, the normalized power-law distribution can be written as follows:

$$f(x;\,D) = \frac{D}{1-X^{-D}}\,x^{-D-1}\,, \tag{4.6.2}$$

where D is the power-law exponent and x is the fragment diameter normalized with the finest diameter $d_{\rm min}$ and X is the maximum value of x, so that the cumulative function (i.e., the fraction of the total number of particles with diameter larger than $x\,d_{\rm min}$ and finer than $d_{\rm max} = X d_{\rm min}$) takes the form:

$$F(x;\,D) = \int_x^X f(x';\,D)\,{\rm d}x' = \frac{x^{-D}-X^{-D}}{1-X^{-D}}$$

with the right normalization: $F(1;\,D) = 1$. Using this distribution I get the following result for the Sauter and the mean diameter:

$$d_{\rm S} = \frac{2(D-2)}{D-3}\frac{X^{D-3}-1}{X^{D-2}-1}\,d_{\rm max} \tag{4.6.3}$$

$$\bar{d} = \frac{2D}{D-1}\frac{X^{D-1}-1}{X^{D}-1}\,d_{\rm max}\,. \tag{4.6.4}$$

As for the log-normal distribution, the mean Sauter diameter is always larger than the mean diameter.

4.6.2 Inversion of the absorption coefficient and retrieval of the Sauter diameter

The solution of the plume model Sect. 3.10 in non-dimensional form is function of the boundary values and model parameters, $(v_q, v_m, q_\chi, q_\psi, \phi, \ell_0)$. The inversion

procedure described in Sect. 4.4 provides the set of parameters which minimizes the difference between the synthetic and the experimental image. In Eqs. (3.4.11) I have given the transformation needed to retrieve the equivalent set of eruption parameters.

The composition of the eruptive mixture can be reconstructed by using Eqs. (3.4.11l), (3.4.11m) and (3.4.11n) to retrieve $Y_{\rm w}$, $Y_{\rm s}$, and Y_α. In this chapter, I have assumed that the erupted gas is composed mainly of water vapor (subscript w), so that the effect of the other gas component could be disregarded at the dynamic level (I should consider them at the optical level, see below). The system can be solved to obtain the mass fractions of ash, volcanic gas and atmospheric gas at $z = 0$. Note that, in general, the gas mass fraction in the mixture at $z = 0$ is $Y_0 = Y_{\rm w} + Y_\alpha$. Since the quota $z = 0$ may not correspond to the vent quota (it is better defined as the quota where the plume starts to be self-similar and stationary), Y_0 in general does not correspond to the gas content in the eruptive mixture but may also contain the fraction Y_α of entrained air.

Finally, the equivalent Sauter diameter of the grain size distribution can be derived by the absorption coefficient A_β by assuming that the absorption by atmospheric air is negligible. Moreover, I here notice that in the above derivation the thermodynamic influence of other gas species is disregarded (e.g., carbon and sulfur dioxides) because generally, in explosive volcanic eruptions, their mass fraction is negligible (less than 1 wt%). However, to compute the optical properties of the mixture, their presence must be taken into account because, as noticed in Figure 4.2.2, their specific absorption coefficient is more than one order of magnitude larger than that of water for the used detector.

In such case, the mixture specific absorption coefficient defined in Eq. (4.3.2) should be written as:

$$\begin{aligned} A_\beta &= A_{\rm s}Y_{\rm s} + A_{\rm w}Y_{\rm w} + A_{\rm SO_2}Y_{\rm SO_2} + A_{\rm CO_2}Y_{\rm CO_2} = \\ &= A_{\rm s}Y_{\rm s} + Y_{\rm w}(A_{\rm w} + A_{\rm SO_2}\kappa_{\rm SO_2} + A_{\rm CO_2}\kappa_{\rm CO_2}) = A_{\rm s}Y_{\rm s} + A_{\rm e}Y_{\rm w}\,, \end{aligned} \quad (4.6.5)$$

where I have used the mass conservation of water, SO_2 and CO_2: $q_i = Y_i, \quad i =$ w, SO_2, CO_2 and the following definitions: $\kappa_{\rm SO_2} \equiv Y_{\rm SO_2}/Y_{\rm w}$, $\kappa_{\rm CO_2} \equiv Y_{\rm CO_2}/Y_{\rm w}$ and $A_{\rm e} = A_{\rm w} + A_{\rm SO_2}\kappa_{\rm SO_2} + A_{\rm CO_2}\kappa_{\rm CO_2}$. Therefore, knowing the specific absorption coefficients and the components mass fraction, the specific absorption coefficient for particles $A_{\rm s}$ can be derived from this expression. By noting that $A_{\rm s} = \dfrac{3}{2d_{\rm S}\hat{\rho}_{\rm s}}$, this can be used to estimate $d_{\rm S}$ (cf. Eq. (4.2.7)).

In this chapter I use $\hat{\rho}_{\rm s} = 1600$ kg/m^3 and I assume average values of magmatic composition for Santiaguito dacitic magmas in order to get gas solubility in the magmatic chamber at 3300 MPa and 950° C [173, 146, 179]. Using these values I obtain $\kappa_{\rm CO_2} = 0.02$ and $\kappa_{\rm SO_2} = 0.004$. From this result and the weight-averaged values of the absorption coefficient reported in Fig. 4.2.2, I obtain $A_{\rm e} = 0.2532\,{\rm m}^2/{\rm kg}$.

Chapter 5

ASHEE numerical model: verification and validation study

In the first part of this chapter the discretization strategy behind the ASHEE model is discussed. Then, a wide set of numerical tests are performed to assess the adequacy of ASHEE for the intended volcanological application and the reliability of the numerical solution method. This section is based on Cerminara et al. [31]. Validation tests are focused on: 1) the dynamics of gas (Sect. 5.2) and multiphase (Sect. 5.3) turbulence; 2) natural convection (Sect. 5.4); 3) turbulent buoyant plumes (Sect. 5.5); 4) turbulent mixing (Sect. 5.7). Compressibility likely exerts a controlling role to the near-vent dynamics during explosive eruptions [e.g., 28]. I briefly discuss in Sect. 5.6 the performance of the model on a standard one-dimensional shock wave numerical test.

5.1 The ASHEE numerical code

The [eqEu] model described in section 1.3 and filtered in section 1.4, is solved numerically to obtain a time-dependent description of all independent flow fields in a three-dimensional domain with prescribed initial and boundary conditions. I have chosen to adopt an open-source approach to the code development in order to guarantee control on the numerical solution procedure and to share scientific knowledge. I hope that this will help building a wider computational volcanology community. As a platform for developing the ASHEE solver, I have chosen the unstructured, finite volume (FV) method based open source C++ library OpenFOAM® (version 2.1.1). OpenFOAM® , released under the Gnu Public License (GPL), has gained a vast popularity during the recent years. The readily existing solvers and tutorials provide a quick start to using the code also to inexperienced users. Thanks to a high level of abstraction in the programming of the source code, the existing solvers can be freely and easily modified in order to create new solvers (e.g., to solve a different set of equations) and/or to implement new numerical schemes. OpenFOAM® is well integrated with advanced tools for pre-processing (including meshing) and post-processing (including visualization). The support of the OpenCFD Ltd, of the OpenFOAM® foundation and of a wide developers and users community guarantees ease of implementation, maintenance

and extension, suited for satisfying the needs of both volcanology researchers and of potential users, e.g. in volcano observatories. Finally, all solvers can be run in parallel on distributed memory architectures, which makes OpenFOAM® suited for envisaging large-scale, three-dimensional volcanological problems.

The new computational model, called `ASHEE` (ASH Equilibrium Eulerian model) is documented in the VMSG (Volcano Modeling and Simulation Gateway) at Istituto Nazionale di Geofisica e Vulcanologia (http://vmsg.pi.ingv.it) and is made available through the VHub portal (https://vhub.org).

5.1.1 Finite Volume discretization strategy

In the FV method [75], the governing partial differential equations are integrated over a computational cell, and the Gauss theorem is applied to convert the volume integrals into surface integrals, involving surface fluxes. Reconstruction of scalar and vector fields (which are defined in the cell centroid) on the cell interface is a key step in the FV method, controlling both the accuracy and the stability properties of the numerical method.

OpenFOAM® implements a wide choice of discretization schemes. In all the presented test cases, the temporal discretization is based on the second-order Crank-Nicolson scheme [75], with a blending factor of 0.5 (0 meaning a first-order Euler scheme, 1 a second-order, bounded implicit scheme) and an adaptive time stepping based on the maximum initial residual of the previous time step [112], and on a threshold that depends on the Courant number ($\mathrm{Co} < 0.2$). All advection terms of the model are treated implicitly to enforce stability. Diffusion terms are also discretized implicit in time, with the exception of those representing subgrid turbulence (see section 1.4). The pressure, gravity and the relative velocity $\boldsymbol{v}_j$ terms in the momentum equations and the continuity equations are solved explicitly. However, as discussed below, the PISO (Pressure Implicit with Splitting of Operators, Issa [105]) solution procedure based on a pressure correction algorithm makes such a coupling implicit. Similarly, the pressure advection terms in the enthalpy equation and the LES subgrid-scale terms are made implicit when the PIMPLE (mixed SIMPLE and PISO algorithm, Ferziger and Perić [75]) procedure is adopted. The same PIMPLE scheme is applied treating all source terms and the additional terms deriving from the equilibrium–Eulerian expansion.

In all described test cases, the spatial gradients are discretized by adopting an unlimited centered linear scheme [which is second-order accurate and has low *numerical diffusion* – 75]. Analogously, implicit advective fluxes at the control volume interfaces are reconstructed by using a centered linear interpolation scheme (also second order accurate). The only exception is for pressure fluxes in the pressure correction equation, for which I adopt a TVD (Total Variation Diminishing) limited linear scheme (in the subsonic regimes) to enforce stability and non-oscillatory behavior of the solution. This choice demonstrated to be a good compromise between stability and accuracy for compressible 3D turbulence in `ASHEE` [see 32]. I will refer to this second order discretization as [linear]. In two-dimensional turbulent simulations I use the TVD limited scheme also for the advective fluxes; I refer to this configuration with [limLin]. In the following sections, I have also used a forth order scheme, based on cubic algorithm. I refer to this scheme as [cubic]. To

enforce stability, the PISO loop in OpenFOAM® usually has incorporated a term of artificial diffusion for the advection term $\nabla \cdot (\rho \boldsymbol{u} \otimes \boldsymbol{u})$. As studied and suggested in Vuorinen et al. [212], I avoid to use this extra term which is not present in the original PISO implementation. I refer to Jasak [106] for a complete description of the discretization strategy adopted in OpenFOAM® .

5.1.2 Solution procedure

Instead of solving the set of algebraic equations deriving from the discretization procedure as a whole, most of the existing solvers in OpenFOAM® are based on a segregated solution strategy, in which partial differential equations are solved sequentially and their coupling is resolved by iterating the solution procedure. In particular, for Eulerian fluid equations, momentum and continuity equation (coupled through the pressure gradient term and the gas equation of state) are solved by adopting the PISO algorithm [105]. The PISO algorithm consists of one predictor step, where an intermediate velocity field is solved using pressure from the previous time-step, and of a number of PISO corrector steps, where intermediate and final velocity and pressure fields are obtained iteratively. The number of corrector steps used affects the solution accuracy and usually at least two steps are used. Additionally, coupling of the energy (or enthalpy) equation can be achieved in OpenFOAM® through additional PIMPLE iterations [which derives from the SIMPLE algorithm by 148]. For each transport equation, the linearized system deriving from the implicit treatment of the advection-diffusion terms is solved by using the PbiCG solver (Preconditioned bi-Conjugate Gradient solver for asymmetric matrices) and the PCG (Preconditioned Conjugate Gradient solver for symmetric matrices), respectively, preconditioned by a Diagonal Incomplete Lower Upper decomposition (DILU) and a Diagonal Incomplete Cholesky (DIC) decomposition. The segregated system is iteratively solved until a global tolerance threshold ϵ_{PIMPLE} is achieved. In numerical simulations, I typically use $\epsilon_{\text{PIMPLE}} < 10^{-7}$ for this threshold.

The numerical solution algorithm is designed as follows:

1. Solve the (explicit) continuity equation (1.4.9a) for mixture density $\bar{\rho}_{\text{m}}$ (predictor stage: uses fluxes from previous iteration).

2. Solve the (implicit) transport equation for all gaseous and particulate mass fractions, Eqs. (1.4.9b), (1.4.9c): $\tilde{y}_i, \quad i = 1, ..., I$ and $\tilde{y}_j, \quad j = 1, ..., J$.

3. Solve the (semi-implicit) momentum equation Eq. (1.4.9d), to obtain $\tilde{\boldsymbol{u}}_{\text{m}}$ (predictor stage: uses the pressure field from previous iteration).

4. Solve the (semi-implicit) enthalpy equation Eq. (1.4.9e) to update the temperature field $\tilde{T}$, the compressibility $\psi_{\text{m}} = \bar{\rho}_{\text{m}}/\bar{p}$ (see Eq. (1.1.20), pressure from previous iteration), and transport coefficients.

5. Solve the (implicit) pressure equation (see Eq. (1.4.9a)) and the relative velocities $\boldsymbol{v_j}$ (cf. (1.4.5)) to update the fluxes $\rho \boldsymbol{u}$:

$$\partial_t(\psi_{\text{m}}\,\bar{p}) + \nabla \cdot (\psi_{\text{m}} \tilde{\boldsymbol{u}}_{\text{m}}\,\bar{p}) = \tilde{S}_{\text{m}} \tag{5.1.1}$$

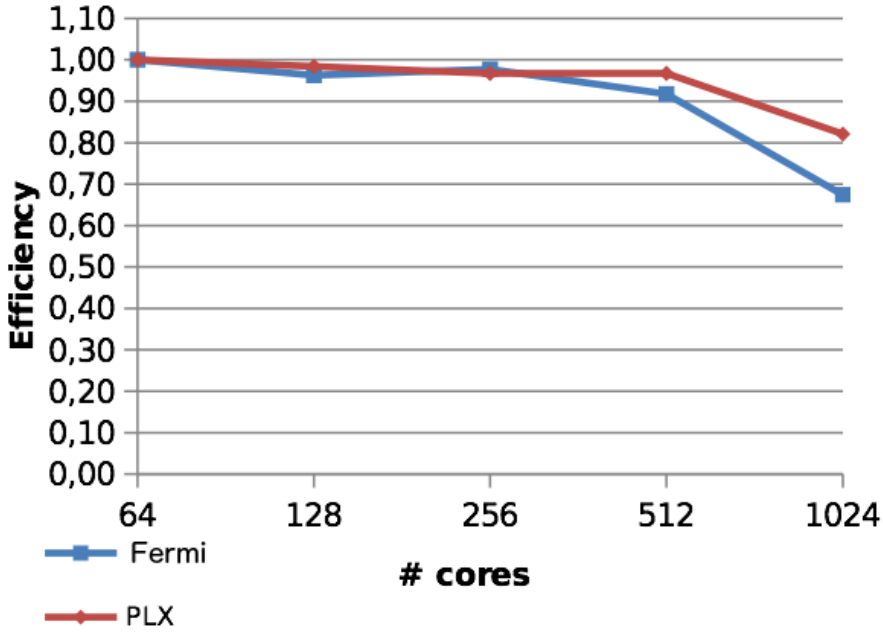

Figure 5.1.1: `ASHEE` parallel efficiency on Fermi and PLX supercomputers at CINECA (`www.cineca.it`).

6. Correct density, velocity with the new pressure field (keeping $\tilde{T}$ and ψ_{m} fixed).
7. Iterate from 5 evaluating the continuity error as the difference between the kinematic and thermodynamic calculation of the density (PISO loop).
8. Compute LES subgrid terms to update subgrid transport coefficients.
9. Evaluate the numerical error $\epsilon_{\mathrm{PIMPLE}}$ and iterate from 2 if prescribed (PIMPLE loop).

With respect to the standard solvers implemented in OpenFOAM® (v2.1.1) for compressible fluid flows (e.g. `sonicFoam` or `rhoPimpleFoam`), the main modification required are the following:

1. The mixture density and velocity replaces the fluid ones.
2. A new scalar transport equation is introduced for the mass fraction of each particulate and gas species.
3. The equations of state are modified as described in Eqs.(1.1.20).
4. First-order terms from the equilibrium–Eulerian model are added in the mass, momentum and enthalpy equations.
5. Equations are added to compute flow acceleration and velocity disequilibrium.
6. Gravity terms and ambient fluid stratification are added.
7. New SGS models are implemented.

Concerning point 5, it is worth remarking that, accordingly to Ferry et al. [74], the first-order term in τ_j in Eq.(1.3.22) must be limited to avoid the divergence of preferential concentration in a turbulent flow field (and to keep the effective Stokes number below 0.2). In other word, I impose at each time step that

$$|\boldsymbol{v}_j - \boldsymbol{w}_j| \leq 0.2|\boldsymbol{u}_\mathrm{g} + \boldsymbol{w}_j| \,. \tag{5.1.2}$$

I tested the effect of this limiter on preferential concentration in Sec. 5.3 below.

5.1.3 Parallel performances

`ASHEE` has been tested on the High Performance Computing (HPC) infrastructures at INGV, Section of Pisa [ING] and at CINECA [CIN]. Fig. 5.1.1 reports the parallel efficiency on both the Fermi and the PLX (a Linux cluster based on Intel Xeon esa- and quad-core processors at 2.4 GHz) machines at CINECA. Here I used a numerical domain with 256^3 cells (cf. Sect. 5.2). The `ASHEE` code efficiency is very good (above 0.9) up to 512 cores (i.e., up to about 30000 cells per core), but it is overall satisfactory for 1024 cores, with efficiency larger than 0.8 on PLX and slightly lower (about 0.7) on Fermi, probably due to the limited level of cache optimization and input/output scalability [42]. The code was run also on 2048 cores on Fermi with parallel efficiency of 0.45 [44].

5.2 Compressible decaying homogeneous and isotropic turbulence

The numerical algorithm is tested in a number of different configurations of decaying homogeneous and isotropic turbulence (DHIT). The flow is initialized in a domain Ω which is a box with side $L = 2\pi$ with periodic boundary conditions. As described in Blaisdell et al. [11], Honein and Moin [103], Pirozzoli and Grasso [150], Lesieur et al. [116], Liao et al. [118], the initial turbulent velocity field is chosen so that its root mean square velocity is u_rms and its energy spectrum is

$$\mathcal{E}(k) = \frac{16}{3}\sqrt{\frac{2}{\pi}}\frac{u_\mathrm{rms}}{k_0}\left(\frac{k}{k_0}\right)^4 e^{-\frac{2k^2}{k_0^2}} \,, \tag{5.2.1}$$

with peak initially in $k = k_0$ and so that the initial kinetic energy and enstrophy are:

$$K_0 = \int_0^\infty \mathcal{E}(k)\mathrm{d}k = \frac{1}{2}u_\mathrm{rms}^2 \tag{5.2.2}$$

$$\mathcal{H}_0 = \int_0^\infty k^2\,\mathcal{E}(k)\mathrm{d}k = \frac{5}{8}u_\mathrm{rms}^2 k_0^2 \,. \tag{5.2.3}$$

As reviewed by Pope [152], the Taylor microscale can be written as a function of the dissipation $\epsilon = 2\nu\mathcal{H}$:

$$\lambda_\mathrm{T}^2 \equiv \frac{5\nu u_\mathrm{rms}^2}{\epsilon} = \frac{5K}{\mathcal{H}} \,, \tag{5.2.4}$$

thus in the present configuration, the initial Taylor microscale is:

$$\lambda_{\mathrm{T},0} = \sqrt{\frac{5K_0}{\mathcal{H}_0}} = \frac{2}{k_0}\,. \tag{5.2.5}$$

As described in Moin et al. [136], the eddy turnover time for the decaying turbulence with this initial spectrum is:

$$\tau_{\mathrm{e}} = \frac{2\sqrt{3}}{k_0 u_{\mathrm{rms}}} = \frac{\sqrt{3}\,\lambda_{\mathrm{T},0}}{u_{\mathrm{rms}}}\,. \tag{5.2.6}$$

The non-dimensionalization is chosen keeping the root mean square of the magnitude of velocity fluctuations ($\boldsymbol{u}'$) equal to u_{rms}:

$$u_{\mathrm{rms}} \equiv \frac{1}{(2\pi)^3}\int_\Omega \sqrt{\boldsymbol{u}'\cdot\boldsymbol{u}'}\mathrm{d}\boldsymbol{x} = 2\int_0^\infty \mathcal{E}(k)\,\mathrm{d}k\,. \tag{5.2.7}$$

I also chose to make the system dimensionless by fixing $\rho_{\mathrm{m},0} = 1$, $T_0 = 1$, $\mathrm{Pr} = 1$, so that the ideal gas law becomes:

$$p = \rho_{\mathrm{m}} R_{\mathrm{m}} T = R_{\mathrm{m}}\,, \tag{5.2.8}$$

and the initial Mach number of the mixture based on the velocity fluctuations reads:

$$\mathrm{Ma}_{\mathrm{rms}} = \sqrt{\frac{u_{\mathrm{rms}}^2}{c_{\mathrm{m}}^2}} = \sqrt{\frac{2K_0\rho_{\mathrm{m}}}{\gamma_{\mathrm{m}} p}} = u_{\mathrm{rms}}(\gamma_{\mathrm{m}}\,p)^{-\frac{1}{2}}\,. \tag{5.2.9}$$

This means that $\mathrm{Ma}_{\mathrm{rms}}$ can be modified keeping fixed u_{rms} and modifying p.

The initial compressibility ratio $\mathcal{C}_0$ is defined as the ratio between the kinetic energy and its compressible component K_c:

$$\mathcal{C}_0 = \frac{K_{c,0}}{K_0} = \frac{1}{2(2\pi)^3 K_0}\int_\Omega \sqrt{\boldsymbol{u}_c'\cdot\boldsymbol{u}_c'}\mathrm{d}\boldsymbol{x}\,. \tag{5.2.10}$$

Here, $\boldsymbol{u}_c'$ is the compressible part of the velocity fluctuations, so that $\nabla\cdot\boldsymbol{u}' = \nabla\cdot\boldsymbol{u}_c'$ and $\nabla\wedge\boldsymbol{u}_c' = 0$.

The last parameter, i.e. the dynamical viscosity, can be given both by fixing the Reynolds number based on $\lambda_{\mathrm{T},0}$ or k_0 (here $\nu = \mu/\rho_{\mathrm{m}}$):

$$\mathrm{Re}_\lambda = \frac{u_{\mathrm{rms}}\lambda_{T,0}}{\sqrt{3}\,\nu} \tag{5.2.11}$$

$$\mathrm{Re}_{k_0} = \frac{u_{\mathrm{rms}}}{k_0\,\nu}\,. \tag{5.2.12}$$

It is useful to define the maximum resolved wavenumber k_{max} on the selected N-cells grid and the Kolmogorov length scale η based on Re_{k_0}. They are, respectively:

$$k_{\mathrm{max}} = \left(\frac{N}{2} - 1\right)\frac{2\pi}{L}\frac{N}{N-1}\,, \tag{5.2.13}$$

$$\eta = \left(\frac{\nu^3}{\epsilon}\right)^{\frac{1}{4}} = \left(\frac{4\nu^2}{5u_{\mathrm{rms}}^2 k_0^2}\right)^{\frac{1}{4}} = \left(\frac{16}{15}\right)^{\frac{1}{4}}\frac{1}{k_0}\,\mathrm{Re}_\lambda^{-\frac{1}{2}} \simeq \frac{1}{k_0}\,\mathrm{Re}_\lambda^{-\frac{1}{2}}\,. \tag{5.2.14}$$

In order to have a DNS, the smallest spatial scale $\delta = 2\pi/N$ should be chosen in order to have $k_{\mathrm{max}}\eta > 2$ [cf. 214, 186, 150].

5.2.1 Single-phase case

In order to validate the numerical code in the single-phase case, the DNS of compressible decaying homogeneous and isotropic turbulence is compared with the well tested numerical solver for Direct Numerical Simulations of compressible turbulence of Sergio Pirozzoli and Matteo Bernerdini [see 150, 7]. For this comparison the following initial parameters are fixed: $p = R_{\mathrm{m}} = 1$, $\gamma_{\mathrm{m}} = 1.4$, $\mathrm{Pr} = 1$, $\mathrm{Ma}_{\mathrm{rms}} = 0.2$, $\mathcal{C}_0 = 0$, $u^2_{\mathrm{rms}} = 2K_0 = 0.056$, $k_0 = 4$, $\lambda_{\mathrm{T}} = 0.5$, $\tau_{\mathrm{e}} \simeq 3.6596$, $\mu = 5.885846 * 10^{-4}$, $\mathrm{Re}_\lambda \simeq 116$, $\mathrm{Re}_{k_0} \simeq 100$. Thus a grid with $N = 256^3$ cells gives $k_{\mathrm{max}} \simeq 127$ and $k_{\mathrm{max}}\eta \simeq 3.0$, big enough to have a DNS. Here I have used the numerical scheme [linear]. The simulation has been performed on 1024 cores on the *Fermi Blue Gene/Q* infrastructure at CINECA [CIN]. It needed about 5 h to be computed completely. In Fig. 5.2.1 the comparison is shown between the energy spectrum

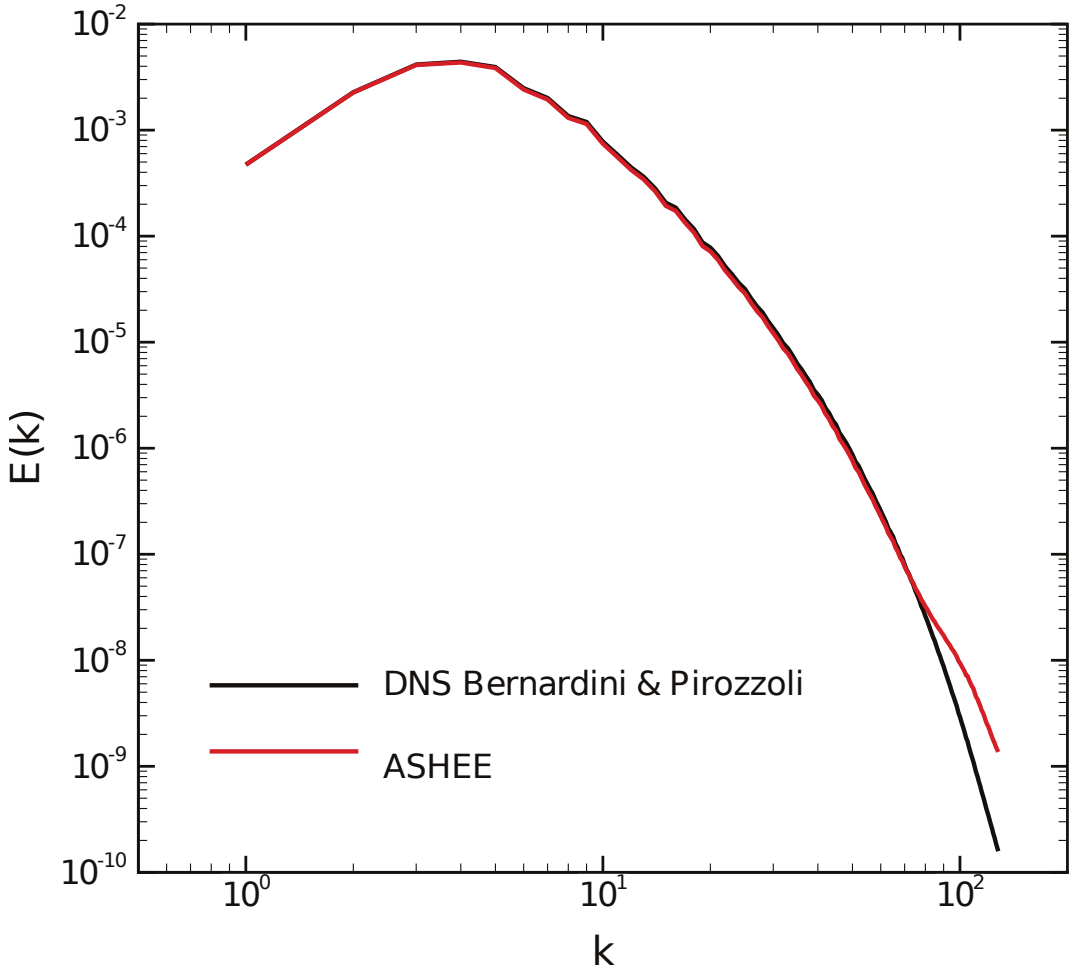

Figure 5.2.1: Comparison of a DNS executed with the eight order scheme by Pirozzoli and Grasso [150] and `ASHEE` code implemented using the `C++` libraries of OpenFOAM® at $t/\tau_{\mathrm{e}} = 1.093$. The L^2 norm between the two spectra is $4.0 * 10^{-4}$. The main parameters are $\mathrm{Re}_\lambda \simeq 116$, $\mathrm{Ma}_{\mathrm{rms}} = 0.2$.

$\mathcal{E}(k)$ obtained with the two algorithms after approximatively 1 eddy turnover time; the L^2 norm of the difference between the two spectra is $4.0 * 10^{-4}$. This validates the accuracy of the `ASHEE` numerical code in the single-phase and shock-free case. Fig. 5.2.2 shows an isosurface based on $T = 1$ colored with the velocity magnitude. There, the eddies generate temperature (and consequently pressure) perturbations

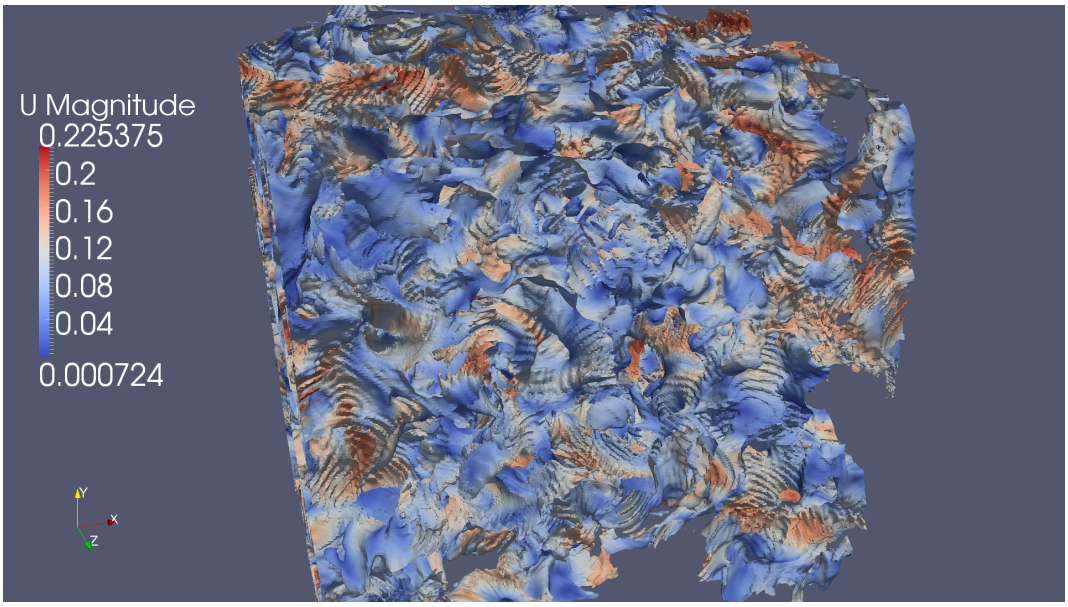

Figure 5.2.2: Isosurface at $T = 1$, coloured with the magnitude of $\boldsymbol{u}$.

(sound), because of the compressibility.

Fig. 5.2.3 shows the kinetic energy spectrum at $t/\tau_e = 0$, 1.093, 5.465 and the evolution of the main integral parameters K, $\mathcal{H}$, λ_T plus the density fluctuations $\rho_{rms} = \sqrt{\langle(\rho - \langle\rho\rangle_\Omega)^2\rangle_\Omega}$, the density contrast ρ_{max}/ρ_{min} and a standard measure of compressibility $\mathcal{C} = \langle|\nabla \cdot \boldsymbol{u}|^2\rangle_\Omega / \langle|\nabla \boldsymbol{u}|^2\rangle_\Omega$ which takes value between 0 (incompressible flow) and 1 (potential flow) [cf. 13]. In Fig. 5.2.3a, the energy spectrum widens from the initial condition until its tail reach $k \simeq k_{max} \simeq 127$. Then system becomes to dissipate and the maximum of the energy spectrum decreases. The largest scales tend to lose energy slower than the other scales and the spectrum widens also in the larger scale direction. In Fig. 5.2.3b, the total kinetic energy decreases monotonically and at $t \simeq 5.5\tau_e$ it remains just $\simeq 15\%$ of its initial value. On the other hand, enstrophy increases until it reaches a maximum at $1.5 < t/\tau_e < 2$. After that moment it start to decrease monotonically. This behavior is related to the two different stages highlighted in the analysis of the energy spectrum evolution. In the first stage of the evolution, the viscous effects are negligible and enstrophy increases due to vortex stretching. During the second stage, viscous diffusion starts to have an important role and to distorted dissipative structures are created [cf. 81]. Also the Taylor micro-scale reflects this behavior, reaching a minimum at the end of the first stage and increasing monotonically during the second stage of the evolution. It is a characteristic of the size of the velocity gradients in the inertial range and comparing it with δ gives an idea of the broadness of the wave number range where the flow can dissipate. In the case of this DNS, $\lambda_T \simeq 10.2\delta$ at $t \simeq 5.5\tau_e$. All the quantities showed in Fig. 5.2.3c depend on the initial Mach number end compressibility. Indeed, very similar result to case $Ma_{rms} = 0.2$ are obtained in Fig. 18 and 19 of Garnier et al. [81].

In [HIT] a movie can be found showing the evolution of an isosurface of the second invariant of the velocity gradient

$$Q_{\boldsymbol{u}} = \frac{1}{2}\left((\mathrm{Tr}(\nabla \boldsymbol{u}))^2 - \mathrm{Tr}(\nabla \boldsymbol{u} \cdot \nabla \boldsymbol{u})\right) , \tag{5.2.15}$$

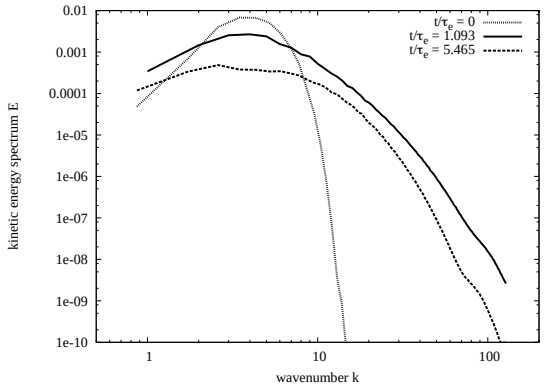

(a) Evolution of $\mathcal{E}(k)$

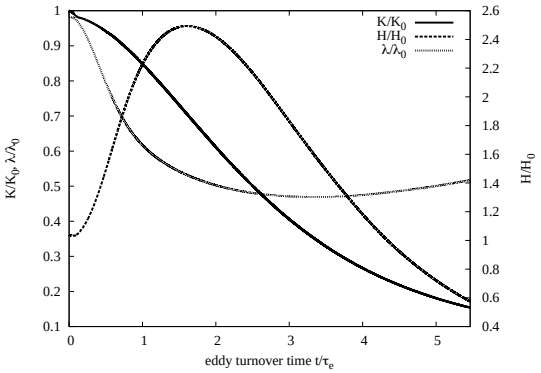

(b) Evolution of K, $\mathcal{H}$ and λ_{T}

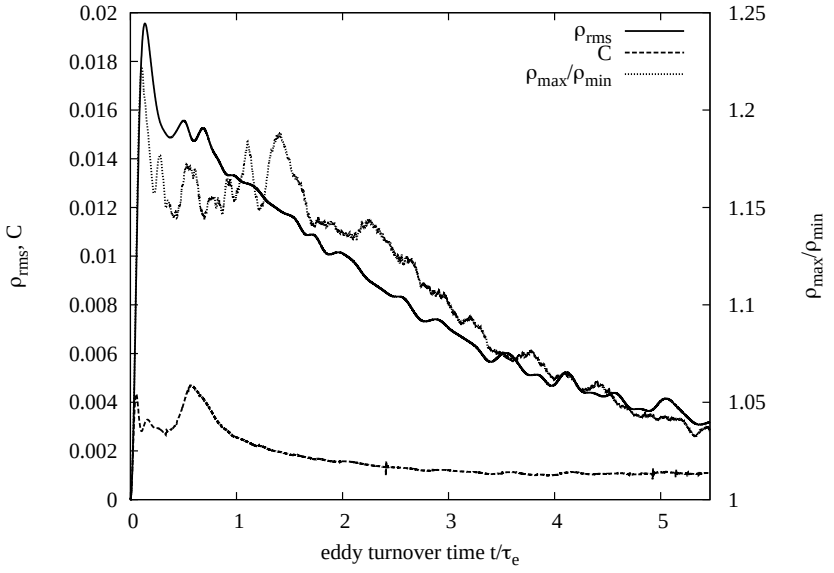

(c) Evolution of ρ_{rms}, $\mathcal{C}$, $\rho_{\mathrm{max}}/\rho_{\mathrm{min}}$

Figure 5.2.3: Evolution of the main integral parameters for DHIT with $\mathrm{Re}_\lambda \simeq 116$ and $\mathrm{Ma}_{\mathrm{rms}} = 0.2$.

in order to show the evolution of the turbulence. Indeed the so called Q-criterion [cf. 80] allows the identification of coherent vortices inside a three dimensional velocity field (see Fig. 5.2.4).

In the next section, I will test the subgrid models reviewed in Sec. 1.4 comparing the DNS described in this section with simulations with resolution $N = 32^3$ and $N = 64^3$ cells.

5.2.2 Large Eddy Simulations

I have tested the subgrid models described in Sec. 1.4 using the DNS described in the previous section as a benchmark. In Fig. 5.2.5 all the LES simulations have been performed with resolution $N = 32^3$ except one of the [dynSma] in Fig. 5.2.5b having $N = 64^3$. In the left panels are represented the simulation without subgrid model [noM] and the subgrid models [sma], [oneEqEddy], [wale], while in the right panels are represented the dynamical models [moin], [dynSma], [dynOneEqEddy] and [dynWale]. [cubic] is the forth order numerical scheme described in Sec. 5.1, all the

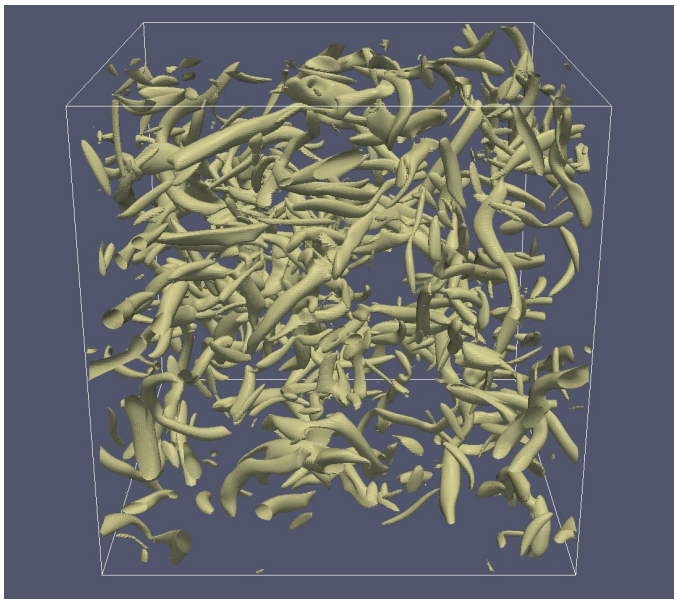

Figure 5.2.4: Isosurface at $Q_{\boldsymbol{u}} \simeq 19$ Hz^2 and $t/\tau_{\mathrm{e}} \simeq 2.2$, representing zones with coherent vortices.

other simulations have been computed with the scheme [linear]. In Fig. 5.2.5, "[noM] 256^3 mapped 32^3" is the DNS with $N = 256^3$ *a posteriori* filtered for comparison into the $N = 32^3$ mesh.

Looking through all the figures it is worth noting that the coarse DNS [noM]–32^3 behaves very well, being the coarse simulation that gives results more similar to the filtered DNS. However, in Fig. 5.2.5a, the simulation without a subgrid model tends to accumulate to much energy at the smallest scales. This behavior should cause numerical instability, especially for long duration LES. On the other hand, subgrid models do not show this behavior, tending to dissipate too much in the inertial range while too much little at integral scale. However, dynamical subgrid models (right panels of Fig. 5.2.5) behaves much better than non-dynamical ones and they gives satisfactory results.

Comparison between non-dynamical subgrid models suggest that: (i) [oneEqEddy] is less diffusive than [sma], while [wale] is the most diffusive; (ii) [oneEqEddy] tends to increase the Taylor micro-scale too fast in last part of the simulation.

Comparison between dynamical models suggest that: (i) all the models have a similar behavior but [dynOneEqEddy] and [dynWale] behave slightly better; (ii) using the [cubic] scheme does not improve substantially the quality of the result, rather it tends to make λ_{T} grow too rapidly; (iii) the two models [moin] and [dynSma] behave very similarly; (iv) increasing the resolution to $N = 64^3$ substantially improves the quality of the results.

5.3 Multiphase isotropic turbulence.

The aim of this section is testing the capability of the `ASHEE` numerical code to capture the right decoupling between solid and gaseous phases whether when the equilibrium–Eulerian hypothesis $\mathrm{St}_j < 0.2$ is fulfilled or not. In the latter case, the limiter for the relative velocity $\boldsymbol{v}_j = \boldsymbol{u}_j - \boldsymbol{u}_{\mathrm{g}}$ defined in Eq. (5.1.2) is applied.

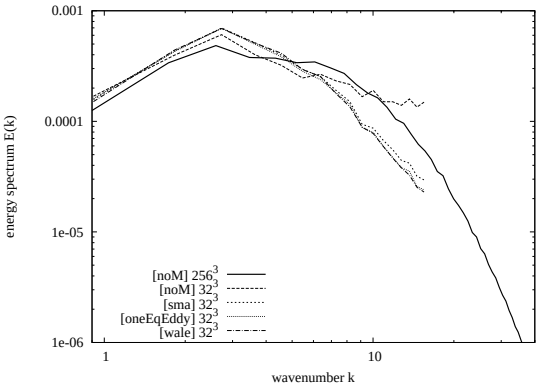

(a) $\mathcal{E}(k)$ at $t/\tau_e = 5.465$

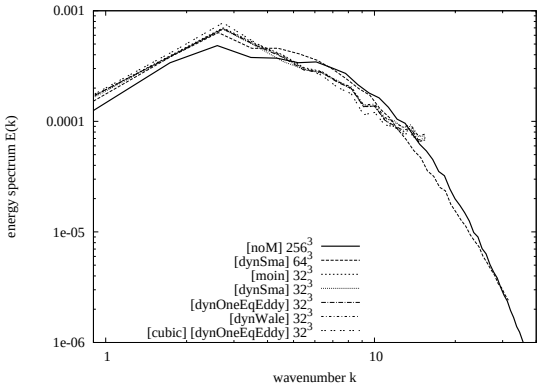

(b) $\mathcal{E}(k)$ at $t/\tau_e = 5.465$

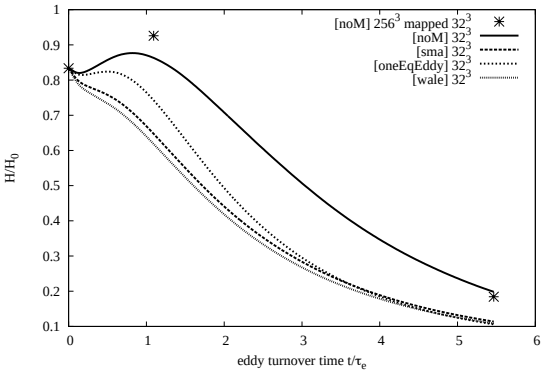

(c) Evolution of $\mathcal{H}/\mathcal{H}_0$

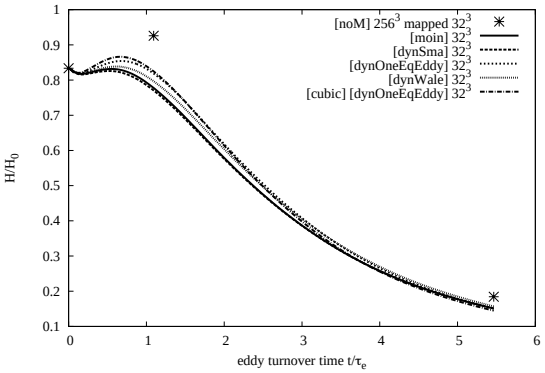

(d) Evolution of $\mathcal{H}/\mathcal{H}_0$

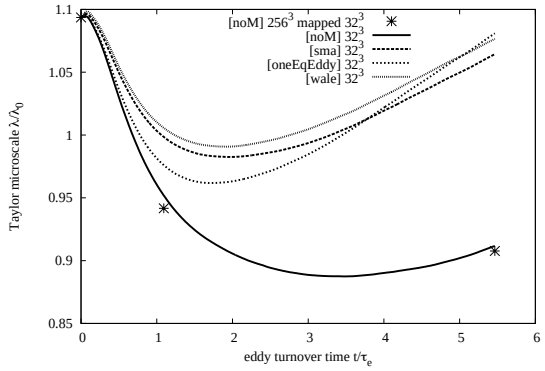

(e) Evolution of $\lambda_T/\lambda_{T,0}$

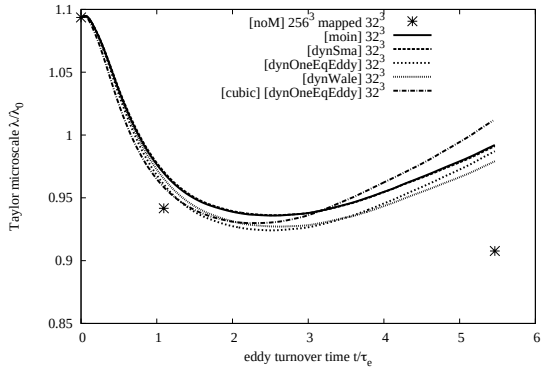

(f) Evolution of $\lambda_T/\lambda_{T,0}$

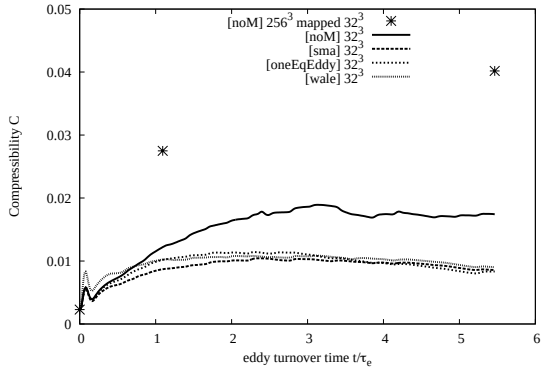

(g) Evolution of $\mathcal{C}$

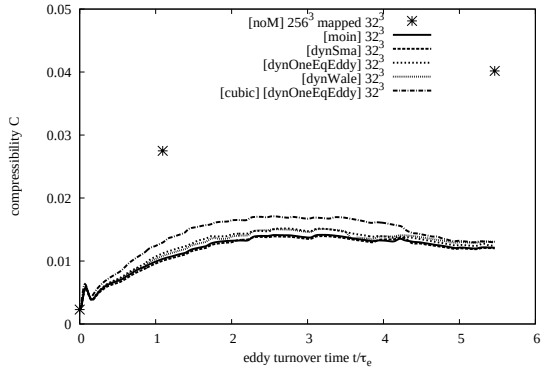

(h) Evolution of $\mathcal{C}$

Figure 5.2.5: Comparison of various subgrid models described in Sec. 1.4 with the DNS described in the previous section.

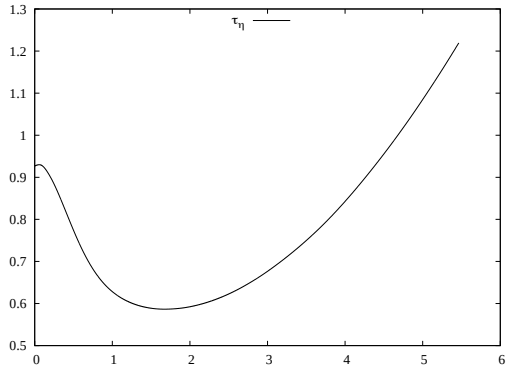

Figure 5.3.1: Evolution of the Kolmogorov time microscale τ_η.

τ_j	$\mathrm{St}_{\max} = \tau_j/0.6$	d_j $(\hat{\rho}_j = 10^3)$
0.60	1.0	$2.521 * 10^{-3}$
0.30	0.5	$1.783 * 10^{-3}$
0.15	0.25	$1.261 * 10^{-3}$
0.075	0.125	$8.914 * 10^{-4}$
0.0375	0.0625	$6.303 * 10^{-4}$

Table 5.3.1: Stokes time, maximum Stokes number and diameter of the solid particles inserted in the turbulent box.

Here, the code is used to simulate the decaying isotropic turbulence in a box filled with 5 different particle species. It is solved both with a DNS (256^3 cells) and a LES (32^3 cells).

5.3.1 One way coupling.

In order to achieve this objective, a numerical simulation of homogeneous and isotropic turbulence is performed with a gas phase initialized with the same initial and geometric conditions described in Sec. 5.2. 5 solid particle classes ($j = 2 \div 6$) are added to that configuration, chosen in such a way that the Stokes number spans the window $\mathrm{St}_j \in [0.03, 1]$. While the Stokes time of each particle class does not change during the evolution, the Stokes number changes because the Kolmogorov time changes. Fig. 5.3.1 shows the evolution of the Kolmogorov time scale τ_η during the evolution of the decaying turbulence.

There approximately $\tau_\eta \in [0.6, 1.2]$ thus, for a given particle class with τ_j fixed, $\mathrm{St}_{\max}/\mathrm{St}_{\min} \simeq 2$ during the time interval $t/\tau_\mathrm{e} \in [0, 5.5]$. Tab. 5.3.1 reports the main properties of the particles inserted in the turbulent box. To evaluate the Stokes time here $\tau_j = \hat{\rho}_j d_j^2/(18\mu)$ is used – i.e. $\phi_\mathrm{c}(\mathrm{Re}_j) = 1$ – because in absence of settling $\mathrm{Re}_j < 1$ when $\mathrm{St}_j < 1$ [cf. 3]. The material density of all the particles is set to $\hat{\rho}_j = 10^3$.

In order to have a small contribution of the particle phases to the fluid dynamics – one way coupling – here the solid particles mass fraction is set to a small value, $y_j = 0.002$, so that $y_\mathrm{g} = 0.99$. Fig. 5.3.2 shows a slice of the turbulent box at $t/\tau_\mathrm{e} \simeq 2.2$.

The global quantity here used to measure the particle decoupling is the preferential concentration. As described in Maxey [131], Rani and Balachandar [158], a good measure for the degree of preferential concentration in incompressible flows is the weighted average on the particle mass fraction of the quantity $(|\mathcal{D}|^2 - |\mathcal{S}|^2)$, where $\mathcal{S}$ is the vorticity tensor, i.e. the skew symmetric part of the gas velocity gradient and $\mathcal{D}$ is its symmetrical part. For compressible flows, I choose to consider

$$\langle \mathcal{P} \rangle_j \equiv \langle \left(|\mathcal{D}|^2 - |\mathcal{S}|^2 - |\,\mathrm{Tr}(\mathcal{D})|^2 \right) \rangle_j \equiv \frac{\langle y_j \left(\mathcal{P} - \langle \mathcal{P} \rangle_\Omega \right) \rangle_\Omega}{\langle y_j \rangle_\Omega} \,. \tag{5.3.1}$$

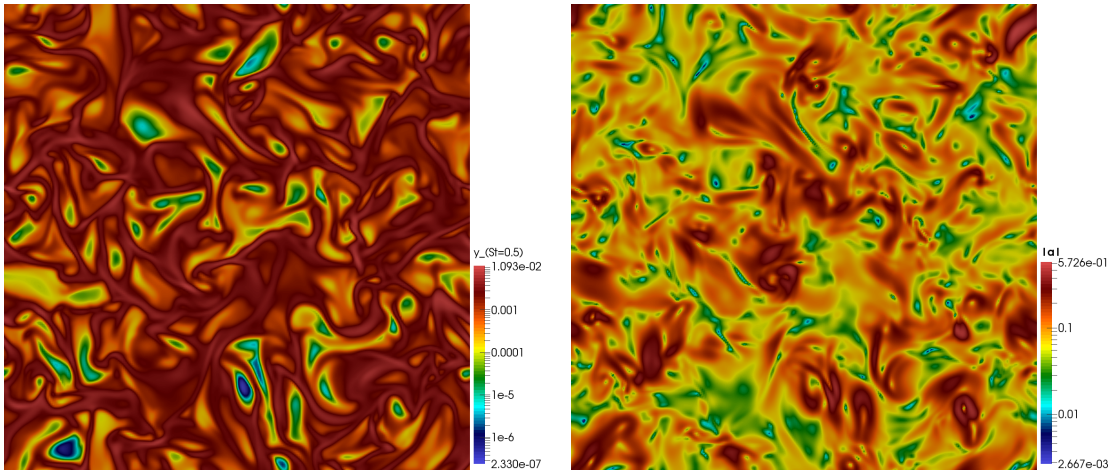

(a) Mass fraction **(b)** Acceleration

Figure 5.3.2: Slice of the turbulent box at $t/\tau_e \simeq 2.2$. The two panels represent respectively a logaritmic color map of y_3 ($\mathrm{St}_{\max} = 0.5$) and of $|\boldsymbol{a}_g|$.

This is a good measure because (use integration by parts, Gauss theorem and Eq. (1.3.21) with $\boldsymbol{w}_j = 0$):

$$\langle \nabla \cdot \boldsymbol{u}_j \rangle_\Omega = -\tau_j \left\langle \sum_{l,m} \left(\partial_l u_m \partial_m u_l - \partial_l u_l \partial_m u_m \right) \right\rangle_\Omega = \\ = -\tau_j \left\langle \left(|\mathcal{D}|^2 - |\mathcal{S}|^2 - |\operatorname{Tr}(\mathcal{D})|^2 \right) \right\rangle_\Omega . \quad (5.3.2)$$

Moreover, it is worth noting that $\langle \mathcal{P} \rangle_j$ vanishes in absence of preferential concentration. By dimensional analysis, preferential concentration is expected to behave as:

$$\langle \mathcal{P} \rangle_j \propto \begin{cases} \tau_j/\tau_\eta^3 & \text{DNS} \\ \tau_j/\tau_\xi^3 & \text{LES}\,, \end{cases} \quad (5.3.3)$$

because it must be proportional to τ_j and have a dimension of $[\mathrm{s}^{-2}]$.

While in DNS τ_η is well defined, a definition for τ_ξ is necessary in LES. As described by Pope [152], the typical time at scale ξ scales along the turbulent energy cascade from the inertial subrange to the dissipation range with dissipation ϵ as:

$$\tau_\xi \overset{inertial\,scales}{=} \left(\frac{\xi^2}{\epsilon} \right)^{\frac{1}{3}} \overset{Kolmogorov}{=} \tau_\eta \left(\frac{\xi}{\eta} \right)^{\frac{2}{3}} \overset{Taylor}{=} \tau_\lambda \left(\frac{\xi}{\lambda_\mathrm{T}} \right)^{\frac{2}{3}} . \quad (5.3.4)$$

Since the time based on the Taylor microscale λ_T is defined as

$$\tau_\lambda = \frac{\sqrt{3}\lambda_\mathrm{T}}{u_\mathrm{rms}} , \quad (5.3.5)$$

the typical time at the smallest resolved LES scale ξ can be evaluated knowing the kinetic energy $K(t)$ and $\lambda_\mathrm{T}(t)$:

$$\tau_\xi(t) = \sqrt{\frac{3}{2K(t)}}\, \xi^{\frac{2}{3}} \lambda_\mathrm{T}(t)^{\frac{1}{3}} . \quad (5.3.6)$$

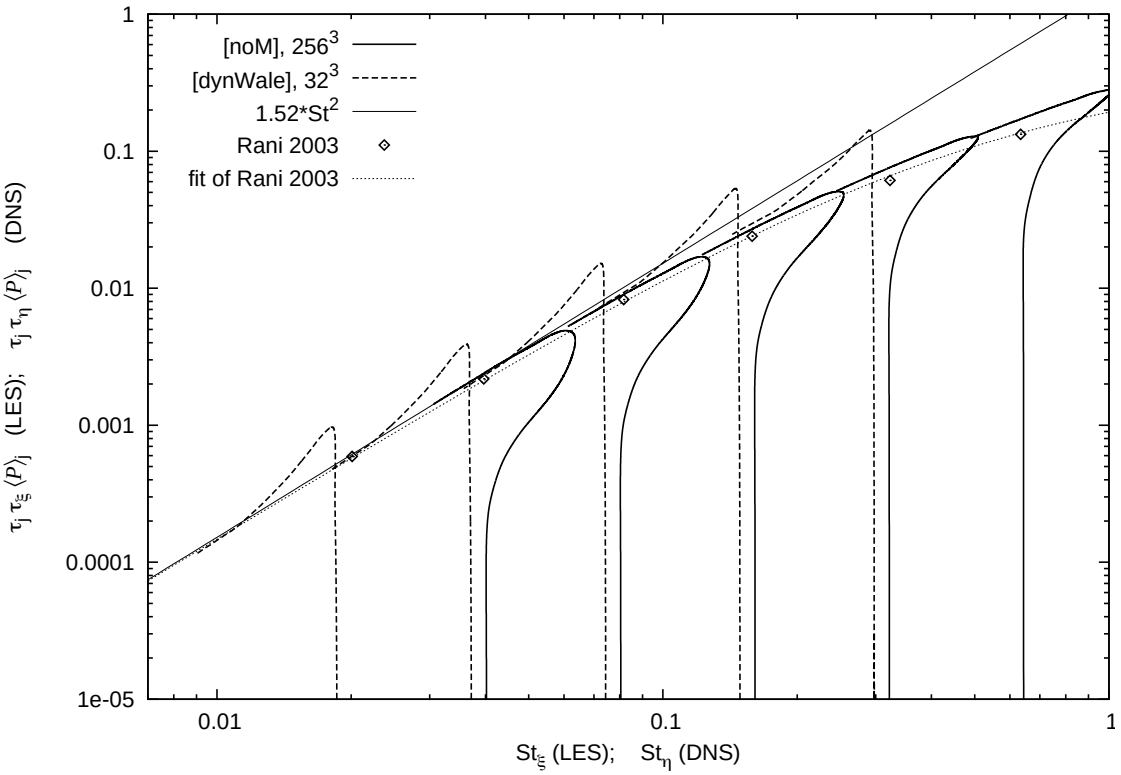

Figure 5.3.3: Evolution of the degree of preferential concentration $\langle \mathcal{P} \rangle_j$ as a function of St_ξ (LES) or St_η (DNS). The evolution is shown for the 5 particle classes of Tab. 5.3.1, in the DNS (bold solid lines) and LES (bold dashed lines) cases. The asymptotic trend St^2 (solid line) is shown with the Lagrangian results by Rani and Balachandar [158] (points) and the fit Eq. (5.3.8) (dotted line). A good agreement is obtained between equilibrium–Eulerian LES/DNS and Lagrangian DNS simulations.

Fig. 5.3.3 shows the evolution of preferential concentration of each of the 5 particle classes of Tab. 5.3.1. The degree of preferential concentration is measured with $\langle \mathcal{P} \rangle_j$, multiplied by $\tau_\xi \tau_j$ (LES) or $\tau_\eta \tau_j$ (DNS) in order to make it dimensionless and to plot on the same graph all the different particles at different times together. The temporal evolution is showed either as a function of the Stokes number St_ξ (LES) or St_η (DNS). Evolution of preferential concentration of each of the 5 particle classes is shown in the LES (bold dashed lines) and DNS (bold solid lines) cases. It is compared with the theoretical asymptotic behavior St^2 (solid line) and the results obtained with Lagrangian DNS (points and dotted line, see below).

Preferential concentration initially is zero because particles are homogeneously distributed in the box. Then, it increases until a maximum value and then it decreases following a particular law function of St. The maximum degree of preferential concentration is reached by the single particle class when τ_η is minimum (at $t/\tau_\mathrm{e} \simeq 1.7$, cf. Fig. 5.3.1). Then, $\langle \mathcal{P} \rangle_j$ decreases until it reaches the maximum value of preferential concentration reached by the next particle class. This kind of behavior is obtained thanks to the particular choice for the Stokes numbers presented in Tab. 5.3.1. It is worth noting that the expected behavior of Eq. (5.3.3) is recovered for $\mathrm{St}_j < 0.2$, in particular I find:

$$\langle \mathcal{P} \rangle_j \simeq \begin{cases} 1.52\,\mathrm{St}_j\,\tau_\eta^{-2} & \text{DNS} \\ 1.52\,\mathrm{St}_j\,\tau_\xi^{-2} & \text{LES}\,. \end{cases} \tag{5.3.7}$$

Moreover, by comparing the present results with the Eulerian-Lagrangian simulation described in Rani and Balachandar [158], it is worth noting that the limiter defined in Eq. (5.1.2) for the preferential concentration when $\mathrm{St} > 0.2$ is well behaving.

For the sake of completeness, I found that the best fit in the range $\mathrm{St} < 2.5$ for the data found by Rani and Balachandar [158] is:

$$\langle \mathcal{P} \rangle_j \simeq 1.52 * \frac{\mathrm{St}_j}{1 + 3.1 * \mathrm{St}_j + 3.8 * \mathrm{St}_j^2} \, \tau_\eta^{-2} \,, \tag{5.3.8}$$

with root mean square of residuals $8.5 * 10^{-3}$.

Moving to comment the 32^3 LES simulation, Fig. 5.3.3 shows that the Stokes number of a particular particle class in the LES case is much smaller than its DNS counterpart. Accordingly with Balachandar and Eaton [4], it holds

$$\mathrm{St}_\xi = \mathrm{St}_\eta \left(\frac{\eta}{\xi} \right)^{\frac{2}{3}} \,, \tag{5.3.9}$$

confirming that the equilibrium–Eulerian model widens its applicability under the LES approximation. Is is also worth noting that the presented LES is able to reproduce the right degree of preferential concentration with a satisfactory level of accuracy when $\mathrm{St} < 0.2$. In particular, the LES slightly overestimate preferential concentration and the time needed to reach the equilibrium and to forget the influence of particles initial condition.

5.4 Natural convection

In this section I want to stress OpenFOAM® and `ASHEE` against a two-dimensional heat exchange problem. Pure air is closed in a box with two horizontal no-slip walls thermally insulated and two vertical no-slip walls kept at a constant temperature, T_0 and $T_0 + \Delta T$ respectively (cf. Sect. 1.5). The filled-air square cavity side is L and it is set initially at constant temperature T_0 and density ρ_0. At the beginning of the transformation, the hot wall starts to heat the air, making it lighter. A convective cell thus creates, moving the heat from the hotter to the colder wall. I refer to these two walls as W_h and W_c respectively. The non-dimensional number associated to buoyancy driven flow is the Rayleigh number. For a perfect gas it is defined:

$$\mathrm{Ra} = \frac{\rho_0 g L^3 \Delta T}{\mu^2 \, T_0} \mathrm{Pr} \,. \tag{5.4.1}$$

Tab. 5.4.1 reports the physical parameters used for this test case.

ρ_0 [kg/m^3]	g [m/s^2]	L [m]	μ [kg/m s]	T_0 [K]	Pr -
1.176824	9.81	0.1	$1.846 * 10^{-5}$	300	0.71

Table 5.4.1: Physical parameters for the natural convection test case.

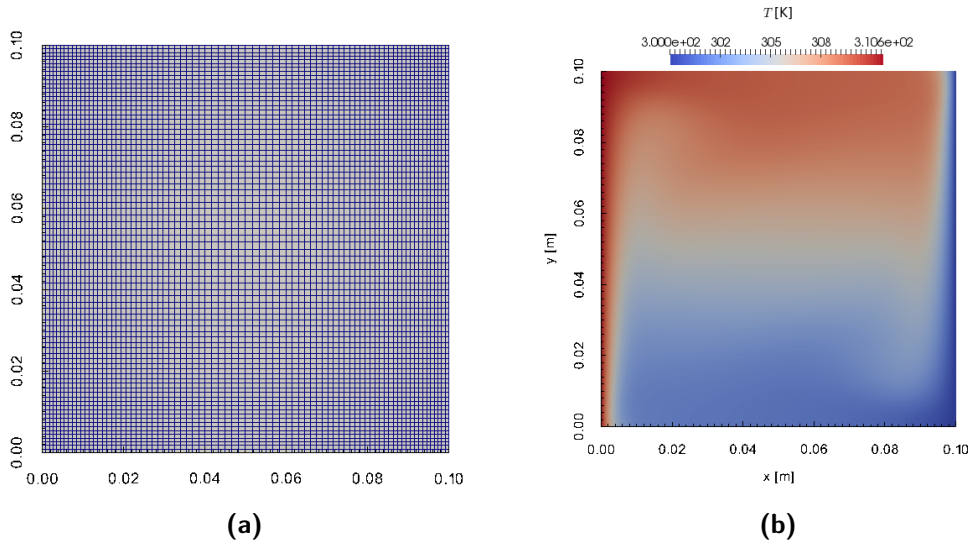

Figure 5.4.1: Configuration for the natural convection test case. a) Mesh with 6400 cells; b) stationary temperature configuration for the $\mathrm{Ra} = 10^6$ case ($\Delta T = 10.59825$ K).

I run four simulations to reproduce the Nusselt number relative, in turn, to the two walls $W_{\mathrm{h,c}}$:

$$\mathrm{Nu}_{\mathrm{h,c}} = \frac{L}{\Delta T |W_{\mathrm{h,c}}|} \int_{W_{\mathrm{h,c}}} |\nabla T \cdot \mathrm{d}S| \,. \tag{5.4.2}$$

At the beginning of the thermodynamic transformation, $\mathrm{Nu_h} > \mathrm{Nu_c}$ because the hotter wall heats the box interior, while the colder is in equilibrium with it. However, when the stationary state is reached, then it must hold $\mathrm{Nu_h} = \mathrm{Nu_c} = \mathrm{Nu}$, because of energy conservation. Thus, at the equilibrium, the box acts as a conductor between the two walls. If conduction dominates (small Ra), $\mathrm{Nu} \simeq 1$; on the contrary if convection dominates (large Ra), Nu increases. In the four simulations the Rayleigh number is left increase, from $\mathrm{Ra} = 10^3$ to $\mathrm{Ra} = 10^6$, in order to compare the present result with the experimental data found in Costa [40], Deng and Tang [50]. Fig. 5.4.1 shows the 6400 cells mesh used, together with the temperature field of the $\mathrm{Ra} = 10^6$ case. The final time for each simulation is t_{f}. Tab. 5.4.2 reports the results of the cited papers, present results and relative errors. Fig. 5.4.2 shows

Ra	Nu [50]	Nu [40]	Nu `ASHEE`	Nu `ASHEE` rel. err.	$\mathrm{Nu_h}/\mathrm{Nu_c} - 1$	t_{f} [s]
10^3	1.118	1.118	1.145	0.02	$1.5 * 10^{-3}$	450
10^4	2.254	2.243	2.251	0.004	$5 * 10^{-4}$	250
10^5	4.557	4.519	4.531	0.003	$2 * 10^{-4}$	150
10^6	8.826	8.800	8.851	0.006	$2 * 10^{-5}$	100

Table 5.4.2: Comparison between the results obtained with `ASHEE` and that measured by Costa [40] and simulated by Deng and Tang [50]. The relative error in the fifth column is relative to Costa [40].

the evolution of $\mathrm{Nu_h}$ and $\mathrm{Nu_c}$ for all the simulated cases. The relative difference between $\mathrm{Nu_h}$ and $\mathrm{Nu_c}$ is reported in Tab. 5.4.2.

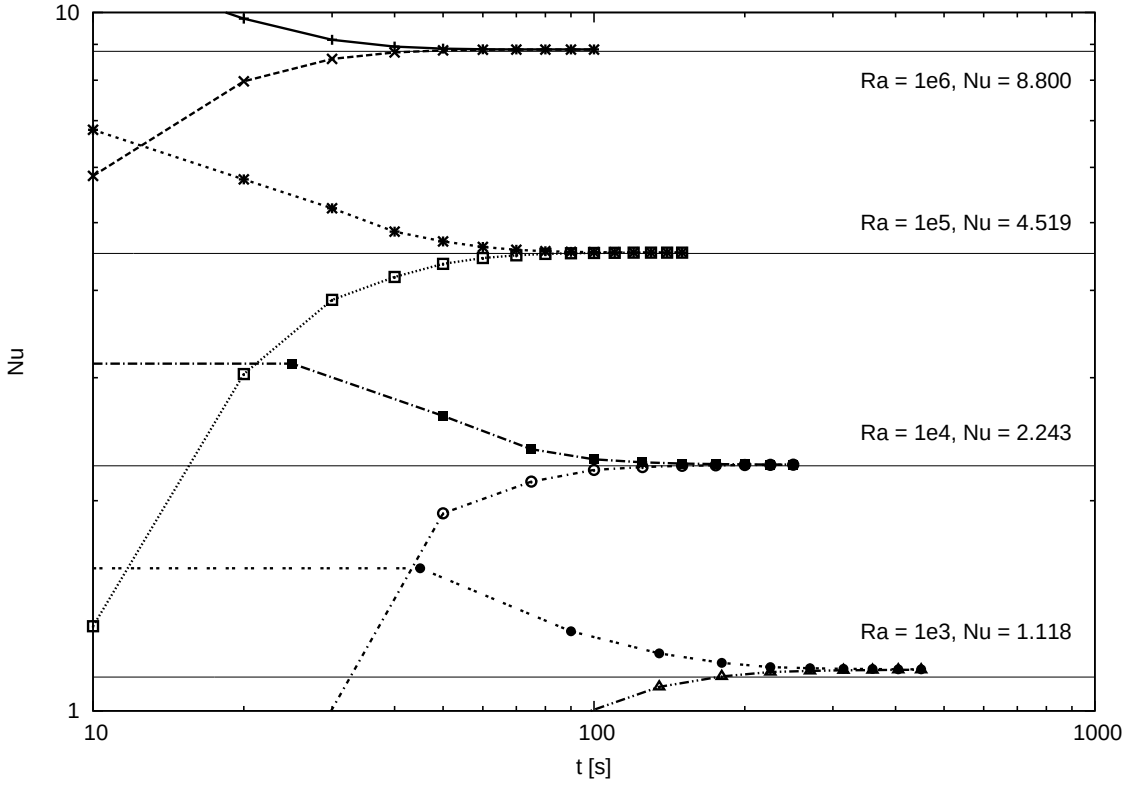

Figure 5.4.2: Evolution of the Nusselt number for all the four simulations presented. For each case, the line above refers to $\mathrm{Nu_h}$, while that below is $\mathrm{Nu_c}$.

The error between the presented simulations is always below 3 %, a satisfactory result with respect the relative coarse resolution of the mesh used. This validates the capability of `ASHEE` to model heat transfer phenomena.

5.5 Turbulent forced plume – [forcedPlume]

In order to test the capability of the `ASHEE` code to capture the fluid dynamics of jets and plumes, present results are compared with the laboratory and numerical experiments described in George et al. [83], Shabbir and George [175], Zhou et al. [233]. Some movie of the numerical simulations described in this section can be found in [TPL].

The numerical test case is designed to reproduce the fluid dynamic configuration of an experimental forced plume. The boundary condition at the inlet consists of a fixed uniform temperature field with $T = T_0$. On the contrary, the velocity field is chosen in order to mimic the experimental radial profile and to include turbulence fluctuations and forcing (see Sect. 1.5.3).

The forced plume is evolved into a hexahedral domain Ω of size $12.8 \times 6.4 \times 6.4$ diameters. No-slip wall boundary conditions are imposed at the bottom and atmospheric boundary conditions at the vertical and top sides (see Sect. 1.5.2). The initial condition is homogeneous for the temperature field $T = T_\alpha$, while the pressure field has been initialized accordingly to the natural stratification $\mathrm{d}_z p = -\alpha g$:

$$p(z, t = 0) = p_0 e^{-\frac{g}{RT_\alpha} z} \,. \tag{5.5.1}$$

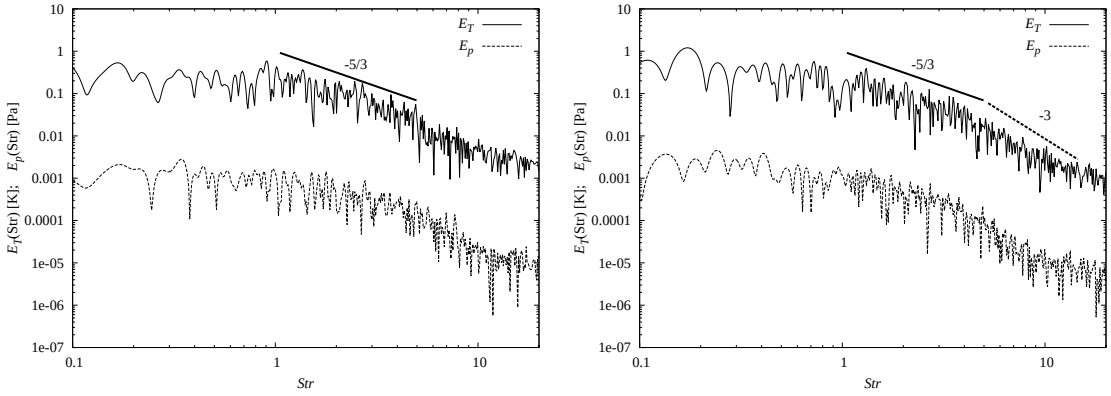

(a) Fluctuations at an axial point **(b)** Fluctuations at an outer edge point

Figure 5.5.1: Temperature (solid) and pressure (dashed) fluctuations energy spectra: a) at a point along the plume axis (0, 0, 0.5715) [m]; b) at a point along the plume outer edge (0, 0.06858, 0.5715) [m]. The slopes $\mathrm{Str}^{-5/3}$ and Str^{-3} are represented with a thick solid and dashed line respectively.

Tab. 5.5.1 summarized the configuration numbers selected for this numerical benchmark. The viscosity is evaluated accordingly to the Sutherland law in Eq. (1.1.25).

U_i [m/s]	b_0 [m]	A_φ -	σ_0 -	N_φ -	Str -	T_0 [K]	T_α [K]	p_0 [Pa]	g [m/s^2]
0.98	0.03175	0.2	0.05	6	0.35	568	300	101325	9.81

Table 5.5.1: Configuration parameters for the [forcedPlume] experiment.

The simulation has been executed up to $t = 10$ s and time averaged fields have been computed in the time window $t \in [4, 10]$ s. Tab. 3.4.2 summarized the main integral-model parameters for this forced plume.

5.5.1 Single-phase case

High-resolution, three-dimensional numerical simulation of a forced gas plume is discussed, produced by the injection of a gas flow from a circular inlet into a stable atmospheric environment at lower temperature (and higher density). Such an experiment allows to test the numerical model behavior against some of the fundamental processes controlling volcanic plumes, namely density variations, non-isotropic turbulence, mixing, air entrainment, and thermal exchange. The present study is mainly aimed at assessing the capability of the numerical model to describe the time-average behavior of a turbulent plume and to reproduce the magnitude of large-scale fluctuations and large-eddy structures. I will mainly refer to laboratory experiments by George et al. [83] and Shabbir and George [175] and numerical simulations by Zhou et al. [233] for a quantitative assessment of model results.

Numerical simulations describe a vertical round forced plume with heated air as the injection fluid. The plume axis is aligned with the gravity vector and is subjected to a positive buoyancy force. As summarized in Tab. 5.5.1, the heat source diameter $2b_0$ is 6.35 cm, the exit vertical velocity on the axis u_0 is 0.98 m/s, the inflow temperature T_0 is 568 K and the ambient air temperature T_α is 300 K. The

corresponding Reynolds number is 1273, based on the inflow mean velocity, viscosity and diameter. Air properties at inlet are $C_p = 1004.5$ J/(K kg); $R = 287$ J/(K kg); $\mu = 3 \times 10^{-5}$ Pa s.

As discussed by Zhou et al. [233] the development of the turbulent plume regime is quite sensitive to the inlet conditions: I therefore tested the model by adding a periodic perturbation and a non-homogeneous inlet profile to anticipate the symmetry breaking, and the transition from a laminar to a turbulent flow. The radial profile is that described in Sect. 1.5.3. A periodical forcing with $A_\varphi = 0.2$, $N_\varphi = 6$, Str $= 0.35$, and a random perturbation of intensity $0.05U_\mathrm{i}$ has been superimposed to mimic a turbulent inlet (see Sect. 1.5.3).

The computational grid is composed of $360 \times 180 \times 180$ uniformly spaced cells (deformed near the bottom plane to conform to the circular inlet) in a box of size $12.8 \times 6.4 \times 6.4$ diameters. In particular, the inlet is discretized with 400 cells. The adaptive time step was set to keep the Courant number less than 0.2. Based on estimates by Plourde et al. [151], the selected mesh refinement is coarser than the required grid to fully resolve turbulent scales in a DNS (which would require about $720 \times 360 \times 360$ cells). Nonetheless, this mesh is resolved enough to avoid the use of a subgrid-scale model. This can be verified by analyzing the energy spectra of fluctuations on the plume axis and at the plume outer edges. Fig. 5.5.1 shows the energy spectra of temperature and pressure as a function of the non-dimensional frequency: the Strouhal number Str $= f * 2b_0/u_0$ (f is the frequency in [Hz]). A result similar to Plourde et al. [151] is recovered, where the inertial–convective regime with the decay $-5/3$ and the inertial–diffusive regime with the steeper decay -3 are observable [122].

Model results describe the establishment of the turbulent plume through the development of fluid-dynamic instabilities near the vent (puffing is clearly recognized as a toroidal vortex in Fig. 5.5.2a). The breaking of large-eddies progressively leads to the onset of the developed turbulence regime, which is responsible of the mixing with the surrounding ambient air, radial spreading of the plume and decrease of the plume average temperature and velocity. Fig. 5.5.2a displays the spatial distribution of gas temperature. Mixing becomes to be effective above a distance of about 4 diameters. Figure 5.5.2b displays the distribution of the vorticity, represented by values of the $Q_{\boldsymbol{u}}$ invariant (Eq. 5.2.15). The figure clearly identifies the toroidal vortex associated to the first instability mode (puffing, dominant at such Reynolds numbers). The other instability modes [helical and meandering, 116] have been observed only by increasing the forcing intensity (not shown).

Experimental observations by George et al. [83] and Shabbir and George [175] reveal that the behavior of forced plumes far enough from the inlet can be well described by integral one-dimensional plume models (cf. Sect. 3 and [138, 137]) provided that an adequate empirical entrainment coefficient is used. In the buoyant plume regime at this Reynolds number George et al. [83] obtained an entrainment coefficient of 0.153.

To compare numerical result with experimental observations and one-dimensional average plume models, the numerical results have been time-averaged between 4 and 10 s (when the turbulent regime was fully developed). Fig. 5.5.3 shows both an instantaneous and time averaged slice of the velocity field in the plume. The averaged velocity field shows the expected behavior, being approximately horizontal

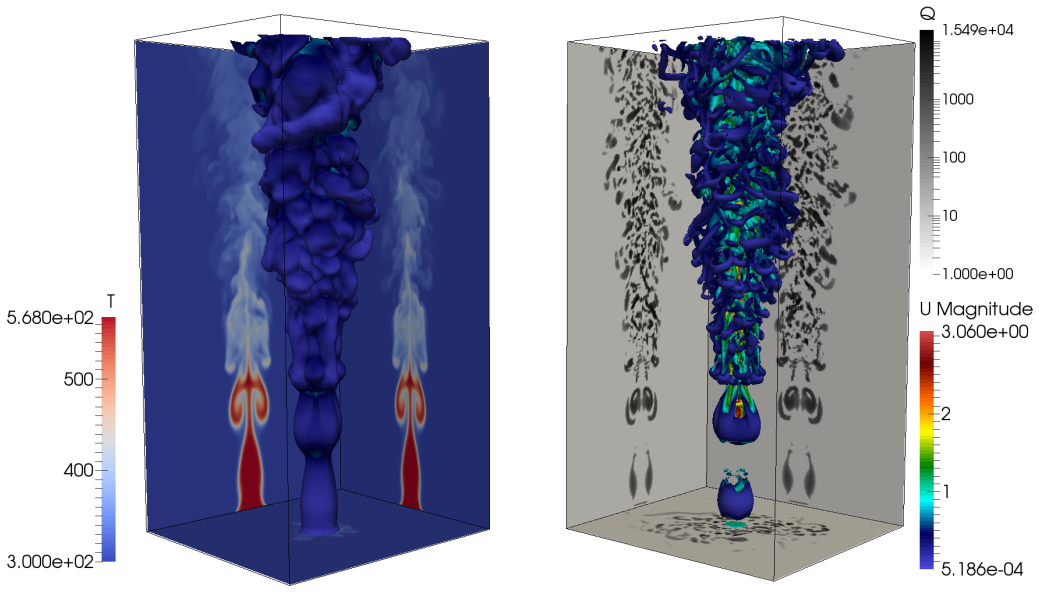

Figure 5.5.2: Three-dimensional numerical simulation of a forced gas plume at $t = 10s$. a) Isosurface of temperature $T = 305$ [K], colored with the magnitude of velocity, and the temperature distribution on two orthogonal slices passing across the inlet center. b) Isosurface of $Q_{\boldsymbol{u}} = 100$ [s^{-2}] colored with the value of the velocity magnitude, and its distribution across two vertical slices passing through the inlet center

outside the plume and vertical inside. Having performed the time average, the vertical mass $Q(z)$, momentum $M(z)$ and buoyancy $F(z)$ fluxes have been computed as a function of the height (see Sect. 3.11).

Fig. 5.5.4 displays the average plume radius and velocity. As previously reported by Fanneløp and Webber [66] and Plourde et al. [151], the plume radius initially shrinks due to the sudden increase of velocity due to buoyancy (at $z = 0.1$ m). Above, turbulent mixing becomes to be effective and increases the plume radius while decreasing the average velocity. The upper inset in Fig. 5.5.4 represents the values of the vertical mass $q = Q/Q_0$, momentum $m = M/M_0$ and buoyancy $f = F/F_0$, normalized with the inlet values. All variables have the expected trends and, in particular, the buoyancy flux is constant (as expected for weak ambient stratification) whereas q and m monotonically increase and attain the theoretical asymptotic trends shown also in Fig. 5.5.5. Indeed, Fanneløp and Webber [66] have shown that an integral plume model for non-Boussinesq regimes (i.e., large density contrasts) in the approximation of weak ambient stratification and adopting the Ricou and Spalding [160] formulation for the entrainment coefficient, has a first integral such that q^2 is proportional to $m^{5/2}$ at all elevations (cf. also Eq. (3.7.8)). Fig. 5.5.5 demonstrates that this relationship is well reproduced by the presented numerical simulations, as also observed in DNS by Plourde et al. [151].

The lower inset in Fig. 5.5.4 shows the computed entrainment coefficient, which is very close to the value found in experiments [83, 175] and numerical simulations [233] of an analogous forced plume. A value around $\varkappa \simeq 0.14$ is found in the buoyant plume region ($6.4 < z/2b_0 < 16$).

The analysis of radial profiles led to a similar conclusions: Fig. 5.5.6, shows

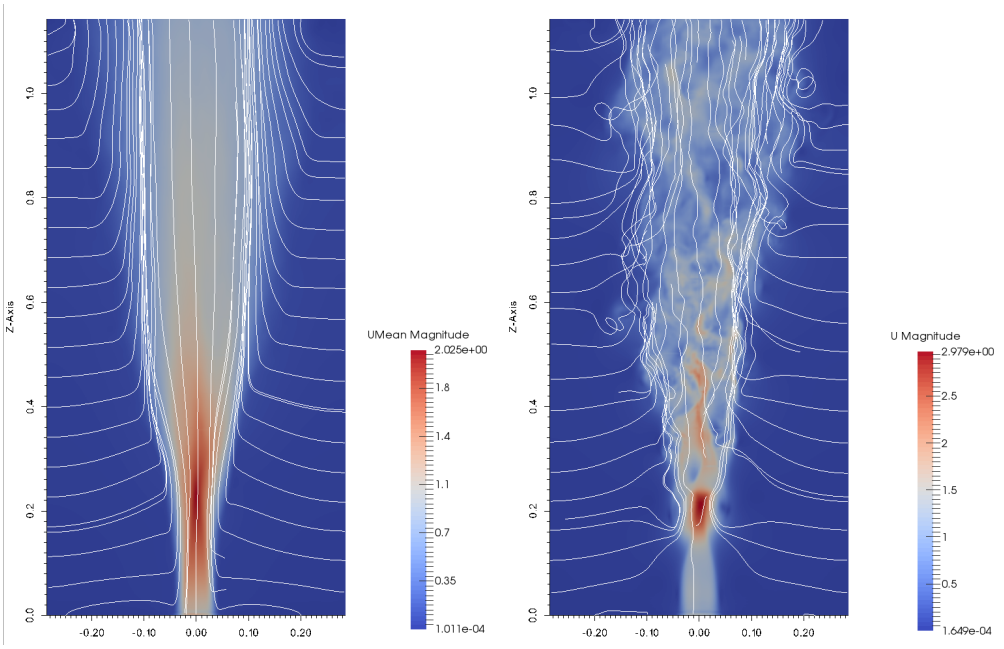

Figure 5.5.3: Two-dimensional slice and streamlines of the velocity field: a) time-averaged velocity field; b) instantaneous velocity field at $t = 10$ s. The mean velocity field outside the plume is approximatively horizontal while in the plume it is approximately vertical. The region where the mean velocity field change direction is the region where the entrainment of air by the plume occurs.

the evolution of the radial profiles for the mean vertical velocity field. This figure, also reports the plume radius as evaluated from Gaussian fits of these profiles on horizontal slices:

$$\bar{u}_z(x, y) = U_{\text{fit}} \exp\left(-\frac{x^2 + y^2}{b_{\text{fit}}^2}\right) . \tag{5.5.2}$$

The slope of the function $b_{\text{fit}}(z)$ has been evaluated in the region $6.4 < z/2b_0 < 16$, to obtain $b_{\text{fit}}/z = 0.142 \pm 0.001$ to be compared with the result of George et al. [83]: $b_{\text{fit}}/z = 0.135 \pm 0.010$.

Finally, Fig. 5.5.7 reports the time-average values of the vertical velocity and temperature along the plume axis. As observed in laboratory experiments, velocity is slightly increasing and temperature is almost constant up to above 4 inlet diameters, before the full development of the turbulence. When the turbulent regime is established, the decay of the velocity and temperature follows the trends predicted by the one-dimensional theory and observed in experiments. The insets displays the average value of the vertical velocity and temperature fluctuations along the axis. Coherently with experimental results [83], velocity fluctuations reach their maximum value and a stationary trend (corresponding to about the 30% of the mean value) at a lower height (about 3 inlet diameters) with respect to temperature fluctuations (which reach a stationary value about the 40% above 4 inlet diameters).

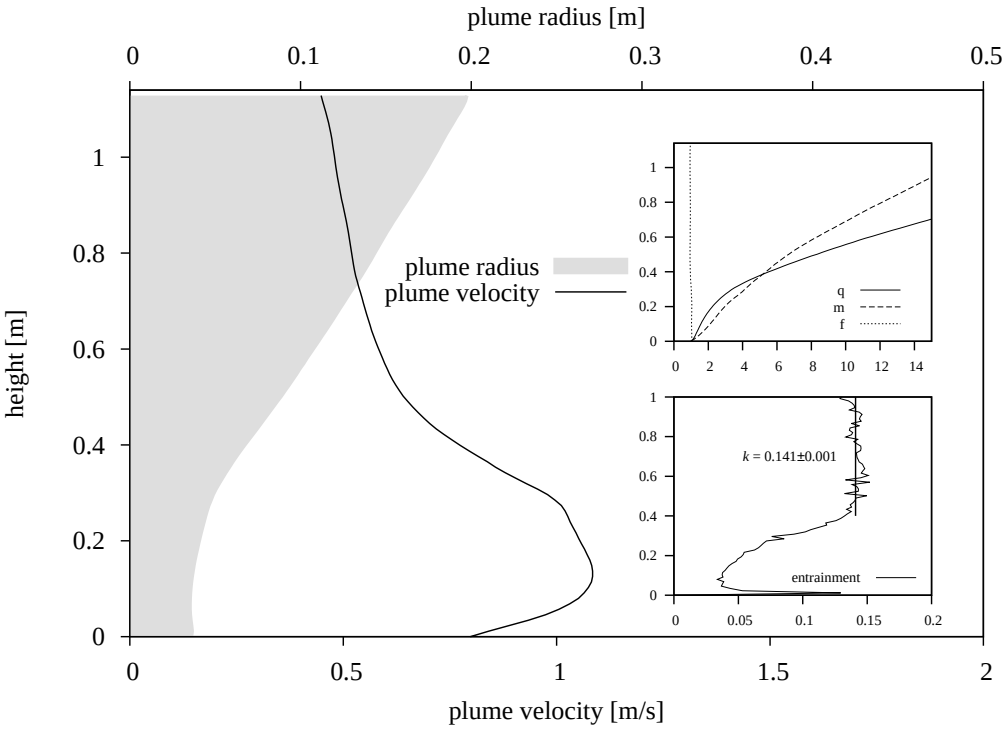

Figure 5.5.4: Time-averaged plume radius and velocity. The insets display the non-dimensional mass, momentum and buoyancy fluxes (top) and the time-averaged entrainment coefficient. The line in the entrainment panel is a constant fit, from which results $\varkappa = 0.141 \pm 0.001$.

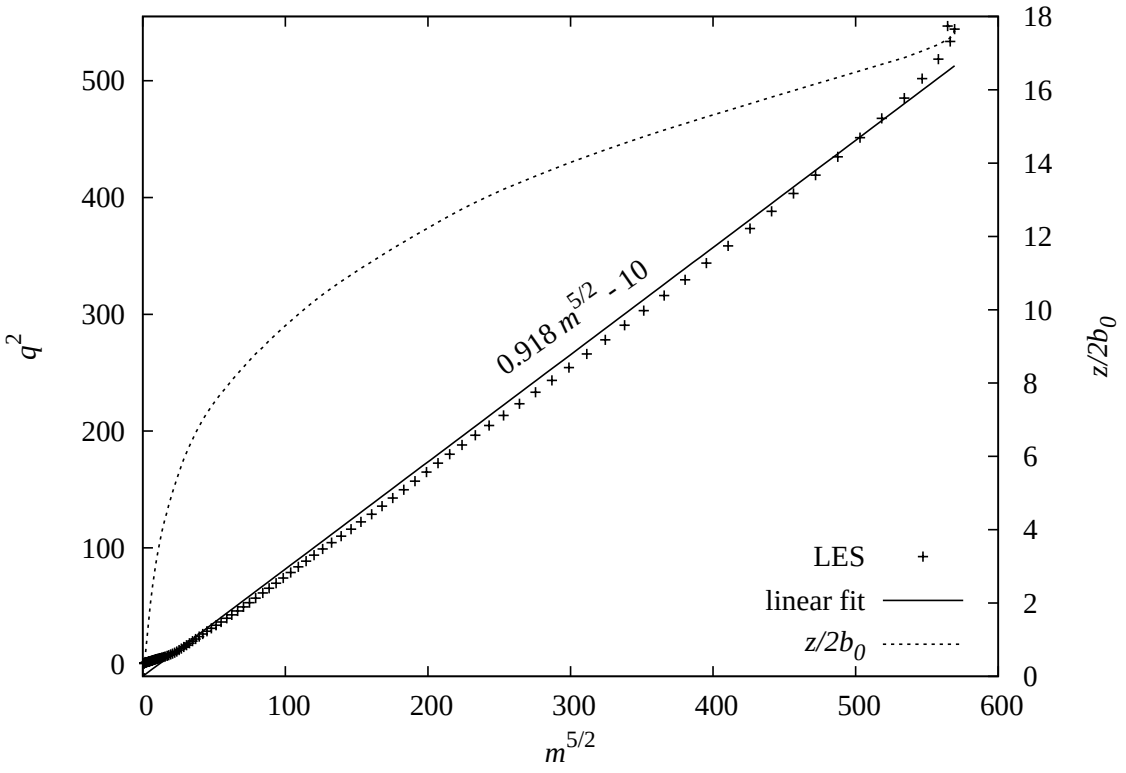

Figure 5.5.5: Linear regression between $m^{5/2}$ and q^2 for the plume simulation with azimuthal forcing.

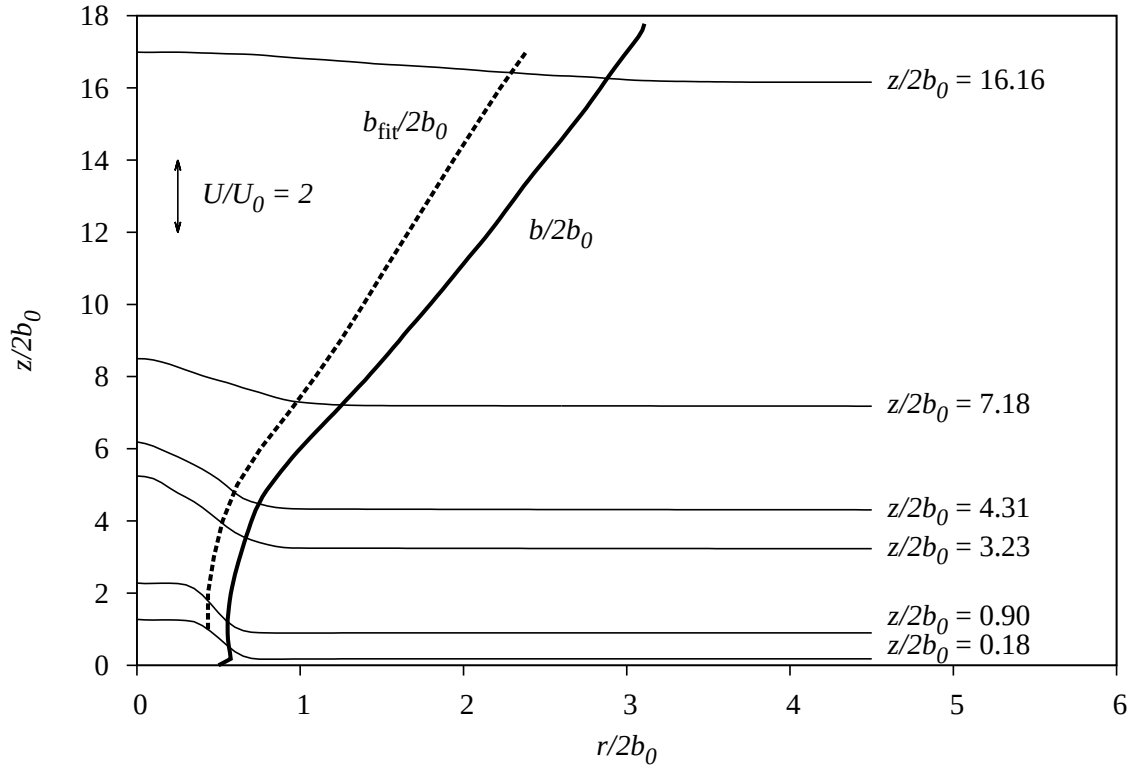

Figure 5.5.6: Radial profiles of the time-averaged velocity field at various height. The scale for these profiles is indicated by the up-down arrow on the left in the panel. The thick solid line is the plume radius evaluated from the mass, momentum and buoyancy fluxes, while the thick dashed line is the plume radius evaluated from Gaussian fits of horizontal profiles.

5.6 Sod's shock tube problem

In this section I want to test the behavior of the `ASHEE` code in presence of shocks. I choose the Sod's shock tube test case [181]. A gas with adiabatic index $\gamma = 1.4$ is let evolve in a one-dimensional domain of length 10 m. Zero gradient boundary conditions ($\partial_x(\cdot) = 0$) are imposed for all the variables u, p, T. Moreover, the numerical simulation is initialized dividing the domain in two symmetric subsets. In the first subset (spatial coordinate $x < 0$) I set $u = 0$, $p = 10^5$ Pa, $T = 348.432$ K, so that $\rho = 1$. In the second subset ($x > 0$), I set $u = 0$, $p = 10^4$ Pa, $T = 278.746$ K, so that $\rho = 0.125$ kg/m^3. I indicate with $c = 374.348$ m/s the speed of sound of the gas in the $x < 0$ part of the domain. As described in Sod [181], a reference analytic solution exists for this problem.

Fig. 5.6.1 shows the density profile obtained with the `ASHEE` numerical solver after 0.007 s of simulation. Two simulations at different resolution are performed. The first has 100 cells and it is compared with the OpenFOAM® solver `rhoCentralFoam` with a second order semi-discrete, non staggered central scheme of Kurganov et al. [114] for the fluxes, and a total variation diminishing limiter [204] for the interpolation. I refer to Greenshields et al. [92] for a presentation of `rhoCentralFoam` and of the Sod's shock tube test case. The inset of Fig. 5.6.1 is the simulation with an higher resolution: 1000 cells. This figure shows that the code performs satisfactorily both at low and high resolution. It is capable to capture the shocks pretty well, with a diffusion that is comparable with that obtained with `rhoCentralFoam`, a code

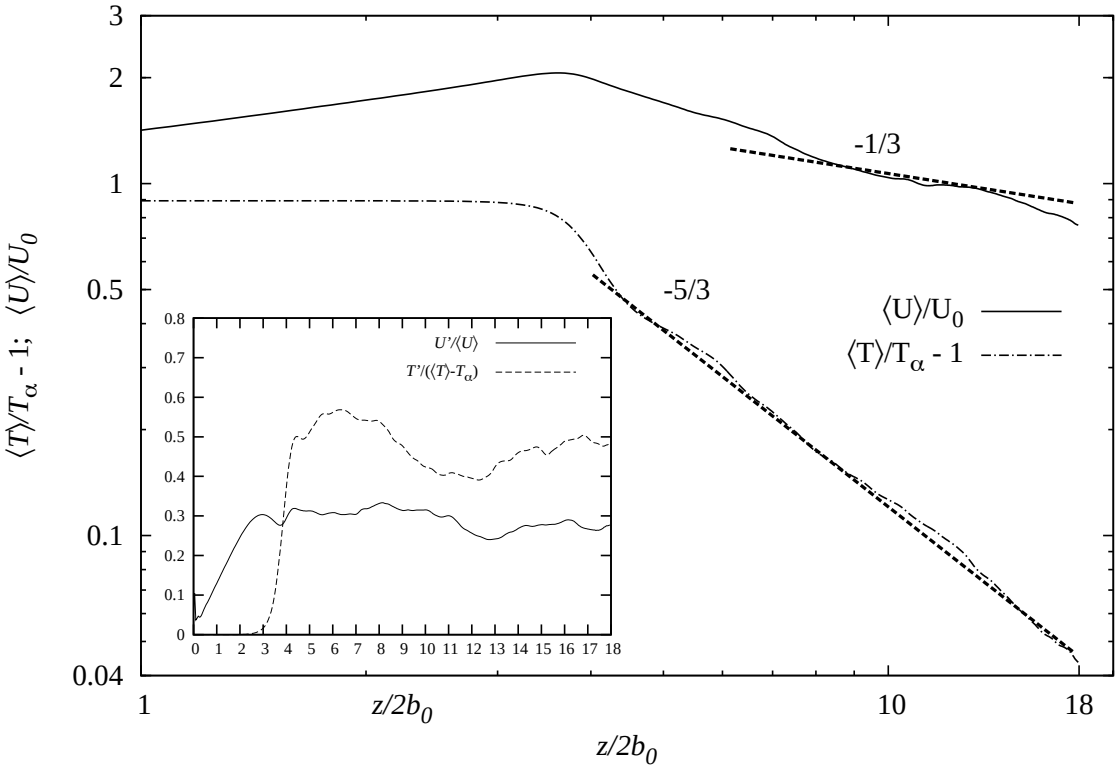

Figure 5.5.7: Centerline time-average axial velocity, and temperature profiles with azimuthal forcing. Inset) centerline correlations of fluctuating velocity and temperature.

thought for simulating shocks.

5.7 Turbulent mixing

In this section I stress `ASHEE` against the two-dimensional lock-exchange benchmark, where a fluid is filling a box separated in two sections by a locker. The locker is left open suddenly at $t = 0$, and the fluid starts to mix because of the gravity field. The reference papers with which I compare results are Özgökmen et al. [145], Berselli et al. [9]. There the density difference is caused by a small temperature contrast between the two sections. That configuration is modified slightly by adding a small amount of dust in one of the two domain section. As discussed in Berselli et al. [8], this configuration is analogous to the previous one, once the Prandtl number is left go to infinity (no molecular particle diffusion in the dusty gas model, cf. Sect. 1.2). The results presented here are an improvement of those published in Berselli et al. [8].

Such an experiment allows to test the capability of the numerical code to capture the turbulent mixing in a two-dimensional, wall bounded configuration.

The numerical domain is bounded with free-slip, thermally insulated wall boundary conditions (See Sect. 1.5). All the parameters have been made non-dimensional in order to mimic the initial conditions of Özgökmen et al. [145]. The two-dimensional domain has size $L \times H = 5 \times 2$, in a gravity field $g = 200$. The initial temperature is $T_0 = 1$, while the initial pressure is $p_0 = 4 * 10^9$ and the

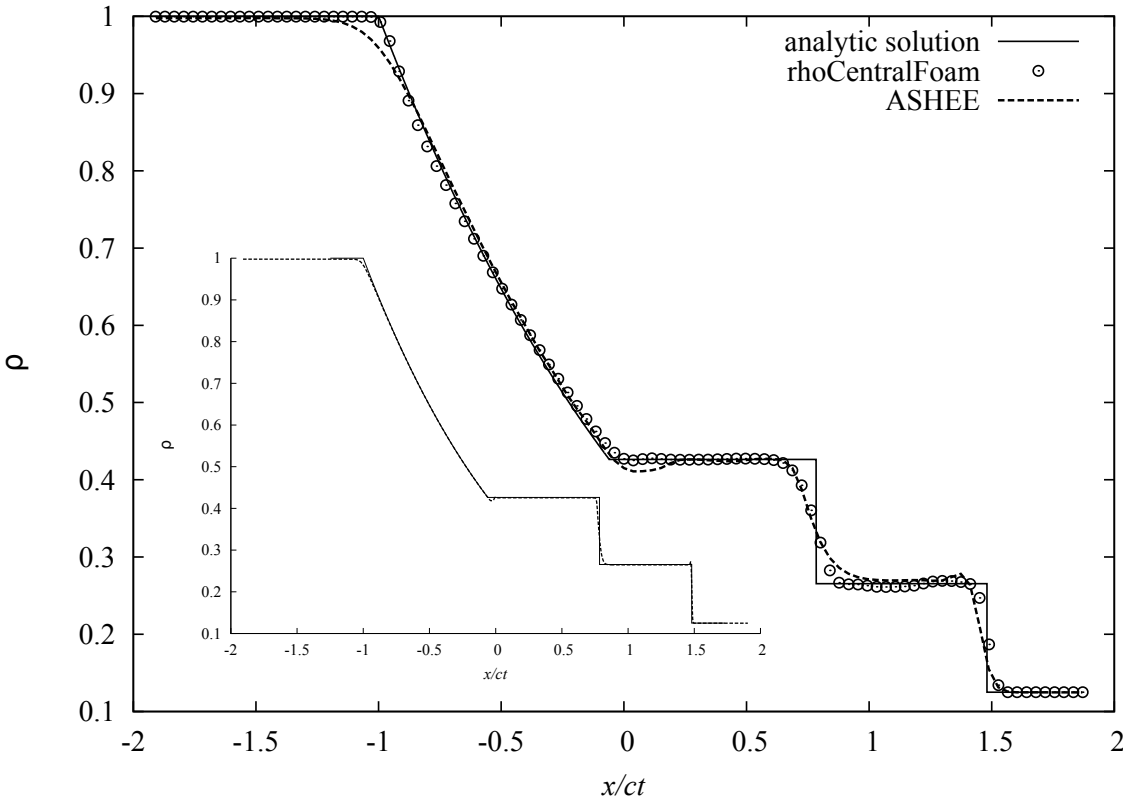

Figure 5.6.1: The Sod's shock tube density after 0.007 s (here $c = 374.348$ m/s). Here the analytic solution (solid) is compared with two simulations performed with `ASHEE` (dashed) and `rhoCentralFoam` (points) codes. The resolution is 100 cells, while in the inlet it is reported the `ASHEE` simulation with resolution equal to 1000 cells.

gas constant of the fluid is $R = 4 * 10^7$. Thus the initial density of the gas is $\rho_0 = 100$. Such a large pressure value is chosen in order to keep the mixture practically incompressible and to avoid fluid stratification ($p_0 \ll \rho_0 g H$). The fluid dynamic viscosity is $\mu = 0.02348837$. Particles with mass fraction $y_s = 0.01$ are added in the left half of the domain, to obtain $\rho_{s,0} = 1$. The Stokes number of the particles is left zero, in order to use the [dusty] model.

With this configuration, the relevant non-dimensional parameters of the lock-exchange benchmark become:

- the typical velocity

$$U = \frac{1}{2}\sqrt{\frac{g\rho_s H}{\rho_0}} = 1\,. \tag{5.7.1}$$

- the Froude number ($g' \equiv g\rho_s/\rho_0$, $\ell \equiv H/2 = 1$)

$$\mathrm{Fr} = \frac{U}{\sqrt{g'\ell}} = 2^{-1/2}\,. \tag{5.7.2}$$

- the Reynolds number

$$\mathrm{Re} = \frac{(\rho_0 + \rho_s)U\ell}{\mu} = 4300\,. \tag{5.7.3}$$

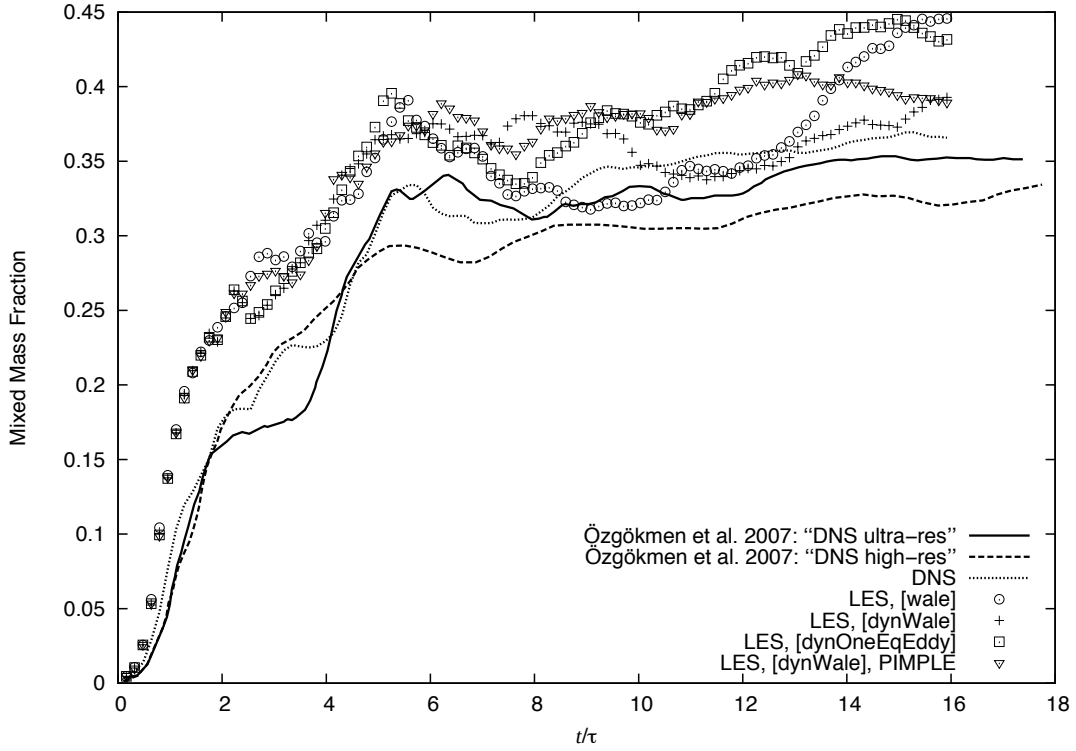

Figure 5.7.1: Evolution of MMF and comparison with the DNS presented in Özgökmen et al. [145]. Point type plots have been obtained by using the LES models described in Sect. 1.4.

- the Brunt-Väisälla buoyancy period, i.e. the natural time for gravity waves,

$$\tau_\omega = 2\pi \frac{H}{g'} = 2\pi \,. \tag{5.7.4}$$

- the Mach number

$$\mathrm{Ma} = \frac{U}{c} \simeq \sqrt{\frac{U^2 \rho_0}{\gamma p}} \simeq 1.34 * 10^{-4} \,. \tag{5.7.5}$$

The Prandtl number of the gas is arranged at 1, while the Prandtl number associated to the diffusion of ρ_s is theoretically infinity, since no dissipation for the solid phase is present in the [dusty] model (cf. 1.2). Only numerical and sub-grid scale diffusion is present.

The domain is discretized with an uniform mesh composed by $2300 \times 460 = 1.058 * 10^6$ square cells. This resolution is close to that which would be necessary to have a DNS [cf. 145]. The simulation have been ran until $t/\tau_\omega \simeq 16$, approximately seven full travel cycles [over $2L$, see 145]. The time-step is adaptive, controlled by the CFL condition $\mathrm{Co} < 0.2$. The Crank-Nicolson scheme and the TVD central interpolation scheme `[limLin]` described in Sect. 5.1 are selected. This simulations is performed on 62 processor in the HPC-SM2 cluster at INGV, Section of Pisa. The cores of this cluster are AMD Opteron$^{\mathrm{TM}}$ Processor 6274@2200 MHz. The DNS simulation took approximatively 5 days, solving the equations in the discretized domain at a velocity of 0.7 Mcells/s.

The accuracy of the DNS (for LES see the next section) is evaluated though *a posteriori* comparison. Two quantities have been used for this scope. The first, used in Özgökmen et al. [145], is the Mixed Mass Fraction MMF. It is the fraction of mixed mass in the range $[\frac{1}{3}, \frac{2}{3}]$ (here m_s is the total mass of the solid phase in Ω):

$$\Omega_3(t) = \left\{ \boldsymbol{x} \in \mathbb{R}^2 \,|\quad \frac{1}{3} < \frac{\rho_\mathrm{s}(\boldsymbol{x},t)}{\rho_{\mathrm{s},0}} < \frac{2}{3} \right\} \tag{5.7.6}$$

$$\mathrm{MMF}(t) = \frac{1}{m_\mathrm{s}} \int_{\Omega_3} \mathrm{d}\boldsymbol{x}\, \rho_\mathrm{s}(\boldsymbol{x},t)\,. \tag{5.7.7}$$

The other quantity is the more correct mathematical formulation for measuring the mixing. It is the Reference/background Potential Energy RPE. It is measuring the potential energy of a density distribution in its adiabatically equivalent minimum potential energy status. The more the mixing increases, the more RPE increases. On his basis, the Available Potential Energy is defined. It is the difference between the Potential Energy and the Reference Potential Energy: $\mathrm{APE} \equiv \mathrm{PE} - \mathrm{RPE}$. Namely, APE is the effective mechanical energy that can be transformed into kinetic energy. These concepts have been introduced by Lorenz [125] and formalized by Winters et al. [221], Winters and Barkan [220]. The faster algorithm I used to calculate it is described in Tseng and Ferziger [198]. To calculate RPE, the reference height must be defined (here $\mathcal{H}$ is the Heaviside step function):

$$z_\mathrm{r}(\rho(\boldsymbol{x},t)) = \frac{1}{L} \int_\Omega \mathrm{d}\boldsymbol{x}'\, \mathcal{H}(\rho(\boldsymbol{x}',t) - \rho(\boldsymbol{x},t))\,, \tag{5.7.8}$$

which is the height of the portion of fluid with density ρ when the fluid is its minimum potential energy state. Starting from this height, the reference potential energy and the available potential energies are defined:

$$\mathrm{RPE}(t) = g \int_\Omega \mathrm{d}\boldsymbol{x}\, \rho_\mathrm{s}(\boldsymbol{x},t) z_\mathrm{r}(\rho_\mathrm{s}(\boldsymbol{x},t)) \tag{5.7.9}$$

$$\mathrm{APE}(t) = \int_\Omega \mathrm{d}\boldsymbol{x}\, \rho_\mathrm{s}(\boldsymbol{x},t) |\boldsymbol{x}\cdot\boldsymbol{g}| - \mathrm{RPE}(t)\,. \tag{5.7.10}$$

These quantities are numerically evaluated by dividing the density range in N_ρ bins, as described in Tseng and Ferziger [198]. RPE is then made dimensionless as follows:

$$\mathrm{RPE}^* = \frac{\mathrm{RPE}(t) - \mathrm{RPE}(0)}{\mathrm{RPE}(0)}\,. \tag{5.7.11}$$

By using MMF and RPE^* the mixing evolution of the present DNS is compared with the DNS results presented in Özgökmen et al. [145]. Figs. 5.7.1 and 5.7.2 show the results obtained.

Fig. 5.7.3 shows a snapshot of ρ_s for the present DNS simulation in $t/\tau_\omega \simeq 1.114$. That snapshot is similar and can be compared with Fig. 3 in Özgökmen et al. [145] for a qualitative analysis. In [LEX] it is possible to find a movie of the numerical simulation commented in Berselli et al. [8].

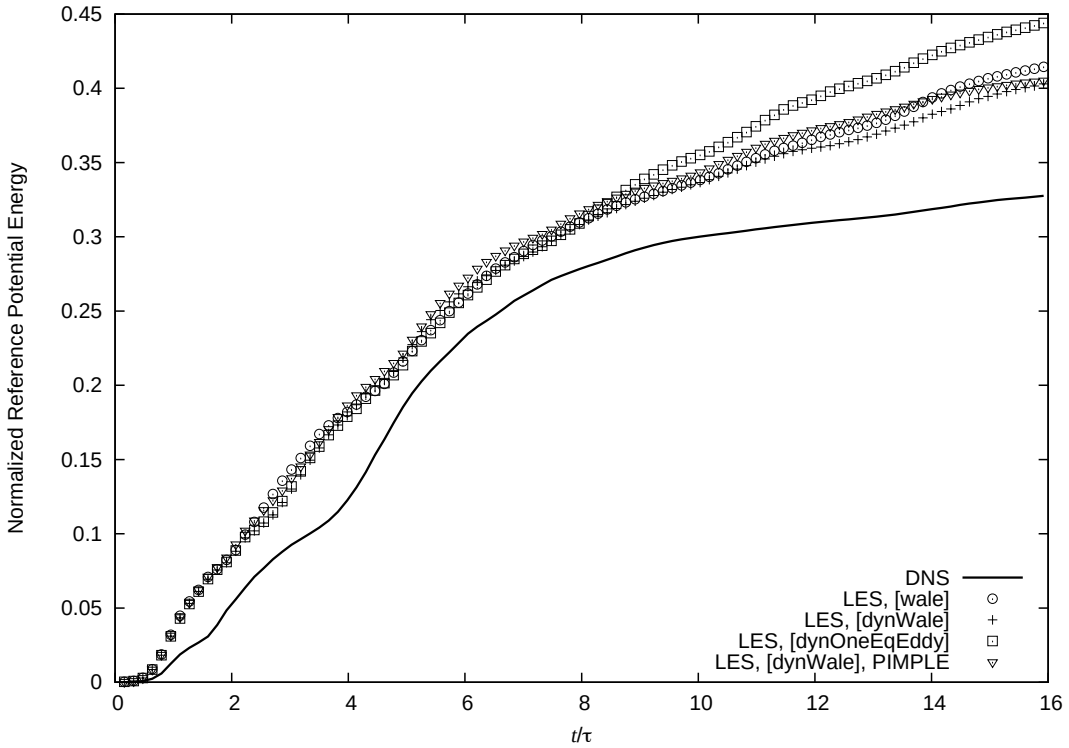

Figure 5.7.2: Evolution of RPE*. Point type plots have been obtained by using the LES models described in Sect. 1.4.

5.7.1 Effect of the subgrid scale models

Large Eddy Simulations in a coarse mesh (230×46 square cells) have been performed to evaluate the performances of the sub-grid models presented in Sect. 1.4. I want to test their capability to capture turbulence mixing when the resolution is low. I selected three among them, because in this test case are present walls. Indeed, LES in presence of walls can be problematic and particular care must be taken into account [see i.e. 145]. Thus, between the static LES models I choose to test only [wale], which naturally send to zero the subgrid terms near the wall. On the other hand, dynamic sub-grid models, can handle the presence of walls, thus I decided to test here two of them: [dynWale] and [dynOneEqEddy]. In the DNS, one PIMPLE loop is enough to reach a good convergence level [as expected, cf. 75]. However, small differences could be seen in the coarse LES. I tested the effect of increasing the number of PIMPLE steps with the [dynWale] model. Results are shown in Fig. 5.7.1, 5.7.2 and 5.7.3. Each simulation took approximatively half an hour on a normal laptop, and one hour with three PIMPLE loops.

5.7.2 Discussion

In this section I have compared the performances of `ASHEE` against the lock-exchange benchmark problem. I analyze results by using two quantities measuring the rate of mixing in a gravity current. The first is the Mixed Mass Fraction MMF. Fig. 5.7.1 compares it with the DNS performed in Özgökmen et al. [145]. The MMF evolution from the presented DNS is comparable with that obtained by Özgökmen et al. [145]. The present MMF is between their "high-res" and "ultra-res" resolution

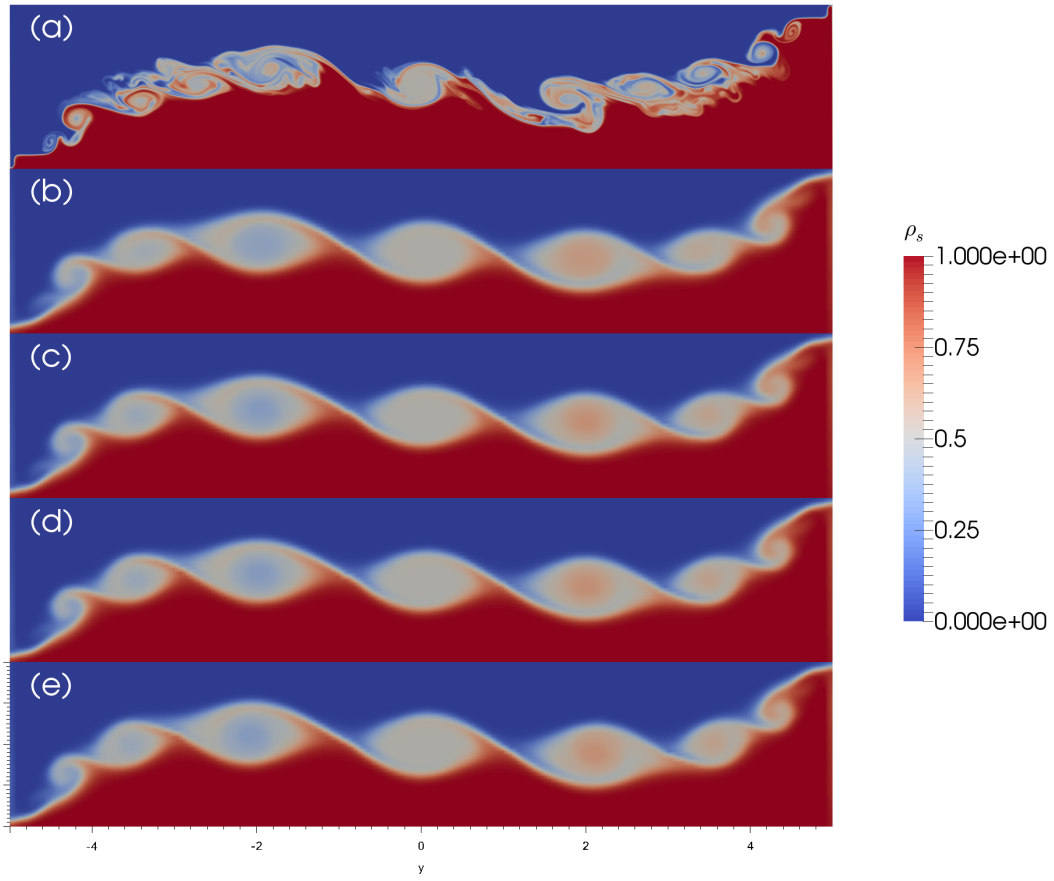

Figure 5.7.3: Snapshot of the solid phase bulk density in the lock exchange simulations after $t/\tau_\omega \simeq 1.114$. Different LES models are compared with the DNS (a): b) [wale]; c) [dynWale]; d) [dynOneEqEddy]; e) [dynWale] with three PIMPLE iterations.

in the fist stage of the evolution and after it is slightly larger than both. However, the error between the `ASHEE` DNS and the Özgökmen et al. [145] "ultra-res" DNS is comparable with that between the latter and the Özgökmen et al. [145] "high-res" DNS. The LES performed are more diffusive than the DNS, implying a larger mixing between the two phases. The [dynWale] subgrid model is that performing well, both in its PISO and PIMPLE configuration.

Even if in Özgökmen et al. [145] MMF has been used, the quantity more suited to measure turbulent mixing is the Reference Potential Energy RPE. In Berselli et al. [9] that quantity has been used to measure the turbulent mixing in a lock-exchange problem analogous to that studied here, but in three-dimensional setting. Moreover, in that simulation they imposed $\mathrm{Re} \simeq 10^4$. By comparing their result with the DNS presented in Fig. 5.7.2, I found that the RPE evolution profile follows the same qualitative behavior. However, in the two-dimensional simulation turbulent mixing is stronger than that obtained from the three-dimensional simulation: $\mathrm{RPE}^*(t = 16\,\tau_\omega) \simeq 0.33$ in two-dimensions while $\mathrm{RPE}^*(t = 16\,\tau_\omega) \simeq 0.26$ in three-dimensions. Consequently, one can expect that gravity currents modeled in two dimensional symmetry would entrain the surrounding fluid at a faster rate than in three-dimensional simulations.

Moving to comment the LES result reported in Fig. 5.7.2, it is worth noting that again the best simulations are those performed with the [dynWale] model, and that the [dynOneEqEddy] model is the most diffusive. The turbulent mixing is overestimated of a factor $\simeq 25$ % for the coarse LES here performed. The result is comparable with that obtained in Özgökmen et al. [145]. For static models, they found that increasing the subgrid model constant decreases the turbulent mixing.

Chapter 6

Volcanic plume simulations.

I apply the ASHEE numerical code to two volcanic eruption benchmarks: [weakPlume] and [strongPlume]. These simulations were conducted in the framework of the IAVCEI (International Association of Volcanology and Geochemistry of the Earth Interior) plume model intercomparison initiative [39], consisting in performing a set of simulations using a standard set of input parameters so that independent results could be meaningfully compared and evaluated, discussing different approaches, and identifying crucial issues of state of the art models. In Costa et al. [39] and Suzuki et al. [188] the results of the ASHEE model are compared with: SK-3D) the dusty gas model by Suzuki et al. [192]; ATHAM) the dusty gas model with particle settling and microphysics by Oberhuber et al. [143], Herzog et al. [100], Graf et al. [90]; PDAC) the multiphase Eulerian-Eulerian model by Neri et al. [141], Esposti Ongaro et al. [64]. Significant differences between the models are present for the [strongPlume] eruption, and further analysis is necessary to better understand why those differences are present. Some additional detail about non-equilibrium processes and large-eddy simulations of volcanic ash plumes can be found respectively in Esposti Ongaro and Cerminara [63] and Cerminara et al. [33].

In Sect. 6.3, I discuss three-dimensional numerical simulation of [weakPlume], a weak volcanic plume in a stratified, calm atmosphere, whose input data were set assuming source conditions and atmospheric profiles similar to those of the 26 January 2011 Shinmoe-dake eruption [191]. Then in Sect. 6.4, I modify initial and boundary conditions to discuss numerical simulations of [strongPlume], a strong volcanic plume, whose conditions are similar to those of the 15 June 1991 Pinatubo eruption [see e.g. 102]. Initial conditions and source parameters for these two eruptions are reported in Table 6.0.1.
The non-dimensional configuration parameters for these two eruptions are summarized in Tab. 3.4.2. Initial atmospheric conditions are described in the Sect. 6.1. The setting for the cylindrical mesh are described in Sec.6.2 and in Tab. 6.2.1.

6.1 Initial atmospheric conditions

The initial conditions for the atmosphere are based on atmospheric measurements provided in the framework of the IAVCEI intercomparison exercise [see 39]. In this thesis, the data provided respectively by the Japan Meteorological Agency's

Parameter	[weakPlume]	[strongPlume]
Vent elevation	1500 m	1500 m
Vent diameter	54 m	1406 m
Mass eruption rate	$1.5 * 10^6$ kg/s	$1.5 * 10^9$ kg/s
Exit velocity	135 m/s	275 m/s
Exit temperature	1273 K	1053 K
Exit water fraction	3 wt.%	5 wt.%
Mixture density at vent	4.85 kg/m^3	3.51 kg/m^3

Table 6.0.1: Vent conditions for the [weakPlume] and [strongPlume] volcanic simulations.

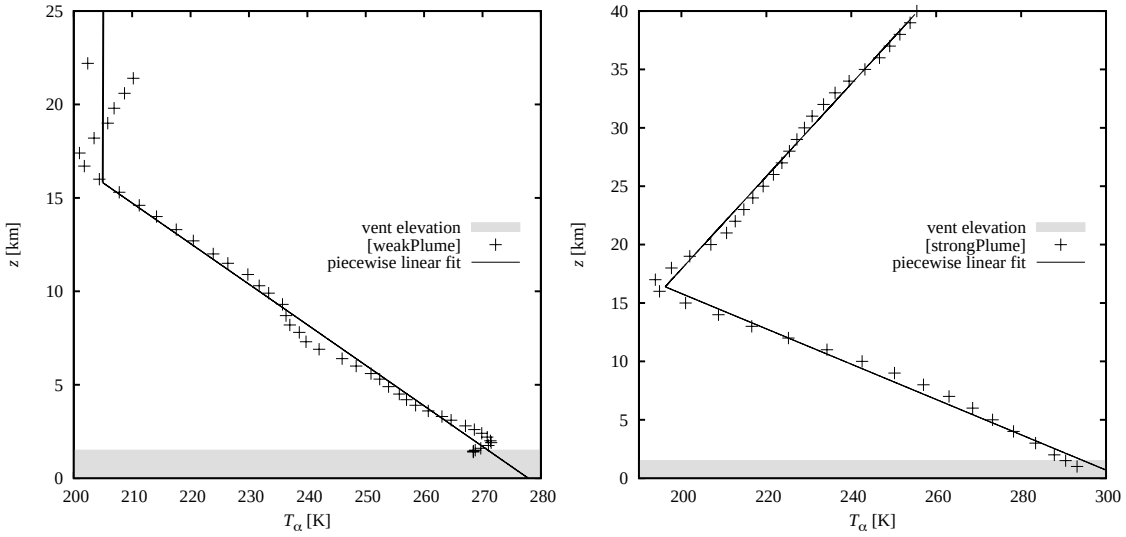

Figure 6.1.1: Atmospheric profiles used for the atmosphere of the two volcanic plume simulations (height z km, with respect atmospheric temperature T_α K): left) [weakPlume]; right) [strongPlume]. The domain for the [strongPlume] case extends up to 50 km. The thermal profile gradient from 40 to 50 km is assumed to be the same obtained below 40 km. The parameters obtained in the piecewise fit are reported in Tab. 6.1.1.

Non-Hydrostatic Model [see 99] and by the European Centre for Medium-Range Weather Forecast [ECMWF, see 38] are fitted with piece-wise linear functions (see Fig. 6.1.1) for the temperature, and a hydrostatic profile for the pressure ($\mathrm{d}_z p = -\alpha g$) is assumed. By using Eq. (3.4.6) and defining the atmospheric thermal gradient $\theta_{\alpha,i}$ when $z \in [z_i, z_{i+1}]$, I obtain for $z \in [z_k, z_{k+1}]$

$$T(z) = T_{\alpha,0} + \sum_{i=0}^{k-1} \theta_{\alpha,i}(z_{i+1} - z_i) + \theta_{\alpha,k}(z - z_k) \tag{6.1.1}$$

$$T_{\alpha,k} = T_{\alpha,0} + \sum_{i=0}^{k-1} \theta_{\alpha,i}(z_{i+1} - z_i) \tag{6.1.2}$$

$$p(z) = p_0 \prod_{i=0}^{k-1} \left(1 + \frac{\theta_{\alpha,i}}{T_{\alpha,i}}(z_{i+1} - z_i)\right)^{-\frac{g}{R_\alpha \theta_{\alpha,i}}} \left(1 + \frac{\theta_{\alpha,k}}{T_{\alpha,k}}(z - z_k)\right)^{-\frac{g}{R_\alpha \theta_{\alpha,k}}} . \tag{6.1.3}$$

In this thesis, the atmosphere is assumed to be dry (no humidity).

U_i [m/s]	b_0 [m]	A_φ -	σ_0 -	N_φ -	Str -	T_0 [K]	T_α [K]	p_0 [Pa]	$\theta_{\alpha,0}$ [K/m]	$\theta_{\alpha,1}$ [K/m]	z_1 [m]
151.8	27.06	0.035	0.05	6	0.35	1273	270.92	85918.7	-0.004607	0	14317.2
306.0	702.8	0.035	0.05	6	0.35	1053	294.66	85496.2	-0.006615	0.002522	14889.1

Table 6.1.1: Configuration parameters for the boundary and initial conditions. The two rows correspond to the [weakPlume] and [strongPlume] numerical experiments, respectively. In both cases $g = 9.80665$ m/s^2.

As already done in Sec. 5.5, the boundary conditions in the vertical and top sides of the domain have atmospheric boundary conditions (see Sect. 1.5.2), while the bottom wall has a thermally insulated no-slip wall condition, see 1.5.1. The inlet velocity has the same profile introduced in (1.5.10) with a superimposed white noise with standard deviation σ_0 and an asymmetric forcing (cf. Eq. (1.5.13) and (1.5.17)). I choose to introduce anisotropy to the forcing at the inlet to emulate small vent instabilities.

At the inlet, temperature is fixed to T_0, pressure is calculated on the basis of the velocity field (I do not consider the effect of overpressured eruptions), and the mass fractions of the gaseous and solid phases are fixed respectively to $y_{i,0}$ and $y_{j,0}$.

Tab. 6.1.1, summarizes the configuration parameters used for the boundary and initial conditions of the volcanic plume simulations.

The particle size distribution of [weakPlume] is composed of two individual classes of pyroclasts in equal weight proportion representing, respectively, fine (diameter $d = 0.0625$ mm; density $\hat{\rho} = 2700$ kg/m^3, volume fraction $\epsilon = 0.00086821$, mass fraction $y = 0.485$) and coarse ash (diameter $d = 1.0000$ mm; density $\hat{\rho} = 2200$ kg/m^3, volume fraction $\epsilon = 0.00106553$, mass fraction $y = 0.485$).

The particle size distribution of [strongPlume] is composed of two individual classes of pyroclasts in equal weight proportion representing, respectively, fine (diameter $d = 0.015625$ mm; density $\hat{\rho} = 2700$ kg/m^3, volume fraction $\epsilon = 0.0006175$, mass fraction $y = 0.475$) and coarse ash (diameter $d = 0.5000$ mm; density $\hat{\rho} = 2500$ kg/m^3, volume fraction $\epsilon = 0.0006669$, mass fraction 0.475).

6.2 Plume domain meshing

The mesh is hexahedral in cylindrical geometry. Its topology is sketched in Fig. 6.2.1. It is composed by four blocks:

- square $(\cdot)_\mathrm{sq}$: an hexahedra with dimensions $2b_\mathrm{sq} \times 2b_\mathrm{sq} \times z_\Omega \times 2r_\mathrm{sq} \times 2r_\mathrm{sq}$
- vent $(\cdot)_\mathrm{vnt}$: a truncated cone with dimensions $b_\mathrm{vnt} \times z_\Omega \times r_\mathrm{vnt}$
- outer cone $(\cdot)_\mathrm{cn}$: a truncated cone with dimensions $b_\mathrm{cn} \times z_\Omega \times r_\mathrm{cn}$
- outer cylinder $(\cdot)_\Omega$: a cylinder with dimensions $r_\Omega \times z_\Omega$

I choose $b_\mathrm{sq} = b_0/2$, $b_\mathrm{vnt} = b_0$ and $b_\mathrm{cn} = 5/2\, b_0 = 5b_\mathrm{sq}$.

I define the resolution n_Ω so that the number of cells in the square inside the inlet circle is n_Ω^2, while it is $3n_\Omega^2$ cells in the inlet and $9n_\Omega^2$ in each horizontal slice of the outer cone. The smallest cell size is defined by $\delta = b_0/n_\Omega$.

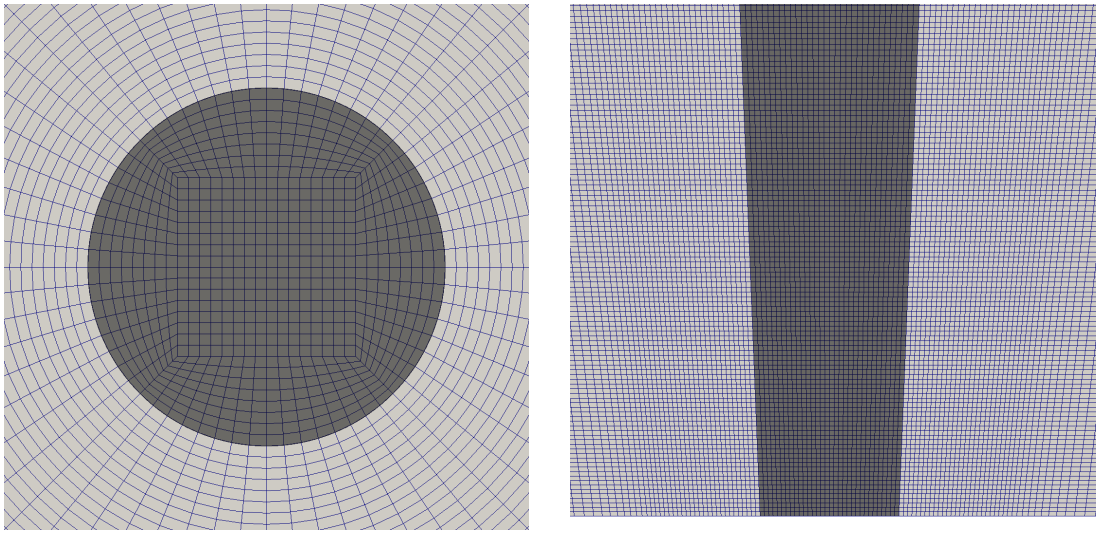

(a) Horizontal cut **(b)** Vertical cut

Figure 6.2.1: Two slices of the mesh for the plume domain with $n_\Omega = 0.16$ and $\tan\theta_\Omega = 0.04$. Shaded surfaces represent the area invaded by the inlet extruded mesh.

It is graded with a geometric progression law in both the axial and radial directions, with a spreading angle of the hexahedra θ_Ω. The size of a cell near the inlet is $\delta_{\text{inlet}} \simeq b_0/n_\Omega$, while at the top of the domain it is $\delta_{\text{top}} \simeq (b_0 + z_\Omega \tan\theta_\Omega)/n_\Omega$.

In order to apply a grading to the mesh cells, a geometric progression for the cell size is used, following the rule:

$$\delta_n = \delta_1\, g^{n-1} \qquad \text{size of the nth cell} \tag{6.2.1}$$

$$\delta = \delta_1 = \ell\frac{g-1}{g^N-1} \qquad \text{size of the smallest cell} \tag{6.2.2}$$

$$g = G^{\frac{1}{N-1}} \qquad G \text{ is the grading factor} \tag{6.2.3}$$

$$\delta_N = G\,\delta_1 = \ell\frac{G^{\frac{N}{N-1}}-G}{G^{\frac{N}{N-1}}-1} \qquad \text{size of the biggest cell}\,, \tag{6.2.4}$$

so that $\sum \delta_n = \ell$ and $\delta_N/\delta_1 = G$. Given ℓ, the number of cells N and the smallest cell δ, the equation giving G is:

$$G^{\frac{N}{N-1}} - N\frac{\ell}{N\delta}G^{\frac{1}{N-1}} + N\frac{\ell}{N\delta} - 1 = 0\,, \tag{6.2.5}$$

which for $N \to \infty$ tends to (to obtain the result make the derivative and do the limit. Then integrate back the limit derivative)

$$G_\infty - 1 - \frac{\ell}{N\delta}\ln G_\infty = 0\,, \tag{6.2.6}$$

with solution represented in Fig. 6.2.2.

The domain extends in the vertical direction with a grading depending on the spreading rate of the mesh from the vent to the top of the domain.

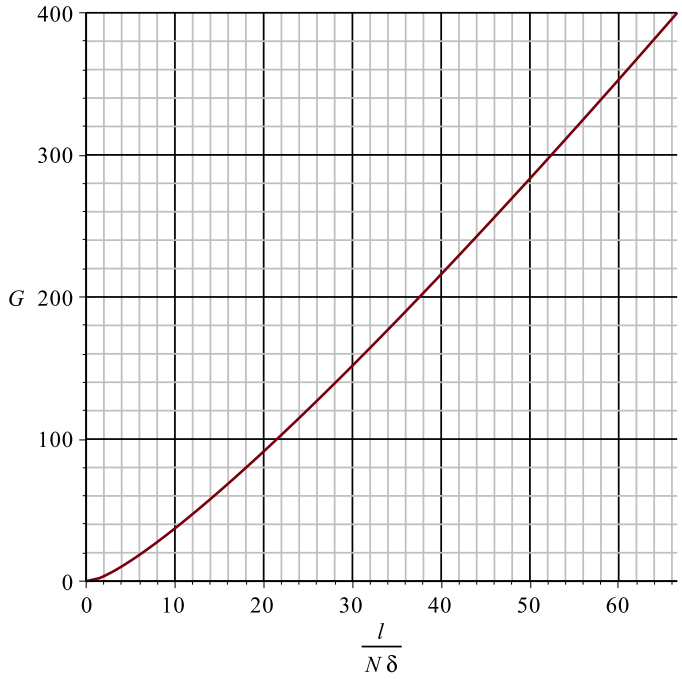

Figure 6.2.2: Dependence of the grading factor G on the stretching $\ell/N\delta$.

I define $\tan\theta_\Omega$ the slope of the spreading of the vent block (from $b_{\rm vnt} = b_0$ to $r_{\rm vnt}$):

$$\tan\theta_\Omega = \frac{r_{\rm vnt} - b_0}{z_\Omega}\,. \tag{6.2.7}$$

Choosing $r_{\rm sq} = r_{\rm vnt}/2$ and $r_{\rm cn} = 5/2\, r_{\rm vnt}$, the slopes of the inner square and outer cone domains are respectively:

$$\frac{r_{\rm vnt}/2 - b_0/2}{z_\Omega} = \frac{1}{2}\tan\theta_\Omega \tag{6.2.8}$$

$$\frac{5r_{\rm vnt}/2 - 5/2 b_0}{z_\Omega} = \frac{5}{2}\tan\theta_\Omega\,. \tag{6.2.9}$$

Because of this mesh spreading, the size of the top cells must be $\delta_{\rm top} = r_{\rm vnt}\,\delta/b_0$ where

$$r_{\rm vnt} = b_0 + z_\Omega\,\tan\theta_\Omega\,. \tag{6.2.10}$$

Thus, the vertical grading is $G_z = r_{\rm vnt}/b_0$. Using Eq. (6.2.6), the number of cells in the vertical direction must be:

$$N_z = \frac{z_\Omega}{\delta}\frac{\ln G_z}{G_z - 1}\,. \tag{6.2.11}$$

Defining N_Ω the number of cells in the outer cylinder, the size δ_Ω has been selected in order to have an homogeneous mesh at the top. Thus:

$$r_\Omega = r_{\rm cn} + N_\Omega\delta_{\rm top} = r_{\rm vnt}\left(\frac{5}{2} + \frac{N_\Omega}{n_\Omega}\right)\,. \tag{6.2.12}$$

Plume	$\tan\theta_\Omega$	z_Ω/b_0	N_Ω/n_Ω	n_Ω	G_z	N_z/n_Ω	r_Ω/b_0	G_Ω
[weakPlume]	0.0588	765	8	$4 \div 16$	46	64	483	287
[strongPlume]	0.0423	71	14	$2 \div 16$	4	33	66	12

Table 6.2.1: Mesh parameters for the two numerical plume cases studied in this chapter. In the [weakPlume] test case $G_\Omega < G_\infty = 353$ (cf. Eq. (6.2.6)) because the stretching is very high and its value is adapted to the mesh resolution.

Now, the right radial grading in the outer cylinder G_Ω must be found, in order to have vertical external walls. At the bottom, the size of the outer cylinder is:

$$\ell_\Omega = r_\Omega - b_{\rm cn} = z_\Omega \left(\frac{5}{2} + \frac{N_\Omega}{n_\Omega}\right) \tan\theta_\Omega + b_0 \frac{N_\Omega}{n_\Omega}\,, \tag{6.2.13}$$

thus

$$\frac{\ell_\Omega}{N_\Omega \delta} = \frac{z_\Omega}{b_0} \left(\frac{5 n_\Omega}{2 N_\Omega} + 1\right) \tan\theta_\Omega + 1\,. \tag{6.2.14}$$

with N_Ω cells and the smallest cell of size δ. Eq. (6.2.6) is used to find G_Ω.

Summarizing, given b_0, the parameters to be furnished in this plume mesh are: $\tan\theta_\Omega$, z_Ω/b_0, N_Ω/n_Ω and n_Ω. Tab. 6.2.1 reports the values of these parameters for the two volcanic plume cases considered in this thesis.

Inside the outer cone, the minimum cell size is b_0/n_Ω, while the maximum is given by the horizontal size of the top plume-edge cell: $\delta_{\rm edge}/\delta = 5\pi G_z/4$. The total number of cells is $(4N_\Omega + 9n_\Omega)N_z n_\Omega$.

6.3 Numerical simulations of [weakPlume]

With respect to the laboratory benchmark case of Sect. 5.5, volcanic plumes are characterized by: 1) a strong density contrast at the vent, with the initial mixture density about 4 times larger than the atmospheric one; 2) buoyancy reversal in a stratified atmosphere (Fig. 6.1.1); 3) a strong temperature contrast ($\simeq 900$ K); 4) the presence of a high particle content affecting the mixing properties of the plume.

The Stokes number of the solid particles is, in general, a nontrivial function of time and space, since the turbulent flow is characterized by a wide spectrum of relevant time and length scales. Generally, the Stokes number is associated with the most energetic turbulent eddy scale which, in analogy with laboratory plumes, has a typical turnover time of the order of $\tau_L \sim {\rm Str}\frac{D}{U_0} \approx 0.12$ s, where D and U_0 are the plume diameter and velocity at the vent, respectively, and Str is the Strouhal number, of the order ${\rm Str} = 0.3$ [233]. Based on this time scale, and computing the particle relaxation time from Eq. 4.2.4, the Stokes number for the two adopted particle classes in the [weakPlume] case is about ${\rm St}_{\rm coarse} \approx 5$ and ${\rm St}_{\rm fine} \approx 0.2$, so one expects to see non-equilibrium phenomena for both particles classes, with more evident effects on the coarsest phase. However, the Stokes number, as an average value in all the plume, is not as high as calculated above. Indeed, by using the Taylor microscale Eq. (5.3.6) as reference time for the turbulent dynamics, I obtain ${\rm St}_{\rm coarse} \approx 0.1$ and ${\rm St}_{\rm fine} \approx 0.005$. This result has been obtained *a posteriori*, for

the finer mesh resolution, having $\xi \approx 40$ m, $K \approx 218$ m^2/s^2 and $\lambda_T \approx 231$ m, when the plume reaches its maximum height. It is worth recalling here that the equilibrium–Eulerian approach is accurate and advantageous for particles having $\mathrm{St} \leq 0.2$ and that, in the `ASHEE` model, the acceleration field is numerically limited in order to keep the turbulent non-equilibrium within this limit, as explained in Sect. 5.1 and tested in Sect. 5.3 (Fig. 5.3.3). The average value of this limit – measuring the importance of the decoupling limiter for this simulation – is approximately 0.6 (limiter equals 1 in the unlimited, while it tends to 0 for a high velocity decoupling).

The computational domain is that described in Sect. 6.2. It is extended $483b_0 \times 765b_0$ in the radial and vertical directions (b_0 being the vent radius). The numerical grid is non-uniform and non-orthogonal. The discretization of the vent is represented in Fig. (6.2.1a). For the highest resolution run, the cell size increases from a minimum grid size $\Delta r = 2b_0/32$ with no radial grading factor in the region where the plume is expected to develop (Fig. 6.2.1b), whose initial radius is equal to $2.5b_0$ and increases linearly with an angle θ such that $\tan\theta = 0.147$, slightly larger than $\tan\theta = 0.12$ predicted by the Morton's plume theory with entrainment $k = 0.1$ [104]. Outside this region, a radial grading factor of 1.0446 is applied. Along z, 2048 cells are utilized. The minimum vertical cell size is $\Delta z = 2b_0/32$, and a grading factor of 1.00187 is imposed. The azimuthal resolution is constant and equal to $\frac{1}{32}\pi$ (5.625 degrees). The resulting total number of cells is $10,747,904$. This numerical mesh guarantees accuracy of the results: the solution procedure utilizes 2 PISO and 2 PIMPLE loops to achieve an absolute residual $\epsilon_{\mathrm{PIMPLE}} = 10^{-7}$ (see Sect. 5.1).

Simulation of 720 s of eruption required about 490,000 time steps (imposing a CFL constrain of 0.2, resulting in an average time-step $\Delta t \approx 1.5$ ms, with a maximum velocity at the vent of about 150 m/s) for a total run-time of about 25 days on 1024 cores on the Fermi architecture at CINECA (meaning about 2.25 millions of cells per second, consistently with estimates of Sect. 5.1).

It is worth noting that having high resolution at the vent is very expensive in terms of computational time in the [weakPlume] simulation. Indeed, the size of the vent in this eruption is small compared with the maximum plume height. The cell-size of the smallest cell is about 35 times smaller than that of the largest because of cell grading. Moreover, the smallest cells are near the vent, where the plume has its larger velocity. Thus, the CFL constrain is controlled by the mesh resolution at the vent. I decided to have high resolution at the vent because jet dynamics is crucial in the dynamics of forced transonic plumes [see e.g. 28]. However, this choice make the time step very small for the mean size of the cells in the whole domain, forcing to use a large number of time steps ($\simeq 490,000$).

Fig. 6.3.1 shows the development of the volcanic plume at $t = 400$ s. Because of the atmospheric stratification, the plume reaches a neutral buoyancy condition at about 10 km above the vent (i.e., 11.5 km above the sea level, still within the troposphere). Due to its inertia, the plume reaches its maximum plume height $H_{\max} \simeq 12$ km, higher than the neutral buoyancy level, before spreading radially to form the so-called volcanic umbrella. The two orthogonal sections highlight the different spatial distribution of the volumetric fraction of fine (right) and coarse (left) ash particles, due to the different coupling regime with the gas phase. Coarse particles have indeed a larger settling velocity $\boldsymbol{w}_s = \tau_s \boldsymbol{g}$ which causes a more intense proximal fallout from the plume margins and a reduced transport by the umbrella.

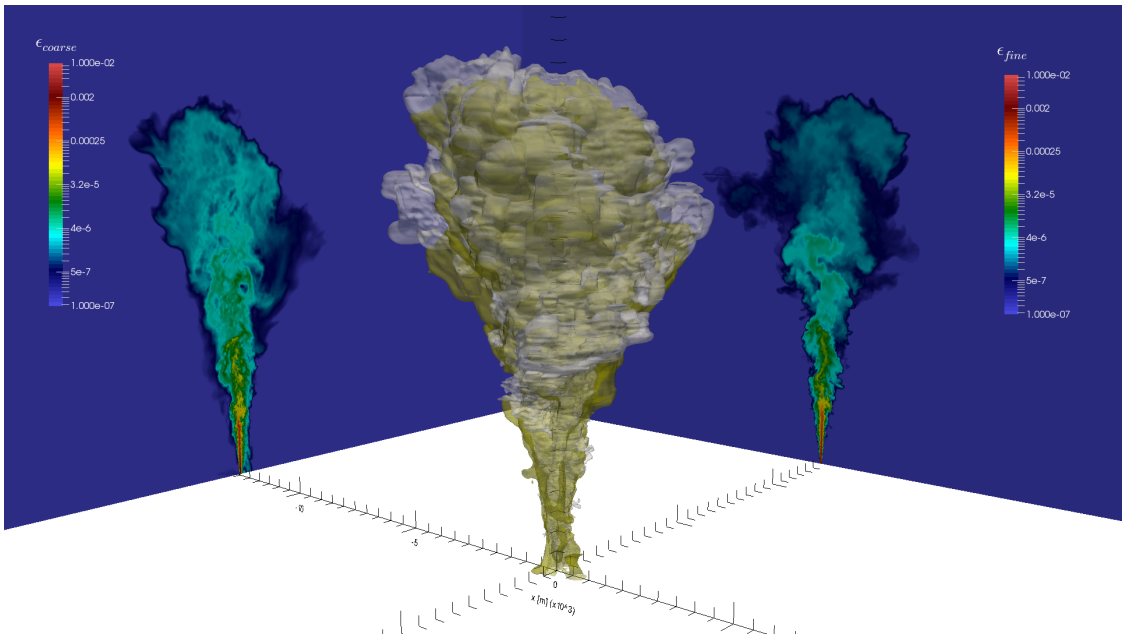

Figure 6.3.1: Three-dimensional numerical simulation of a weak volcanic plume, 400 s after the beginning of the injection (inlet conditions as in Tabs. 6.0.1 and 6.1.1). Isosurfaces and vertical sections of the fine (light white) and coarse (light sand) ash volume fractions. The isosurfaces are given at $\epsilon_s = 10^{-7}$. The maximum height of the fine class isosurface is approximatively 12.1 km. The two-dimensional plots represent the distribution of the volume concentration of coarse (left) and fine (right) particles across vertical orthogonal slices crossing the plume axis.

This is highlighted by the plot of the streamlines of the mixture velocity along a vertical section (Fig. 6.3.2), showing that the plume updraft is surrounded by a shell of settling coarse particles, which also inhibits air entrainment while promoting particle re-entrainment into the plume.

Besides settling, the large inertia of the coarse ash is responsible for the kinematic decoupling, leading to preferential concentration and clustering of particles at the margins of turbulent eddies. To illustrate this phenomenon, in a non-homogeneous flow, the instantaneous preferential concentration is computed as the (normalized) ratio between the jth particle concentration and the concentration of a tracer (in the present case, water vapor), i.e.,

$$\mathcal{C}_j = \frac{y_j}{y_{j,0}} \cdot \frac{y_{\text{tracer},0}}{y_{\text{tracer}}}, \tag{6.3.1}$$

where the 0 subscript corresponds to the value at the vent.

Fig. 6.3.3a shows the distribution of $\mathcal{C}_j$ for the coarsest particles at $t = 400$ s. The color scale is logarithmic and symmetric with respect to 1, which corresponds to the nil preferential concentration. For $\mathcal{C}_j < 1$, the mixture is relatively depleted of particles (green to blue scale); for $\mathcal{C}_j > 1$, particles are clustered (green to red scale). The mass fraction of the coarsest particles is up to 5 times larger (red zones) and 20 times smaller (blue zones) than the value it would have in absence of preferential concentration (green zones). This behavior is expected to affect the mixing and entrainment process. It is also worth remarking that the more uniform red area beyond the plume margins corresponds to the region of settling particles below the incipient umbrella region, that starts to develop on the left hand-side of the domain in Fig. 6.3.3a. On the other hand, the top of the plume is relatively depleted of

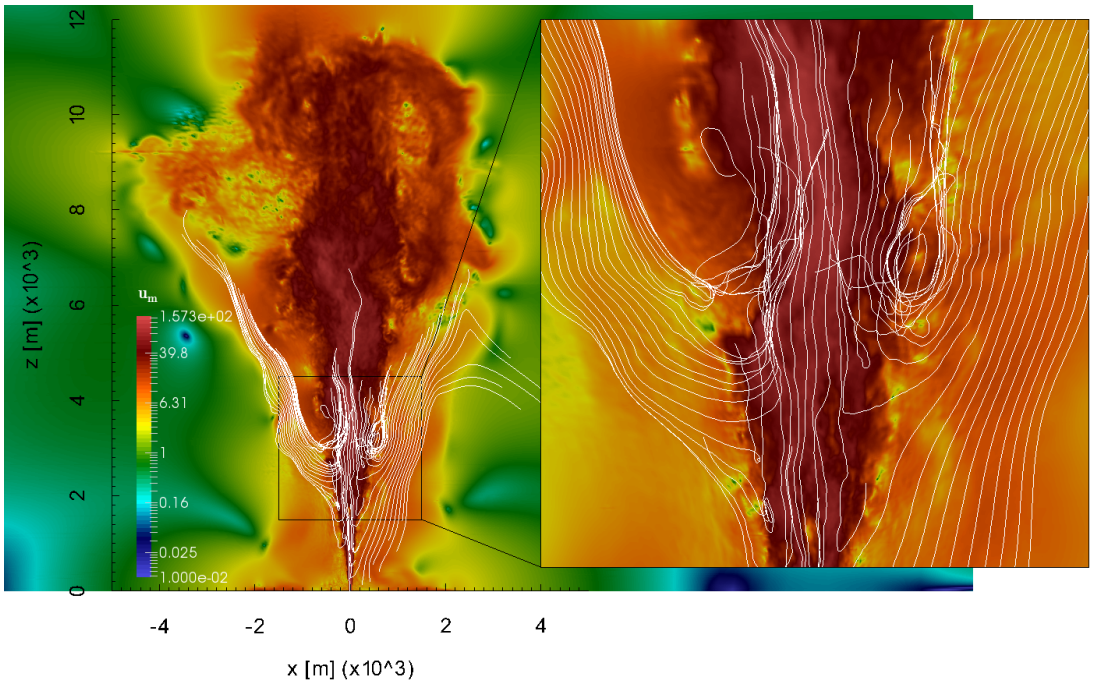

Figure 6.3.2: Vertical section of the instantaneous value of the mixture velocity modulus (in logarithmic scale) at $t = 400$ s and velocity streamlines.

coarse particles. The corresponding Fig. 6.3.3b for fine particles confirms that these are tightly coupled to the gas phase and almost behave as tracers (value of $\mathcal{C}_{\text{fine}}$ is everywhere around 1). These conclusions are coherent with the *a-priori* estimate of St_j given at the beginning of this section, based on the Taylor microscale time.

The instantaneous properties that have just been discussed in the plume region are similar for all the subsequent temporal evolution of the plume, provided that the source conditions are kept stationary. As the plume evolves, the umbrella cloud develops horizontally while the particles settle down reaching the ground as ruled by their terminal velocity in the atmosphere.

In the next section, I present the results obtained by averaging the volcanic plume flow field over time (in a time-window [300-720] s where the plume has reached statistically stationary conditions) and over the azimuthal angle, in order to allow comparison with one-dimensional integral models [e.g. 225] and discuss the effect of numerical resolution. The averaging procedure is explained in Sect. 3.11. The format of the results presented are similar to those described in Fig. 5.5.4 for the laboratory plume test case. Fluctuations fields are calculated during the averaging procedure, but they are not discussed in this thesis, leaving their analysis to future works.

6.3.1 Averaged plume profiles

Fig. 6.3.4 presents the results of the averaging procedure for three multiphase flow simulations at different resolution (panels a–c). In particular, panel a) has the highest resolution (minimum radial cell size $\Delta r = 2b_0/32$ with $2b_0$ equal to the inlet diameter); panel b) has $\Delta r = 2b_0/16$; panel c) has $\Delta r = 2b_0/8$. In panel d) I also present results at the lowest-resolution obtained by imposing the full kinematic

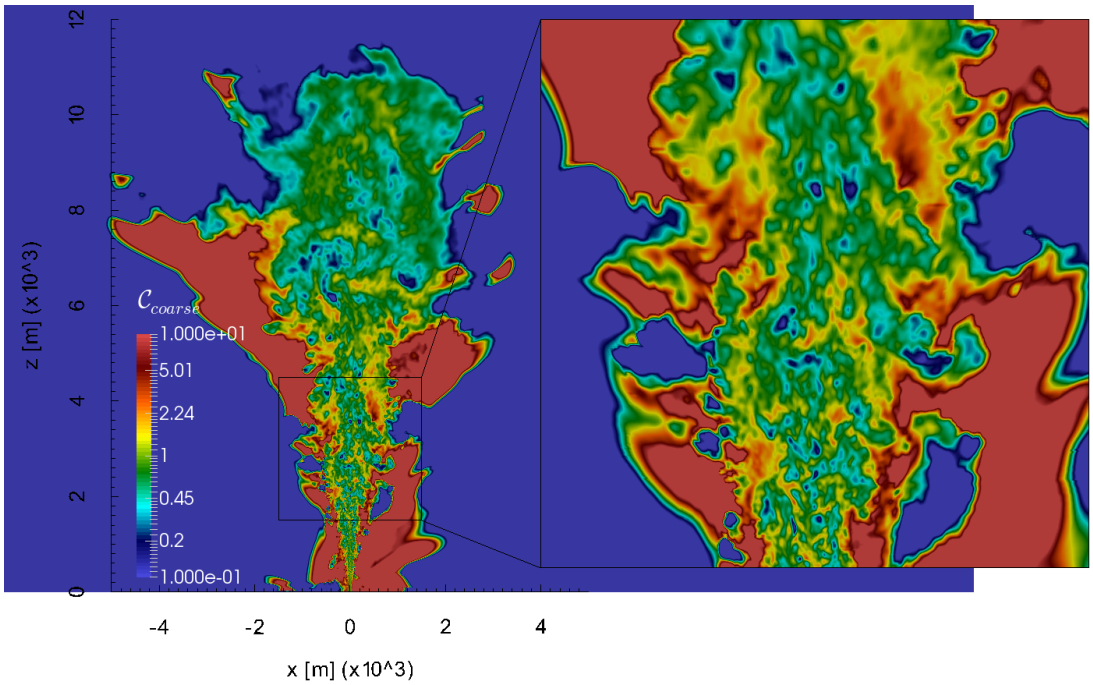

(a) Coarse particles: preferential concentration $\mathcal{C}_{\text{coarse}}$

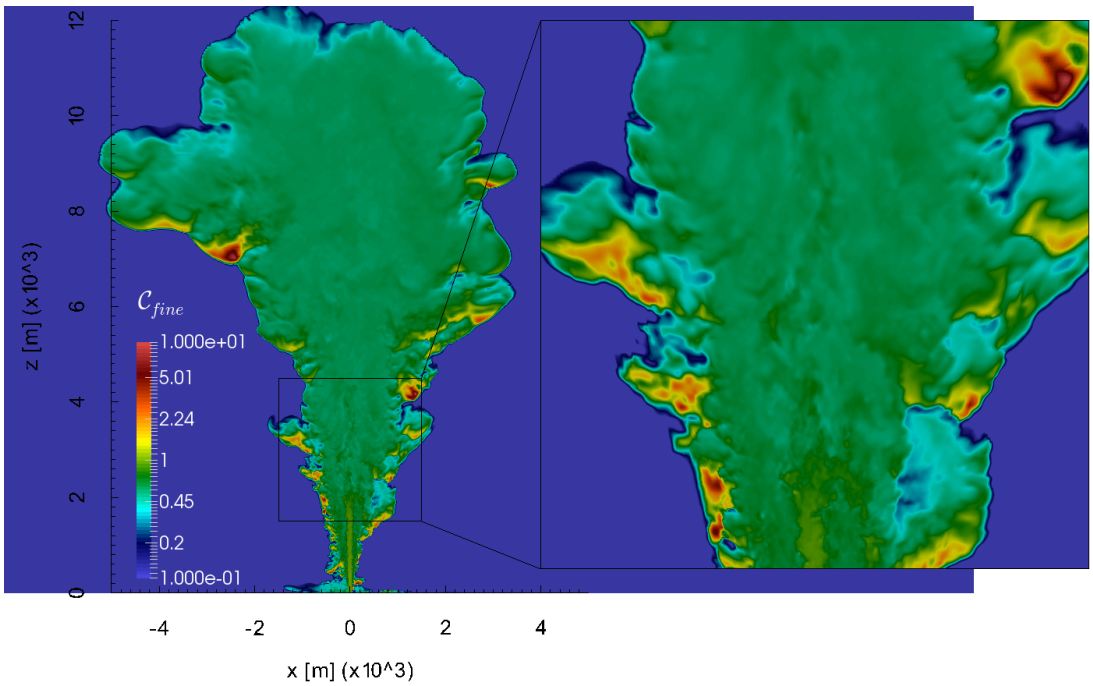

(b) Fine particles: preferential concentration $\mathcal{C}_{\text{fine}}$

Figure 6.3.3: Distribution of $\mathcal{C}_{\text{coarse}}$ (a), and $\mathcal{C}_{\text{fine}}$ (b), for the coarser and finer particles across a vertical section at $t = 400$ s (cf. Eq. 6.3.1).

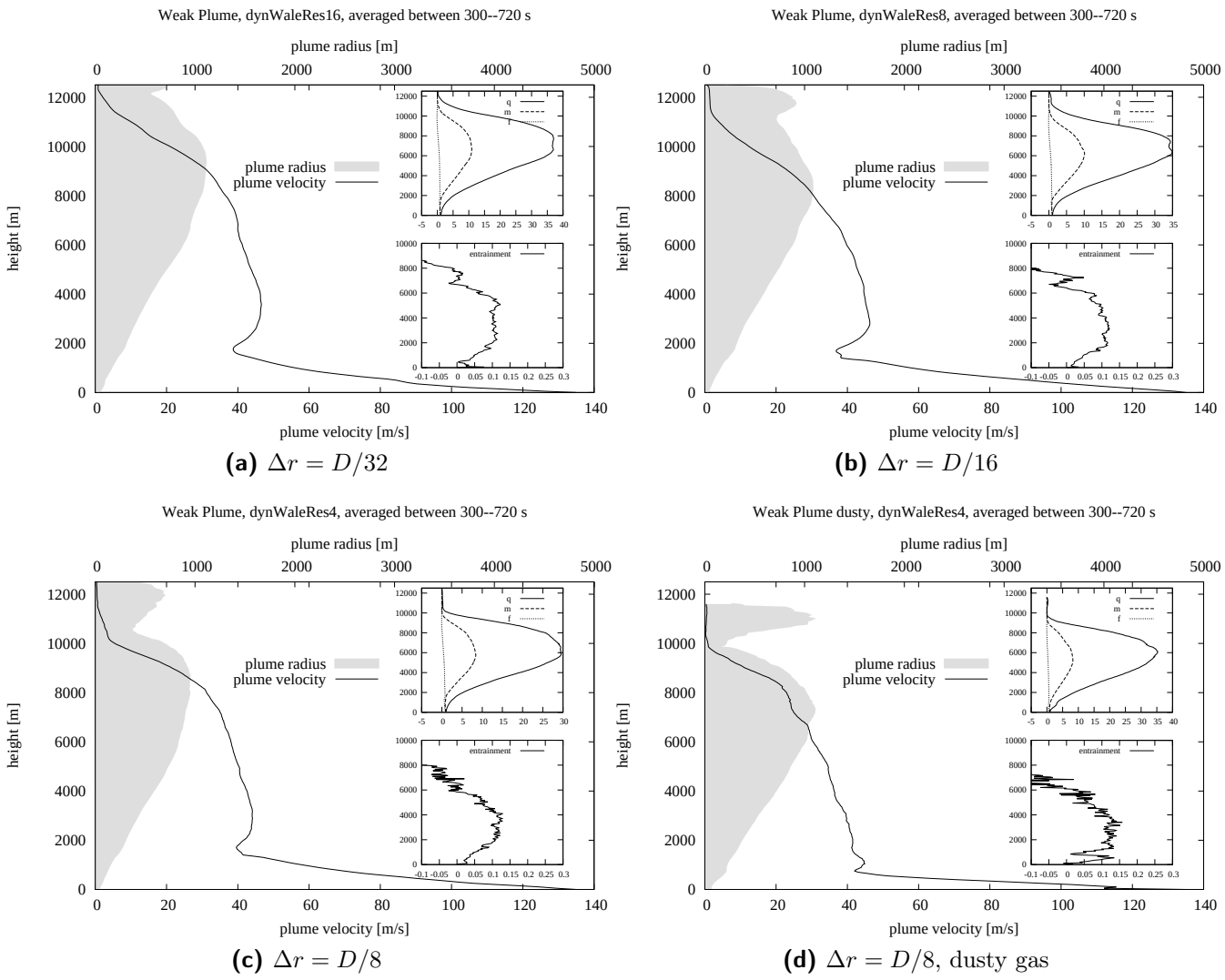

(a) $\Delta r = D/32$ **(b)** $\Delta r = D/16$

(c) $\Delta r = D/8$ **(d)** $\Delta r = D/8$, dusty gas

Figure 6.3.4: Time-averaged plume radius and velocity as a function of plume height. The insets display the non-dimensional mass, momentum and buoyancy fluxes (top) and the time-averaged entrainment coefficient. Panels a–c) `ASHEE` model at different resolutions; panel d) dusty gas model.

equilibrium between gas and particles, i.e., by adopting the [dusty] model [127].

Figs. 6.3.5, show a more detailed comparison, by reporting the evolution along the plume axis of all the plume integral properties described in Sect. 3.11. In particular, they are presented: (a) the mass flow rate $\pi Q(z)$, (b) the momentum flow rate $\pi M(z)$, (c) the enthalpy flow rate $\pi F(z)$, (d) the coarse mass fraction $Y_{\text{coarse}}(z)$, (e) the fine mass fraction $Y_{\text{fine}}(z)$, (f) the entrainment coefficient $\varkappa(z)$, (g) the axial velocity $U(z)$, (h) the plume radius $b(z)$, (i) the plume density $\beta(z)$ (with the atmospheric density as a shadow zone), and (j) the plume temperature $T_\beta(z)$ (with the atmospheric temperature as a shadow zone).

These figures first show the development of the fluxes driving the averaged plume properties (mass, momentum, enthalpy). Then, on the basis of these profiles, the inversion Eqs. (3.4.5) and (3.11.5) are used to recover the mean physical parameters (ash mass fractions, entrainment, velocity, plume radius, density and temperature). The figures show the variability of each mean variable due to the resolution (the

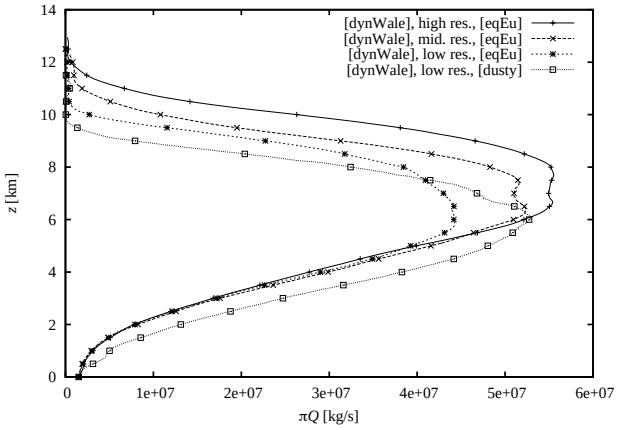

(a) Mass flow rate

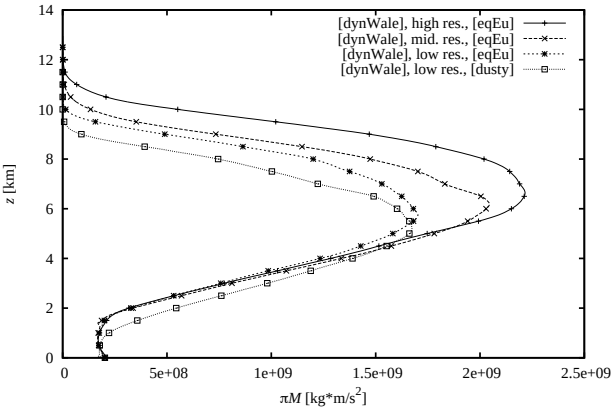

(b) Momentum flow rate

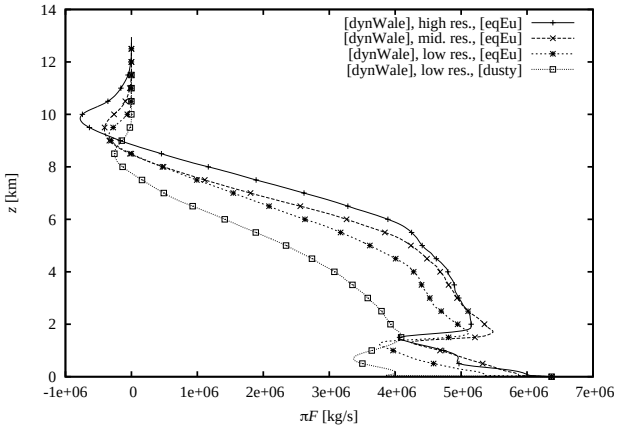

(c) Enthalpy flow rate

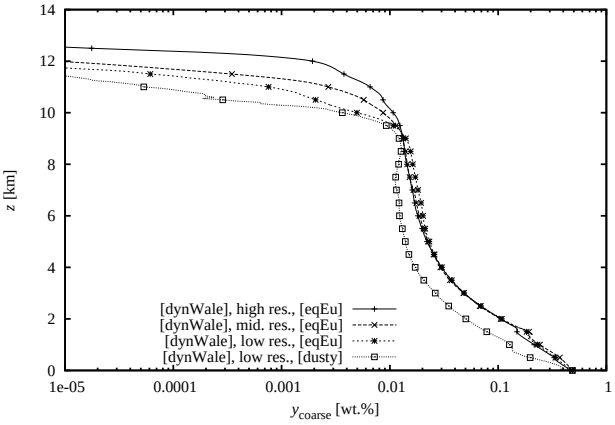

(d) Coarse mass fraction

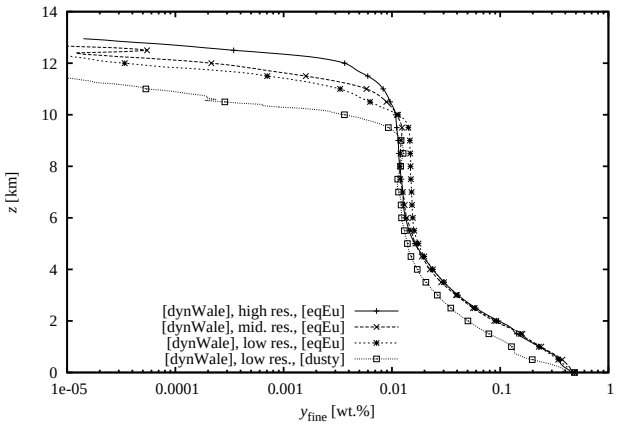

(e) Fine mass fraction

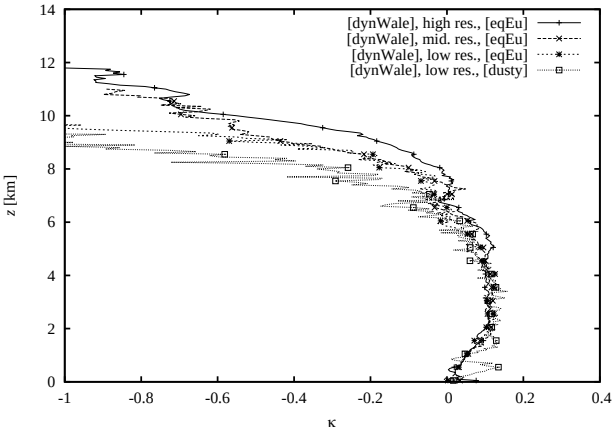

(f) Entrainment coefficient

Figure 6.3.5: (first part) Profiles of all the integral variables of [weakPlume]. Here they are compared by changing the resolution from $\Delta r = D/32$ (high res.) to $\Delta r = D/16$ (mid. res.) and $\Delta r = D/8$ (low res.). In the low resolution case, the results obtained with the dusty gas model [dusty] are also presented.

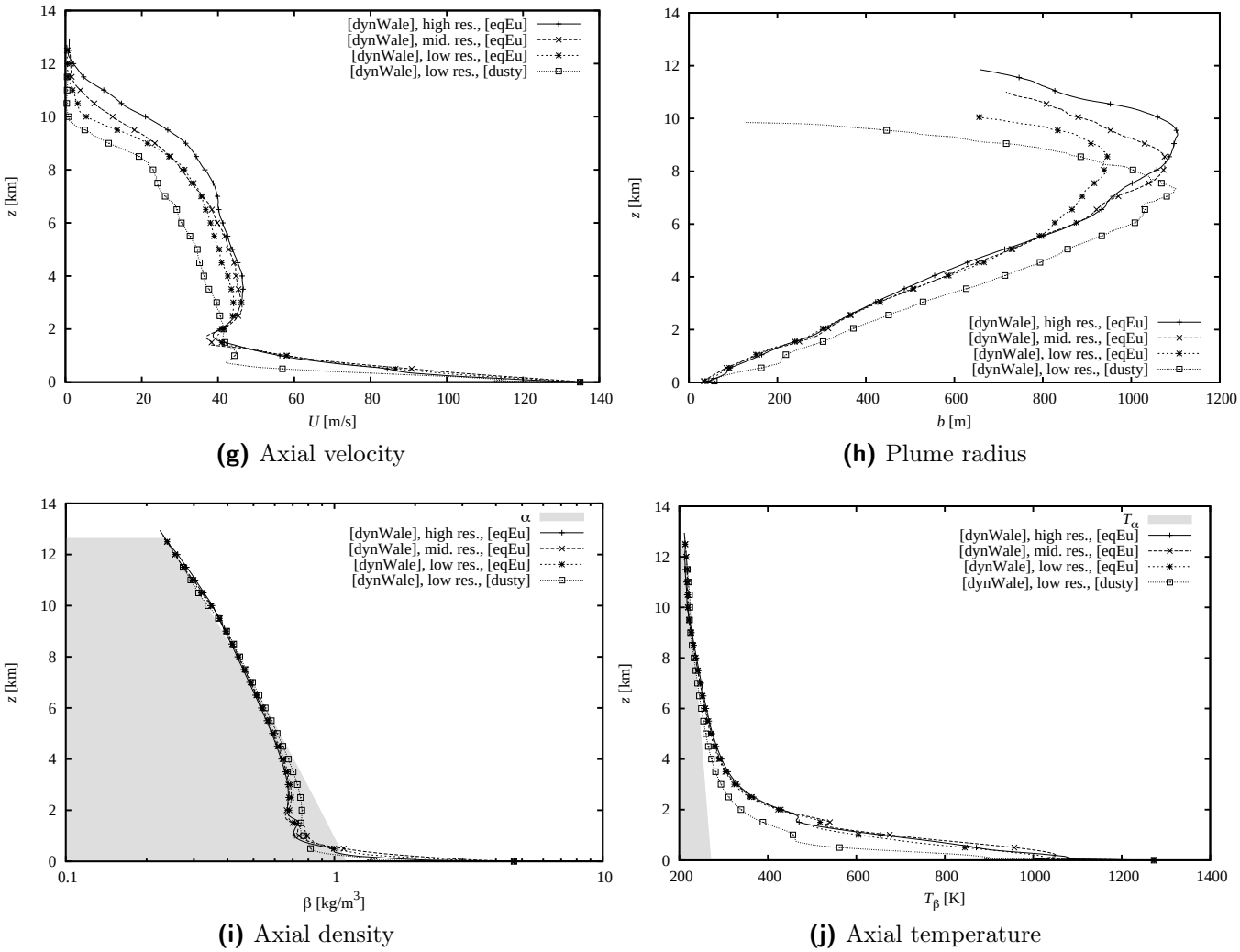

(g) Axial velocity **(h)** Plume radius

(i) Axial density **(j)** Axial temperature

Figure 6.3.5: (second part) Profiles of all the integral variables of [weakPlume]. Here they are compared by changing the resolution from $\Delta r = D/32$ (high res.) to $\Delta r = D/16$ (mid. res.) and $\Delta r = D/8$ (low res.). In the low resolution case, the results obtained with the dusty gas model [dusty] are also presented.

high-res, mid-res and low-res simulations are presented) and to the kinematic decoupling model (the [eqEu] model against the [dusty] model).

In Fig. 6.3.5h, the highest part of the profiles is cut. Indeed, as reported in Fig. 6.3.4, the plume radius starts to fluctuate near $H_{\max}$, i.e. when the mass and momentum fluxes goes to zero (cf. Eq. (3.4.5b)).

Effect of the resolution

Results in Figs. 6.3.4 demonstrate that the numerical model is quite robust and accurate so that even low-resolution simulations are able to capture the main features of the volcanic plume development. However, the maximum plume height systematically decreases from 12100 m (a), to 11300 m (b) to 11000 m (c) by decreasing the resolution. Analogously, the Neutral Buoyancy Level (NBL) decreases from 7800 m (a) to 7200 m (b) to 7100 m (c). Although the lowest resolution run underestimate the maximum plume height and radius by about 10%, the transition

to a super-buoyancy region at about 2000 m above the vent [227] is consistent in the three runs.

In Fig. 6.3.5a-c, the effect of mesh resolution has a significant influence on the development of cross-sectional profile of the flux of mass, momentum and enthalpy. Systematically, the more the resolution increases, the more the fluxes increase. However, these differences are mitigated when looking at the physical variables (see Figs. 6.3.5d-j). Indeed changing the resolution, the profiles for the variables reported in Figs. 6.3.5d-j remain very similar in the plume region, below the umbrella development. The plume velocity is the physical variable influenced more by the resolution.

The computed entrainment coefficient is also consistent in Fig. 6.3.4. It is relatively independent on the grid resolution and shows a different behavior with respect to the laboratory case, associated with the effect of the density contrast. In this case, a mean value of about $\varkappa \simeq 0.1$ is obtained in the buoyant plume region between 2 and 6 km above the vent. The entrainment coefficient assumes smaller values in the jet region $\varkappa \simeq 0.05 \div 0.07$, coherently with experimental results [see e.g. 233, Sect. 5.5, and Fig. 5.5.4]. Interestingly, in three-dimensional simulations the entrainment decreases near the NBL and it becomes negative above that level. This happens because the mass exits from the plume region moving to the umbrella cloud. In this way, the mass flow q of the plume decreases above the NBL and a stationary solution can be achieved. This is not the case in integral plume models with positive entrainment coefficient, where the maximum plume height is reached as a singularity point with divergent mass flow and plume radius [cf. 137, 225]. I plan to address this behavior more thoroughly in future studies. A more detailed analysis of the plume entrainment can be found in Sect. 6.3.2.

Effect of kinematic decoupling: ash jet dragging

In Fig. 6.3.4, the dusty gas model shows a significantly different behavior, with a larger plume radius, a slightly higher entrainment coefficient and a less marked jet-plume transition with no further acceleration (without a super buoyancy transition). The plume height is slightly lower than the non-equilibrium case at the same resolution having maximum plume height and neutral buoyancy level of 9.9 km and 6.1 km, respectively. Numerical simulations thus suggest that the effects of non-equilibrium gas–particle processes (preferential concentration and settling) on air entrainment and mixing are non-negligible. These effects are certainly overlooked in the volcanological literature and will be studied more thoroughly in future studies, by applying the present model to other realistic volcanological case studies. However, in the following I present some first results obtained from the simulations so far carried out.

In Figs. 6.3.5d-j, differences between profiles are influenced more by the decoupling between the gas and particles than by the resolution. As pointed out before, the major effect of mesh resolution is in the plume height. On the other hand, by comparing the low resolution simulations executed with model [eqEu] and model [dusty], it is worth noting that the former tends to shift all plume properties upward. In particular at a fixed height z, the mass and enthalpy flow are higher with [eqEu] model, while the momentum flow is slightly lower. These

facts are reflected in a higher velocity, temperature and ash mass fractions at a fixed height. On the contrary, the plume radius and the plume entrainment are reduced by the gas–particle decoupling at the given Stokes number (for a closer analysis of the plume entrainment see below and Fig. 6.3.6). The motivation for this behavior should be found in the differences between [eqEu] and [dusty] models. In the former gas–particle decoupling is taken into account, while in the latter it is not. Particle decoupling acts on the plume dynamics by two main processes: particle settling and turbulent preferential concentration. The former effect would induce the mass fraction of the coarsest ash phase to decrease with height, while the latter induces particles to accumulate in the direction opposite to gas acceleration (cf. Eq. (1.3.17)). Thus in the jet region, where a strong deceleration is present (as shown in Fig. 6.3.5g), decoupling lets the coarse particles travel more upwards than expected by the dusty gas model. Then, two-way coupling induces all the phases, both the fine particles and the gases, to partially follow the coarse phase. The combined effect of plume decoupling and two-way coupling can be seen in particular in Figs. 6.3.5g, 6.3.5h, 6.3.5j, 6.3.5d, and 6.3.5e. I will refer to this effect in the next sections as ash *jet dragging*. In Fig. 6.3.5j, also the temperature increases because of jet dragging and the plume radius is reduced because the plume is somehow "stretched" by the same effect.

It is worth noting that the present plume is *overexpanded* at the vent, because the pressure of the ejected mixture is equilibrated with that of the surrounding atmosphere. Thus, the gas decelerates in the jet region of [weakPlume]. The opposite case of an *underexpanded* accelerating jet has been studied in Carcano et al. [28]. There, the ash jet dragging has been observed too, but in a different configuration. The particulate phase is dragged by the accelerating gas phase for a significant portion of the jet, decoupling from it and modifying the dynamics if the mixture because of the two-way coupling.

6.3.2 Plume entrainment

Fig. 6.3.6 shows the development of the entrainment coefficient below the umbrella region. To discuss the differences between simulations keeping the plot clear, the entrainment obtained with the high-res simulation and the key fitting parameters of all the other simulations are reported in legend (the complete entrainment evolution for all the simulations can be found in Fig. 6.3.5f).

The first fact I notice is that in the plume region – from $z = 5\,L_{\mathrm{M}}$ to the neutral buoyancy level (see Tab. 3.4.2) – the simulated entrainment coefficient remains nearly constant. Moreover it is weakly influenced by the mesh resolution and by the multiphase flow model. In particular, an entrainment coefficient equal to $\varkappa = 0.103 \pm 0.001$ is obtained in the high resolution case. The middle resolution simulation gives an entrainment coefficient which is in the error band of the high-res simulation: $\varkappa = 0.101 \pm 0.002$. Thus, the middle resolution Large Eddy Simulation is enough refined to capture the correct entrainment coefficient and its error bar. On the other hand the low resolution simulation gives an entrainment coefficient which is underestimated by about 10 %. The comparison of the multiphase models [eqEu] and [dusty] does not present significant differences, because the error bars of the two results are overlapping. Moreover, it is worth noting that the standard

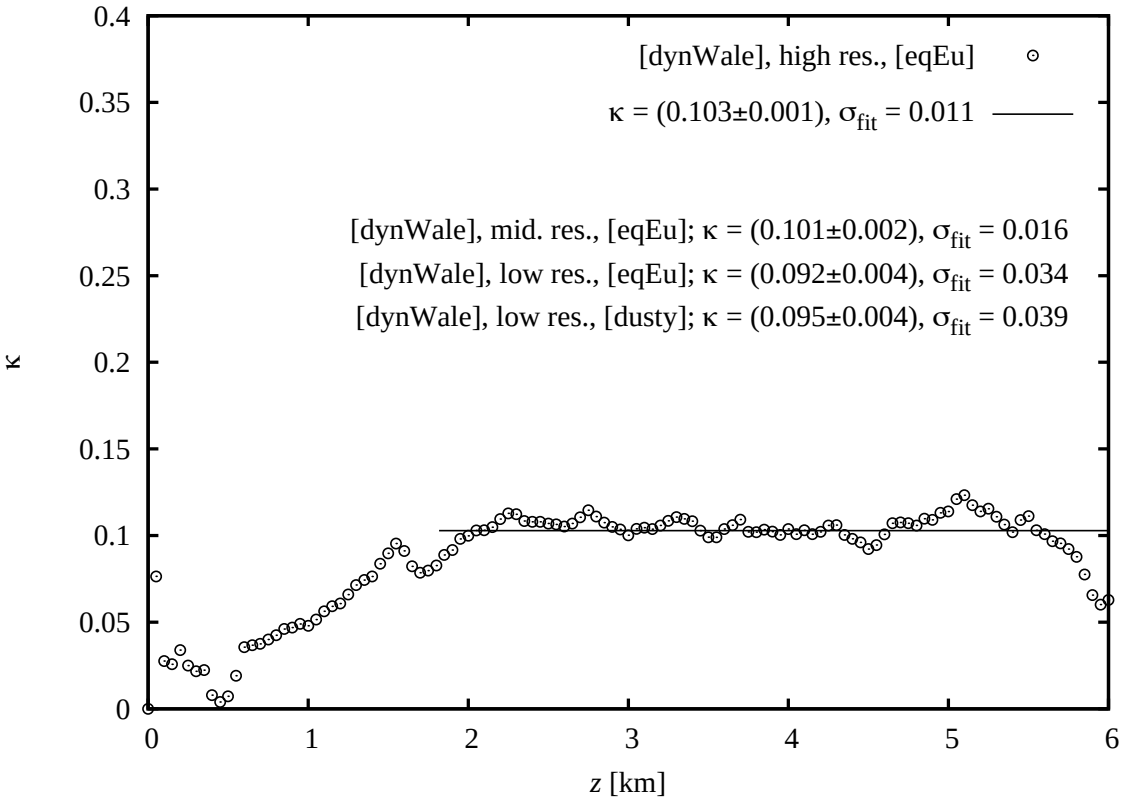

Figure 6.3.6: Entrainment coefficient of [weakPlume]. This is a zoom of Fig. 6.3.5f. The fit graph obtained at high resolution is shown, together with the fit result for the other simulations performed.

deviation between the constant fit and the simulated data is decreasing as the resolution increases. This justifies the use of a constant entrainment coefficient by integral one dimensional models in the plume region, from about five times the Morton length scale [cf. 137] to the neutral buoyancy level.

6.3.3 Comparison with integral models

Results shown in Figs. 6.3.5 can be compared with those obtained from integral models in Fig. 3.10.3. The simulation performed with the [dusty] model is that which can be more coherently compared with them because it uses the same physical assumptions (see Sect. 3.1). I enumerate below the main differences noticed.

- Plume height. The integral models described in Chap. 3 underestimate the plume height with respect to three-dimensional models: the complete model (3.4.1) gives $H_{\max} \simeq 9100$ m, while the analytical asymptotic one (see Sect. 3.10) gives $H_{\max} \simeq 9350$ m. The three-dimensional simulation with the [dusty] model gives $H_{\max} \simeq 9900$ m.

- Neutral buoyancy level. The complete model gives $H_{\mathrm{nbl}} \simeq 6700$ m, the analytic one gives $H_{\mathrm{nbl}} \simeq 7100$ m. Three-dimensional simulation gives $H_{\mathrm{nbl}} \simeq 6100$ m. Integral models overestimate the plume neutral buoyancy level with respect to three-dimensional ones.

- Plume velocity. The plume velocity provided by the integral model is significantly higher than that provided by the three-dimensional simulation. While in the former case the maximum velocity after the super-buoyant transition is around 65 m/s, in the three-dimensional simulation it is about 45 m/s.

- Plume radius. Results from integral models are comparable with that obtained from three-dimensional simulations below the neutral buoyancy level. Above that height the behavior is opposite. While in the former case the plume radius increases, in the latter one it decreases going to zero.

- Plume density, temperature and mass fractions. As a general behavior, the plume dilutes faster in integral models with respect to the three-dimensional simulation. In particular in the jet region the rate of dilution is overestimated by integral models.

Based on these outcomes, some conclusions can be drawn about the use of integral models presented in Chap. 3 vs the three-dimensional ones. The source of discrepancy between the two models seems to be the entrainment assumption. While the entrainment model works reasonably well in the plume region, it does not in the jet region and above the neutral buoyancy level. In the jet part of the evolution, the Ricou and Spalding [160] model is overestimating the quantity of atmospheric air entrained.† Thus, the integral plume model is diluting faster than in three-dimensional simulations, mixing is more efficient and the plume goes higher, reaching a neutral buoyancy level 10 % higher than that provided by three-dimensional simulations. Then, above the neutral buoyancy level, assuming a constant entrainment coefficient led to a completely wrong behavior, where the plume radius diverges instead of going to zero. This discrepancy adds another source of error to the description of the plume evolution since it generates a significant underestimation of the column height. In three-dimensional simulations the entrainment becomes negative above the neutral buoyancy level, the plume thus loses mass and the momentum decrease is slower than in the integral model. Indeed, in the latter model the mass flux keeps increasing causing the momentum flux to go to zero faster.

I plan to further analyze three-dimensional simulations in future studies, to improve the entrainment coefficient of integral models. This can be achieved by studying the behavior of the first integral of motion presented in Chap. 3. In the next section I discuss briefly their behavior in [dusty] three-dimensional simulation.

6.3.4 Plume conserved quantities

In Sect. 3.10 I derived two conserved quantities along the plume height: $\mathcal{U}_{\rm RS}$ (3.7.4) $\mathcal{U}_m$ and (3.9.8). These first integrals of motion depend respectively on $l_{\rm c}(q) \approx q^2$ (see Eq. (3.10.4)) and $m^{\frac{5}{2}}$, and on $(f-\gamma_{\rm c})^2$ and m^2. The first conserved quantity is tied with the entrainment assumption, while the second one is not. Fig. 6.3.7 shows the behavior of these first integral of motions in the three-dimensional simulations. They are represented using the same methodology adopted

†Suzuki and Koyaguchi [189] compared the entrainment computed from three-dimensional simulations with the entrainment model by Carazzo et al. [26]. He found that the entrainment is overestimated also by the Carazzo et al. [26] model.

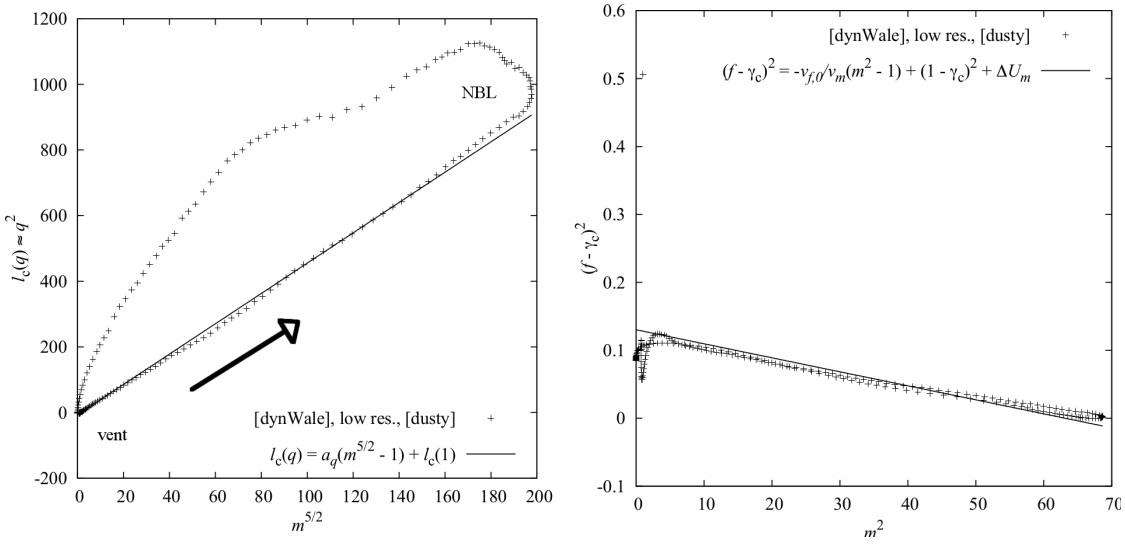

Figure 6.3.7: Behavior of conserved quantities of the asymptotic integral model as calculated from three-dimensional simulations. Here, some of the plume parameters reported in Tab. 3.4.2 have been modified to obtain a better behavior of the conserved quantities (see discussion): $a_q = 1.65 \rightarrow a_q = 4.62$, $\gamma_c = 0.252 \rightarrow \gamma_c = 0.292$. Moreover, the value of $v_{f,0} = 2.66 * 10^{-4}$ is used. It is obtained averaging the atmospheric profile: $\omega_0 \simeq 1.40 * 10^{-2}$ Hz. Each point corresponds to a different height, evolving as indicated by the arrow: from the vent to the maximum height, through the neutral buoyancy level (NBL).

for the experimental forced plume in Fig. 5.5.5. There, the theoretical first integral of motion is used to reduce the dependence of the mass flux on the momentum flux to a linear relationship. In this way, the goodness of the first-integral can be checked against three-dimensional simulations: if the linear fit gives good results, it means that the first integral of motion can be considered as a constant even in three-dimensional simulations.

The theoretical linear behavior can be recovered, provided that some of the parameters of the integral model should be modified. In particular, when testing the conservation of first integral $\mathcal{U}_{\rm RS}$ defined in Eq. (3.7.4) (or, equivalently Eq. (3.10.3)), the parameter a_q should be increased significantly (see Fig. 6.3.7). In this way, the fist integral of motion $\mathcal{U}_{\rm RS}$ remains nearly constant from the vent elevation to the neutral buoyancy level (where m reach its maximum). On the other hand, $\mathcal{U}_{\rm RS}$ is not conserved above the neutral buoyancy level. This is in agreement with the entrainment evolution, which is not constant at all above the neutral buoyancy level. I now move to the other conserved quantity $\mathcal{U}_m$, which is defined independently from the entrainment assumption in Eq. (3.9.8). This time, in order to have $\mathcal{U}_m$ approximately constant along the plume, I increased slightly γ_c (see Fig. 6.3.7). In this way, $\mathcal{U}_m$ can be considered approximately constant all along the plume height, even during the buoyancy transition at the neutral buoyancy level. This result is in agreement with the independence of $\mathcal{U}_m$ on the entrainment assumption. However, in the region near the vent $\mathcal{U}_m$ is subject to a sudden change that I identify in Fig. 6.3.7 with $\Delta\mathcal{U}_m \simeq -0.373$. This behavior can not be attributed to the non-Boussinesq regime to which the plume is subject near the vent, because $\Delta\mathcal{U}_m \simeq 0$ in the complete one-dimensional model (3.4.1). More likely, the motivation can be found in the low resolution of the dusty gas simulation or in the shape of the averaged horizontal profiles of the three-dimensional plume. Indeed, the

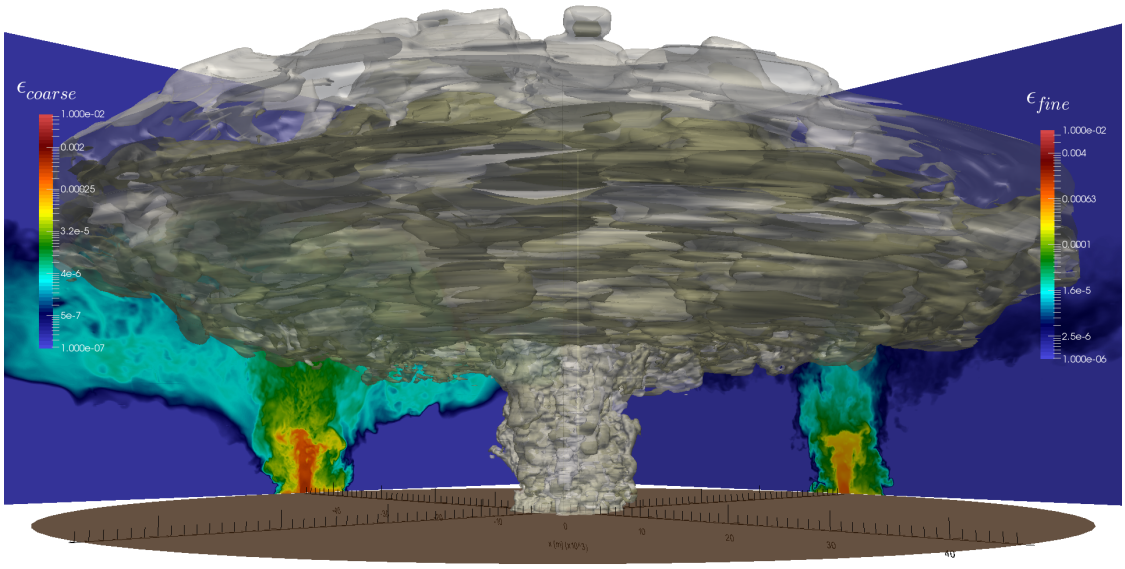

Figure 6.4.1: Three-dimensional simulation of [strongPlume], 1000 s after the beginning of the injection (inlet conditions are in Tabs. 6.0.1 and 6.1.1). Isosurface and vertical sections of the fine (light white) and coarse (light sand) ash volume fractions. The isosurfaces are given at $\epsilon_s = 10^{-7}$. The maximum height of the fine class isosurface is approximatively 43 km. The two-dimensional plots represent the distribution of the volume concentration of coarse (left) and fine (right) particles across vertical orthogonal slices crossing the plume axis.

self-similarity hypothesis could not be met near the vent [63, 33]. Further studies and numerical simulations are needed to better understand the presented behavior.

6.4 Numerical simulations of [strongPlume]

In this section I discuss the results obtained from three-dimensional numerical simulations of the [strongPlume]. The main physical differences between this plume and that presented in the previous section are the following (see Tab. 3.4.2): 1) the plume is supersonic at the vent, since the mixture speed of sound is 157 m/s (cf. Eq. (1.2.17)), while the exit mean velocity is 275 m/s; 2) the plume has more water than [weakPlume], this reflects in a smaller non-Boussinesq parameter ϕ; 3) the multiphase mass flux anomalies q_ψ and q_χ of [weakPlume] and [strongPlume] are comparable; 4) the modified Richardson number v_m is four times larger, thus the non-dimensional Morton length scale decreases by about a factor of 2; 5) however the stratification length scale decreases by about a factor 23, driving the transition between jet and plume at a height comparable with the plume height and the neutral buoyancy level.

A number of different simulations have been performed, modifying both the resolution and the sub-grid scale LES model. In this section, I mainly present the results obtained with the [dynWale] model at the finer resolution $\Delta r = 2b_0/32$. Then I study how the averaged plume properties are influenced by the grid resolution and the LES model. In particular, alongside the high-res simulation, a mid-res grid ($\Delta r = 2b_0/16$) and a low-res grid ($\Delta r = 2b_0/8$) have been used. Then, results obtained with [dynWale] are compared with those obtained with [moin], [oneEqEddy]

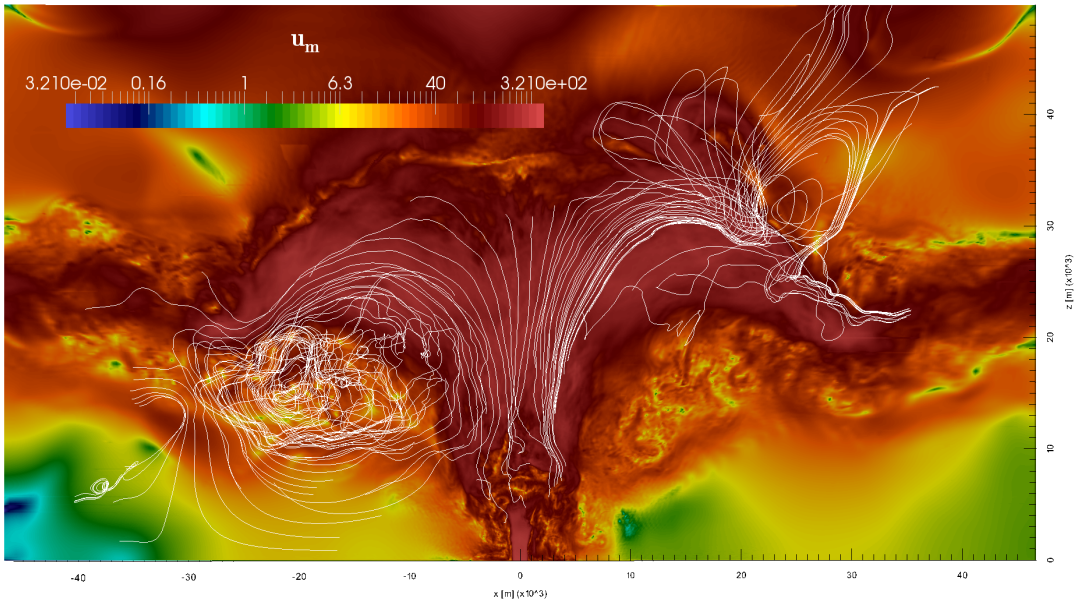

Figure 6.4.2: Vertical section of the instantaneous value of the mixture velocity modulus (in logarithmic scale) at $t = 1000$ s and velocity streamlines.

or without subgrid model [noM]. Finally, results obtained with the [eqEu] model are compared with those obtained using [dusty].

As already done for [weakPlume] in Sect. 6.3, I *a priori* evaluate the Stokes number associated with this eruption, based on the most energetic turbulent eddy scale $\tau_L \simeq 1.5$ s. I obtain $\mathrm{St}_{\mathrm{coarse}} \simeq 0.27$ and $\mathrm{St}_{\mathrm{fine}} \simeq 1.2 * 10^{-3}$. From the a-posteriori analysis based on the Taylor microscale, I found: $\mathrm{St}_{\mathrm{coarse}} \simeq 0.06$ and $\mathrm{St}_{\mathrm{fine}} \simeq 3 * 10^{-4}$, for the finer mesh resolution. Thus, the Stokes number in a [strongPlume] large eddy simulation is expected to rarely exceed the value $\mathrm{St} = 0.2$ and the equilibrium–Eulerian model is well justified for this simulation. Coherently with these results, I have checked a-posteriori that no decoupling limiter have been used during the numerical simulations (cf. Sect. 5.1 for the limiter definition).

The computational grid is described in Sect. 6.2. It is extended $66b_0 \times 71b_0$ in the radial and vertical directions, respectively. For the highest resolution run, the cells have a minimum size $\Delta r = 2b_0/32$. As described in Sects. 6.2 and 6.3, there is no radial grading in the plume region, while outside that region a radial grading factor of 1.011 is applied. Along z, 2112 cells are utilized. The minimum vertical cell size is $\Delta z = 2b_0/32$, and a grading factor of 1.000657 is imposed. The azimuthal resolution is again $\pi/32$, with a total number of cells equal to $8,785,920$. The solution procedure utilizes 2 PISO and 2 PIMPLE loops to achieve an absolute residual $\epsilon_{\mathrm{PIMPLE}} = 10^{-7}$ (see Sect. 5.1).

A 2000 s long numerical simulation at the finer resolution required about $110,000$ time steps with a CFL constrain of 0.2, resulting in an average time step $\Delta t \simeq 20$ ms. It is performed on the Fermi architecture at CINECA [CIN], on 1024 cores for a total run-time of about 5 days (meaning about 2.1 millions of cells per second).

Figs. 6.4.1 and 6.4.2 show the development of the volcanic plume at $t = 1000$ s. The plume at the vent is denser than the surrounding atmosphere, but the initial inertia allows most of the mass to mix with the atmosphere, thus reversing

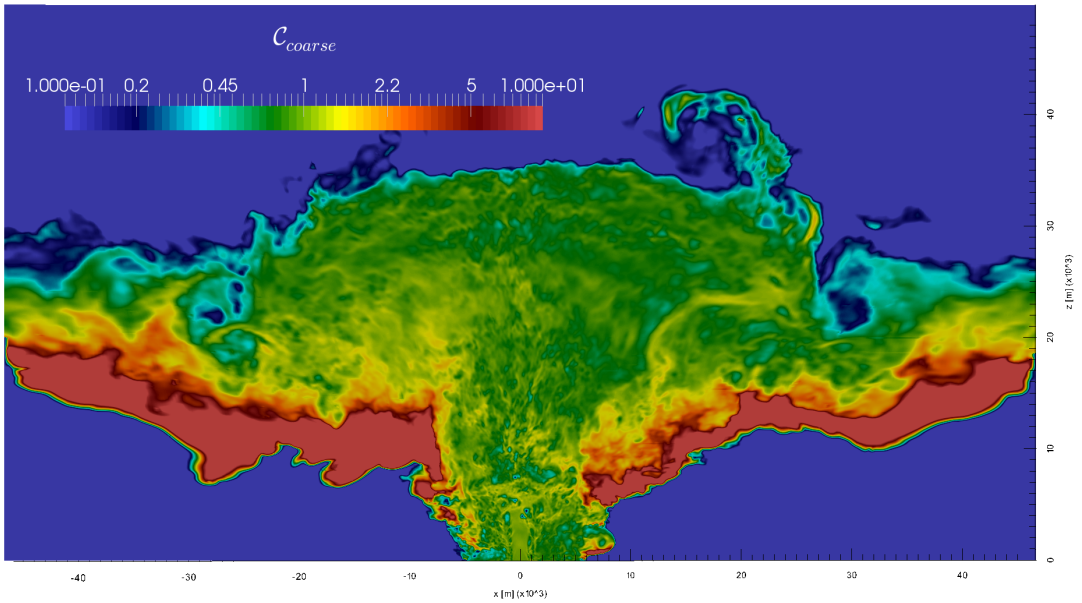

(a) Coarse phase preferential concentration

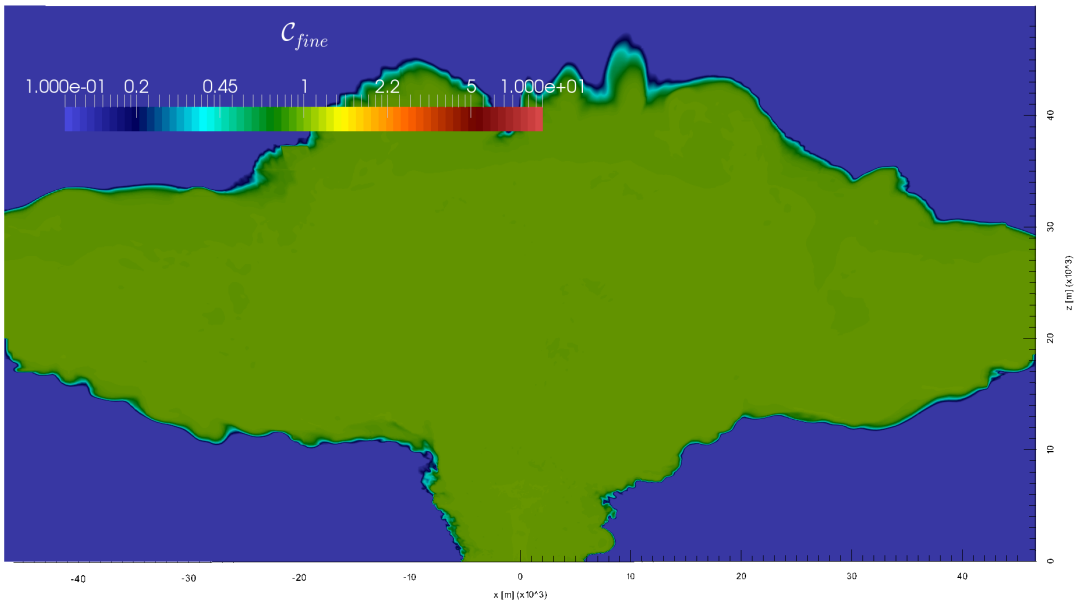

(b) Fine phase preferential concentration

Figure 6.4.3: Distribution of $\mathcal{C}_{\text{coarse}}$ (a), and $\mathcal{C}_{\text{fine}}$ (b), for the coarser and finer particles across a vertical section at $t = 1000$ s (cf. Eq. 6.3.1).

the buoyancy from negative to positive. The transition takes place through the development of a fountain, and a *suspended flow* horizontally spreading over the jet [140, 190]. However in this simulation, part of the mass collapses to the ground, forming pyroclastic density currents and a big co-ignimbrite surrounding the jet core. A quantitative discussion of this partial collapse can be found in Sect. 6.4.5. The plume reaches a neutral buoyancy condition at about 18.9 km above the vent. The inertia of the plume allows it to reach its maximum height at $H_{\max} \simeq 43$ km. Then the top of the plume collapses over the neutral buoyancy level, spreading radially in the umbrella cloud. The updraft induces a significant atmospheric perturbation causing the development of a big gravity current recognizable in the umbrella.

At the beginning of this section, I have highlighted the main physical differences between the [strongPlume] and the [weakPlume] volcanic eruptions. Fig. 6.4.2 (with respect to Fig. 6.3.2) shows how these differences reflect in the global behavior of the velocity field of the plume. The more evident structure, peculiar of the [strongPlume], is the big toroidal eddy under the umbrella cloud. Less apparent, but still very important, is another toroidal eddy developing around the jet, under the suspended flow. These two structures are present in the instantaneous fields through pulsating turbulent events, even if they are more clearly recognizable by analyzing the time-averaged fields [see below and 54]. Figs. 6.4.2 and 6.4.10 show the streamlines of, respectively: 1) the velocity field in a vertical slice of the whole simulated plume; 2) the time-averaged velocity field in the collapsing region, respectively. I notice qualitatively that part of the entrained mass comes from recirculation at the base of the plume. Thus, reentrainment plays an important role, causing part of the settled and collapsing particles to be reentrained into the plume to be transported again upwards. The particles which are closer to the plume margins recirculate because of the large eddies. Part of them fall to the ground, and part are reentrained by the plume. Velocity fluctuations are stronger along the plume margins, while the velocity appears to be more stable near the plume axis. The jet region exhibits an intricate shape, being surrounded by a collapsing layer, a reentrainment region and a big co-ignimbrite. A quantitative discussion of the influence of the plume collapse and particle reentrainment can be found in the next sections, where the time-averaged properties of this volcanic plume are studied. However before discussing that, I focus on two aspects of the instantaneous fields: preferential concentration and turbulent infrasound generation.

6.4.1 Preferential concentration

To illustrate the preferential concentration, I use again the quantity $\mathcal{C}$, Eq. (6.3.1). Fig. 6.4.3 shows the distribution of preferential concentration in an axial slice of the plume. It is worth noting that the fine ash phase is practically coupled with the mixture velocity field, while the coarse phase is not. As already noticed in the [weakPlume] case (see Fig. 6.3.3a), the top of the plume is depleted of coarse particles which tend to settle down. The area of the plume where particle fallout is stronger is red. Inside the plume, turbulence makes the coarse particles to preferentially concentrate, creating zones with higher ash mass fraction (yellow) and zones with lower mass fraction (cyan and blue). Coarse ash clustering is stronger in the jet-plume transition zone and in the zone below the umbrella cloud. Preferential

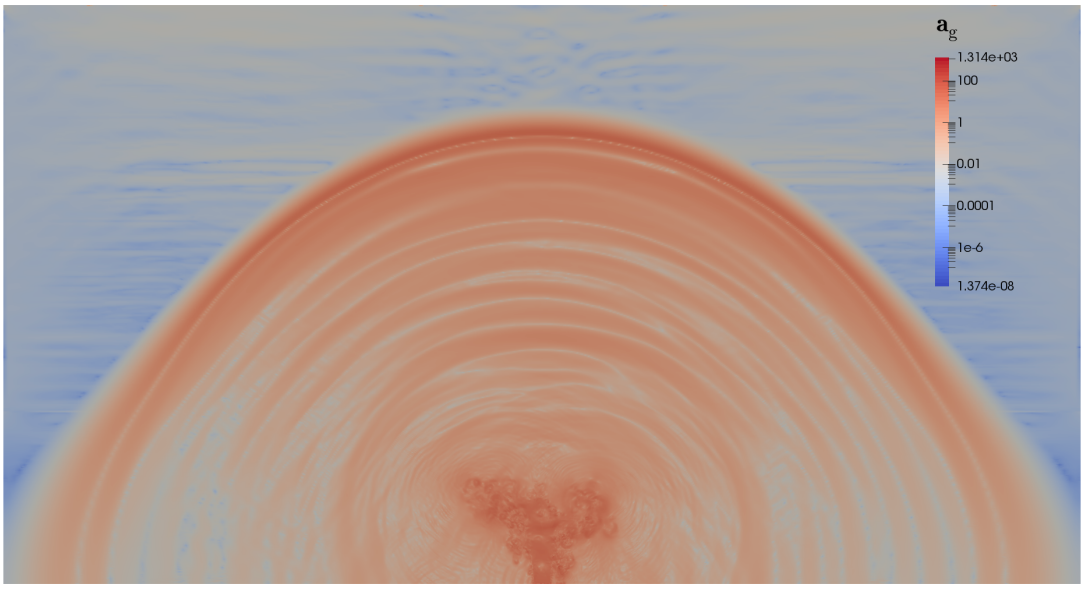

Figure 6.4.4: Infrasonic signal generated by the turbulent eddies. Here the infrasonic perturbation is visualized by using the magnitude of the field of acceleration $\boldsymbol{a}_g$, in logarithmic color scale, after 120 s since the eruption started.

concentration is weaker for this plume with respect to the [weakPlume] case, as expected from the analysis of the Stokes number. For this reason, as discussed below by comparing the models [eqEu] and [dusty], ash jet dragging is present but weakened in the [strongPlume] case.

6.4.2 Turbulent infrasound generation

The plume presented in this section generates big eddies, comparable with the size of the vent ($\simeq 10^3$ m). Turbulent eddies generate pressure perturbations because of their centrifugal acceleration [see e.g. 116]. Fig. 6.4.4 shows qualitatively the shape of these perturbations, highlighting that the source of infrasound is not only the eruptive mixture leaving the vent but also the large eddies. This infrasonic signal can be measured from the ground, extracting important information about the plume dynamics [cf. 108]. In Matoza et al. [130] infrasonic spectra from volcanic eruptions have been compared with large-scale and fine-scale similarity spectra as measured by Tam et al. [193].

Fig. 6.4.5 shows the pressure fluctuation data probed at the ground level, 15 km far from the vent center, in the time window $t \in [0, 13]$ min. As usually done by real infrasound microphones [130], the pressure signal is convoluted with a kernel window cutting the frequencies smaller than 0.03 Hz, to study only pressure fluctuations and not absolute variations. The resulting spectrum is compared with the similarity spectrum generated by large-scale turbulence measured by Tam et al. [193]. The fit is in satisfactory agreement and comparable with results obtained from direct volcanic observation [see 130]. A peak in $E_p(\mathrm{Str}_L)$ is obtained for $\mathrm{Str}_L = 0.32 \pm 0.01$, a value comparable with that expected from experimental results [see 116, and Sect. 6.3]. It is shown also the slope $\mathrm{Str}^{-11/4}$ measured by Tam et al. [193] for

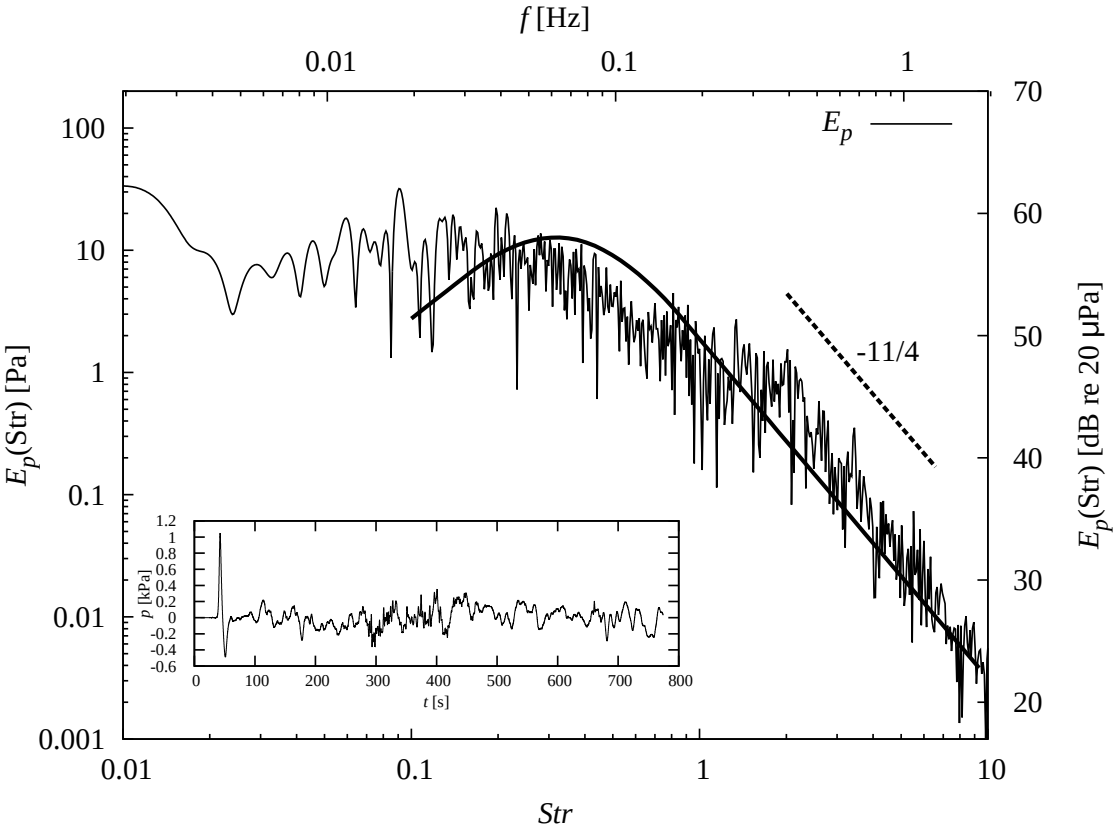

Figure 6.4.5: Infrasonic spectrum of the pressure fluctuations as measured from a probe placed at the ground level 15 km from the vent center, in the time window $t \in [0, 13]$ min. The frequency is expressed both in its dimensional (f) and non-dimensional ($\mathrm{Str} = f\,2b_0/U_0$) formulation. Pressure fluctuations E_p are represented both in logarithmic scale and in dB scale relative to $20\,\mu$Pa. The slope $\mathrm{Str}^{-11/4}$ is shown in bold dashed line. The experimental large-scale similarity spectrum is presented in bold solid line [see 193]. The inset shows the pressure fluctuation signal in [kPa] until $\simeq 13$ min.

supersonic jets for $\mathrm{Str} > 2.5\,\mathrm{Str}_L$. It is worth evidencing that the present result could be influenced by the reflective boundary conditions which have been used. In future studies I plan to modify the atmospheric boundary conditions in order to make them non-reflective.

6.4.3 Averaged plume profiles

Similarly to what presented for the [weakPlume], I here analyze the evolution of the main averaged plume variables along the vertical extension of the plume. The averaging technique is described in Sect. 3.11. Here, the averaging time window $\mathcal{T} = [1000, 2000]$ s has been used. While in the first part of this section I have commented results from the high-res [dynWale] simulation, here results obtained changing the grid resolution, the sub-grid LES model and the kinematic decoupling model are compared. In this section, three groups of figures are presented, to study quantitatively: the effect of the mesh resolution (Fig. 6.4.6); the effect of the subgrid scale model (Fig. 6.4.7); the effect of the kinematic decoupling model (Fig. 6.4.8). Moreover, Fig. 6.4.9 compares the entrainment coefficient as obtained from all the [strongPlume] simulations presented.

Analogously to the [weakPlume] case, in Figs. 6.4.6h, 6.4.7h, and 6.4.8h, the

highest part of the profiles is cut. Indeed, the plume radius starts to fluctuate near $H_{\max}$, when the mass and momentum fluxes go to zero (cf. Eq. (3.4.5b)).

The effect of the resolution can be investigated by comparing the simulations high, mid, and low resolution performed with [dynWale] (see Fig. 6.4.6). The plume heights based on the 1 wt.% of a tracer are respectively: $H_{\max} = 43$, 41, 43 km; the plume neutral buoyancy levels are, respectively, $H_{\rm nbl} = 18.8$, 18.4, 17.7 km. The relative error due to resolution is less than 6 %. Similarly to what has been found for [weakPlume], even in the [strongPlume] case results are quite robust and accurate and even the low resolution simulation is able to capture the main features of the averaged volcanic plume. However, the resolution has a stronger effect on this eruption than on [weakPlume].

Fig. 6.4.6g shows that the velocity is underestimated at lower resolution, while in Fig. 6.4.6j the temperature is slightly overestimated by the low-res simulation. As for the [weakPlume] case, finer resolution seems to have a more efficient mixing. These are the most evident differences due to grid resolution, caused by an underestimation of the momentum flux and of the enthalpy flux (see Fig 6.4.6). I conclude that a simulation with a finer resolution is desirable to lead to convergence the plume averaged results.

Moving to the effect of the subgrid scale model, two groups of simulations are compared in Fig. 6.4.7. The first group analyzes [dynWale] and [noM], both at high resolution. In this way, the net effect of the LES model can be estimated. The height of the plume is, respectively equal to $H_{\max} \simeq 43$ and 40 km; while the neutral buoyancy level $H_{\rm nbl} \simeq 18.8$ and 18.2 km. Thus, the subgrid model tends to increase the plume height and the plume neutral buoyancy level with a relative discrepancy of the order of 7 % and 3 %, respectively. The entrainment coefficient without subgrid model ([noM]) does not significantly change in average although its fluctuations increase ($\sigma_{\rm fit} \simeq 0.20$ vs 0.14 in the legend of Fig. 6.4.9). The main differences in the plume profiles are caused by the underestimation of the mass and enthalpy fluxes by [noM] above the jet-plume transition, inducing the slight underestimation of the plume radius, density, temperature, and solid phase mass fractions. Using a subgrid model improves the quality of the averaged results, because the mid-res simulations with subgrid model are closer to the high-res simulation than the high-res [noM] one.

The second group of profiles presented in Fig. 6.4.7 compares [dynWale], [moin], and [dynOneEqEddy] at middle resolution. As pointed out above, the entrainment coefficient agrees among all the simulations and, this time, also fluctuations are comparable. In particular, $\varkappa$ is underestimated by [dynWale], is comparable with the high-res simulation for [moin] model, and is overestimated by [dynOneEqEddy]. These small differences reflects in the averaged plume profiles, making the mid-res simulation performed with [moin] the most accurate one. However, I can conclude that the effect of the subgrid model used is weaker than the effect of the resolution, in the range of variation investigated.

The last group of profiles is shown in Fig. 6.4.8. In this figure I illustrate the effects of the kinematic decoupling between the ash particles and the gas phase. In this case, the decoupling is much more weaker than what has been found for the [weakPlume] eruption. Indeed, as pointed out above, the Stokes number of these particles can be estimated, on average, as $\mathrm{St}_{\rm coarse} \simeq 0.06$, against $\mathrm{St}_{\rm coarse} \simeq 0.1$

that has been found for the 1 mm particles in [weakPlume]. This apparent slight difference induces a significant effect on the averaged plume properties. The ash jet dragging effect is much weaker and can be seen clearly only on the enthalpy flux profile Fig. 6.4.8c and weakly in the mass flux profile Fig. 6.4.8a. This reflects with more evidence in the plume radius and velocity profiles. As in the [weakPlume] case, the plume radius is initially reduced by the jet dragging inducing a larger plume radius above the neutral buoyancy level. The velocity increases under the neutral buoyancy level due to kinematic decoupling, while above that level, velocity is larger in the dusty gas simulation. The plume height and neutral buoyancy level increase because of kinematic decoupling: they move from $H_{\max} \simeq 39$ km and $H_{\rm nbl} \simeq 18.2$ km with the [dusty] model to $H_{\max} \simeq 41$ km and $H_{\rm nbl} \simeq 18.5$ km with the [eqEu] model.

6.4.4 Entrainment coefficient

Fig. 6.4.9 reports the entrainment coefficient obtained for all the simulations presented in this section. The entrainment coefficient computed by using definition Eq. (3.11.5) is fitted with a constant value from the vent to approximately the neutral buoyancy level: $H = 16$ km. Surprisingly, quite stable results are obtained, even at different resolution, subgrid model and kinematic decoupling model: $\varkappa = 0.24 \pm 0.02$. However, the variability of the entrainment coefficient is larger than that measured in the [weakPlume] simulations. Even if the entrainment coefficient oscillates around a constant value, the standard deviation in this plume is significantly higher: $\sigma_{\rm fit} \simeq 0.14$ for the reference high resolution simulation.

It is worth noting that the entrainment coefficient shown in Figs. 6.4.9 and 6.3.6 has been evaluated by using Eq. (3.11.5), thus without adding in Eq. (3.3.19a) either a sink term due to particle fallout, a source term due to particle reentrainment, or a correction keeping into account partial plume collapse. Consequently, the resulting entrainment coefficient contains all these effects, because they are present in the three-dimensional simulations. This could be an explanation to the strong oscillations registered in the [strongPlume] simulations. Indeed, as it can be noticed from Figs. 6.4.1, 6.4.2 and 6.4.3, the entrainment around the plume edges is not as well organized as for the [weakPlume] case. In this eruption, the plume edge is bounded by nontrivial structures which seem to be quite important from qualitative analysis of the figures mentioned above. Other source of anomaly are the huge eddies underneath the umbrella cloud, which certainly influence the rate of entrainment of the plume under the neutral buoyancy level. Moreover, the plume partially collapses in the jet region, causing the entrainment coefficient to decrease and eventually to go below zero. This fact can be seen in Fig. 6.4.9, above the jet-plume transition at $z \simeq 5$ km. Above that height the entrainment coefficient presents two minima, corresponding to the heights where [strongPlume] loses more mass. I discuss in more detail this point in the next Sect. 6.4.5.

Despite this variability, the results of the fit from the high-res and the mid-res simulations are in agreement, with their respective error bars overlapping. The low resolution simulation is overestimating the entrainment coefficient, modifying the plume properties as commented above. However, all the other simulations at high- and mid-resolution give an entrainment coefficient in agreement with the

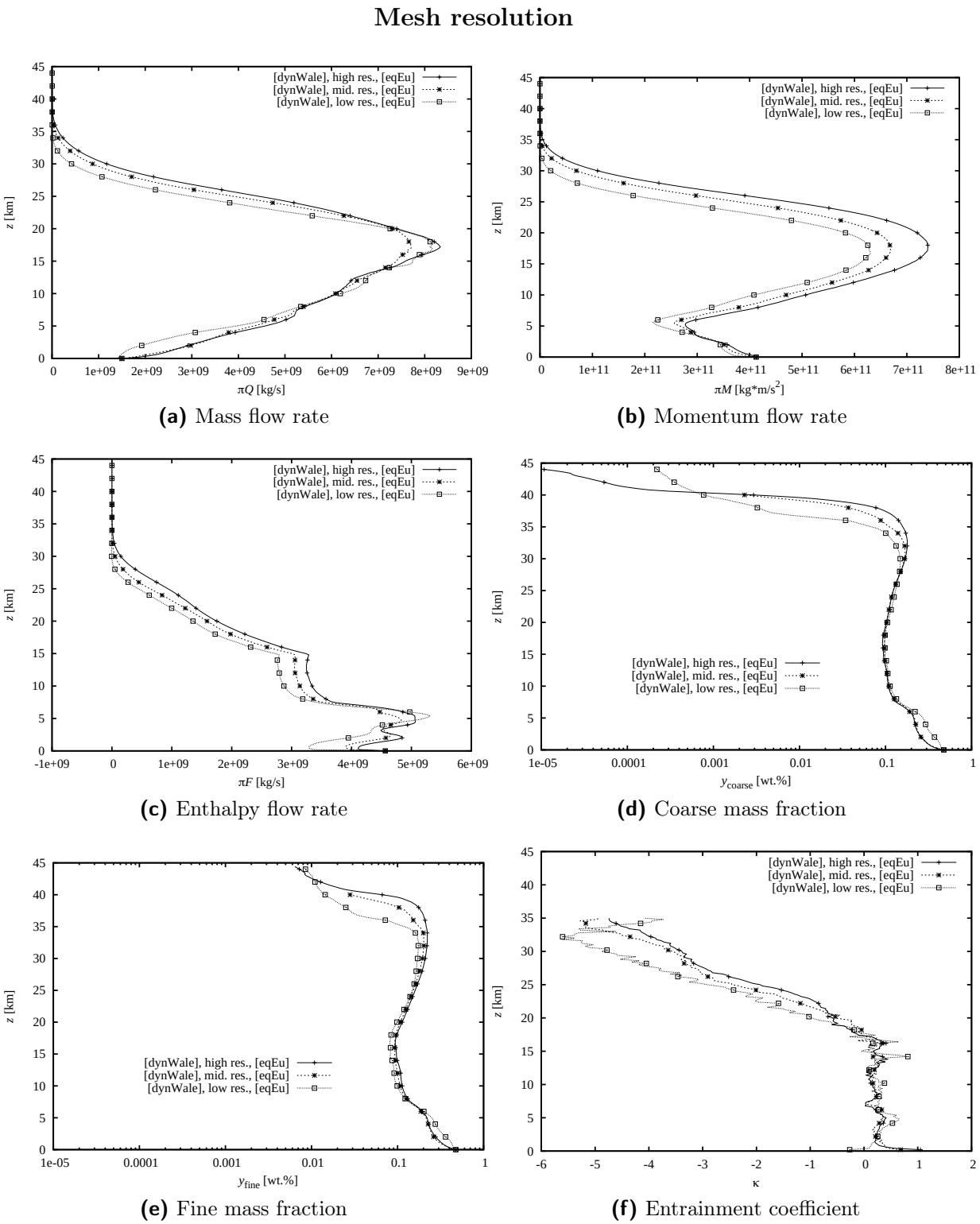

Figure 6.4.6: (first part) Profiles of all the integral variables of [strongPlume]: influence of the mesh resolution. Here, they are compared by changing the resolution from $\Delta r = D/32$ (high res.) to $\Delta r = D/16$ (mid res.) and $\Delta r = D/8$ (low res.).

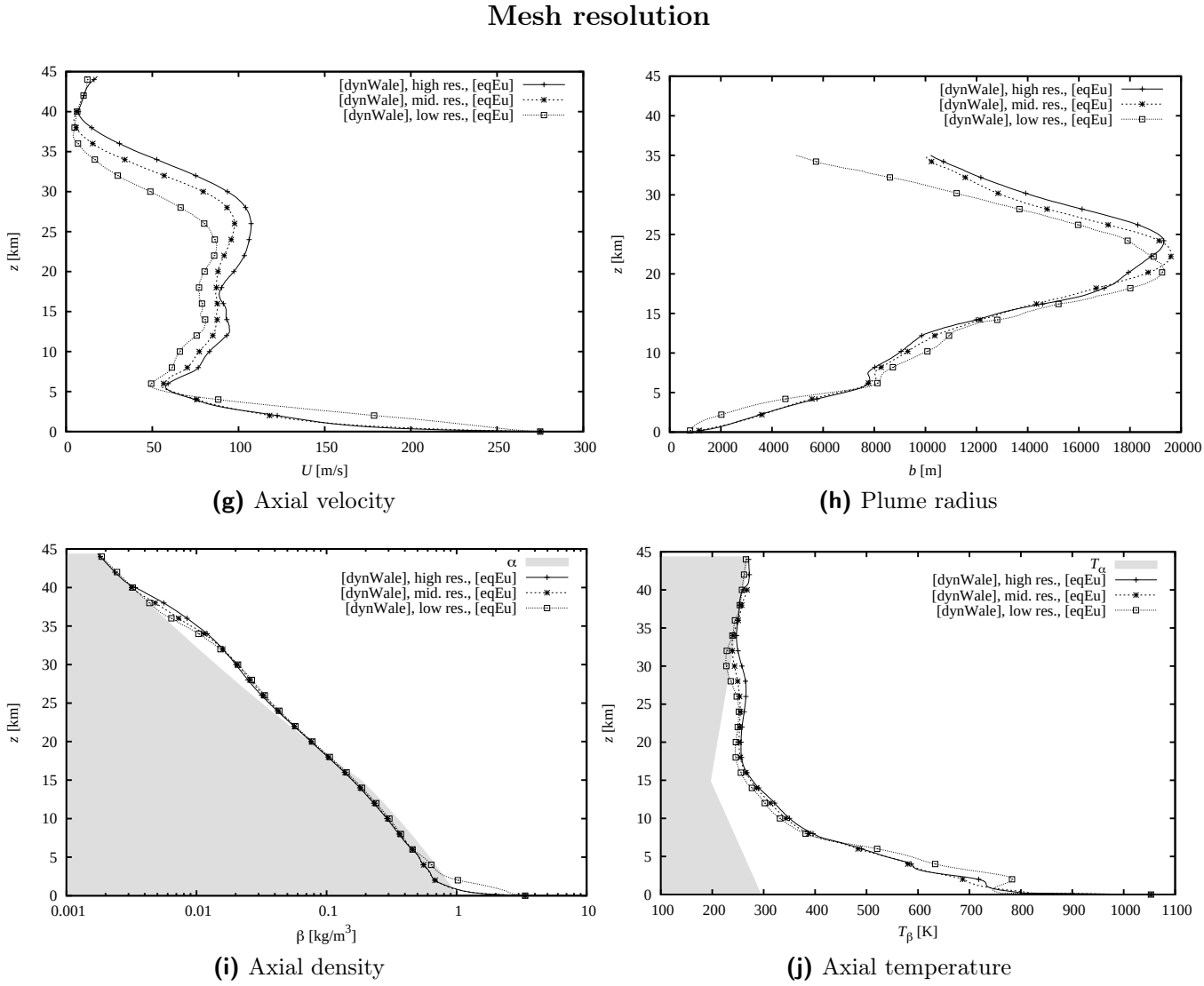

(g) Axial velocity **(h)** Plume radius

(i) Axial density **(j)** Axial temperature

Figure 6.4.6: (second part) Profiles of all the integral variables of [strongPlume]: influence of the mesh resolution. Here, they are compared by changing the resolution from $\Delta r = D/32$ (high res.) to $\Delta r = D/16$ (mid res.) and $\Delta r = D/8$ (low res.).

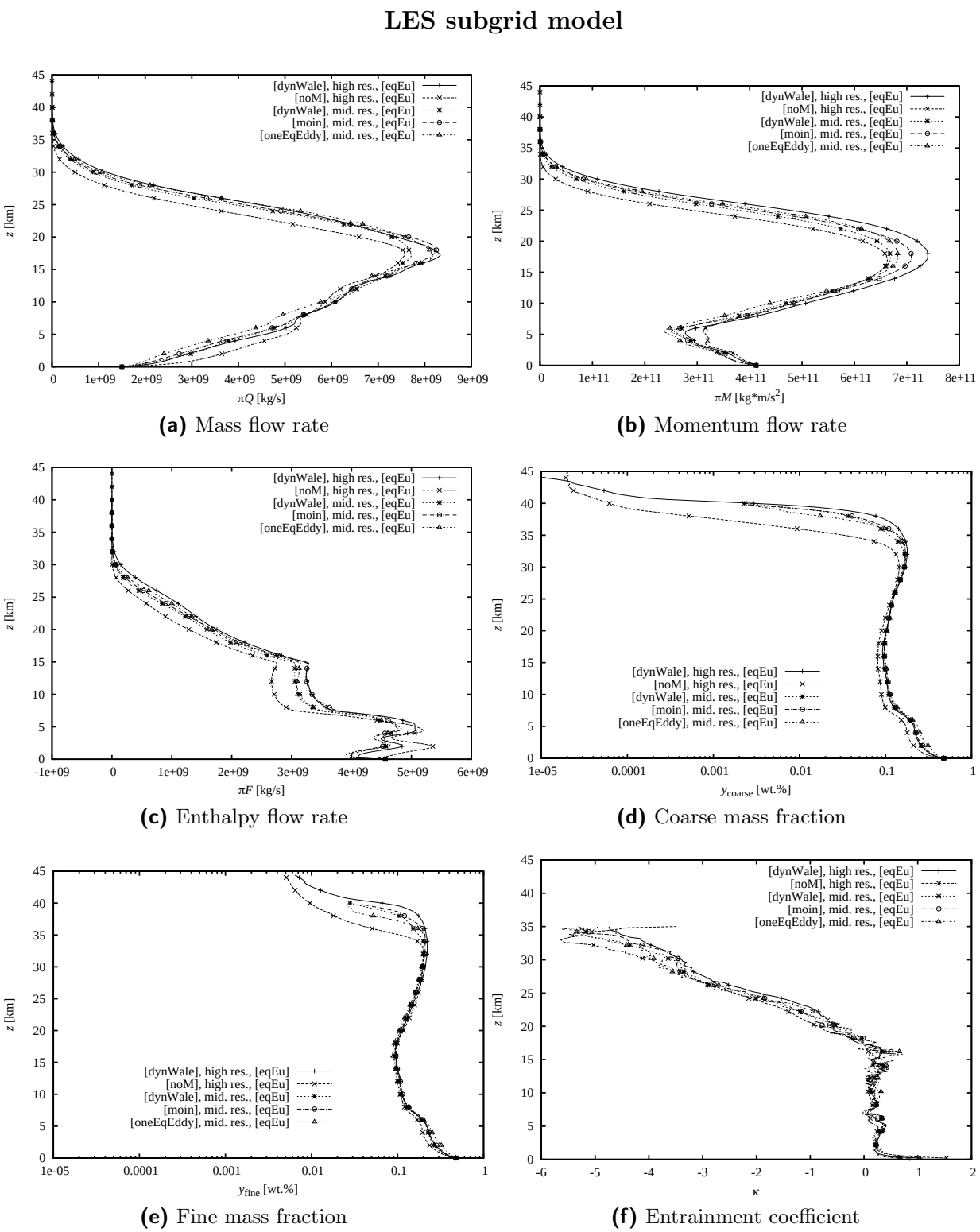

(a) Mass flow rate

(b) Momentum flow rate

(c) Enthalpy flow rate

(d) Coarse mass fraction

(e) Fine mass fraction

(f) Entrainment coefficient

Figure 6.4.7: (first part) Profiles of all the integral variables of [strongPlume]: influence of the subgrid LES models. Here, they are compared by using high and middle resolutions. In the high resolution case, the results obtained without subgrid model [noM] are presented, while in the middle resolution case [moin] and [oneEqEddy] are shown.

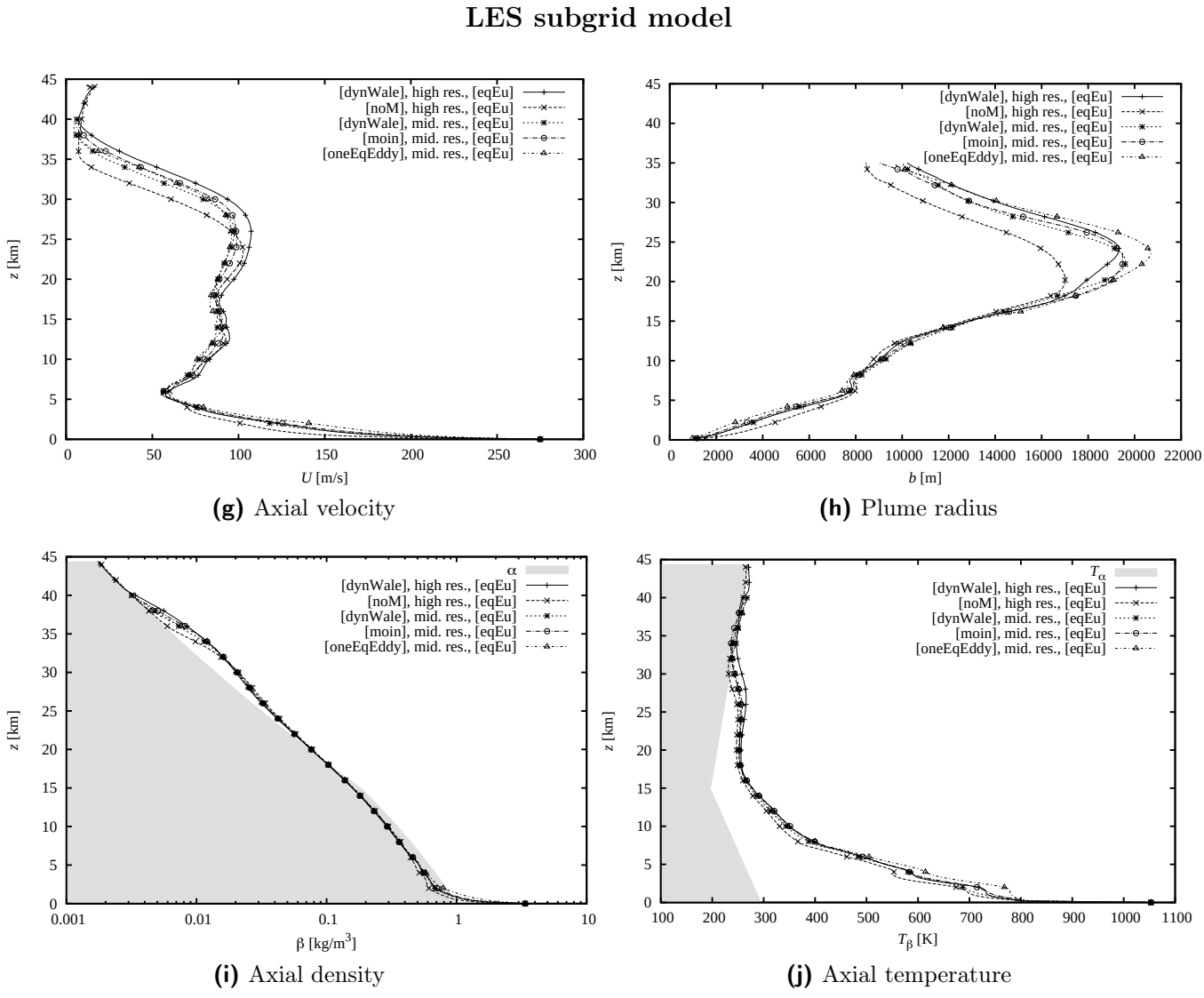

(g) Axial velocity **(h)** Plume radius

(i) Axial density **(j)** Axial temperature

Figure 6.4.7: (second part) Profiles of all the integral variables of [strongPlume]: influence of the subgrid LES models. Here, they are compared by using high and middle resolutions. In the high resolution case, the results obtained without subgrid model [noM] are presented, while in the middle resolution case [moin] and [oneEqEddy] are shown.

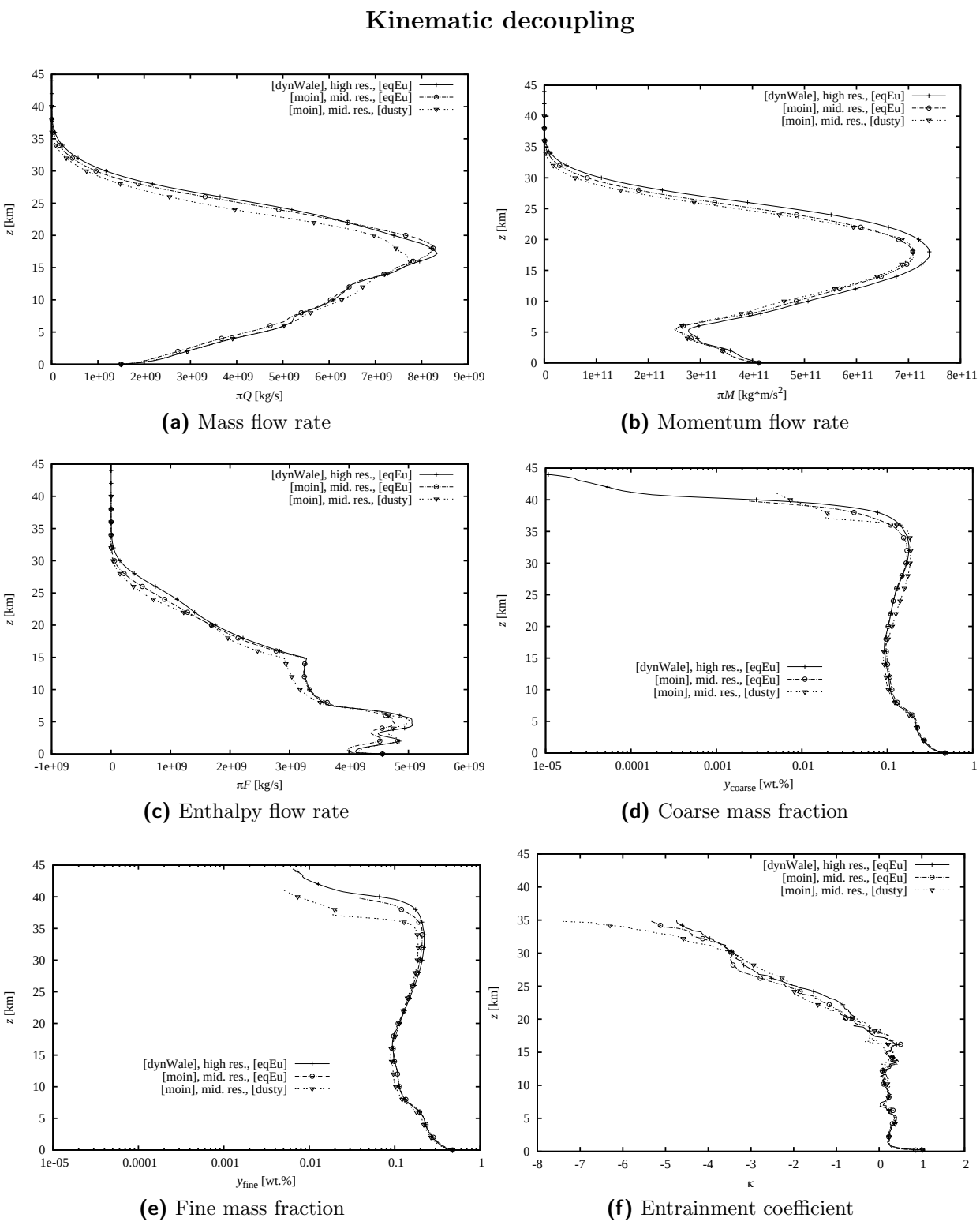

Figure 6.4.8: (first part) Profiles of all the integral variables of [strongPlume]: influence of the kinematic decoupling model. Here, results obtained using the [eqEu] model are compared with those from the [dusty] model. The former is reported in the high and middle resolution case, while the latter in the middle resolution case.

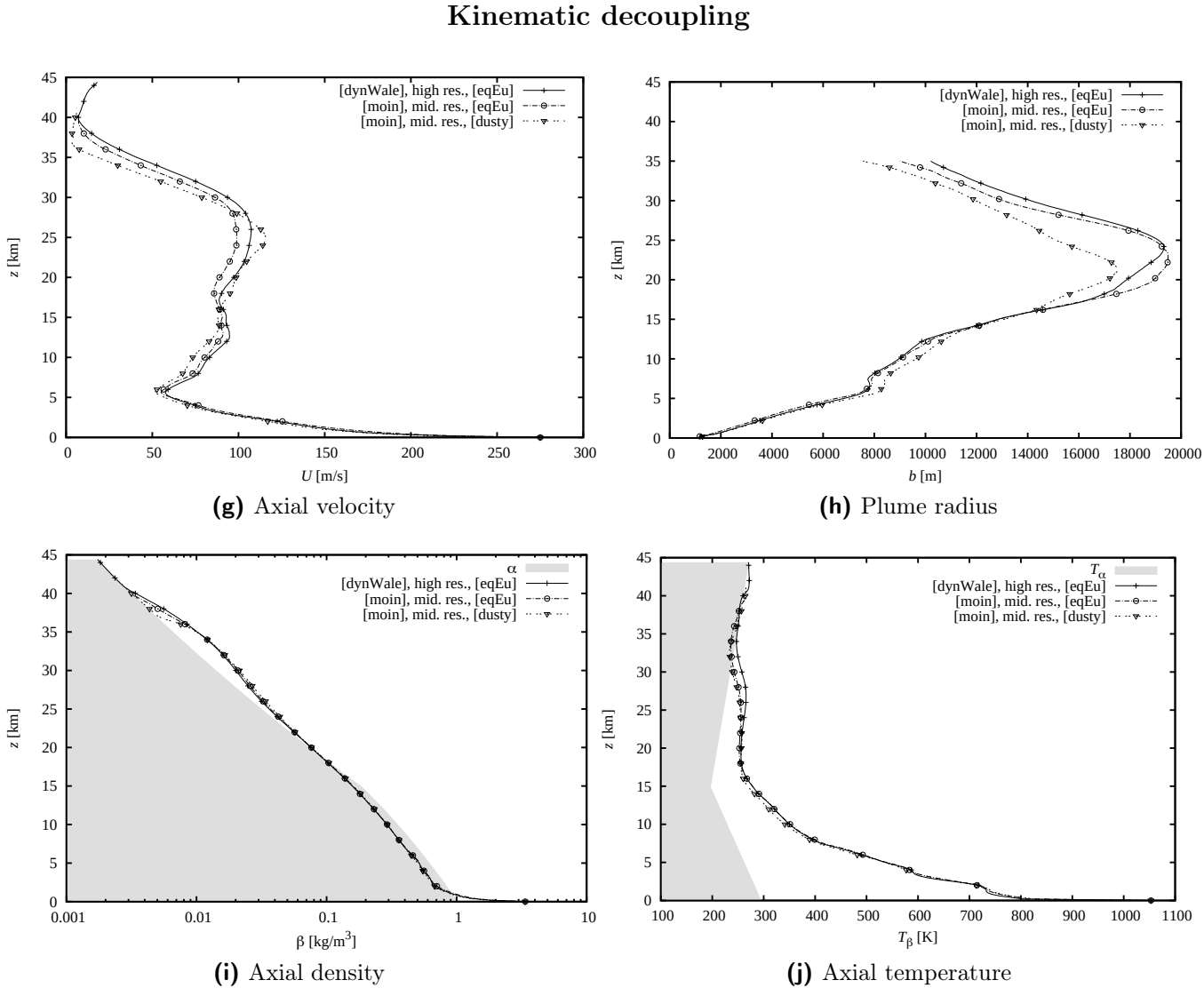

(g) Axial velocity **(h)** Plume radius

(i) Axial density **(j)** Axial temperature

Figure 6.4.8: (second part) Profiles of all the integral variables of [strongPlume]: influence of the kinematic decoupling model. Here, results obtained using the [eqEu] model are compared with those from the [dusty] model. The former is reported in the high and middle resolution case, while the latter in the middle resolution case.

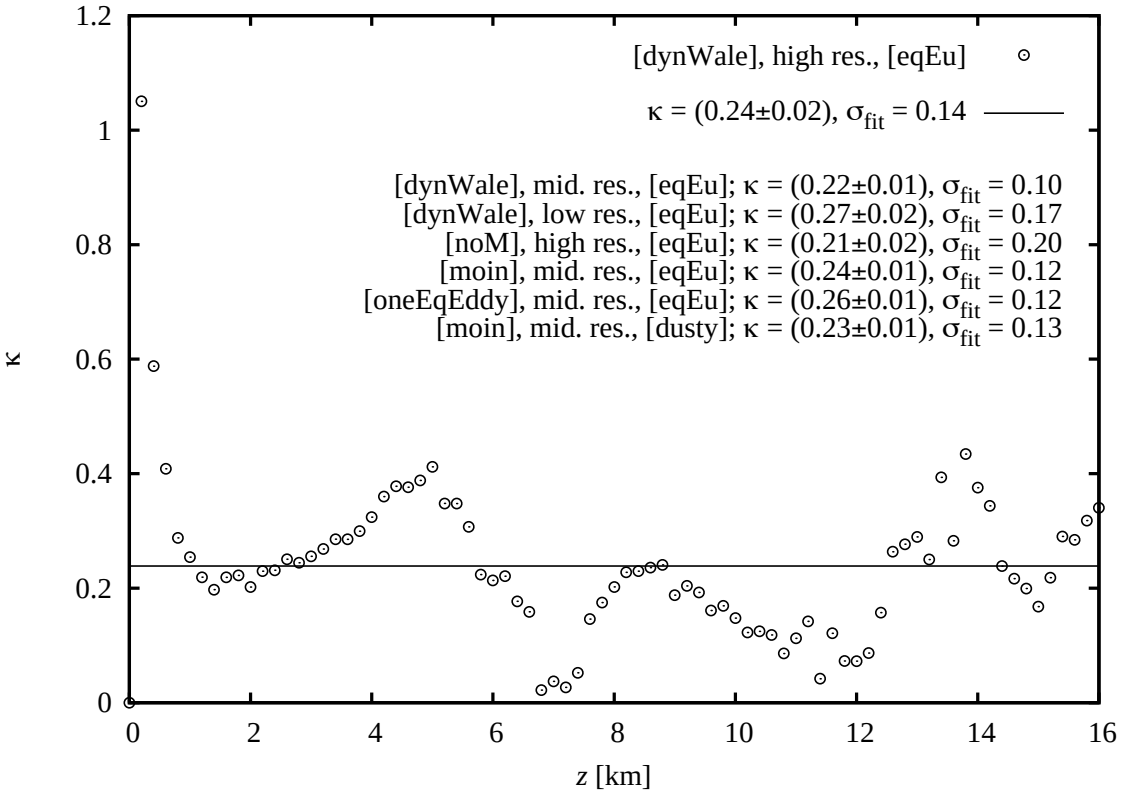

Figure 6.4.9: Entrainment coefficient of [strongPlume]. This is a zoom of Fig. 6.4.6f. The fit graph obtained at high resolution with the [dynWale] sub-grid model is shown, together with, in legend, the fit result for the other simulations performed.

reference simulation. The kinematic decoupling induces a negligible increase of the entrainment coefficient below the neutral buoyancy level: from $\varkappa = 0.23 \pm 0.01$ in the [dusty] case, to $\varkappa = 0.24 \pm 0.01$ in the [eqEu] one.

6.4.5 Plume collapse and reentrainment dynamics

Particle settling, negative buoyancy and two way coupling cause the plume to partially collapse forming pyroclastic density currents at the vent level. Indeed, part of the ash particles tend to collapse, dragging with them all the plume.

Fig. 6.4.10 shows the mean characteristics of the collapsing region, by using the following definition of collapsing flux and collapsing region:

$$q_c \equiv \frac{1}{\pi Q_0} \int_{\Omega_c} (\bar{\rho}_w + \bar{\rho}_{fine} + \bar{\rho}_{coarse})(-\bar{\boldsymbol{u}}_m \cdot \hat{z})\, dx dy \tag{6.4.1a}$$

$$\Omega_c(z) \equiv \{(x,y) \in \mathbb{R}^2 | \, (\bar{\boldsymbol{u}}_m(x,y,z) \cdot \hat{z} < 0) \wedge \sqrt{x^2+y^2} < r_c\}, \tag{6.4.1b}$$

with $r_c = 5$ km. Ω_c is the domain with negative averaged vertical velocity in the vent region, while q_c is the mass flux of the ejected mixture across horizontal slices of Ω_c. I refer to ejected mixture as the flux of ejected water $(\cdot)_w$, and of the solid particles $(\cdot)_{coarse} + (\cdot)_{fine}$. In Fig. 6.4.10a, the connected domain Ω_c is represented through the isosurface at nil vertical velocity $\bar{\boldsymbol{u}}_m \cdot \hat{z} = 0$. It is colored with the magnitude of the mixture flux which is passing through the surface $\bar{\rho}_m(\bar{\boldsymbol{u}}_m \cdot \boldsymbol{n})$. In this figure, it is clearly shown how the jet region is surrounded by a collapsing region with negative

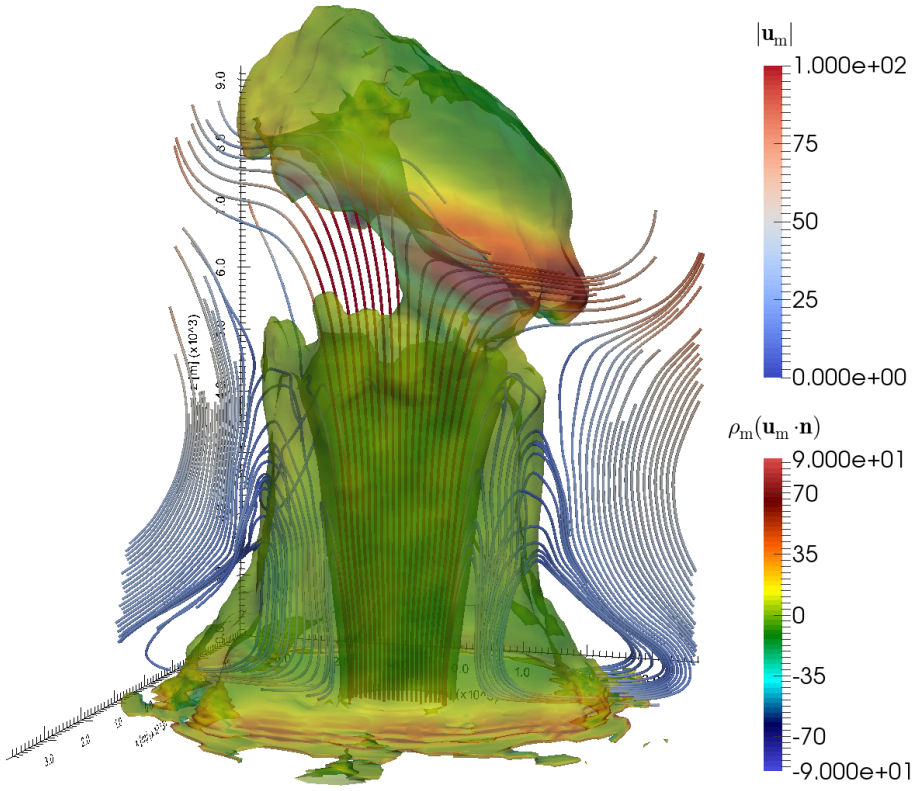

(a) Collapsing region

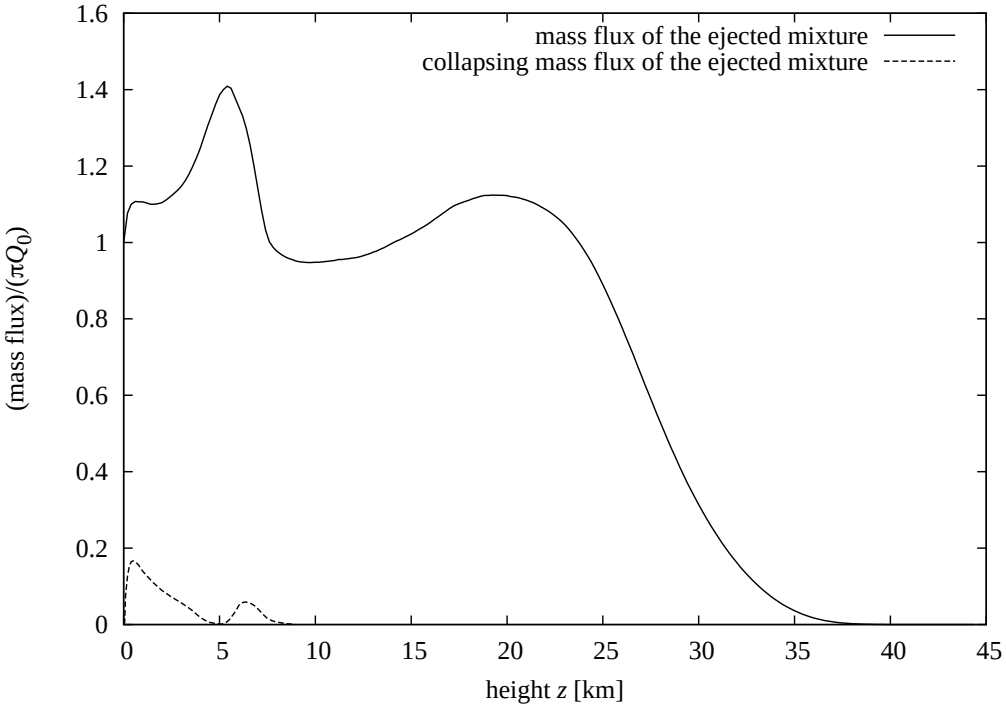

(b) Ejected mixture and collapsing mass fluxes

Figure 6.4.10: Collapsing dynamics: (a) Isosurface at nil vertical velocity ($\bar{\boldsymbol{u}}_m \cdot \hat{z} = 0$), colored with the outflow intensity $\bar{\rho}_m(\bar{\boldsymbol{u}}_m \cdot \boldsymbol{n})$ in kg/m^{2}s. The streamlines of the velocity field $\bar{\boldsymbol{u}}_m$ are also represented, colored with its magnitude in m/s. (b) Vertical evolution of the mass flux of the ejected mixture (water and ash particles) normalized with its vent value $\pi Q_0 = 1.5 * 10^9$ kg/s (solid line). It is also reported in dashed line the vertical evolution of the collapsing flux of the ejected mixture $q_c(z)$. It is calculated following Eq. (6.4.1).

vertical velocity. The collapsing region is fed by the jet itself along its development under the suspended flow above the fountain. The suspended flow stands above the jet at $z \simeq 5$ km. The mean velocity field exhibits an "hat" shaped region with negative vertical velocity above the suspended flow. The streamlines of the velocity field show that the suspended flow divides the part of the jet going directly upwards into the plume from that collapsing. The flow feeding the collapsing region comes from the jet. This flow forms a sharp bend at the jet edges, changing the vertical velocity from positive to negative. The collapsing flux then crashes to the ground and is ejected radially from the feet of the collapsing region. It forms a toroidal eddy all around the jet, which then divides in three parts: the first recirculate entering again in the collapsing region; the second acquires positive buoyancy creating the big co-ignimbrite surrounding the jet region; the third remains negative buoyant and feed the pyroclastic density currents which forms at the base of the co-ignimbrite.

Fig. 6.4.10b quantifies the fraction of collapsing mass flux of the ejected mixture as a function of the height: $q_{\mathrm{c}}(z)$, Eq. (6.4.1). The collapsing mass flux of the ejected mixture reaches its maximum in $z \simeq 500$ m above the vent, with a value approximatively of 17 % of the mass flux at the vent. A second smaller maximum is reached by $q_{\mathrm{c}}(z)$ above the suspended region, in correspondence with the "hat" region above it. Moreover, this figure shows the evolution of the mass flux of the ejected mixture in the plume, i.e. $q_{\mathrm{ej}} = (Q_{\mathrm{w}} + Q_{\mathrm{coarse}} + Q_{\mathrm{fine}})/Q_0$. Q_k is defined in Eq. (3.11.4b) for a generic phase $(\cdot)_k$. It is the mass flux horizontally integrated in the plume region, i.e. in the region with positive vertical velocity. The mass flux of the ejected mixture in the plume reaches its maximum in $z \simeq 5$ km, in correspondence with the suspended flow height. The maximum value is approximatively 1.4 times the mass flux at the vent. Then it decreases in the "hat" region above the suspended flow. In the updraft between the suspended flow and the neutral buoyancy level, q_{ej} keeps a value approximatively constant near to 1. Finally it goes to zero from the neutral buoyancy level to the maximum plume height.

In the ideal case modeled by integral models in Chap. 3, the mass flux of the ejected mixture is assumed to be constant. Indeed, the vector field $\rho_k \boldsymbol{u}$ is divergence-free (see Eqs. (3.2.2a) and (3.2.2b)) and there is not entrainment nor detrainment of the ejected mixture from the plume. Thus the conservation law for the mass fluxes Eqs. (3.2.8) holds. On the other hand in Fig. 6.4.10b, the mass flux found with three-dimensional simulations is not constant. This behavior can be attributed to the following three phenomena: 1) particle decoupling and fallout; 2) ejected mixture partial collapse and recirculation; 3) correlation between the density and velocity fluctuations.

Particle fallout is one of the phenomena causing detrainment of ejected mixture from the mixture. It has been firstly modeled by Woods and Bursik [229] in the framework of the integral models approach. However in [strongPlume], neither particle fall-out nor kinematic decoupling alone are enough to justify the variability of the ejected mixture mass flux. This conclusion has been checked by comparing $q_{\mathrm{ej}}(z)$ obtained with the [dusty] and the [eqEu] models.

Partial collapse and recirculation due to negative buoyancy can participate substantially to the variations of the profile $q_{\mathrm{ej}}(z)$, because they essentially modify the time-averaged velocity field (see Figs. 6.4.10a and 6.4.11). In the forced plume presented in Sect. 5.5, the mean velocity field is directed vertically upwards in

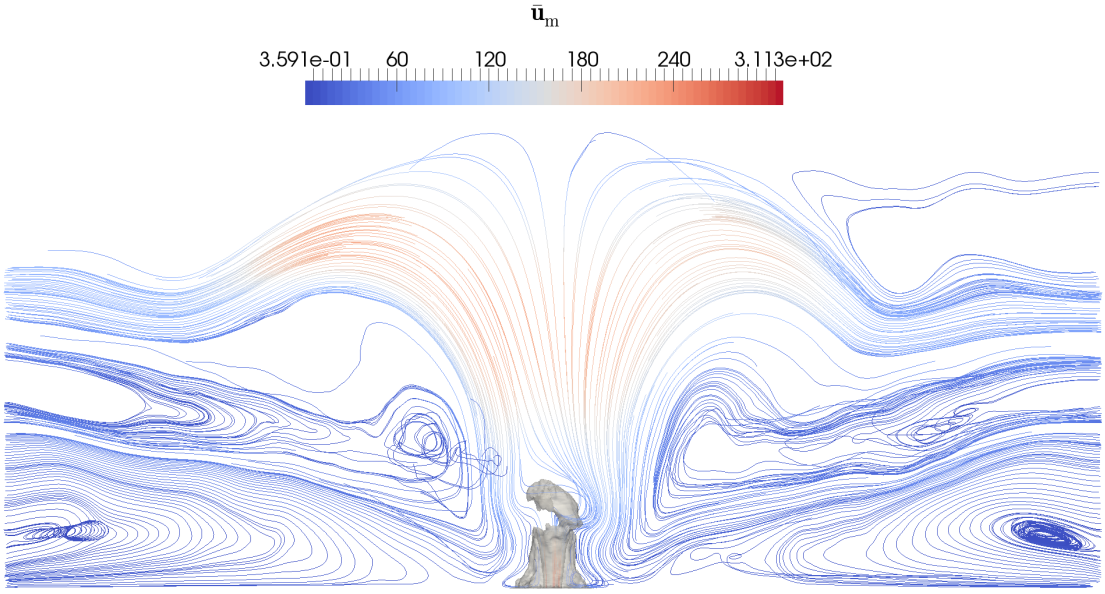

Figure 6.4.11: Streamlines of the time-averaged velocity field of the [strongPlume]

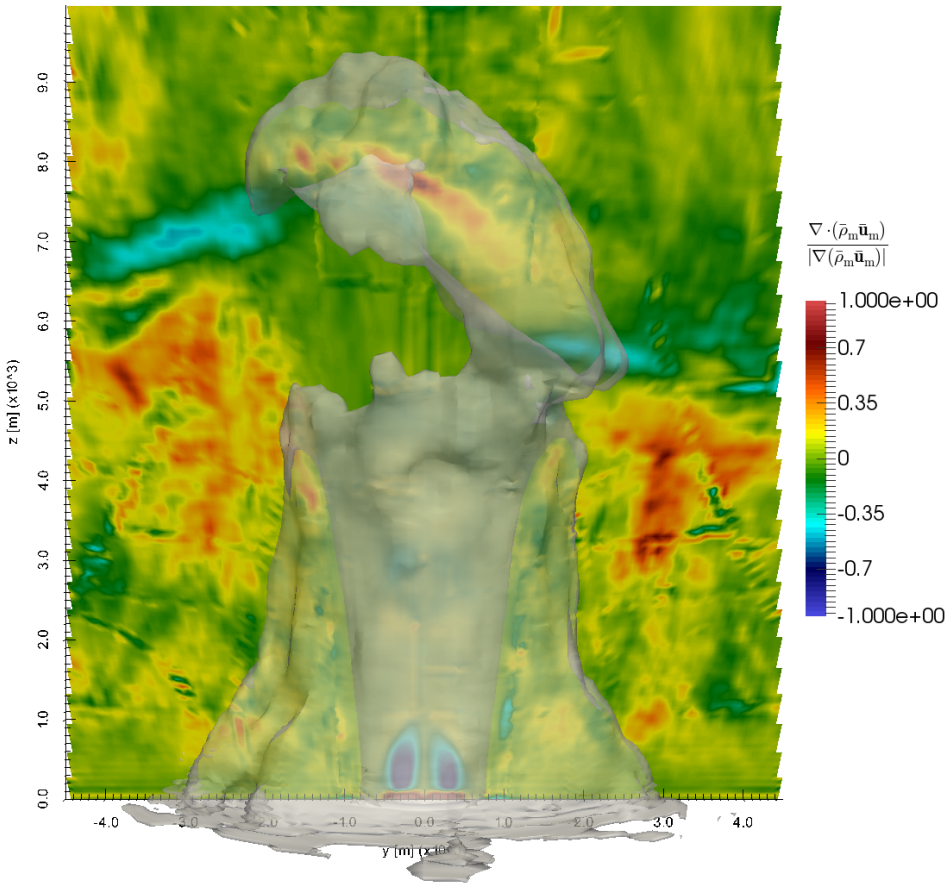

Figure 6.4.12: Divergence coefficient of the mean field $\bar{\rho}_\mathrm{m}\bar{\boldsymbol{u}}_\mathrm{m}$: $\dfrac{\nabla\cdot(\bar{\rho}_\mathrm{m}\bar{\boldsymbol{u}}_\mathrm{m})}{|\nabla(\bar{\rho}_\mathrm{m}\bar{\boldsymbol{u}}_\mathrm{m})|}$. Red and blue zones show where the divergence of $\bar{\rho}_\mathrm{m}\bar{\boldsymbol{u}}_\mathrm{m}$ is big with respect to its gradient.

the plume region and it is horizontal outside (see Fig. 5.5.3). On the other hand, Fig. 6.4.10a shows that the velocity field surrounding the jet region of [strongPlume] has not such a simple configuration. As a consequence, Fig. 6.4.10 shows an increase of $q_{\rm ej}$ below the suspended flow, because the mass flux ejected from the vent is enlarged by the co-ignimbrite, which is fed by the partial collapse. Above the suspended flow, $q_{\rm ej}(z)$ decreases because the mean velocity field in the plume region ceases to be substantially vertical and instead acquires a significant horizontal contribution (Fig. 6.4.11). Then, when $\bar{\boldsymbol{u}}_{\rm m}$ again becomes almost vertical, $q_{\rm ej}$ increases again, until the neutral buoyancy level. Above this level, the plume loses mass in favor of the umbrella cloud. The region between the neutral buoyancy level and the maximum plume height extends for a relevant portion of the total plume height. The huge eddies underneath the umbrella cloud "bend" the plume streamlines, transporting the mass in the plume to the umbrella.

The third phenomenon which, in principle, can affect the conservation of $q_{\rm ej}(z)$ is the statistical correlation between the density and the velocity fluctuations. Indeed, the continuity equation used to write Eqs. (3.2.2a) and (3.2.2b) for the buoyant plume solution, changes slightly if one time-averages directly the three-dimensional fields:

$$0 = \overline{\partial_t \rho_m + \nabla \cdot (\rho_{\rm m} \boldsymbol{u}_{\rm m})} = \nabla \cdot (\overline{\rho_{\rm m} \boldsymbol{u}_{\rm m}}) = \nabla \cdot (\mathrm{cov}(\rho_{\rm m}, \boldsymbol{u}_{\rm m})) + \nabla \cdot (\bar{\rho}_{\rm m} \bar{\boldsymbol{u}}_{\rm m}) \,, \quad (6.4.2)$$

thus $\nabla \cdot (\bar{\rho}_{\rm m} \bar{\boldsymbol{u}}_{\rm m}) = -\nabla \cdot (\mathrm{cov}(\rho_{\rm m}, \boldsymbol{u}_{\rm m})) \neq 0$. In other words, even if $\rho_{\rm m} \boldsymbol{u}_{\rm m}$ is solenoidal, $\bar{\rho}_{\rm m} \bar{\boldsymbol{u}}_{\rm m}$ is not, as long as the divergence of the covariance between $\rho_{\rm m}$ and $\boldsymbol{u}_{\rm m}$ is different from zero. Fig. 6.4.12 quantify this statistical effect, measuring the divergence of $\bar{\rho}_{\rm m} \bar{\boldsymbol{u}}_{\rm m}$ with respect to the norm of its gradient. It is worth noting that – in average – there are two compression zones, immediately above the vent and in the suspended flow, under the "hat" (cyan to blue areas). The decompression zones are essentially in the "hat" and in the co-ignimbrite region below the suspended flow (yellow to red areas).

6.4.6 Comparison with integral models

As done for the [weakPlume] eruption, in this section results obtained from three-dimensional simulations of the [strongPlume] eruption are compared with those presented in Chap. 3. In particular, the profiles obtained with the [dusty] model in Fig. 6.4.8 are compared with profiles shown in Fig. 3.10.4.

Below, the main difference noticed are enumerated.

- Plume height. Integral models described in Chap. 3 capture the plume height. The complete model (3.4.1) gives $H_{\rm max} \simeq 39$ km, as the three dimensional simulation with the [dusty] model. The analytical asymptotic one (see Sect. 3.10) overestimates it $H_{\rm max} \simeq 43.5$ km.

- Neutral buoyancy level. The complete model gives $H_{\rm nbl} \simeq 24.9$ km, the analytic one gives $H_{\rm nbl} \simeq 32.5$ km. Three-dimensional simulation gives $H_{\rm nbl} \simeq 18.2$ km. Integral models overestimate the plume neutral buoyancy level.

- Plume velocity. The plume velocity provided by the integral model is significantly higher than that provided by the three-dimensional simulation. While in the former case the velocity in the jet-plume transition height is around 160 m/s, in the three-dimensional simulation it is about 50 m/s.

- Plume radius. The plume radius is strongly underestimated by integral models. The radius in the jet-plume transition is $\simeq$ 3 km against $\simeq$ 5.5 km in three-dimensional simulations, while close to the neutral buoyancy level ($z \simeq 20$ km) it is $\simeq$ 10 km against $\simeq$ 17.5 km in the three-dimensional simulation. Above that height the behavior is the opposite. While in the former case the plume radius and mass flux increase, in the latter one they decrease down to zero (excluding fluctuations induced by the fact that also momentum goes to zero).

- Plume density, temperature and mass fractions. As a general behavior, the plume dilutes slower in integral models with respect to the three-dimensional simulation. In particular in the jet region the rate of dilution is underestimated by integral models.

- Ejected mixture mass flux. The flux $q_{\rm ej}(z)$ defined in Sect. 6.4.5 is not constant in three-dimensional simulations, while it is constant in integral models.

Based on these outcomes some conclusions can be drawn about the use of integral models presented in Chap. 3 vs the three-dimensional ones. In [strongPlume] as in the [weakPlume] eruption, the main source of discrepancy between the three-dimensional solution and the integral one seems to be the entrainment model (or, in more general terms, the equation for the mass flux). In the three-dimensional simulation, an entrainment coefficient larger than that used in Chap. 3 is found. Thus, the integral plume model is diluting slower than in three-dimensional simulations, the temperature remains hotter, the velocity is larger and the plume goes higher, reaching a neutral buoyancy level 36 % higher than that provided by three-dimensional simulations. Then, above the neutral buoyancy level, assuming a constant entrainment coefficient led to a complete wrong behavior, where the plume radius diverges instead to go to zero. This discrepancy adds another source of error to the plume evolution, which however goes in an opposite direction, decreasing the plume height. In three-dimensional simulations the entrainment becomes negative above the neutral buoyancy level, the plume thus loses mass and the momentum decrease is slower than in the integral model. Indeed, in the latter model the mass flux keeps increasing causing the momentum flux to go to zero faster.

As highlighted in the section devoted to the analysis of the [weakPlume], I plan to further analyze three-dimensional simulations in future studies, to improve the entrainment coefficient of integral models. This can be achieved by studying the behavior of the first integral of motion presented in Chap. 3, and by deepening the knowledge of the influence of the jet region, plume partial collapse and recirculation to the entrainment model. In the next section I discuss briefly the behavior of integral models conserved quantities in [dusty] three-dimensional simulation.

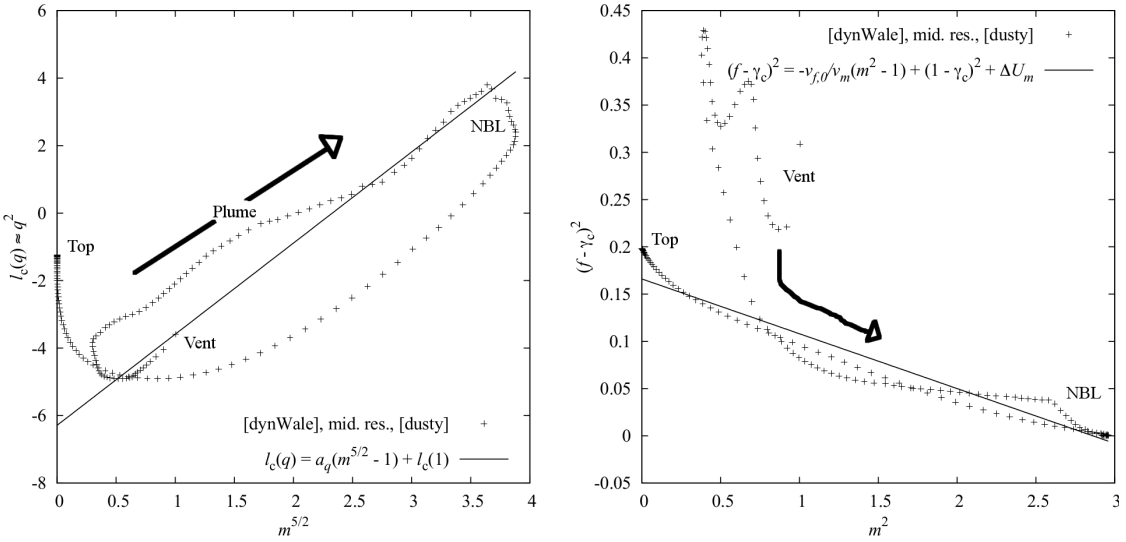

Figure 6.4.13: Behavior of conserved quantities of the asymptotic integral model as calculated from three-dimensional simulations. Here, some of the plume parameters reported in Tab. 3.4.2 have been modified to obtain a better behavior of the conserved quantities (see discussion): $a_q = 0.473 \rightarrow a_q = 2.7$, $\gamma_c = 0.345 \rightarrow \gamma_c = 0.445$. Moreover, it is used the value $v_{f,0} = 3.0 * 10^{-2}$, obtained averaging the atmospheric profile: $\omega_0 \simeq 2.61 * 10^{-2}$ Hz.

6.4.7 Plume conserved quantities

In Sect. 3.10 I used two conserved quantities along the plume height: $\mathcal{U}_{\rm RS}$ Eq. (3.7.4) and $\mathcal{U}_m$ Eq. (3.9.8). These first integral of motion depend respectively on $l_c(q) \approx q^2$ (see Eq. (3.10.4)) and $m^{\frac{5}{2}}$, and on $(f - \gamma_c)^2$ and m^2. The first conserved quantity is tied with the entrainment assumption, while the second one is not. While in Sect. 6.4.5 the conservation of $q_{\rm ej}$ is discussed (hypothesis used by integral models), in this section the behavior of $\mathcal{U}_{\rm RS}$ and $\mathcal{U}_m$ is explored. Fig. 6.3.7 shows the behavior of these first integral of motions in the three-dimensional simulations.

As for the [weakPlume] eruption, even in the [strongPlume] it is found that some of the plume parameters have to be modified to obtain the behavior predicted by integral models. In particular when testing the conservation of first integral $\mathcal{U}_{\rm RS}$ defined in Eq. (3.7.4) (or, equivalently Eq. (3.10.3)), the parameter a_q should be increased significantly (see Fig. 6.4.13). In this way, the evolution of m approximately follows the prevision given by Eq. (3.10.3), from the vent elevation to the neutral buoyancy level (where m reach its maximum). However, in the jet region the prevision works worse than [weakPlume]. On the other hand, $\mathcal{U}_{\rm RS}$ is not conserved above the neutral buoyancy level. This is in agreement with the entrainment evolution, which is not constant at all above the neutral buoyancy level. For what concerns the other conserved quantity $\mathcal{U}_m$, I recall that it is defined independently from the entrainment assumption in Eq. (3.9.8). In order to have $\mathcal{U}_m$ approximately constant along the plume, γ_c is increased slightly (see Fig. 6.3.7). In this way, $\mathcal{U}_m$ can be considered approximately constant all along the plume height, even during the buoyancy transition at the neutral buoyancy level. However, as for the [weakPlume] eruption, in the region near the vent $\mathcal{U}_m$ is subject to a sudden change identified in Fig. 6.4.13 with $\Delta\mathcal{U}_m \simeq -0.2$. In contrast to what seen for the [weakPlume] eruption, in this case part of the motivation changing

$\mathcal{U}_m$ can be found in the non-Boussinesq regime to which the plume is subject near the vent, because $\Delta\mathcal{U}_m \neq 0$ in the complete one-dimensional model (3.4.1). However, the main motivation behind this variation can be found in the composite three-dimensional jet structure obtained and commented in Sect. 6.4.5. Indeed, the self-similar assumption is no longer valid in that region. Further studies and numerical simulations are needed to better understand the presented behavior.

Chapter 7

Summary and concluding remarks

I have presented a comprehensive study of numerical and analytical methods to analyze multiphase flows composed by heavy solid particles dispersed in a carrier fluid. In this thesis, the focus has been the application of such methods to the modeling of volcanic ash plumes. The partial differential equations (PDEs) arising from the laws of conservation of mass, momentum, and energy of the multiphase mixture have been studied analytically to show the existence of weak solutions fulfilling the corresponding natural energy inequalities. By means of Large Eddy Simulations (LES) and Direct Numerical Simulations (DNS) volcanic ash plumes have been modeled in their complete three-dimensional turbulent dynamics. The new three-dimensional numerical solver has been developed by using the `C++` libraries of OpenFOAM® . This solver has been called `ASHEE`, Ash Equilibrium–Eulerian model. The code has been tested against a number of well understood Computational Fluid Dynamics benchmarks in order to verify and validate its capability to capture key physical phenomena in volcanic plumes. Results have been compared with simplified integral plume models, which are faster to solve and widely used in volcanology and operative hazard assessment. I have used both integral and three-dimensional models to calculate quantities that can be measured by volcanologists. In particular, integral models have been used to produce synthetic thermal infrared averaged images of eruption plumes, comparing them with a real eruption occurred in Guatemala in 2005. By means of two alternative inversion techniques, it has been possible to retrieve the key vent parameters from the observed infrared data. On the other hand, I have showed that three-dimensional simulations are capable to reproduce infrasonic spectra measured during volcanic eruptions. Results demonstrated that, despite the difficulties in validating numerical models with field observations, accurate modeling allows to quantitatively interpret observations and laboratory experiments. The developed models are suitable for application to hazard assessment and mitigation of risks associated with the dispersion of volcanic ash and hazardous gases in the atmosphere.

Scientific results

The main scientific results obtained in this thesis are briefly summarized here (chapter by chapter):

- A review of mathematical models for dispersed multiphase turbulence is given.

  The multiphase Eulerian model in dispersed regime has been rewritten in a new "mixture" formulation, solving for the density, momentum, and energy of the mixture instead of those of each individual phase. This formulation has the great advantage to be similar to the classical Navier-Stokes equations, depending explicitly only on the relative velocity $\boldsymbol{v}_j$ and the relative temperature $T_j - T_g$ and not on the explicit form of the drag terms coupling the phases.

  The equilibrium–Eulerian model has been generalized to the compressible two-way coupled regime. The new model has been filtered in order to find all the subgrid terms, and to model them using the existing LES models.

- The two-phase, gas–particle Eulerian model in four-way-coupled and barotropic regime has been studied, by means of techniques of approximations and of functional analysis.

  In particular, I have shown the stability of sequences of smooth solutions fulfilling the natural energy estimates and also some appropriate entropy-type estimates. These sequences converge strongly to weak solutions of the problem.

  I have sketched also how it is possible to construct such sequences, by means of adding certain non-linear terms to the equations.

- The most general multiphase integral model for volcanic plumes in a calm and stratified atmosphere (Woods [225]) has been obtained directly from the dusty gas model (Marble [127]). The resulting ODE system has been closed with the thermodynamics of a gas–particle mixture. A new "enthalpy flux" has been identified, rewriting the model in a compact self-consistent formulation.

  The new ODE system has been made dimensionless, to highlight the six independent parameters characterizing uniquely a volcanic plume in absence of wind. The new model is named `ASH1D`. Different regimes of the integral model have been studied, generalizing literature results to the multiphase regime. In particular, the jet, the Boussinesq, and the stratified/non-stratified regimes have been envisaged. The first integrals of motion conserved by the ODEs have been identified.

  A new "first order" plume height expression has been obtained, refining that found by Morton [137] and allowing to correct to the first order the correlation between the plume height and the neutral buoyancy level reported by Turner [200]. In this way, by measuring the neutral buoyancy level alongside the maximum plume height, it is possible to retrieve not only the mass eruption rate, but also the density of the erupted mixture.

An analytical solution of the `ASH1D` model has been found, allowing to compute the plume profiles in the non-Boussinesq case. It has been called `ASH0D`. It works satisfactorily well (with respect `ASH1D`), capturing both mean profiles and plume heights.

- A model coupling a generic fluid dynamic plume model to a model for the infrared bright emission of a heterogeneous gas–particle mixture has been formulated.

  Using analytical integral plume models, the coupled model has been inverted to retrieve key vent parameters of a volcanic ash plume generated by a real volcanic eruption at Santiaguito (Guatemala). In particular, the model can retrieve: the plume entrainment, the mass flow rate, the plume velocity, the plume temperature, the mass fractions of ash and water, and the mean Sauter diameter of the grain-size distribution of the ash. The minimum of the inversion cost-functional has been studied using the genetic algorithm. This allowed to find the errors associated to all the retrieved parameters.

- A computational algorithm for the DNS/LES of the polydisperse equilibrium–Eulerian model has been implemented taking advantage of an open-source infrastructure. It is named `ASHEE`.

  The new solver has been verified and validated against a variety of experiments and benchmarks. In particular, I have defined a wide set of standardized numerical LES/DNS benchmarks to stress the numerical model: mono/multi-phase decaying isotropic turbulence, natural convection, experimental turbulent forced plume dynamics, shock tube experiment and the lock-exchange mixing experiment.

- The `ASHEE` model has been applied to the numerical simulation of two volcanic eruption scenarios.

  The shape of the infrasonic spectrum measured during persistent volcanic eruptions has been reproduced by the numerical simulations.

  A methodology to measure the mass collapsing from a volcanic plume is introduced.

  The effects of the grid resolution, of the LES subgrid scale model, and of the non-equilibrium decoupling model on the numerical solution have been analyzed, allowing to conclude that the uncertainty on the numerical solution associated with such effects can be significant (of the order of 20%), but still lower than that typically associated with input data and integral model approximations.

  The influence of the non-equilibrium effects is larger than that of the grid resolution and LES models. We have shown that particle non-equilibrium introduces a novel phenomenon, that we have called jet-dragging, clearly observable in the [weakPlume] case. Because of the kinematic decoupling, all profiles are shifted up and the plume radius increases in the buoyant region of about 20%. This reflects systematically in the umbrella region and in the plume height.

In the [weakPlume] case, 3D results are consistent with the predictions of integral models in the jet and plume regions, with an entrainment coefficient around 0.10 in the plume region. In the [strongPlume] case, the self-similarity assumption appears to be more questionable and the entrainment coefficient in the plume region is more unstable, with an average value of 0.24.

A methodology to coherently compare time-averaged 3D and 1D results have been developed and applied to the plumes presented in this thesis. The main discrepancies between 1D and 3D model results derive from the entrainment model.

Plume height predictions of 3D model differ from those of integral models. In the [weakPlume] case, both levels are underestimated by about 10% mainly because of the entrainment assumption in the jet region. In the strong plume case, the NBL is strongly overestimated by integral models, indicating that the assumptions behind such models are weaker both in the jet and plume region. For both cases, integral models description of the umbrella region is incorrect: the entrainment remains constant while in 3D simulations it becomes negative. In the [strongPlume], this effect counterbalances the higher NBL making the total plume height consistent with 3D results.

The present study demonstrates that LES models can reliably describe the dynamics of volcanic plumes and are an irreplaceable tool to identify the critical hypotheses and to calibrate empirical parameters at the base of integral models used in operational studies. In addition, they allow to study unexplored regimes where integral model assumptions are flawed and provide the unprecedented capability to reproduce observables quantities (such as infrasound signals) which can be useful to constrain eruption dynamics in real cases.

Research products

This thesis contains new models and technological products that can be used by researchers. They are:

1. The `ASHEE` model: a well-validated finite volume code based on OpenFOAM® for numerically solve in 1/2/3 dimensions the compressible polydisperse equilibrium–Eulerian model, both in DNS and LES configuration. Since its publication in January 2016, `ASHEE` has been used by other research groups in volcanology and meteorology.

2. A set of standardized numerical benchmarks covering almost entirely the variety of fluid dynamical phenomena behind a volcanic ash plume.

3. The `ASH1D` model: a polydisperse integral plume model based on the top-hat self-similarity assumption. Analytical solutions and conserved quantities are written in particular regimes.

4. The multiphase first-order version of the plume height and neutral buoyancy level in Boussinesq approximation, refining the results by Morton [137], Turner [200].

5. The `ASH0D` model: an analytical approximation of the `ASH1D` model.

6. A coupled fluid-dynamic/electromagnetic model to retrieve vent parameters from infrared videos of volcanic eruptions.

Future directions

For every question it was possible to give a answer, many have opened. In future studies, I would like to exploit the results here described towards the accurate measurement of eruptive vent parameters of a volcanic eruption. In particular, I want to extend the formulation of the coupled fluid dynamic/electromagnetic model to `ASHEE`, in order to produce synthetic infrared images from three-dimensional simulations. Moreover, I plan to deepen the work done with the infrasonic spectrum of volcanic eruptions. Indeed, both the infrared and infrasonic signals are measured in the field by volcanologists, who need theoretical models to interpret data and to retrieve desired quantities. Even the comparison work between 1D and 3D models is far from being completed. Continuing it would offer the possibility to increase the theoretical understanding of volcanic plumes, to better interpreting parameters as the entrainment coefficient and eventually to improve the existing analytical relationships for the plume height and the plume neutral buoyancy level.

To conclude, having in mind hazard mitigation applications, a step forward that I will certainly implement in `ASHEE` is the possibility to add a generic wind field to the atmospheric profile and to add a generic topography able to mimic that of a volcano. Then, to be able to simulate more realistically a volcanic eruption, I want to add to `ASHEE` a set of Lagrangian modeled particles, in order to take into consideration collisions and pyroclastic particles with diameter larger than 1 mm.

Acknowledgements

First and foremost I want to thank my advisors Dr. Tomaso Esposti Ongaro and Luigi Carlo Berselli. They supported me from the very beginning of this Ph.D. thesis, when my research project has been defined in detail. They suggested me the instruments to understand the geophysical and mathematical problem and to face it properly. Their several suggestions made me grow significantly. I would like to thank also Dr. Augusto Neri, whose great experience was of great value for my scientific research in volcanology. I thank Stefano Marmi, as the coordinator of my Ph.D. program at Scuola Normale Superiore. I thank also Maria Vittoria Salvetti for helping me with LES techniques. I am thankful to Sébastien Valade, Andrew J. L. Harris and Tim Druitt for their kind hospitality at the Laboratoire Magmas et Volcans, in Clermont-Ferrand. The two weeks I spent there were very productive, allowing the thesis to make a significant step forward. I am also thankful to Antonio Costa, Yujiro Suzuki and all the research group that participated to the IAVCEI model intercomparison study. Participating to that scientific initiative allows me to compare the models presented in this thesis with the other volcanic plume models used worldwide. It has been a great incentive to improve the quality of the present work. I thank Ivan Spisso, Massimiliano Culpo, Paride Dagna, Luigi Calori and all the SCAI staff at CINECA with Luca Nannipieri, Tomaso Esposti Ongaro and Mattia de' Michieli Vitturi at INGV di Pisa. With their help I was able to use `ASHEE` in parallel on HPC infrastructures. I am thankful to Istituto Nazionale di Geofisica e Vulcanologia (INGV, Sezione di Pisa), Scuola Normale Superiore (SNS) and Università di Pisa (UniPi) for having hosted me and my scientific research. In particular, I am grateful for their financial support through the projects DPC-V1 (founded by the Dipartimento della Protezione Civile, italian civil protection), FP7 Supersites MED-SUV, (founded by the European Commission), MeMoVolc (founded by the European Science Foundation) and 4 ISCRA projects (founded by CINECA).

Bibliography

[1] Bagchi, P. and Balachandar, S. (2002). Steady planar straining flow past a rigid sphere at moderate Reynolds number. *J. Fluid Mech.*, 466:365–407.

[2] Bagheri, G., Bonadonna, C., Manzella, I., Pontelandolfo, P., and Haas, P. (2013). Dedicated vertical wind tunnel for the study of sedimentation of non-spherical particles. *Rev. Sci. Instrum.*, 84(5):054501.

[3] Balachandar, S. (2009). A scaling analysis for point-particle approaches to turbulent multiphase flows. *Int. J. Multiph. Flow*, 35(9):801–810.

[4] Balachandar, S. and Eaton, J. K. (2010). Turbulent Dispersed Multiphase Flow. *Annu. Rev. Fluid Mech.*, 42(1):111–133.

[5] Bardina, J., Ferziger, J. H., and Reynolds, W. C. (1980). Improved subgrid-scale models for large-eddy simulation. In *13th Fluid PlasmaDynamics Conf.*, volume 1, Reston, Virigina. American Institute of Aeronautics and Astronautics.

[6] Bates, D. M. and Watts, D. G. (1988). *Nonlinear regression: iterative estimation and linear approximations*. Wiley Online Library.

[7] Bernardini, M. and Pirozzoli, S. (2009). A general strategy for the optimization of Runge–Kutta schemes for wave propagation phenomena. *J. Comput. Phys.*, 228(11):4182–4199.

[8] Berselli, L. C., Cerminara, M., and Iliescu, T. (2015). Disperse Two-Phase Flows, with Applications to Geophysical Problems. *Pure Appl. Geophys.*, 172(1):181–196.

[9] Berselli, L. C., Fischer, P. F., Iliescu, T., and Özgökmen, T. M. (2011). Horizontal Large Eddy Simulation of Stratified Mixing in a Lock-Exchange System. *J. Sci. Comput.*, 49(1):3–20.

[10] Bisset, D., Hunt, J. C., and Rogers, M. (2002). The turbulent/non-turbulent interface bounding a far wake. *J. Fluid Mech.*, 451:383–410.

[11] Blaisdell, G. A., Mansour, N. N., and Reynolds, W. C. (1991). *Numerical simulation of compressible homogeneous turbulence.* Stanford University, Dept. of Mech. Eng., Thermosciences Div. Rep. TF-50.

[12] Bluth, J. G. S. and Rose, W. I. (2004). Observations of eruptive activity at Santiaguito volcano, Guatemala. *J. Volcanol. Geotherm. Res.*, 136:297–302.

[13] Boffetta, G., Celani, A., De Lillo, F., and Musacchio, S. (2007). The Eulerian description of dilute collisionless suspension. *Europhys. Lett.*, 78(1):14001.

[14] Bombrun, M., Barra, V., and Harris, A. J. (2013). Particle detection and velocity prediction for volcanic eruptions: a preliminary study. In *IAVCEI Gen. Assem.*, Kagoshima, Japan.

[15] Bonadonna, C., Folch, A., Loughlin, S., and Puempel, H. (2012). Future developments in modelling and monitoring of volcanic ash clouds: outcomes from the first IAVCEI-WMO workshop on Ash Dispersal Forecast and Civil Aviation. *Bull. Volcanol.*, 74(1):1–10.

[16] Bonadonna, C., Macedonio, G., and Sparks, R. S. J. (2002). Numerical modelling of tephra fallout associated with dome collapses and Vulcanian explosions: application to hazard assessment on Montserrat. *Geol. Soc. London, Mem.*, 21(1904):517–537.

[17] Bresch, D. and Desjardins, B. (2003). Existence of global weak solutions for a 2D viscous shallow water equations and convergence to the quasi-geostrophic model. *Commun. Math. Phys.*, 238(1-2):211–223.

[18] Bresch, D. and Desjardins, B. (2006). On the construction of approximate solutions for the 2D viscous shallow water model and for compressible Navier-Stokes models. *J. Math. Pures Appl.*, 86(4):362–368.

[19] Bresch, D. and Desjardins, B. (2007). On the existence of global weak solutions to the Navier-Stokes equations for viscous compressible and heat conducting fluids. *J. Math. Pures Appl.*, 87(1):57–90.

[20] Bresch, D., Desjardins, B., and Lin, C.-K. (2003). On some compressible fluid models: Korteweg, lubrication, and shallow water systems. *Commun. Partial Differ. Equations*, 28(3-4):843–868.

[21] Brezis, H. (1983). *Analyse fonctionnelle*. Collection Mathématiques Appliquées pour la Maîtrise. [Collection of Applied Mathematics for the Master's Degree]. Masson, Paris. Théorie et applications. [Theory and applications].

[22] Bürger, R. and Wendland, W. L. (2001). Sedimentation and suspension flows: Historical perspective and some recent developments. *J. Eng. Math.*, 41:101–116.

[23] Bursik, M. I. (2001). Effect of wind on the rise height of volcanic plumes. *Geophys. Res. Lett.*, 28(18):3621–3624.

[24] Bursik, M. I., Sparks, R. S. J., Gilbert, J., and Carey, S. (1992). Sedimentation of tephra by volcanic plumes: I. Theory and its comparison with a study of the Fogo A plinian deposit, Sao Miguel (Azores). *Bull. Volcanol.*, 54(4):329–344.

[25] Cantero, M. I., Balachandar, S., and García, M. H. (2008). An Eulerian–Eulerian model for gravity currents driven by inertial particles. *Int. J. Multiph. Flow*, 34(5):484–501.

[26] Carazzo, G., Kaminski, É., and Tait, S. (2008). On the rise of turbulent plumes: Quantitative effects of variable entrainment for submarine hydrothermal vents, terrestrial and extra terrestrial explosive volcanism. *J. Geophys. Res.*, 113(B9):B09201.

[27] Carcano, S., Bonaventura, L., Esposti Ongaro, T., and Neri, A. (2013). A semi-implicit, second order accurate numerical model for multiphase underexpanded volcanic jets. *Geosci. Model Dev. Discuss.*, 6(1):399–452.

[28] Carcano, S., Esposti Ongaro, T., Bonaventura, L., and Neri, A. (2014). Influence of grain-size distribution on the dynamics of underexpanded volcanic jets. *J. Volcanol. Geotherm. Res.*, 285:60–80.

[29] Cencini, M., Bec, J., Biferale, L., Boffetta, G., Celani, A., Lanotte, A., Musacchio, S., and Toschi, F. (2006). Dynamics and statistics of heavy particles in turbulent flows. *J. Turbul.*, 7:N36. From Duplicate 2 (Dynamics and statistics of heavy particles in turbulent flows - CENCINI, M; BEC, J; BIFERALE, L; BOFFETTA, G; CELANI, A; LANOTTE, A S; MUSACCHIO, S; TOSCHI, F) doi: 10.1080/14685240600675727.

[30] Cerminara, M., Berselli, L. C., Esposti Ongaro, T., and Salvetti, M. V. (2015a). Direct numerical simulation of a compressible multiphase flow through the fast Eulerian approach. In Fröhlich, J., Kuerten, H., Geurts, B. J., and Armenio, V., editors, *Direct Large-Eddy Simul. IX*, volume XX of *ERCOFTAC Series*, page 700. Springer.

[31] Cerminara, M., Esposti Ongaro, T., and Berselli, L. C. (2016a). ASHEE-1.0: a compressible, equilibrium–Eulerian model for volcanic ash plumes. *Geosci. Model Dev.*, 9(2):697–730.

[32] Cerminara, M., Esposti Ongaro, T., and de' Michieli Vitturi, M. (2016b). HPC simulation of volcanic ash plumes and application of OpenFOAM to CFD volcanological problems. In *HPC Enabling OpenFOAM CFD Appl.*, Bologna, Italy. CINECA.

[33] Cerminara, M., Esposti Ongaro, T., and Neri, A. (2016c). Large eddy simulation of gas-particle kinematic decoupling and turbulent entrainment in volcanic plumes. *J. Volcanol. Geotherm. Res.* Accepted.

[34] Cerminara, M., Esposti Ongaro, T., Valade, S., and Harris, A. J. (2015b). Volcanic plume vent conditions retrieved from infrared images: A forward and inverse modeling approach. *J. Volcanol. Geotherm. Res.*, 300:129–147.

[35] Chacón Rebollo, T. and Lewandowski, R. (2013). *Mathematical and numerical foundations of turbulence models*. Birkhäuser, New-York.

[36] Chai, X. and Mahesh, K. (2012). Dynamic k-equation model for large-eddy simulation of compressible flows. *J. Fluid Mech.*, 699(July):385–413.

[37] Clift, R., Grace, J. R., and Weber, M. E. (1978). *Bubbles, drops, and particles*. Academic Press, New York.

[38] Costa, A., Folch, A., and Macedonio, G. (2013). Density-driven transport in the umbrella region of volcanic clouds: Implications for tephra dispersion models. *Geophys. Res. Lett.*, 40(18):4823–4827.

[39] Costa, A., Suzuki, Y. J., Cerminara, M., Devenish, B. J., Esposti Ongaro, T., Herzog, M., Van Eaton, A. R., Denby, L., Bursik, M. I., de' Michieli Vitturi, M., Engwell, S., Neri, A., Barsotti, S., Folch, A., Macedonio, G., Girault, F., Carazzo, G., Tait, S., Kaminski, E., Mastin, L. G., Woodhouse, M. J., Phillips, J. C., Hogg, A. J., Degruyter, W., and Bonadonna, C. (2016). Results of the eruptive column model inter-comparison study. *J. Volcanol. Geotherm. Res.* In press.

[40] Costa, V. (1997). Double diffusive natural convection in a square enclosure with heat and mass diffusive walls. *Int. J. Heat Mass Transf.*, 40(17):4061–4071.

[41] Crowe, C. T., Schwarzkopf, J. D., Sommerfeld, M., and Tsuji, Y. (2011). *Multiphase flows with droplets and particles*. CRC press.

[42] Culpo, M. (2011). Current bottlenecks in the scalability of OpenFOAM on massively parallel clusters. Technical report, PRACE white papers.

[43] da Silva, C. B., Hunt, J. C., Eames, I., and Westerweel, J. (2014). Interfacial Layers Between Regions of Different Turbulence Intensity. *Annu. Rev. Fluid Mech.*, 46(1):567–590.

[44] Dagna, P. (2013). OpenFOAM on BG/Q porting and performance. Technical report, CINECA.

[45] Dartevelle, S., Rose, W. I., Stix, J., Kelfoun, K., and Vallance, J. W. (2004). Numerical modeling of geophysical granular flows: 2. Computer simulations of Plinian clouds and pyroclastic flows and surges. *Geochemistry, Geophys. Geosystems*, 5(8):Q08004.

[46] Dautray, R. and Lions, J.-L. (1988). *Mathematical analysis and numerical methods for science and technology. Vol. 2*. Springer-Verlag, Berlin.

[47] Dautray, R. and Lions, J.-L. (1992). *Mathematical analysis and numerical methods for science and technology. Vol. 5*. Springer-Verlag, Berlin.

[48] de' Michieli Vitturi, M., Neri, A., and Barsotti, S. (2015). PLUME-MoM 1.0: A new integral model of volcanic plumes based on the method of moments. *Geosci. Model Dev.*, 8(8):2447–2463.

[49] Delle Donne, D. and Ripepe, M. (2012). High-frame rate thermal imagery of Strombolian explosions: Implications for explosive and infrasonic source dynamics. *J. Geophys. Res.*, 117(B9).

[50] Deng, Q.-H. and Tang, G.-F. (2002). Numerical visualization of mass and heat transport for conjugate natural convection/heat conduction by streamline and heatline. *Int. J. Heat Mass Transf.*, 45(11):2373–2385.

[51] Devlin, K. J. (2002). *The millennium problems: the seven greatest unsolved mathematical puzzles of our time*. Basic Books.

[52] Di Muro, A., Neri, A., and Rosi, M. (2004). Contemporaneous convective and collapsing eruptive dynamics: The transitional regime of explosive eruptions. *Geophys. Res. Lett.*, 31(10):2001–2004.

[53] DiPerna, R. J. and Lions, P.-L. (1989). Ordinary differential equations, transport theory and Sobolev spaces. *Invent. Math.*, 98(3):511–547.

[54] Dobran, F., Neri, A., and Macedonio, G. (1993). Numerical simulation of collapsing volcanic columns. *J. Geophys. Res.*, 98(B3):4231–4259.

[55] Dongarra, J., Heroux, M. A., and Luszczek, P. (2016). A new metric for ranking high-performance computing systems. *Natl. Sci. Rev.*, 3:1–7.

[56] Donnadieu, F., Freville, P., Hervier, C., Coltelli, M., Scollo, S., Prestifilippo, M., Valade, S., Rivet, S., and Cacault, P. (2016). Near-source Doppler radar monitoring of tephra plumes at Etna. *J. Volcanol. Geotherm. Res.*, 312:26–39.

[57] Druzhinin, O. a. and Elghobashi, S. (1998). Direct numerical simulations of bubble-laden turbulent flows using the two-fluid formulation. *Phys. Fluids*, 10(3):685.

[58] Ducros, F., Comte, P., and Lesieur, M. (1995). Large-eddy simulation of a spatially growing boundary layer over an adiabatic flat plate at low Mach number. *Int. J. heat fluid flow*, 16(5):341–348.

[59] Elghobashi, S. (1991). Particle-laden turbulent flows: direct simulation and closure models. *Appl. Sci. Res.*, 48(3-4):301–314.

[60] Elghobashi, S. (1994). On predicting particle-laden turbulent flows. *Appl. Sci. Res.*, 52(4):309–329.

[61] Erhard, P., Etling, D., Muller, U., Riedel, U., Sreenivasan, K. R., Warnatz, J., Asfaw, K., and Oertel jr, H. (2010). *Prandtl-essentials of fluid mechanics*, volume 158 of *Applied Mathematical Sciences*. Springer, New York, NY.

[62] Erlebacher, G., Hussaini, M. Y., Speziale, C. G., and Zang, T. A. (1990). Toward the large-eddy simulation of compressible turbulent flows. ICASE Report 90-76. Technical report, ICASE/NASA Langley Research Center.

[63] Esposti Ongaro, T. and Cerminara, M. (2015). Non-equilibrium processes in ash-laden volcanic plumes: new insights from 3D multiphase flow simulations. *J. Volcanol. Geotherm. Res.* In press.

[64] Esposti Ongaro, T., Neri, A., Menconi, G., de' Michieli Vitturi, M., Marianelli, P., Cavazzoni, C., Erbacci, G., and Baxter, P. J. (2008). Transient 3D numerical simulations of column collapse and pyroclastic density current scenarios at Vesuvius. *J. Volcanol. Geotherm. Res.*, 178(3):378–396.

[65] Evans, L. C. (1990). *Weak convergence methods for nonlinear partial differential equations*, volume 74 of *CBMS Regional Conference Series in Mathematics*. Published for the Conference Board of the Mathematical Sciences, Washington, DC; by the American Mathematical Society, Providence, RI.

[66] Fanneløp, T. K. and Webber, D. M. (2003). On buoyant plumes rising from area sources in a calm environment. *J. Fluid Mech.*, 497:319–334.

[67] Feireisl, E. (2001). On compactness of solutions to the compressible isentropic Navier-Stokes equations when the density is not square integrable. *Comment. Math. Univ. Carolinae*, 1(1):83–98.

[68] Feireisl, E. (2004). *Dynamics of viscous compressible fluids*, volume 26 of *Oxford Lecture Series in Mathematics and its Applications*. Oxford University Press, Oxford.

[69] Feireisl, E. and Novotny, A. (2009). *Singular limits in thermodynamics of viscous fluids*. Advances in Mathematical Fluid Mechanics. Birkhäuser Verlag, Basel.

[70] Feireisl, E., Novotny, A., and Petzeltová, H. (2001). On the existence of globally defined weak solutions to the Navier-Stokes equations. *J. Math. Fluid Mech.*, 3(4):358–392.

[71] Ferry, J. and Balachandar, S. (2001). A fast Eulerian method for disperse two-phase flow. *Int. J. Multiph. flow*, 27:1199–1226.

[72] Ferry, J. and Balachandar, S. (2002). Equilibrium expansion for the Eulerian velocity of small particles. *Powder Technol.*, 125(2-3):131–139.

[73] Ferry, J. and Balachandar, S. (2005). Equilibrium Eulerian approach for predicting the thermal field of a dispersion of small particles. *Int. J. Heat Mass Transf.*, 48(3):681–689.

[74] Ferry, J., Rani, S. L., and Balachandar, S. (2003). A locally implicit improvement of the equilibrium Eulerian method. *Int. J. Multiph. Flow*, 29(6):869–891.

[75] Ferziger, J. H. and Perić, M. (1996). *Computational methods for fluid dynamics*, volume 3. Springer Berlin.

[76] Fevrier, P., Simonin, O., and Squires, K. D. (2005). Partitioning of particle velocities in gas–solid turbulent flows into a continuous field and a spatially uncorrelated random distribution: theoretical formalism and numerical study. *J. Fluid Mech.*, 533:1–46.

[77] Fisher, R. V. and Schmincke, H.-U. (2012). *Pyroclastic rocks*. Springer Science & Business Media.

[78] Folch, A., Costa, A., Durant, A. J., and Macedonio, G. (2010). A model for wet aggregation of ash particles in volcanic plumes and clouds: 2. Model application. *J. Geophys. Res.*, 115(B9):B09202.

[79] Fureby, C. (1996). On subgrid scale modeling in large eddy simulations of compressible fluid flow. *Phys. Fluids*, 8(5):1301.

[80] Garnier, E., Adams, N., and Sagaut, P. (2009). *Large Eddy Simulation for Compressible Flows*. Scientific Computation. Springer Netherlands, Dordrecht.

[81] Garnier, E., Mossi, M., Sagaut, P., Comte, P., and Deville, M. (1999). On the Use of Shock-Capturing Schemes for Large-Eddy Simulation. *J. Comput. Phys.*, 153(2):273–311.

[82] Garnier, E., Sagaut, P., and Deville, M. (2002). Large Eddy simulation of shock/homogeneous turbulence interaction. *Comput. Fluids*, 31(2):245–268.

[83] George, W. K., Alpert, R. L., and Tamanini, F. (1977). Turbulence measurements in an axisymmetric buoyant plume. *Int. J. Heat Mass Transf.*, 20(11):1145–1154.

[84] Germano, M., Piomelli, U., Moin, P., and Cabot, W. H. (1991). A dynamic subgrid-scale eddy viscosity model. *Phys. Fluids A*, 3(7):1760–1765.

[85] Ghosal, S., Lund, T. S., Moin, P., and Akselvoll, K. (1995). A dynamic localization model for large-eddy simulation of turbulent flows. *J. Fluid Mech.*, 286:229–255.

[86] Gidaspow, D. (1994). *Multiphase flow and fluidization: continuum and kinetic theory descriptions*. Academic press.

[87] Girault, F., Carazzo, G., Tait, S., Ferrucci, F., and Kaminski, É. (2014). The effect of total grain-size distribution on the dynamics of turbulent volcanic plumes. *Earth Planet. Sci. Lett.*, 394:124–134.

[88] Glaze, L. S. and Baloga, S. M. (1996). Sensitivity of buoyant plume heights to ambient atmospheric conditions: implications for volcanic eruption columns. *J. Geophys. Res.*, 101(D1):1529–1540.

[89] Gonnermann, H. M. and Manga, M. (2007). The Fluid Mechanics Inside a Volcano. *Annu. Rev. Fluid Mech.*, 39(1):321–356.

[90] Graf, H.-F., Herzog, M., Oberhuber, J. M., and Textor, C. (1999). Effect of environmental conditions on volcanic plume rise. *J. Geophys. Res.*, 104(D20):24309.

[91] Graham, T. (1846). On the Motion of Gases. *Philos. Trans.*, 136:573–631.

[92] Greenshields, C. J., Weller, H. G., Gasparini, L., and Reese, J. M. (2010). Implementation of semi-discrete, non-staggered central schemes in a colocated, polyhedral, finite volume framework, for high-speed viscous flows. *Int. J. Numer. Methods Fluids*, 63(1):1–21.

[93] Hänel, G. and Dlugi, R. (1977). Approximation for the absorption coefficient of airborne atmospheric aerosol particles in terms of measurable bulk properties. *Tellus*, 29(1):75–82.

[94] Harris, A. J. (2013). *Thermal Remote Sensing of Active Volcanoes*. Cambridge University Press.

[95] Harris, A. J., Flynn, L. P., Matias, O., and Rose, W. I. (2002). The thermal stealth flows of Santiaguito dome, Guatemala: Implications for the cooling and emplacement of dacitic block-lava flows. *Geol. Soc. Am. Bull.*, 114(5):533–546.

[96] Harris, A. J., Flynn, L. P., Matias, O., Rose, W. I., and Cornejo, J. (2004). The evolution of an active silicic lava flow field: an ETM+ perspective. *J. Volcanol. Geotherm. Res.*, 135(1):147–168.

[97] Harris, A. J. and Ripepe, M. (2007). Temperature and dynamics of degassing at Stromboli. *J. Geophys. Res.*, 112(B3):B03205.

[98] Harris, A. J., Ripepe, M., and Hughes, E. A. (2012). Detailed analysis of particle launch velocities, size distributions and gas densities during normal explosions at Stromboli. *J. Volcanol. Geotherm. Res.*, 231-232:109–131.

[99] Hashimoto, A., Shimbori, T., and Fukui, K. (2012). Tephra Fall Simulation for the Eruptions at Mt. Shinmoe-dake during 26-27 January 2011 with JMANHM. *SOLA*, 8(0):37–40.

[100] Herzog, M., Graf, H.-F., Textor, C., and Oberhuber, J. M. (1998). The effect of phase changes of water on the development of volcanic plumes. *J. Volcanol. Geotherm. Res.*, 87(1-4):55–74.

[101] Hoff, D. (1995). Strong convergence to global solutions for multidimensional flows of compressible, viscous fluids with polytropic equations of state and discontinuous initial data. *Arch. Ration. Mech. Anal.*, 132(1):1–14.

[102] Holasek, R. E., Self, S., and Woods, A. W. (1996). Satellite observations and interpretation of the 1991 Mount Pinatubo eruption plumes. *J. Geophys. Res.*, 101(B12):27635–27655.

[103] Honein, A. E. and Moin, P. (2004). Higher entropy conservation and numerical stability of compressible turbulence simulations. *J. Comput. Phys.*, 201(2):531–545.

[104] Ishimine, Y. (2006). Sensitivity of the dynamics of volcanic eruption columns to their shape. *Bull. Volcanol.*, 68(6):516–537.

[105] Issa, R. I. (1986). Solution of the implicitly discretised fluid flow equations by operator-splitting. *J. Comput. Phys.*, 62(1):40–65.

[106] Jasak, H. (1996). *Error Analysis and Estimation for the Finite Volume Method with Applications to Fluid Flows*. Phd thesis, Imperial College London.

[107] Jiang, S. and Zhang, P. (2001). On spherically symmetric solutions of the compressible isentropic Navier-Stokes equations. *Commun. Math. Phys.*, 215(3):559–581.

[108] Johnson, J. B. and Ripepe, M. (2011). Volcano infrasound: A review. *J. Volcanol. Geotherm. Res.*, 206(3-4):61–69.

[109] Jüngel, A. (2010). Global weak solutions to compressible Navier-Stokes equations for quantum fluids. *SIAM J. Math. Anal.*, 42(3):1025–1045.

[110] Kaminski, É. and Jaupart, C. (1998). The size distribution of pyroclasts and the fragmentation sequence in explosive volcanic eruptions. *J. Geophys. Res.*, 103(B12):29759–29779.

[111] Kaminski, É., Tait, S., and Carazzo, G. (2005). Turbulent entrainment in jets with arbitrary buoyancy. *J. Fluid Mech.*, 526:361–376.

[112] Kay, D. A., Gresho, P. M., Griffiths, D. F., and Silvester, D. J. (2010). Adaptive time-stepping for incompressible flow part ii: Navier-stokes equations. *SIAM J. Sci. Comput.*, 32(1):111–128.

[113] Kueppers, U., Perugini, D., and Dingwell, D. B. (2006). "Explosive energy" during volcanic eruptions from fractal analysis of pyroclasts. *Earth Planet. Sci. Lett.*, 248(3-4):800–807.

[114] Kurganov, A., Noelle, S., and Petrova, G. (2001). Semidiscrete central-upwind schemes for hyperbolic conservation laws and Hamilton–Jacobi equations. *SIAM J. Sci. Comput.*, 23(3):707–740.

[115] Landau, L. and Lifshitz, E. (1959). *Fluid Mechanics*. Pergamon Press.

[116] Lesieur, M., Métais, O., and Comte, P. (2005). *Large-Eddy Simulations of Turbulence*, volume 1. Cambridge University Press.

[117] Li, J. and Xin, Z. (2015). Global Existence of of Weak Solutions to the Barotropic Compressible Navier-Stokes Flows with Degenerate Viscosities. Technical Report 1504.06826v1, ArXiv.

[118] Liao, W., Peng, Y., and Luo, L.-S. (2009). Gas-kinetic schemes for direct numerical simulations of compressible homogeneous turbulence. *Phys. Rev. E*, 80(4):046702.

[119] Lilly, D. K. (1992). A proposed modification of the Germano subgrid-scale closure method. *Phys. Fluids A*, 4(3):633.

[120] Lions, P.-L. (1996). *Mathematical Topics in Fluid Mechanics: Volume 1: Incompressible Models*. Oxford University Press, New York, USA, clarendon edition.

[121] Lions, P.-L. (1998). *Mathematical topics in fluid mechanics. Vol. 2*, volume 10 of *Oxford Lecture Series in Mathematics and its Applications*. The Clarendon Press, Oxford University Press, New York. Compressible models, Oxford Science Publications.

[122] List, E. J. (1982). Turbulent Jets and Plumes. *Annu. Rev. Fluid Mech.*, 14(1):189–212.

[123] Lodato, G., Vervisch, L., and Domingo, P. (2009). A compressible wall-adapting similarity mixed model for large-eddy simulation of the impinging round jet. *Phys. Fluids*, 21(3):035102.

[124] Lopez, T., Fee, D., Prata, A. J., and Dehn, J. (2013). Characterization and interpretation of volcanic activity at Karymsky Volcano, Kamchatka, Russia, using observations of infrasound, volcanic emissions, and thermal imagery. *Geochemistry, Geophys. Geosystems*, 14(12):5106–5127.

[125] Lorenz, E. N. (1955). Available Potential Energy and the Maintenance of the General Circulation. *Tellus*, 7(2):157–167.

[126] Magnaudet, J. and Eames, I. (2000). The motion of high-Reynolds-number bubbles in inhomogeneous flows. *Annu. Rev. Fluid Mech.*, 32(1):659–708.

[127] Marble, F. E. (1970). Dynamics of Dusty Gases. *Annu. Rev. Fluid Mech.*, 2(1):397–446.

[128] Mastin, L. G., Guffanti, M., Servranckx, R., Webley, P., Barsotti, S., Dean, K., Durant, A. J., Ewert, J., Neri, A., Rose, W. I., Schneider, D. J., Siebert, L., Stunder, B., Swanson, G., Tupper, A., Volentik, A., and Waythomas, C. F. (2009). A multidisciplinary effort to assign realistic source parameters to models of volcanic ash-cloud transport and dispersion during eruptions. *J. Volcanol. Geotherm. Res.*, 186(1-2):10–21.

[129] Mathew, J. and Basu, A. J. (2002). Some characteristics of entrainment at a cylindrical turbulence boundary. *Phys. Fluids*, 14(7):2065.

[130] Matoza, R. S., Fee, D., Garcés, M. A., Seiner, J. M., Ramón, P. A., and Hedlin, M. A. H. (2009). Infrasonic jet noise from volcanic eruptions. *Geophys. Res. Lett.*, 36(8):L08303.

[131] Maxey, M. R. (1987). The gravitational settling of aerosol particles in homogeneous turbulence and random flow fields. *J. Fluid Mech.*, 174:441.

[132] Mellet, A. and Vasseur, A. F. (2007). On the barotropic compressible Navier-Stokes equations. *Commun. Partial Differ. Equations*, 32(1-3):431–452.

[133] Menow, S. and Rizk, M. (1996). Large-Eddy Simulations of Forced Three-Dimensional Impinging Jets. *Int. J. Comut. Fluid Dyn.*, 7(3):275–289.

[134] Mie, G. (1908). Pioneering mathematical description of scattering by spheres. *Ann. Phys.*, 25:337.

[135] Modest, M. F. (2003). *Radiative heat transfer*. Academic press.

[136] Moin, P., Squires, K. D., Cabot, W. H., and Lee, S. (1991). A dynamic subgrid-scale model for compressible turbulence and scalar transport. *Phys. Fluids A*, 3(11):2746.

[137] Morton, B. R. (1959). Forced plumes. *J. Fluid Mech.*, 5(01):151–163.

[138] Morton, B. R., Taylor, G., and Turner, J. S. (1956). Turbulent Gravitational Convection from Maintained and Instantaneous Sources. *Proc. R. Soc. A Math. Phys. Eng. Sci.*, 234(1196):1–23.

[139] Nagle, R., Saff, E., and Snider, A. (1989). *Fundamentals of Differential Equations*. Addison-Wesley, Pearson, 8th edition.

[140] Neri, A. and Dobran, F. (1994). Influence of eruption parameters on the thermofluid dynamics of collapsing volcanic columns. *J. Geophys. Res.*, 99(B6):11833–11857.

[141] Neri, A., Esposti Ongaro, T., Macedonio, G., and Gidaspow, D. (2003). Multiparticle simulation of collapsing volcanic columns and pyroclastic flow. *J. Geophys. Res.*, 108(B4):2202.

[142] Nicoud, F. and Ducros, F. (1999). Subgrid-scale stress modelling based on the square of the velocity gradient tensor. *Flow, Turbul. Combust.*, 62(3):183–200.

[143] Oberhuber, J. M., Herzog, M., Graf, H.-F., and Schwanke, K. (1998). Volcanic plume simulation on large scales. *J. Volcanol. Geotherm. Res.*, 87(1-4):29–53.

[144] Orsucci, S. (2014). *Multiphase flow modeling and numerical simulation of pyroclastic density currents*. PhD thesis, Università di Pisa.

[145] Özgökmen, T. M., Iliescu, T., Fischer, P. F., Srinivasan, A., and Duan, J. (2007). Large eddy simulation of stratified mixing in two-dimensional dam-break problem in a rectangular enclosed domain. *Ocean Model.*, 16(1-2):106–140.

[146] Papale, P., Moretti, R., and Barbato, D. (2006). The compositional dependence of the saturation surface of H2O+ CO2 fluids in silicate melts. *Chem. Geol.*, 229(1):78–95.

[147] Papanicolaou, P. N. and List, E. J. (1988). Investigations of round vertical turbulent buoyant jets. *J. Fluid Mech.*, 195:341–391.

[148] Patankar, S. V. (1980). *Numerical heat transfer and fluid flow*. Hemisphere Publishing Corporation, New York, USA.

[149] Patrick, M., Harris, A. J., Ripepe, M., Dehn, J., Rothery, D. A., and Calvari, S. (2007). Strombolian explosive styles and source conditions: insights from thermal (FLIR) video. *Bull. Volcanol.*, 69(7):769–784.

[150] Pirozzoli, S. and Grasso, F. (2004). Direct numerical simulations of isotropic compressible turbulence: Influence of compressibility on dynamics and structures. *Phys. Fluids*, 16(12):4386.

[151] Plourde, F., Pham, M. V., Kim, S. D., and Balachandar, S. (2008). Direct numerical simulations of a rapidly expanding thermal plume: structure and entrainment interaction. *J. Fluid Mech.*, 604:99–123.

[152] Pope, S. B. (2000). *Turbulent flows*. Cambridge university press.

[153] Prata, A. J. (1989). Infrared radiative transfer calculations for volcanic ash clouds. *Geophys. Res. Lett.*, 16(11):1293–1296.

[154] Prata, A. J. and Bernardo, C. (2009). Retrieval of volcanic ash particle size, mass and optical depth from a ground-based thermal infrared camera. *J. Volcanol. Geotherm. Res.*, 186(1):91–107.

[155] Prata, A. J. and Bernardo, C. (2014). Retrieval of sulphur dioxide from a ground-based thermal infrared imaging camera. *Atmos. Meas. Tech. Discuss.*, 7(2):1153–1211.

[156] Pyle, D. M. (1989). The thickness, volume and grainsize of tephra fall deposits. *Bull. Volcanol.*, 51(1):1–15.

[157] Ramsey, M. S. and Harris, A. J. (2013). Volcanology 2020: How will thermal remote sensing of volcanic surface activity evolve over the next decade? *J. Volcanol. Geotherm. Res.*, 249:217–233.

[158] Rani, S. L. and Balachandar, S. (2003). Evaluation of the equilibrium Eulerian approach for the evolution of particle concentration in isotropic turbulence. *Int. J. Multiph. Flow*, 29(12):1793–1816.

[159] Reagan, J. A., McCormick, M. P., and SPinhirne, J. D. (1989). Lidar sensing of aerosols and clouds in the troposphere and stratosphere.

[160] Ricou, F. P. and Spalding, D. B. (1961). Measurements of entrainment by axisymmetrical turbulent jets. *J. Fluid Mech.*, 11(01):21.

[161] Rose, W. I. (1972). Notes on the 1902 eruption of Santa Maria volcano, Guatemala. *Bull. Volcanol.*, 36(1):29–45.

[162] Rose, W. I. (1987). Volcanic activity at Santiaguito volcano, 1976–1984. *Geol. Soc. Am. Spec. Pap.*, 212:17–28.

[163] Rose, W. I., Chuan, R., Cadle, R., and Woods, D. (1980). Small particles in volcanic eruption clouds. *Am. J. Sci.*, 280:671–696.

[164] Rothman, L. S., Gordon, I. E., Babikov, Y., Barbe, A., Benner, D. C., Bernath, P. F., Birk, M., Bizzocchi, L., Boudon, V., Brown, L. R., Campargue, A., Chance, K., Cohen, E. A., Coudert, L. H., Devi, V. M., Drouin, B. J., Fayt, A., Flaud, J.-M., Gamache, R. R., Harrison, J. J., Hartmann, J.-M., Hill, C., Hodges, J. T., Jacquemart, D., Jolly, A., Lamouroux, J., Roy, R. J. L., Li, G., Long, D. A., Lyulin, O. M., Mackie, C. J., Massie, S. T., Mikhailenko, S., Müller, H. S. P., Naumenko, O. V., Nikitin, A. V., Orphal, J., Perevalov, V., Perrin, A., Polovtseva, E. R., Richard, C., Smith, M. A. H., Starikova, E., Sung, K., Tashkun, S., Tennyson, J., Toon, G. C., Tyuterev, V., and Wagner, G. (2013). The HITRAN2012 molecular spectroscopic database. *J. Quant. Spectrosc. Radiat. Transf.*, 130(0):4–50. HITRAN2012 special issue.

[165] Sahetapy-Engel, S. T. and Harris, A. J. (2009a). Thermal-image-derived dynamics of vertical ash plumes at Santiaguito volcano, Guatemala. *Bull. Volcanol.*, 71(7):827–830.

[166] Sahetapy-Engel, S. T. and Harris, A. J. (2009b). Thermal structure and heat loss at the summit crater of an active lava dome. *Bull. Volcanol.*, 71(1):15–28.

[167] Sahetapy-Engel, S. T., Harris, A. J., and Marchetti, E. (2008). Thermal, seismic and infrasound observations of persistent explosive activity and conduit dynamics at Santiaguito lava dome, Guatemala. *J. Volcanol. Geotherm. Res.*, 173(1-2):1–14.

[168] Saito, T. (2002). Numerical Analysis of Dusty-Gas Flows. *J. Comput. Phys.*, 176(1):129–144.

[169] Sawyer, G. M. and Burton, M. R. (2006). Effects of a volcanic plume on thermal imaging data. *Geophys. Res. Lett.*, 33(14):L14311.

[170] Scase, M. M. (2009). Evolution of volcanic eruption columns. *J. Geophys. Res.*, 114(F4):F04003.

[171] Scharff, L., Ziemen, F., Hort, M., Gerst, A., and Johnson, J. B. (2012). A detailed view into the eruption clouds of Santiaguito volcano, Guatemala, using Doppler radar. *J. Geophys. Res.*, 117(B4):B04201.

[172] Scollo, S., Boselli, A., Coltelli, M., Leto, G., Pisani, G., Spinelli, N., and Wang, X. (2012). Monitoring Etna volcanic plumes using a scanning LiDAR. *Bull. Volcanol.*, 74(10):2383–2395.

[173] Scott, J. A. J. (2012). *Origin and evlution of the Santiaguito lava dome complex, Guatemala*. Phd thesis, Department of Earth Sciences, University of Oxford & St Anne's College.

[174] Serre, D. (1991). Variations de grande amplitude pour la densité d'un fluide visqueux compressible. *Phys. D Nonlinear Phenom.*, 48(1):113–128.

[175] Shabbir, A. and George, W. K. (1994). Experiments on a round turbulent buoyant plume. *J. Fluid Mech.*, 275:1–32.

[176] Shampine, L. F. and Corless, R. M. (2000). Initial value problems for ODEs in problem solving environments. *J. Comput. Appl. Math.*, 125(1):31–40.

[177] Shotorban, B. and Balachandar, S. (2006). Particle concentration in homogeneous shear turbulence simulated via Lagrangian and equilibrium Eulerian approaches. *Phys. Fluids*, 18(6):65105.

[178] Shotorban, B. and Balachandar, S. (2007). A Eulerian model for large-eddy simulation of concentration of particles with small Stokes numbers. *Phys. Fluids*, 19(11):118107.

[179] Sigurdsson, H., Houghton, B., Rymer, H., Stix, J., and McNutt, S. (1999). *Encyclopedia of Volcanoes*. Academic Press.

[180] Smagorinsky, J. (1963). General circulation experiments with the primitive equations: I. The basic experiment. *Mon. Weather Rev.*

[181] Sod, G. (1978). A Survey of Several of Nonlinear Finite Difference Methods Hyperbolic Conservation Laws. *J. Comput. Phys.*, 27:1–31.

[182] Spampinato, L., Calvari, S., Oppenheimer, C., and Boschi, E. (2011). Volcano surveillance using infrared cameras. *Earth-Science Rev.*, 106(1):63–91.

[183] Sparks, R. S. J. (1978). The dynamics of bubble formation and growth in magmas: A review and analysis. *J. Volcanol. Geotherm. Res.*, 3(1-2):1–37.

[184] Sparks, R. S. J., Bursik, M. I., Carey, S., Gilbert, J., Glaze, L. S., Sigurdsson, H., and Woods, A. W. (1997). *Volcanic Plumes*. John Wiley & Sons, Inc.

[185] Spyropoulos, E. T. and Blaisdell, G. A. (1996). Evaluation of the dynamic model for simulations of compressible decaying isotropic turbulence. *AIAA J.*, 34(5):990–998.

[186] Squires, K. D. and Eaton, J. K. (1991). Measurements of particle dispersion obtained from direct numerical simulations of isotropic turbulence. *J. Fluid Mech.*, 226(1961):1–35.

[187] Stohl, A., Prata, A. J., Elbern, H., Scollo, S., and Varghese, S. (2010). Description of Some European Ash Transport Models. In Zehner, C., editor, *Monit. Volcan. Ash from Space. Proc. ESA-EUMETSAT Work. 14 April to 23 May 2010 Erupt. Eyjafjoll volcano, South Icel.*, number STM-280 in ESA-Pubblication.

[188] Suzuki, Y. J., Costa, A., Cerminara, M., Esposti Ongaro, T., Herzog, M., Van Eaton, A. R., and Denby, L. (2016). Inter-comparison of three-dimensional models of volcanic plumes. *J. Volcanol. Geotherm. Res.* Accepted.

[189] Suzuki, Y. J. and Koyaguchi, T. (2010). Numerical determination of the efficiency of entrainment in volcanic eruption columns. *Geophys. Res. Lett.*, 37(5):L05302.

[190] Suzuki, Y. J. and Koyaguchi, T. (2012). 3-D numerical simulations of eruption column collapse: Effects of vent size on pressure-balanced jet/plumes. *J. Volcanol. Geotherm. Res.*, 221-222:1–13.

[191] Suzuki, Y. J. and Koyaguchi, T. (2013). 3D numerical simulation of volcanic eruption clouds during the 2011 Shinmoe-dake eruptions. *Earth, Planets Sp.*, 65(6):581–589.

[192] Suzuki, Y. J., Koyaguchi, T., Ogawa, M., and Hachisu, I. (2005). A numerical study of turbulent mixing in eruption clouds using a three-dimensional fluid dynamics model. *J. Geophys. Res.*, 110(B8):B08201.

[193] Tam, C. K. W., Golebiowski, M., and Seiner, J. M. (1996). On the two components of turbulent mixing noise from supersonic jets. *AIAA J.*, 96-1716:18.

[194] Taveira, R. M. R., da Silva, C. B., and Pereira, J. C. F. (2011). The Dynamics of Turbulent Scalar Mixing near the Edge of a Shear Layer. *J. Phys. Conf. Ser.*, 318:052049.

[195] Taylor, G. (1945). Dynamics of a mass of hot gas rising in air. *US At. Energy Comm. MDDC, 919, LADC 276*.

[196] Temam, R. (1995). *Navier-Stokes equations and nonlinear functional analysis*, volume 66 of *CBMS-NSF Regional Conference Series in Applied Mathematics*. Society for Industrial and Applied Mathematics (SIAM), Philadelphia, PA, second edition.

[197] Townsend, A. A. (1966). The mechanism of entrainment in free turbulent flows. *J. Fluid Mech.*, 26(689).

[198] Tseng, Y.-h. and Ferziger, J. H. (2001). Mixing and available potential energy in stratified flows. *Phys. Fluids*, 13(5):1281.

[199] Tupper, A., Kinoshita, K., Kanagaki, C., Iino, N., and Kamada, Y. (2003). Observations of volcanic cloud heights and ash-atmosphere interactions. In *WMO/ICAO Third Int. Work. Volcan. Ash, Toulouse, Fr. Sept.*, volume 29.

[200] Turner, J. S. (1979). *Buoyancy effects in fluids*. Cambridge University Press.

[201] Valade, S., Harris, A. J., and Cerminara, M. (2014). Plume Ascent Tracker: Interactive Matlab software for analysis of ascending plumes in image data. *Comput. Geosci.*, 66:132–144.

[202] Valentine, G. A. and Wohletz, K. H. (1989). Numerical models of Plinian eruption columns and pyroclastic flows. *J. Geophys. Res.*, 94(B2):1867–1887.

[203] Van Eaton, A. R., Mastin, L. G., Herzog, M., Schwaiger, H. F., Schneider, D. J., Wallace, K. L., and Clarke, A. B. (2015). Hail formation triggers rapid ash aggregation in volcanic plumes. *Nat. Commun.*, 6:7860.

[204] Van Leer, B. (1997). Towards the ultimate conservative difference scheme. *J. Comput. Phys.*, 135(2):229–248.

[205] Vasseur, A. F. and Yu, C. (2015). Existence of Global Weak Solutions for 3D Degenerate Compressible Navier-Stokes Equations. Technical Report 1501.06803v3, ArXiv. to appear in, Inventiones Mathematicae.

[206] Vasseur, A. F. and Yu, C. (2016). Global weak solutions to the compressible quantum Navier-Stokes equations with damping. *SIAM J. Math. Anal.*, 48(2):1489–1511.

[207] Vauigant, V. A. and Kazhikhov, A. V. (1995). On the existence of global solutions of two-dimensional Navier-Stokes equations of a compressible viscous fluid. *Sib. Mat. Zh.*, 36(6):1283–1316.

[208] Veitch, G. and Woods, A. W. (2002). Particle recycling in volcanic plumes. *Bull. Volcanol.*, 64(1):31–39.

[209] Vetter, J. S. (2013). *Contemporary high performance computing: from Petascale toward exascale*. CRC Press.

[210] Vreman, B. (1995). *Direct and large-eddy simulation of the compressible turbulent mixing layer*. PhD thesis, University of Twente.

[211] Vreman, B., Geurts, B. J., and Kuerten, H. (1995). A priori tests of large eddy simulation of the compressible plane mixing layer. *J. Eng. Math.*, 29(4):299–327.

[212] Vuorinen, V., Keskinen, J. P., Duwig, C., and Boersma, B. J. (2014). On the implementation of low-dissipative Runge-Kutta projection methods for time dependent flows using OpenFOAM® . *Comput. Fluids*, 93:153–163.

[213] Walker, G. P. L. (1971). Grain-size characteristics of pyroclastic deposits. *J. Geol.*, 79:696–714.

[214] Wang, L.-P. and Maxey, M. R. (1993). Settling velocity and concentration distribution of heavy particles in homogeneous isotropic turbulence. *J. Fluid Mech.*, 256(-1):27.

[215] Webb, E. B., Varley, N. R., Pyle, D. M., and Mather, T. A. (2014). Thermal imaging and analysis of short-lived Vulcanian explosions at Volcán de Colima, Mexico. *J. Volcanol. Geotherm. Res.*, 278:132–145.

[216] Westerweel, J., Fukushima, C., Pedersen, J. M., and Hunt, J. C. (2005). Mechanics of the turbulent-nonturbulent interface of a jet. *Phys. Rev. Lett.*, 95(17):1–4.

[217] Wilson, L. (1976). Explosive Volcanic Eruptions-III. Plinian Eruption Columns. *Geophys. J. R. Astron. Soc.*, 45(3):543–556.

[218] Wilson, L. and Self, S. (1980). Volcanic explosion clouds: Density, temperature, and particle content estimates from cloud motion. *J. Geophys. Res. Solid Earth*, 85(B5):2567–2572.

[219] Wilson, L., Sparks, R. S. J., Huang, T., and Watkins, N. D. (1978). The control of volcanic column heights by eruption energetics and dynamics. *J. Geophys. Res.*, 83(B4):1829.

[220] Winters, K. B. and Barkan, R. (2013). Available potential energy density for Boussinesq fluid flow. *J. Fluid Mech.*, 714:476–488.

[221] Winters, K. B., Lombard, P. N., Riley, J. J., and D'Asaro, E. A. (1995). Available potential energy and mixing in density-stratified fluids. *J. Fluid Mech.*, 289:115.

[222] Woodhouse, M. J., Hogg, A. J., Phillips, J. C., and Rougier, J. C. (2015). Uncertainty analysis of a model of wind-blown volcanic plumes. *Bull. Volcanol.*, 77(10):83.

[223] Woodhouse, M. J., Hogg, A. J., Phillips, J. C., and Sparks, R. S. J. (2013). Interaction between volcanic plumes and wind during the 2010 Eyjafjallajökull eruption, Iceland. *J. Geophys. Res.*, 118(1):92–109.

[224] Woodhouse, M. J., Phillips, J. C., and Hogg, A. J. (2016). Unsteady turbulent buoyant plumes. *J. Fluid Mech.*, 794:595–638.

[225] Woods, A. W. (1988). The fluid dynamics and thermodynamics of eruption columns. *Bull. Volcanol.*, 50(3):169–193.

[226] Woods, A. W. (1993). Moist convection and the injection of volcanic ash into the atmosphere. *J. Geophys. Res.*, 98(B10):17627.

[227] Woods, A. W. (2010). Turbulent Plumes in Nature. *Annu. Rev. Fluid Mech.*, 42(1):391–412.

[228] Woods, A. W. and Bower, S. M. (1995). The decompression of volcanic jets in a crater during explosive volcanic eruptions. *Earth Planet. Sci. Lett.*, 131(3-4):189–205.

[229] Woods, A. W. and Bursik, M. I. (1991). Particle fallout, thermal disequilibrium and volcanic plumes. *Bull. Volcanol.*, 53(7):559–570.

[230] Yoshizawa, A. (1986). Statistical theory for compressible turbulent shear flows, with the application to subgrid modeling. *Phys. Fluids*, 29(7):2152.

[231] Yoshizawa, A. (1993). Bridging between eddy-viscosity-type and second-order turbulence models through a two-scale turbulence theory. *Phys. Rev. E*, 48(1):273–281.

[232] Yüceil, K. B. and Ötügen, M. V. (2002). Scaling parameters for underexpanded supersonic jets. *Phys. Fluids*, 14(12):4206.

[233] Zhou, X., Luo, K. H., and Williams, J. J. R. (2001). Large-eddy simulation of a turbulent forced plume. *Eur. J. Mech. B/Fluids*, 20(2):233–254.

Web sites

[CIN] *CINECA, Fermi Blue Gene/Q.* http://www.hpc.cineca.it/content/ibm-fermi-user-guide.

[HIT] *Decaying homogeneous and isotropic turbulence.* http://youtu.be/UeHEXbxd8_o.

[ING] Istituto Nazionale di Geofisica e Vulcanologia, Sezione di Pisa. http://www.pi.ingv.it.

[LEX] *Numerical simulation of the lock exchange problem.* https://youtu.be/fMCPo-pYukw.

[MCW] Personal web site. https://sites.google.com/site/matteocerminara/.

[NIS] *NIST Chemistry WebBook.* http://webbook.nist.gov/chemistry/fluid/.

[SIV] *Smithsonian Institution, Global Volcanism Program.* http://http://volcano.si.edu.

[The] *ThermExcel.* http://www.thermexcel.com/english/tables/.

[TPL] *Numerical simulation of the turbulent forced plume.* https://youtu.be/zBIYteLVmag, https://youtu.be/bvCux7d5uZQ.

[WK1] *List of large volcanic eruptions of the 20th century.* http://en.wikipedia.org/wiki/List_of_large_volcanic_eruptions_of_the_20th_century.